

**Proceedings of the XVII International  
Baldin Seminar on High Energy Physics Problems**

**RELATIVISTIC  
NUCLEAR PHYSICS  
AND QUANTUM  
CHROMODYNAMICS  
VOL. II**



**Editors: A. N. Sissakian, V. V. Burov, A. I. Malakhov**

Dubna 2004

710213

Joint Institute for Nuclear Research

# Relativistic Nuclear Physics and Quantum Chromodynamics

*Proceedings of the XVII International Baldin  
Seminar on High Energy Physics Problems*

Dubna, September 27 – October 2, 2004

## ISHEPP XVII

Volume II

Editors: A. N. Sissakian  
V. V. Burov  
A. I. Malakhov



УДК 539.17(042), 539.12.01(063)  
ББК [22.382+22.315]я431  
R41



Editors: *A. N. Sissakian, V. V. Burov, A. I. Malakhov*

Preparing proceedings to print: *S. G. Bondarenko, E. B. Plekhanov*

Photos by *Yu. A. Tumanov, E. B. Plekhanov, I. G. Zarubina*

The contributions are reproduced directly from the originals  
presented by the Organizing Committee.

**Relativistic Nuclear Physics and Quantum Chromodynamics:**  
R41 Proc. of the XVII Intern. Baldin Seminar on High Energy Physics Problems (Dubna, September 27 – October 2, 2004). — Dubna: JINR, 2005. — V. 2. — 377 p., photos.

ISBN 5-9530-0090-1

The Proceedings present the invited talks given by leading scientists in the field of relativistic nuclear physics at the traditional XVII International Baldin Seminar on High Energy Physics Problems «Relativistic Nuclear Physics and Quantum Chromodynamics» (Dubna, September 27 – October 2, 2004).

**Релятивистская ядерная физика и квантовая хромодинамика:**  
Тр. XVII Междунар. Балдинского семинара по проблемам физики высоких энергий (Дубна, 27 сентября – 2 октября 2004 г.). — Дубна: ОИЯИ, 2005. — Т. 2. — 377 с., фото.

ISBN 5-9530-0090-1

В сборнике представлены доклады, которые были сделаны ведущими специалистами в области релятивистской ядерной физики на традиционном XVII Международном Балдинском семинаре по проблемам физики высоких энергий «Релятивистская ядерная физика и квантовая хромодинамика» (Дубна, 27 сентября – 2 октября 2004 г.).

УДК 539.17(042), 539.12.01(063)  
ББК [22.382+22.315]я431

ISBN 5-9530-0090-1

© Joint Institute for Nuclear  
Research, 2005

# Contents

## Volume I

Preface .....	13
<b>I. QUANTUM CHROMODYNAMICS AT THE LARGE DISTANCES</b>	
PROTON FORM FACTOR MEASUREMENTS AT JEFFERSON LAB <i>C. Perdrisat, V. Punjabi (for the Jefferson Lab <math>G_{Ep}(III)</math> Collaborations)</i> .....	17
MESONIC EXCHANGE CURRENTS IN THE DEUTERON. THE BRIDGE FROM NONRELATIVISTIC TO RELATIVISTIC NUCLEAR PHYSICS <i>S. G. Bondarenko et al.</i> .....	32
COULD LEPTONS BE COMPOSED FROM QUARKS OR ANTIQUARKS? <i>Y. E. Pokrovsky</i> .....	42
INSTANTON VACUUM BEYOND CHIRAL LIMIT <i>M. Musakhanov</i> .....	54
ON THE MOTION OF MATTER IN THE GEOMETRICAL GAUGE FIELD THEORY <i>N. P. Konopleva</i> .....	65
RANDOM LATTICE QCD AND CHIRAL BORN-INFELD THEORY <i>O. V. Pavlovsky</i> .....	70
THE NUCLEON-NUCLEON SCATTERING DESCRIPTION AT $E_{lab}=0.6$ GeV, THE DEUTERON PROPERTIES AND DEUTERON PHOTODISINTEGRATION IN THE RELATIVISTIC QUASIPOTENTIAL OPTICAL MODEL, BASED ON THE MOSCOW POTENTIAL <i>N. A. Khokhlov, V. A. Knyr, V. G. Neudatchin</i> .....	78
PRODUCTION OF CUMULATIVE PROTONS IN DIS OF NUCLEI, THE ROLE OF FLUCTONS, LPM EFFECT AND ALL THAT <i>S. M. Eliseev</i> .....	84
ON ELECTRODYNAMICS OF CONSTITUENT QUARKS AND QCD POTENTIAL <i>I. B. Pestov</i> .....	89
INSTANTONS AND STRUCTURE OF PENTAQUARK <i>H.-J. Lee</i> .....	96

ON THE RELATIONS BETWEEN TWO-PHOTON AND LEPTONIC WIDTHS OF LOW-LYING S-WAVE STATES OF CHARMONIUM <i>S. B. Gerasimov, M. Majewski</i> .....	102
CLOTHED PARTICLE REPRESENTATION IN QUANTUM FIELD THEORY: MASS RENORMALIZATION <i>V. Yu. Korda, A. V. Shebeko</i> .....	111
ELECTROPRODUCTION OF VECTOR MESONS AT SMALL $x$ <i>S. V. Goloskokov</i> .....	120
THE INFLUENCE OF FRAGMENTATION MODELS IN PRODUCTION OF HADRON JETS IN ELECTRON-POSITRON ANNIHILATION <i>M. E. Zomorrodian</i> .....	126
PHYSICAL NATURE OF LOBACHEVSKY PARALLEL LINES AND A NEW INERTIAL FRAME TRANSFORMATION <i>N. G. Fadeev</i> .....	132
<b>II. STRUCTURE FUNCTIONS OF HADRONS AND NUCLEI</b>	
JET ENERGY DENSITY IN HADRON-HADRON COLLISIONS AT HIGH ENERGIES <i>J. V. Ilić, G. P. Škoro, M. V. Tokarev</i> .....	143
Z-SCALING AT RHIC <i>M. V. Tokarev</i> .....	151
ANISOTROPY IN RELATIVISTIC NUCLEAR COLLISIONS AND MICHELSON'S EXPERIMENTS WITH LIGHT <i>I. Zborovský</i> .....	167
Z-SCALING OF JET PRODUCTION AT TEVATRON <i>M. V. Tokarev, T. G. Dedovich</i> .....	173
SCALING IN INCLUSIVE ELECTRON SCATTERING FROM NUCLEI <i>M. K. Gaidarov et al.</i> .....	186
NEW ASPECTS IN THE ASYMPTOTICS OF THE DEUTERON ELECTROMAGNETIC FORM FACTORS <i>A. F. Krutov, V. E. Troitsky, N. A. Tsirova</i> .....	194
METHOD OF THE POLARIZED SEMI-INCLUSIVE DEEP INELASTIC SCATTERING DATA ANALYSIS IN THE NEXT-TO-LEADING QCD ORDER <i>A. N. Sissakian, O. Yu. Shevchenko, O. N. Ivanov</i> .....	200
MEASUREMENT OF HADRON PRODUCTION CROSS-SECTION IN COLLISIONS OF HIGHLY VIRTUAL PHOTONS <i>V. Pozdnyakov, Yu. Vertogradova</i> .....	206

### III. RELATIVISTIC HEAVY ION COLLISIONS

MULTIPLICITY AND $p_t$ CORRELATIONS IN RELATIVISTIC NUCLEAR COLLISIONS <i>R. S. Kolevatov, V. V. Vechernin</i> .....	213
LONG-RANGE CORRELATIONS IN Pb-Pb COLLISIONS AT 158 A*GeV <i>G. Feofilov (for NA49 Collaboration and SPbSU group)</i> .....	222
ON SPATIAL AND EVENT-BY-EVENT FLUCTUATIONS IN RELATIVISTIC HEAVY-ION COLLISIONS <i>Sh. Ahmad</i> .....	232
NEUTRINO OPACITY TO COLD NEUTRON MATTER <i>O. Benhar, A. Fabrocini, S. Fantoni, G. I. Lykasov</i> .....	238
SEARCH FOR SIGNAL ON PERCOLATION CLUSTER FORMATION IN NUCLEUS- NUCLEUS COLLISIONS AT RELATIVISTIC ENERGIES <i>O. B. Abidinov et al.</i> .....	246
INVESTIGATION OF CHARMONIUM STATES PRODUCTION IN $p$ -A AND NUCLEUS- NUCLEUS COLLISIONS AT THE CERN SPS <i>N. S. Topilskaya (for the NA50 Collaboration)</i> .....	255
STRUCTURE FUNCTION $F_L$ AT FIXED $W$ IN THE $K_T$ -FACTORIZATION APPROACH <i>A. V. Kotikov, A. V. Lipatov, N. P. Zotov</i> .....	263
MODEL FOR RESTORATION OF HEAVY-ION POTENTIALS AT INTERMEDIATE ENERGIES <i>K. M. Hanna et al.</i> .....	269
AZIMUTHAL STRUCTURES OF PRODUCED PARTICLES IN HEAVY-ION INTERACTIONS <i>S. Vokál et al.</i> .....	280
THE EXTRAORDINARY INTERACTION OF $^{14}\text{N}$ -NUCLEUS IN PHOTOEMULSION <i>G. Orlova</i> .....	288
$\rho$ MESON PRODUCTION IN ULTRAPERIPHERAL $d\text{Au}$ COLLISION <i>S. L. Timoshenko (for the STAR Collaboration)</i> .....	292
RANDOM MATRIX THEORY AND ANALYSIS OF NUCLEUS-NUCLEUS COLLISION AT HIGH ENERGIES <i>E. I. Shahakiev et al.</i> .....	296

## IV. MULTIPARTICLE DYNAMICS

$\Lambda$ AND $K_s^0$ PRODUCTION IN $pC$ COLLISIONS AT 10 GeV/c <i>P. Zh. Aslanyan, V. N. Emelyanenko, G. G. Rikhkvitzkaya</i> .....	305
SEARCH FOR SCALING PROPERTIES IN MANY-PARTICLE STOCHASTIC PROCESSES <i>B. Słowiński</i> .....	314
STUDY OF MULTIPARTICLE PRODUCTION BY GLUON DOMINANCE MODEL (Part I) <i>E. S. Kokoulina, V. A. Nikitin</i> .....	319
STUDY OF MULTIPARTICLE PRODUCTION BY GLUON DOMINANCE MODEL (Part II) <i>P. F. Ermolov et al.</i> .....	327
THE LOBACHEVSKY SPACE IN RELATIVISTIC NUCLEAR PHYSICS <i>A. A. Baldin</i> .....	337
STRANGENESS CONSERVATION AND STRUCTURE OF PAIR CORRELATIONS OF NEUTRAL KAONS WITH LOW RELATIVE MOMENTA IN INCLUSIVE PROCESSES <i>V. L. Lyuboshitz, V. V. Lyuboshitz</i> .....	361

## V. ACCELERATOR FACILITIES: STATUS AND PERSPECTIVES

BEAM-BASED MEASUREMENT OF DYNAMICAL CHARACTERISTICS IN NUCLOTRON <i>N. Blinnikov et al.</i> .....	369
SPIN AS AN ADDITIONAL TOOL FOR QGP INVESTIGATIONS <i>Yu. Karachuk, S. S. Shimanskiy</i> .....	375
TRANSMUTATION RESEARCH USING THE NUCLOTRON <i>W. Westmeier et al.</i> .....	379
ELECTRON-POSITRON PAIR CREATION IN THE FIELDS OF HIGH-INTENSITY OPTICAL LASERS <i>D. B. Blaschke, A. V. Prozorkevich, S. A. Smolyansky</i> .....	383

VI. HADRON SPECTROSCOPY

BARYONIC RESONANCES WITH THE STRANGENESS  $S = +1$  IN THE SYSTEM OF  $nK^+$  FROM THE REACTION  $np \rightarrow npK^+K^-$  AT THE MOMENTUM OF INCIDENT NEUTRONS  $P_n = (5.20 \pm 0.12) \text{ GeV}/c$   
*Yu. A. Troyan et al.* ..... 13

OBSERVATION OF  $S = +1$  NARROW RESONANCES IN THE SYSTEM  $K_s^0 p$  FROM  $p + C_3H_8$  COLLISION AT 10 GeV/c  
*P. Zh. Aslanyan, V. N. Emelyanenko, G. G. Rikhkvitzkaya* ..... 26

WAVELET ANALYSIS OF DATA IN PHYSICS OF RESONANCES  
*V. I. Henner, T. S. Belozeroва, P. G. Frick* ..... 37

DIBARYONS IN HADRONIC PHYSICS AND NUCLEAR STRUCTURE  
*V. I. Kukul'in, M. A. Shikhalev* ..... 45

FURTHER EVIDENCE OF NARROW BARYONIC STRUCTURES WITH HADRONIC AS WELL AS LEPTONIC PROBES  
*B. Tatischeff, E. Tomasi-Gustafsson* ..... 56

INSTANTONS IN HIGH ENERGY QCD PROCESSES: INSTANTONS AND THE SOFT POMERON FORMATION  
*A. E. Dorokhov, I. O. Cherednikov* ..... 63

TWO-QUARK BOUND STATES: MESON SPECTRA AND REGGE TRAJECTORIES  
*G. Ganbold, G. V. Efimov* ..... 67

SOLVING THE INHOMOGENEOUS BETHE-SALPETER EQUATION  
*S. S. Semikh et al.* ..... 75

DETERMINATION OF THE GLUEBALL MASS SPECTRUM WITH THE SPIN-ORBIT INTERACTION IN NONPERTURBATIVE QCD APPROACH  
*M. Dineykhаn, S. A. Zhaugasheva, T. A. Kozhamkulov* ..... 82

VII. APPLIED USE OF RELATIVISTIC BEAMS

INVESTIGATION OF TRANSMUTATION OF RADIOACTIVE WASTE OF ATOMIC REACTORS  $^{129}\text{I}$ ,  $^{237}\text{Np}$  AND NEUTRONS GENERATION WITH 1.5 GEV PROTONS FROM THE NUCLOTRON AT THE SETUP "ENERGY PLUS TRANSMUTATION" (JINR, DUBNA)  
*M. I. Krivopustov et al.* ..... 91

THOROUGH COMPARISON OF THE NEUTRON FLUXES GENERATED IN THE LEAD-URANIUM ASSEMBLY (INSTALLATION "ENERGY PLUS TRANSMUTATION") UNDER IRRADIATION WITH PROTONS AT ENERGY IN THE RANGE FROM 0.7 TO 2.0 GeV <i>A. N. Sosnin et al.</i> .....	110
---	-----

EXPERIMENTAL STUDIES OF SPATIAL DISTRIBUTIONS OF NEUTRONS INSIDE AND AROUND THE SET-UP CONSISTED FROM A THICK LEAD TARGET AND A LARGE URANIUM BLANKET IRRADIATED BY RELATIVISTIC PROTONS <i>V. Wagner et al.</i> .....	111
---	-----

EXPERIMENTAL AND THEORETICAL DETERMINATION OF $^{235}\text{U}$ , $^{238}\text{U}$ AND $^{\text{NAT}}\text{Pb}$ FISSION RATE DISTRIBUTIONS IN THE U/PB ASSEMBLY BOMBARDED WITH 1.5 GEV PROTONS <i>I. V. Zhuk et al.</i> .....	117
---	-----

ON SOLUTION OF THE NUCLEAR PROBLEMS REDUCED TO A SYSTEM OF FIRST ORDER INTEGRAL FREDHOLM EQUATIONS <i>S. V. Korneev et al.</i> .....	124
---	-----

ON THE EXPERIMENT OF NEUTRON SPECTRUM INVESTIGATION ON U/Pb-ASSEMBLY USING 0.7 GeV PROTON BEAM FROM THE JINR NUCLOTRON (DUBNA) <i>M. Bielewicz et al.</i> .....	125
--	-----

INVESTIGATION OF TEMPERATURE FIELDS AND HEAT GENERATION IN THE LEAD BLOCK AND THE LEAD TARGET WITH THE URANIUM BLANKET OF THE INSTALLATION "ENERGY PLUS TRANSMUTATION" USING PROTON BEAMS FROM THE JINR SYNCHROPHASOTRON/NUCLOTRON <i>A. V. Voronkov et al.</i> .....	133
--	-----

EXPERIMENTAL STUDIES OF TRANSMUTATION OF $^{129}\text{I}$ BY SPALLATION NEUTRONS USING JINR DUBNA PHASOTRON <i>M. Majerle (for Collaboration "Energy plus Transmutation")</i> .....	135
--	-----

INVESTIGATION OF NEUTRON FIELDS ON THE SURFACE OF THE MASSIVE LEAD TARGET UNDER IRRADIATIONS WITH PROTONS AT ENERGIES OF 1.5 AND 5.0 GeV USING SYNCHROPHASOTRON (JINR, DUBNA) <i>M. K. Kievets et al.</i> .....	141
--	-----

## VIII. POLARIZATION PHENOMENA AND SPIN PHYSICS

INVESTIGATION OF THE ANGULAR DEPENDENCE OF THE TENSOR ANALYZING POWER OF 9 GeV/c DEUTERON BREAKUP <i>L. S. Azhgirey et al.</i> .....	153
---	-----

MEASUREMENTS OF ENERGY BEHAVIOURS OF SPIN-DEPENDENT  
 $np$ -OBSERVABLES OVER 1.2-3.7 GEV REGION

*V. I. Sharov et al.* ..... 161

SENSITIVITY OF THE POLARIZATION OBSERVABLES  $A_Y$ ,  $A_{YY}$ ,  $A_{XX}$  AND  $A_{XZ}$   
 OF THE  $\vec{d}d \rightarrow p\ ^3H$  AND  $\vec{d}d \rightarrow pX$  REACTIONS TO THE DEUTERON SPIN  
 STRUCTURE AT 270 MEV

*T. A. Vasiliev et al.* ..... 178

SPIN AS A KINEMATICAL EFFECT OF THE RELATIVITY

*O. S. Kosmachev* ..... 185

THE POLARIZED CHARGE-EXCHANGE REACTION  $\vec{d} + p \rightarrow (pp)_{1s_0} + n$

*V. Glagolev (for the ANKE Collaboration)* ..... 192

SINGLE SPIN ASYMMETRY IN HIGH  $P_T$  CHARGED HADRON PRODUCTION OFF  
 NUCLEI AT 40 GeV

*V. V. Abramov et al.* ..... 202

LONGITUDINAL POLARIZATION OF  $\Lambda$  AND  $\bar{\Lambda}$   
 IN DEEP-INELASTIC SCATTERING AT COMPASS

*M. G. Sapozhnikov (for the COMPASS Collaboration)* ..... 208

DEUTERON-PROTON CHARGE EXCHANGE REACTION  
 AT SMALL TRANSFER MOMENTUM

*N. B. Ladygina, A. V. Shebeko* ..... 214

NUCLEAR SPIN IN DIRECT DARK MATTER SEARCH

*V. A. Bednyakov, F. Šimkovic, I. V. Titkova* ..... 221

CHARM PRODUCTION IN  $NN$  AND  $\gamma N$  COLLISIONS

*E. Tomasi-Gustafsson* ..... 231

TENSOR  $A_{yy}$  AND VECTOR  $A_y$  ANALYZING POWERS  
 OF THE  $(d,p)$  AND  $(d,d)$  REACTIONS AT 5 GeV/c AND 178 MR

*V. P. Ladygin et al.* ..... 241

MEASUREMENTS OF THE TENSOR  $A_{xx}$ ,  $A_{yy}$ ,  $A_{zz}$  AND VECTOR  $A_y$  ANALYZING  
 POWERS FOR THE  $d + d \rightarrow\ ^3H + p$  AND  $d + d \rightarrow\ ^3He + n$  REACTIONS AT 270 MeV

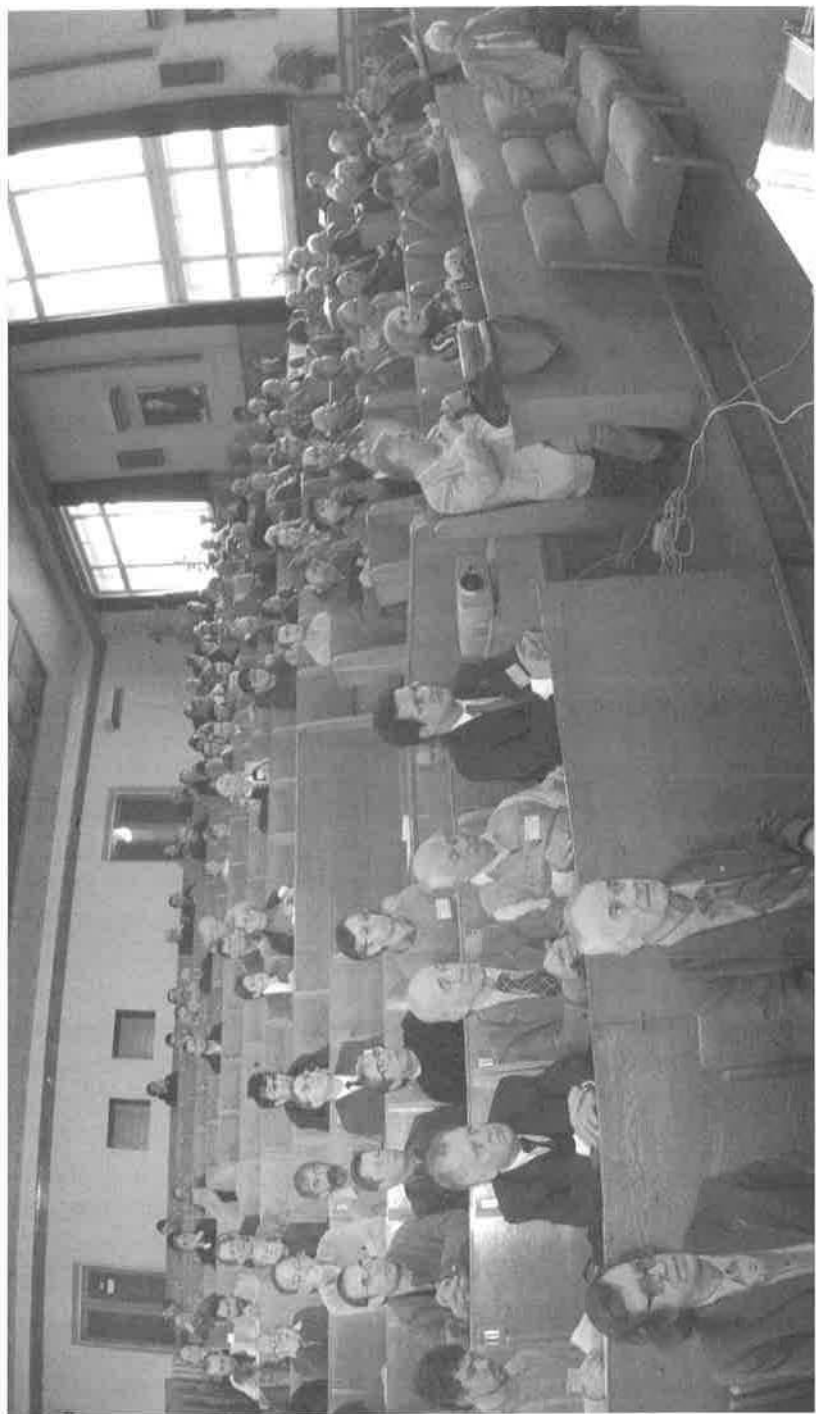
*M. Janek et al.* ..... 249

INCLUSIVE AND SEMI-INCLUSIVE ASYMMETRIES AT COMPASS

*A. Yu. Korzenev (for the COMPASS Collaboration)* ..... 255

## IX. PROGRESS IN EXPERIMENTAL STUDIES AT THE HIGH ENERGY ACCELERATORS

FULL SIMULATION OF HIGGS BOSON DECAYS INTO FOUR LEPTONS FOR ATLAS AT THE LHC <i>A. Khodinov, M. Rijssenbeek, S. Padhi</i> .....	263
STUDY OF A POSSIBILITY TO DETECT $\Upsilon$ IN $p$ -Pb AND Pb- $p$ COLLISIONS AT THE LHC IN THE MUON SPECTROMETER OF ALICE <i>A. Morsch et al.</i> .....	268
PERFORMANCE OF THE SILICON DRIFT DETECTOR IN THE CASE OF PERPENDICULAR TRACKS AND INCLINED TRACKS <i>S. Kouchpil (for the ITS ALICE Collaboration)</i> .....	276
PRODUCTION AND IDENTIFICATION OF THE SUPERHEAVY HYDROGEN HYPERNUCLEUS ${}^{\infty}\text{H}$ <i>L. Majling et al.</i> .....	282
THE DIPOLE MAGNET IRON YOKE DESIGN FOR THE ALICE DIMUON ARM SPECTROMETER <i>V. Arefiev et al.</i> .....	291
INCLUSIVE $\pi^0$ PRODUCTION BY PROTONS AND LIGHT NUCLEI ON C AND Cu TARGETS AT A MOMENTUM OF 4.5 GeV/c PER NUCLEON <i>Kh. U. Abraamyan et al.</i> .....	301
CLUSTER-FLUCTONS REVELATION IN NUCLEAR INTERACTIONS AT 4.2 (GeV/c)/N <i>V. N. Penev, A. I. Shklovskaya, E. N. Kladnitskaya</i> .....	311
INVESTIGATIONS IN VEKSLER AND BALDIN LABORATORY OF HIGH ENERGIES <i>A. I. Malakhov</i> .....	319
INVARIANT ANALYSIS OF THE FRAGMENTATION OF RELATIVISTIC NUCLEI IN EMULSION <i>P. I. Zarubin et al.</i> .....	339
PHYSICS AT COSY <i>H. Machner</i> .....	347
POLARIZED DEUTERONS AT THE NUCLOTRON <i>Yu. K. Pilipenko et al.</i> .....	353
Scientific Programme .....	358
List of Participants .....	370









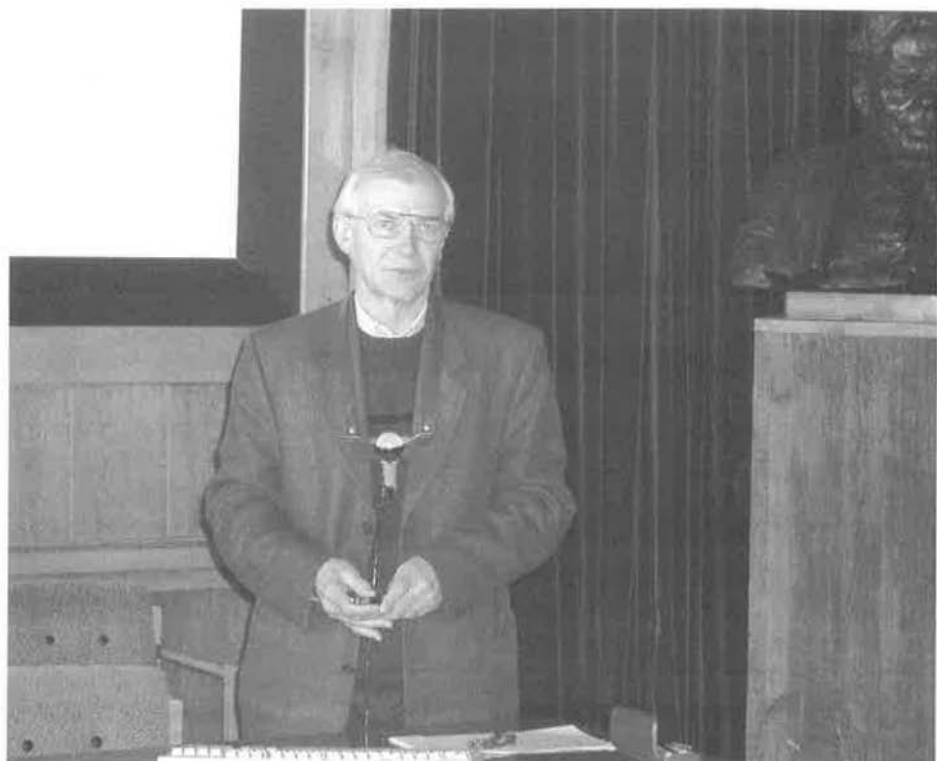


# Investigations in Veksler and Baldin Laboratory of High Energies

*A. Malafayev*

High Energy Accelerator Institute, Moscow, in High Energy  
Physics, Khabarovsk, September 27 - October 2, 1991







**VI.**  
**HADRON**  
**SPECTROSCOPY**



# BARYONIC RESONANCES WITH THE STRANGENESS $S = +1$ IN THE SYSTEM OF $nK^+$ FROM THE REACTION $np \rightarrow npK^+K^-$ AT THE MOMENTUM OF INCIDENT NEUTRONS $P_n = (5.20 \pm 0.12) GeV/c$

Yu.A.Troyan<sup>1</sup>, A.V.Beljaev, A.Yu.Troyan, E.B.Plekhanov, A.P.Jerusalimov, G.B.Piskaleva,  
S.G.Arakelian<sup>2</sup>

The investigation has been performed at the Veksler and Baldin Laboratory of High Energies, JINR,  
within the framework of the theme 03-1-0983092/2004  
(JINR.D1-2004-39, Dubna,2004.)

<sup>1</sup> E-mail: [atroyan@jinr.ru](mailto:atroyan@jinr.ru)

<sup>2</sup> Lebedev Institute of Physics, Russian Academy of Sciences, Moscow

The production and properties of baryon resonances with the strangeness  $S = +1$  in the  $nK^+$  system have been studied in the reaction  $np \rightarrow npK^+K^-$  at the momentum of incident neutrons  $P_n = (5.20 \pm 0.12) GeV/c$ . A number of peculiarities have been found in the effective mass spectrum of the above system. All these resonances have a large statistical significance. Their widths are comparable with the mass resolution. The estimation of spins of the resonances has been carried out, and the rotational band connecting the resonance masses and their spins has been constructed.

## 1. Introduction

In the papers [1, 2] D.Diakonov, V.Petrov and M.Polyakov have suggested the extension of a  $SU(3)$  symmetry scheme for states with the strangeness  $S = +1$ . It was claimed the existence of antidecuplet  $\overline{10}$ , which includes states consisting of five quarks ( $uudd\bar{s}$ ). The dynamics of new resonances was based on the model of chiral scliton. This made it possible to estimate the masses, widths and quantum numbers of expected new states, to propose a formula of the rotational band that give a dependence of the resonance masses to their spins. In the paper [1],  $\Theta$ -resonance at the mass  $M = 1.530 GeV/c^2$ , width  $\Gamma \leq 15 MeV/c^2$  and with quantum numbers  $Y = 2, I = 0, J^P = 1/2^+$  is on the top of antidecuplet.

The hypothesis of the authors [1] is discussed in detail in many theoretical works the number of which is close to 50. Detailed review of theoretical works one can find in papers [3,4,5] together with the number of critical remarks. The quite different approaches to the problem of these resonances have been developed in papers [6,7]: integration of quarks into diquarks, which is accompanied by a rise of superconducting layers [6]; a pure quark picture where isoscalar, isovector and isotensor states consisting of five quarks (both usual and strange) can arise, which greatly extends both the possible quantum numbers, resonances masses and probability of their decays (for example,  $\Theta$ -resonances may have the quantum numbers  $1/2^-, 3/2^-, 5/2^-$ ) [7].

Papers of D.Akher's [8] represents a rotation-vibration model giving a set of predicts about masses and other quantum numbers of discussing resonances. In review of A.Arkipov [9] these effects are rated on unified structure of hadronic spectrum.

The properties of the particles from antidecuplet predicted in [1,2] allow a direct search for effects. These are both comparatively low masses and widths accessible for a direct measurement. This simulated a number of experimental works [10] in which a resonance with the mass of  $\sim 1.540 \text{ GeV}/c^2$  and width from 3 to 25  $\text{MeV}/c^2$  was discovered in  $nK^+$  or  $pK_s^0$  system.

But none of these experimental works observe the rotational band or more than one resonance state. Also neither spin of resonance nor its parity was determined. This is primarily due to the small statistics of the experiments, insufficient accuracy and some kinds of samplings.

In the present work we have attempted to study the characteristics of the observed effects in greater detail.

## 2. Experiment

The study was carried out using data obtained in the exposure of 1- $m$  H<sub>2</sub> bubble chamber (HBC) of JINR's LHE to a quasi-monochromatic neutron beam, constructed in 1972 due to the acceleration of deuterons by the LHE Synchrophasotron. The purpose of the neutron experiment was to study pentaquarks in  $\Delta^{++}\pi^+$  system (described below).

Quasi-monochromatic neutrons ( $\Delta P_n / P_n \approx 2.5\%$ ) were generated due to the stripping of accelerated deuterons in a 1  $\text{cm}$  Al target placed inside the vacuum chamber of the Synchrophasotron. The neutrons were extracted from the accelerator at the angle of  $0^\circ$  to the direction of accelerated deuterons.

The cleaning of the neutron beam from charged particles was provided by the magnetic field of the accelerator in which the neutrons passed about 12 meters before leaving the Synchrophasotron. The bubble chamber was at a distance of 120  $m$  from the Al target. The neutron beam was well collimated and had an angular spread of  $\Delta\Omega_n \approx 10^{-7}$  st. The beam had no admixture from either charged particles or  $\gamma$  quanta. The detailed description of the neutron channel was made in [11].

The 1- $m$  HBC was placed in a magnetic field of  $\sim 1.7$  T. As a result we have had a good accuracy for the momenta of secondary charged particles ( $\delta P \approx 2\%$  for protons and  $\delta P \approx 3\%$  for  $K^+$  and  $K^-$  from the reaction  $np \rightarrow npK^+K^-$ ). The angular accuracy was  $\leq 0.5^\circ$ .

The reaction channels were separated by the standard  $\chi^2$  method with regard to the corresponding constraints [12]. For the reaction  $np \rightarrow npK^+K^-$  there is only one constraint for the parameters (energy conservation law), and the experimental  $\chi^2$  distribution must follow the theoretical  $\chi^2$  distribution with one degree of freedom.

The experimental (histogram) and theoretical (solid curve)  $\chi^2$  distributions for the above reaction are shown in fig. 1a. One can see a good agreement between them up to  $\chi^2 = 1$  and some difference for  $\chi^2 > 1$ . Therefore, we have used only the events with  $\chi^2 \leq 1$  (limit is marked off by an arrow) for the further analysis. 15% of events with this cut satisfy the two hypotheses: the channel  $np \rightarrow npK^+K^-$  and the channel  $np \rightarrow np\pi^+\pi^-$ . In this case  $\chi^2$  value for the  $K$ -mesons hypothesis ("K") is always less than  $\chi^2$  value for the  $\pi$ -mesons hypothesis (" $\pi$ "). All these events are attributed to the "K" hypothesis. No difference was ob-

served between some test distributions for single-valued ( $\chi^2_{K^+} < 1$ ,  $\chi^2_{\pi^+} > 6.5$ ) and two-valued ( $\chi^2_{K^+} < 1$ ,  $\chi^2_{\pi^+} < 1$ ) events.

Figure 1b shows missing mass distribution for the  $\chi^2 \leq 1$  events. One can see that the distribution has a maximum at the missing mass equal to the neutron mass with an accuracy of  $0.1 \text{ MeV}/c^2$  and is symmetric about the neutron mass. Subsequently a small number of events with missing masses outside the range marked off in the plot by arrows were excluded for higher purity of data.

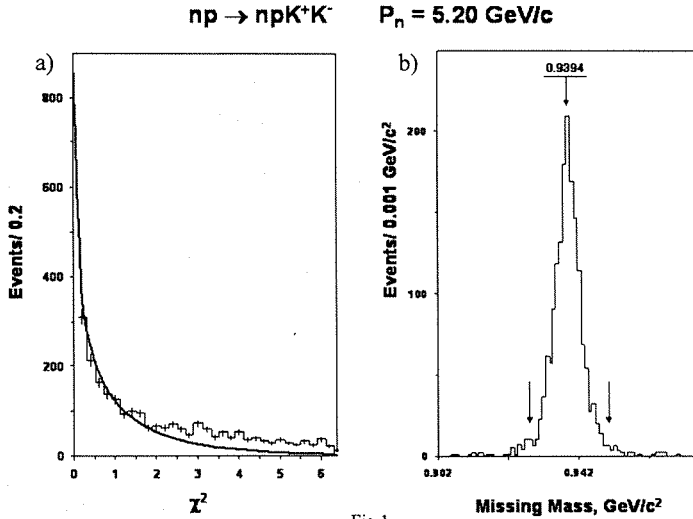


Fig.1.

- a) - The experimental (histogram) and the theoretical (solid curve)  $\chi^2$ -distribution for the reaction  $np \rightarrow npK^+K^-$ ;
- b) - missing mass distribution for the events of  $\chi^2 \leq 1$

As a result, 1558 events were selected from the reaction  $np \rightarrow npK^+K^-$  at  $P_n = (5.20 \pm 0.12) \text{ GeV}/c$  under the  $4\pi$  geometry (the absence of any angular selections).

### 3. Results

Figure 2 shows the effective mass distribution of  $nK^+$  combinations for all the events from the reaction  $np \rightarrow npK^+K^-$  at  $P_n = (5.20 \pm 0.12) \text{ GeV}/c$ . The distribution is approximated by an incoherent sum of the background curve (taken in the form of a superposition of Legendre polynomials up to 8<sup>th</sup> power, inclusive) and by 10 resonance curves taken in the Breit-Wigner form. The contribution of the background to this distribution is 75.8 %. The requirements to the background curve are the following: firstly, the errors of the coefficients must be no more than 50 % for each term of the polynomial; secondly, the polynomial must describe the experimental distribution after "deletion" of the resonance regions with  $\overline{\chi^2} = 1.0$  and  $\sqrt{D} = 1.4$  (the parameters of  $\chi^2$  distribution with one degree of freedom). The parameters for the distribution in Fig. 2 are  $\overline{\chi^2} = 0.92 \pm 0.29$  and  $\sqrt{D} = 1.33 \pm 0.20$ . The same values

for the background curve normalized to 100 % of events (with resonance regions included) are  $\overline{\chi^2} = 1.40 \pm 0.19$  and  $\sqrt{D} = 2.38 \pm 0.14$ . The significance level of the resonance at  $M = 1.541 \text{ GeV}/c^2$  is 4.5 SD.

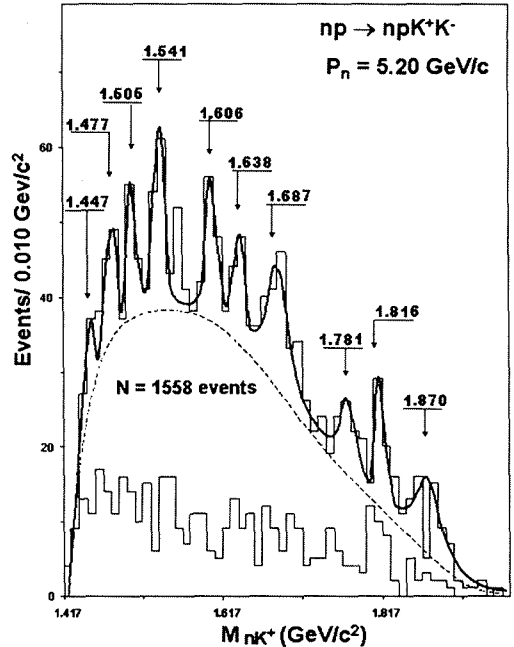
Fig.2.

The effective mass distribution of  $nK^+$  combinations for all events from the reaction  $np \rightarrow npK^+K^-$  at  $P_n = (5.20 \pm 0.12) \text{ GeV}/c$ .

The dotted line is the background curve taken in the form of Legendre polynomial of 8<sup>th</sup> power.

The solid line is the sum of the background curve and the ten resonance curves taken in the Breit-Wigner form.

The histogram in the bottom is the effective mass distribution of  $nK^+$  combinations selected under condition  $\{\cos \Theta_n^* < -0.85 \cup \cos \Theta_n^* > 0.85\}$



The same plot (Fig. 2) shows the distribution of effective masses for  $nK^+$  combinations selected under condition  $\{\cos \Theta_n^* < -0.85 \cup \cos \Theta_n^* > 0.85\}$ , where  $\Theta_n^*$  - the angle of secondary neutron emission in general c.m.s. One can see that this distribution has no essential bumps and a deletion of such kind events can decrease the background.

Fig. 3 shows the distribution of effective masses of  $nK^+$  combinations for the events selected under condition  $\{-0.85 < \cos \Theta_n^* < 0.85\}$ . The distribution is approximated by an incoherent sum of the background curve taken in the form of superposition of Legendre polynomials up to 8<sup>th</sup> power and by eight resonance curves taken in the Breit-Wigner form. The statistical significance increased slightly for resonances to the right of the mass  $M = 1.541 \text{ GeV}/c^2$  and decreased slightly for the narrow resonances to the left of it.

To gain a better understanding of low-masses resonances, the distribution of the effective masses of  $nK^+$  combinations was constructed with bins of  $5 \text{ MeV}/c^2$  (up to a mass of  $\sim 1.663 \text{ GeV}/c^2$ ). This distribution (Fig. 4) was approximated by an incoherent sum of the background curve taken in the form of a superposition of Legendre polynomials up to 4<sup>th</sup> power and by six resonance curves taken in the Breit-Wigner form.

The resonance at  $M = 1.541 \text{ GeV}/c^2$  exceeds the background by 5.2 SD, the resonance at  $M = 1.605 \text{ GeV}/c^2$  by 5.4 SD and the resonance at  $M = 1.505 \text{ GeV}/c^2$  by 3.1 SD. The widths of the resonances are determined more precisely by means of this distribution (see Tab. I).

Fig.3

The effective mass distribution of  $nK^+$  combinations for the events selected under condition  $\{-0.85 < \cos \Theta_n^* < 0.85\}$

from the reaction  $np \rightarrow npK^+K^-$  at  $P_n = (5.20 \pm 0.12) \text{ GeV} / c$ .

The dotted line is the background curve taken in the form of Legendre polynomial of 8<sup>th</sup> power. The solid line is the sum of the background curve and the eight resonance curves taken in the Breit-Wigner form

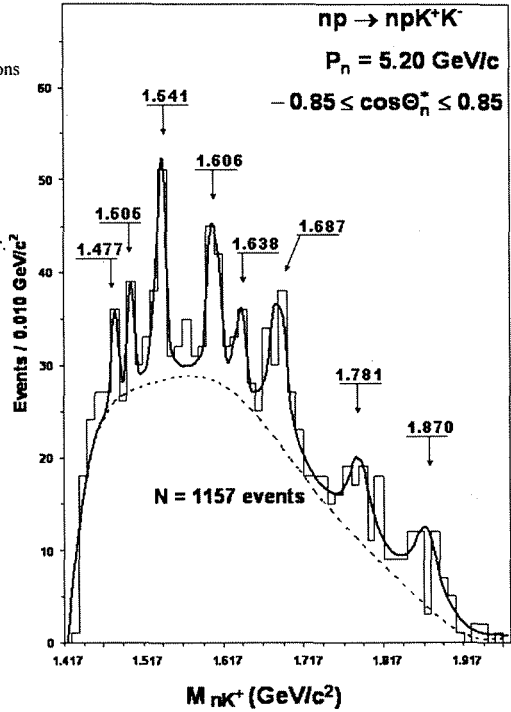
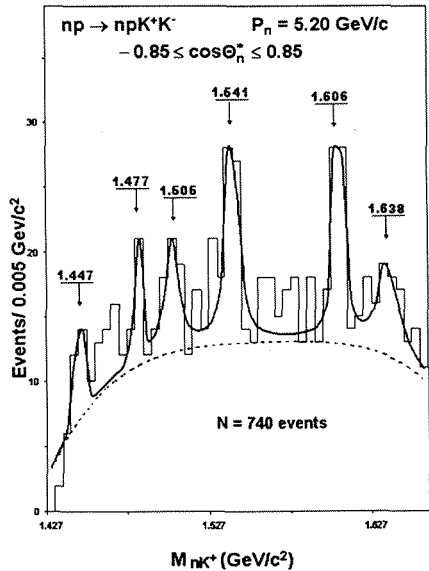


Fig.4.

The effective mass distribution of  $nK^+$  combinations from the reaction  $np \rightarrow npK^+K^-$  at  $P_n = (5.20 \pm 0.12) \text{ GeV} / c$  for the events selected under condition  $\{-0.85 < \cos \Theta_n^* < 0.85\}$ .

The dotted line is the background curve taken in the form of Legendre polynomial of 4<sup>th</sup> power.

The solid line is the sum of the background curve and the six resonance curves taken in the Breit-Wigner form



We made an effort to increase the statistical significances of some resonances. This attempt was based under the assumption that resonances are generated by means of  $K$ -exchange mechanism: a well known resonance ( $\Sigma^*$  or  $\Lambda^*$ ) decaying through  $pK^-$  mode is produced in one of the vertices of the corresponding diagram and a resonance in the  $nK^+$  system was produced in another vertex. The  $K^-$  meson from the decay of the known resonance can be correlated kinematically with the resonance in the  $nK^+$  system. In consequence kinematically produced peaks can occur in the effective mass distribution of  $nK^+K^-$  system.

Figure 5 shows the effective mass distribution of  $nK^+K^-$  combinations. A number of peculiarities can be clearly seen in this distribution. No corresponding resonances decaying through the mode  $R \rightarrow nK\bar{K}$  are available in PDG tables. These are just the kinematic reflections mentioned above. Fig. 5 also shows the effective masses distribution of  $nK^+K^-$  combinations selected so that the effective mass of the  $nK^+$  system lies within the range of the  $M = 1.541 GeV/c^2$  resonance. Two clusters are readily apparent in this distribution in the  $nK^+K^-$  mass region from 2.020 to 2.150 and from 2.240 to 2.280 ( $GeV/c^2$ ). The corresponding clusters exist also for resonances in  $nK^+$  system with  $M = 1.606 GeV/c^2$  and  $M = 1.678 GeV/c^2$ .

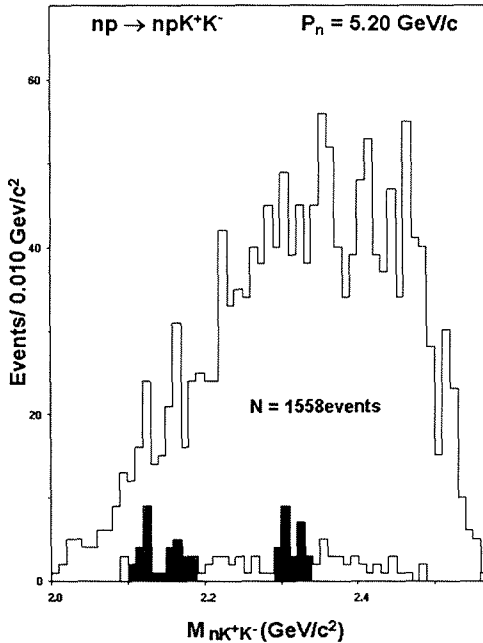


Fig.5.

The effective mass distribution of  $nK^+K^-$  combinations from the reaction  $np \rightarrow npK^+K^-$  at  $P_n = (5.20 \pm 0.12) GeV/c$ .

The bottom histogram corresponds to the effective mass distribution of  $nK^+K^-$  combinations selected so that the effective mass of  $nK^+$  combinations is within the resonance range at  $M = 1.541 GeV/c^2$

Selecting the mass region of  $nK^+K^-$  combinations that correspond to the resonance reflections in the  $nK^+$  system at these masses, we obtain distributions of the effective masses of  $nK^+K^-$  combinations (Fig. 6).

The selected mass bands of  $nK^+K^-$  combinations and additional cuts on the emission angles of the secondary neutron in the general c.m.s. are given under each plot. The additional cuts on emission angle somewhat decrease the background but the major effect of enhancement results from the sample on masses of  $nK^+K^-$  combinations.

Each of obtained distributions is approximated by an incoherent sum of background curve taken in the form of Legendre polynomial and by resonance curves in the Breit-Wigner form.

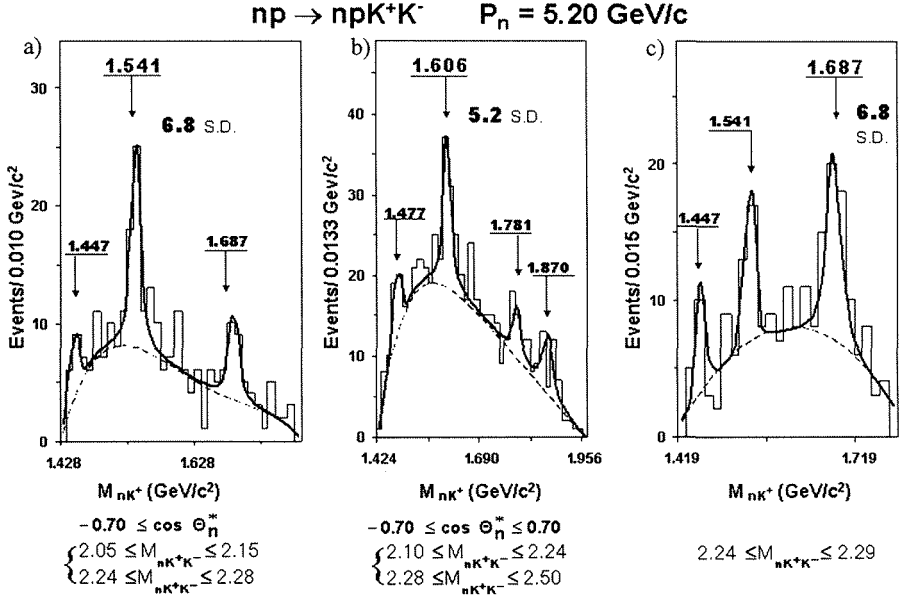


Fig. 6.

The effective mass distribution of  $nK^+$  combinations from the reaction  $np \rightarrow npK^+K^-$  at  $P_n = (5.20 \pm 0.12) \text{ GeV}/c$  for the resonances at:

(a)  $M = 1.541 \text{ GeV}/c^2$ ;    (b)  $M = 1.606 \text{ GeV}/c^2$ ,    (c)  $M = 1.678 \text{ GeV}/c^2$ .

Selected mass regions of  $nK^+K^-$  combinations and the additional cuts for emission angles of secondary neutrons in the general c.m.s. are presented under the plot.

Dotted lines denote background curves. Solid lines are approximating curves

As a consequence, we get a considerable enhancement of the effects of three resonances processed in this manner (the values of SD are listed in the plot of Fig. 6). In this case, the number of events in the peaks does not decrease as compared with the processed data shown in Fig. 2-4.

Figure 7 presents the distributions of the effective masses of  $pK^-$  combinations under the same sampling conditions as in Fig. 6. Peculiarities are evident in the distribution of the effective masses of  $pK^-$  combinations corresponding to the known  $\Sigma^*$  or  $\Lambda^*$  resonances (these peculiarities are also easily observed in the distributions of the effective masses of  $pK^-$  combinations constructed without cuts mentioned above).

We have tried to estimate the values of spins of the observed resonances in  $nK^+$  system. To do this, we constructed distributions of emission angles of neutrons from the resonance decay with respect to the direction of resonance emission in general c.m.s of the reaction. All values are taken in the rest system of resonance (helicity coordinate system). In the helicity coordinate system, the angular distributions have to be described by a sum of even-power Legendre polynomials with maximum power being equal to  $(2J-1)$ , where  $J$  is a spin of the resonance (for half-integer spins). In such a manner the value of lower limit of the resonance spin is estimated. The authors are grateful to Dr. V.L.Luboshits for the arrangement of the corresponding formulas.

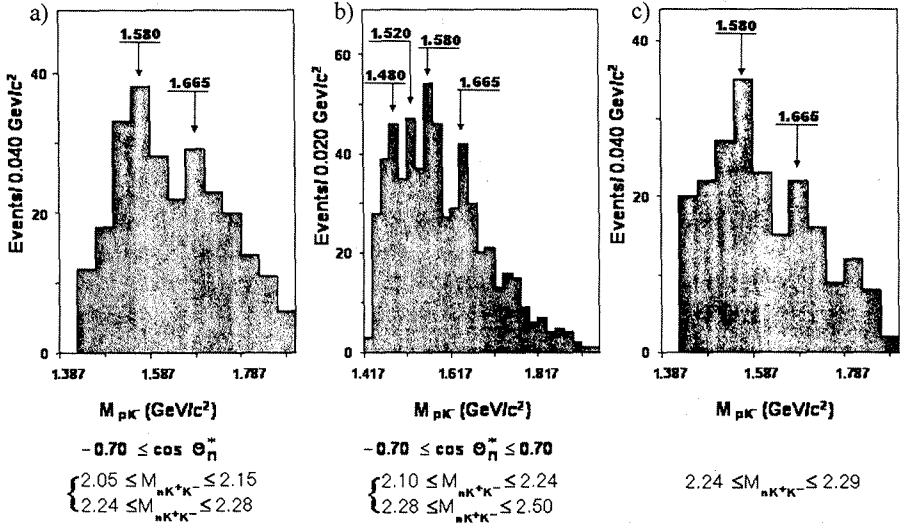


Fig. 7. The effective mass distribution of  $pK^-$  combinations from the reaction  $np \rightarrow npK^+K^-$  at  $P_n = (5.20 \pm 0.12) \text{ GeV}/c$ .

Selected mass intervals of  $nK^+K^-$ -combinations and the additional cuts of emission angles of secondary neutron in the general c.m.s. are given under the histogram (a-c correspond to fig. 6)

Figure 8 presents the angular distributions for six resonances whose masses are in the ranges given in the plots. The background distributions are constructed on the intervals to the left and to the right of the corresponding resonance band and subtracted with a factor corresponding to the background fraction in the resonance region. No cuts on emission angles of secondary particles were used in constructing these distributions (cuts on the emission angle of secondary neutron leave the results unchanged). When approximating it was essential that errors in coefficients of the selected Legendre polynomials should be less than 50%.

From the plots presented in fig. 8 one can see that the distribution for the resonance at  $1.467 < M < 1.487 \text{ GeV}/c^2$  is isotropic and polynomials of high power are not needed for an approximation. Therefore, its spin is  $J \geq 1/2$ . The most likely spin value for the resonance at  $1.500 < M < 1.510 \text{ GeV}/c^2$  is  $J \geq 3/2$ , although the value  $J \geq 1/2$  also has enough large confidence level. The spin value  $J \geq 1/2$  for the resonance at  $1.530 < M < 1.550 \text{ GeV}/c^2$  (the most

widely discussed in papers) has a confidence level significantly less than the higher ones. Of the highest confidence level is the spin value  $J \geq 5/2$ . The resonance at  $1.595 < M < 1.615 \text{ GeV}/c^2$  has a rather confident estimation for the spin value  $J \geq 7/2$ .

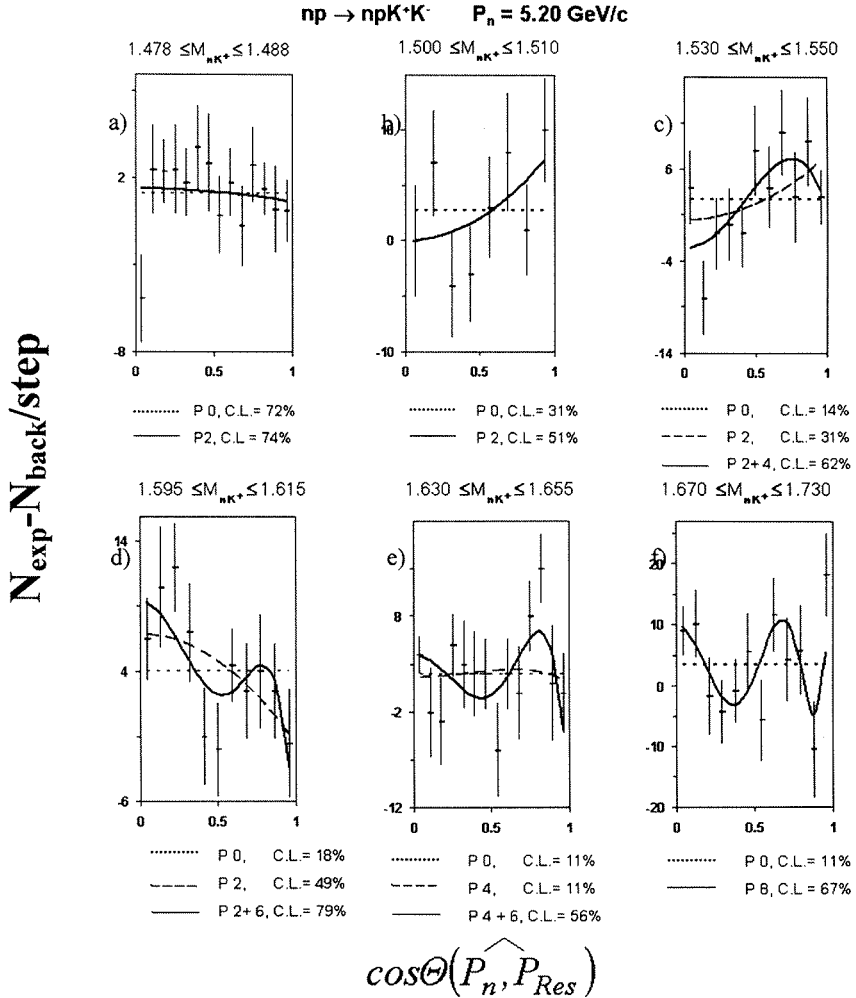


Fig.8. The distribution of the emission angles of a secondary neutron in the helicity coordinate system for the resonances with mass equal to: (a)  $M = 1.477 \text{ GeV}/c^2$ , (b)  $M = 1.505 \text{ GeV}/c^2$ , (c)  $M = 1.541 \text{ GeV}/c^2$ , (d)  $M = 1.606 \text{ GeV}/c^2$ , (e)  $M = 1.638 \text{ GeV}/c^2$ , (f)  $M = 1.687 \text{ GeV}/c^2$

Qualitative estimation can be made by examining the shape of the plots: they must have  $(2J-3)/2$  extrema and a “trivial” one at  $\cos\Theta = 0$ . That is, for spin  $J \geq 7/2$  there must be two extrema and a “trivial” extremum at  $\cos\Theta = 0$ , which is reasonably well exemplified by the plot of fig. 8d.

Figures 8e and 8f present the results of spin studies for heavier resonances. The resonance at  $1.630 < M < 1.655 \text{ GeV}/c^2$  has a spin value  $J \geq 7/2$  with a good confidence level, the resonance at  $1.670 < M < 1.730 \text{ GeV}/c^2$  has the spin value  $J \geq 9/2$  with an even larger confidence level. The high-mass resonance has week estimation, which is due to a rather low mass resolution at this region and the growing effect of the background on spin estimation in this region.

The results of the present work are presented in Tab. I.

Table I

$M_{exp} \pm \Delta M_{exp}$ $\text{GeV}/c^2$	$\Gamma_{exp} \pm \Delta \Gamma_{exp}$ $\text{GeV}/c^2$	$\Gamma_R \pm \Delta \Gamma_R$ $\text{GeV}/c^2$	$J_{exp}$	$S.D.$
$1.447 \pm 0.007$	$0.005 \pm 0.004$	$0.004 \pm 0.004$		3.2
$1.467 \pm 0.003$	$0.008 \pm 0.003$	$0.008 \pm 0.004$		2.3
$1.477 \pm 0.002$	$0.005 \pm 0.003$	$0.002^{+0.006}_{-0.002}$	1/2	3.0
$1.505 \pm 0.004$	$0.008 \pm 0.003$	$0.005 \pm 0.005$	3/2	3.5
$1.541 \pm 0.004$	$0.011 \pm 0.003$	$0.008 \pm 0.004$	5/2	6.8
$1.606 \pm 0.005$	$0.014 \pm 0.005$	$0.011 \pm 0.006$	7/2	5.2
$1.638 \pm 0.005$	$0.016 \pm 0.011$	$0.012^{+0.015}_{-0.012}$	7/2	3.6
$1.687 \pm 0.007$	$0.027 \pm 0.007$	$0.024 \pm 0.008$	9/2	6.8
$1.781 \pm 0.008$	$0.029 \pm 0.012$	$0.023 \pm 0.015$		4.1
$1.870 \pm 0.019$	$0.036 \pm 0.010$	$0.032 \pm 0.011$		5.9

The first column contains the experimental values of the resonance masses and their errors.

The second column contains the experimental values of the total width of the resonances.

The third column contains the true widths of the resonances and their errors.

The true widths of the resonances are found by a quadratic subtraction of the value of the mass resolution from the experimental value of the width. The mass resolution function [13] grows with increasing mass as:

$$\Gamma_{res}(M) = 4.2 \left[ \left( M - \sum_{i=1}^2 m_i \right) / 0.1 \right] + 2.8 ,$$

where  $M$  – the mass of the resonance,  $m_i$  – the rest mass of the particles composing this resonance,  $M$  and  $m_i$  are in  $\text{GeV}/c^2$ , coefficients 4.2 and 2.8 are in  $\text{MeV}/c^2$ . For instance, the value of the total width of the resolution function for the resonance with  $M = 1.541 \text{ GeV}/c^2$  is found to be  $\approx 7 \text{ MeV}/c^2$ .

The fourth column contains the values of the resonance spins. These are the lower limits of spins as explained in the discussion of the spin estimation procedure.

The fifth column lists the statistical significances of the resonances determined as the ratio of the number of events in the resonance to the square root of the number of background events under the resonance curve.

The estimation of the production cross section for the resonance at  $M = 1.541 \text{ GeV}/c^2$  in the  $nK^+$  system from the reaction  $np \rightarrow npK^+K^-$  at  $P_n = (5.20 \pm 0.12) \text{ GeV}/c$  is  $\sigma = (3.5 \pm 0.7) \mu\text{b}$ .

## 4. Discussion

We have attempted to systematize the obtained results using the formula for rotational bands suggested by Diakonov et al. [1, 2]:

$$M_J = M_0 + kJ(J+1), \quad (1)$$

where:  $M_J$  – the mass of the resonance,  $J$  – its spin,  $M_0$  – rest mass of the soliton,  $k$  – the inverse of twice the soliton moment of inertia (we use the terminology of paper [2]).

Under closer examination, the plots of the effective mass distribution of  $nK^+$  combinations (especially those in Fig. 4 constructed with a bin of  $5 \text{ MeV}/c^2$ ) one can observe that strong peculiarities are accompanied by weaker ones: a weak peculiarity at  $M = 1.467 \text{ GeV}/c^2$ , the bump in the mass region of  $M = 1.565 \text{ GeV}/c^2$  etc. That is why we performed the approximation of the mass distributions versus spin using two variants. Both of them are given in Tab. II, which shows good agreement between the experimental data and the formula (1). In Tab. IIa the largest predicted mass at  $1.901 \text{ GeV}/c^2$  ( $J = 13/2$ ) can be cut by the phase space on the right and be observed in experiments at a lower mass. In Tab. IIb no experimental values of masses and spins are available in the third and fifth lines. There are only bumps at these masses that are not provided statistically as resonances.

a)

$M_0 = 1.462 \text{ GeV}/c^2 \quad k = 0.0090$			
$J$	$M_J$	$M_{exp} \pm \Delta M_{exp}$	$J_{exp}$
1/2	1.469	$1.467 \pm 0.003$	
3/2	1.496	$1.505 \pm 0.004$	3/2
5/2	1.541	$1.541 \pm 0.004$	5/2
7/2	1.604	$1.606 \pm 0.005$	7/2
9/2	1.685	$1.687 \pm 0.007$	9/2
11/2	1.784	$1.781 \pm 0.008$	
13/2	1.901	$1.870 \pm 0.019$	

Table II

b)

$M_0 = 1.471 \text{ GeV}/c^2 \quad k = 0.0107$			
$J$	$M_J$	$M_{exp} \pm \Delta M_{exp}$	$J_{exp}$
1/2	1.479	$1.477 \pm 0.002$	1/2
3/2	1.511	$1.505 \pm 0.004$	3/2
5/2	1.565		
7/2	1.640	$1.638 \pm 0.005$	7/2
9/2	1.736		
11/2	1.854	$1.870 \pm 0.019$	

Taking the moments of inertia in the form of  $I = M_0 \cdot r^2$  and using the value of  $k = 1/2I$  from Tab. II one can determine the radius of the soliton. It proves to be approximately  $1.2 \text{ fm}$ , which is close to the  $\pi$ -meson radius ( $\approx 1.35 \text{ fm}$ ).

We have carried out another approximation of the observed rotational bands where the mass of an excited state depends not on of a resonance spin but on its orbital moment  $l$ :

$$M_l = M_0 + kl(l+1). \quad (2)$$

The results are presented in Tab. III: (a) – for “strong” resonances and (b) – for “weak” ones (as in Table II). The values of orbital moments are taken arbitrarily but so that they do not contradict the estimations of the spins. This approximations gives a better agreement with the experimental data. In addition, it takes in account the resonance with  $M = 1.447 \text{ GeV}/c^2$ , which is observed in most of presented distributions and is widely discussed in theoretical analysis.

With the assumption made about the orbital moments, the parity of the resonance at  $M = 1.541 \text{ GeV}/c^2$  is negative. When the value of its spin  $J = 5/2$  is also considered, it may be concluded that this resonance is not located on the top of the antidecuplet suggested in [1, 2].

But there exists a probability that on the top occurs the resonance with  $M = 1.501 GeV/c^2$ , with positive parity and spin equal to  $1/2$ . Our determination of the spin for the resonance with  $M \approx 1.505 GeV/c^2$  does not contradict to the fact that there can be found a resonance with  $M = 1.501 GeV/c^2$  ( $J^P = 1/2^+$ ) and a resonance with  $M = 1.507 GeV/c^2$  ( $J^P = 3/2^-$ ). In this case both of them are very narrow and are shifted relative to each other. This results in an average value of the experimental mass equal to  $M = 1.505 GeV/c^2$ . Thus, it is necessary to carry out very precise experiments both in mass resolution and in terms of the statistics.

Table III

a)			b)		
$M_0 = 1.481 GeV/c^2 \quad k = 0.0100$			$M_0 = 1.447 GeV/c^2 \quad k = 0.0100$		
$\ell$	$M_\ell$	$M_{exp} \pm \Delta M_{exp}$	$\ell$	$M_\ell$	$M_{exp} \pm \Delta M_{exp}$
0	1.481	$1.477 \pm 0.002$	0	1.447	$1.447 \pm 0.007$
1	1.501	$1.505 \pm 0.004$	1	1.467	$1.467 \pm 0.003$
2	1.541	$1.541 \pm 0.004$	2	1.507	$1.505 \pm 0.004$
3	1.601	$1.606 \pm 0.005$	3	1.567	
4	1.681	$1.687 \pm 0.007$	4	1.647	$1.638 \pm 0.005$
5	1.781	$1.781 \pm 0.008$	5	1.747	
6	1.901	$1.870 \pm 0.019$	6	1.867	$1.870 \pm 0.019$

**One further remark needs to be made.**

The problem of pentaquarks evolved as early as the 1960s. Ya.B.Zel'dovich and A.D.Saharov [14] were the first in interpreting the effects observed at that time in the  $p\pi^+\pi^+$  system as a manifestation of pentaquark states. Our first investigations [15] concerning this problem have given an impetus to the creation of a unique neutron beam [11] for 1-m HBC of LHE upon acceleration of deuterons at LHE's Synchrophasotron. In 1979 we reported [16] the observation of a rather narrow ( $\Gamma = 43 MeV/c^2$ ) resonance in the effective masses of  $\Delta^{++}\pi^+$  ( $\Delta^-\pi^-$ ) combinations with  $M = 1.440 GeV/c^2$  with a statistical significance of 5.5 SD. These resonances could be interpreted as five-quark states —  $uuuud$  ( $ddd\bar{d}\bar{u}$ ) for  $\Delta^{++}\pi^+$  ( $\Delta^-\pi^-$ ). Also, in [16] a Regge trajectory was constructed for the states with  $J=T$  and  $N, \Delta, E_{55}$  (observed by us at  $M = 1.440 GeV/c^2$ ) were shown to be on this trajectory. The slope of the trajectory was about  $1.680 (GeV/c^2)^{-2}$ .

The existence of such new resonances with  $J = T$  was predicted by A.Grigorian and A.Kaidalov in their studies of superconverged sum rules for Reggeon-particle scattering [17]. Their predictions agreed with our data.

In 1983 we have published another study with increased statistic [18]. Two more states were observed at  $M = 1.522 GeV/c^2$  and  $M = 1.894 GeV/c^2$ . Thus, the problem of states with more than three quarks is discussed for a long time and there are theories predicting them.

The problem of the number of quarks is, in our opinion, of no importance in the assumptions made by D.Diakonov, V.Petrov and M.Polyakov. The symmetry approach does not use the notion "quark" at all. This approach is very general and thus is much more important than the model approach.

As regards the experimental situation, we think of it as being very complicated. All experiments investigated the effects in the systems  $nK^+$  or  $pK_S^0$  reveal only one peak at the mass region from 1.530 to 1.540  $GeV/c^2$ . This is likely due to low incident energy, insufficient mass resolution, small statistics and a variety of samples in the experiments.

It seems to be now of crucial importance to observe at least one more resonance, to determine spins of at least two resonances and to estimate precisely their widths. The predicted law of increase in resonance width with an increase in its spins  $\Gamma \sim J^3/M^2$  [2] is very stringent. The width increases 125 times as the spin increases by a factor of 5, and the experiment will give some observations only if the masses of resonances do increase considerably, which is difficult for an observation and provokes a question as to whether the nonrelativistic approach used in the model of chiral soliton is valid.

### Acknowledgements

The authors are grateful to Dr. V.L.Lyuboshitz for the persistent help he has rendered us in our work for many years. We also thank Dr. E.A.Strokovsky and Dr. M.V.Tokarev for drawing our attention to the physical problem in question and for permanently providing us with valuable physical information. We are grateful to Dr. E.N.Kladnitskaya for some useful remarks.

Our thanks are also to all the researchers of JINR, who help us in data processing: laboratory assistants of LHE, and engineers of LIT attending the respective apparatus.

### References

1. D.Diakonov, V.Petrov, M.Polyakov. *Z.Phys.* A359, 305-314 (1997).
2. D.Diakonov *Acta Physica Polonica B*, No.1-2, Vol.25 (1994).
3. J.Ellis, M.Karliner, M.Praszalowich, hep-ph/0401127.
4. D.Borisyuk, M.Faber, A.Kobushkin, hep-ph/0307370.
5. D.Borisyuk, M.Faber, A.Kobushkin, hep-ph/0312213.
6. R.Jaffe, F.Wilczek, hep-ph/0307341.
7. S.Capstick, P.R.Page, W.Roberts, hep-ph/0307019.
8. D.Akers, hep-ph/0403142.
9. A.A.Arkipov, hep-ph/0403284.
10. T.Nakano et al. [LEPS Collaboration], *Phys.Rev.Lett.*91(2003)012002, hep-ex/0301020;  
V.V.Barmin et al. [DIANA Collaboration], *Phys.Atom.Nucl.*66(2003) 1715 [*Yad.Fis.*vol.66(2003) p.1763], hep-ex/0304040;  
S.Stepanyan et al. [CIAS Collaboration], hep-ex/0307018;  
J.Barth et al. [SAPHIR Collaboration], hep-ex/0307083;  
V.Kubarovsky AND S. Stepanyan and [CLAS Collaboration], hep-ex/0307088;  
A.E.Asratyan, A.G.Dolgolenko AND V.A.Kubantsev, hep-ex/0309042;  
V.Kubarovsky et al., [CLAS Collaboration], hep-ex/0311046;  
A.Airapetian et al., [HERMES Collaboration], hep-ex/0312044;  
S.Chekanov. [ZEUS Collaboration], <http://www.desy.de/f/seminar/Chekanov.pdf>;  
R.Togoo et al., *Proc.Mongolian Acad. Sci.*, 4(2003) 2;  
A.Aleev et al., [SVD Collaboration], hep-ex/0401024.  
P.Zh.Aslyanyan et al., hep-ex/0403044.
11. A.P.Gasparian et al. *JINR*, 1-9111, Dubna, 1975, *Pribory i Teknika Eksp.*, 1977, v.2, p.37.
12. Yu.A.Troyan et al., *Phys.Atom.Nuc.*, Vol.63, No.9, 2000, pp.1562-1573 [*Yad.Fiz.*, vol.63, No.9. 2000, pp.1648-1659].
13. Yu.A.Troyan et al., *JINR Rapid Communications* No.6[80]-96.
14. Y.A.B.Zeldovich, A.D.SAHAROV, *Yad.Fiz.*, 4, 395, 1966.
15. V.I.Moroz, A.V.Nikitin, Yu.A.Troyan, *JINR*, E1-3940, Dubna, 1968, *Yad.Fiz.*9, v.2, 1969.
16. A.Abdivaliev, C.Besliu et al., *Yad.Fiz.*29, v.6, 1979.
17. A.Grigorian, A.Kaidalov, *Yad.Fiz.*32, 1980, p.540;  
A.Grigorian, A.Kaidalov, *Pisma v JETF* 28, 318, 1978
18. A.Abdivaliev, C.Besliu et al., *Yad.Fiz.*37, v3, 1983.

# OBSERVATION OF $S=+1$ NARROW RESONANCES IN THE SYSTEM $K_s^0 p$ FROM $p+C_3H_8$ COLLISION AT 10 GeV/c

P.Zh.Aslanyan<sup>1,2†</sup>, V.N.Emelyanenko<sup>1</sup>, G.G. Rikhkvitzkaya<sup>1</sup>

(1) *Joint Institute for Nuclear Research*

(2) *Yerevan State University* † *E-mail: paslanian@jinr.ru*

## Abstract

Experimental data from the 2m propane bubble chamber have been analyzed to search for an exotic baryon state, the  $\Theta^+$  -baryon, in the  $pK_s^0$  decay mode for the reaction  $p+C_3H_8$  at 10 GeV/c. The  $pK_s^0$  invariant mass spectrum shows resonant structures with  $M_{K_s^0 p}=1540\pm 8$ ,  $1613\pm 10$ ,  $1821\pm 11$  MeV/ $c^2$  and  $\Gamma_{K_s^0 p}=9.2\pm 1.8$ ,  $16.1\pm 4.1$ ,  $28.0\pm 9.4$  MeV/ $c^2$ . The statistical significance of these peaks has been estimated as 5.5, 4.8 and 5.0 s.d., respectively. There are also small peaks in mass regions of 1690( 3.6 s.d.) and 1980(3.0 s.d.) MeV/ $c^2$ .

The investigation has been performed at the Veksler and Baldin Laboratory of High Energies, JINR.

## 1. Introduction

Recent experimental efforts have been strongly motivated by Diakonov, Petrov, Polyakov [1] who studied antidecuplet baryons by using the chiral soliton (Skyrme) models. The lightest member of the pentaquarks antidecuplet,  $\Theta^+(1530)$  -baryon predicted in [1], has positive strangeness, the mass of  $M=1530$  MeV/ $c^2$ ,  $1/2$  spin and even parity. Jaffe and Wilczek have suggested an underlying quark model structure of this state [2]. There are other theoretical speculations which have predicted this state [3]-[6]. The rotational states of the  $S=+1$   $\Theta^+$  baryon are shown in the paper by Akers[5]. Experimental evidence for  $\Theta^+(1530)$ -baryon with positive strangeness has come recently from several experimental groups (LEPS[7]), DIANA-ITEP [8], CLAS [9], SAPHIR [10], HERMES [11], SVD-2 experiment ,IHEP [12]). The bubble chamber method has observed a resonant structure in the  $pK_s^0$  and  $nK^+$  invariant mass spectrum [8],[13]-[16].

## 2. Method

A reliable identification of the above mentioned resonance needs to use 4 $\pi$ -detectors and high precision measurements of the sought objects. The bubble chamber is the most suitable instrument for this purpose [8],[13]-[18]. The experimental information of more than 700000 stereo photographs are used to select the events with  $V^0$  strange particles . The GEOFIT based on the Grind-CERN program[19] is used to measure the kinematics parameter of tracks momenta,  $tg\alpha$ ( $\alpha$  - depth angle) and azimuthal angle( $\beta$ ) in the photographs. The relative error of measuring momentum  $p$  and the average track length  $L$  of charged particles are found to be  $\langle \Delta p/p \rangle = 2.1\%$ ,  $\langle L \rangle = 12$  cm for stopping particles and  $\langle \Delta p/p \rangle = 9.8\%$ ,  $\langle L \rangle = 36$  cm for non stopping particles. The mean values of measurement errors for the dip and azimuthal angles are equal to  $\langle \Delta tg\alpha \rangle = 0.0099 \pm 0.0002$  and  $\langle \Delta \beta \rangle = 0.0052 \pm 0.0001$  (rad.).

The estimation of ionization, the peculiarities of the end track points of the stopping particles (protons,  $K^\pm$ ) allowed one to identify them. Protons can be identified over the following momentum range:  $0.150 \leq p \leq 0.900$  GeV/c. In the momentum range,  $p > 0.900$  GeV/c, protons couldn't be separated from other particles. Therefore, the experimental information has been analyzed similarly in two separate ranges.

## 2.1. Identification of $\Lambda$ and $K_s^0$

The events with  $V^0$  ( $\Lambda$  and  $K_s^0$ ) were identified by using the following criteria [20]-[22]: 1)  $V^0$  stars from the photographs were selected according to  $\Lambda \rightarrow \pi^- + p$ , neutral  $K_s \rightarrow \pi^- + \pi^+$  or  $\gamma \rightarrow e^+ + e^-$  hypothesis. A momentum limit of  $K_s^0$  and  $\Lambda$  is greater than 0.1 and 0.2 GeV/c, respectively ; 2)  $V^0$  stars should have the effective mass of  $K_s^0$  and of  $\Lambda$ ; 3) these  $V^0$  stars are directed to some vertices (complanarity); 4) they should have one vertex, a three constraint fit for the  $M_K$  or  $M_\Lambda$  hypothesis and after the fit,  $\chi^2_{\nu}$  should be selected over range less than 12; 5) The analysis has shown [21] that the events with undivided  $\Lambda$ ,  $K_s^0$  were appropriated events as  $\Lambda$  (Fig.1).

Figures 2(a,c) and 2(b,d) show the effective mass distribution of 8657-events with  $\Lambda$ , 4122-events with  $K_s^0$  particles and their  $\chi^2$  from kinematics fits, respectively. The measured masses of these events have the following Gaussian distribution parameters  $\langle M(K_s) \rangle = 497.7 \pm 3.6$ , s.d. = 23.9 MeV/c<sup>2</sup> and  $\langle M(\Lambda) \rangle = 1117.0 \pm 0.6$ , s.d. = 10.0 MeV/c<sup>2</sup>. The masses of the observed  $\Lambda$ ,  $K_s^0$  are consistent with their PDG values [23]. The effective mass of the  $\Theta^+ \rightarrow K_s^0 p$  system, like that of the  $\Lambda \rightarrow \pi^- p$  system, has been measured with a precision of  $\langle \Delta M_{(K_s^0 p)} / M_{(K_s^0 p)} \rangle \approx 1.1\%$ . Then the effective mass resolution of  $K_s^0 p$  system was estimated to be on the average 0.6% for identified protons with a momentum of  $0.150 \leq p \leq 0.900$  GeV/c.

The preliminary estimate of the experimental total cross sections is equal to  $\sigma = 3.8 \pm 0.6$  mb for  $K_s^0$  production in the  $p + ^{12}C$  collisions at 10 GeV/c.

## 3. $pK_s^0$ - spectrum analysis

### 3.1. $pK_s^0$ - spectrum for identified protons with a momentum of $0.350 \leq p_p \leq 0.900$ GeV/c

The  $pK_s^0$  effective mass distribution for 2300 combinations is shown in Fig.3. The solid curve is the sum of the background and 4 Breit-Wigner resonance curves.

The total experimental background has been obtained by two methods. In the first method, the experimental effective mass distribution was approximated by the polynomial function after cutting out the resonance ranges because this procedure has to provide the fit with  $\chi^2=1$  and polynomial coefficient with errors less than 10%. This distribution was fitted by the eight- order polynomial. The second of the randomly mixing method of the angle between  $K_s^0$  and p for experimental events is described in [24]. Then, these background events were analyzed by using the same experimental condition and the effective mass distribution  $pK_s^0$  was fitted by the eight-order polynomial. The analysis done by two methods has shown that while fitting these distributions had the same coefficients and order of polynomial.

The background for  $\overline{K}^0p$  combinations is estimated with FRITIOF model [25, 26] and no more than 10% has been obtained. No obvious structure in  $\overline{K}^0p$  spectrum is seen in Fig.3.

The statistical significance for the fit in Fig.3 has been calculated as  $NP/\sqrt{NB}$ , where NP is the number of events corresponding to the signal on the fitted background top and NB is the number of events corresponding to the background in the chosen area. There are significant enhancements in mass regions of 1540,1612 and 1821 MeV/c<sup>2</sup>. There are small peaks in mass regions of 1480 and 1980 MeV/c<sup>2</sup>.

### 3.2. $pK_s^0$ - spectrum for positively charged tracks with a momentum of $0.9 \leq p_p \leq 1.7$ GeV/c

The  $pK_s^0$  invariant mass spectrum shows resonant structures with  $M = 1515$  (5.3 s.d.) and 1690 MeV/c<sup>2</sup>(3.8 s.d.) in Fig.4. No obvious structure in mass regions of 1540,1610 and 1821 MeV/c<sup>2</sup> is seen in Fig.4. The FRITIOF [25, 26] model shows that the average multiplicity in this range for all positive tracks, protons and  $\pi^+$  is equal to 1.2, 0.4 and 0.8, respectively. The background for  $K_s^0\pi^+$  and  $K_s^0K^+$  combinations is equal to 46.6% and 4.4%, respectively. These observed peaks can be a reflection from resonances  $\Lambda(1520)$  and  $\Lambda(1700)$ . The ( $n\overline{K}^0$ ) invariant mass spectrum for events where  $\pi^+$ -meson was detected in reactions  $p+C_3H_8 \rightarrow \pi^+\overline{K}^0nX$  and its mass was substituted by the mass of neutron.

### 3.3. $pK_s^0$ - spectrum with a momentum of $p_p \geq 1.7$ GeV/c

The  $pK_s^0$  invariant mass distribution with a momentum  $p_p \geq 1.7$  GeV/c (3500 combinations) is shown in Fig.5. The histogram is approximated by a polynomial background curve and by 5 resonance curves taken in the Breit-Wigner form. The dashed curve is the background taken in the form of a superposition of Legendre polynomials up to the 6 -th degree, inclusive. The analysis done by two methods has shown that while fitting these distributions had the same coefficient and order of polynomial. The average multiplicity(FRITIOF) in this range for all positive tracks, protons and  $\pi^+$  is equal to 1.3, 0.8 and 0.5, respectively. Therefore the background for  $K_s^0\pi^+$  and  $K_s^0K^+$  combinations is equal to 20% and 5%, respectively. The estimate of contribution for  $\overline{K}^0p$  combinations with FRITIOF model is equal to 8%. No obvious structure in  $\overline{K}^0p$  spectrum is seen in Fig.5.

There are significant enhancements in mass regions of 1487, 1544, 1612 and 1805 MeV/c<sup>2</sup> (Fig.5). Their excess above background is 3.0, 3.9, 3.7 and 4.0 S.D.. There is a small peak in the mass region of 1685 MeV/c<sup>2</sup>.

### 3.4. The sum of $pK_s^0$ - spectrum

The total  $pK_s^0$  invariant mass distribution for identified protons and positively charged tracks  $p_p \geq 1.7$  GeV/c is shown in Fig.6. The solid curve is the sum of the background and 4 Breit-Wigner resonance curves. The background was fitted by the six-order polynomial. The total experimental background(dashed histogram) with the same experimental condition has been also obtained by the second method [24]. The dashed curve is the background taken in the form of a superposition of Legendre polynomials up to the 6 -th

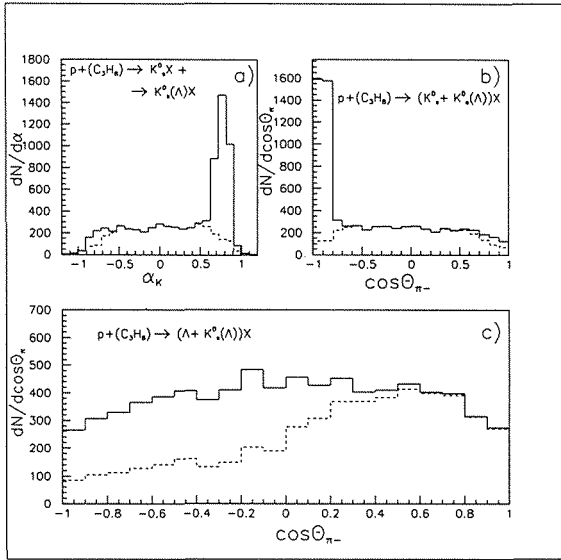


Figure 1: Distributions of  $\alpha$  (Armenteros parameter) and  $\cos\Theta^*$  are used for correctly identification of the undivided V0s.  $\alpha = (P_{\parallel}^+ - P_{\parallel}^-)/((P_{\parallel}^+ + P_{\parallel}^-))$ . Where  $P_{\parallel}^+$  and  $P_{\parallel}^-$  are the parallel components of momenta positive and negative charged tracks.  $\cos\Theta^*$  is the angular distribution of  $\pi^-$  from  $K_s^0$  decay. Distributions of  $\alpha$  and  $\cos\theta^*$  were isotropic in the rest frame of  $K_s^0$  when undivided  $\Lambda K_s^0$  were assumed to be events as  $\Lambda$

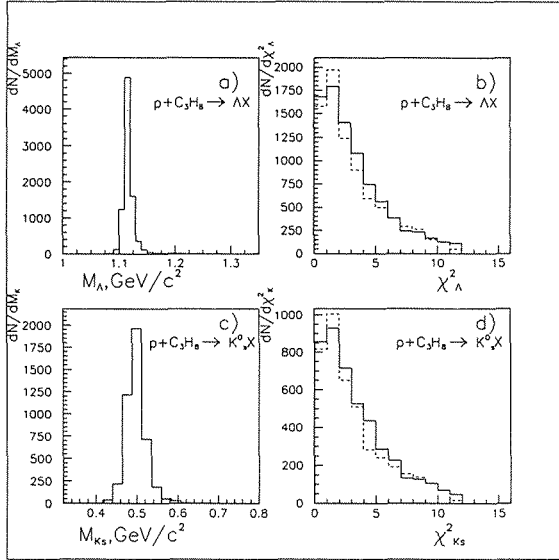


Figure 2: The distribution of experimental  $V^0$  events produced from interactions of beam protons with propane: a) for the effective mass of  $M_\Lambda$ ; b) for  $\chi_\Lambda^2(1V - 3C)$  of the fits via the decay mode  $\Lambda \rightarrow \pi^- + p$ ; c) for the effective mass of  $M_{K_s}$ ; d) for  $\chi_{K_s}^2(1V - 3C)$  of the fits via decay mode  $K_s^0 \rightarrow \pi^- + \pi^+$ . The expected functional form for  $\chi^2$  is depicted with the dotted histogram

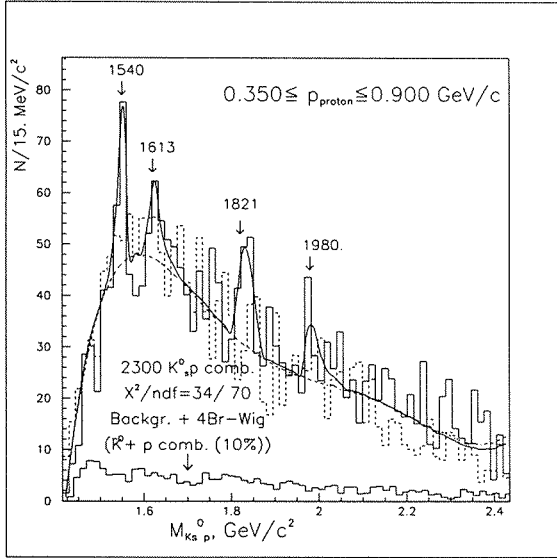


Figure 3: The  $(pK_s^0)$  invariant mass spectrum with a momentum of  $0.350 \leq p_p \leq 0.900 \text{ GeV}/c$  for identified protons in the reaction  $p + C_3H_8 \rightarrow (pK_s^0) + X$ . The solid curve is the sum of the experimental background (by the first method) and 4 Breit-Wigner resonance curves ( $\chi^2/ndf = 34/70$ ). The dashed histogram is the experimental background[24] taken in the form of by the eight-order polynomial (the dashed curve). The below histogram shows the simulated background for the spectrum of  $\overline{K^0}p$  combinations

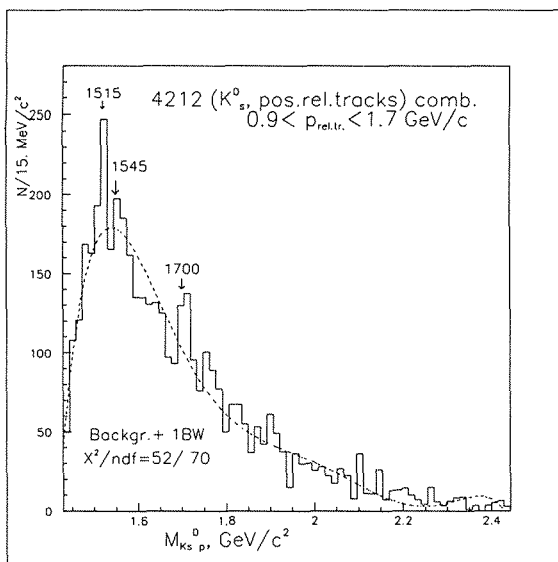


Figure 4: The  $(pK_s^0)$  invariant mass spectrum in the reaction  $p + C_3H_8 \rightarrow (pK_s^0) + X$ , where protons were selected as positively charged tracks with the cuts of a momentum  $0.9 \leq p \leq 1.7 \text{ GeV}/c$ . The dashed curve is the background distribution taken by the six-order polynomial

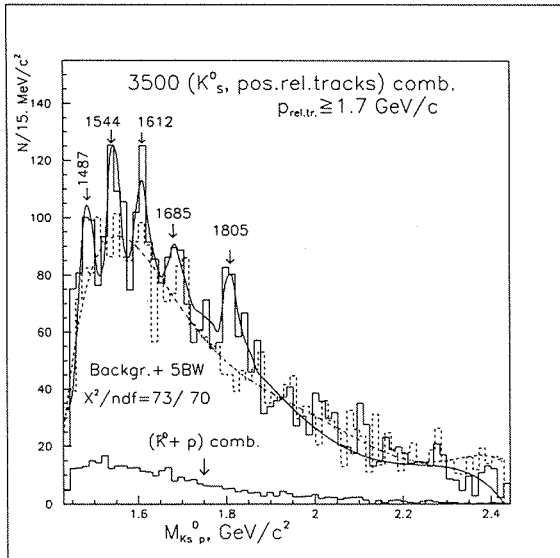


Figure 5: The  $(pK_s^0)$  invariant mass spectrum in the reaction  $p + C_3H_8 \rightarrow (pK_s^0) + X$ , where protons were selected as positively charged tracks with the cuts of a momentum  $p > 1.7 \text{ GeV}/c$ . The solid curve is the sum of the experimental background (by the first method) and 5 Breit-Wigner form resonance curves. The dashed histogram is the experimental background [24] taken in the form of by the six-order polynomial (dashed curve). The below histogram shows the simulated background for the spectrum of  $\bar{K}^0 p$  combinations

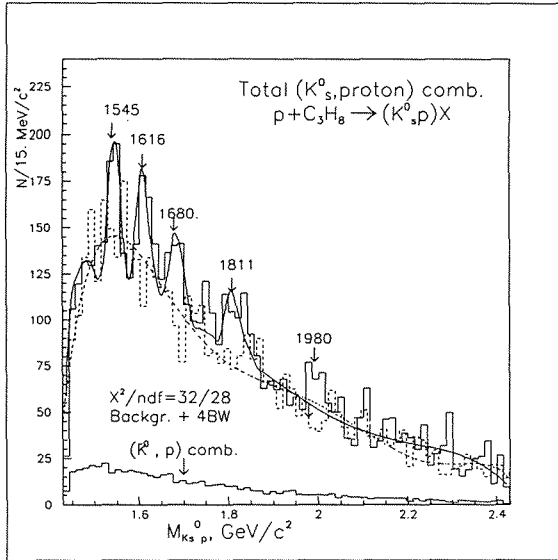


Figure 6: The sum of the effective mass distribution of  $(K_s^0, p)$  combinations for protons with a momentum  $0.350 \leq p \leq 0.9$  GeV/c and  $p > 1.7$  GeV/c. The solid curve is the sum of the experimental background (by the first method) and 4 Breit-Wigner resonance curves. The dashed histogram is the experimental background[24] taken in the form of by the six-order polynomial(the dashed curve). The below histogram shows the simulated background for the spectrum of  $K_s^0 p$  combinations

Table 1: The effective mass spectra  $K_s^0 p$  have resulted in the discovery of the peaks presented below

Resonance system	M MeV/ $c^2$	$\Gamma_e$ MeV/ $c^2$ Experiment	$\Gamma$ MeV/ $c^2$	The statistical significance $N_{sd}$
$K_s^0 p$	1540 $\pm$ 8	18.2 $\pm$ 2.1	9.2 $\pm$ 1.8	5.5 $\pm$ 0.5
$K_s^0 p$	1613 $\pm$ 10	23.6 $\pm$ 6.0	16.1 $\pm$ 4.1	4.8 $\pm$ 0.5
$K_s^0 p$	1821 $\pm$ 11	35.9 $\pm$ 12.0	28.0 $\pm$ 9.4	5.0 $\pm$ 0.6

degree, inclusive. In Fig.6, the below histogram shows the simulated background for the spectrum of  $\overline{K^0} p$  combinations.

There are significant enhancements in mass regions of (1545 $\pm$ 12), (1616 $\pm$ 10) and (1811 $\pm$ 11) MeV/ $c^2$ . Their excess above background by the second method is (5.5 $\pm$ 0.5), (4.8 $\pm$ 0.5) and (5.0 $\pm$ 0.6) S.D., respectively. There are small peaks in mass regions of 1690(3.6 s.d.) and 1980(3.0 s.d.) MeV/ $c^2$ .

## 4. Conclusion

The effective mass spectra  $K_s^0 p$  in collisions protons of a 10.0 GeV/c momentum with  $C_3H_8$  nuclei, have resulted in the discovery of the peaks presented below(Table 1). Table 1 shows the width( $\Gamma$ ) and the effective mass resonances which are based on the data from Fig. 3. The statistical significance in Table 1 is the based on the data from Fig.6. There are small peaks in mass regions of 1690 and 1980 MeV/ $c^2$ (Fig.6), their excess above background is 3.6 and 3.0 S.D., respectively. The primary total cross section for  $\Theta^+$ (1540) production in  $p + C_3H_8$ -interactions is estimated to be  $\approx 90\mu b$ .

## References

- [1] D. Diakonov, V. Petrov, and M. Polyakov, Z. Phys. A 359 , 305,1997.
- [2] R.L. Jaffe, SLAC-PUB-1774 Talk presented at th Topical Conf. on Baryon Resonances, Oxford, Eng., Jul 5-9, 1976;arXiv:hep-ph/0307341, 2003.
- [3] M. Karliner and H.J. Lipkin, Phys. Lett. B, 575 , 249, 2003.
- [4] J.Ellis, M.Karliner,M.Praszalowich, hep-ph/0401127, 2004.
- [5] D. Akers, arXiv.org:hep-ph/0311031, 2004.
- [6] A.A.Arkipov, arXiv:hep-ph/0403284, 2004.
- [7] LEPS Coll., T. Nakano et al., arXiv:hep-exp/0301020; Phys. Rev. Lett. 91 , 012002, 2003.
- [8] DIANA Coll., V. Barmin et al., arXiv:hep-exp/0304040; Phys. At. Nucl., 66 , 1715-1718, 2003;

- [9] CLAS Coll., V. Kubarovsky and S. Stepanyan, presented at the CIPANP2003, New York, NY, USA, May 19-24, arXiv:hep-ex/0307088, 2003.
- [10] SAPHIR Coll., J. Barthet et al., Phys. Lett., B 572, 2004.
- [11] HERMES Coll., A. Airapetian et al., arXiv:hep-ex/0312044, 2004.
- [12] SVD-2 experiment IHEP, A.Aleev et al., arXiv:hep-ex/0401024, 2004.
- [13] A.E. Asratayn et al., arXiv:hep-ex/0309042, 2003.
- [14] A.A.Kuznetsov, R.Togoo et al., Proc. of the Mangolian Academy of Sciences, v.170, N4, p.3, 2003.
- [15] P.Z.Aslyan et al., hep-ex/0403044, 2004.
- [16] Yu.A.Troyan et al., JINR, D1-2004-39, Dubna, 2004; arXiv:hep-ex/0404003(2004).
- [17] M.Balandin et al., Nucl.Instr. and Meth., 20., p.110, 1963.
- [18] A.I. Bondarenko et al., JINR Commun., Dubna, P1-98-292, 1998.
- [19] N.F.Markova, et al., JINR Commun., P10-3768, 1968.
- [20] G.N.Agakashiev et al., Yad. Fiz., 1986, 43(2), p.366, 373.
- [21] E.N.Kladnitskaya, K.J.Jovchev, P1-86-166 JINR, S.G. Arakelian et al., JINR Commun., 1-82-683, 1982.
- [22] P.Zh.Aslyan et al., JINR Communications, E1-2001-265, 2002.
- [23] Particle Data Group, K. Hagiwara et al., Phys. Rev. D. 66, 010001 (2002).
- [24] V.L.Lyuboshits et al., JINR Rapid Comm., N6(74), p209, 1995.
- [25] FRITIOF, H. Pi, Comput. Phys. Commun. 71, 173, 1992.
- [26] A.S.Galoian et al., JINR Commun., P1-2002-54, 2002.

# WAVELET ANALYSIS OF DATA IN PHYSICS OF RESONANCES

V.K.Henner <sup>1</sup>, T.S.Belozerova, P.G.Frick

*Perm State University, Perm, Russia*

## Abstract

The advantages that the wavelet analysis (WA) provides for resolving the structures in experimental data are demonstrated. Due to good scaling properties of the wavelets one can consider the data with various resolution which allows to separate the resonances from background and from each other. The WA is much less sensitive to the noise than any other analysis and allows substantially reduce the role of statistical fluctuations in data.

Key-words: wavelets, resonances, vector mesons.

1. In this short paper we would like to demonstrate the efficiency of wavelet transforms to reduce the role of fluctuations in experimental data. While the number of "candidates" to resonances rapidly grows, we think that some criteria helping to resist a temptation to associate so many peaks with resonances might be useful. In some cases the WA, that is independent on physical models and statistical arguments like  $\chi^2$ -level, can be a very good tool to separate noise contribution and peaks. Some peaks are stable to such separation (to small variation of noise), otherwise they can not be considered as possible resonance states. Then the stable peaks, distinguished from an experimental noise and background, can be easier associated with, for instance Breit-Wigner, resonance contributions that allows to extract resonance parameters more reliable.

As an example, we apply the WA to some data relevant to vector  $\rho'$  mesons.

The continuous wavelet transformation of a function  $f(t)$  representing the data is defined as:

$$w(a, t) = C_\psi^{-\frac{1}{2}} a^{-\frac{1}{2}} \int_{-\infty}^{+\infty} \psi^* \left( \frac{t-t'}{a} \right) f(t') dt'. \quad (1)$$

Argument  $t$  in our case is an energy. The decomposition (1) is performed by convolution of the function  $f(t)$  with a biparametric family of self-similar functions generated by dilatation and translation of the analyzing function  $\psi(t)$ :

$$\psi_{a,b}(t) = \psi \left( \frac{t-b}{a} \right), \quad (2)$$

where a scale parameter  $a$  characterizes the dilatation, and  $b$  characterizes the translation.  $C_\psi$  is a constant defined through the Fourier transformation of  $\psi(t)$ . Wavelet function  $\psi(t)$  is a sort of "window function" with a nonconstant window's width: high-frequency wavelets are narrow (due to the factor  $1/a$ ), while low-frequency wavelets are much broader. The function  $\psi(t)$  should be well localized in both time and Fourier spaces and must obey the admissibility condition,  $\int_{-\infty}^{+\infty} \psi(t) dt = 0$ . This condition implies that  $\psi$

---

<sup>1</sup>e-mail: [henner@psu.ru](mailto:henner@psu.ru)

is an oscillatory (but with the limited support) function and provides the existence of the inverse transformation:

$$f(t) = C_{\psi}^{-\frac{1}{2}} \int_{-\infty}^{+\infty} \int_0^{+\infty} \psi\left(\frac{t-t'}{a}\right) w(a, t') \frac{dt' da}{a^{5/2}}. \quad (3)$$

When the goal of WA is to recognize the local features of data, to find the parameters of dominating structures (location and scale/width), the so-called "Mexican Hat" (MH) wavelet is very often used:

$$\psi(t) = (1 - t^2)e^{-t^2/2}. \quad (4)$$

Let us give two examples similar to real data in physics of resonances. The first example is the model signal composed of several Gaussians with different widths and intensities:

$$f(t) = e^{-5(t-1)^2} + 2e^{-(t-6)^2/20} + 3e^{-10(t-10)^2} + e^{-(t-14)^2/10} + e^{-(t-18)^2}. \quad (5)$$

Then it was discretized with a step 0.1 on the interval  $0 < t < 20$  ( $f(t) \approx 0$  outside this interval) and a random high-frequency noise was added at each point to make it similar to real experimental data which will be analyzed in the next section. These simulated data are shown at the bottom of Fig.1*b*. In the left-hand part of this figure, above the simulated data, the Fourier reconstructions of the signal are given for different numbers of the Fourier harmonics. Keeping 20 harmonics is enough to localize all maxima except for the one at  $t = 14$  which is not resolved due to the noise that still exists in a smoother form in the restored signal. Moreover, many false maxima appear. When the number of harmonics decreases, the restored signal becomes smoother, but the localization of maxima changes significantly. The widths and amplitudes of all maxima have essentially changed.

The situation is quite different when the WA is applied. A very helpful representation of the WT, which allows to see the features of the signal, gives the "time-frequency" plane. This is a multiresolution spectrogram which shows the frequency (scale) contents of the signal as a function of time. Each pixel on the spectrogram represents  $w(a, t)$  for a certain  $a$  and  $t$ . Fig.1*a* shows the wavelet transformation  $w(a, t)$  performed by the MH. The sequences of dark and light spots indicate variations at corresponding scales. The location of a spot on the vertical axis (scale axis,  $a$ ) corresponds to the width of the extremum. The intensity of dark spots shows the amplitudes of maxima. The highest maximum at  $t = 10$  corresponds to the darkest spot that is located at the smallest value of  $a \approx 0.2$  corresponding to this narrowest maximum. The spot at  $t \approx 1$  is located at larger  $a \approx 0.35$  and is not so dark (lower and wider maximum in (5)). The dark region at the top of the figure demonstrates that in the large-scale region the whole signal is nothing but a wide maximum. The reconstructed signal is stable under small perturbations, that enables one to distinguish between "useful" large-scale stains (low frequencies in Fourier space) and contributions of the small-scale features usually generated by noise. The noise is located at the bottom of the wavelet plane (small-scale regions, or high frequencies). In order to separate the signal from the background noise, the wavelet reconstruction is performed for scales (scale parameter values) greater than a certain boundary scale  $a_{\text{noise}}$ . Reconstructions for different boundary scales are shown in Fig.1*b* (right-hand side). On

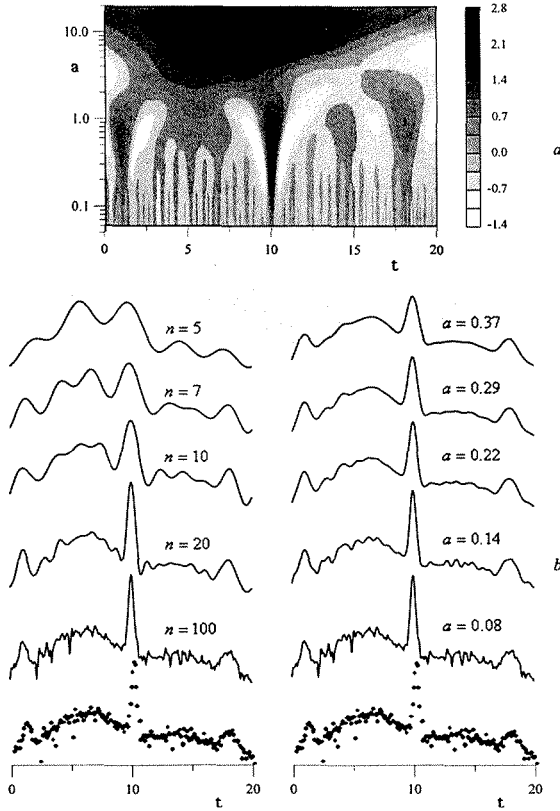


Figure 1: (a) Wavelet plane. (b) Model signal based on (5) and its Fourier reconstruction for different  $n$  – number of harmonics (left side); wavelet reconstruction with MH wavelet for different values of the boundary scale (the right side).

the upper two graphs the noise is practically damped, and even then the localization of all the maxima and their widths remains intact except for the width of the narrowest one at  $t = 10$ . The latter happens because the width of this peak is close to the width of noise-like fluctuations and this part of the signal alters with noise filtering. The actual experimental data we analyze below do not have very narrow peaks and we included such a peak in the model signal (5) in order to be able to discuss more general cases. Thus, Fig.1 illustrates that the WA is a substantially better description of the data at large enough values  $a$  than the Fourier description is at small numbers  $n$  – both these cases correspond to damped noise.

Another signal, similar to physics-of-resonances data, is generated by discretizing of a combination of several Lorentz-like peaks

$$f(t) = \frac{8}{(t-2)^2+4} + \frac{1}{(t-5)^2+1} + \frac{48}{(t-10)^2+16} + \frac{1}{4(t-15)^2+1}. \quad (6)$$

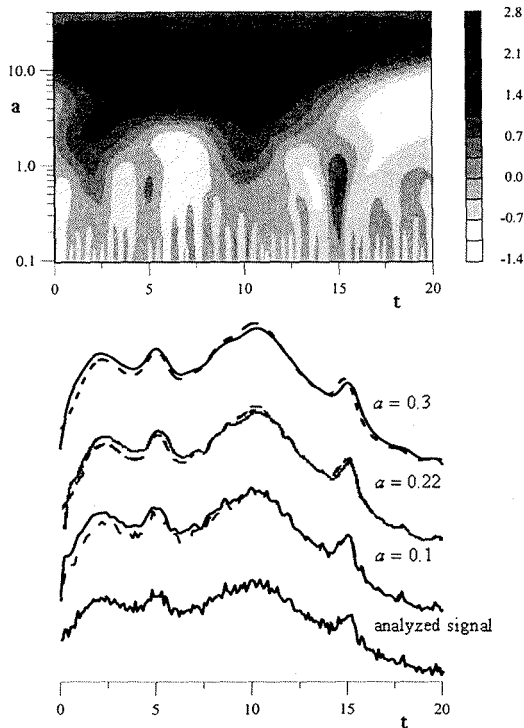


Figure 2: (a) Wavelet plane. (b) Model signal based on (6) and its reconstructions for different boundary scale  $a$  and different continuations below  $t_{\min}$ :  $f(t < 0) = 0$  – solid line,  $f(t < 0) = f(0)$  – dashed line

The peaks have very different widths, some of them substantially overlap. The signal was discretized with a step 0.1 on the interval  $0 < t < 20$  and a random high frequency noise was added at each point (in Fig.2b we use solid line for analyzed signal). Two different continuations for  $f(t)$  below  $t = 0$  were used to see the effect of the boundary conditions:  $f(t) = 0$  and  $f(t) = f(0)$ . (Since  $f(20) \approx 0$ , a natural continuation above  $t = 20$  is  $f(t) = 0$ .) Fig.2 gives the wavelet plane for the MH and the wavelet reconstruction of this signal. It is seen that the results of the WA of the signal (6) + noise are similar to those obtained for the signal based on (5).

The reconstructed data are obtained using the inverse transformation (3):

$$f_r(t) = \langle f \rangle + C_\psi^{-\frac{1}{2}} \int_{a_{\text{noise}}}^{a_{\text{max}}} \int_{t_{\text{min}}}^{t_{\text{max}}} \psi_{a,t}(t') w(a, t') \frac{dt' da}{a^{5/2}}. \quad (7)$$

The  $\langle f \rangle$  must be added to the reconstructed signal to restore the mean value of the original signal (recall, that the mean value of the WT is zero because an average value of any wavelet is zero). Formula (7) in the limit  $a_{\text{noise}} \rightarrow 0$ ,  $a_{\text{max}} \rightarrow \infty$ ,  $t_{\text{min}} \rightarrow -\infty$ ,  $t_{\text{max}} \rightarrow +\infty$  is equivalent to the exact relation (3), but in practice a limited number of experimental points on the restricted energy interval leads to a limited domain in the integral (7). To fill in the gaps between experimental points we use a linear interpolation. In practice different interpolations lead to a small difference in the restored signal (that produces a very small difference on a lower part of the wavelet plane corresponding to noise). To show that, in the case of rather rare coverage in the energy scale in the data we used two interpolations: linear and quadratic spline. Also note one of the big advantages of the WA: very low sensitivity of the restored signal to any physically reasonable continuation of the "data" outside the interval  $(t_{\text{min}}, t_{\text{max}})$ , where the data are known.

2. Here we have room for three figures relevant to  $\rho'$  states. The WT localizes the structures in a fashion that allows to estimate the masses of the resonances and their widths before the reconstruction of the data and their physical analysis is made.

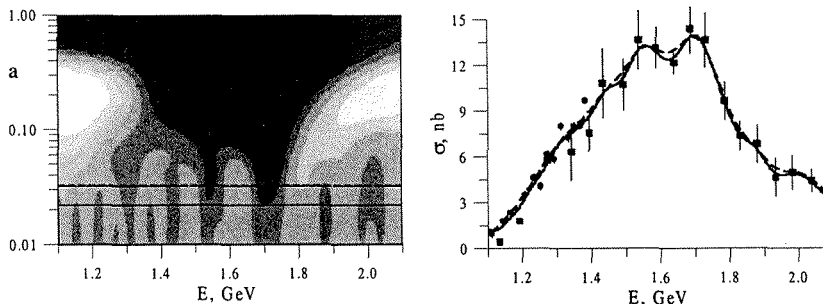


Figure 3: Cross section  $e^+e^- \rightarrow \pi^+\pi^-2\pi^0$  with subtracted contribution from  $\omega\pi^0$ . Wavelet plane and two reconstructions of the data [5, 6] for different cutoff values  $a_{\text{cutoff}}$

The straight horizontal lines correspond to the boundary scale  $a_{\text{noise}}$  which cuts off the small scale structures. The curves in the figures are the reconstructed data obtained using the inverse transformation (7). The cutoff value  $a_{\text{noise}}$  corresponds to the smallest structure included in the reconstructed data. The width of such structure can be estimated with the width of the MH wavelet at its half-height,  $\Gamma \approx 1.5a$ . It is reasonable to assume that a resonance structure to be reliably resolved should include at least three experimental points. In the data we analyze, a distance between experimental points is 0.01 GeV or larger, and the smallest structures we are looking for have  $\Gamma_{\text{min}}$  not less than 0.03 GeV. This value 0.03 GeV corresponds to the value  $a_{\text{noise}} = 0.02$  GeV which we use in this section.

For  $e^+e^- \rightarrow \pi^+\pi^-\pi^0\pi^0$  with subtracted contribution from  $\omega\pi^0$ , Fig.3, two obvious maxima are seen around 1.55 and 1.7 GeV with widths about 0.08 and 0.1 GeV. Two other maxima are seen to occur around 1.3 and 2.0 GeV. All these structures are stable for variation of  $a_{\text{noise}}$ : its reduction by a factor of almost two does not change the locations of the peaks and their shapes.

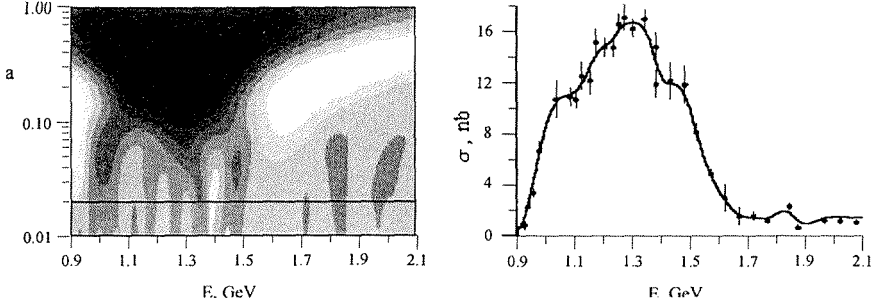


Figure 4: Cross section  $e^+e^- \rightarrow \omega\pi^0$ . Wavelet plane and reconstruction of the data [5, 7]

For  $e^+e^- \rightarrow \omega\pi^0$ , Fig.4, a wide structure is located at about 1.25 GeV. A decrease of the cutoff scale causes splitting of that major maximum – two maxima occur at 1.05 and 1.45 GeV. Three more smaller structures can be recognized between these two. There are also two structures at about 1.85 and 2.0 GeV. The scale values corresponding to these structures are close to reliable values of  $a_{\text{noise}}$ . It can be observed that except 1.25 and 1.45 GeV states no dominating scales can be attributed to other states.

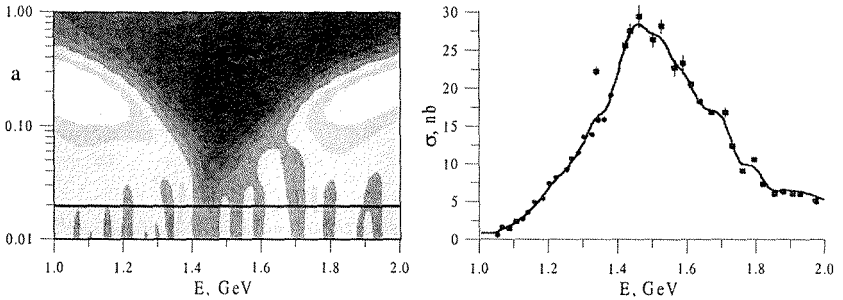


Figure 5: Cross section  $e^+e^- \rightarrow 2\pi^+2\pi^-$ . Wavelet plane and reconstruction of the data [5, 6] for cutoff value  $a_{\text{cutoff}} = 0.018$

For  $e^+e^- \rightarrow \pi^+\pi^+\pi^-\pi^-$ , Fig.5, the most obvious maxima are located at about 1.45 and 1.7 GeV with widths about 0.1 and 0.05 GeV, respectively. At greater value of  $a$  these two maxima appear as one wide maximum around 1.55 GeV and width about 0.2 GeV. The situation we are describing reminds a former  $\rho'(1600)$  that was later resolved in two states. For energy above the 1.7 GeV maximum, several small and unstable to  $a_{\text{noise}}$  variation maxima are seen.

Let us note one more thing related to fluctuations. While small-scale structures located at the bottom of wavelet plane correspond to experimental noise, the structures in intermediate part of the wavelet plane can be of different nature. Dark spots (related to big amplitude of the wavelet coefficient  $w(a, E)$ ), resolved in frequency, occur where the structure of the signal is similar to the wavelet shape and size at this location  $(a, E)$ . Thus, such spots are most likely associated with resonances. There might also be dark "horns" (usually less intense than in the previous case) reaching high frequencies from the area of low or intermediate frequencies, and not having relatively well resolved maximum intensity (looking like a "knee-cap"). Such "horns" should also be checked for association with resonances (using some physical models), but most likely they are related to noise fluctuations with big amplitude (when one or few experimental points substantially "jump" up or down with respect to their neighbors).

Thus, the WA indicates the  $\rho'$  states with masses 1.05–1.25, 1.4, 1.6–1.85, and 2.0–2.2 GeV and widths of about 0.1 GeV which makes sense to include in further analysis that should be based on some physical models. The first and the last states are sensitive to high-frequency noise that makes them questionable. A discussion above on a stability of those states under noise contribution can help evaluate a reliability of the results of further analyses. The PDG[1] contains the references to experimental works related to  $\rho'$  states with masses close to all the listed above. Some of these states are questionable and the parameters of all states are known with a large uncertainty mostly due to fluctuations in experimental data. The WA shows that some experimental data are statistically inadequate in sense that they do not allow to separate the noise fluctuations. The method gives the criteria for distinguishing between "stable" and "unstable" data – the latter do not reproduce the same essential structures when a contribution of the experimental noise changes slightly. Technically it means that the structure (resonance) is questionable if it is sensitive to the noise cutoff value. Interestingly this criterion supports  $\rho'$  at about 1.45 and 1.65–1.70 GeV, in accord with the assessment in the current PDG[1] compilation.

3. Numerous applications of wavelets to data analysis in different fields of mathematics and physics have proved themselves to be a powerful tool for studying the fractal signals and data (see, for instance [2]). This technique can be successfully applied to some problems of nuclear and high-energy physics where the wavelet analysis can work as a tool for studying the energy scaling of the process.

In the case of one isolated resonance, or several resonances with the same quantum numbers that are very distant from each other, the wavelet image of data gives practically direct information about the mass and total width of each resonance. When resonances overlap, their physical parameters can be found with an appropriate partial wave analysis, for instance with modified Breit-Wigner approach preserving unitarity for the case, when resonances overlap[3, 4]. Fitting the data with suppressed noise gives more reliable results for resonances' parameters.

## References

- [1] D.E.Groom *et al.*, Eur.Phys.J. C **15**, 1 (2000).
- [2] I.M. Dremin, O.V. Ivanov, V.A. Nechitailo, Usp. Fiz. Nauk, **171**, 465 (2001).
- [3] V.K. Henner and T.S. Belozerova, Yad. Fiz. **60**, 1998 (1997).

- [4] T.S. Belozerova and V.K. Henner, *Phys. Part. Nucl.* **29**, 63 (1998).
- [5] L. Stanco, in *Proceedings of the International Conference on Hadron Spectroscopy, College Park, Maryland, 1991*, p.84.
- [6] R.R. Akhmetshin *et al.*, *Phys. Lett. B* **446**, 392 (1999).
- [7] M.N. Achasov *et al.*, *Phys. Lett. B* **486**, 29 (2000).

# DIBARYONS IN HADRONIC PHYSICS AND NUCLEAR STRUCTURE

V.I. Kukulin<sup>1†</sup> and M.A. Shikhalev<sup>2</sup>

(1) *Institute of Nuclear Physics, Moscow State University*

(2) *Veksler and Baldin Laboratory of High Energies, JINR, Dubna*

† *E-mail: kukulin@nucl-th.sinp.msu.ru*

## Abstract

Numerous phenomena in hadronic physics and nuclear structure where the incorporation of dibaryonic degrees of freedom gives the keys for their proper understanding and consistent quantitative interpretation have been analysed. Main focus is on the following topics: formulation of the dibaryon model for nuclear force in terms of an effective field theory; effects of new  $3N$ - and  $4N$ -scalar forces on nuclear structure; enhancement of the near-threshold  $\pi^0$  and  $2\pi$  production in  $pp$ ,  $pd$ , etc. collisions; the hint for an explanation of the long-term ABC-puzzle and an enhanced yield of cumulative mesons and other hadrons (studied experimentally mainly by Baldin and coworkers at JINR in  $pA$ ,  $dA$ , etc. collisions); new electromagnetic currents in deuteron and few-nucleon systems, and large effects in electroweak processes accompanying with high momentum transfer.

## 1. Introduction. Key problems in traditional OBE-picture of strong interaction of nucleons

One of the main difficulties in conventional one-boson-exchange (OBE) models of  $NN$  interaction is their inability to describe in a consistent way many phenomena accompanying with a large momentum transfer from one nucleon to the others at physically acceptable values of cut-off parameters  $\Lambda_{\pi NN}$ ,  $\Lambda_{\pi N\Delta}$ , etc. ( $\sim 0.5 - 0.7$  GeV). This difficulty with the proper description of the short-range  $NN$ -correlations in nuclei is tightly interrelated to (generally poorly known) nature of short-range  $NN$ -force. For example, there are numerous problems [1, 2, 3, 4] with a consistent interpretation of the short-range  $NN$ -force in terms of OBE-model via scalar and vector meson exchanges. This general difficulty can clearly be illustrated by two recent experiments:  $d(e, e'p)$  [5] and  ${}^3\text{He}(e, e'pp)$  [6] and the respective theoretical efforts to interpret these consistently in terms of conventional meson-exchange currents. Disagreement with the data for  ${}^3\text{He}(e, e'pp)$  is especially evident because even the trends of theoretical curves and the experimental data are opposite, and also since the experiment with  ${}^3\text{He}$  measures just the  $pp$  short-range correlation in the nucleus. The above discrepancy between the traditional force models and the experiments can be followed up also much farther both in high-energy experiments  ${}^3\text{He}(e, e'NN)$  performed recently at JLab [7, 8] and in intermediate-energy experiments  $A(\gamma, 2p)$  done at Mainz facility [9]. Semi-quantitative theoretical interpretations suggested for these data seems put even more questions than give answers.

Another fundamental difficulty with conventional OBE-models for the  $NN$ -interaction is a source for intermediate-range  $NN$  attraction associated usually with the scalar-isoscalar  $\sigma$ -meson exchange. As was demonstrated in two recent independent works [10, 11], the two-pion exchange supplemented with the  $S$ -wave  $\pi\pi$  interaction giving the

$\sigma$ -meson leads to a strong central  $NN$  repulsion and fully repulsive spin-orbit force, which is just opposite to those one needs in real situation. Thus, the  $t$ -channel  $\sigma$ -meson exchange which is responsible in traditional OBE-models for the basic  $NN$  attraction at intermediate ranges is not valid and the fundamental problem arises: what is the source for such strong  $NN$  attraction. In our previous works [2, 3, 4], we have given some (very plausible) answer to this question (see below).

Still another difficulty with the conventional OBE-models is heavy meson (e.g.  $\rho$ ,  $\omega$ , etc.) exchange which is responsible for the short-range  $NN$ -interaction within the OBE-approach. In fact, if the heavy meson mass takes the value  $m \simeq 800$  MeV the characteristic radius for the respective exchange force  $r_m \sim m^{-1} \simeq 0.2 - 0.3$  fm (the Compton scattering length) which is much less than the quark radius of the nucleon ( $r_N \simeq 0.6$  fm). So, two nucleons are filling the above heavy-meson exchange when they are overlapped strongly to each other. Thus, the heavy meson is moving simultaneously in the field of two  $3q$  cores. And in such a case one should first justify the employment of free space  $g_{\rho NN}$  and  $g_{\omega NN}$  coupling constants and even a local character for such a coupling (it should be highly nonlocal).

There are also many other problems in the traditional OBE-picture for the basic  $NN$ -force, but those mentioned above can be considered as the most important ones (see e.g. some review in Refs [2, 3, 4]).

## 2. Dibaryon model for nuclear force: new effective-field theory approach

The developed field theoretical picture [4] allows to carry out a natural matching between the field theory approach at low-energies (where ChPT is fully applicable) and the high energy region. In both regions one can now formulate a field theoretical language. In our approach, the peripheral, i.e. the “external” part of  $NN$ -interaction is described by the conventional  $\pi$ - and  $2\pi$ -exchanges in the  $t$ -channel while the intermediate and short range interaction is described via generation of an intermediate dressed dibaryon which can be represented as a color quantum string able to vibrate and rotate. The schematic evolution for this process is depicted in Fig. 1. To be more specific, we assume when the

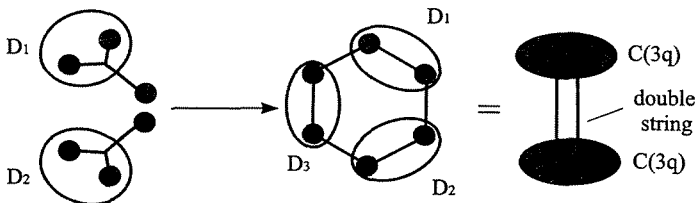


Figure 1: Possible mechanism of dibaryon formation.  $D_i$  means that there are possible diquark correlations in dibaryon.

two quarks belonging to different  $3q$ -clusters interact and exchange a color, this can lead to the formation of either a nonconfined six-quark state (i.e.  $NN$ ,  $N\Delta$ , etc.) or a confined

6 $q$ -state. The first non-resonance process is, in fact, analogous in action to conventional meson exchange, while the second leads to formation of a hidden color  $CC$ -state.

The  $NN \rightarrow D(CC) \rightarrow NN$  transition amplitude is described through the non-local Lagrangian density:

$$M_{fi} = i\langle 4, 3|T \left[ e^{i \int dx dx' \mathcal{L}_{\text{int}}(x, x')} \right] |2, 1\rangle - i\langle 4, 3|I|2, 1\rangle. \quad (1)$$

Here  $T$  means time-ordering while the bra and ket  $|2, 1\rangle$  and  $\langle 4, 3|$  relates to the initial and final nucleons with 4-momenta  $p_2, p_1$  and  $p_4, p_3$  respectively. The second term in (1), where  $I$  is the unit matrix, corresponds to the propagation of noninteracting nucleons and thus must be subtracted.

The nonlocal Lagrangian density in Eq. (1) corresponding to transition from the two-nucleon to a bare dibaryon state, and the subsequent dibaryon dressing can be written in the form:

$$\mathcal{L}_{\text{int}}(x_1, x_2) = \mathcal{L}_{DN} + \mathcal{L}_{Dm}, \quad (2)$$

where the Lagrangian

$$\mathcal{L}_{DN} = \tilde{N}(x_2)\{\Psi(x_1, x_2)V_0(x_1 - x_2) + \gamma_5\gamma^\mu\Psi_\mu(x_1, x_2)V_1(x_1 - x_2)\}N(x_1) + \text{h.c.} \quad (3)$$

is odd on dibaryon field operators  $\Psi$  and  $\Psi_\mu$ , and the Lagrangian  $\mathcal{L}_{Dm}$  describing the interaction of 6 $q$ -bag with its meson cloud, is even on  $\Psi$ 's. The function  $\Psi(x_1, x_2)$  describes the dibaryon with spin  $S = 0$ , while  $\Psi_\mu(x_1, x_2)$  corresponds to the  $S = 1$  dibaryon (in both cases the isospin is assumed to have the value  $I = 0$ , for the case of isospin  $I = 1$  we should make a replacement  $\Psi \rightarrow \tilde{\tau}\tilde{\Psi}$  in (2)). The bispinor  $\tilde{N} \equiv N^T C^{-1} \gamma_5 i \tau_2$  has the same transformation properties as the Dirac-conjugated nucleon-field operator  $\bar{N} = N^\dagger \gamma_0$  in the Lorentz and isospin groups,  $C = i\gamma_2 \gamma_0$  is the charge-conjugation operator,  $\tau_2$  is a Pauli matrix, and  $N^T$  stands for a transposed matrix. The interaction  $V(x)$  (where  $x = x_1 - x_2$ ) relates to the transition vertex  $NN \rightarrow D$ . The dibaryon wavefunctions are taken as a convolution of orbital and total spin parts:  $\Psi(x_1, x_2) = \Phi(x; P) \otimes S(X; P)$ , where the orbital part  $\Phi(x; P)$  is a superposition of covariant harmonic oscillator eigenfunctions.

From Eqs. (1) and (3), it is evident that the transition amplitude must be even on dibaryon field operator and is at least of the second order in interaction with a nucleon current. As a result, one has the following expression for  $M_{fi}$  (in  $I = 0$  channel):

$$M_{fi} = \frac{1}{2!} \sum_S \int d^4x_1 d^4x_2 d^4x_3 d^4x_4 \langle 4, 3| \bar{N}(x_4) \Gamma_S^\dagger \tilde{N}(x_3) \times \mathcal{G}^S(x_3, x_4; x_1, x_2) \tilde{N}(x_1) \Gamma_S N(x_2) |2, 1\rangle V_S(x_1 - x_2) V_S(x_3 - x_4), \quad (4)$$

where  $\mathcal{G}^S(x_3, x_4; x_1, x_2)$  is an exact dibaryon propagator that takes into account the dressing of the dibaryon with meson fields. The vertices  $\Gamma_S$  are equal:

$$\Gamma_S = \begin{cases} 1, & S = 0, \\ \gamma_5 \gamma_\mu, & S = 1. \end{cases} \quad (5)$$

The dressed dibaryon propagator is found by solving the respective Dyson equation

$$\mathcal{G}^S(x_3, x_4; x_1, x_2) = G^S(x_3, x_4; x_1, x_2) + \int d^4x'_1 d^4x'_2 d^4x'_3 d^4x'_4 G^S(x_3, x_4; x'_3, x'_4) \Pi^S(x'_3, x'_4; x'_1, x'_2) \mathcal{G}^S(x'_1, x'_2; x_1, x_2), \quad (6)$$

where the bare dibaryon propagator expanded into the string eigenstates (with  $J, L$  being the total and orbital angular momenta and  $N_e$  being the number of excitation quanta of the string) is:

$$G^S(x_3, x_4; x_1, x_2) = -i \sum_{J, L, N_e} \langle 0 | T_{X, X'} [\Psi_{LS}^{JN_e}(x_3, x_4) \Psi_{LS}^{JN_e}(x_1, x_2)] | 0 \rangle. \quad (7)$$

and  $\Pi^S$  stands for a polarization operator of the dibaryon. Here, the time-ordering is performed with respect to the coordinates  $X$  and  $X'$  of the dibaryon center of mass.

The dibaryon polarization operator  $\Pi^S$  is determined, for example, in even partial waves mainly by the  $D\sigma$  and  $D\pi$  loops, while its imaginary part is largely determined by the  $NN$  loops and these loops are responsible for dibaryon decay back to two real nucleons. Hence, in our case, if we want to construct the  $NN$ -potential, we must exclude coupling to an intermediate nucleon-nucleon state. This is because of the fact that in the scattering equation (e.g. Bethe–Salpeter or any quasipotential equation), such channels are automatically taken into account by virtue of the requirement that the scattering equation satisfies two-particle unitarity. Therefore, the main contribution to the polarization operator comes from the dressing of the dibaryon with its meson cloud. This interaction induces a transition of the dibaryon (featuring  $N_e \geq 2$  string-excitation quanta) to the ground state  $|s^6\rangle$  at low energies.

We also note that, in the present model, the polarization operators (and consequently the  $NN$ -potential as well) are complex-valued functions. Their imaginary parts are related to open inelastic channels and are determined by the discontinuities of these quantities at the unitary cut in the complex energy plane. In the example considered here, we have two inelastic channels corresponding to real intermediate states,  $NN\pi$  and  $NN\pi\pi$  (shown in Fig. 2), where the latter is associated with the mechanism of  $\sigma$ -meson decay to two real pions.

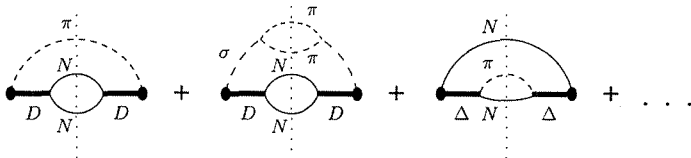


Figure 2: Several of the possible loops taken into account in calculation of polarization operator of dibaryon. They correspond to the dressed bag state

After some algebra manipulations, it is straightforward albeit quite lengthy to write down from the amplitude (4) the expressions for the dibaryonic part of  $NN$  potential in different partial channels [4]. It is worth to emphasize here that, at the value of the string excitation quantum  $\Omega \approx 300 - 350$  MeV, taking up to two-quanta excitations of the string will be sufficient for description of  $NN$ -interaction from zero energy until 1 GeV or even higher, while account of four-quanta excitations is sufficient for description of interaction in  $NN$ -channel or the  $NN$  meson-production processes up to energies of  $E_{\text{lab}} \approx 3$  GeV.

After the complete derivation of the covariant  $NN$ -potential in various partial waves we should add this short-range interaction to the peripheral one-pion and two-pion exchange potentials derived previously in ChPT (but with the short-range contact terms being

parameterized in a purely phenomenological manner) or alternatively, we should replace the contact terms in the ChPT-approach with the covariant short-range potential derived in our field-theoretical approach. The resulting full  $NN$ -potential can be fitted first in the low-energy region,  $E_{\text{lab}} \leq 300$  MeV and by this way the main input parameters of the short-range part of interaction (e.g. the coupling constants of the meson fields with the string) can be established. This procedure is similar in some degree to fitting the parameters of contact terms in higher-order ChPT.

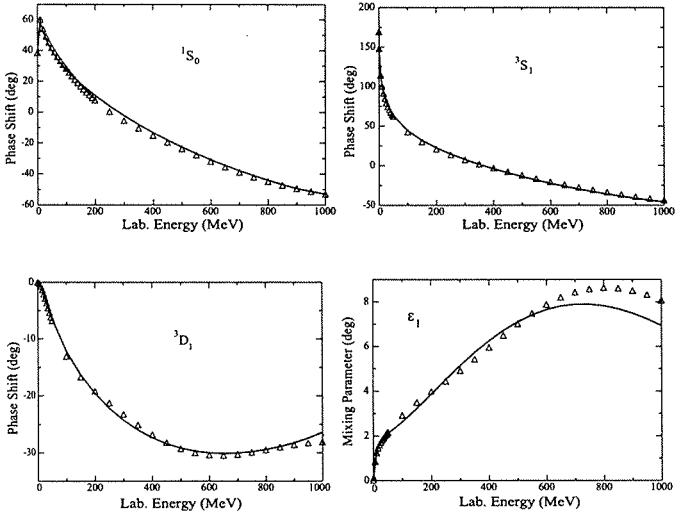


Figure 3: The comparison between the theoretical fits (with the  $NN$  potential model similar to that derived here) for some lower  $NN$  phase shifts and respective phase shift analysis (taken from SAID)

Thus, by combining the low-energy and high-energy effective field theories one can reach a very consistent and fully dynamical description of elastic and inelastic  $NN$ -interaction from zero energy up to the GeV region. It has been shown [4] that when doing the nonrelativistic reduction of the derived relativistic potentials we get the formulas very similar to those obtained in our previous fully microscopic semi-relativistic approach [3, 4] and thus the derived forms for the low partial waves can fit almost perfectly the  $NN$  lower phase shifts up to energies of 1GeV (see Fig. 3) as well as static deuteron properties shown in Table 1.

### 3. Dibaryons in hadronic physics

Incorporation of the dressed dibaryon mode into the  $NN$ -collisions has very numerous implications in hadronic physics and also in the dynamics of heavy nucleus collisions. One of the most indicative manifestation for the dibaryon mode should be in  $\pi^0$ - and

Table 1: Deuteron properties in the dressed bag model

Model	$E_d(\text{MeV})$	$P_D(\%)$	$r_m(\text{fm})$	$Q_d(\text{fm}^2)$	$\mu_d(\mu_N)$	$A_S(\text{fm}^{-1/2})$	$\eta(D/S)$
RSC	2.22461	6.47	1.957	0.2796	0.8429	0.8776	0.0262
Moscow 99	2.22452	5.52	1.966	0.2722	0.8483	0.8844	0.0255
Bonn 2001	2.224575	4.85	1.966	0.270	0.8521	0.8846	0.0256
DBM (1) $P_{\text{in}} = 3.66\%$	2.22454	5.22	1.9715	0.2754	0.8548	0.8864	0.0259
DBM (2) $P_{\text{in}} = 2.5\%$	2.22459	5.31	1.970	0.2768	0.8538	0.8866	0.0263
experiment	2.224575		1.971	0.2859	0.8574	0.8846	0.0263

$2\pi$ -productions in  $pp$ ,  $pd$ , etc. collisions at GeV region. It has to be noted that the above production processes should be tightly interrelated to the strong  $\sigma$ -field in dibaryon, which, on the other hand, is responsible for the strong effective attraction in  $NN$ -channel within our approach. Thus, the enhancement of the  $2\pi$ -production in scalar-isoscalar channel can be explained quite naturally by a disclosing  $\sigma$ -meson loops in the dibaryon dressing graph with subsequent breakup of the  $\sigma$ -meson into the two-pion state (see Fig. 4(a)). Within

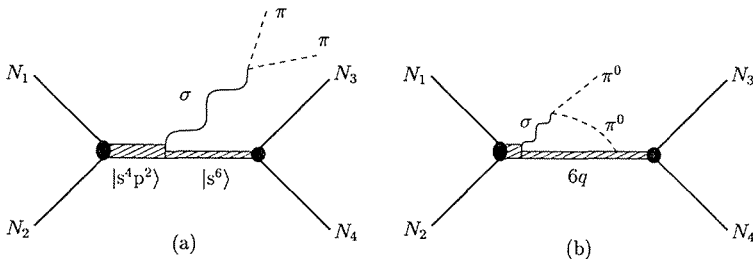


Figure 4: Example of diagrams describing a new possible mechanisms of meson production. Diagram (a) corresponds to an enhancement of the double pion production in the scalar-isoscalar channel, whereas diagram (b) describes the new mechanism for the near-threshold  $\pi^0$  production

the same framework the enhancement of the near-threshold  $\pi^0$  production in  $pp$ -collision can be described by the diagram shown in Fig. 4(b). In such an approach, the strong  $\sigma$ -field in the dibaryon leads very naturally to an enhancement for the near-threshold  $\pi^0$  production rate. It should be compared to the conventional OBE-dynamics [12] where one adds coherently many different graphs to describe such an enhancement.

Quite similar very natural explanation arises within our model for the near-threshold heavy meson production [13, 14, 15]. Here two basic mechanisms shown in Figs. 5(a) and 5(b) can be responsible for the vector (e.g. the  $\omega$ ) meson production. The first graph (Fig. 5(a)) represents a near-threshold or subthreshold  $\omega$ -meson production through the intermediate  $N^*(1535)$  isobar production from the dibaryon while the second graph (Fig.

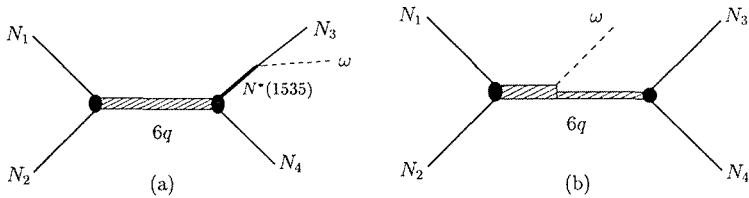


Figure 5: New mechanisms for  $\omega$ -meson emission in a nucleon-nucleon collision

5(b)) describes the vector meson production in  $pp$ -collision via the deexcitation of  $6q$ -bag and at higher energies, far from threshold. We should emphasize that the meson production mechanisms through the intermediate dibaryon, if there are no suppression of some partial channels due to quantum numbers, will lead generally to an enhancement for near-threshold meson production as compared to the any OBE-mechanism due to natural enhancement of the meson fields near the dibaryon. In other words, the six-quark system produces more strong meson fields than two well-separated three-quark clusters. Moreover, as was shown in our previous works [2, 3, 4], the bare dibaryon produced at the first stage (from two nucleons) is in a  $2\hbar\Omega$ -excited state even at a zero kinetic energy in  $NN$ -channel. At higher energies in  $NN$ -collision the excitation energy of the dibaryon string becomes even higher and thus the strongly excited dibaryon may produce a lot of cumulative particles, like  $\pi$ ,  $\eta$ , etc. mesons and also antiprotons (when the excited string gets broken). This production mechanism can explain quite naturally the production of far-subthreshold and cumulative hadrons.

## 4. Dibaryons in nuclei

Appearance of the dibaryon mode in the fundamental  $NN$ -interaction must result in the appearance of the dibaryon components in nuclear wavefunctions. The reality turns out even more reach! In fact, it was shown recently [16, 17] in the extensive  $3N$ -calculations within the dibaryon model for  $NN$  force that the presence of the strong  $\sigma$ -field in the dibaryon leads inevitably to an emergence of new strong three-nucleon force due to the interaction of nucleons surrounding the dibaryon with its rather extended  $\sigma$ -field, see Fig. 6.

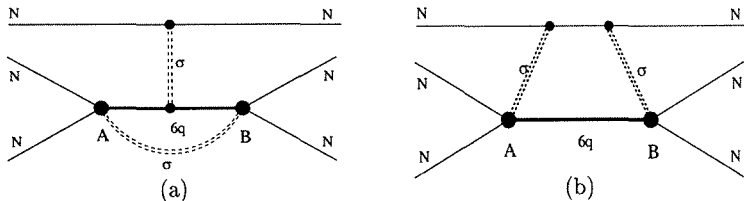


Figure 6: The graphs illustrating the new  $3N$  scalar force induced by  $\sigma$ -exchange between the dressed bag and third nucleon.

Table 2: Results of the  $3N$  calculations with two- and three-body forces for two variants of the dressed-bag model

	$E$ MeV	$P_D$ %	$P_S$ %	$P_{6qN}$ %	Individual contributions to $H$ , MeV		
					$T$	$T + V^{(2N)}$	$V^{(3N)}$
${}^3\text{H}$							
DBM(I) $g = 9.577^*$	-8.482	6.87	0.67	10.99	112.8	-1.33	-7.15
DBM(II) $g = 8.673^*$	-8.481	7.08	0.68	7.39	112.4	-3.79	-4.69
AV18+UIX <sup>1)</sup>	-8.48	9.3	1.05	-	51.4	-7.27	-1.19
${}^3\text{He}$							
DBM(I)	-7.772	6.85	0.74	10.80	110.2	-0.90	-6.88
DBM(II)	-7.789	7.06	0.75	7.26	109.9	-3.28	-4.51
AV18+UIX <sup>1)</sup>	-7.76	9.25	1.24	-	50.6	-6.54	-1.17

<sup>\*</sup>) These values of  $\sigma NN$  coupling constant in  ${}^3\text{H}$  calculations have been chosen to reproduce the exact binding energy of  ${}^3\text{H}$  nucleus. The calculations for  ${}^3\text{He}$  have been carried out without any free parameters.

<sup>1)</sup> The values are taken from [18].

This strong scalar  $3N$ -force between the dibaryon and third nucleon has been demonstrated to give, at least, a half of the total nuclear binding and contributes strongly to other  $3N$  observables [16, 17]. So the  $2N$ - and  $3N$ -force contributions to the total nuclear binding are redistributed largely as compared to conventional OBE-models (see Table 2).

The new picture of nuclear forces, emerged from these studies, has been checked in some independent way [17] in precise calculation of the Coulomb displacement energy between  ${}^3\text{H}$  and  ${}^3\text{He}$ . In fact, the accurate magnitude for the displacement energy could not be reproduced for 40 last years in any accurate and consistent  $3N$  calculations without involving rather serious charge-symmetry breaking effects. Our precise parameter-free  $3N$  calculation have demonstrated that this displacement energy can be accurately reproduced without any serious CSB-effects.

Another pleasant feature of such model for  $3N$  scalar force is its nice compatibility with well known Walecka–Serot model for heavy nuclei and nuclear matter, in which strong self-consistent  $\sigma$ -field presents a main source for nuclear binding.

## 5. New electromagnetic currents in deuteron and few-nucleon systems

According to a general principle of quantum theory, a new carrier of interaction leads inevitably to a new current. So that the introduction of dibaryon mode will result in an appearance of the respective new  $s$ -channel currents in deuteron and other few-nucleon systems. These “interaction” currents are of short-range character and can carry a large momentum transferred from one nucleon to another ones, or from an external probe to nucleons in a nuclear target. Some of the  $s$ -channel currents are displayed in Fig. 7.

It is evident that this  $s$ -channel currents are in some correspondence with respective (conventional)  $t$ -channel currents and thus they represent the proper short-range parts of these currents.

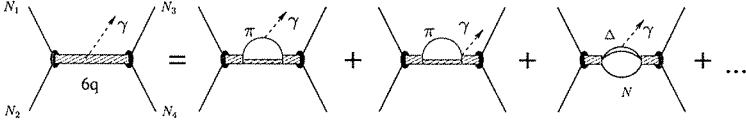


Figure 7: Examples of diagrams involving new meson-exchange electromagnetic currents that arise in the present model

One of the most interesting problems in the field is isoscalar currents in low-energy  $np \rightarrow d\gamma$  process, associated to the isoscalar  $M1$  transition  ${}^3S_1 \rightarrow {}^3S_1$  forbidden for a pure  $NN$  component (due to orthogonality between initial and final wavefunctions). These isoscalar currents can be described by a Lagrangian density  $\mathcal{L}_{\sigma qq} = \mathcal{L}^{(0)} + \mathcal{L}^{(2)}$ , where

$$\mathcal{L}^{(0)} = g_{\sigma qq} \bar{\psi}_q(x) \psi_q(x) \varphi_\sigma(x) \quad (8)$$

$$\mathcal{L}^{(2)}(x) = \frac{\kappa_\sigma}{4M_N^2} g_{\sigma qq} \bar{\psi}_q(x) \gamma^\mu \partial_\mu^{(+)} \gamma^\nu \partial_\nu^{(-)} \psi_q(x) \varphi_\sigma(x) + h.c. \quad (9)$$

Here  $\mathcal{L}^{(2)}$  incorporates the derivatives on fermion fields,  $g_{\sigma qq}$  and  $\kappa_\sigma$  is respective coupling constants of a quark with the  $\sigma$ -meson field the both should be determined from independent observables. By making use a standard minimal gauge substitution in Lagrangian  $\mathcal{L}^{(2)}$ , one can get a contact  $qq\sigma\gamma$  interaction Lagrangian:

$$\mathcal{L}_{\gamma\sigma qq}(x) = ie \frac{\kappa_\sigma g_{\sigma qq}}{4M_N^2} \bar{\psi}_q(x) \gamma^\mu \partial_\mu^{(+)} \gamma^\nu A_\nu \psi_q(x) \varphi_\sigma(x) + h.c. \quad (10)$$

This contact term corresponds to the vertex operator of the form:

$$\Gamma_{\gamma\sigma qq} = e \frac{\kappa_\sigma g_{\sigma qq}}{4M_N^2} \sigma^{\mu\nu} \left( -\frac{i}{2} \mathcal{F}_{\mu\nu} + k_\mu A_\nu \right), \quad (11)$$

in which the (second) term linear on  $k$  will vanish in integration over directions of the  $k$ -vector.

After a non-relativistic reduction of the vertex one gets a vertex

$$\Gamma_{e.m.}^{(\lambda)}(\vec{p} - \vec{p}') \cong \frac{e\kappa_\sigma}{4M_N^2} \begin{pmatrix} [\vec{\sigma} \times (\vec{p} - \vec{p}')] \cdot \vec{\varepsilon}^{(\lambda)*} & 0 \\ 0 & [\vec{\sigma} \times (\vec{p} - \vec{p}')] \cdot \vec{\varepsilon}^{(\lambda)*} \end{pmatrix}, \quad \lambda = \pm 1, \quad (12)$$

which can be factorized out the strong interaction diagram series. We ought to omit here any calculational details, so that the final results for  $M1$  and  $E2$   $s$ -channel transition matrix elements can be written in the form:

$$\begin{aligned} \mathcal{M}_{M1}(I=0) &= \\ &= \kappa_\sigma \mu_N^{I=0} \frac{q}{2M_N} \frac{\lambda_{00}(\epsilon_T)}{2M_N} \int_0^\infty u(r) j_0(qr/2) \varphi_{2S}(r) dr \int_0^\infty Z(r', p, {}^3S_1) \varphi_{2S}(r') dr' + \\ &+ \kappa_\sigma \mu_N^{I=0} \frac{q}{2M_N} \frac{\lambda_{00}(E_d)}{2M_N} \int_0^\infty u(r) \varphi_{2S}(r) dr \int_0^\infty Z(r', p, {}^3S_1) j_0(qr'/2) \varphi_{2S}(r') dr', \quad (13) \end{aligned}$$

$$\begin{aligned} \mathcal{M}_{E2}(I=0) &= -\frac{e\kappa_\sigma}{4M_N^2} < \chi_{M'}^1(d) | (\vec{\sigma}_1 \cdot \vec{q}) (\vec{\sigma}_2 \cdot \vec{\varepsilon}^{(\lambda)}) + (\vec{\sigma}_2 \cdot \vec{q}) (\vec{\sigma}_1 \cdot \vec{\varepsilon}^{(\lambda)}) | \chi_M^1(NN) > \times \\ &\times \int d^3r \int d^3r' ( < \psi_d({}^3D_1)(r) | j_0(qr/2) \lambda_{02}(E_i) \varphi_{2D}(r) \varphi_{2S}(r') | \psi_{NN}({}^3S_1)(r') > + \\ &+ < \psi_d({}^3D_1)(r) | \lambda_{20}(E_f) \varphi_{2D}(r) \varphi_{2S}(r') j_0(qr'/2) | \psi_{NN}({}^3S_1)(r') > ), \quad (14) \end{aligned}$$

where  $\chi_{M'}^1(d)$  and  $\chi_M^1(NN)$  are spin parts of the respective  $NN$  wavefunctions and  $\psi_d(^3D_1)$  and  $\psi_{NN}(^3S_1)$  are the orbital parts of the  $NN$  wavefunctions<sup>1</sup>.

The eventual results for circular  $\gamma$ -quantum polarization  $P_\gamma^{th}$  take the form:

$$P_\gamma^{th} = |P_n|\sqrt{2}(R_{M1} - R_{E2}), \quad R_{M1} = \frac{M1(I=0)}{M1(I=1)}, \quad R_{E2} = \frac{E2(I=0)}{M1(I=1)}. \quad (15)$$

The value of coupling constant  $\kappa_\sigma$  has been found by fitting the exact magnitude for the deuteron magnetic moment within our force model. The result for  $P_\gamma^{th}$  derived earlier within conventional OBE-model is  $P_\gamma^{th} \simeq -0.95 \cdot 10^{-3}$ , while the additional contribution from the above transitional  $M1$  current  $P_\gamma^{th} \simeq -0.40 \cdot 10^{-3}$ , which makes the total value for  $P_\gamma^{th}$  much closer to the respective experimental value  $P_\gamma^{exp} \simeq -1.5 \cdot 10^{-3}$ . Thus the circular polarization of  $\gamma$ -quanta  $P_\gamma$  in radiation capture of polarized neutrons in hydrogen:  $\bar{n}p \rightarrow d\bar{\gamma}$  gets with new  $s$ -channel currents much closer to the respective experimental value than with the traditional OBE-picture.

We should emphasize here that the contribution of the new  $s$ -channel currents will rise fastly with momentum transfer  $|\vec{q}|$ . So that we predict a large contribution from the new isoscalar currents to many deuteron observables, like  $M1$  elastic form factors,  $C2$  quadrupole form factor,  $T_{20}$  quantity at  $ed$  scattering, etc. Moreover, besides of the traditional currents considered here, our model predicts automatically also a diagonal quark and meson currents from the dressed bag itself. While these currents are of low significance at small momentum transfer, their contribution at intermediate and high momentum transfer should be crucial. E.g. these diagonal  $s$ -channel quark and meson currents will lead to well known quark counting rules for all deuteron form factors and structural functions at  $q \rightarrow \infty$ .

We must stress that the above dibaryon model is alone which leads to (potentially very adequate) explanation for electromagnetic properties of deuteron (and other few-nucleon systems) in whole region of the momentum transfer, from zero to very high  $q^2$ . It is because the model includes all three major components of the full wavefunction in a natural way: (i) nucleon currents, (ii) meson-exchange currents (both in  $t$  and  $s$  channel) at intermediate  $q^2$  and (iii) quark currents at high  $q^2$ . This universality is a unique feature of the new force model.

## 6. Conclusion

We have demonstrated in the talk that the introduction of the dibaryon degrees of freedom into description of hadronic processes and nuclear structure leads to much more consistent picture for many processes than with incorporation of only nucleonic and mesonic degrees of freedom. In particular, the description of intermediate- and short-range correlations can be improved considerably. Among these we discussed the following topics:

- fully covariant effective-field theory formulation for intermediate- and short-range  $NN$  interaction;
- two- and three-nucleon forces due to production of the dressed dibaryon in intermediate state;

---

<sup>1</sup>These calculations have been done by I.T. Obukhovskiy.

- an enhancement of the  $\pi^0$  and  $2\pi$  near-threshold production in  $pp$ ,  $pd$ , etc. collisions and ABC-puzzle tightly interrelated to these processes;
- near- and subthreshold production of vector mesons in  $pp$  collisions;
- explanation for the Coulomb displacement energy in  ${}^3\text{H}$  and  ${}^3\text{He}$  systems;
- new  $s$ -channel electromagnetic currents in deuteron and  $2N$ -system.

## References

- [1] D. Plaemper, J. Flender, M.F. Gari, Phys. Rev. C **49**, 2370 (1994).
- [2] V.I. Kukulín, I.T. Obukhovskiy, V.N. Pomerantsev, A. Faessler, Phys. At. Nucl. **64**, 1667 (2001).
- [3] V.I. Kukulín, I.T. Obukhovskiy, V.N. Pomerantsev, A. Faessler, Int. J. Mod. Phys. **E11**, 1 (2002).
- [4] V.I. Kukulín, M.A. Shikhalev, Phys. At. Nucl. **67**, 1536 (2004).
- [5] K.I. Blomqvist *et al.*, Phys. Lett. **B424**, 33 (1998).
- [6] D.L. Groep *et al.*, Phys. Rev. C **63**, 014005 (2001).
- [7] S.J. Brodsky, L. Frankfurt, R. Gilman, J.R. Hiller, G.A. Miller, E. Piasetzky, M. Sargsian, M. Strikman, Phys. Lett. **B578**, 69 (2004).
- [8] E. Piasetzky, R. Gilman, M. Sargsian, in Proceedings of 6th Workshop on “e-m induced Two-Hadron Emission”, Pavia, September 24-27, 2003, p.211.
- [9] M. Schwamb, S. Boffi, C. Giusti, F.D. Pacati, in Proceedings of 6th Workshop on “e-m induced Two-Hadron Emission”, Pavia, September 24-27, 2003, p.16.
- [10] E. Oset, H. Toki, M. Mizobe, T.T. Takahashi, Progr. Theor. Phys. **103**, 351 (2000).
- [11] M.M. Kaskulov, H. Clement, Phys. Rev. C **70**, 014002 (2004).
- [12] C. Hanhart, Phys. Rep. **397**, 155 (2004).
- [13] A. Faessler, C. Fuchs, M.I. Krivoruchenko, and B.V. Martemyanov, J. Phys. G **29**, 603 (2003).
- [14] C. Fuchs, M.I. Krivoruchenko, H.L. Yadav, A. Faessler, B.V. Martemyanov, and K. Shekhter, Phys. Rev. C **67**, 025202 (2003).
- [15] K. Tsushima, K. Nakayama, Phys. Rev. C **68**, 034612 (2003).
- [16] V.I. Kukulín, V.N. Pomerantsev, M.M. Kaskulov, A. Faessler, J. Phys. **G30**, 287 (2004).
- [17] V.I. Kukulín, V.N. Pomerantsev, A. Faessler, J. Phys. **G30**, 309 (2004).
- [18] S. C. Pieper, V. R. Pandharipande, R. B. Wiringa, and J. Carlson, Phys. Rev. C **64**, 014001 (2001).

# FURTHER EVIDENCE OF NARROW BARYONIC STRUCTURES WITH HADRONIC AS WELL AS LEPTONIC PROBES

B. Tatischeff<sup>1</sup> and E. Tomasi-Gustafsson<sup>2</sup>

<sup>1</sup>*Institut de Physique Nucléaire, CNRS/IN2P3, F-91406 Orsay Cedex, France*

<sup>2</sup>*DAPNIA/SPhN, CEA/Saclay, 91191 Gif-sur-Yvette Cedex, France*

† *E-mail: tati@ipno.in2p3.fr, etomasi@cea.fr*

## Abstract

Although extracted from several experiments using hadronic probes [1], narrow baryonic structures have been sometimes met with disbelief. New signatures are presented, which appear from already published data, obtained with hadronic probes as well as with leptonic probes. The authors of these results did not take into account the possibility to associate the discontinuities of their spectra with the topic of narrow baryonic low mass structures. The stability of the observed narrow structure masses, represents a confirmation of their genuine existence.

## 1. Narrow baryons produced by hadrons

Using mainly the  $pp \rightarrow p\pi^+X$  and  $pp \rightarrow ppX$  reactions, studied at SPES3 (Saturne), a spectrum of narrow baryonic structures was observed [1]. A high statistic missing mass spectrum of the  $p(\alpha, \alpha')X$  reaction ( $T_\alpha=4.2$  GeV,  $\theta=0.8^\circ$ ) was obtained twelve years ago at SPES4 (Saturne) in order to study the radial excitation of the nucleon in the  $P_{11}(1440$  MeV) Roper resonance [2]. A first large peak around  $\omega \approx 240$  MeV was associated with the projectile excitation, and a second large peak around  $\omega \approx 510$  MeV was associated with the target excitation. Above them lie narrow peaks, defined by a large number of standard deviations (see Fig. 1). Their masses (see table 1) agree fairly well with the masses of narrow structures extracted from  $pp \rightarrow p\pi^+$  and  $pp \rightarrow ppX$  reactions studied at SPES3 (Saturne) [1]. Fig. 2 shows the spectra of the same reaction at  $\theta=2^\circ$  [3]. The empty circles, in both figures, which correspond to the scale, are the published number of events versus the energy loss. The full circles and full squares show the same data in an expanded scale [4]. Table 1 and Fig. 3 give the quantitative informations concerning the masses extracted from the previous figures, and the comparison with the masses previously extracted from SPES3 cross-sections [1]. Nearly all peaks are seen in both experiments. At  $\theta=0.8^\circ$ , the incident beam enters the SPES4 spectrometer, preventing a possible confirmation of the lower mass structure at  $M=1004$  MeV. Above  $M=1470$  MeV, a lot of peaks are observed. The same situation is observed in the SPES3 data [5], and all masses observed in both reactions are about the same. The peak at  $M=1394$  MeV observed in the SPES4 experiment, was not kinematically accessible in the SPES3 data, since the mass range  $1400 \leq M \leq 1470$  MeV lie between two incident proton energies.

We observe a nice agreement between the masses obtained using data from different physicists, studying different reactions with different probes and different experimental equipments.

This correlation is shown in Fig. 3, where the masses of the structures observed at SPES4 are shown versus the ones at SPES3. The straight lines correspond to the same masses, and all points are located along these lines. Peaks observed in one experiment

only are shown as empty circles. Some other structures were observed in a few  $p(d,d')X$  spectra, which masses correspond with a high accuracy to the SPES3 masses.

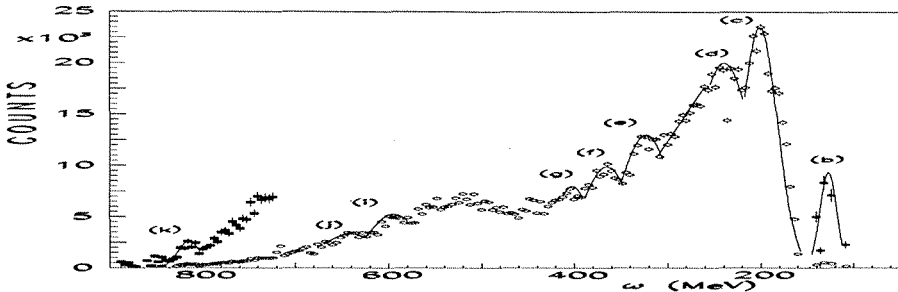


Figure 1: Spectra of the  $p(\alpha, \alpha')X$  reaction studied at SPES4 (Saturne) with  $T_\alpha=4.2$  GeV and  $\theta=0.8^\circ$  [2]

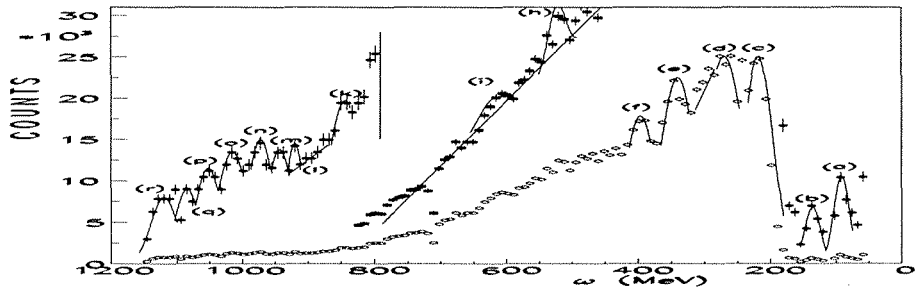


Figure 2: Spectra of the  $p(\alpha, \alpha')X$  reaction studied at SPES4 (Saturne) with  $T_\alpha=4.2$  GeV and  $\theta=2^\circ$  [3]

## 2. Narrow baryons produced by leptons

Recent precise attempts, fail to point out the narrow baryonic structures observed with leptonic probes below pion threshold [6] [7] [8]. However, at masses above pion threshold, as it was done before with hadronic probes, several narrow structures can be extracted from previous experiments performed to study other topics. A more detailed paper which reviews similar results is in progress [9]. In order to illustrate the previous comment, we show four different data in the next figures.

Among the numerous experiments of Compton scattering on proton, some results from

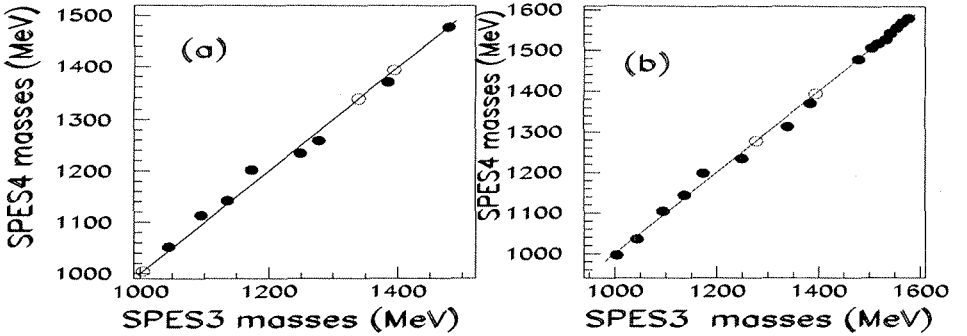


Figure 3: Comparison between masses of narrow baryons extracted from SPES3 and SPES4 data. Inserts (a) and (b) correspond respectively to  $\theta=0.8^\circ$  and  $\theta=2^\circ$

Table 1: Masses (in MeV) of narrow exotic baryons, observed previously in SPES3 data and extracted from previous  $p(\alpha, \alpha')X$  spectra measured at SPES4 [2] [3]

SPES3 mass	1004	1044	1094	1136	1173	1249	1277	1339	1384	1479
pic marker	(a)	(b)	(c)	(d)	(e)	(f)	(g)	(h)	(i)	(j)
SPES4 mass $0.8^\circ$		1052	1113	1142	1202	1234	1259	1370	1394	1478
SPES4 mass $2^\circ$	996	1036	1104	1144	1198	1234	1313	1370		1477
SPES3 mass	1505	1517	1533	1542	(1554)	1564	1577			
pic marker	l	(m)	(n)	(o)	(p)	(q)	(r)			
SPES4 mass $2^\circ$	1507	1517	1530	1543	1557	1569	1580			

Saskatchewan [10] are shown in Fig. 4. A peak not discussed by the authors, is easily extracted at  $M \approx 1094$  MeV, at the same mass where it was seen before in the  $pp \rightarrow p\pi^+X$  reaction at SPES3. Inserts (a) and (b) correspond to  $\theta_{c.m.}^0 = 90^\circ$  and  $141^\circ$  respectively, with a peak at  $T_\gamma = 166.5$  (169) MeV. The total c.m. energies are respectively  $\sqrt{s} = 1092.2$  and 1094.3 MeV, the width of the peaks is  $\sigma = 5.7$  (5.2) MeV and the number of standard deviations S.D. = 3.3 (5.5).

Fig. 5 illustrates total cross-sections of two pion photoproduction measured at MAMI, namely  $\gamma p \rightarrow \pi^0 \pi^0 p$  [11] and  $\gamma n \rightarrow \pi^- \pi^0 p$  [12]. Both peaks correspond to  $\sqrt{s} = 1387$  MeV, close to  $M = 1384$  MeV (mass of a narrow structure already seen [4]).

Fig. 6 illustrates total cross-sections of one pion photoproduction measured at INS (Tokyo) [13]. Insert (a) and (b) correspond respectively to the  $\gamma p \rightarrow \pi^+ n$  and  $\gamma n \rightarrow \pi^- p$  reactions. Insert (a) shows a peak at  $M = 1389$  MeV, ( $M = 1384$  MeV observed at SPES3). Insert (b) shows peaks at  $M = 1171$  MeV (1173),  $M = 1252$  MeV (1249), and  $M = 1387$  MeV (1384).

Fig. 7 illustrates total cross-sections of one pion photoproduction on  $^1\text{H}$  and  $^2\text{H}$  targets. The  $\gamma n \rightarrow \pi^- p$  total cross-section data are from different laboratories [14], when the  $\gamma d \rightarrow \pi^- pp$  total cross-sections are quoted from the CERN-Hera Compilation [15]. Both

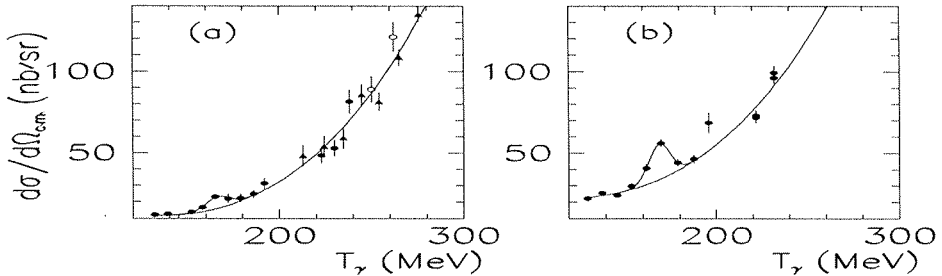


Figure 4: Selection of Compton scattering from the proton data, measured at Saskatchewan [10] (see [9])

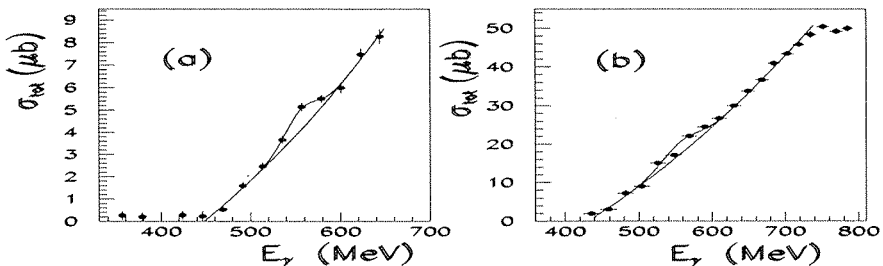


Figure 5: Total cross-sections of two pion production measured at MAMI. Insert (a) shows  $\sigma_{tot}$  of  $\gamma p \rightarrow \pi^0 \pi^0 p$  [11]; insert (b) shows  $\sigma_{tot}$  of  $\gamma n \rightarrow \pi^- \pi^0 p$  [12]. The quantitative informations are given in [9]

spectra exhibit a peak at  $M=1094$  MeV and  $M=1095$  MeV, to compare to  $M=1094$  MeV (a SPES3 peak mass).

Other examples can be given [9], sometimes the peaks are smaller than those which are illustrated in this paper; they always show an astonishing correspondance with the masses previously extracted with hadronic probes.

Fig. 8 shows a comparison of masses observed with leptons, versus masses observed with hadrons. Here the solid symbols give this comparison and the empty circles show the peak masses not observed with leptonic probes. We observe less structures extracted from reactions with leptonic probes, but when a peak was seen, its mass reproduces well a peak mass from SPES3 experiments.

### 3. Conclusion

New dedicated precise experiments must be done to confirm the masses of the narrow baryons observed in many previous experiments, mainly performed at Saturne on the SPES3 and SPES4 beam lines. However, the stability of the structures already extracted from data obtained to study other topics, is noteworthy. This comment concerns as

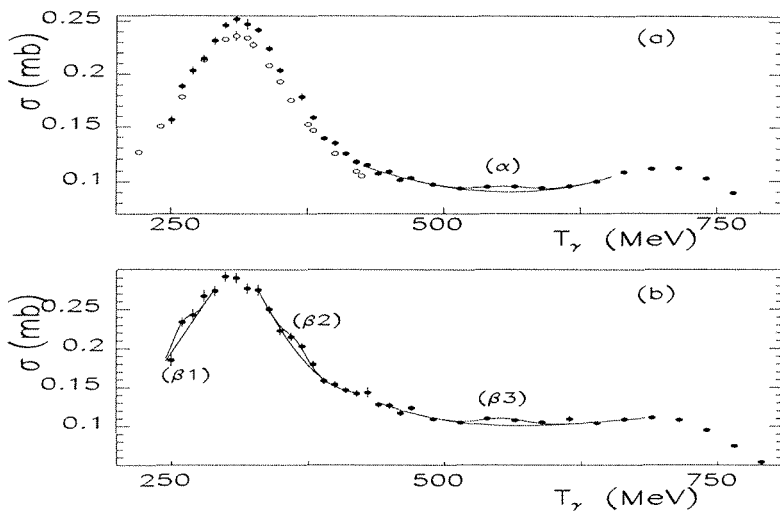


Figure 6: Total cross-sections of the  $\gamma p \rightarrow \pi^+ n$  and  $\gamma n \rightarrow \pi^- p$  reactions measured at the INS (Tokyo). The quantitative informations are given in [9]

well data obtained with hadronic probes as data obtained with leptonic probes, although these last are less numerous. It is worthwhile to mention that the few baryons with mass lower than the pion threshold, were not seen in recent experiments using leptonic probes. Then it is possible to speculate that the excitation of these baryons is favoured through dibaryonic states.

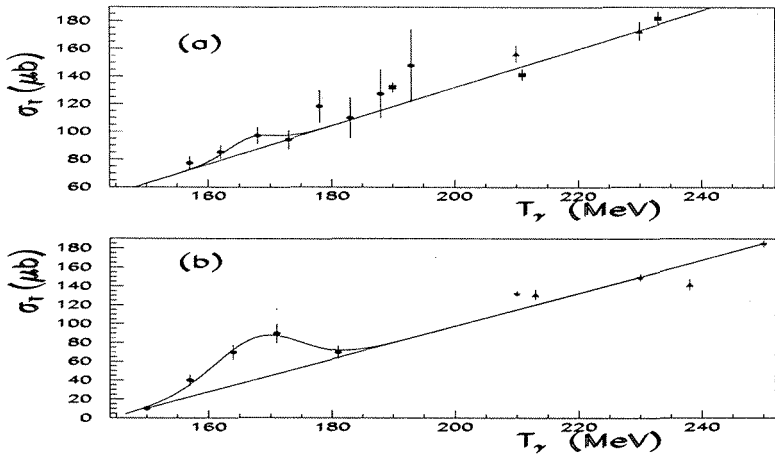


Figure 7: Total cross-sections of the  $\gamma n \rightarrow \pi^- p$  (insert (a)) and  $\gamma d \rightarrow \pi^- pp$  (insert (b)) reactions measured at various laboratories. The quantitative informations are given in [9]

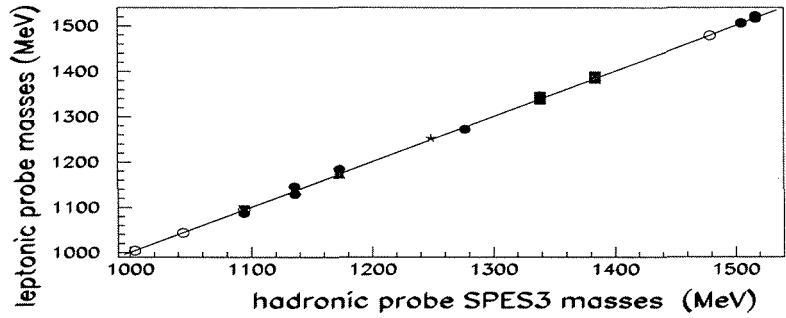


Figure 8: Comparison of masses of narrow baryonic structures observed with leptonic probes, versus masses of narrow baryonic structures observed with hadronic probes. The empty circles show data not seen with incident leptons

## References

- [1] B. Tatischeff et al., Eur. Phys. J. A **17**, 245 (2003).
- [2] H.P. Morsch et al., Phys. Rev. Lett. **69**, 1336 (1992).
- [3] H.P. Morsch, Proceedings of the Dixieme Journee Thematique de l'IPN d'Orsay, p.76 (1995).
- [4] B. Tatischeff, arXiv:nucl-ex/0404042 Apr (2004).
- [5] B. Tatischeff *et al.* to be published.
- [6] X. Jiang *et al.*, Phys. Rev. **C67**, 028201 (2003).
- [7] M. Kohl *et al.*, Phys. Rev. **C67**, 065204 (2003).
- [8] P.A. Zolnierczuk *et al.*, nucl-ex/0403046 v1 (2004).
- [9] B. Tatischeff and E. Tomasi-Gustafsson, to be published.
- [10] E.L. Hallin *et al.*, Phys. Rev. **C48**, 1497 (1993).
- [11] F. Härter *et al.*, Phys. Lett. **B 401**, 229 (1997).
- [12] A. Zabrodin *et al.*, Phys. Rev. **C55**, R1617 (1977).
- [13] T. Fijii *et al.*, Nucl. Phys. **B120**, 395 (1977).
- [14] Goldwasser *et al.*, Dubna64-64, CERN-HERA Compilation, 87-01, p66.
- [15] Adamovit., *et al.*, JETP38, 1078-60, CERN-HERA Compilation, 87-01, p78.

# INSTANTONS IN HIGH ENERGY QCD PROCESSES: INSTANTONS AND THE SOFT POMERON FORMATION

A.E. Dorokhov<sup>1†</sup>, I.O. Cherednikov<sup>1,2‡</sup>

(1) *Joint Institute for Nuclear Research, RU-141980 BLTP JINR, Dubna, Russia*

(2) *Dipartimento di Fisica, Università di Cagliari  
and INFN-Cagliari, C.P. 170, I-90142 Monserrato (CA), Italy*

† *E-mail: dorokhov@theor.jinr.ru*

‡ *E-mail: igorch@theor.jinr.ru*

## Abstract

The role of the QCD vacuum effects in high energy diffractive quark-quark and quark-antiquark scattering is studied with the Instanton Liquid Model. Special attention is given to the problem of formation of the soft Pomeron. We show that in the leading approximation in instanton density the  $C$ -odd instanton contribution to the diffractive amplitude is suppressed by  $1/s$  compared to the  $C$ -even one.

Strong interaction processes in the Regge regime:  $s \gg -t$ , *i.e.*, collisions with large total center-of-mass energy and small momentum transfer, yield the main contribution to the hadronic cross sections at high energy. These processes are described successfully within the Regge phenomenology, with the Pomeron exchange being dominant in this regime [1]. The Pomeron is treated as an effective exchange in the  $t$  channel with vacuum quantum numbers and positive charge parity  $C = +1$ . Within perturbative QCD, the pioneer calculations of the Pomeron properties were performed in Refs. [2], which lead to the supercritical “hard” Pomeron violating the Froissart bound. Further, it was shown that the NLO corrections can change significantly this leading logarithmic approximation result [3]. From the other point of view, it is natural to expect that the QCD dynamics at large distances and the nontrivial structure of the QCD vacuum are relevant for such processes with small momentum transfer [4]. A fruitful approach is to try to reformulate the complicated QCD dynamics in terms of some effective theory which would be easier to solve in a given regime. The convenient effective degrees of freedom at high energy are the Wilson path-ordered exponentials evaluated along the straight-line trajectories of colliding particles [5, 6, 7, 8].

In this work, we consider the high energy diffractive quark-quark scattering using the Instanton Liquid Model (ILM) of the QCD ground state [9, 10, 11] in order to take into account nonperturbative effects in formation of the soft Pomeron. A similar situation was first analysed in Refs. [12, 13] from a somewhat different point of view. The quark-quark scattering amplitude is expressed in terms of the vacuum average of the gauge invariant path-ordered Wilson exponential [5, 6, 14]

$$T_{mn}^{kl}(s, t) = -2is \int d^2b_{\perp} e^{ib_{\perp}q} W_{mn}^{kl}(\chi, b_{\perp}^2), \quad (1)$$

where the Wilson integral  $W_{mn}^{kl}$  reads

$$W_{mn}^{kl}(\chi, b_{\perp}^2) = \left\langle \mathcal{P} e^{ig \int_{C_{qq}} dz_{\mu} \hat{A}_{\mu}(x)} \right\rangle_{0, mn}^{kl} . \quad (2)$$

In Eq. (2), the corresponding integration path goes along the closed contour  $C_{qq}$ : two infinite lines separated by the transverse distance  $b_{\perp}$  and having relative scattering angle  $\chi$ . We parameterize the integration path as  $C_{\chi} = \{z_{\mu}(\lambda); \lambda = [-\infty, \infty]\}$  where  $z_{\mu}(\lambda) = v_1 \lambda$ ,  $-\infty < \lambda < \infty$ , and  $z_{\mu}(\lambda) = v_2 \lambda + \mathbf{b}$ ,  $-\infty < \lambda < \infty$ . with  $(v_1 v_2) = \cosh \chi$  and  $\mathbf{b} = (0_{\parallel}, b_{\perp})$  being the impact parameter in the transversal plane.

To calculate the amplitude (1) in the instanton background, we use the explicit expression for the instanton field

$$\hat{A}_{\mu}(x; \rho) = \frac{1}{g_s} \mathbf{R}^{ab} \sigma^a \eta^{\pm b}_{\mu\nu} (x - z_0)_{\nu} \varphi(x - z_0; \rho) . \quad (3)$$

The averaging  $\langle \dots \rangle_0$  over the nonperturbative vacuum consists in integration over the coordinate of the instanton center  $z_0$ , the color orientation  $\mathbf{R}^{ab}$  and the instanton size  $\rho$ :  $dI = d\mathbf{R} d^4 z_0 dn_{\rho}$ , where the instanton size distribution  $dn_{\rho}$  is chosen according to ILM as [9]  $dn_{\rho} = n_c \delta(\rho - \rho_c) d\rho$ ,  $n_c \approx 1 fm^{-4}$ ,  $\rho_c \approx 1/3 fm$ . Evaluating the path-ordered exponential Eq. (2) and averaging over all possible embeddings of  $SU_c(2)$  into  $SU_c(3)$  by using the relations from Ref. [15] we get (for further technical details, see Ref. [16])

$$W_{mn}^{kl}(\gamma, \mathbf{b}^2) = n_c \left\{ \frac{4}{9} \delta_{kl} \delta_{mn} w_c(\gamma, \mathbf{b}^2) + \frac{1}{8} \lambda_{kl}^a \lambda_{mn}^a \left[ \frac{1}{3} w_c(\gamma, \mathbf{b}^2) + w_s(\gamma, \mathbf{b}^2) \right] \right\} , \quad (4)$$

$$w_c(\gamma, \mathbf{b}^2) = \int d^4 z_0 (\cos \alpha_1 - 1) (\cos \alpha_2 - 1) , \quad (5)$$

$$w_s(\gamma, \mathbf{b}^2) = - \int d^4 z_0 (\hat{n}_1^a \hat{n}_2^a) \sin \alpha_1 \sin \alpha_2 , \quad (6)$$

where the color correlation factor is

$$\hat{n}_1^a \hat{n}_2^a = \frac{(v_1 v_2)(z_0, z_0 - \mathbf{b}) - (v_1 z_0)(v_2 z_0)}{s_1 s_2} . \quad (7)$$

The phases are defined as

$$\alpha_1 = s_1 \cdot \int_{-\infty}^{\infty} d\lambda \varphi \left[ (z_0 + v_1 \lambda)^2; \rho \right] , \quad (8)$$

$$\alpha_2 = s_2 \cdot \int_{-\infty}^{\infty} d\lambda \varphi \left[ (z_0 - v_2 \lambda - \mathbf{b})^2; \rho \right] . \quad (9)$$

with  $s_1^2 = z_0^2 - (v_1 z_0)$ ;  $s_2^2 = (z_0 - \mathbf{b})^2 - (v_2 z_0)$ . Here  $\gamma$  is the scattering angle in Euclidean space, whereas in the final expressions one must make a transition back to Minkowski space-time (see below). By means of the proper change of variables, the energy dependence is trivially factorized

$$w_c(\gamma, b_{\perp}^2) \rightarrow \frac{1}{\sin \gamma} w_c(\pi/2, b_{\perp}^2) , \quad w_s(\gamma, b_{\perp}^2) \rightarrow \cot \gamma w_s(\pi/2, b_{\perp}^2) . \quad (10)$$

The differential cross section of the quark-quark scattering is expressed through the amplitude (4) as

$$\frac{d\sigma_{qq}}{dt} \approx \frac{1}{9} \frac{1}{s^2} \sum_{kl} \sum_{mn} |T_{mn}^{kl}(s, t)|^2. \quad (11)$$

Making analytical continuation to Minkowski space [17, 18]:  $\gamma \rightarrow -i\chi$ , one finds

$$\frac{d\sigma_{qq}(t)}{dt} = \frac{2}{9} n_c^2 \left[ \coth^2 \chi F_s^2(t) + \frac{2 \coth \chi}{3 \sinh \chi} F_c(t) F_s(t) + \frac{11}{3} \frac{1}{\sinh^2 \chi} F_c^2(t) \right], \quad (12)$$

where

$$F_{s,c}(t) = \int d^2 \mathbf{b} e^{i \mathbf{b} \mathbf{q}} w_{s,c}(\pi/2, \mathbf{b}^2). \quad (13)$$

In the asymptotic limit ( $\sinh \chi \sim s$ ,  $\coth \chi \rightarrow 1$ ) the result (12) coincides with the result of Ref. [12]:  $\frac{d\sigma}{dt} \approx \frac{2}{9} n_c^2 F_s^2(t)$ . In the weak field limit we reproduce the one-loop single instanton results (see Ref. [16]).

For the quark-antiquark scattering one can treat an antiquark with velocity  $v_2$  as a quark moving backward in time with velocity  $-v_2$ . As a result, the scalar product of velocities changes its sign ( $v_1^q v_2^q = -(v_1^q v_2^{\bar{q}})$ ) and the scattering angles are related as  $\chi_{q\bar{q}} \rightarrow i\pi - \chi_{q\bar{q}}$ . Then one gets

$$\frac{d\sigma_{q\bar{q}}(t)}{dt} = \frac{2}{9} n_c^2 \left[ \coth^2 \chi F_s^2(t) - \frac{2 \coth \chi}{3 \sinh \chi} F_c(t) F_s(t) + \frac{11}{3} \frac{1}{\sinh^2 \chi} F_c^2(t) \right]. \quad (14)$$

The second terms in Eqs. (12) and (14) correspond to the contribution of the  $C$ -odd amplitude.

The spin averaged total quark-quark cross section in the instanton-antiinstanton approximation reads

$$\sigma_{qq} \approx \frac{2}{9} n_c^2 \int_0^\infty d\mathbf{q}^2 \left[ F_s^2(\mathbf{q}^2) + \frac{4}{3} \frac{m^2}{s} F_c(\mathbf{q}^2) F_s(\mathbf{q}^2) \right] \quad (15)$$

which is constant in the high energy limit. It is finite if the constrained instanton solution is used [19]. In Eq. (15), the only term corresponding to the  $C = +1$  exchange, Pomeron, survives in the asymptotics, while the  $C = -1$  contribution (second term in Eq. (15)) is suppressed by the small factor  $\sim m^2/s$ . The leading  $C = -1$  part of the scattering amplitude, odderon, will arise at higher orders in instanton density, which corresponds to diagrams like three nonperturbative gluon exchange. The growing part of the total cross section  $\Delta\sigma_{qq} \sim (n_c \rho_c^4)^2 \Delta(t) \ln s$  can arise only if *inelastic* quark-quark scattering in the instanton-antiinstanton background is taken into account [12].

It is important to note that the original Wilson exponential, Eq. (2), has essentially Minkowskian light-cone geometry whereas the instanton calculations of Wilson loop are performed in the Euclidean QCD. The mapping from the Minkowski space to the Euclidean one is possible since the dependence of the Wilson integral on the total energy  $s$  and transverse momentum squared  $t$  is factorized in Eqs. (10), (10). At high energy, the amplitude is  $s$ -independent both in the perturbative and nonperturbative cases. At the same time, the  $t$ -dependence of the amplitude is naturally expressed through the nonperturbative instanton field.

Supported in part by RFBR (04-02-16445, 03-02-17291) and the Russian Federation President's Grant 1450-2003-2.

## References

- [1] A.B. Kaidalov, Phys. Usp. **46** (2003) 1121.
- [2] V.S. Fadin, E.A. Kuraev, L.N. Lipatov, Phys. Lett. **B60** (1975) 50; Zh. Eksp. Teor. Fiz. **71** (1976) 840; *ibid.* **72** (1977) 377; I.I. Balitsky, L.N. Lipatov, Yad. Fiz. **28** (1978) 1597.
- [3] L.N. Lipatov, V.S. Fadin, JETP Lett. **49** (1989) 352; Yad. Fiz. **50** (1989) 1141; Phys. Lett. **B429** (1998) 127; Nucl. Phys. **B477** (1996) 767 M. Ciafaloni, G. Camici, Phys. Lett. **B430** (1998) 349.
- [4] F.E. Low, Phys. Rev. **D12** (1975) 163; S. Nussinov, Phys. Rev. Lett. **34** (1975) 1286; P.V. Landshoff, O. Nachtmann, Z. Phys. **C35** (1987) 405.
- [5] A. Bassetto, M. Ciafaloni, G. Marchesini, Phys. Reports **100** (1983) 201; O. Nachtmann, Ann. Phys. (N.Y.) **209** (1991) 436.
- [6] H. Verlinde, E. Verlinde, hep-th/9302104.
- [7] L.N. Lipatov, Nucl. Phys. **B452** (1995) 369; Phys. Rept. **286** (1997) 131; Phys. Usp. **47** (2004) 325.
- [8] I. Balitsky, Nucl. Phys. **B463** (1996) 99; Phys. Rev. **D60** (1999) 014020; hep-ph/0101042; Phys. Lett. **B518** (2001) 235; A. Babansky, I. Balitsky, Phys. Rev. **D67** (2003) 054026.
- [9] E. Shuryak, Nucl. Phys. **B203** (1982) 93, 116, 140; D. Diakonov, V. Petrov, *ibid.* **B245** (1984) 259.
- [10] A.E. Dorokhov, Yu.A. Zubov, N.I. Kochelev, Sov. J. Part. Nucl. **23** (1992) 522.
- [11] T. Schäfer, E.V. Shuryak, Rev. Mod. Phys. **70** (1998) 323.
- [12] E. Shuryak, *et al.* Phys. Rev. **D62** (2000) 085014; *ibid.* **D64** (2001) 034008. *ibid.* **D65** (2002) 074034.
- [13] D.E. Kharzeev, Y.V. Kovchegov, E. Levin, Nucl. Phys. **A690** (2001) 621; F. Schrempf, A. Utermann, Phys. Lett. **B543** (2002) 197.
- [14] G. Korchemsky, Phys. Lett. **B325** (1994) 459.
- [15] M.A. Shifman, A.I. Vainshtein, V.I. Zakharov, Nucl. Phys. **B163** (1980) 46.
- [16] A.E. Dorokhov, I.O. Cherednikov, Ann. Phys. (NY) **314** (2004) 321.
- [17] G.P. Korchemsky, A.V. Radyushkin, Yad. Fiz. **45** (1987) 1466; Nucl. Phys. **B283** (1987) 342.
- [18] E. Meggiolaro, Z. Phys. **C76** (1997) 523; Eur. Phys. J. **C4** (1998) 101; Phys. Rev. **D53** (1996) 3835.
- [19] A.E. Dorokhov, S.V. Esaibegyan, A. E. Maximov, S.V. Mikhailov, Eur. Phys. J. **C13** (2000) 331.

# TWO-QUARK BOUND STATES: MESON SPECTRA AND REGGE TRAJECTORIES

G. Ganbold<sup>1,2†</sup> and G.V. Efimov<sup>1</sup>

(1) *Bogoliubov Laboratory of Theoretical Physics, JINR, Dubna*

(2) *Institute of Physics and Technology, MAS, Ulaanbaatar*

† *E-mail: ganbold@thsun1.jinr.ru*

## Abstract

We consider simple relativistic quantum field models with the Yukawa interaction of quarks and gluons. In the presence of the analytic confinement there exist bound states of quarks and gluons at relatively weak coupling. By using a minimal set of free parameters (the quark masses and the confinement scale) and involving the mass-dependent coupling constant of QCD we satisfactorily explain the observed meson spectra and the asymptotically linear Regge trajectories.

## 1. Introduction

The conventional theoretical description of colorless hadrons within the QCD implies they are bound states of quarks and gluons considered under the color confinement. A realisation of the confinement is developed in [1, 2] by using an assumption that QCD vacuum is realized by the self-dual homogeneous vacuum gluon field. Accordingly, this can lead to the quark and gluon confinement as well as a necessary chiral symmetry breaking. Hereby, propagators of quarks and gluons in this field are entire analytic functions in the  $p^2$ -complex plane, i.e. the analytic confinement takes place. On the other hand, there exists a prejudice to the idea of the analytic confinement (for example, [3]).

Therefore, it seems reasonable first to consider simple quantum field models in order to investigate only qualitative effects. In our earlier paper [4] we considered simple scalar-field models to clarify the "pure role" of the analytic confinement in formation of the hadron bound states. In doing so, we have demonstrated just a mathematical sketch of calculations of the mass spectrum for the "mesons" consisting of two "scalar quarks" by omitting some quantum degrees of freedom such as the spin, color and flavor. These models gave a quite reasonable sight to the underlying physical principles of the hadron formation mechanism and the spectra, and have resulted in qualitative descriptions of "mesons", their Regge trajectories and "glueballs" [5].

In this paper we present a more realistic extension of our earlier consideration by taking into account the omitted quantum characteristics associated with color, flavor and spin degrees of freedom for constituent quarks and gluons. Below we calculate the mass spectrum of pseudoscalar and vector mesons as well as glueballs.

## 2. The Model

Conventionally, considering this problem within QCD one deals with complicated and elaborate calculations, because the confinement is achieved as a result of strong interaction – by involving high-order corrections [6]. Then, there arises a problem of correct and effective summation of these contributions.

On the other hand, the use of a QFT method is effective when the coupling is not large. Then, lower orders of a perturbative technique can result in satisfactory accurate estimates (e.g., in QCD) of observables. Particularly, one can effectively use the one-gluon exchange approximation.

We consider a relativistic physics and for the hadronization processes use the Bethe-Salpeter equation. Because, when the binding energy is not negligible the relativistic corrections are considerable. Of course, in doing so, we use a minimal set of free parameters.

Consider the quark and gluon fields:  $\Psi_{\alpha f}^a(x) = \Psi_{\text{spin flavour}}^{\text{color}}(x)$ ,  $\phi_{\mu}^a(x) = \phi_{\text{vector}}^{\text{color}}(x)$

The Lagrangian of the Yukawa-type interaction reads:

$$\begin{aligned} \mathcal{L}(x) = & \left( \bar{\Psi}_{\alpha}^i [S^{-1}]_{\alpha\beta}^{ij} \Psi_{\beta}^j \right) + \frac{1}{2} \left( \phi_{\mu}^a [D^{-1}]_{\mu\nu}^{ab} \phi_{\nu}^b \right) \\ & + g \left( \bar{\Psi}_{\alpha}^i (\Gamma^{\alpha})_{\alpha\beta}^{ij} \Psi_{\beta}^j \phi^{\alpha} \right) + h\Lambda \left( \phi_{\mu}^a \phi_{\nu}^b F_{\mu\nu}^c \right) f^{abc} \\ & \left( \Gamma_{\mu}^{\alpha} \right)_{\alpha\beta}^{ij} = (i\gamma)^{\alpha\beta} t_{ij}^{\alpha}, \quad F_{\mu\nu}^c = \partial_{\mu} \phi_{\nu}^c - \partial_{\nu} \phi_{\mu}^c \end{aligned}$$

We guess that the matrix elements of hadron processes at large distance (in the confinement region) are in fact integrated characteristics of quark (gluon) propagators and their vertices. Their tiny detailed behaviors may be not so important, but important is to take into account the correct symmetry features.

Our aim is to find the most plain forms of these propagators which keep the essential properties and result in a qualitative and semi-quantitative description of the hadron spectra. For this purpose, we consider the following propagators:

$$\begin{aligned} D_{ab}^{\mu\nu}(x) &= \delta_{ab} \delta^{\mu\nu} \frac{\Lambda^2}{(4\pi)^2} e^{-x^2 \Lambda^2/4} \\ \tilde{S}_{\alpha\beta}^{ij}(\hat{p}) &= \delta^{ij} \frac{1}{m^2} [i\hat{p} + m(1 + \gamma_5 \omega(m))]_{\alpha\beta} \cdot e^{-\frac{p^2 + m^2}{2\Lambda^2}}, \end{aligned}$$

where  $\Lambda$  - the confinement energy scale,  $m$  - the quark mass and

$$\omega(m) = \int_0^1 du \left( \frac{1-u}{1+u} \right)^{\frac{m^2}{4}} \frac{u^2}{1-u^2} \cdot \left\{ \int_0^1 du \left( \frac{1-u}{1+u} \right)^{\frac{m^2}{4}} \frac{1}{1-u^2} \right\}^{-1}$$

These are entire analytic functions and represent reasonable approximations of the exact quark and gluon propagators.

Consider the partition function and take an explicit integration over  $\phi$ -variable:

$$\begin{aligned} Z &= \iint \delta\bar{\Psi} \delta\Psi e^{-\mathcal{L}_F[\bar{\Psi}, \Psi]} \int \delta\phi e^{-\mathcal{L}_B[\phi] - \mathcal{L}_{int}[\bar{\Psi}, \Psi, \phi]} \\ &= \iint \delta\bar{\Psi} \delta\Psi e^{-\mathcal{L}_F[\bar{\Psi}, \Psi] - \mathcal{L}_2[\bar{\Psi}, \Psi] - \mathcal{L}_3[\bar{\Psi}, \Psi] - \mathcal{L}_G + \dots} \end{aligned}$$

Then, the lowest bound states of quarks and gluons are expressed as follows.  
Mesons:

$$\mathcal{L}_2 = \frac{g^2}{2} \int \delta\phi e^{-\mathcal{L}_B|\phi|} (\bar{\Psi}\Gamma\Psi) D(\bar{\Psi}\Gamma\Psi)$$

Glueballs:

$$\mathcal{L}_G = \frac{3(3h)^2}{2} \int \delta\phi e^{-\mathcal{L}_B|\phi|} (\phi\phi D\phi\phi)$$

Baryons:

$$\mathcal{L}_3 = \frac{g^3 h}{6} \int \delta\phi e^{-\mathcal{L}_B|\phi|} (\bar{\Psi}\Gamma\Psi) D(\bar{\Psi}\Gamma\Psi) D(\bar{\Psi}\Gamma\Psi) D$$

### 3. Two-Quark Bound States

Omitting elaborous details of intermediate calculations, we write shortly only important steps of our approach for describing two-quark (mesonic) stable bound states.

i. Allocation of one-gluon exchange between quark currents

$$L_2 = \frac{g^2}{2} \iint dx_1 dx_2 \sum_{f_1 f_2} (\bar{q}_{f_1}(x_1) \gamma_\mu t^a q_{f_1}(x_1) D_{\mu\nu}^{ab}(x_1, x_2) (\bar{q}_{f_2}(x_2) \gamma_\nu t^b q_{f_2}(x_2))).$$

ii. Introduction of the centre-of-masses system:

$$x_1 = x + \xi_1 y, \quad x_2 = x - \xi_2 y, \quad \xi_1 = \frac{m_{f_2}}{m_{f_1} + m_{f_2}}, \quad \xi_2 = \frac{m_{f_1}}{m_{f_1} + m_{f_2}}.$$

iii. Fierz transformation for colorless bilocal quark currents

$$i(\gamma_{\mu_1})_{\alpha_1\beta_1} i(\gamma_{\mu_2})_{\alpha_2\beta_2} = -1 \cdot S - \frac{1}{2} \cdot V + 0 \cdot T + \frac{1}{2} \cdot A - 1 \cdot P$$

$$\delta^{\mu\mu'} \delta^{\nu\nu'} = \frac{1}{4} \cdot S - \frac{1}{4} \cdot V + \frac{1}{4} \cdot T - \frac{1}{4} \cdot A - \frac{1}{4} \cdot P$$

$$L_2 = \frac{g^2}{2} \iint dx dy \sum_{J_{f_1 f_2}} \mathcal{J}_{J_{f_1 f_2}}(x, y) \mathcal{J}_{J_{f_2 f_1}}(x, y).$$

iv. Orthonormal basis  $\{U_Q(x)\}$  indexed by quantum numbers  $Q = \{n\kappa l m\}$ :

$$\mathcal{J}_{J_{f_1 f_2}}(x, y) = \sqrt{D(y)} (\bar{q}_{f_1}(x + \xi_1 y) \Gamma_J q_{f_2}(x - \xi_2 y)) = \sum_Q J_{J Q_{f_1 f_2}}(x) U_Q(y),$$

v. Diagonalization of  $L_2$  on colorless quark currents:

$$L_2 = \frac{g^2}{2} \sum_{\mathcal{N}} \int dx \mathcal{J}_{\mathcal{N}}^\dagger(x) \mathcal{J}_{\mathcal{N}}(x), \quad \mathcal{N} = J Q_{f_1 f_2}, \quad \mathcal{J}_{J Q}(x) = \bar{q}_{f_1}(x) V_{J Q}(\vec{\partial}) q_{f_2}(x).$$

vi. Gaussian representation by using auxiliary meson fields:

$$e^{g^2(\mathcal{J}_N^+ \mathcal{J}_N)} = \iint DB_N DB_N^+ e^{-(B_N^+ B_N) + g[(B_N^+ \mathcal{J}_N) + (\mathcal{J}_N^+ B_N)]}$$

vii. Integration over  $\bar{q}, q$  and introduction of an effective action

$$\mathcal{S}_N[B] = -\frac{1}{2}(B_N^2) + \text{Tr} \ln[1 + g(B_N V_N)S]$$

viii. *Hadronization Ansatz* to identify  $B_N(x)$  as meson fields with  $\mathcal{N} = \{JQff\}$ .

$$\mathcal{S}_N[B] = -\frac{1}{2}(B_N^2) + \text{Tr} \ln[1 + g(B_N V_N)S], \quad \text{Tr} = \text{Tr}_c \text{Tr}_\gamma$$

ix. Partition function for mesons and extraction of the full quadratic (kinetic) term:

$$Z_N = \int DB_N e^{-\frac{1}{2}(B_N^2) + \text{Tr} \ln[1 + g(B_N V_N)S]} = \int DB_N e^{-\frac{1}{2}(B_N[1 + g^2 \text{Tr} V_N S V_N S] B_N) + W_I[B_N]}$$

x. The diagonalization of the quadratic form is equivalent to solution of the Bethe-Salpeter equation (in the ladder approximation) on the orthonormal system  $U_N$ :

$$g^2 \text{Tr}(V_N S V_N S) = \langle U_N \Pi_p U_N \rangle = \lambda_N (-p^2) \delta_{JJ'} \delta_{QQ'}$$

xi. The mass spectrum and vertex-functions are defined from:

$$1 = \lambda_N (M_N^2), \quad V_N(\partial) = \Gamma_J \int dy U_Q(y) \sqrt{D(y)} e^{\frac{y}{2} \partial}$$

xii. Below we investigate only two-quark bound states for mesons and will not consider remaining interaction between mesons is described by functional  $W_I[B_N] = O[B_N^3]$ .

### 3.1. Bethe-Salpeter Equation for Mesons

The diagonalization of  $g^2 \Pi_p(x, y)$  is equivalent to the solution of the corresponding Bethe-Salpeter equation:

$$\iint dx dy U_{JQ}(x) g^2 \Pi_p(x, y) U_{J'Q'}(y) = \delta^{QQ'} \delta^{JJ'} \lambda_{JQ} (-p^2)$$

Note, the polarization kernel  $\Pi_p(x, y)$  is real and symmetric that allows one to use a variational technique. Choose a normalized trial wave function (for simplicity consider  $n = 0, l \geq 0$ ) as an approximation for  $U_Q(x)$ :

$$\Psi_{l(\mu)}(x, a) = C_l T_{l(\mu)}(x) \sqrt{D(x)} e^{-\frac{\Lambda^2}{4} c x^2},$$

$$C_l = \Lambda^{l+1} \sqrt{\frac{(1+2c)^{l+1}}{2^l (l+1)!}}, \quad \sum_{\{\mu\}} \int dx |\Psi_{l(\mu)}(x, c)|^2 = 1,$$

where  $c > 0$  - variational parameter;  $T_{l(\mu)}(x)$  - four-dimensional orthogonal polynomials.

### 3.2. Mass Equation

Variational solution (on the mass shell  $p^2 = -M_l^2$ ) for the Bethe-Salpeter equation for mesons reads:

$$\begin{aligned}
 1 &= \max_{\Psi_Q} \sum_{\{\mu\}} \iint dy_1 dy_2 \Psi_Q(y_1) g^2 \Pi_p(y_1, y_2) \Psi_Q(y_2) = \lambda_Q(M_l) \quad (1) \\
 &= \alpha_s \cdot \frac{4}{3\pi m_1^2 m_2^2} \exp \left\{ \frac{M_l^2(\mu_1^2 + \mu_2^2) - (m_1^2 + m_2^2)}{2} \right\} \frac{2^l}{(l+1)!} \\
 &\cdot \max_{0 < b < 1} \left\{ [b(1-b/2)]^{l+2} (-1)^l \frac{d^l}{dA^l} \frac{1}{A^2} \exp \left\{ -\frac{M_l^2(\mu_1 - \mu_2)^2}{4A} \right\} \right\} \\
 &\cdot \left[ \frac{2\rho}{A} + \frac{M_l^2(\mu_1 - \mu_2)^2}{4} \left( \frac{2}{A} - \frac{1}{A^2} \right) + M_l^2 \mu_1 \mu_2 + m_1 m_2 (1 + \chi \omega_1 \omega_2) \right] \Big\}
 \end{aligned}$$

$$A = 1 + 2b, \quad m_i = m_{f_i}/\Lambda, \quad M_l = M_{meson}/\Lambda$$

$$\rho = \left\{ 1, \frac{1}{2} \right\}, \quad \chi = \{+1, -1\} \quad \text{for } \{P - Pseudoscalar, V - Vector\}$$

### 3.3. Mass-dependent Coupling Constant

Generally, the coupling constant  $\alpha_s = g^2/4\pi$  is a free parameter of our model and it can be found as a good fitting parameter for known meson masses. However, it is interesting to consider  $\alpha_s$  in dependence on meson masses, for example, by using known results for the QCD running coupling [7, 8]. For this purpose we have tested various versions of such mass dependence (Fig.1):

$$\frac{1}{\alpha_s(M)} = \frac{1}{\alpha_s(M_0)} + \frac{\beta_0}{4\pi} \ln \left( \frac{M^2}{M_0^2} \right), \quad [\text{QCD asymptotics}]$$

$$\alpha_s(M) = \frac{4\pi}{\beta_0} \frac{1}{\ln(M^2/Q^2)} \left( 1 - \frac{1}{(M^2/Q^2)} \right), \quad [\text{A.Nesterenko(2002)}]$$

$$\alpha_s(M) = \frac{4\pi}{\beta_0} \left( \frac{1}{\ln(M^2/Q^2)} - \frac{1}{(M^2/Q^2) - 1} \right), \quad [\text{I.Solovtsev, D.V.Shirkov(2003)}]$$

where  $\beta_0 = 11 - 2 N_{flav}/3$  and,  $\alpha_s(1777 \text{ MeV}) = 0.34$  is known from  $\tau$ -lepton decay data.

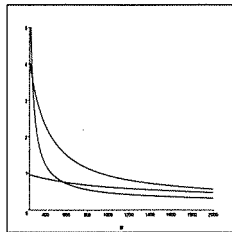


Figure 1: Some mass-dependent versions of  $\alpha_s$

Note, this mass dependence allows one to explain the mass splitting effect between  $\pi(140)$  and  $\eta(547)$  mesons when the quark content is the same for both of them (Fig.2). Besides, the mass-dependent formula due to [7] is found more acceptable for our consideration with  $Q = 600 \text{ MeV}$ .

### 3.4. Ground State: $l = 0$

Obtained results of our estimations for  $l = 0$  are shown in Tables 1 and 2, and Figure 2.

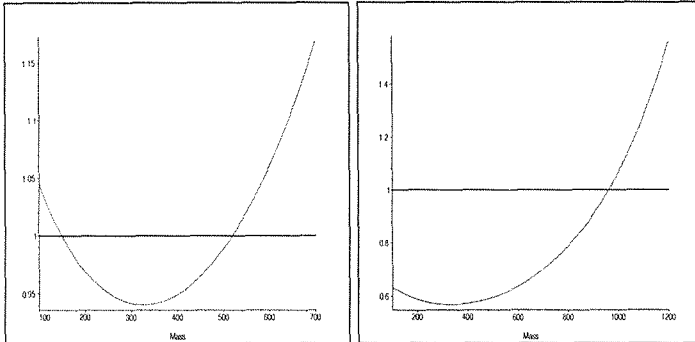


Figure 2: Solutions of the mass equation for  $\pi, \eta$  and  $\eta'$  mesons.

Note, there appears a mass splitting effect between  $\pi(140)$  and  $\eta(547)$  mesons when the quark content is the same for both of them (Fig.2). This is possible only for relatively light quarks  $m_u = m_d = 219 \text{ MeV}$  and the reason is a relevant combination of the decreasing function  $\alpha_s(M)$  and an increasing function standing behind it in (1). But this does not appear for heavier quarks (e.g.,  $m_s = 249 \text{ MeV}$  and the unique solution is the meson  $\eta'(958)$ ).

$J^{PC} = 0^{-+}$	$M_P$	$J^{PC} = 0^{-+}$	$M_P$
$\pi(140)$	140	$D(1870)$	1975
$\eta(547)$	547	$D_s(1970)$	1969
$\eta_c(2979)$	2979	$B(5279)$	5333
$\eta_b(9300)$	9300	$B_s(5370)$	5330
$K(495)$	495	$B_c(6400 \pm 400)$	6087

Table 1: Estimated masses for the pseudoscalar mesons.

We see (Table 1) that our model with a set of parameters:

$$\{\Lambda = 600 \text{ MeV}, m_u = m_d = 219 \text{ MeV}, m_s = 249 \text{ MeV}, m_c = 844 \text{ MeV}, m_b = 4303 \text{ MeV}\}$$

leads to quantitatively well description of both light and heavy meson masses.

$J^{PC} = 1^{--}$	$M_P$	$J^{PC} = 1^{--}$	$M_P$
$\rho(770)$	770	$K^*(892)$	892
$\omega(782)$	782	$D^*(2010)$	2034
$\Phi(1019)$	1019	$D_s^*(2112)$	2102
$J/\Psi(3097)$	3097	$B^*(5325)$	5397
$\Upsilon(9460)$	9460		

Table 2: Estimated masses for the vector mesons

For the vector mesons, the optimal set of parameters is found:

$$\{\Lambda = 600\text{MeV}, m_u = m_d = 203\text{MeV}, m_s = 226\text{MeV}, m_c = 887\text{MeV}, m_b = 4387\text{MeV}\}.$$

### 3.5. Orbital Excitations: Regge Trajectories

Correct description of the mesonic orbital excitations can serve as an additional testing ground for our model. In fact, the orbital excitations take place in larger distances and therefore, should be less sensitive to the tiny short-range details of the chosen propagators.

The experimental data and our estimates for the  $\rho$ -meson and  $K$ -meson families are:

$$\rho(770) - a_2(1320) - \rho_3(1640) - a_4(2040),$$

$$M_1(770) - M_2(1367) - M_3(1702) - M_4(2005),$$

and

$$K^*(892) - K_2^*(1430) - K_3^*(1780) - K_4^*(2045)$$

$$M_1(892) - M_2(1487) - M_3(1791) - M_4(2064) - M_5(2317) - M_6(2551) - M_7(2770)$$

correspondingly (see Fig.3).

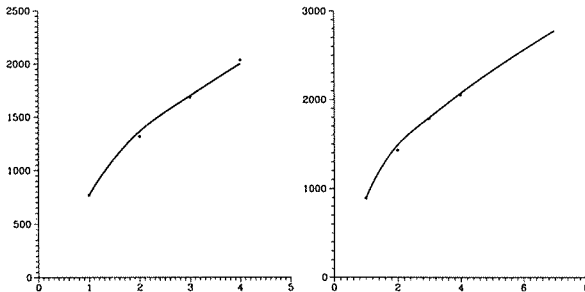


Figure 3: Regge trajectories of  $\rho$ - and  $K$ -meson families

As is expected, our model describes well the Regge trajectories of mesons. The most sensitive parameter  $\Lambda$  governs the slope of the Regge trajectories and its optimal value  $\Lambda = 600\text{MeV}$  is used in previous section.

## 4. Glueballs

The experimental status of glueballs is not clear up to now, although they are very interesting objects from the theoretical point of view. Indeed, it is quite intriguing how can massless gluons be merged into massive object? It is evident that the structure of QCD vacuum plays the main role in formation of glueballs, any direct guess about its explicit structure is avoided.

Omitting details, we just write down the polarization kernel for the  $gg$  bound state with quantum numbers  $J^{PC} = 0^{++}$ :

$$\tilde{\Pi}(p^2) = 6(3h)^2 \max \frac{\int d\xi \int d\eta e^{-c(\xi^2+\eta^2)} D(\xi) D(\eta) \int dz e^{-ipz} D\left(z + \frac{\xi-\eta}{2}\right) D\left(z - \frac{\xi-\eta}{2}\right)}{\int d\xi e^{-2c\xi^2} D(\xi)}.$$

Taking into account:

$$D(\xi) = \frac{\Lambda^2}{(4\pi)^2} e^{-\Lambda^2 \xi^2/4}, \quad \kappa = \max \left\{ \frac{c + 1/8}{(c + 3/8)(c + 3/8 - 1/48/(c + 3/8))} \right\} = 1.2122\dots$$

we write the mass equation and obtain the glueball mass:

$$1 - \tilde{\Pi}(-M_G^2) = 0, \quad M_G = \Lambda \sqrt{2 \ln \frac{128\pi}{27\lambda\kappa}}.$$

Substituting the coupling constant and  $\Lambda$  we obtain:

$$\lambda = \frac{h^2}{4\pi} = 0.33, \quad \Lambda = 600 \text{ MeV} \quad \Rightarrow \quad M_G = 1614 \text{ MeV}$$

This result may be compared with other predictions of the glueball mass:

1730 ± 130 MeV	M.Pearidon [1999]
1740 ± 150 MeV	M.Teper [1999]
1580 MeV	Y.A.Simonov [2000]
1530 ± 200 MeV	H.Forkel [2001]

## References

- [1] H. Leutwyler, Phys. Lett. **96B** 154 (1980) Nucl. Phys. **B179** 129 (1981)
- [2] Ja.V.Burdanov, G.V.Efimov, S.N.Nedelko, S.A.Solunin, Phys.Rev. **D54** 4483 (1996)
- [3] A. Ahlig et al., Phys. Rev. **D64** 014004 (2001)
- [4] G.V. Efimov and G. Ganbold, Phys. Rev. **D65** 054012 (2002)
- [5] G. Ganbold, Hadron Spectroscopy AIP **717** 285 (2004)
- [6] M.Baldicchi and G.M.Prosperi, hep-ph/0310213 (2003)
- [7] D.V.Schirkov, Theor. Math. Phys. **132** 484 (2002)
- [8] A.V.Nesterenko, Int. J. M. Phys. **A18** 5475 (2003)

# SOLVING THE INHOMOGENEOUS BETHE-SALPETER EQUATION

S.S. Semikh<sup>1†</sup>, S.M. Dorkin<sup>2</sup>, M. Beyer<sup>3</sup>, L.P. Kaptari<sup>1</sup>

(1) *BLTP, Joint Institute for Nuclear Research*

(2) *SNPI, Moscow State University*

(3) *University of Rostock, Germany*

† *E-mail: semikh@thsun1.jinr.ru*

## Abstract

We develop an advanced method of solving homogeneous and inhomogeneous Bethe-Salpeter equations by using the expansion over the complete set of 4-dimensional spherical harmonics. We solve Bethe-Salpeter equations for bound and scattering states of scalar and spinor particles for the case of one meson exchange kernels. Phase shifts calculated for the scalar model are in agreement with the previously published results. We discuss possible manifestations of separability for one meson exchange interaction kernels.

## 1. Introduction and preliminaries

Obtaining solutions of inhomogeneous Bethe-Salpeter (BS) equations is a long standing problem with clear motivation – BS amplitude in continuum (or half-off-shell  $T$ -matrix) is a necessary ingredient for description of final state interaction in numerous processes with the correlated nucleon-nucleon pair in final state. As an example one can mention, for instance, charge-exchange reaction on deuteron  $pD \rightarrow n(pp)$  [1], deuteron break-up with fast forward  $pp$ -pair [2], electro- and photo-disintegration of deuteron [3] etc. One of the possible ways to obtain the BS amplitude in continuum is the so-called one iteration approximation scheme [4], when the relativistic  $P$ -components are obtained as first iteration from the non relativistic wave function with a certain interaction kernel. In [5] the inhomogeneous BS equation for spinor particles is regularly treated with a 2-dimensional Gaussian mesh. Although there are no doubts in correctness of these results, it can be shown that, in general, inappropriate choice of a 2-dimensional mapping in integration procedure can lead to under- or overestimation of the solutions. In this sense a 2-dimensional change of variables that one has to apply in partial BS equation for transforming the limits of integration to finite ones is not well defined procedure. Thus, the search of the rigorous method to solve such an equations should be continued.

In [6] the expansion of the BS amplitude and interaction kernel over hyperspherical basis is employed to formulate a method of solving the BS equation for bound states of scalar particles,

$$\Gamma(k) = i \int \frac{d^4 p}{(2\pi)^4} V(k, p) S(p_1) S(p_2) \Gamma(p), \quad (1)$$

$p_{1,2} = P/2 \pm p$ , and  $S(p) = (p^2 - m^2 + i\varepsilon)^{-1}$ . The corresponding expansions after the Wick rotation looks like

$$\Gamma(ik_4, \mathbf{k}) = \sum_{nlm} \varphi_l^n(\tilde{k}) Z_{nlm}(\omega_k), \quad (2)$$

$$\begin{aligned}
V(k, p) &= \frac{g^2}{(k-p)^2 + \mu^2} = 2\pi^2 \sum_{nlm} \frac{1}{n+1} V_n(\tilde{k}, \tilde{p}) Z_{nlm}(\omega_k) Z_{nlm}^*(\omega_p), \\
V_n(a, b) &= \frac{4g^2}{(\Lambda_+ + \Lambda_-)^2} \left( \frac{\Lambda_+ - \Lambda_-}{\Lambda_+ + \Lambda_-} \right)^n, \\
\Lambda_{\pm} &= \sqrt{(a \pm b)^2 + \mu^2},
\end{aligned} \tag{3}$$

where by definition  $\tilde{k} = \sqrt{k_4^2 + \mathbf{k}^2}$ , and  $\omega_k = (\chi, \theta, \phi)$  - angles of vector  $k = (k_4, \mathbf{k})$  in 4-dimensional Euclidean space. Hyperspherical harmonics

$$Z_{nlm}(\chi, \theta, \phi) = X_{nl}(\chi) Y_{lm}(\theta, \phi), \quad X_{nl}(\chi) \sim \sin^l \chi C_{n-l}^{l+1}(\cos \chi),$$

are proportional to the product of usual spherical harmonics for orbital momentum  $l$  and Gegenbauer polynomials  $C_{n-l}^{l+1}$ .

Performing a Wick rotation in (1) and substituting (2) and (3) one reduces the BS equation to the infinite set of 1-dimensional integral equations. Thus, there is only one degree of freedom left in the choice of the mapping for integration. It is shown in [6], that this approach is very effective for numerical purpose. In particular, due to rapid convergence of hyperspherical expansion, the consideration of only first few equations from the set is sufficient.

## 2. Inhomogeneous BS equation for scalar particles

In this paper the method introduced in [6] is applied to the scalar inhomogeneous BS equation, and generalized to spinor equations, both homogeneous and inhomogeneous. Let us first consider the BS equation for the scattering of scalar particles:

$$T(k) = V(k, q) + i \int \frac{d^4 p}{(2\pi)^4} V(k, p) S(p_1) S(p_2) T(p). \tag{4}$$

Here  $T(k)$  is half-off-shell  $T$ -matrix for the scattering of real particles with momenta  $q_{1,2}$ , and in c.m.s., where the real 3-momentum of particles  $|\mathbf{q}| = \hat{p}$ ,

$$s = (q_1 + q_2)^2 = (2E_{\hat{p}})^2, \quad E_{\hat{p}} = \sqrt{m^2 + \hat{p}^2}, \quad q = \frac{q_1 - q_2}{2}, \quad (2m)^2 < s < (2m + \mu)^2$$

Before Gegenbauer decomposition of type (2) and (3) the Wick rotation should be applied. It is more convenient to perform firstly in (4) the usual partial expansion over the spherical harmonics  $Y_{lm}$  (see also [7]):

$$T_l(k_0, k) = g^2 Q_l(k_0, k; 0, \hat{p}) - i \int \frac{dp_0 dp}{(2\pi)^3} g^2 Q_l(k_0, k; p_0, p) S(p_1) S(p_2) T_l(p_0, p). \tag{5}$$

Here  $Q_l(k_0, k; p_0, p) \equiv Q_l([k^2 + p^2 + \mu^2 - (k_0 - p_0)^2 - i\varepsilon]/2kp)$  is the adjoint Legendre function of the 2nd kind. The normalization of  $T$ -matrix is fixed by the free term in (5) and leads to the following expression for the phase shifts:

$$T_l(0, \hat{p}) = 16\pi \hat{p} \sqrt{s} e^{i\delta_l} \sin \delta_l. \tag{6}$$

To eliminate the removable singularity at  $(p_0, p) = (0, \hat{p})$ , we present the  $T$ -matrix in the following factorized form [8]:

$$T_l(k_0, k) \sim \varphi_l(k_0, k) t_l(s), \quad t_l(s) \sim e^{i\delta_l} \sin \delta_l,$$

thus obtaining from (5) the equation for  $\varphi_l$ ,

$$\begin{aligned} \varphi_l(k_0, k) = & g^2 Q_l(k_0, k; 0, \hat{p}) - i \int \frac{dp_0 dp}{(2\pi)^3} \{g^2 Q_l(k_0, k; p_0, p) \\ & - \frac{g^2}{Q_l(s)} Q_l(k_0, k; 0, \hat{p}) Q_l(0, \hat{p}; p_0, p)\} S(p_1) S(p_2) \varphi_l(p_0, p), \end{aligned} \quad (7)$$

$Q_l(s) \equiv Q_l(0, \hat{p}; 0, \hat{p})$ . In the following only the cases  $l = 0, 1$  will be considered. After the Wick rotation the Gegenbauer decomposition of  $\varphi_l$  for  $l = 0$  takes the form

$$\varphi_0(ik_4, k) = k\hat{p} \sum_{j=1}^{\infty} g_j(\bar{k}) X_{2j-2,0}(\chi), \quad (8)$$

and for the coefficient functions  $g_j$  the system of integral equations is obtained:

$$\begin{aligned} g_j(\bar{k}) = & \frac{\pi}{2j-1} V_{2j-2}(\bar{k}, \hat{p}) X_{2j-2,0} \left( \frac{\pi}{2} \right) \\ & + \sum_{l=1}^{\infty} \int_0^{\infty} \frac{d\bar{p} \bar{p}^3}{8\pi^2} \left[ \frac{1}{2j-1} V_{2j-2}(\bar{k}, \bar{p}) S_{2j-2,2l-2}^0(\bar{p}) \right. \\ & - \left. \frac{\hat{p}^2}{2j-1} V_{2j-2}(\bar{k}, \hat{p}) X_{2j-2,0} \left( \frac{\pi}{2} \right) \frac{1}{Q_0(s)} N_{0,2l-2}(\hat{p}, \bar{p}) \right] g_l(\bar{p}) \\ & - \int_0^{\hat{p}} \frac{dp}{8\pi^2} \frac{1}{E_p \sqrt{s} (\sqrt{s} - 2E_p)} \left[ \frac{p}{\hat{p}} g^2 W_{2j-2,0}(\bar{k}, p) \right. \\ & - \left. \frac{2}{Q_0(s)} \frac{\pi}{2j-1} V_{2j-2}(\bar{k}, \hat{p}) X_{2j-2,0} \left( \frac{\pi}{2} \right) Q_0(0, \hat{p}; p_2^0, p) \right] \tau_0(p), \end{aligned} \quad (9)$$

$$\begin{aligned} \tau_0(k) = & g^2 Q_0(k_2^0, k; 0, \hat{p}) + g^2 \hat{p} \sum_{l=1}^{\infty} \int_0^{\infty} \frac{d\bar{p} \bar{p}^3}{(2\pi)^3} [k N_{0,2l-2}(k, \bar{p}) \\ & - \frac{\hat{p}}{Q_0(s)} Q_0(k_2^0, k; 0, \hat{p}) N_{0,2l-2}(\hat{p}, \bar{p})] g_l(\bar{p}) \\ & - g^2 \int_0^{\hat{p}} \frac{dp}{8\pi^2} \frac{1}{E_p \sqrt{s} (\sqrt{s} - 2E_p)} [k p U_0(k, p) \\ & - \frac{2}{Q_0(s)} Q_0(k_2^0, k; 0, \hat{p}) Q_0(0, \hat{p}; p_2^0, p)] \tau_0(p). \end{aligned} \quad (10)$$

The additional unknown function  $\tau_0$  comes after the Wick rotation from the residue at the pole  $p_2^0 = \sqrt{s}/2 - E_p + i\varepsilon$ , which is able to cross the imaginary  $p_0$  axis. It is

proportional to the  $T$ -matrix in Minkowsky space for certain value of relative energy,  $\tau_0(p) \sim T_0(\sqrt{s}/2 - E_p, p)$ . The partial kernels are

$$\begin{aligned}
 S_{k'k}^l(\tilde{p}) &= \int_0^\pi d\chi \sin^2 \chi \frac{X_{k'l}(\chi)X_{kl}(\chi)}{(\tilde{p}^2 - \hat{p}^2)^2 + s\tilde{p}^2 \cos^2 \chi}, \\
 N_{ml}(k, \tilde{p}) &= \int_0^\pi d\chi_p \sin^2 \chi_p \frac{1}{2kp} \{Q_m(k_2^0, k; ip_4, p) \\
 &\quad + Q_m(-k_2^0, k; ip_4, p)\} \frac{X_{lm}(\chi_p)}{(\tilde{p}^2 - \hat{p}^2)^2 + s\tilde{p}^2 \cos^2 \chi_p}, \\
 W_{nl}(\tilde{k}, p) &= \int_0^\pi d\chi_k \sin^2 \chi_k X_{nl}(\chi_k) \frac{1}{kp} \{Q_l(ik_4, k; p_2^0, p) + Q_l(ik_4, k; -p_2^0, p)\}, \\
 U_l(k, p) &= \frac{1}{kp} \{Q_l(k_2^0, k; p_2^0, p) + Q_l(k_2^0, k; -p_2^0, p)\}.
 \end{aligned}$$

It is easy to see that all the partial kernels are real expressions.

### 3. Numerical results and separability

As all the integrations in system (9), (10) are 1-dimensional, the integrals can be replaced by finite sums by using the gaussian mesh. In this way this system is reduced to the usual system of linear equations, which can be solved by any appropriate method. Besides, the solution of integral equations (9), (10) can be obtained by iterating the free term, thus constructing the Neumann series, which represents the solution of an inhomogeneous integral equation. It was explicitly checked that these two procedures of finding a solution lead to the same results.

Taking the first five terms in the expansion (8), the system (9), (10) was numerically considered for the following set of parameters:

$$\frac{g^2}{4\pi} = 4\pi, \quad m = \mu = 1 \text{ GeV}, \quad \hat{p} = 0.77 \text{ GeV}/c$$

In Fig. 1 the numerical results for the first three coefficient functions from (8) are shown. It was established that convergence of this expansion is quite rapid, that is why only 3 components are presented and  $g_2$  and  $g_3$  are multiplied by 10 and 100 respectively. Centered symbols correspond to the points of the mesh, where the solution is defined. Lines connecting the points reproduce the results of the fit for the obtained Gegenbauer components with the fitting functions

1. For  $g_1(p), p \equiv \tilde{p}$

$$F(p) = \sum_{j=1}^4 \frac{a_j^1 p^{2j-2}}{(p^2 + b_1^2)^j}, \quad (11)$$

2. For  $g_2(p)$

$$F(p) = \frac{p^2}{p^2 + b_2^2} \sum_{j=1}^4 \frac{a_j^2 p^{2j-2}}{(p^2 + b_2^2)^j}, \quad (12)$$

3. For  $g_3(p)$

$$F(p) = \left[ \frac{p^2}{p^2 + b_3^2} \right]^2 \sum_{j=1}^4 \frac{a_j^3 p^{2j-2}}{(p^2 + b_3^2)^j} \quad (13)$$

For the sake of brevity we don't show here the numerical values of the parameters  $a_j^{1,2,3}$  and  $b_{1,2,3}$ , which can be adjusted by any appropriate method (for instance, the built-in fitting procedure in Microcal Origin 7.0 can be employed). It should be mentioned that the quality of this analytical fit is excellent in the whole range of the argument  $\bar{p}$  despite the very simple form of the functions (11)-(13). This fact can be treated as an indication to some kind of separability in the one meson exchange interaction and will be discussed below. Besides, it was found that such a fit is valid for Gegenbauer components of solutions of any BS equation in ladder approximation (scalar and spinor equations, both homogeneous and inhomogeneous). Hence, it is very useful for practical purposes, e.g. to represent the numerical results in a compact form.

To discuss the manifestations of separability in more details, let us now turn to the homogeneous BS equation (1). After Wick rotation and usual partial decomposition it gives

$$\Gamma_l(ik_4, k) = \int \frac{dp_4 dp p^2}{(2\pi)^3} V_l(ik_4, k; ip_4, p) S(p_1) S(p_2) \Gamma_l(ip_4, p). \quad (14)$$

It is generally known that for the conventional separable kernel of the form (see e.g. [9])

$$V_l(ik_4, k; ip_4, p) = \sum_{ij} \lambda_{ij}(s) g_i(\vec{k}^2) g_j(\vec{p}^2)$$

the vertex functions are expressed in terms of functions  $g$ :

$$\Gamma_l(ik_4, k) = \sum_i c_i g_i(\vec{k}^2).$$

In our case, solving equation (14) for kernel (3) by the method given above and fitting the calculated Gegenbauer components with analytical expressions like (11)-(13), we obtain the following approximate representation for the solution (cf. (8)):

$$\Gamma_l(ik_4, k) = \sum_{j=1}^N c_j^l R_{jl}(\vec{k}^2) X_{jl}(\chi_k), \quad (15)$$

where the fitting functions are

$$R_{jl}(\vec{k}^2) = \frac{(\vec{k}^2)^{\mu_{jl}}}{(\vec{k}^2 + \beta_{jl}^2)^{\nu_{jl}}}.$$

It is clear that constructing the expression for the separable kernel like

$$V_l(ik_4, k; ip_4, p) = \sum_{ij} \lambda_{ij}(s) g_{il}(p_4, p) g_{jl}(k_4, k) \quad (16)$$

with

$$g_{jl}(k_4, k) = R_{jl}(\vec{k}^2) X_{jl}(\chi_k) \quad (17)$$

one identically reproduces the analytical form of the solution (15). Therefore, the kernel (16), (17) can be referred to as some general form for constructing separable kernels. Note that it has the following properties:

- A dependence on mass (or  $s$ ) in the functions  $g$
- An explicit dependence on  $k_4$  in  $g$  coming from Gegenbauer polynomials being the functions of  $\cos \chi_k = k_4/k$
- At low  $k^2$  (16) tends to a Yamaguchi kernel, because  $g(k^2) \rightarrow \frac{C}{k^2 + \beta^2}$

A concrete example of the solution of eq. (14) is given in Table 1. The parameters  $\lambda_{ij}$  [GeV<sup>5</sup>] for the partial kernel (16) of rank 3 are

$$\begin{aligned} \lambda_{11} &= 0.19613 & \lambda_{22} &= 0.13734 & \lambda_{33} &= -0.01644 \\ \lambda_{12} &= -0.09675 & \lambda_{13} &= 0.00236 & \lambda_{23} &= -0.00034. \end{aligned}$$

$j$	$c_j^0$	$\beta_{j0}$ [GeV]	$\mu_{j0}$	$\nu_{j0}$
0	0.17904	0.39736	0	1
2	-0.00923	0.41533	1	2
4	0.00127	0.43362	2	3
6	-0.00055	0.45127	3	4
8	0.00017	0.47019	4	5

Table 1. Numerical values of parameters in (15) for  $l = 0$ ,  $m = 1$  GeV, mass of bound state  $M = 1.9$  GeV,  $\mu = 0.1$  GeV. Coefficients  $c_j^0$  for odd values of  $j$  are equal to zero.

Analyzing the obtained solutions for the system (9), (10) it is also informative to calculate corresponding phase shifts. The results for  $l = 0$  are presented in Fig. 2 for different values of coupling constant  $\lambda$  connected with  $g^2$  as  $\frac{g^2}{4\pi} = 4\pi\lambda$ . It is obvious, that for  $\lambda = 0.7$  there are no bound states in this system due to the Levinson's theorem. For the values  $\lambda = 1, 3, 5$  there is one bound state, and two bound states for  $\lambda = 7$ . Obtained results for the phase shifts are in a good agreement with [8].

Further development of the formalism and results of solving the inhomogeneous equations for spinor particles can be found in [11].

## 4. Acknowledgments

We are grateful to K.Yu. Kazakov for valuable discussions. S.M.D. and S.S.S. acknowledge the warm hospitality of the Elementary particle physics group of the University of Rostock, where part of this work was performed. This work is supported by the Heisenberg - Landau program of JINR - FRG collaboration and by the Deutscher Akademischer Austauschdienst.

## References

- [1] L.P. Kaptari, B. Kämpfer, S.S. Semikh, S.M. Dorkin, Eur. Phys. J. **A17** (2003) 119.

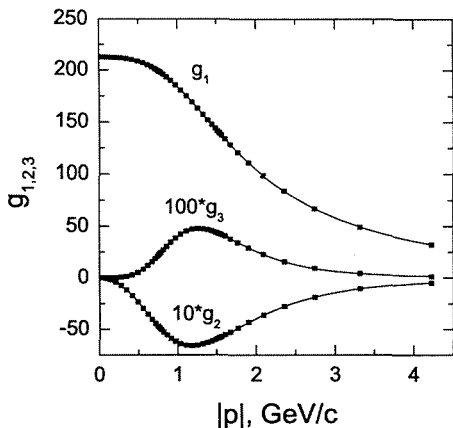


Figure 1: Gegenbauer components from (8). Functions  $g_2$  and  $g_3$  are multiplied by 10 and 100 respectively in view of their smallness

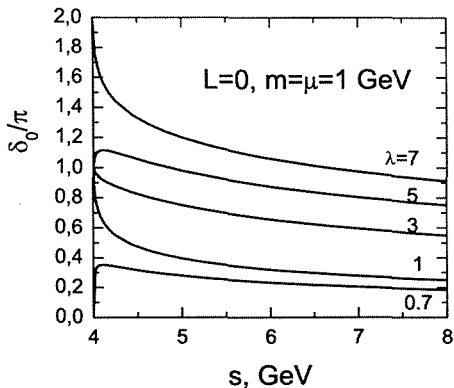


Figure 2: Phase shifts (in the units of  $\pi$ ) for  $l = 0$  and different values of coupling constant

- [2] L.P. Kaptari, B. Kämpfer, S.S. Semikh, S.M. Dorkin, Eur. Phys. J. **A19** (2004) 301.
- [3] C. Ciofi degli Atti, L.P. Kaptari, e-Print Archive: nucl-th/0407024; C. Ciofi degli Atti, L.P. Kaptari, D. Treleani, Phys. Rev. **C63** (2001) 044601.01; S.G. Bondarenko, V.V. Burov, M. Beyer, S.M. Dorkin, e-Print Archive: nucl-th/9612047.
- [4] L.P. Kaptari, B. Kämpfer, S.M. Dorkin, S.S. Semikh, Phys. Rev. **C57** (1998) 1097; S.G. Bondarenko, V.V. Burov, M. Beyer, S.M. Dorkin, Phys. Rev. **C58** (1998) 3143.
- [5] M.J. Zuilhof, J.A. Tjon, Phys. Rev. **C22** (1980) 2369 *and references therein*.
- [6] T. Nieuwenhuis, J.A. Tjon, Few-Body Syst. **21** (1996) 167.
- [7] S.M. Dorkin, L.P. Kaptari, S.S. Semikh, Phys. Atom. Nucl. **60** (1997) 1629; Yad. Fiz. **60** (1997) 1784.
- [8] M.J. Levine, J. Wright, J.A. Tjon, Phys. Rev. **154** (1967) 1433; M. Fortes, A.D. Jackson, Nucl. Phys. **A175** (1971) 449.
- [9] G. Rupp, J.A. Tjon, Phys. Rev. **C41** (1990) 472.
- [10] L.P. Kaptari, A.Yu. Umnikov, S.G. Bondarenko, K.Yu. Kazakov, F.C. Khanna, B. Kämpfer, Phys. Rev. **C54** (1996) 986.
- [11] S.S. Semikh, S.M. Dorkin, M. Beyer, L.P. Kaptari, e-Print Archive: nucl-th/0410076.

# DETERMINATION OF THE GLUEBALL MASS SPECTRUM WITH THE SPIN-ORBIT INTERACTION IN NONPERTURBATIVE QCD-APPROACH

M. Dineykhani<sup>1</sup>, S. A. Zhaugasheva<sup>1,2</sup>, T. A. Kozhamkulov<sup>2</sup>

(1) *Bogoliubov Laboratory of Theoretical Physics, Joint Institute for Nuclear Research, Dubna*

(2) *al-Farabi Kazak National University, 480012, Almaty, Kazakhstan*

## Abstract

The mass spectrum of the bound state is analytically derived. The mechanism for arising of the constituent mass of the bound state forming particles is explained. Change of the bound state mass and of the constituent mass of particles is analyzed by the varying the coupling constant. The mass spectrum of the two-gluon glueball is calculated taking into account spin-orbit and spin-spin interactions.

## 1. Introduction

For the last three decades theorists have been trying to derive the effective potential of the quark interaction, starting from the basic principle of the QCD which explains the requirement of the confinement and deconfinement of the constituent particles [1]. There is a lot of potential models of quarks which are constructed on the basis of non-relativistic picture of confinement. These models are mainly applicable to physics of hadrons consisting of heavy quarks. The properties of hadrons consisting of light quarks are dominated by the relativistic character of the interactions, which requires additional efforts to incorporate relativistic effects. It is known (for instance, [2]) that relativistic effects in the bound state formation in the quantum field systems can be taking into account as small corrections only in the weak coupling regime, but the strongly coupled systems like hadrons in QCD ultimately require fully relativistic consideration which can be adequately realised only by means of genuine field theoretical methods. One of the most powerful method of this kind is based on the Bethe-Salpeter equation. Application of Bethe-Salpeter equation in QCD assumes an appropriate approximate choice of the kernel, which is usually chosen on the basis of physical assumptions about nonperturbative QCD vacuum (see, for example [3, 4]).

Another field theoretical method based on the Fock-Feynman-Schwinger representation was suggested in [5]. This method successfully applied [6] for the description of the hadron and glueball mass spectra. The keynote of this approach is the presentation of the polarized loop function as a functional integral and the main problem is its integration. Of course, this integral is not evaluated in general but only in certain physical assumptions. One of the alternative methods of the functional integral evaluation and determination of the glueball mass with taking into account the nonperturbative and relativistic character of the interaction is suggested in the [7]. In this work, we present one of the alternative methods of the bound state mass determination. The bound state mass determined in the form

$$M = \sqrt{m_1^2 - 2\mu^2 E'(\mu)} + \sqrt{m_2^2 - 2\mu^2 E'(\mu)} + \mu E'(\mu) + E(\mu). \quad (1)$$

The parameter  $\mu$  can be determined from the equation

$$\frac{1}{\mu} = \frac{1}{\mu_1} + \frac{1}{\mu_2} = \frac{1}{\sqrt{m_1^2 - 2\mu^2 \cdot E'(\mu)}} + \frac{1}{\sqrt{m_2^2 - 2\mu^2 \cdot E'(\mu)}}, \quad (2)$$

where the following notation is used:

$$E'(\mu) = \partial E(\mu) / \partial \mu. \quad (3)$$

We will consider the parameters  $\mu_1$  and  $\mu_2$  as masses of the constituent particles in the bound state. These masses differ from  $m_1$  and  $m_2$  which represent the masses of a free state. To describe the mass spectrum of the relativistic bound state, the constituent mass, which differs from the mass of the initially free particle. Particularly, when describing the hadron mass spectrum, the masses of the valence and current quarks are introduced. On the other hand, if the bound state consists of two gluons, then the constituent mass of gluons is nonzero, according to (2). In this case, one can identify the two-gluon bound state with the pomeron which is broadly used in describing the mechanism of the inelastic scattering of particles. The quantity  $E(\mu)$  is defined as eigenvalues of the interaction Hamiltonian with the nonperturbative correction. The nonperturbative correction to the interaction Hamiltonian represented as (the detail see [7])

$$H^0 = \frac{1}{2\mu} \cdot \vec{P}^2 - \frac{4\alpha_s}{3r} + V(0);$$

$$\Delta H_{nonper}^0 = -\frac{4\alpha_s}{3r} \cdot \left[ \frac{1}{\sqrt{1 + \ell(\ell + 1)/(c^2 r^2 \mu^2)}} - 1 \right]. \quad (4)$$

## 2. Calculation of the glueball mass spectrum taking into account the spin-orbit interaction

Let us determine the mass spectrum of the two-gluon bound state when all effects of the gluon-gluon interaction such as the one-gluon exchange, nonperturbative character, and spin-orbit corrections are taken into account. The total Hamiltonian can be written as a sum of two parts. The first one is the central Hamiltonian which corresponds to the conditions of the one-gluon exchange and nonperturbative character of interaction and also to the confinement. The second one is the Hamiltonian of the spin-orbit interaction

$$H = H_c + H_{spin}, \quad (5)$$

where  $H_c$  is the central part

$$H_c = \frac{1}{2\mu} \vec{P}^2 + \sigma_{ad} r - \frac{4\alpha_s}{3r} - \frac{4\alpha_s}{3r} \left[ \frac{1}{\sqrt{1 + \ell(\ell + 1)/(r^2 \mu^2)}} - 1 \right]. \quad (6)$$

The second part of the Hamiltonian is defined in the standard form

$$H_{spin} = H_{SS} + H_{LS} + H_{TT}. \quad (7)$$

where  $H_{SS}$  is the spin-spin interaction Hamiltonian

$$H_{SS} = \frac{(\mathbf{S}_1 \mathbf{S}_2)}{\mu^2} \Delta V_v, \quad (8)$$

and also the spin-orbit interaction Hamiltonian

$$H_{LS} = \frac{(\mathbf{L} \mathbf{S})}{8\mu^2} \left[ \frac{3}{r} \frac{\partial}{\partial r} V_v - \frac{1}{r} \frac{\partial}{\partial r} V_s \right], \quad (9)$$

and, at last, the tensor interaction Hamiltonian

$$H_{TT} = \frac{S_{12}}{48\mu^2} \left[ \frac{1}{r} \frac{\partial}{\partial r} V_v - \frac{\partial^2}{\partial r^2} V_v \right]. \quad (10)$$

Here  $V_v$  is the vector potential corresponding to the one-gluon exchange

$$V_v = -\frac{4\alpha_s}{3} \frac{1}{\sqrt{r^2 + \ell(\ell+1)/\mu^2}}; \quad (11)$$

$V_s$  is the confinement potential

$$V_s = r\sigma_{ad}; \quad (12)$$

and also the following notation is used:

$$\begin{aligned} \mathbf{S} &= \mathbf{S}_1 + \mathbf{S}_2 \\ S_{12} &= \frac{4}{(2\ell+3)(2\ell-1)} \left[ \mathbf{L}^2 \mathbf{S}^2 - \frac{3}{2}(\mathbf{L} \mathbf{S}) - 3(\mathbf{L} \mathbf{S})^2 \right]. \end{aligned} \quad (13)$$

Using the explicit form of the Hamiltonian introduced in equations (7)-(13), let us start to determine the mass of the glueball with the spin-spin interactions when  $\ell = 0$ . In this case, for the energy spectrum we have

$$\varepsilon_0(E) = \varepsilon_0^C(E) + \varepsilon_0^{SS}(E), \quad (14)$$

where  $\varepsilon_0^C(E)$  and  $\varepsilon_0^{SS}(E)$  are the contributions of the Hamiltonians of the central and spin-spin interactions, respectively:

$$\begin{aligned} \varepsilon_0^C(E) &= \frac{(1+\rho)\omega}{2} + \frac{4\rho^2\mu\sigma_{ad}}{\omega^{3\rho-1}} \frac{\Gamma(4\rho)}{\Gamma(1+\rho)} - \frac{4\rho^2\mu E}{\omega^{2\rho-1}} \frac{\Gamma(3\rho)}{\Gamma(1+\rho)} - \\ &\quad - \frac{16\alpha_s\rho^2\mu\omega^{1+\rho}}{3\Gamma(1+\rho)} \int_0^\infty du \frac{u^{3\rho-1} e^{-u\omega}}{\sqrt{u^{2\rho} + \ell(\ell+1)/\mu^2}}; \\ \varepsilon_0^{SS} &= \frac{\alpha_s\rho(\mathbf{S}_1 \mathbf{S}_2)}{36\mu} \frac{\omega^{1+\rho}}{\Gamma(1+\rho)}, \end{aligned} \quad (15)$$

After some simplifications we obtain for the energy spectrum

$$E(\mu) = \sqrt{\sigma_{ad}} \cdot \min_{\{\rho, Z\}} \left[ xA + \frac{1}{x}B \right], \quad (16)$$

where the following notation is used:

$$A = \frac{Z^2 \Gamma(2+\rho)}{8\rho^2 \Gamma(3\rho)} - \frac{4Z\alpha_s \Gamma(2\rho)}{3 \Gamma(3\rho)} - \frac{\alpha_s \rho (\mathbf{S}_1 \mathbf{S}_2) Z^3}{144\rho^2 \Gamma(3\rho)}; \quad (17)$$

$$B = \frac{1 \Gamma(4\rho)}{Z \Gamma(3\rho)}; \quad x = \frac{\mu}{\sqrt{\sigma_{ad}}},$$

and the  $x$  parameter is derived from (1), (2). Using this parameter for the glueball mass we have

$$M = \sqrt{\sigma_{ad}} \left[ 2x + \frac{E(\mu)}{\sqrt{\sigma_{ad}}} \right]. \quad (18)$$

In this case, the mass glueball corresponding to the following states, is determined

$$J^{PC} = 0^{++}, 1^{+-}, 2^{++}.$$

Our numerical results are presented in Table 1.

**Table 1.** The mass spectrum of the glueball with taking into account the nonperturbative character of interaction and spin-spin interaction for the case of  $\ell = 0$ . In  $GeV$  units.  $\sigma_{ad} = 0.45 GeV^2$ ,  $\alpha_s = 0.3$

$J^{PC}$	<i>our result</i>	<i>lattice data</i>	<i>Exp.</i>	<i>other works</i>
$0^{++}$	1.64	1.73 [8]		
		1.63 [9]	1.50 [12]	
		1.61 [10]	2.11 [12]	1.98 [14]
		1.75 [11]	2.32 [13]	2.69 [15]
$2^{++}$	1.97	2.40 [17]		
		2.35 [9]	2.02 [16]	2.42 [14]
		2.26 [10]		2.70 [15]
		2.42 [11]		

From Table 1, we can see that our results are in good agreement with the results of other authors. Let us now consider the general case when  $\ell \neq 0$ . We obtain the energy spectrum  $E(\mu)$  for the total Hamiltonian from SE

$$E = E^{(C)} + E^{(SS)} + E^{(LS)} + E^{(TT)}. \quad (19)$$

Here  $E^{(C)}$  is the contribution of the central interaction Hamiltonian

$$E^{(C)} = \frac{x^2 \sqrt{\sigma_{ad}} \Gamma(2+\rho+2\rho\ell)}{8\rho^2 \Gamma(3\rho+2\rho\ell)} + \frac{\sqrt{\sigma_{ad}} \Gamma(4\rho+2\rho\ell)}{xz \Gamma(3\rho+2\rho\ell)} - \frac{4\alpha_s xz \sqrt{\sigma_{ad}}}{3\Gamma(3\rho+2\rho\ell)} \int_0^\infty du \frac{u^{3\rho+2\rho\ell-1} e^{-u}}{\sqrt{u^{2\rho} + z^2 \ell(\ell+1)}}; \quad (20)$$

$E^{(LS)}$  is the spin-orbit interaction contribution

$$E^{(LS)} = \frac{z^2 \sqrt{\sigma_{ad}} (\mathbf{L} \mathbf{S})}{8\Gamma(3\rho+2\rho\ell)} \left\{ -\frac{\Gamma(2\rho+2\rho\ell)}{xz} + 4\alpha_s xz \int_0^\infty du \frac{u^{3\rho+2\rho\ell-1} e^{-u}}{[u^{2\rho} + z^2 \ell(\ell+1)]^{3/2}} \right\}; \quad (21)$$

$E^{(TT)}$  is the inclusion for the tensor interaction

$$E^{(TT)} = \frac{\alpha_s x z^3 \sqrt{\sigma_{ad}} S_{12}}{12\Gamma(3\rho + 2\rho\ell)} \int_0^\infty du \frac{u^{5\rho+2\rho\ell-1} e^{-u}}{[u^{2\rho} + z^2\ell(\ell+1)]^{5/2}} ; \quad (22)$$

and  $E^{(SS)}$  is the contribution of the spin-spin interaction

$$E^{(SS)} = \frac{\alpha_s \ell \sqrt{\sigma_{ad}} (\mathbf{S}_1 \mathbf{S}_2)}{18\Gamma(3\rho + 2\rho\ell)} \cdot x z^3 \rho^2 \int_0^\infty du \frac{u^{3\rho+2\rho\ell-1} e^{-u}}{[u^{2\rho} + z^2\ell(\ell+1)]^{5/2}} \times \left[ u^{2\rho} + \frac{z^2}{2} (3 + 2\ell)(1 + \ell) \right] . \quad (23)$$

The parameter  $x$  is derived from the equation

$$2 + \frac{1}{\sqrt{\sigma_{ad}}} \frac{\partial E}{\partial x} - 0 , \quad (24)$$

and then the energy spectrum is determined in the following form:

$$E(\mu) = \min_{\{\rho, z\}} [E(x, \rho, z)] . \quad (25)$$

The numerical results are in Table 2.

**Table 2.** The mass spectrum of the glueball for the general case. In  $GeV$  units.

$\sigma_{ad} = 0.45 GeV^2$ ,  $\alpha_s = 0.3$

	$\ell = 1$			$\ell = 2$			$\ell = 3$		
	$J^{PC}$	<i>our result</i>	<i>other works</i>	$J^{PC}$	<i>our result</i>	<i>other works</i>	$J^{PC}$	<i>our result</i>	<i>other works</i>
$S = 0$	$0^{--}$	2.95		$0^{++}$	3.39	1.72 [8]	$0^{--}$	3.95	
	$1^{--}$	2.99		$1^{++}$	3.42		$1^{--}$	3.97	3.81 [8]
				$2^{++}$	3.47	3.50 [11]	$2^{--}$	4.00	3.90 [8]
							$3^{--}$	4.05	4.10 [8]
$S = 1$	$0^{-+}$	2.92	2.59 [17]	$0^{+-}$	3.36	4.82 [8]	$0^{-+}$	3.90	3.64 [10]
	$1^{-+}$	2.95		$1^{+-}$	3.39	2.95 [8]	$1^{-+}$	3.95	
	$2^{-+}$	3.02	3.10 [17]	$2^{+-}$	3.44	4.10 [8]	$2^{-+}$	3.99	3.89 [10]
				$3^{+-}$	3.52	3.53 [8]	$3^{-+}$	4.03	
							$4^{-+}$	4.10	
$S = 2$	$0^{--}$	2.86		$0^{++}$	3.31	2.67 [8]	$0^{--}$	3.90	
	$1^{--}$	2.89		$1^{++}$	3.33		$1^{--}$	3.92	
	$2^{--}$	2.95		$2^{++}$	3.38	2.38 [8]	$2^{--}$	3.95	
	$3^{--}$	3.05		$3^{++}$	3.46	3.69 [10]	$3^{--}$	4.00	

The mass spectrum of the two-gluon glueball is calculated taking into account spin-orbit and spin-spin interactions.

Our approach allows a unified description of the mass spectrum of glueball for various states with various spin and orbit quantum numbers. Further, we will apply our approach for the description of the glueball mass spectrum taking radial excitation into consideration and for determination of the hadron mass spectrum.

## References

- [1] Ball, G. S., Schilling, K., Wachter, A.: Phys. Rev. **D56**, 2556 (1997), hep-lat/9703019; Ball, G. S., Boyle, P.: Phys. Rev. **D59**, 114504 (1999), hep-lat/9809180
- [2] Efimov, G. V.: Few-Body Systems **33**,199(2003)
- [3] Efimov, G. V., Nedelko, S. N.: Phys. Rev. **D51**, 170 (1995); Phys.Rev. **D54**, 4483 (1996)
- [4] Roberts, C.D. and Cahill, R.T.: Aust.J. Phys. **40**, 499(1987); Prashifka, J., Roberts, C.D. and Cahill, R.T.: Phys. Rev. **D36**, 209 (1987); **D41**, 627 (1990): Ann.Phys.(N.Y.) **188**, 20(1987)
- [5] Dosch, H. G.: Phys. Lett. **B190**, 177 (1987); Dosch, H. G., Simonov, Yu. A.: Phys.Lett. **B205**, 339 (1998); Simonov, Yu. A.: Nucl. Phys. **B307**, 512 (1988)
- [6] Kaidalov, A. B., Simonov, Yu. A.: Yad. Fiz **63**, 1428 (2000)
- [7] Dineykhon, M., Zhaugasheva S. A., Kozhamkulov T. A., Petrov Ye. V.:Few-Body Systems **34**,(2004)(in press)
- [8] Godfrey, S.: hep-ph/0211464
- [9] Niedermayer, F., Rufenacht, P., Wenger, U.: Nucl. Phys. **B597**, 413 (2001)
- [10] Teper, M. J.: hep-lat/9711011
- [11] Liu, D. Q., Wu, I. M., Chen, Y.: High Energy, Nucl. Phys. **26**, 222 (2002)
- [12] Bugg, D. V., Peardon, M. J., Zou, B. S.: Phys. Lett. **B476**, 49 (2000)
- [13] Anisovich, A. V., et al.: Phys. Lett. **B471**, 271 (1999); Nucl. Phys. **A662**, 319 (2000)
- [14] Szczepaniak, P., Swanson, E. S.: hep-ph/0308268
- [15] Hou, W. S., Wong, G. G.: hep-ph/0207292
- [16] Zou, B. S.: Nucl. Phys. **A655**, 41 (1999)
- [17] Morningstar, C. J., Peardon, M. J.: Phys. Rev. **D31**, 034509(1999); **D56**, 4043 (1997)



**VII.**  
**APPLIED**  
**USE OF**  
**RELATIVISTIC**  
**BEAMS**



# Investigation of Transmutation of Radioactive Waste of Atomic Reactors $^{129}\text{I}$ and $^{237}\text{Np}$ and Neutrons Generation with 1.5 GeV Protons from the Nuclotron at the Setup „Energy plus Transmutation (JINR, Dubna)

M.I. Krivopustov\*, J. Adam, Yu.A. Batusov, A.R. Balabekyan, P. Chaloun, D. Chultem, A.F. Elishev, V.G. Kalinnikov, I.I. Mariin, A.V. Pavliouk, V.S. Pronskikh, V.I. Stegailov, A.A. Solnyshkin, A.N. Sosnin, V.M. Tsoupko-Sitnikov, O.S. Zaverioukha  
*Joint Institute for Nuclear Research, 141980 Dubna, Russian Federation*  
R. Brandt, H. Robotham, K. Siemon, W. Westmeier  
*Fachbereich Chemie, Philipps-Universität, Marburg, Germany*  
R. Odoj

*Institut für Sicherheitsforschung und Reaktortechnik, FZJ, 52425 Jülich, Germany*

V. Henzl, D. Henzlová, A. Krása, F. Krizek, A. Kugler, V. Wagner

*Nuclear Physics Institute of CAS, 250 68 Řež, Czech Republic*

M. Bielewicz, S. Kilim, M. Shuta, A. Vojechowski

*Institute of Atomic Energy, 05-400 Otwock-Swierk, Poland*

S. R. Hashemi-Nezhad

*University of Sydney, Department of High Energy Physics, NSW2006, Australia*

M. Fragopoulou, M. Manolopoulou, S. Stoulos, M. Zamani-Valasiadou

*Physics Department, Aristotle University, Thessaloniki 54124, Greece*

M.K. Kievets, I.V. Zhuk

*Joint Institute of Power and Nuclear Research-Sosny NASB, Minsk, Belarus*

Ts. Damdinsuren, Zh. Ganzorig, S. Gerbish, Ts. Tumendelger

*National University, Ulan –Bator, Mongolia*

A. Nourreddine, J.C. Adloff, M. Debeauvais

*Institut de Recherche Subatomique in Lue Paster Univesrity, Strasbourg, France*

J.S. Wan

*Northwest Institute of Nuclear Technology, Xian, China*

V. Kumar, H. Kumawat

*HENP Laboratory, University of Rajasthan, Jaipur, 302004, India*

\*) Corresponding author : [Krivopustov@jinr.ru](mailto:Krivopustov@jinr.ru)

Collaboration «ENERGY PLUS TRANSMUTATION»

## Abstract

Experiments which are part of the scientific program „*Investigations of physical aspects of electronuclear method of energy production and transmutation for radioactive waste of atomic energetic using relativistic beams from the JINR Synchrophasotron/Nuclotron*“ - the project is „*Energy plus Transmutation*“ (Kerntechnik 2003, 68, 48-55) are described in this report. A large lead target (diameter 8.4 cm, length 48 cm) surrounded by a four-section uranium blanket with total weight of 206.4 kg natural uranium was irradiated with 1.5 GeV protons from the new cryogenic accelerator Nuclotron (JINR, Dubna). Radiochemical sensors were exposed to the secondary particle fluences inside and on top of the target assembly. Two long-lived radioactive waste of atomic energetic sensors,  $^{129}\text{I}$  and  $^{237}\text{Np}$  (approximately 1 g weight each) and stable nuclides  $^{27}\text{Al}$ ,  $^{59}\text{Co}$ ,  $^{127}\text{I}$ ,  $^{139}\text{La}$ ,  $^{197}\text{Au}$  and  $^{209}\text{Bi}$  as well as natural and enriched uranium were used. In addition, various solid state nuclear track detectors and nuclear emulsions were exposed simultaneously. The experimental results confirm the theoretical estimations that the neutron spectra around this U/Pb-assembly are dominated by medium and high energy neutrons as shown by the observation of (n, xn)-reaction products in Co-, Au- and Bi-sensors. The yield of thermal neutrons on the surface of the U-blanket is strongly reduced as compared to the surface of a smaller Pb target surrounded with paraffin. The latter data were determined with (n,  $\gamma$ )-reactions in stable La sensors. In this experiment the technique of nuclear emulsions has for the first time been applied to measurements of neutron spectra in an accelerator driven system.

## INTRODUCTION

The Veksler-Baldin Laboratory of High Energies within the Joint Institute for Nuclear Research (JINR) in Dubna (Russia) is carrying out extended „*Investigations of physical aspects of electronuclear method of energy production and transmutation for radioactive waste of atomic energetic using relativistic beams from the JINR Synchrophasotron/Nuclotron*“ -- the project is „*Energy plus Transmutation*“. It has been introduced into the nuclear science community by Krivopustov et al.<sup>[1,2]</sup>. The scientific program (see next page), the experimental setup „Energy plus transmutation“ schema with lead target and uranium blanket and complex of detectors forming *uranium fission calorimeter* are presented on Fig. 1. It is part of the experimental program at the new cryogenic accelerator *Nuclotron*, as outlined by Baldin et al.<sup>[3]</sup>. Basic technical details of this new accelerator have been described by Kovalenko et al.<sup>[4]</sup>. Results from the first experiment within this series with protons of 1.5 GeV energy impinging onto a lead target that was surrounded by a two-section uranium blanket (with total of 103.2 kg natural uranium) have been published<sup>[1,2]</sup> and various other papers describe some special aspects of this work<sup>[5-11]</sup>.

The present article describes the experiment with 1.5 GeV protons irradiating a lead target inside a four-section uranium blanket (containing a total of 206.4 kg natural uranium). This continuation of the earlier experiment is dealing with following aspects:

- Transmutation studies on long-lived radioactive waste nuclides  $^{129}\text{I}$  and  $^{237}\text{Np}$  in the field of secondary neutrons that complement earlier studies (ecological aspect)<sup>[13-16]</sup>.
- Energy and intensity distributions of neutrons inside and around the U/Pb-assembly studied with (n,  $\gamma$ )- and (n, xn)-reactions using Al, Co, Au, Bi and La as radiochemical sensors.
- Energy and intensity distributions of neutrons around the target assembly using Solid State Nuclear Track Detectors (SSNTD) and uranium sensors.
- Energy spectra of neutrons using nuclear emulsion techniques (see Ref. 2, 12).
- Theoretical model calculations of neutron spectra.

The experiment was carried out in 11-12 December 2001 by several groups forming an international team. At first a description of the experimental setup consisting of the lead target, the uranium blanket and the biological shielding will be presented. Second, various experimental studies using different detection systems will be described in detail together with results and theoretical interpretations.

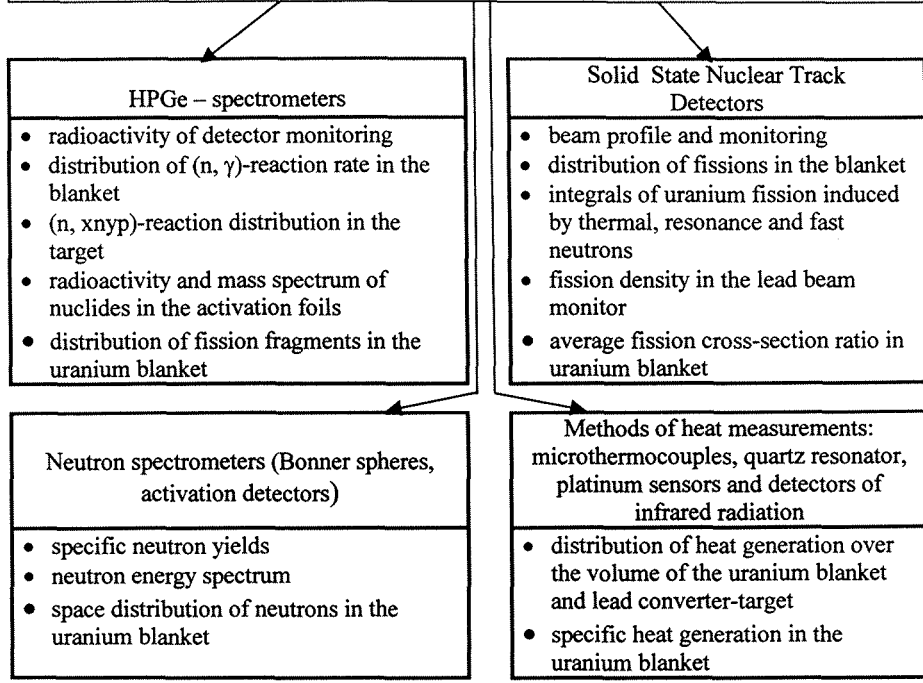
## 1. EXPERIMENTAL APPARATUS

The lead target together with the four-section uranium blanket is called U/Pb-assembly and it is shown in Fig. 1. The lead target has a length of 48 cm and a diameter of 8.4 cm. It is surrounded by four sections of a natural uranium blanket. Each section contains 30 uranium rods. The uranium rods of 10.4 cm length, 3.6 cm diameter and 1.72 kg weight are hermetically sealed in an aluminum cladding. Each section contains 51.6 kg natural uranium and the total uranium content in four sections is 206.4 kg. The construction of the metal structure used to mount the blanket provides a rigid and safe fixation of the uranium rods. The three gaps between the four sections as well as the front and back end of the setup are measuring positions for five large planar detector holder plates (called „Activation and SSNT-detectors“) as shown in Fig. 1. These detector plates are covered with various SSNTD and activation sensors. In addition to these detectors measuring radial distributions, various sensors were placed on the outside surfaces of each of the four uranium sections. As an

**Program for the experimental studies within the frame of the project „Energy plus transmutation“ (JINR, Dubna) with lead target and uranium blanket and complex of detectors forming uranium fission calorimeter<sup>[1, 2]</sup>**

P R O G R A M	<ul style="list-style-type: none"> <li>• heat generation and energy costs of neutron generation</li> <li>• neutron multiplication and balance</li> <li>• energetic gain (power amplification coefficient)</li> <li>• accumulation of long-lived radioactive products</li> <li>• transmutation cross-sections of radioactive wastes: <math>\alpha</math>-actinides, fission fragments and activation products</li> <li>• optimization of parameters of electronuclear installation</li> <li>• practical recommendations on development of a prototype transmutation installation</li> <li>• benchmark data to modernize computer codes and programs to simulate electronuclear processes</li> </ul>
---------------------------------	--

*The uranium fission calorimeter* includes the following detector systems on relativistic beams from the JINR synchrophasotron/nuclotron:



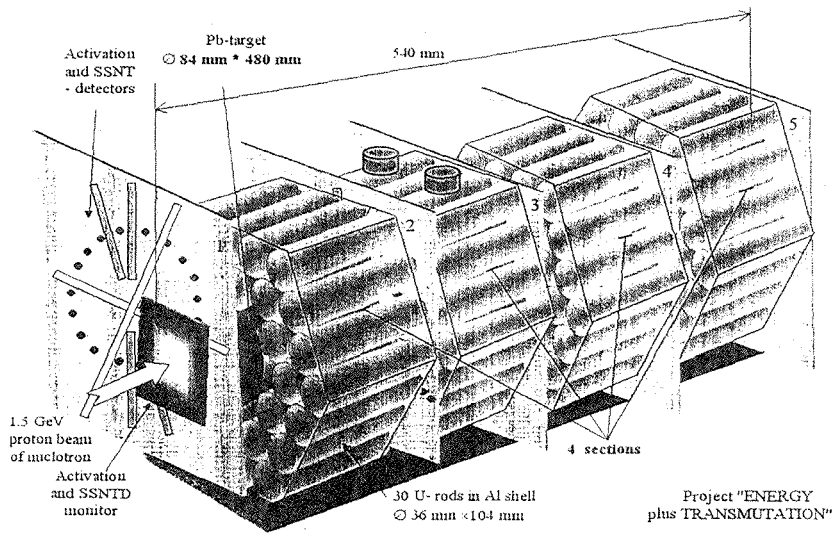
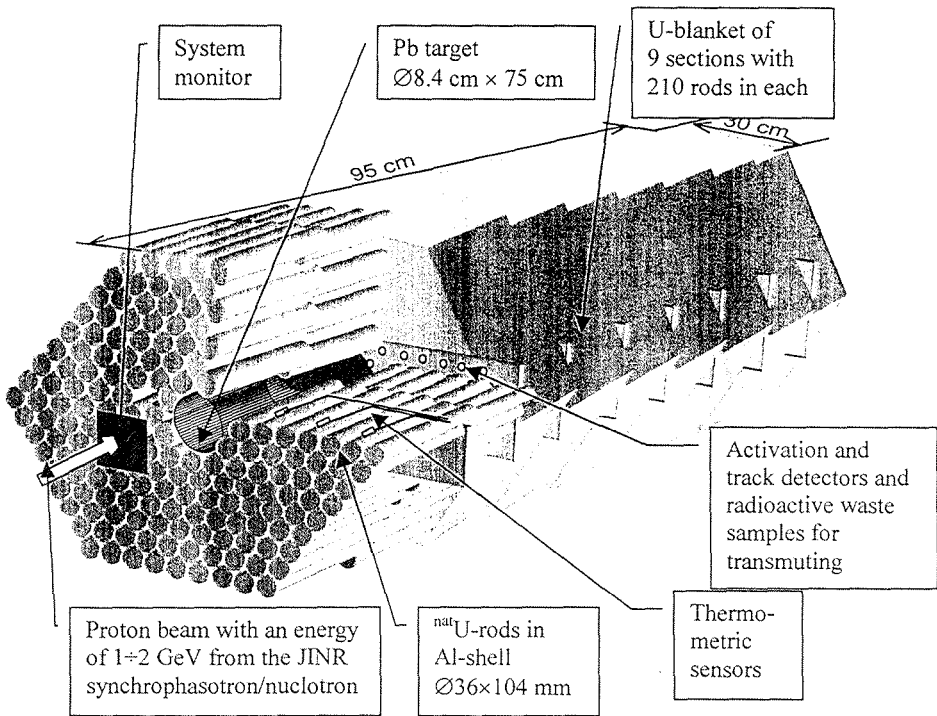


Figure 1. Schema of full scale (upper part) and four sections (down part) U/Pb-assembly with uranium blanket around a massive lead target<sup>[1,2]</sup>

example, the position of the placement for the radioactive waste nuclides  $^{129}\text{I}$  and  $^{237}\text{Np}$  on top of the second section is also indicated in Fig. 1.

The U/Pb-assembly was placed into an external shielding as shown in Fig. 2. The technical design of this shield was made by the Design Institute of Nuclear Power Maschine Building (VNIAM, Moscow, Russian Federation). This biological shielding is an important safety requirement for such massive uranium blanket around a lead target that is irradiated with relativistic protons. The big shielding consists of a container filled with granulated polyethylene, and the walls are plated with sheets of cadmium and lead. High energy neutrons are moderated within the polyethylene down to thermal energies. The 1 mm thick Cd-absorbers located at the inner walls of the container reduce significantly the backscattering of

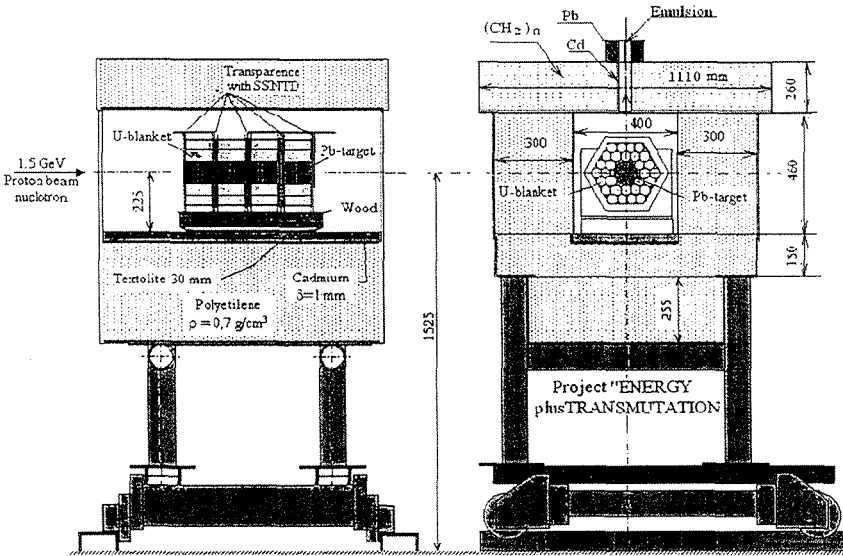


Figure 2. Technical details of the U/Pb-assembly<sup>[1, 2]</sup> inside a massive shielding and placed into a mobile platform, which can be moved into and out of the proton beam line. The left-side of this figure gives a cut through the assembly along the proton beam line, the right-side shows a cut through the assembly perpendicular to the proton beam line in the position, where there is a hole within the upside shielding between the 1<sup>st</sup> and 2<sup>nd</sup> uranium section

thermalized neutrons into the target and detector volume. The outside dimensions of this shielding container are  $100 \cdot 106 \cdot 111 \text{ cm}^3$  and it has a total weight of 950 kg. It is mounted onto a mobile platform, that can be moved into and later out of the irradiation position called „Focus F3“ of the proton exit channel for the Nuclotron beam in the experimental hall. The metallic structure of the biological shielding was manufactured in the Laboratory of High Energy JINR (Dubna). The left part of Fig. 2 shows a „cut“ through the entire assembly along the proton beam line, and the right part of this figure shows the cut through the entire assembly perpendicular to the proton beam line in the position, where there is a hole within the upside shielding. On top of this hole one can directly measure high-energy neutrons emitted from the U/Pb-assembly with nuclear emulsions<sup>[2, 12]</sup>, as described in Section 3.3. A more detailed description and technical drawings of details have been published elsewhere<sup>[1]</sup>.

The extracted 1.5 GeV proton beam from the Nuclotron enters the experimental hall with a nominal intensity of  $1.5 \cdot 10^{10}$  protons per pulse, the duration of a slow extraction of one pulse lasts 0.3 s, and the repetition rate is one pulse per 9 s. The exact geometrical adjustment

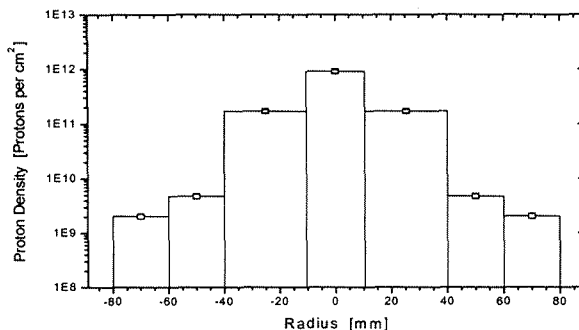


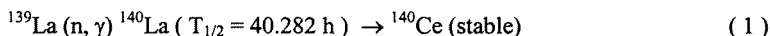
Figure 3. The beam profile of the 1.5 GeV proton beam from the Nuclotron as it enters the U/Pb-assembly (experiment of 11-12 December 2001)

of the U/Pb-assembly with respect to the proton beam direction is performed with sensitive Polaroid films and ionisation chambers<sup>[1,2]</sup>. The accurate monitoring of the proton beam together with the determination of the integral proton fluence is carried out during the entire run using standard aluminum foil activation detectors. The Al-monitor foils were placed 60 cm upstream the entrance of the protons into the lead target in order to avoid interactions of backscattered neutrons with the monitor foils. Details on the beam monitoring system in the „Focus F3“ position have already been published<sup>[1,2]</sup>. The monitor reaction  $^{27}\text{Al}(p, 3p\text{n})^{24}\text{Na}$  was used to determine the proton fluence where the decay of the  $^{24}\text{Na}$  activity was measured using gamma-ray spectrometry<sup>[1,2,17-20]</sup>. The Al-foil of thickness 0.05 mm was cut into 3 concentric rings with external diameters of 80, 120 and 160 mm. From the central part of the Al-foil a circle with diameter of 21 mm was cut out. The cross section used for the  $^{27}\text{Al}(p, 3p\text{n})^{24}\text{Na}$  reaction at 1.5 GeV proton energy is  $(9.93 \pm 0.17) \text{ mb}^{[20]}$ . The results of beam monitoring are shown in Fig. 3. The total beam intensity in F3 was  $(1.14 \pm 0.06) \cdot 10^{13}$  protons. The central part of the beam with 84 mm diameter, i.e. the diameter of the Pb-target in Fig. 1, contained  $(1.10 \pm 0.05) \cdot 10^{13}$  protons or  $(95.8 \pm 4.7)\%$  of the entire beam. This measurement shows that the Nuclotron delivers well-focussed proton beams into the external experimental hall.

## 2. EXPERIMENTAL RESULTS BASED ON RADIOCHEMICAL TECHNIQUES (METHOD OF ACTIVATION ANALYSIS)

2.1 The results of investigation of neutron fields in the volume of U/Pb-assembly with help of (n,  $\gamma$ )- and (n, xn)-reactions on activation threshold detectors (Al, Co, Au and Bi) are presented in the report V. Wagner (Nuclear Physics Institute, Rez/Praha, Czech Republic) „Experimental studies of spatial distributions of neutrons inside and around the set-up consisted from thick lead target and large uranium blanket irradiated by relativistic protons Nuclotron (JINR, Dubna)“ (see Proceeding present Seminar and our work<sup>[2]</sup>).

**2.2. Radiochemical Studies of the Transmutation of Stable  $^{139}\text{La}$ .** The stable and monoisotopic sensor  $^{139}\text{La}$  was used to measure thermal neutron fluences within a small and well-defined volume of approximately  $2.5\text{ cm}^3$  during irradiations with relativistic hadrons onto massive targets, as it was described recently<sup>[17, 20, 21]</sup>. The same  $^{139}\text{La}$  sensors were also used in our studies, using the thermal neutron induced reaction:



Ten small plastic vials of 15 mm diameter and 50 mm length containing about 1 g La each in the form of  $\text{LaCl}_3 \cdot 7\text{H}_2\text{O}$  have been placed along the top surface of the 48 cm long U/Pb-assembly (Fig. 1 and 2) and irradiated with secondary particles. No particular moderator material was inserted between the U/Pb-assembly and the La-sensors. The induced  $^{140}\text{La}$ -activity was measured after the end-of-irradiation using HPGe detection systems together with well-known analysing techniques<sup>[18, 19]</sup>. The resulting production rate for  $^{140}\text{La}$  is given in the form of an experimental  $B(^{140}\text{La})$ -value, as defined in next equation.

Activities at the end-of-bombardment were converted into production rates  $B(A)$  of the produced isotopes A according to the definition<sup>[17, 20]</sup>:

$$B(A) = (\text{number of A-atoms produced}) / [(1\text{ g sensor}) \cdot (1\text{ primary proton})] \quad (2)$$

$B(A)$  is an absolute number of atoms A produced in the given experimental setup. This production rate is strictly an experimental value which is sensitive to the neutron spectrum at the actual geometric location of the sensor. B-values on a given setup are comparable among each other; however, B-values measured on different setups are not.

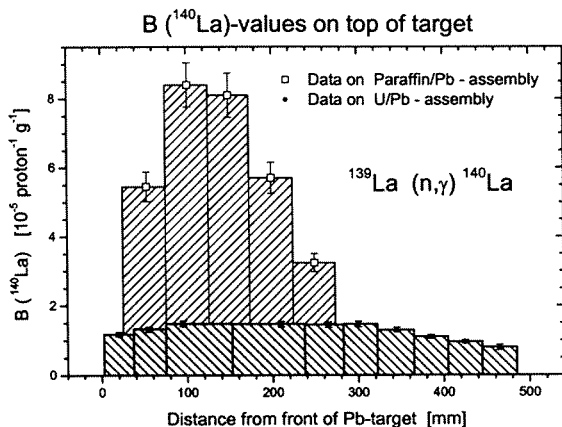
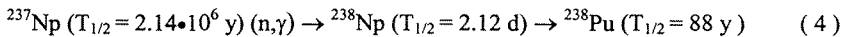
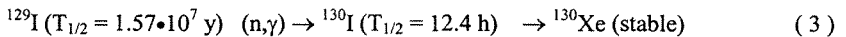


Figure 4. The dependence of the measured  $B(^{140}\text{La})$  yields along the proton beam direction on top of the target in two experiments: U/Pb-assembly (this experiment; see Fig. 1 and 2) and Pb-target with paraffin moderator<sup>[17]</sup>

The experimental  $B(^{140}\text{La})$  values are presented in Fig. 4 together with equivalent data measured on a Pb/paraffine-assembly<sup>[17]</sup>. The neutron spectrum in the latter experiment was

softened through a 6 cm thick paraffin moderator but there was no shield around the setup. Both data sets were measured with 1.5 GeV proton energy. It is found that the 48 cm long Pb-target with the four section uranium blanket has an almost constant thermal neutron fluence over nearly its entire length. In contrast, the much shorter 20 cm Pb-target with paraffin moderator<sup>[17, 20]</sup> has a considerably higher and well accumulated fluence of thermal neutrons. The reason for the missing enhancement of slow neutrons around 15 cm after beam impact into the U/Pb-assembly is qualitatively clear. There is experimental evidence for an enhancement of fast neutrons around 15 cm after beam impact but there is no suitable moderating material available to slow these fast neutrons down. The inner side of the external shield is covered with a Cd-layer, thus preventing thermalized neutrons from moving back from the shielding or from the environment into the target area. Therefore one expects to find only those thermal neutrons on top of the U/Pb-assembly that were actually produced in the thermal energy region or that were thermalized through collisions with atoms in the target and blanket or that migrated back from the shield without being caught by the Cd-layer. As the energy loss in a collision between a neutron and heavy atoms like Pb or U is small one needs many collisions to slow down neutrons to thermal energies. As a consequence, the initially focussed direction of motion of the neutrons is lost and the measured distribution is flat.

**2.3. Transmutation of radioactive waste nuclides  $^{129}\text{I}$  and  $^{237}\text{Np}$  and stable  $^{127}\text{I}$ .** The transmutation of long-lived radioactive waste into stable or short-lived radioactive nuclides is of major interest in these studies. Transmutation cross-sections (B-values) are ideal benchmark data to test theoretical models that describe the complex process of interactions of the primary beam, the production of spallation neutrons, secondary reactions in the assembly, particle transport properties and finally the interaction with the sensor nuclide. The correct description of all processes is an essential premise for credible results from the necessary calculations that must be made in order to design a real transmutation setup on the technical or even industrial scale. The nuclides  $^{129}\text{I}$  and  $^{237}\text{Np}$  are of particular practical interest, as they are long-lived radioactive waste nuclides from nuclear facilities and they can be transmuted with neutrons into stable or short-lived isotopes:



As available  $^{129}\text{I}$ -sensors from radioactive waste reprocessing are a mixture of 15% stable  $^{127}\text{I}$  and 85% radioactive  $^{129}\text{I}$ , it appeared to be useful to study simultaneously the transmutation of pure  $^{127}\text{I}$ -samples. The available  $^{237}\text{Np}$ -sensor is isotopically pure. Sample containers used are shown schematically in <sup>[13]</sup>. The  $^{127, 129}\text{I}$  in the form of NaI salt is hermetically sealed in a welded aluminium container and the sensor has been manufactured at the Institute of Physics and Power Engineering (Obninsk, Russia). The radioactive sample contained 0.772 g  $^{129}\text{I}$  plus 0.136 g  $^{127}\text{I}$ . Two inactive iodine control sensors contained 1.439 g  $^{127}\text{I}$  each. The radioactive  $^{237}\text{Np}$  sample contained 1.061 g  $^{237}\text{Np}$  in the chemical form  $\text{NpO}_2$ . All sensors were placed on top of the second uranium section, as counted downstream from the beam entrance into the lead target and irradiated during the entire experiment. Afterwards, all sensors were investigated with standard gamma-ray spectroscopy as described earlier. Because of the high level of radioactivity induced in the massive Al container (78.8 g Al) the gamma detector was shielded with 2 mm Cd and 2 mm Cu filters in order to reduce the

background. Further details of the gamma-spectrum analysing procedures for this special case are given in [22]. Changes in the beam intensity during the irradiation were taken into account for the calculation of the experimental  $B(A)_{\text{exp}}$  values for the various radioactive transmutation products. Results are given in Table 1.

The calculation of  $B(^{128-121}\text{I})_{\text{exp}}$  for a pure  $^{127}\text{I}$ -sensor is carried out by taking the results of measured  $B_{\text{exp}}$ -values for the mixture of the ( $^{129}\text{I}$  plus  $^{127}\text{I}$ )-sensor and for a pure  $^{127}\text{I}$ -sensor, using straightforward arithmetic.

**Table 1. Experimental B(A)-values in neptunium, iodine and aluminum sensors at 1.5 GeV proton energy**

Isotope	$T_{1/2}$	$B(A)_{\text{exp}} \cdot 10^6$ in $^{237}\text{Np}$ -, $^{129}\text{I}$ - and $^{27}\text{Al}$ -sensors	$B(A)_{\text{exp}} \cdot 10^6$ in $^{127}\text{I}$ - or $^{27}\text{Al}$ -sensors
$^{238}\text{Np}$	2.12 d	$378 \pm 18$	-
$^{130}\text{I}$	12.3 h	$32.5 \pm 1.7$	-
$^{128}\text{I}$	25 min	-	$93 \pm 7$
$^{126}\text{I}$	13.1 d	$1.28 \pm 0.11$	$5.0 \pm 0.5$
$^{124}\text{I}$	4.17 d	$0.362 \pm 0.030$	$1.40 \pm 0.10$
$^{123}\text{I}$	13.3 h	-	$0.82 \pm 0.10$
$^{121}\text{I}$	2.12 h	-	$0.28 \pm 0.07$
$^{120}\text{I}$	81 min	-	$0.084 \pm 0.015$
$^{24}\text{Na}$	14.95 h	$2.00 \pm 0.16$ *)	$5.14 \pm 0.30$

\*) This value agrees fairly well with an independent determination given in [2].

In other experiments the transmutation of  $^{129}\text{I}$  was investigated using a massive setup and higher proton energy. Due to the different beam energy and geometric differences of setups the results of the measurements of this and the other experiment are incomparable. Details are given in [21, 23]

In contrast to other transmutation studies<sup>[13, 14, 20, 21]</sup> with thermalised neutrons, one observes in this experiment some  $(n, \gamma)$ -reactions as well as substantial contributions from  $(n, xn)$ -reactions, leading to very neutron deficient iodine isotopes such as  $^{120}\text{I}$ . A model-based calculation was carried out for reaction rates  $R_{\text{calc}}$  according to the equation

$$R_{\text{calc}} = \int_{E_{\text{thr}}}^{E_{\text{max}}} \sigma(E_n) \Phi(E_n) dE_n \quad (5)$$

where  $E_{\text{thr}}$  is the threshold energy for a particular reaction channel. The value  $\Phi(E_n)$  is the neutron fluence [ $\text{n} \cdot \text{cm}^{-2} \cdot \text{MeV}^{-1} \cdot \text{proton}^{-1}$ ] and it is calculated using the program DCM/CEM<sup>[24, 25]</sup> for the given geometry of the experiment (see below). The calculated reaction rate  $R_{\text{calc}}$  is related to the calculated  $B_{\text{calc}}$  value as follows:

$$R_{\text{calc}} (^{130-121}\text{I}) = B_{\text{calc}} (^{130-121}\text{I}) \cdot A / N_A \quad (6)$$

whose  $A$  is the mass number and  $N_A$  is Avogadro's number. Cross sections for  $^{129}\text{I}$   $(n, xn)$ - and  $^{127}\text{I}$   $(n, xn)$ -reactions are calculated by means of a modified program LAHET<sup>[23]</sup> depending on the neutron energy. Calculated values  $B_{\text{calc}}$  and experimental data  $B_{\text{exp}}$  from Table 1 show

that the agreement of these values is far from being satisfactory due to the inaccuracy of calculations of either neutron cross sections and/or the energy dependent neutron fluence.

In order to estimate the neutron spectrum from our experimental data, an approach was suggested starting with experimental reaction rates  $R_{\text{exp}}$  (or  $B_{\text{exp}}$ -values) from Table 1 and calculated values of cross sections of  $(n, xn)$ -reactions as a function of neutron energy [23].

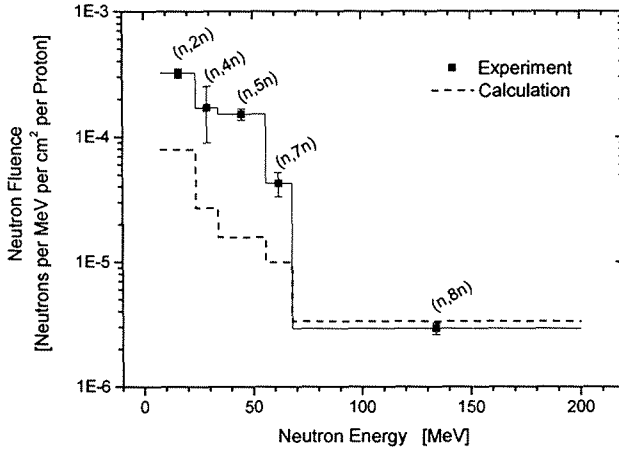


Figure 5. Experimental neutron spectrum at 1.5 GeV extracted from product yields of  $(n, xn)$ -reactions in  $^{127}\text{I}$  on top of the U/Pb-assembly and comparison with the calculated neutron spectrum based on the DCM/CEM-code<sup>[24, 25]</sup>

Let  $R_i(\text{exp})$  and  $\sigma_i(E_n)$  correspond to the reaction rate to the reaction with emission of  $i$  neutrons and  $\sigma_i$  correspond to the calculated cross section of this reaction for the neutron energy  $E_n$ . Reactions with removal of a maximum of 8 neutrons are observed in our experiment starting with  $^{127}\text{I}$ . Thus

$$R_8(\text{exp}) = \int_{E_{\text{thr}}^{(8)}}^{E_{\text{max}}} \varphi_8(E_n) \sigma_8(E_n) dE_n \approx \overline{\varphi_8(E_n)} \int_{E_{\text{thr}}^{(8)}}^{E_{\text{max}}} \sigma_8(E_n) dE_n \quad (7)$$

Therefore  $\overline{\varphi_8(E_n)}$  was calculated, which is the average value of the neutron fluence in the energy range from  $E_{\text{thr}}^{(8)} = 68$  MeV up to  $E_{\text{max}} = 300$  MeV. In the case of a reaction with emission of 7 neutrons the following relation applies:

$$R_7(\text{exp}) = \overline{\varphi_7(E_n)} \int_{E_{\text{thr}}^{(7)}}^{E_{\text{thr}}^{(8)}} \sigma_7(E_n) dE_n + \overline{\varphi_8(E_n)} \int_{E_{\text{thr}}^{(8)}}^{E_{\text{max}}} \sigma_7(E_n) dE_n \quad (8)$$

which allows one to determine  $\overline{\varphi_7(E_n)}$ . Experimental values of  $R_5(\text{exp})$ ,  $R_4(\text{exp})$  and  $R_2(\text{exp})$  were used in a similar manner to determine average neutron fluences  $\overline{\varphi_5(E_n)}$ ,

$\bar{\varphi}_4(E_n)$  and  $\bar{\varphi}_2(E_n)$  in the energy ranges  $(E_{thr}^{(5)}, E_{thr}^{(7)})$ ,  $(E_{thr}^{(4)}, E_{thr}^{(5)})$  and  $(E_{thr}^{(2)}, E_{thr}^{(4)})$ , respectively.

The resulting experimental neutron spectrum and the appropriately averaged calculated neutron spectrum are shown in Fig. 5. The agreement between these two spectra is not at all satisfactory.

**2.4. Further computer simulations on neutron induced transmutation of  $^{127}\text{I}$  and  $^{129}\text{I}$ .** The spectra of secondary particles (neutrons and protons) crossing the external surface of the U/Pb-assembly were calculated with the assumption of an ideal non-absorbing detector by means of the program DCM/CEM<sup>[24, 25]</sup>. The range of neutron energies extends from thermal up to 300 MeV. It is assumed in the calculations that the temperature of the lead target and the uranium blanket is thermal (0,0252 eV).

In principle one can register particles with larger energies up to the initial bombarding energy of 1.5 GeV. However, due to an insignificant amount of such particles present these were not considered in our calculations. The energy range of secondary protons is considered within the limits from the cut-off energy (~2 MeV) up to 300 MeV. Calculations of energy spectra of secondary particles were performed as before<sup>[1, 2, 7, 24, 25]</sup>.

The energy range of secondary particles below 10.5 MeV is divided up according to the 26 group system. Additional splitting of the energy range < 0.1 eV is introduced to describe the thermalized spectrum. The energy range > 10.5 MeV is divided with a step width of 10 MeV. Additional calculations of the neutron spectra above the threshold of several nuclear reactions  $^{129}\text{I}(n, 4n)^{126}\text{I}$  and  $^{127}\text{I}(n, 2n)^{126}\text{I}$  were carried out with smaller step (2 MeV) to study the features of these reactions under conditions of irradiation of the samples of  $^{127}\text{I}$  and  $^{129}\text{I}$ .

Neutron spectra are registered in geometrical positions corresponding to the actual locations of radioactive  $^{129}\text{I}$ ,  $^{127}\text{I}$  and  $^{237}\text{Np}$  sensors in this experiment. Geometrical features and chemical composition of the lead target, natural uranium blanket and radiation shielding and moderator containing sheets of cadmium, lead and granulated polyethylene (see Fig. 2) are considered in very detail in our calculations. However, we had to make the assumption that the medium in the limits of separate geometrical zones is homogeneous (in the case of the blanket this assumption is a crude approximation because in the real assembly this volume is filled with cylindrical uranium rods). Therefore we introduced a correction to the density of the volume taking into account the porosity of the medium. Furthermore, we also made an assumption concerning the shape of the blanket. The hexagonal sections (see Fig. 1 and 2) were replaced in the calculations with an equivalent cylinder. There was no acceptable agreement between the calculated neutron spectra and other experimental data.

The cross sections of (n, xn)-reactions on  $^{127}\text{I}$  and  $^{129}\text{I}$  using the same programs were also calculated (see Table 1). The calculation was performed by modeling of inelastic interactions of neutrons with subsequent normalization of the fraction of the given reaction channel on the calculated inelastic cross section. Reactions for the production of isotope  $^{126}\text{I}$  from  $^{129}\text{I}$  and  $^{127}\text{I}$  nuclei are characterized by a pronounced peak in the energy distribution of the cross section which is in the region of 30 MeV for the reaction  $^{129}\text{I}(n, 4n)^{126}\text{I}$  and around 20 MeV for the reaction  $^{127}\text{I}(n, 2n)^{126}\text{I}$ , correspondingly.

The data data of this section were compared with the data received by means of the modified program LAHET<sup>[23]</sup>. It is found that the results calculated with the program LAHET appear to be systematically lower by a factor of 2.5 in the region of the maximum in comparison to the data received with the program DCM/CEM<sup>[1, 2, 24, 25]</sup>. The overall agreement between experimental and calculated results, however, is poor.

It is necessary to note the contribution of the proton component to the amount of induced activities. Cross sections of threshold reactions  $^{129}\text{I}(p, p3n)^{126}\text{I}$  and  $^{127}\text{I}(p, pn)^{126}\text{I}$  differ from corresponding neutron reactions by a shift in the reaction threshold to higher energies. The shift is in value approximately equal to the binding energy of the nucleon in the nucleus. The contribution of the proton component to the total  $^{126}\text{I}$  activity is about two orders of magnitude below the corresponding contribution of the neutron fluence.

### 3. EXPERIMENTS USING SOLID STATE NUCLEAR TRACK DETECTORS

**3.1.** The results of investigations of space and energy distribution of neutrons with using mica detectors are presented in the report I.V. Zhuk "Experimental and theoretical determination of  $^{235}\text{U}$ ,  $^{238}\text{U}$  and  $^{210}\text{Po}$  fission rate distributions in the U/Pb assembly bombarded with 1.5 GeV protons" (see the Proceeding of present Seminar and our work [2]).

**3.2. Measurement of neutron fluence and neutron energy regimes using SSNTD.** Neutron fluence measurements were performed in the gaps between the U-blanket sections, on surface of the blanket as well as on top of the target shielding using various forms of solid state nuclear track detectors, as indicated on Fig. 6. In each gap between the U-blanket sections, twelve sets of SSNT-detectors were placed along the diagonal of the hexagon (along the strip on Fig. 6). On the surface of each section of the U-blanket four sets of the detectors were parallel to the beam axis. In addition, at three different positions on the top of the shielding, five sets of SSNT-detectors were placed parallel to the beam axis, in order to measure the neutrons escaping from the setup.

Each set of SSNTD provided three different detection areas and it consisted of a CR-39 foil on polyethylene, half-covered with  $^6\text{Li}_2\text{B}_4\text{O}_7$  convertor material. The area with the  $^6\text{Li}_2\text{B}_4\text{O}_7$  converter was partially covered on both sides with 1 mm of Cd. Such detection system can simultaneously detect thermal and intermediate + fast neutrons. The difference in track density between the Cd-covered and uncovered part of the CR-39 foil plus  $^6\text{Li}_2\text{B}_4\text{O}_7$  converter comes from thermal neutrons which induce  $(n, \alpha)$ -processes in  $^{10}\text{B}(n, \alpha)^7\text{Li}$ - and  $^6\text{Li}(n, \alpha)^3\text{H}$ -reactions. The track density in the completely uncovered CR-39 foil (no convertor, no Cd) originates from recoil protons from  $(n, p)$  scattering reactions giving indirect information about intermediate-energy and fast neutrons in the energy range of  $0.3 < E_n < 3$  MeV, which is the range with an about constant response of CR-39 to protons<sup>[26]</sup>. Details on the operation of these systems and their response are given in<sup>[27]</sup>. Moreover, SSNTD acting as fission detectors for fast neutrons detection above  $\sim 1.4$  MeV were placed on the top of the middle sections of the U-blanket (see Fig. 6). These detectors consisted of Makrofol foils with about  $1 \text{ mg}\cdot\text{cm}^{-2}$  of  $^{238}\text{U}$  evaporated on one surface. Details of this method to detect neutrons with energies above  $\sim 1.4$  MeV are given in<sup>[28]</sup>. After the irradiation with a total of approximately  $10^{11}$  protons the SSNTD etching and track-scanning under an optical microscope was carried out.

Neutron fluence distributions in units of [neutrons per  $\text{cm}^2$  per proton] measured between the sections of the U-blanket are presented in Fig. 7, as a function of the radial distance R from the Pb-target symmetry axis. These neutron distributions are attributed to fast neutrons alone. Thermal neutrons were not detected because their contribution is lower than

the detection limit of the detector ( $<10^5 \text{ n}\cdot\text{cm}^{-2}$ ). In all three gaps the neutron density is

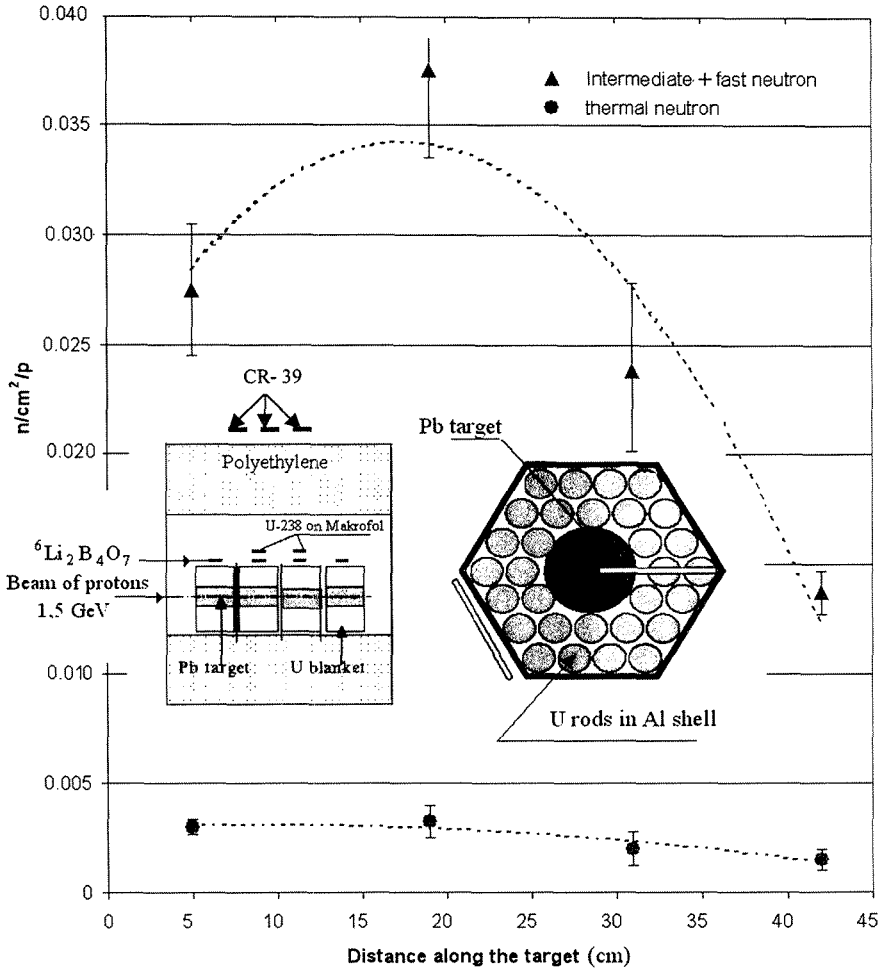


Figure 6. Thermal and intermediate + fast neutron densities on the surface of the four U-blanket sections setup "Energy plus Transmutation"<sup>[1, 2]</sup>. In the middle of the figure show the scheme of the experiment. On this figure the lines connecting experimental data are displayed with dots.

highest at the target axis and it drops off towards the surface of the U-blanket. The decrease of neutron density in the first and second gap scales approximately with  $1/R^{1.5}$ , where R is the radial distance from the beam axis. The neutron distribution in the third gap looks quite different, possibly because protons come to rest after about 30 cm inside the target. Thus, there are no spallation neutrons produced in the central region of the target around the third gap and the detected neutrons are only those emitted in forward directions.

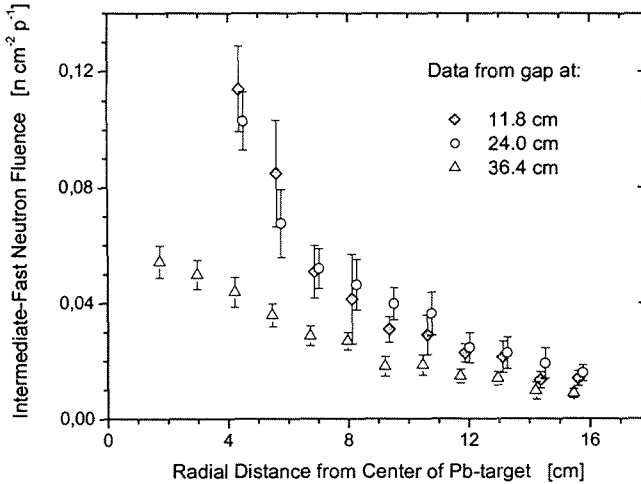


Figure 7. Intermediate-fast neutron distributions between sections of the U-blanket as a function of the radial distance  $R$  from the axis of symmetry of the Pb-target. The data set from the third gap (at 36.4 cm) is shifted 0.15 cm to the left, the data set from the second gap (at 25.0 cm) is shifted 0.15 cm to the right.

The different origin of neutrons in the third gap is also evident from the results of a fitting process to the neutron fluence distributions in the radial direction  $R$ . The neutron fluence distribution in the fourth gap is described well by the exponential form  $Y = A \cdot e^{BR}$ , in contrast to the second and third gap where a power law  $Y = A \cdot R^B$  fits best, as shown in Table 2.

**Table 2. Fitting parameters describing the radial decrease of the neutron fluence (see Fig. 7)**

Distance along the target, cm	Fitting model	Parameter A	Parameter B
12.0	$Y = A \cdot R^B$	$1.26 \pm 0.19$	$-1.61 \pm 0.09$
24.2	$Y = A \cdot R^B$	$0.71 \pm 0.08$	$-1.33 \pm 0.07$
36.4	$Y = A \cdot e^{BR}$	$0.073 \pm 0.002$	$-0.13 \pm 0.01$

The four sets of SSNT-detectors placed on the surface of each U-blanket section showed essentially identical results among each other. So, results presented in Fig. 6 represent the mean value of the four measurements, where the longitudinal distance is measured from the beam entry into the target. Both, thermal and intermediate + fast neutrons were detected in the four positions. The intermediate + fast neutron distribution peaks slightly on the second section and then drops significantly towards the end of the target. In contrast to that, the thermal neutrons distribution is essentially flat with only minor deficiencies on the fourth

section. The thermal neutron distribution resembles the shape of the radiochemically determined B(<sup>140</sup>La)-value distribution shown in Fig. 4. Densities of thermal neutrons on top of the blanket are one order of magnitude less than intermediate-fast neutrons (see Fig. 6).

The neutron fluence measured with fission detectors on the surface of the second and third sections of the U-blanket is presented in Table 3. For comparison, measurements by proton recoils with CR-39 at the same positions are also tabulated. There is a reasonable agreement between the two methods considering the different energy ranges covered by each method.

**Table 3. Fluence of fast neutrons on the surface of the middle sections of the U-blanket measured with two different SSNTD methods**

Neutron energy range, eV	Neutron fluence, $10^{-3} \cdot \text{n} \cdot \text{cm}^{-2} \cdot \text{p}^{-1}$	
	Proton recoil detectors	Fission fragment detectors
$3 \cdot 10^5$ to $3 \cdot 10^6$	$2.5 \pm 0.9$	-
Above $1 \cdot 10^6$	-	$7.5 \pm 1.7$

**3.3. Measurements of fast neutron spectra with nuclear emulsions.** The preceding sections gave a detailed account on neutron spectra measured inside and around the U/Pb-assembly with major emphasis on neutrons with energies below several MeV. An accurate measurement of the neutron spectrum, in particular of the high energy part above 1 MeV neutron energy, was carried out using nuclear emulsions. Details of this technique have been described in our article (see<sup>[2, 12]</sup>). The measurement was performed on the outside of the biological shielding above the uranium blanket between the first and second uranium section, such as indicated in Fig. 2. The figure shows a cut through the entire U/Pb-assembly and also the hole in the top part of the shielding.

Cd-foils aligned around and over this hole prevented the transfer of thermal neutrons through this opening. High sensitivity thick nuclear emulsions G-5 BR (baseless, relativistic) were exposed to neutrons emitted from the uranium blanket that were moving in the  $90^\circ$ -direction to beam axis during an irradiation with a few pulses of 1.5 GeV protons. The nuclear emulsion sheet had the size  $100 \cdot 25 \cdot 1.4 \text{ mm}^3$  and it was positioned in 500 mm distance above the top surface of the U-blanket. The hole of 30 mm diameter in the top shielding was used as a collimator for the neutrons (see Fig. 2). High energy neutrons produce recoil protons inside the nuclear emulsion which in turn produce tracks for analysis. After the irradiation proton tracks inside the nuclear emulsion were developed and about 3000 events were scanned and measured with an optical microscope. The accurate measurement of the recoil proton track length allows a very precise determination of the proton energy  $E_p$ . The direction of motion of each proton is measured and the scattering angle  $\Theta$  relative to the direction of the collimating hole is calculated. Thus, it is possible to determine the primary neutron energy  $E_n$  of the elastically scattered neutron using the equation  $E_n = E_p \cdot (\cos \Theta)^2$ .

The resulting neutron spectrum is shown in Fig. 8 where the maximum of the registered distribution is at  $(1.5 \pm 0.5)$  MeV neutron energy. Neutron energies up to 200 MeV have been observed. The barycenter of the spectrum from 0 MeV to 20 MeV is at  $(4.3 \pm 0.5)$  MeV. If statistics could be improved through extensive scanning of additional tracks one would surely have also registered neutrons of higher energies and the barycenter of the distribution would be slightly over 4.3 MeV. Thus the barycenter of the same spectrum in

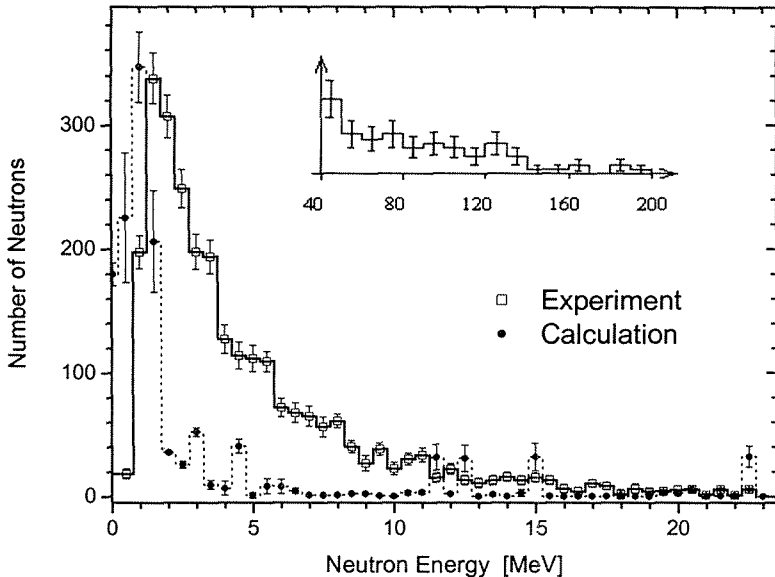


Figure 8. Experimental and calculated neutron spectrum above the U/Pb-assembly during the irradiation with 1.5 GeV protons

range from 0 MeV to 50 MeV is at  $(6.6 \pm 0.5)$  MeV. This neutron spectrum measured over the uranium blanket is much harder than the fission neutron spectrum in a conventional nuclear reactor where the barycenter is  $(1.58 \pm 0.12)$  MeV (see<sup>[29]</sup>).

The neutron spectrum on top of the shielding is determined experimentally with very good resolution and high statistical significance. This spectrum is therefore very suitable to serve as a benchmark set of data for comparison with model calculations. The theoretical spectrum as calculated with the program DCM/CEM<sup>[24, 25]</sup> is also indicated in Fig. 8. Significant discrepancies found, especially in the low- and medium-energy regions, clearly show that the modelling of neutron production and transport processes needs improvement. As the modelling of the interaction environment was very elaborate in the calculations it may seem that the basic modelling of the physics of interactions has to be improved. Discrepancies found in the emulsion method confirm results from radiochemical measurements with threshold detectors (see section 2.3 and Fig. 5) where similar discrepancies between experimental and calculated neutron spectra were encountered.

## CONCLUSIONS

An extended U/Pb-assembly [1, 2] containing a massive 43 kg Pb-target surrounded by 206.4 kg natural uranium as blanket without any low-Z moderators was irradiated with 1.5

GeV protons. Quantitative details of the neutron induced transmutation of nuclides as well as neutron yields and neutron spectra have been investigated within this assembly.

- Due to very hard neutron spectra, one could observe products in stable Co-, Au- and Bi-sensors from (n, xn)-reactions yielding neutron deficient isotopes produced through the emission of up to  $x = 9$  neutrons. This is in contrast to the transmutation yields restricted essentially to (n,  $\gamma$ )-processes as observed in an accelerator driven model system containing an efficient low-Z moderator that produced a high thermal neutron fluence<sup>[13, 14, 20, 21]</sup>.

- For the same reasons, one observed in transmutation studies on the stable nuclide <sup>127</sup>I not only the direct (n,  $\gamma$ ) transmutation product <sup>128</sup>I but also considerable yields of neutron deficient iodine isotopes down to <sup>120</sup>I. Transmutation yields in both systems with hard or soft neutron spectra depend in detail on the actual geometrical construction of the setups.

- Results of <sup>235, 238</sup>U fission rates are confirmed by a second set of SSNTD experiments using CR-39 and macrofol plastic track detectors, where the fast neutron fluence on the U-blanket surface is studied over its total length. Taking the measured neutron fluences on the surface of the U-blanket as shown in Fig. 6, one can estimate the expected fluence for a 1 mA proton beam of 1.5 GeV in the present system as follows:

$$\Phi(\text{thermal} + \text{epithermal neutrons}) = 1 \cdot 10^{13} \text{ neutrons} \cdot \text{cm}^{-2} \cdot \text{s}^{-1}$$

$$\Phi(\text{intermediate} + \text{fast neutrons}) = 2 \cdot 10^{14} \text{ neutrons} \cdot \text{cm}^{-2} \cdot \text{s}^{-1}$$

Such neutron fluences are a quite substantial achievement towards the realisation of a transmutation facility on a larger scale. However, they request the technical ability to remove considerably more than 1.5 MW of thermal energy out of the assembly which is a difficult technical task.

- The neutron spectrum was measured with high resolution and good statistical precision using a nuclear emulsion method (Fig. 8). The comparison of experimental and calculated data unambiguously shows that current model descriptions for neutron production and transport need improvement. In this experiment the technique of nuclear emulsions has for the first time been applied to measurements of neutron spectra in an accelerator driven system.

- It is evident from all comparisons shown between experimental data and the results from model calculations that the theoretical modeling of neutron production and transmutation processes needs a lot of improvement. Differences between measured and calculated data are frequently encountered. Such differences are unacceptable when large transmutation facilities shall designed on a technical or even on an industrial scale.

It is shown, that the project „Energy plus Transmutation“ [1, 2] provides valuable results and useful technical informations [5 - 14] towards the realisation of scientifically and industrially relevant future constructions employing accelerator-driven systems (ADS).

**Acknowledgements.** Authors are grateful to Professors A.I. Malakhov, N.A. Rusakovich, V.N. Penev and V.B. Brudanin, Drs. Yu.S. Anisimov and P.I. Zarubin for their help with the construction of the installation, preparation and carrying out of the experiments and gamma-spectroscopic measurements. We thank the technical personnel of the Laboratory of High Energies under the leadership of A.D. Kovalenko for providing reliable operation of the Nuclotron. Authors are grateful to the Workshop of the Laboratory of High Energies headed by Yu.I. Tyatyushkin for mechanical construction work and to A.F. Elishev and I.I. Mar'in for their help in preparation and performing of the irradiation of the uranium-lead assembly at the Nuclotron beam. Authors express thanks to E.M. Pavlyuk for assistance in figuring this article.

The enthusiastic scientific and experimental help over many years of Dr. E.-J. Langrock (FBL, Hoyerswerda, Germany) is gratefully acknowledged.

Authors are grateful to the Ministry of Atomic Energy of the Russian Federation for providing the material to build the uranium blanket, the main part of the experimental installation "Energy plus Transmutation". Results described in the present work were obtained with the financial support of the FZJ (Jülich, Germany), Russian Foundation for Basic Research (Moscow, Russia), Czechia Commission for collaboration with JINR (Dubna) and of the JINR Directorate who provided the operation of the accelerator and reactor installations of the Institute.

One of the authors (M.I.K.) is grateful to Prof. W. Ensinger (Kernchemie Institut, Fachbereich Chemie Philipps-Universität, Marburg, Germany) for creating favorable conditions on the ending stage of work on this report.

#### REFERENCES

- 1.) M.I. Krivopustov et al. On the First Experiments on the Calorimetry of the Uranium Blanket Using the Model of the U/Pb Electro-Nuclear Assembly „Energy plus Transmutation“ on a 1.5 GeV Proton Beam of the Dubna Synchrotron. JINR-Preprint P1-2000-168, Dubna, 2000// Kerntechnik, 2003, V 68, p.p. 48–55.  
M.I. Krivopustov, D. Chultem. Experiments on Electronuclear Technology and Radioactive Waste of Atomic Energetic Transmutation on Beams of the Synchrotron JINR Dubna // JINR News, 1998, 3, p.p. 27-30;  
M. I. Krivopustov et al. On the first experiment on calorimetry of uranium blanket of the model U/Pb-assembly of the electronuclear installation „Energy plus transmutation“ in the 1.5 GeV proton beam from the JINR synchrotron. In „Proc. of the International Seminar on High Energy Physics Problem. Relativistic Nuclear Physics and Quantum Chromodynamics“ (Dubna, September 25-29, 2000), Dubna, 2001, V 2, p.p. 3–21.
- 2.) Krivopustov M.I. et al. Investigation of Neutron Spectra and Transmutation of  $^{129}\text{I}$ ,  $^{237}\text{Np}$  and Other Nuclides with 1.5 GeV Protons from the Dubna Nuclotron Using the Electronuclear Setup „Energy plus Transmutation“, JINR-Preprint, E1-2004-79, 2004, Dubna (submitted to NIM A).
- 3.) A.M. Baldin, A.I. Malakhov, A.N. Sisakyan. Selected problems of relativistic nuclear physics and multiple particle production. „Physics of Elementary Particles and Atomic Nuclei“ 2001, 32, 1, p.p. s4-s30. МАИК «НАУКА»/INTERPERIODIKA PUBLISHING.
- 4.) A.D. Kovalenko et al. The Nuclotron – New Superconducting Ion Synchrotron at JINR // Proc. of the COSPAR Colloquium, Dubna, 2003(in print); Nuclotron: Main Results and Development Plans // Journal Atomic Energy, 2002, V. 93, p.p. 479 – 485.
- 5.) D. Chultem et al. JINR-Preprint P1-2002-16, Dubna, 2002.
- 6.) M. I. Krivopustov et al. In Proceeding „Research Program of the Laboratory of High Energy JINR, Dubna“. Editor A.M. Baldin. JINR-Communication 99 - 266, Dubna, 1999, p.p. 135-139.
- 7.) B.A. Martsynkevich et al. JINR Communication P1-2002-165, Dubna, 2002 and Vesti NASB (Physics-mathematic series), Minsk, Belarus, 2004, 1, p.p. 90 – 95.
- 8.) I.V. Zhuk et al. JINR-Preprint P1-2002-184, Dubna, 2002 and Vesti NASB (Physics-technic series), Minsk, Belarus, 2003, 12, p.p. 31 – 35.
- 9.) D. Chultem, Ts. Tumendelger, M.I. Krivopustov. JINR-Communication P1-2001-128, Dubna, 2001.
- 10.) L.A. Goncharova et al. Preprint 25, RAS Lebedev Institute of Physics (Moscow, Russian Federation), 2001.

- 11.) R. Brandt et al. JINR-Communication P1-99-117, Dubna, 1999.
- 12.) D. Chultem et al. JINR-Preprint P1-2003-59, Dubna, 2003.
- 13.) M.I. Krivopustov et al. JINR-Preprint E1-97-59, Dubna, 1997 and Journal of Radioanalytic and Nuclear Chemistry Letters 1997, 222, p.p. 267 – 270.
- 14.) J.S. Wan et al. Journal Kerntechnik 1998, 63, p.p. 167 – 177 // Journal Nuclear Instruments and Methods A, 2001, 463, p.p. 634 – 652.
- 15.) J. Adam et al. "Jaderna Physica / Nuclear Physics" 2002, 65, p.p. 797 – 809.
- 16.) J. Adam et al. Journal of Nuclear Science and Technology, 2002. Supplement 2, p.p. 272 – 275.
- 17.) J. Adam et al. Journal Kerntechnik 2003, 68, p.p. 214 – 218.
- 18.) W. Westmeier. Handbuch des Gamma-Spektrenanalyse Programms GAMMAW. Gesellschaft für Kernspektrometrie. Ebsdorfergrund, Germany.
- 19.) U. Reus, W. Westmeier. At. Data and Nuclear Tables 1983, V. 29, p.p. 1 – 406.
- 20.) W. Westmeier et al. Transmutation experiments on  $^{129}\text{I}$ ,  $^{139}\text{La}$  and  $^{237}\text{Np}$  using the Nuclotron accelerator (submitted in Radiochemica Acta), 2004.
- 21.) J. Adam et al. Radiochemica Acta 2002, 90, p.p. 431 – 442.
- 22.) J. Adam et al. Izmeritalnaya Tekhnika, 2001, p.p. 57 – 61 (Russian).
- 23.) D. Ganusheva. Diploma Thesis (Karlovy University, Prague, Czech Republic), 2001.
- 24.) A. Polanski, A.N. Sosnin, V.D. Toneev. On anomalous Na-24 production in high energy nuclear interactions. JINR-Preprint E2-91-562, Dubna, 1991.
- 25.) A.N. Sosnin et al. Izvestiya RAS (Physics Series), 2002, 66, p.p. 1494 – 1496.
- 26.) J.R. Harvey et al. Radiation Protection and Dosimetry 1998, 77, p.p. 267 – 304.
- 27.) M. Zamani, D. Sampsonidis and E. Savvidis. Journal Radiation Measurements 1996, 26, p.p. 87 – 92 // J.C. Adloff et al. Radiation Measurements 1999, 31, p.p. 551 – 554.
- 28.) G. Remy et al. Journal de Physique, 1970, 31, p. 27.
- 29.) L. Steward. Journal Nuclear Science and Engineering, 1960, 8, p.p. 595 – 597.

# Thorough Comparison of the Neutron Fluxes Generated in the Lead-Uranium Assembly (Installation “Energy plus Transmutation”) under Irradiation with Protons at Energy in the Range from 0.7 to 2.0 GeV

A.N.Sosnin<sup>1</sup>, M.I.Krivopustov<sup>1</sup>, M.Zamani-Valasiadou<sup>2</sup>, M.Manolopoulou<sup>2</sup>,  
M.Fragopoulou<sup>2</sup>, W.Westmeier<sup>3</sup>, H.Botham<sup>3</sup>, R.Brandt<sup>3</sup>, R.Odoj<sup>4</sup>,  
S.R.Hashemi-Nezhad<sup>5</sup>

For collaboration “Energy plus Transmutation”

<sup>1</sup> Joint Institute for Nuclear Research, 141980 Dubna, Russian Federation

<sup>2</sup> Physics Department, Aristotle University, Thessaloniki 54124, Greece

<sup>3</sup> Fachbereich Chemie, Philipps Universität, 35032 Marburg, Germany

<sup>4</sup> Institut für Sicherheitsforschung und Reaktortechnik, FZJ, 52425 Jülich, Germany

<sup>5</sup> Sydney University, Australia

Several irradiations of the lead-Uranium assembly (Installation “Energy plus Transmutation” [1,2]) have been carried out in the wide energy range from 0.7 up to 2.0 GeV using proton beam from the Synchrotron and Nuclotron (LHE, JINR, Dubna) to study generation of secondary neutron fields. In the present work neutron fluxes in the assembly are calculated using computer Monte-Carlo modeling codes, DCM/CEM in particular [3,4]. Calculated results are thoroughly compared in the frame of the carried research.

## References

1. M.I.Krivopustov, D.Chultem, Ts.Tumendelger, A.N.Sosnin et al. On a First Experiment on the Calorimetry of an Uranium Blanket Using the Model of the U/Pb Electronuclear Assembly “Energy plus Transmutation” on a 1.5 GeV Proton Beam from the Dubna Synchrotron. JINR Preprint P1-200-168, Dubna 200 // Journal “Kerntechnik” 2003, 68, pp. 48-55.
2. M.I.Krivopustov, W.Westmeier, A.N.Sosnin et al. Investigation of Neutron Spectra and Transmutation of <sup>129</sup>I, <sup>237</sup>Np and Other Nuclides Using the Electronuclear Setup “Energy plus Transmutation” Exposed to 1.5 GeV Proton Beam from the Nuclotron (JINR, Dubna). JINR-Preprint E1-2004-79, Dubna, 2004 (Submitted to Journal “Nuclear Instruments and Methods in Physics Research A”)
3. A.N.Sosnin, M.I.Krivopustov, M.Zamani-Valasiadou et al. Modelling of NEUTRON Spectra in U/Pb Assembly Irradiated with Protons by Means of Monte-Carlo Method. International Seminar “Features of Nuclear Excitation States and Mechanisms of Nuclear Reactions” (September 3-8, Sarov, Russia), 2001. Published in Izvestiya RAN (Physics Series), 2002, 66, pp.1494-1496.
4. Stoulos S, M.Fragopoulou, M.Manolopoulou, A.N.Sosnin, M.I.Krivopustov, W.Westmeier, R.Brandt, M.Debeauvais, M.Zamani. Neutron Measurement by Passive Methods in the Dubna Transmutation Assemblies. NIM A, 519, issue 3, 2004, pp. 651-658.

# EXPERIMENTAL STUDIES OF SPATIAL DISTRIBUTIONS OF NEUTRONS INSIDE AND AROUND THE SET-UP CONSISTED FROM A THICK LEAD TARGET AND A LARGE URANIUM BLANKET IRRADIATED BY RELATIVISTIC PROTONS

V. Wagner<sup>1,†</sup>, A. Krása<sup>1</sup>, F. Křížek<sup>1</sup>, A. Kugler<sup>1</sup>, M. Majerle<sup>1</sup>,  
O. Svoboda<sup>1</sup>, J. Adam<sup>1,2</sup>, M.I. Krivopustov<sup>2</sup>

for collaboration "Energy plus transmutation"

(1) *Nuclear Physics Institute of the Academy of Sciences of the Czech Republic, Řež near Prague, 25068, Czech Republic*

(2) *Joint Institute for Nuclear Research, Dubna, Russia*

† E-mail: [wagner@ujf.cas.cz](mailto:wagner@ujf.cas.cz)

## Abstract

We studied the spatial and energetic distribution of neutrons produced by spallation reactions at different places around and inside a simple thick lead target or in more complex installation Energy plus transmutation (consisted of lead target and uranium blanket) irradiated by relativistic protons of different energies from energies 0.5 GeV up to 2.5 GeV using JINR Dubna Synchrophasotron and Nuclotron. The activation detectors were used for neutron field determination. The comparison between experimental and simulated production rates of many threshold reactions makes it possible to test the accuracy of the description of neutron production in the wide neutron energy interval. Experimental results were analyzed and were compared with Monte Carlo simulations provided by LAHET+MCNP and MCNPX code. Simulations were also used for study of possible background and systematic errors produced by biological shielding around our set-ups.

## 1. Introduction

Spallation reactions induced by intense high energy proton beam in heavy target are ideal source of neutrons for the transmutation of radioactive waste. Accelerator Driven Transmutation Systems (ADTS), where an accelerator is coupled with a reactor, will use such source of neutrons [1]. Detailed studies of neutron production and transport inside a thick target and also more complicated set-ups, consisting of target and blanket, are important for verification and improvement of currently available simulation codes suitable for design of ADTS.

## 2. Experiments of collaboration Energy plus transmutation

The needed studies of neutron production and transmutation of different radioactive waste materials using simple and also complex set-ups are performed by collaboration "Energy

plus transmutation" using JINR Dubna accelerators (Synchrotron, Nuclotron, and Phasotron). These accelerators provide proton beam in suitable energy range (0.5 - 5 GeV). Collaboration carry out experiments using three types of set-up.

The first is a simple thick lead target. The target is sectioned and has standard diameter 9.8 cm and length 50 cm. Second is the "Energy plus transmutation" set-up which consists of a cylindrical lead target and an uranium blanket. The lead target has length of 48 cm and a diameter of 8.4 cm. It is surrounded by four sections of a natural uranium blanket. Each section contains 51.6 kg natural uranium and the total uranium content in four sections is 206.4 kg.

Both set-ups were placed into a big external shielding (during some of the simple lead target experiments and during all of "Energy plus transmutation" experiments). The shielding consists of a container filled with granulated polyethylene. Inner walls are plated with 1 mm sheets of cadmium. Outside dimensions of this container are 100x106x111 cm and total weight is 950 kg. Detailed description and technical drawings of details have been published in [2, 3].

Third set-up is named GAMMA-2. This set-up has target consisting of 20 lead discs, each 1 cm in thickness and 8 cm in diameter and it is surrounded by a 6 cm paraffin moderator [4].

The neutron field in different places inside and around these set-ups were measured using activation detectors. In activation detectors produced neutrons induced  $(n, xn\gamma)$ ,  $(n, \alpha\gamma)$  and  $(n, \gamma)$  reactions, and  $\gamma$ -decaying radioisotopes were produced. Different thresholds of these reactions allow us to probe energy spectra of neutrons. Activation detectors (Au, Al, Bi, Cu, Co, and La) were placed at different positions of the used setup (also inside the lead target or uranium blanket) [3]. This approach allowed us the determination of production rates of radioactive nuclides, which were compared directly with the results of simulations or were used for deconvolution of neutron energy spectra.

### 3. Simulations using MCNPX

We made series of simulations to understand influence of different parts of set-ups on accuracy of data, to estimate systematic errors and also to compare obtained experimental data and model assumptions. Simulations were performed by MCNPX 2.3.0 code[5]. Calculations were done in two steps. First, neutron and proton energy spectra were obtained using MCNPX code. Second, the yields of nuclei produced in activation foils were calculated by convolution of these spectra with the corresponding cross-sections. The cross-sections were taken from ENDF/B-IV library [6], for higher energies were taken from EXFOR/CSISRS or calculated by LAHET code.

### 4. Influence of shielding container

The main task of the shielding container is biological shielding. The high energy neutrons in the MeV region are moderated to the low energies (thermal, epithermal and resonance). The Cd layer significantly absorbs thermal neutrons going back to the space inside the container, but influence of epithermal and resonance neutrons from container is still important.

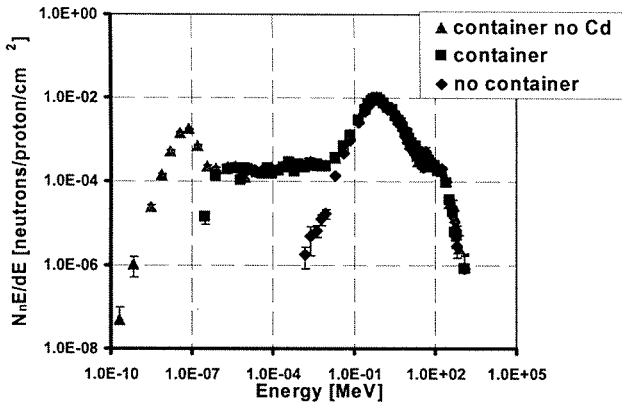


Figure 1: Example of simulated (MCNPX) neutron spectra inside shielding container with set-up Energy plus transmutation (spectrum on the top of U blanket 11 cm from the front). Simulations with container and Cd layer, with container and without Cd layer, without container are compared.

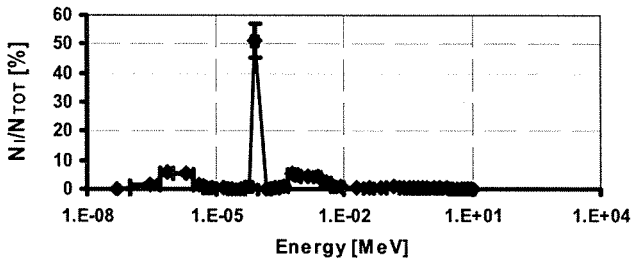


Figure 2: Contribution of different part of neutron energy spectra to the reaction  $^{139}\text{La}(n,\gamma)^{140}\text{La}$  in the case of set-up "Energy plus transmutation" with container

We studied influence of container on neutron spectra inside and around our set-up using MCNPX code to find out which parts of spectra are significantly changed and which are not influenced. The comparison of three types of simulation for neutron energy spectra on the top of U blanket is on Fig. 1. The spectra for these three simulations are the same for energy higher than 0.5 MeV. The spectrum for energy lower than 0.1 MeV starts to drop very quickly in the case of the set-up without container. Spectrum is constant and the same in the energy range from 1 eV up to 0.1 MeV for two simulated cases with container. Peak of thermal neutrons is not visible in the case with container with Cd layer (thermal neutrons are absorbed by Cd).

The main contribution of radioactive nuclei produced by no threshold neutron capture reactions in our experiment (set-up with container and Cd layer) is due to by resonance neutrons. This is true not only for La production (see Fig. 2.) but also for very often used  $^{197}\text{Au}(n,\gamma)^{198}\text{Au}$  reaction.

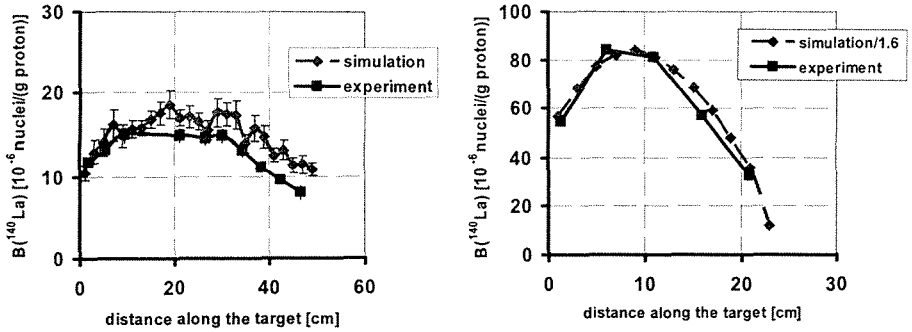


Figure 3: Spatial distribution of  $^{140}\text{La}$  production in  $^{139}\text{La}$  samples on the top of uranium blanket (set-up "Energy plus transmutation" with container) - left. The same for La samples on the top of paraffin moderator (set-up GAMMA-2 without container) - right

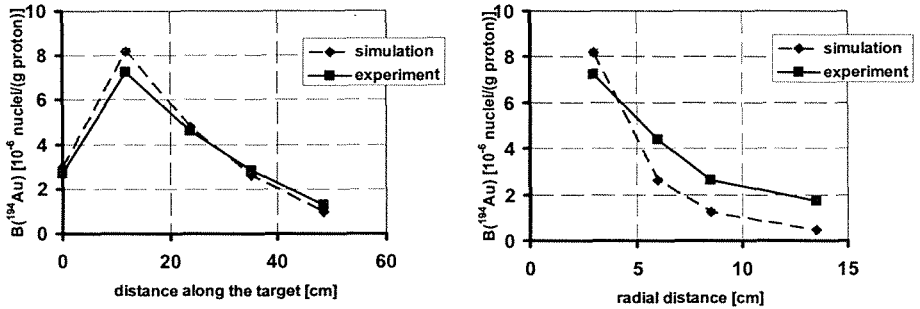


Figure 4: Spatial distribution of  $^{194}\text{Au}$  production for experiment with "Energy plus transmutation" set-up irradiated by 1.5 GeV neutrons. Longitudinal distribution (radial distance is 3 cm) - left side, radial distribution (longitudinal distance is 11.8 cm) - right side

## 5. Comparison of experiments and simulations

The results of three experiments with different set-up each are presented as example. There are shown some results from experiment with "Energy plus transmutation" set-up [3], GAMMA-2 set-up [6] and simple lead target [7]. Presented results are compared with MCNPX code simulations.

Spatial distribution of low energy neutrons were measured using production rates of the reaction  $^{139}\text{La}(n,\gamma)^{140}\text{La}$  during the experiment with "Energy and transmutation" set-up and proton energy 1.5 GeV from Nuclotron. Lanthanum samples were placed on the top of uranium blanket. In this case shielding container was used [3]. The experiment with GAMMA-2 set-up with the same proton energy was made without container. The  $^{139}\text{La}$  samples were placed on the top of the paraffin moderator [6]. Comparison of experimental data and MCNPX simulations for these cases is on the Fig. 3.. There is nice qualitative agreement between the experiments and the simulations.

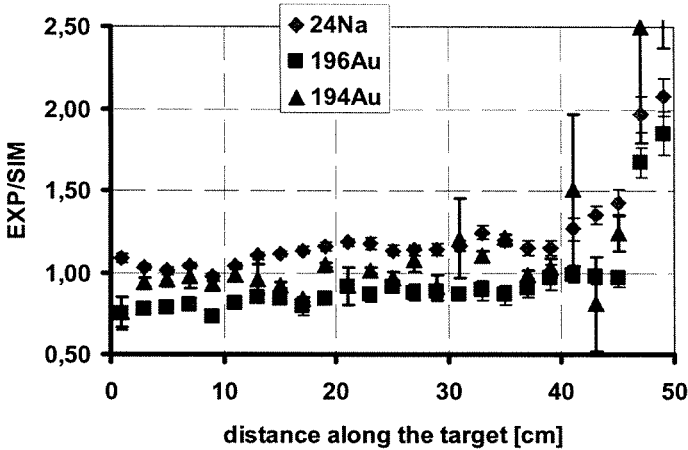


Figure 5: Ratio between experimental and simulated data for spatial distribution of production of different radioisotopes along the simple lead target irradiated by 885 MeV protons

Neutrons with MeV energies were measured by different threshold reactions. We compared experimental and simulated data for mentioned experiment with "Energy plus transmutation" set-up [3]. The production of  $^{194}\text{Au}$  isotope by  $(n,4n)$  reaction with energy threshold 23.2 MeV is shown as an example on Fig.4. We see good agreement for longitudinal distribution. However simulated radial distribution is much steeper than experimental one.

Spatial distribution of produced neutrons along the simple lead target (diameter 9.8 cm, length 50 cm) irradiated by protons with energy 0.885 GeV was measured during experiment on the JINR Synchrophasotron [7]. The comparison of obtained experimental data and MCNPX simulations is shown on the Fig.5. Nice agreement is possible to see. Difference starts to be visible for last ten centimeters of the target. It looks like the simulations underestimate the development of relativistic particles inside the target.

## 6. Conclusions and Outlooks

The collaboration "Energy plus transmutation" performed series of experiments with production and transport of neutrons with thick lead target or more complicated set-up irradiated by relativistic protons for benchmark tests of simulation codes. JINR Dubna accelerators are nice tool for such studies and relevant needed data were obtained.

The used shielding container has no influence on the part of the neutron spectra of energy higher than 0.5 MeV. Threshold reactions at activation detectors are produced only by neutrons coming directly from the target. Contribution of MeV neutrons from the container is negligible. Different situation is for radioactive nuclei produced by  $(n,\gamma)$  reactions, which have maximal cross-sections in the thermal, epithermal and resonance range. These nuclei are mainly produced by neutrons which come from the container. Moderation and scattering of neutrons by the container polyethylene produced homoge-

neous field of epithermal, and resonance neutrons (thermal neutrons are absorbed by Cd layer). Container is useful for the experiment, where MeV neutrons are measured. These neutrons are moderated in the container polyethylene and MeV neutrons cannot return back to the interior of the container. But number of neutrons with energy lower than 0.1 MeV is significantly influenced by the shielding container. Production of neutrons with energy lower than 0.1 MeV from set-up is necessary to measure only without the shielding container only.

Overall we observed good qualitative agreement between experimental and simulated data. It is possible to see some underestimation of relativistic particle shower inside the lead target by simulation. Simulated falling of radial distribution of neutrons inside the uranium blanket of "Energy plus transmutation" set-up is steeper than experimental, too. Running analysis of performed experiments and preparing further experiments will help to understand these discrepancies.

**Acknowledgements.** The authors are grateful to the staff of the Synchrotron and Nuclotron of the VBLHE at JINR Dubna. These experiments were supported by the Czech Committee for collaboration with JINR Dubna. This work was carried out partly under support of the Grant Agency of the Czech Republic (grant No. 202/03/H043) and ASCR K1048102 (Czech Republic).

## References

- [1] C.D. Bowman, Nucl. Instr. and Meth. **A332**, 336 (1992).
- [2] M.I. Krivopustov et al, Kerntechnik. **68**, 48 (2003).
- [3] M.I. Krivopustov et al, Preprint JINR **E1-2004-79**, Dubna (2004).
- [4] J. Adam et al, Preprint JINR. **E1-2004-16**, Dubna (2004).
- [5] L.S. Waters, MCNPX User's Manual Version 2.3.0, LANL report **LA-UR-02**, 1 (2002).
- [6] J. Adam et al, Kerntechnik **68**, 214 (2003).
- [7] A. Krása et al, Proceedings of the International Workshop on Nuclear Data for the Transmutation of Nuclear Waste, September 1-5, 2003. ISBN **3-00-012276-1**, [wnt.gsi.de/tramu/proceedings/krasa.pdf](http://wnt.gsi.de/tramu/proceedings/krasa.pdf)

# EXPERIMENTAL AND THEORETICAL DETERMINATION OF $^{235}\text{U}$ , $^{238}\text{U}$ AND $^{\text{nat}}\text{Pb}$ FISSION RATE DISTRIBUTIONS IN THE U/Pb ASSEMBLY BOMBARDED WITH 1.5 GEV PROTONS

I.V. Zhuk<sup>1</sup>, M.K. Kievets<sup>1</sup>, M.I. Krivopustov<sup>2</sup>, A.N. Sosnin<sup>2</sup>,  
R. Brandt<sup>3</sup> and W. Westmeier<sup>4</sup>

<sup>1</sup>*Joint Institute of Power and Nuclear Research - Sosny NASB, Krasin Str., 99,  
220109 Minsk, Belarus, e-mail: zhuk@sosny.bas-net.by*

<sup>2</sup>*Joint Institute of Nuclear Research, 141980 Dubna, Russia*

<sup>3</sup>*Institut fuer Physikalische Chemie, Kernchemie und Makromolekulare  
Chemie, Philipps-Universitaet, 35032 Marburg, Germany*

<sup>4</sup>*Dr. Westmeier GmbH, 35085 Ebsdorfergrund, Germany*

Collaboration "Energy plus Transmutation"

## Abstract

Results of a joint experiment with 1.5 GeV Protons from the Nuclotron (Laboratory of High Energies of the JINR, Dubna, Russia) irradiating the target assembly of the installation "Energy plus Transmutation" consisting of an extended lead target and a 206 kg natural uranium blanket [1,2] are presented.

Results of measurements and calculations of fission rates distributions for  $^{235}\text{U}$ ,  $^{238}\text{U}$  and  $^{\text{nat}}\text{Pb}$  and as well as threshold spectral index  $\frac{\overline{\sigma}_f^{238\text{U}}}{\overline{\sigma}_f^{235\text{U}}}$  and  $\frac{\overline{\sigma}_f^{\text{natPb}}}{\overline{\sigma}_f^{235\text{U}}}$  and considering the geometry of target and blanket of the uranium-lead assembly will be used to determine total number of fission events. Experimental fission rates are determined using solid state nuclear track detectors and theoretical rates are calculated using the Monte-Carlo simulation code DCM/CEM [3].

**Keywords:** Spectral index, fission rate, spallation reaction, Synchrophasotron, lead target, ADS, protons, secondary neutrons, track detectors.

## 1. Introduction

The work presents investigations of spatial and energy distribution of neutrons in the system "lead target - blanket from natural uranium" under bombardment with protons with the energy of 1.5 GeV including the measurements of distributions of  $^{235}\text{U}$ ,  $^{238}\text{U}$  and  $^{\text{nat}}\text{Pb}$  fission rates, as well as a threshold spectral indices ( $SI$ )  $\frac{\overline{\sigma}_f^{238\text{U}}}{\overline{\sigma}_f^{235\text{U}}}$  and  $\frac{\overline{\sigma}_f^{\text{natPb}}}{\overline{\sigma}_f^{235\text{U}}}$  as to the volume of the target and the blanket of U/Pb assembly. The research is carried out within the framework of a series of experiments using the model of subcritical heterogeneous electronuclear system at the Laboratory of High Energies, JINR, Dubna ("Investigation of Physical Aspects of Electronuclear Method of Energy Production and Transmutation of Radioactive Waste Using Beams from JINR Synchrophasotron/Nuclotron" - "Energy plus Transmutation").

The aim of the investigation specified was to obtain information about a neutron field of the system, integral nuclear data (as to fission rates and spectral indices). The comparison of the experimental values obtained was carried out with the calculation results executed by the

method of Monte-Carlo simulation using computer code *DCM/CEM* [3] and the library of adron-nuclear cross-sections [4]. When calculating the fission rates and *SI* the libraries of neutron cross-sections were applied [5,6].

## 2. Experiment

Measurements were carried out with SSNTD as described earlier [1,2]. The sensors consisting of fissionable sources and track detectors for fission fragments were placed onto detector plates. On each of the five detector plates in the U/Pb-assembly we used six sensor positions, radially distributed from the center of the lead target to the outer surface of the U-blanket. The two innermost positions were situated inside of the lead target, three positions within the uranium blanket, and one position outside of the blanket at the same distance from the axis of the target as transmutation samples. All five detector plates were identically constructed. Layout of the U/Pb-assembly is shown in Fig. 1.

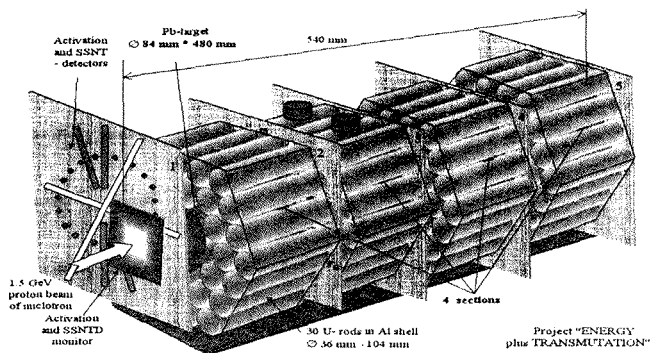


Fig. 1. Layout of the U/Pb-assembly

Metallic foils from 90% enriched  $^{235}\text{U}$  and from natural uranium of 7 mm diameter and approx. 0.1 mm thickness were used as fissionable sources. They were manufactured by cold rolling and vacuum annealing of the material [7]. Foils natural lead ( $\varnothing$  7 mm, thickness  $\sim$  0.07 mm) were the same as described in work [8]. The advantage of using thick sources is the fact that there is no necessity for thickness calibration of each individual source and that the sensitivity is optimized. Artificial mica (fluoroflogopite) was used as the fission fragment detector.

## 3. Results and discussion

Fig. 2 presents the results of measurements and calculations of the radial distribution of  $^{235}\text{U}$  and  $^{238}\text{U}$  fission rates as measured in the second detector plate, which is at 11.8 cm from the front of the lead target. Fission rates of both nuclides  $^{235}\text{U}$  and  $^{238}\text{U}$  decrease inside the blanket with increasing radial distance  $R$  from the axis of the U/Pb-assembly by factors of approx. 1.3 for  $^{235}\text{U}$  and, depending on the detector plate, between 2.6 and 3.5 for  $^{238}\text{U}$ , as compared to the calculated decrease by factors of 1.6 and between 2.2 and 3.8, respectively. It is seen,

that the value of decrease of the fission rate for  $^{238}\text{U}$  is much larger than for the  $^{235}\text{U}$  fission rate. It can be explained by the fact that the decrease of neutron fluence density in radial direction connected with an absorption in the blanket material and the effect of geometric factor is compensated by an increase of the average cross-section of  $^{235}\text{U}$  fission caused by a decrease in the average energy of neutrons in the processes of inelastic scattering on nuclei of the blanket.

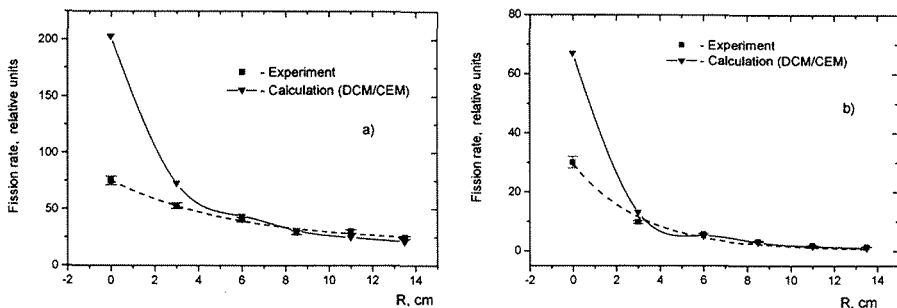


Fig. 2. Radial distributions of fission rates for  $^{235}\text{U}$ (a) and  $^{238}\text{U}$ (b) inside the Pb-target and U-blanket (see Fig. 1) measured in the second detector plate. The central Pb-target extends up to  $R=4.2$  cm and the U-blanket up to  $R=13.5$  cm.  $R$  is the radial distance from the axis of the lead target. Lines are drawn to guide the eyes

The experimental and calculated axial distributions of  $^{235}\text{U}$  and  $^{238}\text{U}$  fission rates exhibit similar features on all five detector plates along the entire target-assembly with a maximum of the fission rates in the second detector plate. In Fig. 3 the fission rates of  $^{238}\text{U}$  and  $^{235}\text{U}$  are shown for all detector plates at a radial distance  $R=13.5$  cm. These positions are on top of the blanket and close to the locations where the radiochemical transmutation sensors were mounted on the surface of the blanket. A satisfactory agreement of the results of the calculation and the experiment (in the limits of 25%) is seen in this Figure.

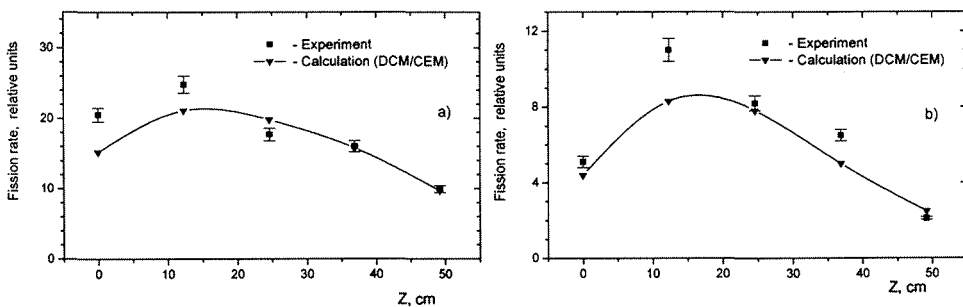


Fig. 3. Axial distributions of  $^{235}\text{U}$ (a) and  $^{238}\text{U}$ (b) fission rates along the top surface of the blanket of U/Pb-assembly (solid lines are drawn as guide for eyes)

The results of measurements and calculations of the  $SI \frac{\sigma_f^{-238U}}{\sigma_f^{-235U}}$  in dependence of the radial distance R within the U/Pb-assembly for the second detector plate are given in Fig. 4(a). The good agreement between measurement and calculation of the radial distributions in the ratio of  $^{235}\text{U}$  and  $^{238}\text{U}$  fission rates shows that the model calculation describes consistently the particles' energy transfer within the blanket. The spectral index, which is an indicator of the neutron spectrum hardness, decreases with increasing distance R from the target axis, thus showing the softening of the neutron spectrum in the radial direction. Experimental values of axial distribution of  $SI \frac{\sigma_f^{-238U}}{\sigma_f^{-235U}}$  are not changed in the blanket of U/Pb-assembly (in the limit of experimental uncertainties) along the axis of the proton beam, that indicates a steady-state neutron spectrum in the axial direction inside of the blanket of the assembly for energy region ~ up to 30 MeV, because the contribution of fissions  $^{238}\text{U}$  is not considerable under the more greater energies.

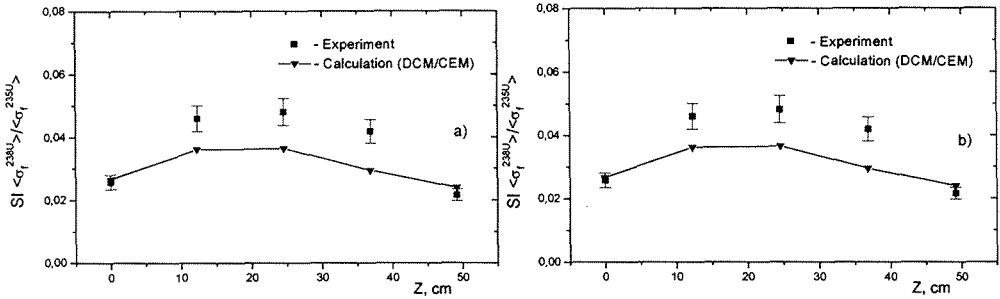


Fig. 4. Radial distribution of spectral index  $\frac{\sigma_f^{-238U}}{\sigma_f^{-235U}}$  (a) in the target and the blanket of U/Pb-assembly for the second plate and axial distribution of spectral index  $\frac{\sigma_f^{-238U}}{\sigma_f^{-235U}}$  (b) along the top surface of the blanket of U/Pb-assembly (lines are drawn as guide for eyes)

Fig. 4(b) shows this for points placed on the top surface of the blanket of U/Pb-assembly. As it is seen in Fig. 4(b) experimental values of  $SI \frac{\sigma_f^{-238U}}{\sigma_f^{-235U}}$  exceed the calculated ones (by ~25%). This points the more hard character of neutron spectrum than the calculation gives. It is probably caused by a certain overestimation by the calculation of a real influence of construction materials of the shielding container

Fig. 5(a, b) presents the results of measurements of the radial distribution of  $^{nat}\text{Pb}$  fission rate as measured in the second detector plate (a) and along the entire target – assembly (b). Fission rate of  $^{nat}\text{Pb}$  decreases inside the U/Pb-assembly blanket with increasing radial distance R from the axis of the U/Pb-assembly by factors of approx. 430 and decreases inside the U/Pb-assembly blanket by the factor 30. It is seen, that the value of decrease of the fission rate for  $^{nat}\text{Pb}$  is much larger than for the  $^{238}\text{U}$  fission rate. It can be explained by the fact that the decrease of neutron fluence density of ultrafast neutrons ( $En > 30$  MeV) in radial direction which are mainly produced in lead target connected only with effect of geometric factor. At the same time the fast neutrons ( $En > 1.4$  MeV) are produced in the target and in the blanket (due to fission of uranium). The experimental axial distributions of  $^{nat}\text{Pb}$  fission rate exhibit

similar features as  $^{235}\text{U}$  and  $^{238}\text{U}$  fission rates (in the limit of experimental uncertainties) on all five detector plates along the entire target-assembly with a maximum of the fission rates in the second detector plate. In Fig.5(b) the fission rates of  $^{\text{nat}}\text{Pb}$  are shown for all detector plates at a radial distance  $R=13.5$  cm.

The results of measurements of the  $SI \frac{\sigma_f^{-\text{natPb}}}{\sigma_f^{-235\text{U}}}$  ( $SI$  normalized on value  $SI$  in the second detector plate at a radial distant  $R=8,5$  cm) in dependence of the radial distance  $R$  within the  $\text{U/Pb}$ -assembly for the second detector plate are given in Fig. 6(a). This spectral index shows the softening of the neutron spectrum for ultrafast neutrons in the radial direction. Comparison of distributions  $SI \frac{\sigma_f^{-238\text{U}}}{\sigma_f^{-235\text{U}}}$  and  $\frac{\sigma_f^{-\text{natPb}}}{\sigma_f^{-235\text{U}}}$  shows, that the fraction of ultrafast neutrons in the neutron spectrum decreases rather faster than the fraction of fast neutrons.

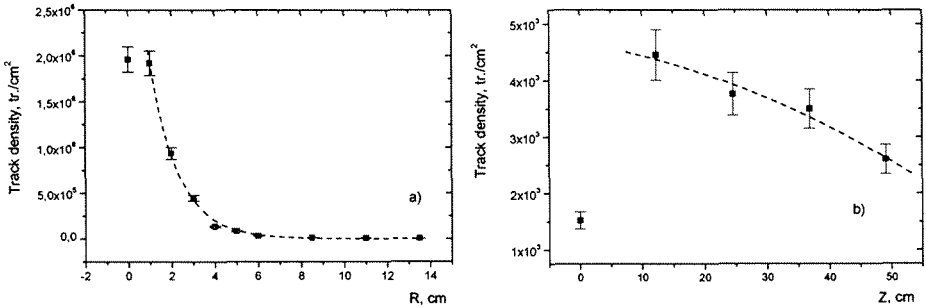


Fig. 5. Radial distribution of  $^{\text{nat}}\text{Pb}$  fission rate as measured in the second detector plate (a) and along the entire  $\text{U/Pb}$  - assembly (b). Lines are drawn to guide the eyes

In Fig. 6(b) experimental values of axial distribution the  $SI \frac{\sigma_f^{-\text{natPb}}}{\sigma_f^{-235\text{U}}}$  sensitive to neutrons with energies  $> 30$  MeV along the surface of the  $\text{U}$  - blanket show of the neutron spectrum became harder as to removal from the beginning of the target. This can be explain that neutrons formed in spallation reactions escape forward preferably.

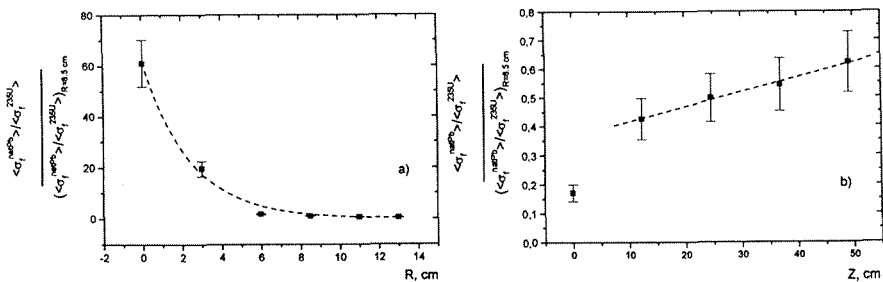


Fig. 6. Radial distribution of spectral index  $\frac{\overline{\sigma}_f^{natPb}}{\overline{\sigma}_f^{235U}}$  (a) in the target and the blanket of U/Pb-assembly for the second plate and axial distribution of spectral index  $\frac{\overline{\sigma}_f^{natPb}}{\overline{\sigma}_f^{235U}}$  (b) along the top surface of the blanket of U/Pb-assembly (lines are drawn as guide for eyes)

#### 4. Conclusions

- Experimental radial and axial distributions of  $^{235}\text{U}$ ,  $^{238}\text{U}$  and  $^{nat}\text{Pb}$  fission rates, as well as spectral indices  $\frac{\overline{\sigma}_f^{238U}}{\overline{\sigma}_f^{235U}}$  and  $\frac{\overline{\sigma}_f^{natPb}}{\overline{\sigma}_f^{235U}}$  have been obtained with the *SSNTD*-technique for the entire Pb-target and the U-blanket.
- Calculated results using the modified computer code *DCM/CEM* show a reasonable agreement with the experimental radial and axial distributions of  $^{235}\text{U}$  and  $^{238}\text{U}$  fission rates inside the U-blanket and a less satisfactory agreement on the surface of the U-blanket.
- Experimental and calculated results for the *SI*  $\frac{\overline{\sigma}_f^{238U}}{\overline{\sigma}_f^{235U}}$  do not change in the limit of experimental uncertainties on the surface of the U-blanket in the axial direction. This indicates a rather constant neutron spectrum for fast neutron part of the neutron spectrum in the U/Pb-assembly along the proton beam direction for energy region ~ up to 30 MeV, because the contribution of fissions  $^{238}\text{U}$  is not considerable under the more greater energies.
- The results of measurements of the *SI*  $\frac{\overline{\sigma}_f^{natPb}}{\overline{\sigma}_f^{235U}}$  show that ultrafast part of the neutron spectrum became harder with increasing distance from the front face of the lead target. This can be explained that neutrons formed in spallation reactions escape forward preferably.
- The agreement of the measured and calculated results confirms the fact that the calculation model describes correctly the relative energy transfer due to scattering within the blanket material.

#### References

1. Krivopustov M.I., Chultem D., Tumendelger Ts. et al. On a First Experiment on the Calorimetry of an Uranium Blanket Using the Model of the U/Pb Electronuclear Assembly "Energy plus Transmutation" on a 1.5 GeV Proton Beam from the Dubna Synchrophasotron // –Dubna, 2000. –( Preprint JINR; P1-2000-168) and –Kerntechnik, 2003, Vol. 68, pp. 48–55.
2. Krivopustov M.I., estmeier W.W, Sosnin A.N. et al. Investigation of Neutron Spectra and Transmutation of  $^{129}\text{I}$ ,  $^{237}\text{Np}$  and Other Nuclides Using the Electronuclear Setup "Energy plus Transmutation" Exposed to 1.5 GeV Proton Beam from the Nuclotron (JINR, Dubna). JINR-Preprint EI-2004-79, Dubna, 2004 (Submitted to Journal "Nuclear Instruments and Methods in Physics Research A").
3. Software "KASKAD" for Monte-Carlo simulation of nuclear and physical processes, initiated by high-energy particles and nuclei in gaseous and condensed media / Barashenkov V.S., Le van Ngok, L.G. Levchuk et al. –Dubna, 1985. –17 p. –(Preprint JINR; P2-85-173).
4. Barashenkov V.S., Gudowski W., Polanski A. Integral high-energy nucleon-nucleus cross-sections for mathematical experiments with electronuclear facilities. // Proc. of the

- 3<sup>rd</sup> Intern. Conf. on Accelerator Driven Transmutation Technologies and Applications (99'ADTTA), Praha (Pruhonice), Czech Republic, 7–11 June 1999. –1999. –P. 1–6, MO-O-C10 (CD ROM Edition).
5. Group constants for calculation of reactors and shielding. Reference book / L.P. Abagyan, Bazazyants N.O., Nikolaev M.N., Tsybulya A.M.. –M.: Energoizdat, 1981. –231 p.
  6. Neutron induced fission cross section ratios for <sup>232</sup>Th, <sup>235,238</sup>U, <sup>237</sup>Np and <sup>239</sup>Pu from 1 to 400 MeV / Lisowski P.W., Ullmann J.L., Balestrini S.J. e.a. // Proc. of the Intern. Conf. on Nuclear Data for Science and Technology, 30 May–3 June 1988, JAERI, Mito, Japan; ed. by S. Igarasi. –Mito, 1988. –P. 97–103.
  7. Investigation of space and energy distributions of neutrons generated in lead target and uranium blanket of the electronuclear system “Energy plus transmutation” under irradiation with protons at 1.5 GeV / Zhuk I.V., Kievets M.K., Krivopuskov M.I. et al. –Dubna, 2002. –29 p. –( Preprint JINR; P1-2002-184).
  8. Perelygin V.P., et. al. SSNTD Studies of lead nuclei fission induced by relativistic p, d, He and C projectiles inside massive Pb and U targets.–Radiation Measurements, 31, (1999), 567.

# On Solution of the Nuclear Problems reduced to a System of First Order Integral Fredholm Equations

S.V.Korneev<sup>1</sup>, Yu.G.Fokov<sup>1</sup>, S.E.Chigrinov<sup>1</sup>, T.N.Korbut<sup>2</sup>, B.A.Martsynkevich<sup>2</sup>,  
A.M.Khilmanovich<sup>2</sup>, M.I.Krivopustov<sup>3</sup>, A.N.Sosnin<sup>3</sup>

1. JIPNP – Sosny, NAS Belarus, Minsk, Belarus
2. Stepanov Institute of Physics, NAS Belarus, Minsk, Belarus
3. Joint Institute for Nuclear Research, Dubna, Russia

(Collaboration «Energy plus Transmutation»)

## Abstract

Methods to solve some physical problems reducible to a system of the first order integral Fredholm equations are considered in the report. A case when equation kernels possess thresholds, below which they are equal to zero are considered. Equation kernels and absolute terms are deduced during the solution by using the experimental results.

Research data on unfolding fast neutron spectra in a wide energy range from 1 up to 100 MeV are presented. This study is performed in relation to a wide series of experiments using a model U/Pb electronuclear system driven with a proton beam from the LHE JINR Synchrophasotron/Nuclotron in the frame of the Project “Energy plus Transmutation”[1-3] and subcritical assembly “Yalina” driven with a JIPNP, Sosny neutron generator [4].

Methods to unfold the spectra proposed in the report are using the method of effective threshold cross sections. It is pointed out that for neutron energies exceeding 20 MeV there is as a rule a lack of reliable data on effective reaction cross sections. Therefore two approaches to solve the problem are considered: reference spectrum obtained by means of numerical calculation is used or effective cross sections taken from published data are employed. It is shown that the approach based on using the reference spectrum is preferable.

## References

1. M.I.Krivopustov, D.Chultem, A.N.Sosnin et al. On a First Experiment on the Calorimetry of an Uranium Blanket Using the Model of the U/Pb Electro-Nuclear Assembly «Energy Plus Transmutation» on a 1,5 GeV Proton Beam from the Dubna Synchrophasotron. JINR-Preprint R1-200-168, Dubna, 2000; //Journal Kerntechnik 2003, 68, p.p. 48-55.
2. B.A.Martsynkevich, A.M.Khilmanovich, S.V.Korneev et al. Unfolding of Fast Neutron Spectra in a Wide Energy Range (up to 200 MeV) in the Subcritical Uranium-Lead System “Energy plus Transmutation”. JINR Preprint P1-2002-65, Dubna, 2002 // Vesti NASB. Physics-Mathematics Series. Minsk, 2004. V.1. p.p. 90-95.
3. M.Zamani, M.Fragopoulou, M.Manolopoulou, M.I.Krivopustov, A.N.Sosnin et al. Spallation neutron production in the new Dubna transmutation assembly. NIM, A 508. 2003, p.p.454-459.
4. S.F.Bulyga, V.G.Gulo, I.V.Zhuk et al. Neutron Generator NG-12 – Basic Installation to Carry Research at the Neutron Center of the National Academy of Sciences, Belarus. Preprint IRPhChP, Minsk, 1998.

# ON THE EXPERIMENT OF NEUTRON SPECTRUM INVESTIGATION ON U/Pb-ASSEMBLY USING 0,7 GeV PROTON BEAM FROM THE JINR NUCLOTRON (DUBNA)

M.Bielewicz<sup>1</sup>, M.Szuta<sup>1</sup>, A.Wojciechowski<sup>1</sup>, E.Gola-Strugalska<sup>1</sup>,  
M.I.Krivopustov<sup>2</sup>, I.Adam<sup>2</sup>, A.Kugler<sup>3</sup>, V.Wagner<sup>3</sup>, A.Krasa<sup>3</sup>, M.Majerle<sup>3</sup>, P. Chaloun<sup>3</sup>.  
(for collaboration "Energy plus Transmutation")

1. Institute of Atomic Energy, 05-400 Otwock-Świerk, Poland
2. Joint Institute for Nuclear Research, 141980 Dubna, Russia
3. Nuclear Physics Institute of CAS, 25068 Rez, Czech Republic

## Abstract

Within the program of "Investigation of physical aspects of energy production and study of radioactive waste transmutation using relativistic beams of Synchrotron / Nuclotron accelerator complex of the Laboratory of High Energies JINR" – project "Energy plus Transmutation" [1-3] – was carried on an experiment (June 2004) of irradiation the lead target surrounded by an uranium blanket (206,4 kg of natural uranium) with proton beam of 0.7 GeV. To study the spectrum of neutrons generated in the U/Pb - assembly the following activation detectors Al, Cu, Y, Au and Bi were used. Preliminary results obtained from the Yttrium-89 detectors show that the  $(n, xn)$  - reactions are observed with the "x" up to 6. Those results will be used to determine the neutron spectrum in the U/Pb - assembly in the wide range of energy until 200 MeV.

## 1. Introduction

The presented here experiment was carried out on JINR Dubna experimental set-up 'Energy plus Transmutation'. 0.7 GeV proton beam struck at a cylindrical lead target surrounded by uranium blanket, which was surrounded by shielding polyethylene container. Produced spallation neutrons were multiplied in process of uranium fission. Our experiment was focused on neutron field measurement. We determined neutron field using pure Yttrium (99.9% Y89) samples as activation detectors. Neutron capture led in Y89 to various  $(n, xn)$ , reactions where 'x' is an integer number. Resulted isotopes were unstable, gamma active. The gamma activity was measured with Ge(Li) detectors. As a result we got isotope production/neutron flux distribution in various locations of 'Energy plus Transmutation' facility.

## 2. Experiment

The base part of the experimental facility was a U/Pb assembly consisting of a lead cylindrical core and natural uranium cylinders. More detailed drawing of the assembly is shown in [1-3]. The assembly was divided into 4 identical sections separated by foils with detectors. The same foils were also on front and rear side of the assembly. This gave us 5 possible locations of detectors along the axis. Y89 samples were located on each mentioned foil. The exact sample location is shown in Table 1 and Fig.1. Thanks to such location one could investigate axial and radial distribution of generated isotopes. The experiment was carried out June 27-28, 2004. The time of irradiation in proton beam was equal 31860 sec to collect about  $2 \cdot 10^{13}$  protons (still only preliminary determination of this value).

Table 1. Y89 sample location

Nr	Symbol	Foil Number	Position along the target axis [cm]	Distance from the Axis [cm]	Mass [g]	Comments
1	Y1 0	F1	0	0,0	1,98	Powder
2	Y1 1	F1	0	3,0	0,80	
3	Y2 1	F2	11.8	3,0	0,825	
4	Y2 2	F2	11.8	6,0	0,78	
5	Y2 3	F2	11.8	8,5	0,79	
6	Y2 4	F2	11.8	10,5	0,91	
7	Y2 5	F2	11.8	13,5	0,90	
8	Y3 1	F3	24.2	3,0	1,33	
9	Y4 1	F4	36.4	3,0	1,16	
10	Y5 0	F5	48.4	0,0	0,9	
11	Y5 1	F5	48.4	3,0	1,57	

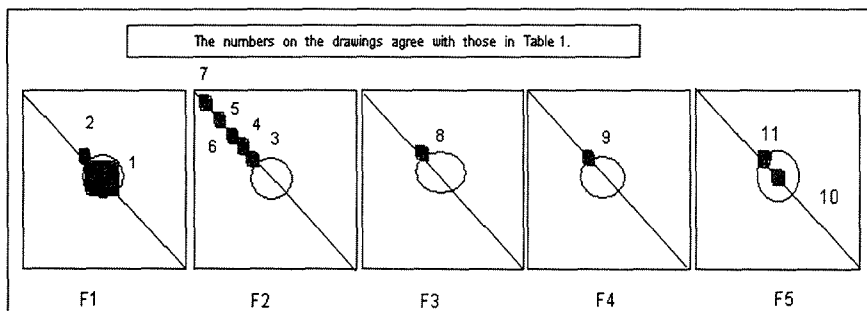


Fig.1. Y89 sample location. F1 – plastic foil located in front of target; F2, F3 and F4 – located between target sections; F5 – located on rear of the target. For target construction details see Fig. 1 in [2].

### 3. Measurements

After the end of the experiment all samples were transported to another building where their gamma activity was measured with HPGe detector. The measurements started in about two hours after the end of the experiment and lasted several consecutive days. Two series of measurements were carried out, the first one about 400 sec for each measurement and the second one about 4000 sec.

Several standard target and background measurements (without sample) were carried out for calibration purpose. Each series of the measurements was recorded in a separate file.

#### 4. Analysis and calibration

The first stage of the analysis was executed by means of the computer program DEIMOS [4]. Using this program one performed the gamma line energy calibrations, line absolute intensity and half width of the line (FWHM) and respective errors.

The second stage of analysis was an identification of isotopes the spectra line came from. One used the "manual" procedure for this basing a gamma line library.

At the third stage the results were corrected for duration of the experiment elapsed time from the end of the experiment to the beginning of the measurement, duration of the measurement, mass of the sample, absolute intensity of the line value (from tables), relative detector efficiency for the given energy.

Below is the calibration formula:

$$B = \frac{N_1}{m \times \frac{N_{abs}}{100} \times \varepsilon_p(E) \times COI(E,G) \times I} \times \frac{\left( \frac{\ln(2)}{t_{1/2}} \times t_{ira} \right)}{\left( 1 - \exp \left[ - \frac{\ln(2)}{t_{1/2}} \times t_{ira} \right] \right)} \times \left( \exp \left[ \frac{\ln(2)}{t_{1/2}} \times t_+ \right] \right) \times \frac{\frac{t_{real}}{t_{live}}}{\left( 1 - \exp \left[ - \frac{\ln(2)}{t_{1/2}} \times t_{real} \right] \right)}$$

where

B	number of nuclei per gram of a sample material and per one primary proton
$N_1$	peak (line) area
$N_{abs}$	the absolute intensity of given line in percent [%]
$\varepsilon_p(E)$	detector efficiency function of energy (polynomial)
COI(E,G)	cascade effect coefficient function of energy and geometry
I	total number of primary protons
$t_{1/2}$	half life time
$t_{ira}$	elapsed time of irradiation
$t_+$	elapsed time from the end of irradiation to the beginning of measurement
$t_{real}$	elapsed time of the measurement
$t_{live}$	"live" time of measurement
m	mass of the sample (target) in grams

So calibrated results were averaged in relation to all lines, measurements and samples and shown on the summary graphs.

## 5. Results

The results are shown below in Table 2 and in consecutive graphs.

Table 2. The identified gamma lines and the isotopes they come from [5]

Nr	Reaction	Produced Isotope	Half Life	Ethr [Mev]	Energy [keV]	Intensity [%]
1	(n,g)	Y90	3,19h	-6,9	202,5	97,3
					497,2	90,74
2	(n,2n)	Y88	106,65d	11,5	898,0	93,7
					1836,1	99,2
3	(n,3n)	Y87	79,8h	20,8	388,5	82,00
			13,37h		380,8	78
4	(n,4n)	Y86	14,74h	32,7	627,7	32,6
					703,3	15,4
					777,4	22,4
					1076,6	82,00
					1153,0	30,50
					1854,4	17,2
1920,7	20,8					
5	(n,5n)	Y85	2,68h	42,1	231,7	84
					504,5	60
			913,9		9,00	
			4,86h		231,7	22,8
1404,8	3,08					
2123,8	5					
2172,1	2,27					
6	(n,6n)	Y84	39,5m	54,4	793,3	99
					974,6	75
					1040,2	56
7		Sr85	64,84d	38,1	514,0	96
			67,63m		151,2	12,9
					231,7	84,4
8		Sr83	32,41h	58,6	381,5	14,1

Nr	Reaction	Produced Isotope	Half Life	Ethr [Mev]	Energy [keV]	Intensity [%]
					762,7	30
9		Rb83	86,2d	55,6	520,4 552,6	44,7 16
10		Rb82	6,47h	66,4	554,3 619,1 698,4 1007,6 1044,0 1317,5 1474,9	62,4 37,975 26,3 7,17 32,068 23,7 15,53
11		Rb81	4,576h	75,3	190,5 446,2	64 23,2
12		Kr77	74,4m		129,6 146,6	81 37,3
13		Br77	57,036h		239,0 520,6	23 22,4
14		Br75	96,7m		141,3 286,5 377,4 427,9	6,6 88 39,3 4,4
15		Se73	7,15h		67,0 360,8	78 108

The below graphs (Fig 2-4) show the axial and radial distribution of generation of some isotopes listed in Table 2

Y86,  $t_{1/2}=14,74\text{h}$ , axial distribution

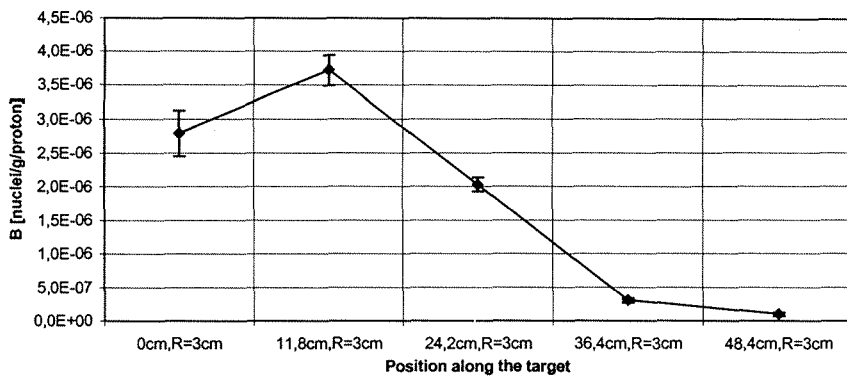


Fig.2 Axial distribution of Y86 generation (see Fig. 1)

Kr 77,  $t_{1/2}=74.4\text{m}$ , axial distribution

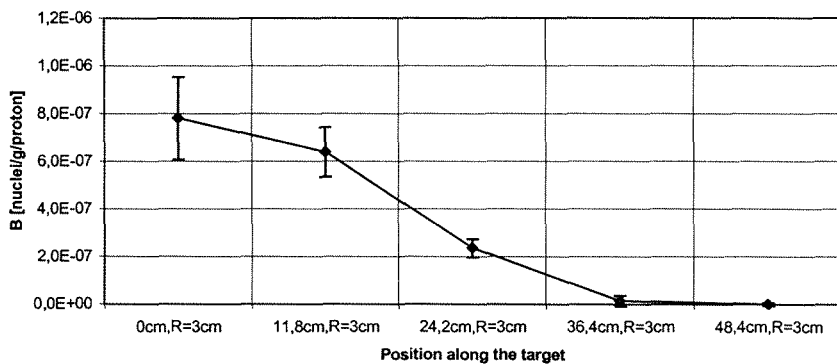
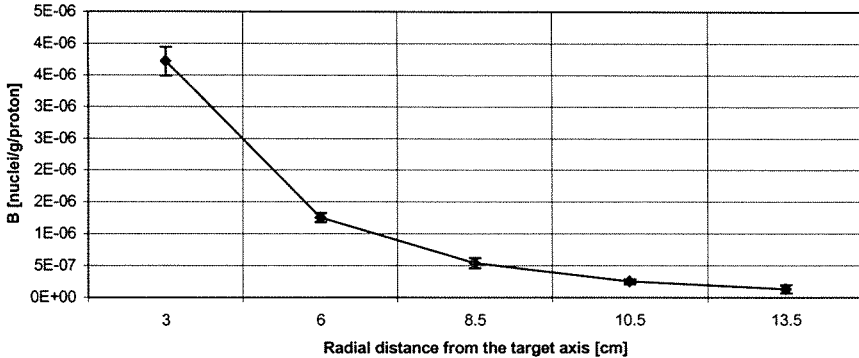


Fig.3 Axial distribution of Kr77 generation (see Fig. 1)

### Y86, $t_{1/2}=14,74\text{h}$ , radial distribution



**Fig.4 Radial distribution of Y86 generation (see Fig. 1)**

## 6. Conclusions and remarks

Presented hereby results are the partial ones only, not final, just to show the tendencies.

Preliminary results obtained from the Yttrium-89 detectors show that the  $(n, xn)$  - reactions are observed with the "x" up to 6.

Looking at the above graphs one can see that isotope creation axial distribution changes when going from one to another isotope. Y88 to Y84 distribution has maximum on the second foil (11,4 cm from the front side) (Fig.2) while for the other isotopes the maximum is right on the front side (Fig.3). The maximum position seems to depend on threshold energy of the reaction leading to given isotope. More detailed analysis will be the subject of later work over.

Yttrium seems to be a very good detector because of its simple and well defined isotope composition, many possible reaction channels leading to isotopes with suitable, very convenient for measurement half life time.

It's very important to underline that this paper referring to the Y89 detector is only a small part of the bigger work which will be prepared later.

## References

- [1] M. Krivopustov et al.- *On a First Experiment on the Calorimetry of the Uranium Blanket Using the Model of the U/Pb Electro-Nuclear Assembly "Energy plus Transmutation" on a 1.5 GeV Proton Beam of the Dubna Synchrophasotron*. JINR Preprint P1-2000-168, Dubna, 2000. Kerntechnik, 2003. V.68. p 48-55.
- [2] M. Krivopustov et al.- *Investigation of Neutron Spectra and Transmutation of I129, Np237 and other Nuclides with 1,5 GeV Protons from the Dubna Nuclotron Using the Electronuclear Setup "Energy plus Transmutation"*. JINR Preprint, E1-2004-79, Dubna, 2004, (submitted in NIM).

- [3] B. A. Martsynkevich et al. – *Unfolding of Fast Neutron Spectra in the Wide Energy Range (up to 200 MeV) in a Heterogenous Subcritical Assembly of an Electronuclear System “Energy Plus Transmutation”* JINR Comm., P1-2002-65, Dubna, 2002. (Russian)
- [4] J. Frana – *Program DEIMOS32 for Gamma Ray Spectra Evaluation*. Radioanal. and Nucl. Chem., V. 257, p.583, 2003.
- [5] LANDOLT-BORNSTEIN Numerical Data and Functional Relationships in Science and Technology. *New Series Q-Values and the Excitation Functions of Nuclear Reactions*. Vol.5, Part a and b, Editor. H.Schopper, Springer-Verlag Berlin, Heidelberg-New York, 1973.

# Investigation of Temperature Fields and Heat Generation in the Lead Block and the Lead target with the Uranium blanket of the Installation "Energy plus Transmutation" Using Proton Beams from the JINR Synchrophotron/Nuclotron

A.V.Voronkov<sup>1</sup>, A.V.Efremov<sup>1</sup>, E.A.Zemskov<sup>2</sup>, N.M.Sobolevsky<sup>1</sup>, A.G.Churbanov<sup>1</sup>,  
S.P.Kaznovsky<sup>3</sup>, S.G.Lobanov<sup>3</sup>, V.F.Mischenkov<sup>3</sup>, B.I.Fonarev<sup>3</sup>, Yu.L.Shapovalov<sup>3</sup>,  
M.I.Krivopustov<sup>4</sup>, A.V.Pavlyuk<sup>4</sup>, A.N.Sosnin<sup>4</sup>, Ts.Tumendelger<sup>4</sup>, D.Chultem<sup>4</sup>

<sup>1</sup> Keldysh Institute of Applied Mathematics, RAS, Moscow, Russia

<sup>2</sup> Institute of Physics and Power Engineering, Obninsk, Russia

<sup>3</sup> All Russian Design and Research Institute of Atomic Power Machine Building, Moscow, Russia

<sup>4</sup> Joint Institute for Nuclear Research, 141980 Dubna, Russia

(for collaboration "Energy plus transmutation")

Space-time distributions of temperature fields and dynamics of heat generation in the volume of the lead block ( $50 \times 50 \times 80 \text{ cm}^3$ ) and in the lead target and uranium blanket (total mass 206.4 kg of natural uranium) of the electronuclear installation "Energy plus Transmutation" irradiated with proton beams at energy 0.5 and 1.5 GeV correspondingly [1,2]. Measurements of non-stationary distributions of temperatures during the irradiation of the block and the assembly with relativistic protons have been performed using thermometric methods based on highly-sensitive low-inertial microthermocouples and semiconductor resistors.

Theoretical calculations of thermal fields have been performed using computer program TEMP [3], calculation of the external source of heat generation are carried out using program complexes SHIELD [4], PFRSE [5] and LAHET [6]. Calculated data and their comparison are discussed in [7]. Values of specific heat generation in the cells of the large lead block are calculated. Results of computer modeling of non-stationary temperature fields in the lead block and target-blanket assembly show qualitative agreement with experimental data [1,2].

## References

1. R.Brandt, S.P.Kaznovsky, M.I.Krivopustov, A.N.Sosnin, D.Chultem, Ts.Tumendelger et al. Investigation of Temperature and Neutron Fields in Lead Medium During the Interactions with Relativistic Protons. JINR Preprint P1-99-117, Dubna, 1998.
2. M.I.Krivopustov, D.Chultem, A.N.Sosnin, S.P.Kaznovsky, S.G.Lobanov, V.F.Mischenko, B.I.Fonarev, Yu.L.Shapovalov et al. First Experiments with a Large Uranium Blanket within the Installation "Energy plus Transmutation" Exposed to 1.5 GeV Protons. JINR Preprint P1-2000-168, Dubna, 2000; // Journal Kerntechnik, 2003, 68, pp.48-55.
3. A.N.Pavlov, A.A.Ionkin, A.V.Voronkov, A.G.Churbanov. Uniform Method of Heat and Mass Transfer in the Regions with Complex Internal Structure. Preprint N8 of the Keldysh Institute of Applied Mathematics, RAS, Moscow, 1998.
4. A.V.Dementyev, N.M.Sobolevsky. SHIELD – Universal Monte-Carlo Hadron Transport Code: Scope and Applications. Radiation Measurements, 1999, 30, p.553.
5. E.V.Efremov, N.A.Ivanov, O.B.Moskalev. PARSE-2 – Code Complex to Calculate Hadronic Cascades in Three Dimensional Geometry by Means of the Monte-Carlo

- Method. Report Abstracts of the VI All-Russian Scientific Conference on Protection from Radiation Sources from Nuclear Installations, Obninsk, 1998.
6. R.E.Prael and H.Lichtenstein. User Guide to LCS: The LAHET Code System. LANL Report LA-UR-89-3014 (September 1989).
  7. A.V.Voronkov, A.V.Efremov, E.A.Zemskov, N.M.Sobolevsky, S.P.Kaznovsky, M.I.Krivopustov. Computational Analysis of the Fields of Heat Generated in Targets Irradiated with Relativistic Proton Beams. Preprint N75 of the Keldysh Institute of Applied Mathematics, RAS, Moscow, 2000.
  8. A.V.Voronkov, E.A.Zemskov, A.G.Churbanov, S.P.Kaznovsky, M.I.Krivopustov. Calculation Analysis for an Experiment on Thermomeasuring the massive lead target Irradiated by a Beam of Relativistic Protons. Preprint N76 of the Keldysh Institute of Applied Mathematics, RAS, Moscow, 2000.
  9. A.V.Voronkov, A.V.Efremov, E.A.Zemskov, S.P.Kaznovsky, M.I.krivopustov, A.G.Churbanov. Computational Analysis of the Experiment on Thermometric Measurements of Uranium-Lead Assembly Irradiated with Relativistic Proton Beams at 1.5 GeV. Preprint N23 of the Keldysh Institute of Applied Mathematics, RAS, Moscow, 2000.

# EXPERIMENTAL STUDIES OF TRANSMUTATION OF $^{129}\text{I}$ BY SPALLATION NEUTRONS USING JINR DUBNA PHASOTRON

M. Majerle<sup>1†</sup>, V. Wagner<sup>1</sup>, A. Kugler<sup>1</sup>, A. Krása<sup>1</sup>, F. Křížek<sup>1</sup>, V. Henzl<sup>1</sup>, D. Henzlová<sup>1</sup>,  
J. Adam<sup>1,2</sup>, V. Bradnová<sup>2</sup>, P. Čaloun<sup>1,2</sup>, D. Chultem<sup>2</sup>, V. G. Kalinnikov<sup>2</sup>,  
M. I. Krivopustov<sup>2</sup>, A. A. Solnyshkin<sup>2</sup>, V. I. Stegailov<sup>2</sup>, V. M. Tsoupko-Sitnikov<sup>2</sup>,  
Ts. Tumendelger<sup>2</sup>, and S. I. Vasiliev<sup>2</sup>

(1) *Nuclear Physics Institute of CAS, 250 68 Řež, The Czech Republic*

(2) *JINR Dubna*

† *E-mail: majerle@ujf.cas.cz*

## Abstract

An intensive beam of 660 MeV protons was directed towards a lead target (not surrounded by shielding or neutron reflectors) for 10 minutes. On the top of the target were placed detectors and iodine samples. The neutron field and the transmutation of  $^{129}\text{I}$  were studied by the neutron activation analysis method. First simulations were compared to the experimental data.

## 1. Description of the experiment

The collaboration "Energy plus transmutation" works on benchmark experiments intended to test simulation programs, which shall be used in design of Accelerator Driven Systems. The work consist of a series of similar experiments, of which each is concentrated on a specific topic. Generally said, we study production of neutrons by spallation reactions on massive targets, their transport, and use for transmutation. Our experimental setups consist of heavy metal (Pb, W, Bi, U) targets of cylindrical shape to which a narrow beam of relativistic protons is directed. In the target protons cause spallations of heavy nuclei to nucleons, and smaller fractions of nucleus. Relativistic nucleons cause further spallations, and mostly neutrons of all energies - from thermal up to the energy of the proton beam - exit the target sideways. Such neutron production shall be used in the devices called ADS (Accelerator Driven Systems), which will be able to use a wider spectrum of nuclear fuel ( $^{232}\text{Th}$ , nuclear waste from thermal reactors), and their waste should be much less radioactive than the waste from thermal reactors. These systems cannot be built in smaller scale as a test model, and the accelerators to be added to the reactors will not be a cheap extension. That is why we need the precise descriptions of what will be going on in these systems. Our experiments are simplified setups of them, and are used as benchmark tests for the computer simulations that will be used to describe larger and more complicated systems.

One of the experiments was held on Dubna Phasotron in December, 2003, and was focused on the studies of short-lived iodine isotopes production. We needed to make our measurements as soon as possible after the irradiation, and use as intensive proton beam as possible. The proton beam was provided by Dubna Phasotron, which accelerated the intensive proton beam to the energy 660 MeV. The beam was directed to the bare lead

target, which was composed of four cylinders ( $r = 4.8$  cm,  $d = 12$  cm). Before the target were placed two metal (Al and Cu) monitor foils to determine the proton beam integral. Between the first and the second cylinder there was a 7 mm empty interval, where were placed 5 detectors to determine the dislocation of the beam from the central axis. Other detectors (Al, Au, and Bi foils of dimensions  $2 \times 2$  cm<sup>2</sup>) were put on the top of the target along its entire length. At the 9<sup>th</sup> cm, we put two iodine samples, one of natural iodine (<sup>127</sup>I), and the other of iodine from radioactive waste (mixture of 10% <sup>127</sup>I and 90% <sup>129</sup>I). Two identical samples were put at the 21<sup>st</sup> cm. The iodine was packed in Al cases for safety reasons. Similar samples were already used in previous experiments [1, 2], and the aluminum shielding was remodeled for this experiment: to provide reasonable safety at the minimum of Al used (Al is activated during the irradiation, and the radiation of its products adversely affects the measurements). After 10 minutes of irradiation with the intensive proton beam, the detectors and samples were collected from the setup, and the measurements with three HPGe detectors started. The  $\gamma$ -spectra of foils were measured at least twice, firstly soon after the irradiation for a short time, to detect short-lived isotopes, and secondly for a longer time, to accurately detect the amount of produced longer lived isotopes. The iodine samples were measured more times (10 times). Finally the spectra of calibration samples were measured to determine the efficiencies of the detectors.

With the analysis of these spectra we determined: the yields of produced isotopes in the monitor foils, in the neutron detectors, and in the iodine samples, and we further deduced the parameters of the proton beam, the neutron spectrum and distribution, and the production rates of transmutation of <sup>129</sup>I to shorter lived isotopes.

## 2. Experimental data

### 2.1. Longitudinal neutron field

For calculations concerning neutron production, we needed to know the parameters of the proton beam: the integral of the proton flux (measured with Al and Cu foils of  $8 \times 8$  cm<sup>2</sup> at the front of the target), and the displacement of the beam from the central axis (measured with five Al and Au foils of  $2 \times 2$  cm<sup>2</sup> inserted after the first segment of the target).

During the irradiation, the beam intensity and size were measured by wire chamber:  $10^{13}$  protons/s, the horizontal and the vertical diameters of the beam were 1.6 cm - 1.9 cm. The beam profile had a Gaussian profile, so the word "diameter" does not define the exact beam borders but the limit, where we can find most of protons. Our beam was focused enough that all of the protons passed through  $8 \times 8$  cm foils before continuing to the target. In monitor foils, protons produced radioactive isotopes, which were later detected by the means of the  $\gamma$ -spectroscopy. The library of the experimental cross-sections for reactions with protons of energy 660 MeV is voluminous and precise, and the results calculated from different produced elements were in good concordance with each other, and with the expected number of protons. Through the monitor foils passed  $1.58 \cdot 10^{15}$  protons, the accuracy of this result is 6% (included are systematic and statistic errors), which is in accordance with the given intensity multiplied by the time of irradiation.

Two sets of five  $2 \times 2$  cm<sup>2</sup> foils were placed after the first segment of the target, one foil on the central axis, and four others around it with the space 0.5 cm between their sides.

In the left and in the right foil the numbers of produced elements were 3 times smaller than in the central foil, in the lower foil it was 5 times smaller, and in the upper foil it was smaller by a factor of 0.8. This agrees with the results measured by the wire chambers: the beam diameter was roughly limited to 2 cm. From the results in the upper and lower foils, we concluded that the center of the beam was shifted upwards for cca 1 cm.

Three types of detector foils were used to study longitudinal neutron field: Al, Au ( $2 \times 2$  cm<sup>2</sup>) and Bi ( $2.5 \times 2.5$  cm<sup>2</sup>) foils in the square shape placed on the top of the target along its length. In the foils, neutrons produced radioactive isotopes via reactions  $(n, \alpha)$ ,  $(n, \gamma)$  or  $(n, xn)$  (see Table 1). After the irradiation, we measured the  $\gamma$ -spectra of the foils, and could calculate the yields of produced isotopes.

Material	Reaction	Product	Threshold (MeV)
<sup>27</sup> Al	$(n, \alpha)$	<sup>24</sup> Na	3.24996
<sup>197</sup> Au	$(n, \gamma)$	<sup>198</sup> Au	0
	$(n, 2n)$	<sup>196</sup> Au	8.11245
	$(n, 3n)$	<sup>195</sup> Au	14.78950
<sup>209</sup> Bi	$(n, 4n)$	<sup>206</sup> Bi	22.55228
	$(n, 5n)$	<sup>205</sup> Bi	29.62538
	$(n, 6n)$	<sup>204</sup> Bi	38.13866

Table 1: Some reactions and their thresholds for Al, Au, and Bi foils [3]

The yields of produced isotopes were recalculated to the number of produced atoms of isotope  $A$  per 1 gram of the detector material and per 1 incident proton. This value is called production rate  $B(A)$  [4, 5], and is defined as:

$$B(A) = (\text{number of } A \text{ -atoms produced}) / [(1 \text{ g sensor}) \cdot (1 \text{ primary proton})]. \quad (1)$$

In the figures (Fig. 1 and 2) are plotted the experimental production rates against the position along the target for all three types of detector foils (errors at the graphs are only statistic errors; systematic errors, such as imprecisely placed foils in the detectors, should contribute another 5%). All graphs show a specific shape: the maximum at around 10<sup>th</sup> cm, and the point near 30<sup>th</sup> cm, from where the neutron field starts to decrease faster - the particles lost so much energy by that point that they cannot cause further spallations. Moreover, the graphs of the elements produced with higher energy neutrons show a slower falling trend - higher energy neutrons are directed mostly in a forward direction, and cause the hardening of the neutron spectrum approaching the end of the target. The exception is the graph for <sup>198</sup>Au, which is produced via  $(n, \gamma)$  reaction by low-energy neutrons (thermal, epithermal and resonance neutrons). The neutrons from the target were partly reflected back by concrete walls, resulting in a homogenous low-energy neutron field in the place with the target, which is seen as flat distribution of production rates of <sup>198</sup>Au.

## 2.2. Transmutation of iodine

Our basic interest here was to observe and measure the production rates of higher order reactions -  $(n, 5n)$ ,  $(n, 6n)$ ,... in iodine samples. Because the isotopes produced via such

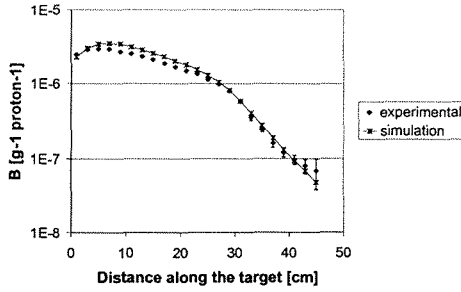


Figure 1:  $B$ -values for  $^{24}\text{Na}$  in Al foils along the target, and comparison with calculated values (MCNPX)

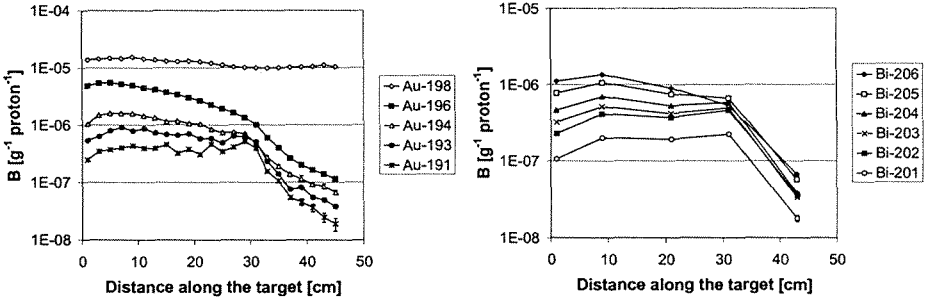


Figure 2:  $B$ -values for different isotopes in Au and Bi foils along the target

reactions are far away from the line of stability and have short lifetimes, we needed to use a series of prompt measurements immediately after the experiment. We could determine the yields of produced isotopes up to  $^{118}\text{I}$  with good accuracy (10%), and detect the products decayed from iodine isotopes up to  $^{116}\text{I}$ , which will be used to calculate the yields of produced iodine isotopes to the isotope  $^{116}\text{I}$ . The yields of produced isotopes for  $^{129}\text{I}$  were calculated with the subtraction of  $^{127}\text{I}$  contribution in the samples with the mixture of radioactive and stable iodine.

The graphs in Fig. 3 show the production rates of measured iodine isotopes at the 9<sup>th</sup> cm and the 21<sup>st</sup> cm for  $^{127}\text{I}$  and  $^{129}\text{I}$ . The production rates for iodine isotopes are comparable with each other and with the production rates for other elements ( $10^{-6} \text{ g}^{-1}\text{proton}^{-1} > B > 10^{-7} \text{ g}^{-1}\text{proton}^{-1}$ ).

### 3. MCNPX calculations

We have compared the experimental data with the calculations done by the simulation code MCNPX v2.3.0. MCNPX simulates the exact paths of incident particles through the setup, simulates nuclear reactions, and stores the history of the particles. From this history, we can extract neutron and proton spectra along the target (Fig. 4). If we convolute the calculated spectrum with the cross-sections for nuclear reactions, we can

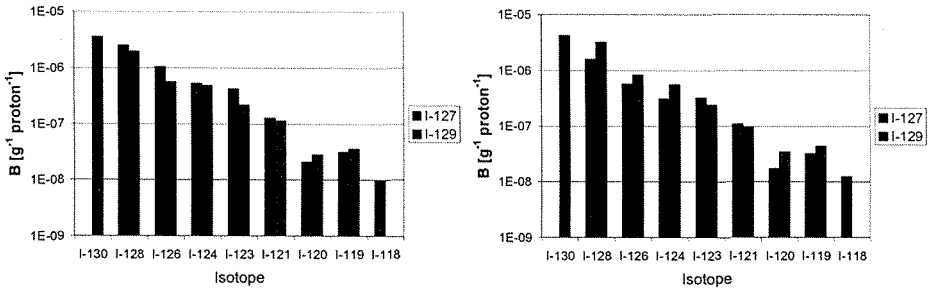


Figure 3:  $B$ -values for different isotopes in  $^{127}\text{I}$  and  $^{129}\text{I}$ . Samples were placed at 9<sup>th</sup> (left) and 21<sup>st</sup> cm (right).

calculate the production rates for our detectors, and compare them with experimental values (Fig. 1).

The calculations agree well with the experimental data (discrepancies do not exceed 20%). One general discrepancy of the MCNPX simulations is that they underestimate the neutron field after the 40<sup>th</sup> cm of a target [6], what was also our case.

Our calculations differed from experimental values in two more points. The field of low-energy neutrons is not correctly calculated, probably because in the calculations were not included the concrete walls, where neutrons from the target were moderated and partly reflected. Also, the calculated production rates for high-energy neutrons were systematically higher from the experimental values by a factor 1.2. This is supposed to be due to the dislocation of the beam to the upper part of the target, where monitor foils were placed. New simulations shall include these two corrections.

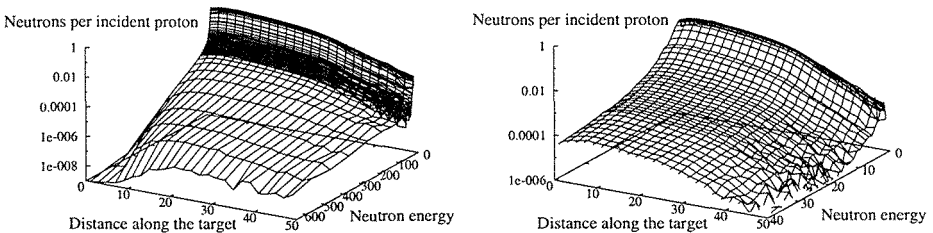


Figure 4: Longitudinal neutron spectra calculated with MCNPX. The graph on right shows the neutron energy range from 0-40 MeV in detail

## 4. Conclusion

We obtained a lot of experimental data from the Phasotron experiment, and found out that it corresponds well to the expectations. This experiment is going to be a good tool to test the simulation codes. The calculations agree to the experimental data inside 20%, and we are trying to improve this agreement with a more accurate definition of the experiment

in MCNPX. In the iodine samples, we measured the production rates for the reactions up to  $(n, 9n)$ , and we are determining the production rates of higher order reactions with the analysis of the decay products of produced iodine isotopes.

The benchmark experiments done on Dubna accelerators have become routine experiments already. Each half a year, a new experiment is done, and we try to provide as much various experimental data as possible. Our future plans include targets from different materials (Bi/Pb), minor modifications of the setup, different energy and intensity of the beam, and different beam particles. Currently we are working on the experiment with deuterons from Nuclotron impinging upon the "Energy plus transmutation" setup. An another experiment is planned on Phasotron as well.

**Acknowledgements.** The authors are grateful to the staff of Phasotron for their essential contribution to this work. The analysis of this experiment especially showed that they have done good work, and provided a stable and well focused beam. These experiments were supported by the Czech Committee for collaboration with JINR Dubna. This work was carried out partly under support of the Grant Agency of the Czech Republic (grant No. 202/03/H043) and ASCR K1048102 (The Czech Republic).

## References

- [1] V. Henzl et al., Journal of Nuclear Science and Technology, Supplement 2., p.1248, August 2001
- [2] M.I. Krivopustov et al., Journal of Radioanalytical and Nuclear Chemistry Letters 222(1997)267
- [3] <http://t2.lanl.gov/data/qtool.html>
- [4] Adam J. et al., First Nuclear Activation Experiments Using the New Accelerator Nuclotron in Dubna, Kerntechnik., 2003., V.68., P.214
- [5] Westmeier W. et al., Transmutation experiments on  $^{129}\text{I}$ ,  $^{139}\text{La}$  and  $^{237}\text{Np}$  Using the Nuclotron Accelerator (submitted to Radiochimiae Acta).
- [6] A. Krása, V. Wagner, A. Kugler, et al., Experimental Studies of Spatial Distributions of Neutron Production Around Thick Lead Target Irradiated by 0.9 GeV Protons, Proceedings of the International Workshop on Nuclear Data for the Transmutation of Nuclear Waste GSI-Darmstadt, Germany, September 1-5, 2003, ISBN 3-00-012276-1, Editors: A. Kelic and K.-H. Schmidt

# INVESTIGATION OF NEUTRON FIELDS ON THE SURFACE OF THE MASSIVE LEAD TARGET UNDER IRRADIATIONS WITH PROTONS AT ENERGIES OF 1.5 AND 5.0 GEV USING SYNCHROPHASOTRON (JINR, DUBNA)

M.K. Kievets<sup>1</sup>, I.V. Zhuk<sup>1</sup>, A.N. Sosnin<sup>2</sup>, M.I. Krivopustov<sup>2</sup>, V.M. D'yachenko<sup>2</sup>

<sup>1</sup>Joint Institute of Power and Nuclear Research - NASB, Sosny, Krasin str., 99,  
220109 Minsk, Belarus, e-mail: kievets@sosny.bas-net.by

<sup>2</sup>Joint Institute of Nuclear Research, 141980 Dubna, Russia

Collaboration "Energy plus Transmutation"

## Abstract

Some spatial and energy characteristics of neutron fields formed on the surface of a massive lead target ( $50 \times 50 \times 80 \text{ cm}^3$ ) under irradiation with protons at energies of 1.5 and 5.0 GeV have been investigated. The irradiations were carried out at the Synchrophasotron of the Laboratory of High Energies, JINR (Dubna, Russia) [1].

Distributions of fission rates of threshold nuclides  $^{232}\text{Th}$  and  $^{209}\text{Bi}$  on the outer surface of the lead target in two directions (transverse and longitudinal) were measured. Fission rates of nuclides  $^{235}\text{U}$  (with and without a cadmium filter),  $^{234}\text{U}$ ,  $^{236}\text{U}$ ,  $^{237}\text{Np}$ ,  $^{238}\text{U}$  were measured on the surface of the target; corresponding spectral indices  $\frac{\sigma_f^i}{\sigma_f^{235\text{U}}}$  and cadmium ratio for  $^{235}\text{U}$  were obtained.

Obtained experimental values for two energies of protons are intercompared as well as comparison with the results of the calculations by means of Monte-Carlo modelling using the computer code *DCM/CEM* is performed [2].

**Keywords:** Spectral index, fission rate, spallation reaction, Synchrophasotron, lead target, ADS, protons, secondary neutrons, track detectors.

## 1. Introduction

The progress of accelerator engineering caused promotion of scientific ideas to create and use intensive neutron sources developed in accelerator driven systems (ADS), which operation is based on spallation reaction. These systems are envisaged to solve in perspective such applied problems as safe generation of nuclear energy, transmutation of radioactive waste, research of material properties etc. At the present stage of research of ADS experimental investigations of their characteristics are of special importance. Such investigations allow one to receive integral nuclear data necessary to test and improve computer codes used for calculation of parameters of ADS.

It's been proposed to use the system which is a rectangular lead target with dimensions of  $50 \times 50 \times 80 \text{ cm}^3$  (massive lead target) irradiated with protons at energies in the range from 1.5 and 5 GeV performed at the Synchrophasotron of the Laboratory of High Energies (JINR, Dubna, Russia). The target specified has a quite simple configuration, which is convenient for calculations and interpretation. At the beginning of 90<sup>th</sup> of the last century the target has been investigated by the group of Prof. K.D. Tolstov within the framework of the project "Lead block" intended to study physical aspects of secondary neutron generation [3]. Experiments with a target assembly of similar configuration but with larger dimensions were carried out at CERN in the frame of the "TARC" experiment [4]. Description and results of other

investigations within the scope of the same experiment are presented in [1]. Present investigation is carried out within the framework of the project “Energy plus Transmutation” and its aim is as follows:

- investigation of spatial distribution of fast neutrons over a lateral surface of the massive lead target, bombarded by protons at energies 1.5 and 5 GeV;
- obtaining of the integral nuclear data on fission rates of a number of fissile nuclides and correspondent spectral indices in the system under investigation;
- intercomparison of experimental data obtained at two energies of protons, as well as their comparison to the calculated results.

The method of solid state nuclear track detectors is chosen as an experimental technique.

## 2. Experiment

### 2.1 Target

The target is a rectangular lead block made in with dimensions of  $50 \times 50 \times 80 \text{ cm}^3$  assembled from lead bricks with the dimensions  $5 \times 10 \times 20 \text{ cm}^3$ . There was the recess hole with the dimensions of  $10 \times 10 \times 20 \text{ cm}^3$  along the longitudinal axis of the target to introduce the proton beam. Layout of the target is shown in Fig. 1.

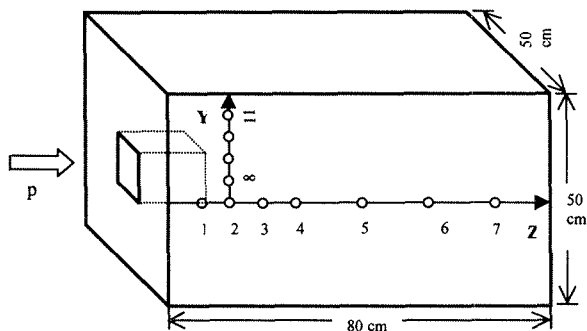


Fig. 1 Layout of the massive Pb-target

The target was irradiated with protons at energies of 1.5 and 5 GeV provided from the slow extraction line of the Synchrophasotron of Laboratory of High Energies (JINR, Dubna). Cross section of the proton beam is in a shape of the ellipse with axes 2.5 and 3 cm.

### 2.1. Measuring positions and detectors used in the experiment

Measuring positions (points) are distributed over the side surfaces of the target along the two axes – Z and Y. Z axis is parallel to the trajectory of the proton beam; Y axis is perpendicular to it. The beginning of the Z axis coincides with a front end surface of the target, and the beginning of the Y axis corresponds to the point 2 of the Z axis. Seven measuring positions are located along the Z axis, and five – along the Y axis. The chart of their locations is presented in Fig. 1. Experimental detectors consisting of a radiator, which is a source of fission fragments, and a track detector are located in each measuring position. These detectors are supplied with radiators made of  $^{232}\text{Th}$  (Th) and  $^{209}\text{Bi}$  (Bi). Th- radiators consist of foils with a diameter of 7 mm and thickness of 0.1 mm and are manufactured from metal  $^{232}\text{Th}$ .

They are considered to be “thick” radiators which is determined by the identical yield of fission fragments. The latter fact appears to be convenient because it excludes the necessity of individual calibration for each detector. Bi -radiators are manufactured with a diameter of 10 mm and they are composed of layers of  $^{209}\text{Bi}$  metal foils with thickness of about  $1 \text{ mg/cm}^2$  put on top of Al- substrate. Detectors with radiators containing  $^{234}\text{U}$ ,  $^{236}\text{U}$ ,  $^{237}\text{Np}$  and  $^{238}\text{U}$  nuclides, as well as  $^{235}\text{U}$  (with and without Cd-cover with thickness of 1 mm) were placed in the detector position 2. All these radiators appear to be made as a thin layer ( $d=0.12\text{--}1.14 \text{ mg/cm}^2$ ) with a diameter of 7 mm containing corresponding fissile material applied over the Al- substrate. All materials used for radiators are pure with the content of the isotope of interest exceeding 99%. Individual calibration of each radiator is required. Lavan (analog of lexan) is used as a track detector. All sensors are allocated in the measuring points in the  $2\pi$ - geometry. All sensors, except for sensors with Bi-radiator, were calibrated in a standard thermal and fast (with  $E_n=14.7 \text{ MeV}$ ) neutron fields.

Fission rate  $Q_f^i$  of one fissile nucleus is equal to an activation integral (or fission integral). It is determined in the ADS under investigation in compliance with the following formula:

$$Q_f^i = \int_0^{\infty} \sigma_f^i(E) \varphi^p(E) dE = \frac{N_q^i}{k_q^{\text{sens}}} P, \quad (1)$$

where  $\varphi^p(E)$  – differential energy density of the neutron flux;  $\sigma_f^i(E)$  – differential microscopic fission cross-section of the  $i$ -th nuclide when fission is induced by neutrons;  $N_q^i$  – track density registered in the track detector, exposed to the neutron flux in contact with the  $q$ -th radiator, containing  $i$ -th nuclide;  $k_q^{\text{sens}}$  – sensitivity coefficient of a sensor;  $P$  – number of incident particles striking the target. Spectral index  $(SI) \frac{\sigma_f^i}{\sigma_f^{235U}}$  is equal to the ratio of fission rates of  $i$ -th nuclide and  $^{235}\text{U}$  nuclide; it is determined in the ADS under investigation in compliance with the following formula:

$$\frac{\sigma_f^i}{\sigma_f^{235U}} = \frac{\int_0^{\infty} \sigma_f^i(E) \varphi(E) dE}{\int_0^{\infty} \sigma_f^{235U}(E) \varphi(E) dE} = \left( \frac{N_q^i}{N_j^{235U}} \right)_{inv} \left( \frac{N_j^{235U}}{N_q^i} \right)_{st} \left( \frac{\sigma_f^i}{\sigma_f^{235U}} \right)_{st}, \quad (2)$$

where indices  $st$  and  $inv$  relate to the values obtained for standard and the investigated neutrons fields [5].

### 3. Calculation

Calculation of neutron spectra at the measuring positions is performed by means of Monte-Carlo simulation using the computer code *DCM/CEM* (Dubna cascade-evaporation model [2]). Neutron cross sections for the above mentioned nuclides are well known in the range up to 20 MeV. There are also experimental data available up to energies 400 MeV. It allows one to carry out comparison of experimental and calculated results for these fissile nuclides. Group neutron sections from the libraries ABBN-78 and IRDF-90 and experimental data obtained by P. Lisowski and others at the LANL for energies of neutrons exceeding 20 MeV [6,7] were used to determine the values of fission rates and spectral indices. Two types of calculation were implemented:

- the first type is the calculation for the "bare" target (calculation 1);
- the second type is the calculation for the target surrounded with a concrete reflector having rectangular shape with thickness 1m and placed at a distance of 2.0 m which simulates the reflection of neutrons from the walls of the experimental hall (calculation 2). Calculated neutron spectra for both cases are presented in fig. 2.

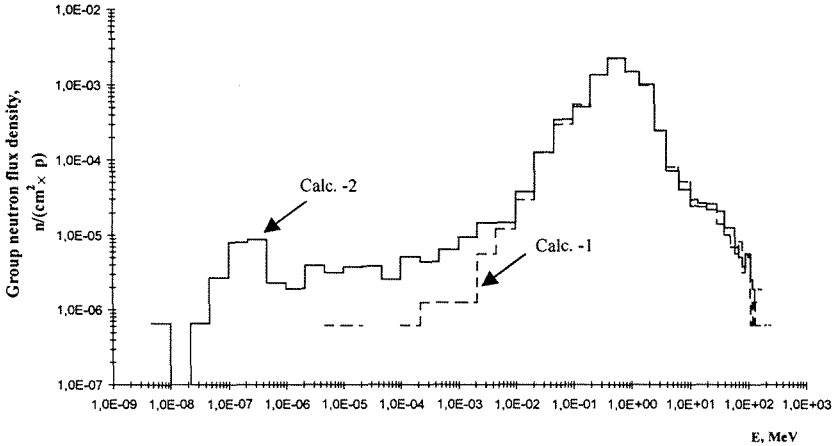


Fig. 2. Calculated (DCM/CEM) neutron spectra at point 2 on the side surface of the massive Pb-target with the concrete reflector surrounded the target (Calc.-2) and without it (Calc. -1)

#### 4. Results and discussion

Distribution of  $^{232}\text{Th}$  fission rate characterizes spatial distribution of fast neutrons in a system with energy exceeding or equal to the energy of its fission threshold (1.4 MeV). During the carried research the distributions of  $^{232}\text{Th}$  fission rate along the axes Z (Z-distribution) and Y (Y- distribution) for both proton energies are measured. Experimental and calculated distributions of  $^{232}\text{Th}$  fission rate on both axes for kinetic energy 1.5 GeV protons are shown in fig. 3.

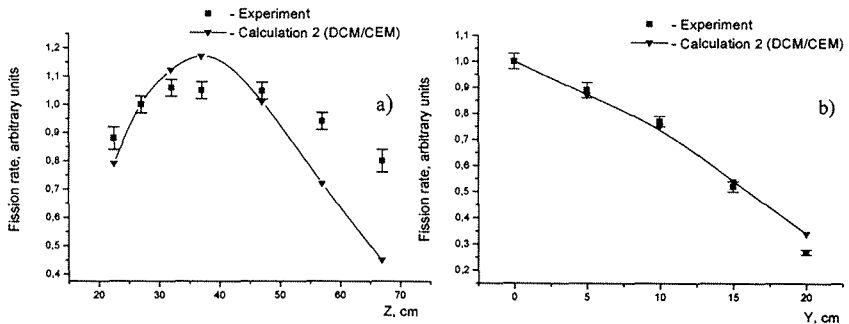


Fig. 3. Experimental and calculated Z- (a) and Y- (b) distributions of  $^{232}\text{Th}$  fission rate on the side surface of Pb-target at  $E_p=1.5$  GeV (solid lines are drawn to guide the eyes)

As it is seen from this figure the shapes of the two distributions for the Z axis differ, and the shapes of distributions for the Y axis practically coincide (within the limits of experimental errors) in case of calculation and experiment. The shape of the experimental distribution is not as sharp as the calculated one (maximal decrease of fission rate is ~20% in case of experiment and ~55 % in case of calculation). Experimental distributions of fission rate for  $^{232}\text{Th}$  along both axes for both kinetic energies of the proton beam (1.5 and 5 GeV) are shown in fig. 4 for comparison.

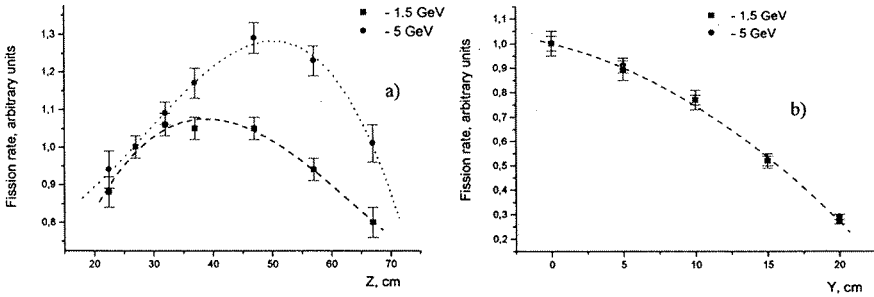


Fig. 4. Experimental Z-(a) and Y - (b) distributions of  $^{232}\text{Th}$  fission rate on the side surface of the Pb-target at  $E_p=1.5$  and 5 GeV (dashed lines are drawn to guide the eyes)

As it is seen from the given figure the shapes of the Y-distributions coincide (within the limits of an experimental errors) and the shape of the Z-distribution differ for both energies of protons. The maxima of distributions of  $^{232}\text{Th}$  fission rate on the Z axis for both energies are at the distances of 32 and 47 cm from the front end surface of the target for proton energies 1.5 and 5 GeV, respectively. Maximum decrease of the fission rate, as it has been already discussed, is ~20 % at energy 1.5 GeV and ~30% at energy 5 GeV. Distributions of fission rate for  $^{232}\text{Th}$  could be approximated rather well by 2 and 3 order polynomial fits for Y and Z axes, respectively. According to calculations the absolute values of fission rate for  $^{232}\text{Th}$  at the measuring point 2 are  $2.78 \times 10^{-28}$  and  $7.76 \times 10^{-28}$  fissions / (proton  $\times$  nucleus) for proton energies 1.5 and 5 GeV, respectively.

$^{209}\text{Bi}$  has a neutron fission threshold at about 30 MeV, therefore distribution of fission rate for  $^{209}\text{Bi}$  characterizes spatial distribution of ultrafast neutrons with energy exceeding or equal to 30 MeV. Unfortunately, the events of fission for  $^{209}\text{Bi}$  could be registered only for proton energy of 5 GeV. Experimental distributions of  $^{209}\text{Bi}$  fission rate along both axes for the given energy are shown in fig. 5.

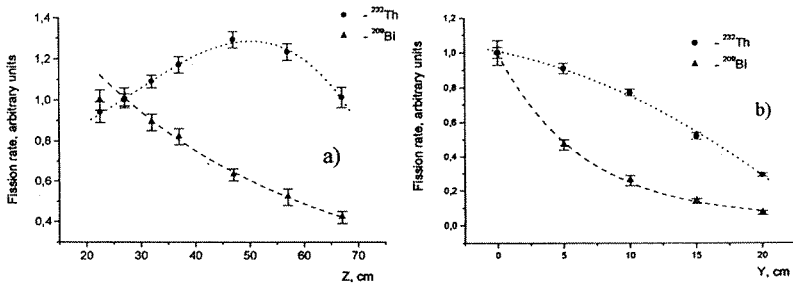


Fig. 5. Experimental Z-(a) and Y(b) - distributions of fission rates of  $^{209}\text{Bi}$  and  $^{232}\text{Th}$  on the side surface of Pb-target at  $E_p=5$  GeV (dashed lines are drawn to guide the eyes) Experimental distributions of fission rate for  $^{232}\text{Th}$  are shown in the same figure for comparison. As it is seen from this figure the distributions of fission rates for  $^{209}\text{Bi}$  and  $^{232}\text{Th}$  differ considerably. The distribution of  $^{209}\text{Bi}$  fission rate is characterized by the decrease which is close to exponential and is equal to the factor of  $\sim 2.4$  and  $14$  for axes Z and Y, respectively.

There is a threshold in the fission cross section of  $^{234}\text{U}$ ,  $^{236}\text{U}$ ,  $^{237}\text{Np}$ ,  $^{238}\text{U}$  as well as  $^{232}\text{Th}$  (fission thresholds are in the interval from 0.5 to 1.4 MeV). The nuclide  $^{235}\text{U}$  is fissile over the whole range of the neutron spectrum, and it's fission threshold is  $\sim 0.5$  eV in the case when it is covered with cadmium sheets with thickness 1 mm. Threshold  $SI \frac{\sigma_f^-}{\sigma_f^i}$  and cadmium ratio for  $^{235}\text{U}$  characterize energy distribution of neutrons in the system under investigation. Measured and calculated values for  $SI \frac{\sigma_f^-}{\sigma_f^i}$  ( $i$ -  $^{232}\text{Th}$ ,  $^{234}\text{U}$ ,  $^{236}\text{U}$ ,  $^{237}\text{Np}$ ,  $^{238}\text{U}$ ), as well as  $R_{\text{Cd}}(^{235}\text{U})$  at the measuring point 2 are presented for both proton energies in table 1.

Table 1. Values of spectral indices  $\frac{\sigma_f^-}{\sigma_f^i}$  at the measuring point 2 on the side surface of the Pb-target

i- nuclide	$\frac{\sigma_f^-}{\sigma_f^i}$		
	Experiment	Calc.-1	Calc.-2
<b>1.5 GeV</b>			
Th-232	0.0105±0.0009	0.0270	0.0172
U-234	0.185±0.016	0.60	0.37
U-236	0.076±0.006	0.211	0.130
Np-237	0.193±0.015	0.66	0.41
U-238	0.034±0.003	0.097	0.061
R <sub>Cd</sub> (U-235)	1.34±0.09	1.00	1.48
<b>5 GeV</b>			
Th-232	0.0106±0.0009	0.0294	0.0172
U-234	0.178±0.015	0.61	0.36
U-236	0.071±0.006	0.217	0.127
Np-237	0.199±0.015	0.67	0.39
U-238	0.034±0.003	0.102	0.059
R <sub>Cd</sub> (U-235)	1.40±0.10	1.02	1.55

As it is seen from this table the values of all the threshold  $SI \frac{\sigma_f^-}{\sigma_f^i}$  ( $i$ -  $^{232}\text{Th}$ ,  $^{234}\text{U}$ ,  $^{236}\text{U}$ ,  $^{237}\text{Np}$ ,  $^{238}\text{U}$ ), as well as  $R_{\text{Cd}}(^{235}\text{U})$  at the measuring point 2 on the side surface of the lead target coincide (within the limits of an experimental error) for proton energies of 1.5 and 5 GeV. Comparison of the experimental and calculated data for  $SI \frac{\sigma_f^-}{\sigma_f^i}$  and  $R_{\text{Cd}}(^{235}\text{U})$  has shown their significant difference. The calculated values (calculation 1) exceed experimental by a factor of 2.8–3.5 for  $SI$ , and by a factor of 1.5 for  $R_{\text{Cd}}(^{235}\text{U})$ . The given fact indicates that

the calculated spectrum is harder in comparison with the experimental one. The account of reflection effect of neutrons from the walls of the experimental hall allows one to reduce this difference down to 1.7–2.2 for  $SI$ , and allows one to receive good agreement for  $R_{Cd}(^{235}U)$ .

Experimental and calculated values for ratios of fission rate for the  $i$ -th nuclide to the fission rate of  $^{232}Th$   $Q_f^i/Q_f^{232Th}$  ( $i$ -  $^{234}U$ ,  $^{235}U$ ,  $^{236}U$ ,  $^{237}Np$ ,  $^{238}U$ , ( $^{235}U$ ) $_{Cd}$ ) at the measuring point 2 for both investigated proton energies are shown in table 2. As it is seen from this table good and satisfactory agreement between the experimental and calculated values for this parameter is observed (within the limits of 8–30%), with the exception of  $^{235}U$  and  $^{235}U$  in Cd-cover. The deviations of values for these cases are somewhat larger and come up to 60 and 40% for  $^{235}U$  and ~45 % for  $^{235}U$  in Cd-cover for calculations 1 and 2, respectively.

Table 2. Values of ratio of fission rates  $Q_f^i/Q_f^{232Th}$  at the measuring point 2 on the side surface of the Pb-target

$i$ - nuclide	$Q_f^i/Q_f^{232Th}$		
	Experiment	Calc.-1	Calc.-2
<b>1.5 GeV</b>			
U-234	17.6±1.4	22.2	21.3
U-235	95±8	37	58
U-236	7.3±0.6	7.8	7.6
Np-237	18.3±1.4	24.6	23.5
U-238	3.3±0.3	3.6	3.5
(U-235) $_{Cd}$	71±5	37	39
<b>5 GeV</b>			
U-234	16.9±1.4	20.7	20.8
U-235	94±8	34	58
U-236	6.8±0.6	7.4	7.4
Np-237	19.0±1.5	22.9	23.0
U-238	3.2±0.3	3.5	3.5
(U-235) $_{Cd}$	68±5	35	38

Values of fission rates for  $^{232}Th$  and  $^{237}Np$ , measured by track detectors inside the experimental channels of the massive lead target ( $3.3 \times 3.3 \times 3 \text{ m}^3$ ), irradiated with protons at kinetic energy 2.75 GeV are given in the report of the group from CERN which was carried out the "TARC" experiment. The values of fission rates for  $^{232}Th$  and  $^{237}Np$  at the measuring point located at a distance 12–14 cm from the entrance point of the proton beam in the target and at a distance of 15 cm from the longitudinal axes of the target, are equal to  $3.0 \times 10^{-27}$  and  $1.3 \times 10^{-25}$  fissions/(proton×nucleus), respectively. It follows from these data that the fission rate ratio for these nuclides is equal 43.3. This figure exceeds the value obtained in the present work (19.0) by a factor of 2.3. Our value agrees satisfactorily (within the limits of 30–35%) with the calculated data.

## 5. Conclusions

- Spatial and energy distribution of neutrons is experimentally determined on the side surface of the massive lead target irradiated with protons at energies 1.5 and 5 GeV.

- Distributions of fission rates for  $^{232}\text{Th}$  and  $^{209}\text{Bi}$  over the surface of the target are obtained as a result of the carried experimental research.
- Values of the spectral indices  $\bar{\sigma}_f^i / \bar{\sigma}_f^{235\text{U}}$  ( $i = ^{232}\text{Th}, ^{234}\text{U}, ^{236}\text{U}, ^{237}\text{Np}, ^{238}\text{U}$ ), as well as the cadmium ratio for  $^{235}\text{U}$  are measured on the surface of the target.
- The calculation of these parameters by means of Monte-Carlo simulation using the computer code *DCM/CEM* with the account and without the account of neutrons reflected from the walls of the experimental hall is carried out.
- The distributions of fission rate for  $^{232}\text{Th}$ , as well as the behaviour of fast neutrons (with  $En \geq 1.4$  MeV), in the direction of the Z axis, which is parallel to the proton beam, differ considerably for proton energies of 1.5 and 5 GeV, as well as the calculated and measured distributions at the same energy.
- Distributions of  $^{232}\text{Th}$  fission rate in the transverse direction agree (within the limits of an experimental error) for proton energies of 1.5 and 5 GeV, and also for calculated and measured data for the same energy.
- Distributions of fission rates for  $^{232}\text{Th}$  and  $^{209}\text{Bi}$ , as well as the behaviour of fast (with  $En \geq 1.4$  MeV) and ultrafast neutrons (with  $En \geq 30$  MeV), differ considerably in the investigated system for proton energies 1.5 and 5 GeV both in longitudinal and transverse directions to the proton beam.
- The values of  $SI \bar{\sigma}_f^i / \bar{\sigma}_f^{235\text{U}}$  ( $i = ^{232}\text{Th}, ^{234}\text{U}, ^{236}\text{U}, ^{237}\text{Np}, ^{238}\text{U}$ ) and cadmium ratio for  $^{235}\text{U}$  are independent (within the limits of an experimental error) on energy of protons, irradiating on the target.
- The calculated values of  $SI \bar{\sigma}_f^i / \bar{\sigma}_f^{235\text{U}}$  exceed significantly (by a factor of 1.73–3.5) the experimental ones, which indicates that the calculated neutron spectrum is harder.
- Good and satisfactory agreement (in limits 8–38 %) of the calculated and experimental values of the ratio of fission rates  $Q_f^i / Q_f^{232\text{Th}}$  ( $i = ^{234}\text{U}, ^{236}\text{U}, ^{237}\text{Np}, ^{238}\text{U}$ ) is observed.

Authors thank the crew of the Synchrophasotron of Laboratory for High Energies (JINR) for their excellent work during the irradiations and Professor A.I. Malachov and Professor A.D. Kovalenko for their continuous support of this work.

## References

1. R. Brandt, M.I. Krivopustov, D. Chultem, A.N. Sosnin et al. Investigation of temperature and neutron fields in a lead medium under interaction of relativistic protons // –Dubna, 1999. –17 p. –(Preprint / Joint Institute of Nuclear Research; P1-99-117) (in Russian).
2. A.N. Sosnin, M.I. Krivopustov, M. Zamani et al. Monte Carlo Modeling of Neutron Spectra in the U/Pb-Assembly Irradiated with Protons. // *Izvestiya RAS. Physics Series.* – 2002. –Vol. 66. –pp. 1494 – 1496.
3. V.A.Voronko, V.M.D'yachenko, V.A. Kostin,..K.D. Tolstov.. et al. Generation of neutrons in an extended lead target // *Atomnaya Energiya.* –1990. –Vol. 68, Issue. 6. –pp.449–452 (in Russian).
4. A. Abanades, J. Aleixandre, S. Andriamonje et al. Results from TARC experiment spallation neutron phenomenology in lead and neutron-driven nuclear transmutation by adiabatic resonance crossing. The TARC collaboration // –Geneva, 2001. –174 p. – (Report / European Organization for Nuclear Research; CERN/SL/2001–033(BET)).
5. I.V. Zhuk, N.M. Grusha, E.M. Lomonosova et al. Measurement of ratios of average cross-sections threshold reactions  $^{234}\text{U}(n,f)$ ,  $^{236}\text{U}(n,f)$ ,  $^{237}\text{Np}(n,f)$ , to the average cross-

- section of  $^{235}\text{U}(n,f)$  reaction at the critical assembly BTS-4// *Vestsi AS BSSR, Ser. Phys.-energ. Navuk.* – 1987. –N: 2. –pp. 18–22 (*in Russian*).
6. P.W. Lisowski, J.L. Ullmann, S.J. Balestrini et al. Neutron induced fission cross section ratios for  $^{232}\text{Th}$ ,  $^{235,238}\text{U}$ ,  $^{237}\text{Np}$  and  $^{239}\text{Pu}$  from 1 to 400 MeV // Proc. of the Intern. Conf. on Nuclear Data for Science and Technology, 30 May–3 June 1988, JAERI, Mito, Japan; ed. by S. Igarasi. –Mito, 1988. –pp. 97–103.
  7. P.W. Lisowski, A. Gavron, W.E. Parker et al. Fission cross section ratios for  $^{233, 234, 236}\text{U}$  relative to  $^{235}\text{U}$  from 0.5 to 400 MeV // Proc. of the Intern. Conf. on Nuclear Data for Science and Technology, 13–17 May 1991, Juelich, Germany; ed. by S.M. Qaim, – Berlin, Heidelberg: Springer-Verlag, 1992. –pp.732–737.



**VIII.**  
**POLARIZATION**  
**PHENOMENA**  
**AND SPIN**  
**PHYSICS**



# INVESTIGATION OF THE ANGULAR DEPENDENCE OF THE TENSOR ANALYZING POWER OF 9 GEV/C DEUTERON BREAKUP

L.S. Azhgirey<sup>1†</sup>, S.V. Afanasiev<sup>1</sup>, V.V. Arkhipov<sup>1</sup>, V.K. Bondarev<sup>1,2</sup>, Yu.T. Borzounov<sup>1</sup>, G.Filipov<sup>1,3</sup>, L.B. Golovanov<sup>1</sup>, A.Yu. Isupov<sup>1</sup>, A.A. Kartamyshev<sup>4</sup>, V.A. Kashirin<sup>1</sup>, A.N. Khrenov<sup>1</sup>, V.I. Kolesnikov<sup>1</sup>, V.A. Kuznezov<sup>1</sup>, V.P. Ladygin<sup>1</sup>, A.G. Litvinenko<sup>1</sup>, S.G. Reznikov<sup>1</sup>, P.A. Rukoyatkin<sup>1</sup>, A.Yu. Semenov<sup>1</sup>, I.A. Semenova<sup>1</sup>, G.D. Stoletov<sup>1</sup>, A.P. Tzvinev<sup>1</sup>, N.P. Yudin<sup>5</sup>, V.N. Zhmyrov<sup>1</sup> and L.S. Zolin<sup>1</sup>

(1) *Joint Institute for Nuclear Researches, 141980 Dubna, Russia*

(2) *St.-Petersburg State University, 198350 St.-Petersburg, Russia*

(3) *Institute of Nuclear Research and Nuclear Energy, 1784 Sofia, Bulgaria*

(4) *Russian Scientific Center "Kurchatov Institute", 123182 Moscow, Russia*

(5) *Moscow State University, 117234 Moscow, Russia*

† *E-mail: azhgirey@jinr.ru*

## Abstract

An angular dependence of the tensor analyzing power of the breakup of polarized deuterons at 9 GeV/c has been investigated. The measurements have been made on hydrogen and carbon targets at angles in the range from 85 to 160 mr. The data obtained are analyzed within the framework of the light-front dynamics using the deuteron wave functions for Paris and Bonn CD potentials, and the relativistic deuteron wave function by Karmanov et al. The experimental data are in rough agreement with calculations with the use of Karmanov's deuteron wave function.

## 1. Introduction

Investigations of polarization properties of the deuteron fragmentation reaction ( $d, p$ ) have amassed a convincing body of evidence that the description of the deuteron structure by means of wave functions derived from non-relativistic functions through the kinematical transformation of variables is liable to break down at short distances between nucleons. The main discrepancies between the expected and observed behaviour of data manifest themselves in the following facts.

(i) The expression for the tensor analyzing power  $T_{20}$  of deuteron breakup,  $A(d, p)X$ , in the impulse approximation (IA) has the form  $T_{20} \sim w(k)[\sqrt{8}u(k) - w(k)]$ , where  $u(k)$  and  $w(k)$  are the deuteron momentum space wave functions for  $S$  and  $D$  states, respectively, and  $k$  is the internal momentum of the nucleons in the deuteron (defined in the light-front system). With standard deuteron wave functions, the  $T_{20}$  dependence on  $k$  can be expected to change the sign at  $k \sim 0.5$  GeV/c, but this expectation lacks support from experiment [1].

(ii) The recent measurements of the tensor analyzing power  $A_{yy}$  of the breakup of relativistic deuterons on nuclei at non-zero angles of emitted protons [2, 3] show that the measured  $A_{yy}$ -values at fixed value of the longitudinal proton momentum have the dependence on the transverse proton momentum that differs from that calculated with standard deuteron wave functions.

(iii) The above-mentioned data show that the values of  $A_{yy}$  being plotted at fixed values of  $k$  tend to decrease as the variable ( $\mathbf{n} \cdot \mathbf{k}$ ) grows (vector  $\mathbf{n}$  is the unit normal to the surface of the light front).

(iv) The pion-free deuteron breakup process  $dp \rightarrow ppn$  in the kinematical region close to that of backward elastic  $dp$  scattering at a given value of  $k$  depends on the incident momentum of deuteron [4].

The foregoing forces one to suggest that an additional variable is required to depict the deuteron structure function at short distances, where relativistic effects are significant.

One approach that gives a relativistic description of the deuteron is light-front dynamics, one of several forms of Hamiltonian dynamics, first discussed by Dirac [5]. Each form of dynamics is associated with a hypersurface on which the commutation relations for the generators of the Poincaré group are defined. There are many desirable features of the light-front dynamics [6].

(i) High-energy experiments are naturally described using light-front coordinates: the fraction of the longitudinal momentum of the bound state taken away by the constituent particle in the infinite momentum frame is simply the ratio of the plus momentum of the constituent to the total plus momentum of the bound state.

(ii) There is a clean separation between center-of-momentum (internal) and relative (external) momentum variables in the light-front dynamics.

(iii) The vacuum for a theory with massive particles can be very simple on the light front: the vacuum with  $p^+ = 0$  is empty, and diagrams that couple to this vacuum are zero.

(iv) The generators of boosts in one, two, and plus directions are kinematic, meaning they are independent of the interaction. Thus, even when the Hamiltonian is truncated, the wave functions will transform correctly under boosts.

These attractive features have led to the possibility that light-front dynamics is the best approach for calculating the spectrum and wave functions of relativistic composite system from an underlying field theory, such as quantum chromodynamics.

In previous papers [7] the global features of proton spectra in the region of transverse momenta of  $0.5 - 1$  GeV/c, produced in the reaction  $(d, p)$  by unpolarized deuterons with an initial momentum of 9 GeV/c, were satisfactorily described on the basis of the pole diagrams within the framework of the light-front dynamics. In those calculations the light-front deuteron wave function was connected with the non-relativistic deuteron wave function in a simple way, by the kinematical transition from the equal-time variables to the light-front variables. However, attempts to describe the tensor analyzing power  $A_{yy}$  of the reaction  $^{12}\text{C}(d, p)X$  at an incident deuteron momentum of 9 GeV/c and a proton emission angle of 85 mr within the same approach have not met with the success [3]. The simple kinematical transition from a non-relativistic deuteron wave function to the light-front one [8] presumably does not take into account essential features of the spin structure of a relativistic deuteron.

The relativistic deuteron wave function in the light front dynamics was found in ref. [9]. It is determined by six invariant functions  $f_1, \dots, f_6$  instead of two ones in the non-relativistic case, each of them depending on two scalar variables  $k$  and  $z = \cos(\mathbf{k}\mathbf{n})$ . The quantities  $\mathbf{k}$  (the momentum of nucleons in the deuteron in their rest frame) and  $\mathbf{n}$  (the unit normal to the light front surface) are defined by

$$x = \frac{E_p + p_{pl}}{E_d + p_d}, \quad k = \sqrt{\frac{m_p^2 + \mathbf{p}_T^2}{4x(1-x)} - m_p^2}, \quad (\mathbf{n} \cdot \mathbf{k}) = \left(\frac{1}{2} - x\right) \cdot \sqrt{\frac{m_p^2 + \mathbf{p}_T^2}{x(1-x)}}, \quad (1)$$

where  $E_d$  and  $p_d$  are the energy and the momentum of the incoming deuteron, respectively,  $p_{pl}$  is the longitudinal component of  $\mathbf{p}_1$ , and  $m_p$  is the mass of the nucleon. It will be assumed further that  $\mathbf{n}$  is directed opposite to the beam direction, i.e.  $\mathbf{n} = (0, 0, -1)$ .

The expressions for the tensor analyzing power of the  $(d, p)$  reaction using the above function are given in ref. [10].

Within the framework of this approach the following results on the description of the tensor analyzing power of the reaction  $A(d, p)X$  have been obtained previously.

(i) It was shown [11] that calculations with Karmanov's deuteron wave function are in reasonably good agreement with the experimental data on the  $T_{20}$  parameter of deuteron breakup on  $H$  and  $C$  targets with the emission of protons at  $0^\circ$  in the  $k$  region from 0.4 to 0.8 GeV/c.

(ii) A qualitative description of the momentum behaviour of the  $A_{yy}$  parameter of the  ${}^9\text{Be}(d, p)X$  reaction at a deuteron momentum of 4.5 GeV/c and a detected proton angle of 80 mr [2] was obtained [10].

(iii) Rather good description of the  $A_{yy}$  data for the  ${}^{12}\text{C}(d, p)X$  reaction at 9 GeV/c and 85 mr [3] was achieved [10].

(iv) The experimental data on the tensor analyzing power  $A_{yy}$  of the reaction  ${}^9\text{Be}(d, p)X$  at an initial deuteron momentum of 5 GeV/c and a proton emission angle of 178 mr are rather well reproduced with Karmanov's relativistic deuteron wave function as opposed to the calculations with the standard deuteron wave functions [12].

To get a more comprehensive picture of the angular behaviour of the tensor analyzing power of the deuteron breakup reaction, the  $A_{yy}$  parameter in the interactions of polarized deuterons with hydrogen and carbon at 9 GeV/c has been measured. The measurements have been made on hydrogen and carbon targets at angles in the range from 85 to 160 mr.

## 2. Experiment

The measurements have been made at a polarized deuteron beam of the JINR Synchrophasotron using the SPHERE setup described elsewhere [3]. The polarized deuterons were produced by the ion source POLARIS [13].

The tensor polarization of the beam was determined from the asymmetry of protons with a momentum of  $p_p \sim \frac{2}{3}p_d$  emitted at  $0^\circ$  in the  $A(d, p)X$  reaction [14], and it was  $p_{zz}^+ = 0.798 \pm 0.002(stat) \pm 0.040(syst)$  and  $p_{zz}^- = -0.803 \pm 0.002(stat) \pm 0.040(syst)$  for positive and negative polarization directions, respectively. The vector polarization of the beam was monitored during the experiment by measuring the asymmetry of quasi-elastic  $pp$ -scattering on a thin  $\text{CH}_2$  target placed in the beam [15], and its values in different spin states were  $p_z^+ = 0.231 \pm 0.014(stat) \pm 0.012(syst)$  and  $p_z^- = 0.242 \pm 0.014(stat) \pm 0.012(syst)$ .

A slowly extracted beam of tensor polarized 9-GeV/c deuterons with an intensity of  $\sim 5 \cdot 10^8 \div 10^9$  particles per beam spill with a duration of 0.5 s fell on a liquid hydrogen target of 30 cm length or on carbon targets with varied length. The beam intensity was monitored by an ionization chamber. The beam positions and profiles at certain points of the beam line were monitored by the control system of the accelerator during each spill. The beam size at the target point was  $\sigma_x \sim 0.4$  cm and  $\sigma_y \sim 0.9$  cm in the horizontal and vertical directions, respectively.

The data were obtained at secondary particle emission angles of 85, 130 and 160 mr (two measurements were made at 115 and 145 mr), and secondary momenta between 4.5

and 9 GeV/c. Along with the secondary protons, the apparatus detected the deuterons from inelastic scattering. The particles detected at given momentum were identified off-line on the basis of two independent time-of-flight (TOF) measurements with a base line of  $\sim 34$  m. The TOF resolution was better than 0.2 ns ( $1\sigma$ ). Useful events were selected as the ones with two measured TOF values correlated. This allowed one to rule out the residual background completely. The values of the tensor analyzing power  $A_{yy}$  obtained in the experiment are shown in Figs. 2, 3. The reported error bars are statistical only; possible systematic errors are estimated to be  $\sim 5\%$ .

The acceptance of the setup was determined by means of Monte Carlo simulation; the momentum and polar angle acceptances were  $\Delta p/p \sim \pm 2\%$  and  $\pm 8$  mr, respectively.

### 3. Formalism

The mechanism of the deuteron fragmentation ( $d, p$ ) can be represented by the Feynman diagrams shown in Fig. 1. Here  $d$  is the incoming deuteron,  $p$  is the target proton,  $p_1$  is the detected proton,  $b$  is the virtual (off-shell) nucleon, and  $p_2, p_3$  are nucleons. In addition to nucleons, one or more pions may be produced at low vertices. Diagram (a) corresponds to the case where the detected proton results from deuteron stripping, and at the low vertex elastic  $np$  scattering takes place. In diagrams (b) and (c) the low vertices correspond to the charge exchange  $np$  and elastic  $pp$  scatterings, respectively.

The analyzing power  $T_{\kappa q}$  of the ( $d, p$ ) reaction is given by the expression

$$T_{\kappa q} = \frac{\int d\tau Sp\{\mathcal{M} \cdot t_{\kappa q} \cdot \mathcal{M}^\dagger\}}{\int d\tau Sp\{\mathcal{M} \cdot \mathcal{M}^\dagger\}}, \quad (2)$$

where  $d\tau$  is the phase volume element,  $\mathcal{M}$  is the reaction amplitude, and the operator  $t_{2q}$  is defined by

$$\langle m | t_{\kappa q} | m' \rangle = (-1)^{1-m} \langle 1 m 1 - m' | \kappa q \rangle,$$

with the Clebsh-Gordan coefficients  $\langle 1 m 1 - m' | \kappa q \rangle$ .

The amplitude for the reaction  ${}^1H(d, p)X$  in the light-front dynamics is

$$\mathcal{M}_a = \frac{\mathcal{M}(d \rightarrow p_1 b)}{(1-x)(M_d^2 - M^2(k))} \mathcal{M}(bp \rightarrow p_2 p_3), \quad (3)$$

where  $\mathcal{M}(d \rightarrow p_1 b)$  is the amplitude of the deuteron breakup on a proton-spectator  $p_1$  and an off-shell particle  $b$ , and  $\mathcal{M}(bp \rightarrow p_2 p_3)$  is the amplitude of the reaction  $bp \rightarrow p_2 p_3$  (in the case of diagram (a), and with evident replacements of indices for diagrams (b) and (c)).

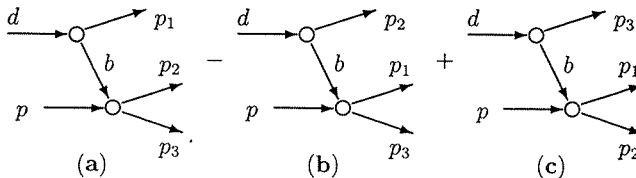


Fig. 1. Feynman diagrams describing fragmentation of deuterons on protons.

The ratio

$$\psi(x, p_{1T}) = \frac{\mathcal{M}(d \rightarrow p_1 b)}{M_d^2 - M^2(k)} \quad (4)$$

is the wave function in the channel  $(b, N)$  given in [9]; here  $p_{1T}$  is the component of the momentum  $p_1$  transverse to the  $z$  axis. The light-front variables  $p_T \equiv p_{1T}$  and  $x$  (the fraction of the deuteron longitudinal momentum taken away by the proton in the infinite momentum frame) are given above. The quantity  $M^2(k)$  is given by

$$M^2(k) = \frac{m^2 + p_{1T}^2}{x} + \frac{b^2 + p_{1T}^2}{1-x}, \quad (5)$$

where  $b^2$  is the four-momentum squared of the off-shell particle  $b$ .

The final expressions for the tensor analyzing power of the  $(d, p)$  reaction are given in ref. [10].

#### 4. Results and discussion

It should be emphasized that the problem has no adjusted parameters. The invariant differential cross sections of processes taking place in the low vertices of the pole diagrams of Fig. 1, on the one hand, and the values of the invariant functions  $f_1, \dots, f_6$  taken from ref. [9], on the other, were taken as input data. The contributions of the elastic and inelastic processes in the low vertex of the pole diagram were taken into account according to the parameterizations given in ref. [18]. To account for the off-shell nature of particle  $b$ , the analytic continuations of the cross section parameterizations to the values of invariant variables  $s' = (b+p)^2$ ,  $t' = (b-p_1)^2$  defined in the low vertex of the pole diagram at  $b^2 \neq m^2$  were used in the calculations. To obtain the values of functions  $f_i(k, z)$  required for calculations, the spline-interpolation procedure between the table values given in ref. [9] was used.

The experimental data on the tensor analyzing power  $A_{yy}$  of the reactions  $^1H(d, p)X$  and  $^{12}C(d, p)X$  at an initial deuteron momentum of 9 GeV/c and proton emission angles of 85, 130 and 160 mr are compared with the calculation results in Fig. 2. The data obtained on hydrogen and carbon targets are shown with empty and full circles, respectively. Above all it should be pointed out that data for both targets agree. By this is meant that nuclear targets are also appropriate to obtain information on the deuteron structure, as indicated before [7]. The previous data obtained at 9 GeV/c on carbon at a proton emission angle of 85 mr [3] are shown with full triangles.

It is seen that the experimental data at an angle of 85 mr are rather well reproduced with Karmanov's relativistic deuteron wave function as opposed to the calculations with the standard deuteron wave functions [16, 17]. The data at angles of 130 and 160 mr are only in rough agreement with calculations using Karmanov's deuteron wave function, and, as before, they are in contradiction with calculations using standard deuteron wave functions.

The dependences of the analyzing power  $A_{yy}$  on the transverse momentum of the protons  $p_T$  at fixed values of total proton momenta  $p$  close to 4.5, 5.0, 5.5, 6.0, 6.5, and 7.0 GeV/c are shown in Fig. 3. These values of the total momentum of protons correspond to their longitudinal momentum fractions  $x = 0.503, 0.558, 0.614, 0.670, 0.724$ , and 0.791. It may be noted that the dependence of  $A_{yy}$  on  $p_T$  in the range of  $p_T$  between 0.4 and 0.9 GeV/c investigated in the present experiment is considerably more flat than

in the range of  $p_T$  from 0 to 0.6 GeV/c as it was found in ref. [2]. It is seen as well that  $p_T$ -behaviour of  $A_{yy}$  counts in favour of Karmanov's relativistic deuteron wave function and definitely contradicts the predictions based on Paris and Bonn CD deuteron wave functions particularly at  $p = 4.5, 5.0, 6.5,$  and  $7.0$  GeV/c.

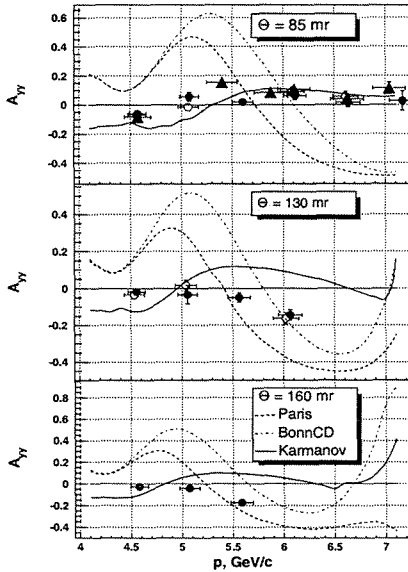


Fig.2. Parameter  $A_{yy}$  of the reactions  ${}^1H(d,p)X$  (empty circles)  ${}^{12}C(d,p)X$  (full circles) at an initial deuteron momentum of 9 GeV/c and proton emission angles of 85, 130 and 160 mr as a function of the detected proton momentum. The data obtained in ref. [3] are shown with full triangles. The calculations were made with the deuteron wave functions for the Paris [16] (dashed curves) and Bonn CD [17] (dash-dotted curves) potentials. The solid curves were calculated with Karmanov's relativistic deuteron wave function [9].

## 5. Conclusion

The results of this work can be summarized as follows.

(i) The tensor analyzing power  $A_{yy}$  of the reactions  ${}^1H(d,p)X$  and  ${}^{12}C(d,p)X$  has been measured at an initial deuteron momentum of 9 GeV/c and proton emission angles of 85, 115, 130, 145 and 160 mr in the laboratory. The range of measurements corresponds to transverse proton momenta between 0.4 and 0.9 GeV/c.

(ii) The  $A_{yy}$  data from the present experiment at 85 mr are in good agreement with the data obtained earlier [3].

(iii) The  $A_{yy}$  data demonstrate an approximate independence on the A-value of the target, as it was pointed previously [12].

(iv) The proton momentum dependences of  $A_{yy}$  at the fixed values of proton emission angles and the transverse proton momentum dependences of  $A_{yy}$  at the fixed values of longitudinal proton momentum fractions are in a better agreement with calculations using Karmanov's relativistic deuteron wave function instead of standard non-relativistic deuteron wave functions. While a quantitative description is not always achieved, the results obtained favours the description of the relativistic deuteron structure with a function depending on more than one variable.

(v) Additional measurements of  $A_{yy}$  and other polarization observables at different initial deuteron momenta and various  $p_T$  and  $x$  are strongly desirable to provide the necessary

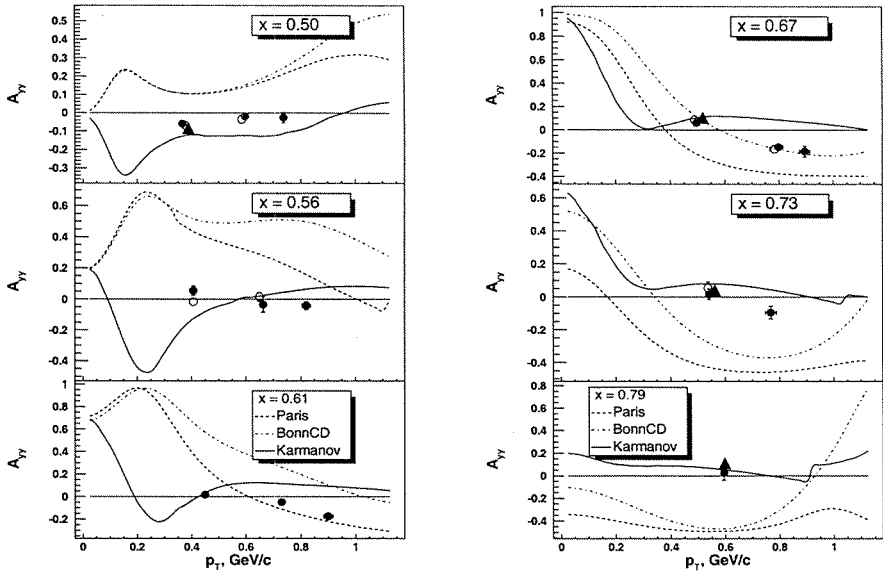


Fig. 3. Parameter  $A_{yy}$  of the reactions  $^1H(d,p)X$  (empty circles)  $^{12}C(d,p)X$  (full circles) at an initial deuteron momentum of 9 GeV/c and proton emission momenta of 4.5, 5.0, 5.5 (left panel) and 6.0, 6.5, 7.0 GeV/c (right panel) as a function of the transverse proton momentum  $p_T$ . The data obtained in ref. [3] are shown with full triangles. The calculations were made with the deuteron wave functions for the Paris [16] (dashed curves) and Bonn CD [17] (dash-dotted curves) potentials, and with the relativistic deuteron wave function [9] (solid curves)

experimental base to develop relativistic models describing the short-range structure of deuteron.

*Acknowledgment.* The authors are grateful to the LHE accelerator staff and the POLARIS team for providing good conditions for the experiment. They thank L.V. Budkin, V.P. Ershov, V.V. Fimushkin, A.S. Nikiforov, Yu.K. Pilipenko, V.G. Perevozchikov, E.V. Ryzhov, A.I. Shirokov, and O.A. Titov for their assistance during the experiment. They are indebted to Profs. V.A. Karmanov, V.I. Komarov, and J. Carbonell for helpful discussions. This work was supported by the Russian Foundation for Basic Research under grant No. 03-02-16224.

## References

- [1] See, for example, V.G. Ableev et al., Pis'ma Zh. Eksp. Teor. Fiz. **47**, 558 (1988); JINR Rapid Comm. **4[43]-90**, 5 (1990); V. Punjabi et al., Phys. Rev. **C39**, 608 (1989); T. Aono et al., Phys. Rev. Lett. **74**, 4997 (1995); L.S. Azhgirey et al., Phys. Lett. **B387**, 37 (1996).
- [2] V.P. Ladygin et al., Few-Body Systems **32**, 127 (2002); L.S. Azhgirey et al., Yad. Fiz. **66**, 719 (2003).
- [3] S.V. Afanasiev et al., Phys. Lett. **B434**, 21 (1998).
- [4] L.S. Azhgirey et al., Phys. Lett. **B391**, 22 (1997); Yad. Fiz. **61**, 494 (1998).
- [5] P.A.M. Dirac, Rev. Mod. Phys., **21**, 392 (1949).
- [6] See, for example, M.G. Fuda, Ann. Phys. (N.Y.) **197**, 265 (1990).
- [7] L.S. Azhgirey et al., Nucl. Phys. **A528**, 621 (1991); Yad. Fiz., **46** 1134 (1987); Yad. Fiz. **53**, 1591 (1991).
- [8] See, for example, L.S. Azhgirey and N.P. Yudin, Yad. Fiz. **57**, 160 (1994); C.E. Carlson, J.R. Hiller and R.J. Holt, Ann. Rev. Nucl. Part. Sci. **47**, 395 (1997).
- [9] J. Carbonell and V.A. Karmanov, Nucl. Phys. **A581**, 625 (1994).
- [10] L.S. Azhgirey and N.P. Yudin, to be published in Yad. Fiz.; see also Preprint arXiv:nucl-th/0311052 (2003).
- [11] L.S. Azhgirey and N.P. Yudin, Preprint arXiv:nucl-th/0212033 (2002).
- [12] L.S. Azhgirey et al., Phys. Lett. **B595**, 151 (2004).
- [13] N.G. Anishchenko et al., in *Proceedings of 5th International Symposium on High Energy Spin Physics, Brookhaven, 1982*, AIP Conf. Proc. **95**, 445 (1983).
- [14] L.S. Zolin et al., JINR Rapid Comm. **2[88]-98**, 27 (1998).
- [15] L.S. Azhgirey et al., PTE **1** 51 (1997) [Instr. and Exp. Tech. **40**, 43 (1997)]; L.S. Azhgirey et al., Nucl.Inst.and Meth. in Phys.Res. **A497**, 340 (2003).
- [16] M. Lacombe et al., Phys. Lett. **B101**, 139 (1981).
- [17] R. Machleidt, Phys. Rev. **C63**, 024001 (2001).
- [18] L.S. Azhgirey, S.V. Razin and N.P. Yudin, Yad. Fiz. **46** 1657 (1987).

MEASUREMENTS OF ENERGY BEHAVIOURS OF SPIN-DEPENDENT  
 $np$  - OBSERVABLES OVER 1.2 - 3.7 GEV REGION

*Dubna "Delta-Sigma" Experiment*

V.I. Sharov<sup>1,a</sup>, N.G. Anischenko<sup>1</sup>, V.G. Antonenko<sup>2</sup>, S.A. Averichev<sup>1</sup>, L.S. Azhgirey<sup>3</sup>,  
V.D. Bartenev<sup>1</sup>, N.A. Bazhanov<sup>3</sup>, A.A. Belyaev<sup>5</sup>, N.A. Blinov<sup>1</sup>, N.S. Borisov<sup>3</sup>,  
S.B. Borzakov<sup>6</sup>, Yu.T. Borzunov<sup>1</sup>, Yu.P. Bushuev<sup>1</sup>, L.P. Chernenko<sup>6</sup>, E.V. Chernykh<sup>1</sup>,  
V.F. Chumakov<sup>1</sup>, S.A. Dolgii<sup>1</sup>, A.N. Fedorov<sup>3</sup>, V.V. Fimushkin<sup>1</sup>, M. Finger<sup>3,7</sup>,  
M. Finger, Jr.<sup>3</sup>, L.B. Golovanov<sup>1</sup>, G.M. Gurevich<sup>8</sup>, D.K. Guriev<sup>11</sup>, A. Janata<sup>3</sup>,  
A.D. Kirillov<sup>1</sup>, V.G. Kolomiets<sup>3</sup>, E.V. Komogorov<sup>1</sup>, A.D. Kovalenko<sup>1</sup>, A.I. Kovalev<sup>4</sup>,  
V.A. Krasnov<sup>1</sup>, P. Krstonoshich<sup>3</sup>, E.S. Kuzmin<sup>3</sup>, N.A. Kuzmin<sup>11</sup>, V.P. Ladygin<sup>1</sup>,  
A.B. Lazarev<sup>3</sup>, F. Lehar<sup>9</sup>, A. de Lesquen<sup>9</sup>, M.Yu. Liburg<sup>1</sup>, A.N. Livanov<sup>1</sup>,  
A.A. Lukhanin<sup>5</sup>, P.K. Maniakov<sup>1</sup>, V.N. Matafonov<sup>3,†</sup>, E.A. Matyushevsky<sup>1</sup>,  
V.D. Moroz<sup>1,†</sup>, A.A. Morozov<sup>1</sup>, A.B. Neganov<sup>3</sup>, G.P. Nikolaevsky<sup>1</sup>, A.A. Nomofilov<sup>1</sup>,  
Tz. Panteleev<sup>6,10</sup>, Yu.K. Pilipenko<sup>1</sup>, I.L. Pisarev<sup>3</sup>, Yu.A. Plis<sup>3</sup>, Yu.P. Polunin<sup>2</sup>,  
A.N. Prokofiev<sup>4</sup>, V.Yu. Prytkov<sup>1</sup>, P.A. Rukoyatkin<sup>1</sup>, V.A. Schedrov<sup>4</sup>, O.N. Schevelev<sup>3</sup>,  
S.N. Shilov<sup>3</sup>, R.A. Shindin<sup>1</sup>, M. Slunečka<sup>3,7</sup>, V. Slunečková<sup>3</sup>, A.Yu. Starikov<sup>1</sup>,  
G.D. Stoletov<sup>3,†</sup>, L.N. Strunov<sup>1</sup>, A.L. Svetov<sup>1</sup>, Yu.A. Usov<sup>3</sup>, T. Vasiliev<sup>1</sup>, V.I. Volkov<sup>1</sup>,  
E.I. Vorobiev<sup>1</sup>, I.P. Yudin<sup>11</sup>, I.V. Zaitsev<sup>1</sup>, A.A. Zhdanov<sup>4</sup>, V.N. Zhmyrov<sup>3</sup>

- 1) Joint Institute for Nuclear Research, Veksler and Baldin Laboratory of High Energies, 141980 Dubna, Russia
- 2) Russian Scientific Center "Kurchatov Institute", 123182 Moscow, Russia
- 3) Joint Institute for Nuclear Research, Dzhelapov Laboratory of Nuclear Problems, 141980 Dubna, Russia
- 4) St.Petersburg Nuclear Physics Institute, High Energy Physics Division, 188350 Gatchina, Russia
- 5) Kharkov Institute of Physics and Technology, 310108 Kharkov, Ukraine
- 6) Joint Institute for Nuclear Research, Frank Laboratory of Neutron Physics, 141980 Dubna, Russia
- 7) Charles University, Faculty of Mathematics and Physics, V Holešovičkách 2, 180 00 Praha 8, Czech Republic
- 8) Institute for Nuclear Research, Russian Academy of Sciences, 117312 Moscow, Russia
- 9) DAPNIA, CEA/Saclay, 91191 Gif-sur-Yvette Cedex, France
- 10) Institute for Nuclear Research and Nuclear Energy, Bulgarian Academy of Sciences, Tsarigradsko shaussee boulevard 72, 1784 Sofia, Bulgaria
- 11) Joint Institute for Nuclear Research, Laboratory of Particle Physics, 141980 Dubna, Russia

<sup>a</sup> e-mail: sharov@sunhe.jinr.ru

<sup>†</sup> Deceased

## Abstract

New accurate data on the neutron-proton spin-dependent total cross section difference  $\Delta\sigma_L(np)$  at the neutron beam kinetic energies 1.4, 1.7, 1.9 and 2.0 GeV are presented. A number of physical and methodical results on investigation of an elastic  $np \rightarrow pn$  charge exchange process over a few GeV region are also presented. Measurements were carried out at the Synchrophasotron and Nuclotron of the Veksler and Baldin Laboratory of High Energies of the Joint Institute for Nuclear Research.

**Keywords:** relativistic polarized neutron beam, polarized proton target, total cross section difference, spin correlation parameters, charge exchange process.

## 1. Introduction

The investigations were performed under the program of the first priority JINR project "Delta-Sigma" Experiment. (For more detailed information see [http://www.jinr.ru/PAC\\_2003\\_nov/PAC-PP/](http://www.jinr.ru/PAC_2003_nov/PAC-PP/)). Full name of the project is "Determination of spin-dependent elastic  $np$  forward scattering amplitudes over 1.2 - 3.7 GeV region: measurements of  $\Delta\sigma_{L,T}(np)$  and  $A_{00kk}(np)$  and  $A_{00nn}(np)$  - total  $np$  cross sections differences and spin-correlation parameters from  $np \rightarrow pn$  scattering".

The aim of the project is to extend investigations of  $NN$  interaction over the new high energy region (1.2 - 3.7 GeV) of free polarized neutron beams, *provided only by the JINR VBLHE accelerators at present*. The main task of these studies is to determine the imaginary and real parts of spin dependent forward scattering  $np$  amplitudes over this energy region for the first time. For this purpose a sufficient data set of  $np$  spin dependent observables has to be obtained for the direct reconstruction of scattering amplitudes at several energies.

### THE "DELTA-SIGMA" EXPERIMENT RESEARCH PROGRAM.

Using longitudinally ( $L$ ) and transverse ( $T$ ) *polarized neutron beams* and the Dubna movable *polarized proton target* (PPT) to measure the energy dependences of following quantities:

a) the  $\Delta\sigma_L(np)$  and  $\Delta\sigma_T(np)$  - the total cross section differences for parallel and antiparallel directions of beam and target polarizations, with energy steps of 100-200 MeV and expected statistical errors of  $\sim 1$  mb;

b) simultaneously and independently of the  $\Delta\sigma_{L,T}(np)$  experiment, measurements of spin correlation parameters  $A_{00kk}(np)$  (together with  $\Delta\sigma_L(np)$ ) and  $A_{00nn}(np)$  (together with  $\Delta\sigma_T(np)$ ) with expected statistical errors 0.02-0.05.

c) using *the high intensity unpolarized neutron beam* and the *liquid hydrogen or deuterium targets*, to measure at the same energies as for item a) the ratio  $R_{dp} = d\sigma/d\Omega(nd)/d\sigma/d\Omega(np)$  for elastic charge exchange process  $np \rightarrow pn$  at  $0^\circ$  with statistical errors of  $\sim 5\%$ .

The observables  $\Delta\sigma_L$  and  $\Delta\sigma_T$  as well as  $\sigma_{\text{tot}}$  are obtained in transmission measurements. They are linearly related to the imaginary parts of forward scattering  $NN$  invariant amplitudes via optical theorems and allow to extract their imaginary parts.

The  $A_{00kk}(np)$  and  $A_{00nn}(np)$  values will be obtained by a registration of yields of protons from elastic charge exchange process  $np \rightarrow pn$  at  $0^\circ$ . They are bilinearly related to real parts of amplitudes which can be extracted from measured data.

The ratio  $R_{dp}$  of differential cross sections on deuterium and hydrogen targets gives one additional relation between  $NN$ -amplitudes and a set of such data allows to avoid one uncertainty of the real parts determination.

The data set of energy dependences of observables  $\Delta\sigma_{L,T}(np)$ ,  $A_{00kk}(np)$ ,  $A_{00nn}(np)$  and  $R_{dp}$  will be obtained for the first time over the energy range of neutron beam of 1.2-3.7 GeV. Besides the direct amplitude reconstruction, this data set will contribute to extend  $NN$  phase shift analysis (PSA) to high energies and to check the predictions of dynamical models.

### THE ACCELERATORS AND TOOLS.

1. The Synchrophasotron and Nuclotron of the JINR VBLHE.
2. Relativistic (1-5 GEV)
  - a) *polarized neutron beams* with  $L$  or  $T$  orientation of polarization, reversion of polarization direction cycle by cycle and average polarization value of  $\sim 0.53$ ;
  - b) *high intensity*  $(2 - 3) \cdot 10^{10}$  d/cycle *unpolarized deuteron beam*.
3. Large *polarized proton target (PPT)* with volume of  $140\text{cm}^3$  and polarization value of 0.7-0.8.
  4. Cryogenic *liquid hydrogen  $H_2$  and deuterium  $D_2$  targets* 30 cm long.
5. Experimental set-up "DELTA-SIGMA" with
  - a) monitor and transmission neutron detectors;
  - b) magnetic spectrometer with multiwire proportional chambers (MPC);
  - c) detectors for target surrounding (DTS);
  - d) time-of-flight (TOF) system and
  - e) data acquisition system.

In the following sections a determination of the  $NN$  spin-dependent observables and some results of investigations under the "Delta-Sigma experiment" program will be done. The last accurate data [1, 2] on the neutron-proton spin-dependent total cross section difference  $\Delta\sigma_L(np)$  at the neutron beam kinetic energies 1.4, 1.7, 1.9 and 2.0 GeV will be presented. A number of physical and methodical results on investigation of the elastic  $np \rightarrow pn$  charge exchange process over the energy region under discussion will be also presented.

## 2. The $\Delta\sigma_{L,T}(np)$ observables

In this contribution, we use  $NN$  formalism and the notations for elastic nucleon-nucleon scattering observables from [3].

The general expression for the total cross section of a polarized nucleon beam transmitted through a polarized proton target, with arbitrary directions of beam and target polarizations is

$$\sigma_{\text{tot}} = \sigma_{0\text{tot}} + \sigma_{1\text{tot}}(\mathbf{P}_B, \mathbf{P}_T) + \sigma_{2\text{tot}}(\mathbf{P}_B, \mathbf{k})(\mathbf{P}_T, \mathbf{k}), \quad (1)$$

where  $\mathbf{P}_B$  and  $\mathbf{P}_T$  are the beam and target polarizations, and  $\mathbf{k}$  is a unit vector in the direction of the beam momentum. The term  $\sigma_{0\text{tot}}$  is the total cross section for unpolarized particles,  $\sigma_{1\text{tot}}$  and  $\sigma_{2\text{tot}}$  are the spin-dependent contributions. They are related to the measurable observables  $\Delta\sigma_T$  and  $\Delta\sigma_L$  by:

$$-\Delta\sigma_T = 2\sigma_{1\text{tot}}, \quad (2)$$

$$-\Delta\sigma_L = 2(\sigma_{1\text{tot}} + \sigma_{2\text{tot}}), \quad (())3$$

Values of  $\sigma_{0\text{tot}}$ ,  $\Delta\sigma_T$  and  $\Delta\sigma_L$  are connected with the imaginary parts of three invariant forward scattering amplitudes  $a + b$ ,  $c$  and  $d$  via three optical theorems

$$\sigma_{0\text{tot}} = (2\pi/K) \text{Im} [a(0) + b(0)], \quad (())4$$

$$-\Delta\sigma_T = (4\pi/K) \text{Im} [c(0) + d(0)], \quad (())5$$

$$-\Delta\sigma_L = (4\pi/K) \text{Im} [c(0) - d(0)], \quad (())6$$

where  $K$  is the c.m. momentum of the incident nucleon. Relations (5) and (6) allow one to extract the imaginary parts of the spin-dependent invariant amplitudes  $c(0)$  and  $d(0)$  at an angle of  $0^\circ$  from the measured values of  $\Delta\sigma_L$  and  $\Delta\sigma_T$ .

Using the measured values of  $\Delta\sigma_{L,T}(np)$  and the existing  $\Delta\sigma_{L,T}(pp)$  data at the same energy, one can deduce  $\Delta\sigma_{L,T}(I=0)$  as

$$\Delta\sigma_{L,T}(I=0) = 2\Delta\sigma_{L,T}(np) - \Delta\sigma_{L,T}(pp). \quad (())7$$

### 3. Results of the $\Delta\sigma_L(np)$ measurements

A large amount of results for  $np$  elastic scattering and transmission experiments at energies up to 1.1 GeV was accumulated by the end of the 80-th. (See for example review [4].) The possibility to extend measurements of the  $np$  spin-dependent observables to higher energies exists now at the JINR VBLHE accelerators only.

The measurements of energy dependences of the  $np$  total cross sections differences  $\Delta\sigma_L(np)$  and  $\Delta\sigma_T(np)$  for parallel and antiparallel particle spins oriented longitudinally or transverse were proposed [5, 6] at the beginning of the 90-th and started [7-10] in Dubna. To implement the proposed  $\Delta\sigma_{L,T}(np)$  experimental program, a large Argonne-Saclay polarized proton target (PPT) was reconstructed in Dubna [11-13], and a new polarized neutron beam line with suitable parameters [14, 15] was constructed and tested. A set of necessary neutron detectors with corresponding electronics, and up-to-date data acquisition system and other needed equipment were also prepared, tuned and tested. Two successful data taking runs were carried out in 1995 and 1997. The energy dependence of  $\Delta\sigma_L(np)$  was measured at 1.19, 1.59, 1.79, 2.2, 2.49, and 3.66 GeV [7-10].

This contribution presents new results for the spin-dependent  $np$  total cross section difference  $\Delta\sigma_L(np)$  obtained in 2001 with longitudinally polarized both the quasi-monochromatic polarized neutron beam and the PPT. The values of  $\Delta\sigma_L(np)$  were measured at neutron beam kinetic energies of 1.4, 1.7, 1.9 and 2.0 GeV. The measured  $-\Delta\sigma_L(np)$  values are presented in [1, 2] and shown in Fig. 1. Statistical and systematic errors are taken into account. Total errors are the quadratic sums of experimental and systematic uncertainties. The results of our earlier measurements [7-10] together with the existing  $\Delta\sigma_L(np)$  data [4], obtained with free polarized neutrons at lower energies, are also shown in Fig. 1. One can see that the new results smoothly connect with the lower energy data and confirm a fast decrease to zero within a 1.2-2.0 GeV energy region, observed previously [7-10].

The solid curves show the last energy-dependent GW/VPI PSA fits [16, 17] (FA95, SP99 and SP03 solutions) of this observable over the interval from 0.1 to 1.3 GeV. Above 1.1 GeV (Saturne II), the  $np$  database is insufficient and a high energy part of the  $\Delta\sigma_L(np)$  PSA predictions still disagrees with the measured data.

Below 2.0 GeV, a usual meson exchange theory of NN scattering [18] gives the  $\Delta\sigma_L(np)$  energy dependence as shown by the dotted curve in Fig. 1. It can be seen that this model provides a qualitative description only.

More detailed and accurate  $-\Delta\sigma_L(np)$  measurements around 1.8 GeV and obtaining of new  $-\Delta\sigma_T(np)$  data using coming high intensity ( $\geq 2 \cdot 10^{10}$  d/cycle) relativistic polarized deuteron beam from the JINR VBLHE Nuclotron are planned.

## 4. Measurements of the $A_{00kk}(np)$ and $A_{00nn}(np)$ observables from $np \rightarrow pn$ process

An expression for the differential cross sections for scattering of polarized nucleon beam with energy  $E$  on the polarized target nucleons with the scattered particle detection at an angle of  $\theta$  is [3, 4]

$$\begin{aligned} [d\sigma/d\Omega]_{pol}(E, \theta) = d\sigma/d\Omega(E, \theta) \cdot [1 + A_{00n0}(E, \theta) \cdot P_{B^n} + A_{000n}(E, \theta) \cdot P_{T^n} + \\ A_{00nn}(E, \theta) \cdot P_{B^n} \cdot P_{T^n} + A_{00ss}(E, \theta) \cdot P_{B^s} \cdot P_{T^s} + A_{00kk}(E, \theta) \cdot P_{B^k} \cdot P_{T^k} + \\ A_{00sk}(E, \theta)(P_{B^s} \cdot P_{T^k} + P_{B^k} \cdot P_{T^s})], \quad (())8 \end{aligned}$$

where  $d\sigma/d\Omega$  is the cross section for unpolarized nucleons.

If the scattered particles are detected at  $0^\circ$  then analyzing powers  $A_{00n0}(E, 0) = A_{000n}(E, 0) = 0$  and parameters  $A_{00sk}(E, 0) = 0$  and  $A_{00ss}(E, 0) = A_{00nn}(E, 0)$ . Thus, only two different non-vanishing spin-dependent quantities  $A_{00nn}(E, 0)$  and  $A_{00kk}(E, 0)$  remain in Eq.(8).

Due to symmetries of amplitudes, which hold separately for isospins  $I = 0$  and  $I = 1$ , the same relations are valid at  $\theta_{c.m.} = \pi$ . Moreover the amplitude  $e(0) = e(\pi) = 0$  for any isospin. The measured  $np$  observables at  $\theta_{c.m.} = \pi$  are connected with the invariant amplitudes as follows

$$d\sigma/d\Omega = \frac{1}{2}[|a|^2 + |b|^2 + |c|^2 + |d|^2], (())9$$

$$d\sigma/d\Omega \cdot A_{00nn} = \frac{1}{2}[|a|^2 - |b|^2 - |c|^2 + |d|^2], (())10$$

$$d\sigma/d\Omega \cdot A_{00kk} = Re a^* \cdot d + Re b^* \cdot c, (())11$$

where all experimental quantities and amplitudes are at  $\theta_{c.m.} = \pi$ . These equations can be transformed to

$$d\sigma/d\Omega(1 + A_{00kk}) = A + (Re b + Re c)^2, (())12$$

$$d\sigma/d\Omega(1 - A_{00kk} - 2 \cdot A_{00nn}) = B + (Re b - Re c)^2, (())13$$

$$d\sigma/d\Omega(1 - A_{00kk} + 2 \cdot A_{00nn}) = C + (Re b + Re c - 2 \cdot Re d)^2, ((14)$$

where terms  $A, B, C$  contain the imaginary parts of amplitudes only. The real parts of the amplitudes  $b, c$ , and  $d$  can be determined from Eq.s (12)-(14) using known imaginary ones. A knowledge of  $I = 1$  system is assumed in order to use the amplitude symmetries for the transformation of  $I = 0$  amplitudes from  $\theta = 0$  to  $\theta = \pi$  and vice versa [19].

Measurements of the  $A_{00kk}(np)$  and  $A_{00nn}(np)$  observables were examined for example in [19, 20]. Obtaining of data set on energy dependences of  $A_{00kk}(np)$  and  $A_{00nn}(np)$  spin observables over the JINR VBLHE accelerators energy region were discussed [1, 2, 7-10] and planned under the program of "Delta-Sigma" experiment. The  $A_{00kk}(np)$  and  $A_{00nn}(np)$  values will be determined from the asymmetry measurements of yields of  $np \rightarrow pn$  charge exchange process at  $0^\circ$  (i.e. elastic scattering at  $\theta = \pi$ ) for parallel and antiparallel orientations of polarizations of the  $L$  and  $T$  polarized neutron beam and PPT.

Energy dependence of the ratio

$$R_{dp} = d\sigma/d\Omega(nd)/d\sigma/d\Omega(np)((15)$$

for the elastic charge exchange process  $np \rightarrow pn$  at  $0^\circ$  in Lab. (or elastic  $np \rightarrow np$  backward scattering in c.m.s) will be measured with high intensity unpolarised neutron beam from Nuclotron using the magnetic spectrometer and liquid hydrogen and deuterium targets.  $R_{dp}$  is connected with helicity  $NN$  amplitudes by (see for example [20])

$$R_{dp} = \frac{2}{3} \cdot \frac{1}{(1 + R')}, ((16)$$

$$R' = \frac{|\Phi_4 - \Phi_2|^2}{2 \cdot |\Phi_1|^2 + |\Phi_4 + \Phi_2|^2}, ((17)$$

where  $\Phi_i$  are the helicity  $NN$  amplitudes and  $R'$  is the ratio of "spin non-flip" to "spin flip" contributions to the cross sections of  $np \rightarrow pn$  process. For  $R' = 0$  we have

$$d\sigma/d\Omega(nd) = 2/3 d\sigma/d\Omega(np).((15)$$

The values of  $R_{dp}$  give an additional relation between spin-dependent  $NN$ -amplitudes and a set of such data allows to avoid one uncertainty of real parts extraction.

The first measurement of the ratio  $R_{dp}$  was carried out [21] at the Dubna synchrotron at neutron energy of 380 MeV.

## 5. Magnetic spectrometer for investigation of elastic $np \rightarrow pn$ charge exchange process

In the last few years the measurements of spin-correlation parameters  $A_{00kk}(np)$  and  $A_{00nn}(np)$  from  $np \rightarrow np$  elastic charge exchange at  $0^\circ$  (Lab.) were prepared in frame of the "Delta-Sigma experiment" project. These spin-correlation  $np$  observables can be measured simultaneously (and independently) with the transmission measurements of  $\Delta\sigma_{L,T}(np)$ .

The method of scattered particle detection is used to measure the yield of charge exchanged protons and differential cross section for  $np \rightarrow pn$  process at  $0^\circ$ . A magnetic spectrometer for detection of protons from  $np \rightarrow np$  elastic charge exchange at  $0^\circ$  (*Lab.*) was installed and tested at the polarized neutron beam line (see Fig. 2).

The spectrometer consist of analyzing dipole SP-94, two sets of multiwire proportional chambers before and after SP-94 for momentum analyzis of detected secondaries, time-of flight system (*S1, TOF1, 2*) for particle identification, liquid  $H_2$  or  $D_2$  targets, surrounded by a device for detecting of recoils and gammas, and trigger counters *A, S1, ST*.

Investigations of the charge exchange  $np \rightarrow pn$  process at  $0^\circ$  were performed during a number of last metodical and physical runs using a high intensity unpolarized neutron beam from the JINR VBLHE Nuclotron. Some characteristics of the spectrometer and studied process and a number of physical results, obtained in these runs, are shown in Figs 3-10.

The momentum spectra of charged secondaries, detected by spectrometer using  $H_2$  and  $D_2$  liquid targets, at the neutron beam energies of 1.0 and 1.2 GeV are shown in Figs 3 and 4. The momentum resolution of spectrometer, measured using primary monochromatic deuteron beam, was estimated as  $\Delta P/P = 1.65\%$ .

An information from the detectors for target surrounding DTS allows to suppress the contributions from other (inelastic)  $np$ -reaction channels. The upper histograms in Figs 5 and 6 present spectra of charged secondaries as function of angle of deflection in analyzing magnet obtained without using the information from the DTS. The middle and bottom histograms in Figs 5 and 6 show the same as the upper ones but when the signal from the DTS is in anticoincidence or in coincidence with the spectrometer trigger, respectively.

The detected particle identification, using both the magnetic analyzis and time-of-flight spectra is demonstrated by Fig. 7. An angular acceptance of spectrometer in polar  $\theta$  and asimuthal  $\varphi$  angular planes is shown in Fig. 8.

Two examples of angular dependences of differential cross sections of the  $np \rightarrow pn$  process near  $0^\circ$ , obtained with  $H_2$  and  $D_2$  targets at  $T_n = 1.0$  GeV, are presented in Fig. 9 and an estimation of the ratio  $R_{dp}$  at neutron energy of 1.0 GeV is shown in Fig. 10.

A sufficient statistics to determine the differential cross sections for  $np \rightarrow pn$  process at  $0^\circ$  were accumulated over 1-2 GeV energy region, using liquid  $H_2$  and  $D_2$  targets. Our preliminary results on the momentum spectra of elastic charge exchange protons and  $d\sigma/d\Omega(np)$  at 1.0, 1.2 GeV are in good agreement with the existing data [22, 23]. The accumulated data treatment and analyzis are in progress.

## 6. Conclusion

1. New  $-\Delta\sigma_L(np)$  results complete in the main the measurement of the  $-\Delta\sigma_L(np)$  energy dependence at the Dubna Synchrophasotron energy region.
2. Measured  $-\Delta\sigma_L(np)$  values are in accordance with the existing  $np$  results at low energies, obtained with free neutron beams. The rapid decrease of  $-\Delta\sigma_L(np)$  values above 1.1 GeV was observed in the first data taking runs and is confirmed in the latest run and a minimum or a shoulder around 1.8 GeV is observed.
3. The necessity of more detailed and accurate  $-\Delta\sigma_L(np)$  measurements around 1.8

GeV and new  $-\Delta\sigma_T(np)$  data in the kinetic energy region above 1.1 GeV is emphasized.

4. A number of physical and methodical results on investigation of the elastic  $np \rightarrow pn$  charge exchange process over a few GeV region are also presented. The possibilities for  $A_{00kk}(np)$ ,  $A_{00nn}(np)$  and  $R_{dp}$  measurements, using prepared magnetic spectrometer, were demonstrated.

We are grateful to the JINR, JINR VBLHE, DLNP and LPP Directorates for these investigations support. The investigations were supported in part by the Russian Foundation for Basic Research (Grant No 02-02-17129).

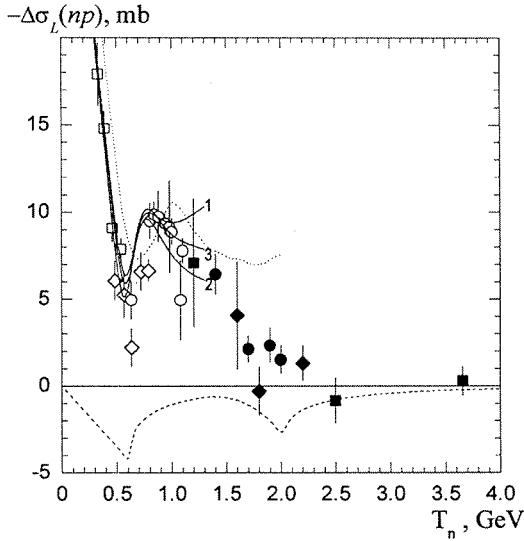


**Fig. 1.** Energy dependence of the  $-\Delta\sigma_L(np)$ . Black circles – the last JINR results [1, 2], black squares – JINR [7, 8], black rhombes – JINR [9, 10], open squares – PSI, open rhombes – LAMPF and open circles – Saturne II (see [4]), solid curves – ED GW/VPI PSA [16, 17](1-FA95 solution, 2-SP99 solution and 3-SP03 solution), dotted curve – meson-exchange model [18], dashed curve – contribution from nonperturbative QCD interaction induced by instantons [7, 8, 10]

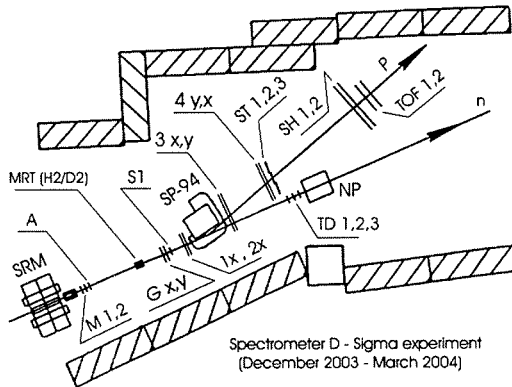


**Fig. 2.** Magnetic spectrometer for detection of protons from  $np \rightarrow np$  elastic charge exchange at  $0^\circ(Lab)$ . SP-94 – analyzing dipole, Gx,y, 1x, 2x, 3x,y, 4x,y – two sets of multiwire proportional chambers, MPT, $H_2/D_2$  – polarized proton target or liquid  $H_2$  or  $D_2$  targets, S1, TOF1,2 and A, S1, ST – time-of flight and trigger counters

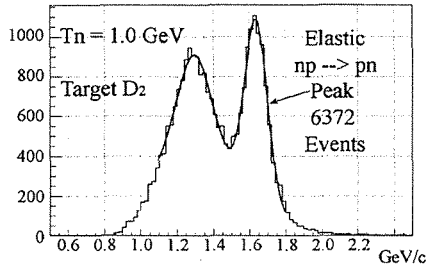
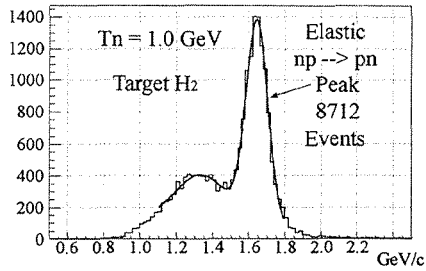


Fig. 3. The momentum spectra of charged secondaries, detected by spectrometer using  $H_2$  and  $D_2$  liquid targets, at the neutron beam energy of 1.0 GeV

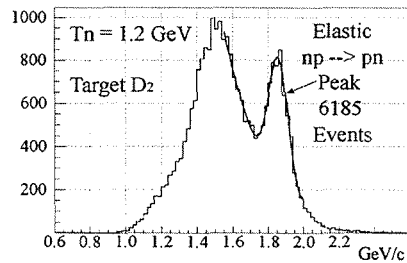
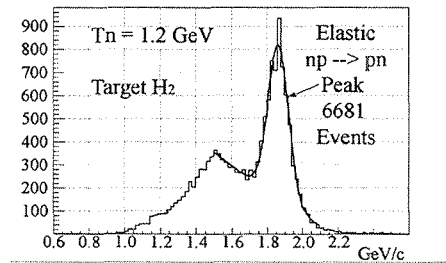
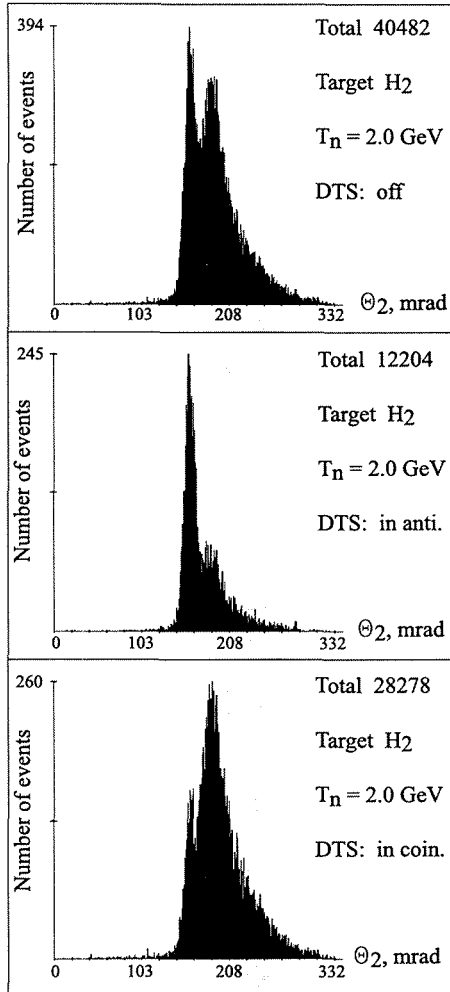


Fig. 4. The same as in Fig. 3 but at the neutron beam energies of 1.2 GeV



**Fig. 5.** The "on-line" histograms as function of angle of deflection in analyzing magnet of charged secondaries, detected by spectrometer using H<sub>2</sub> liquid target, at the neutron beam energy of 2.0 GeV. Information from the detectors for target surrounding DTS allows to suppress the contributions from other (inelastic) *np*-reaction channels. The upper histogram shows the spectrum of charged secondaries obtained without using the information from the DTS. The middle and bottom histograms show the spectra when the signal from the DTS is in anticoincidence and in coincidence with the spectrometer trigger, respectively

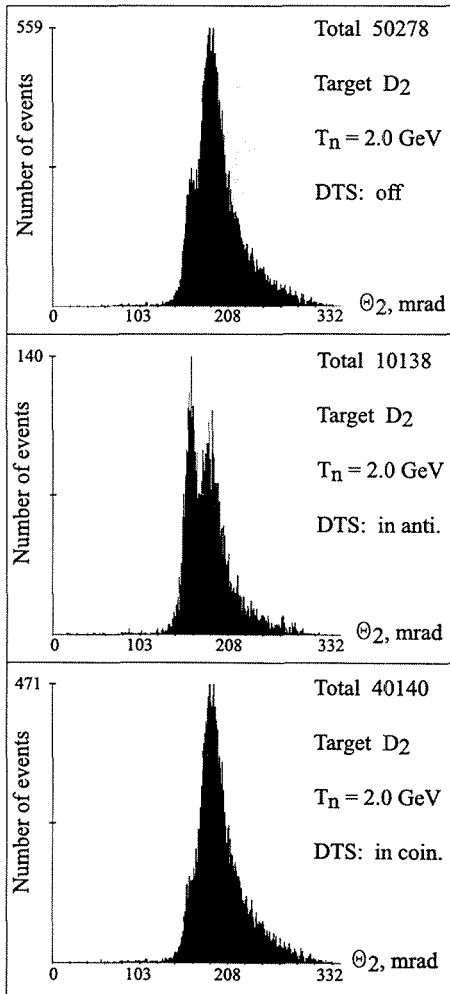


Fig. 6. The same as in Fig. 5 but with  $D_2$  liquid target

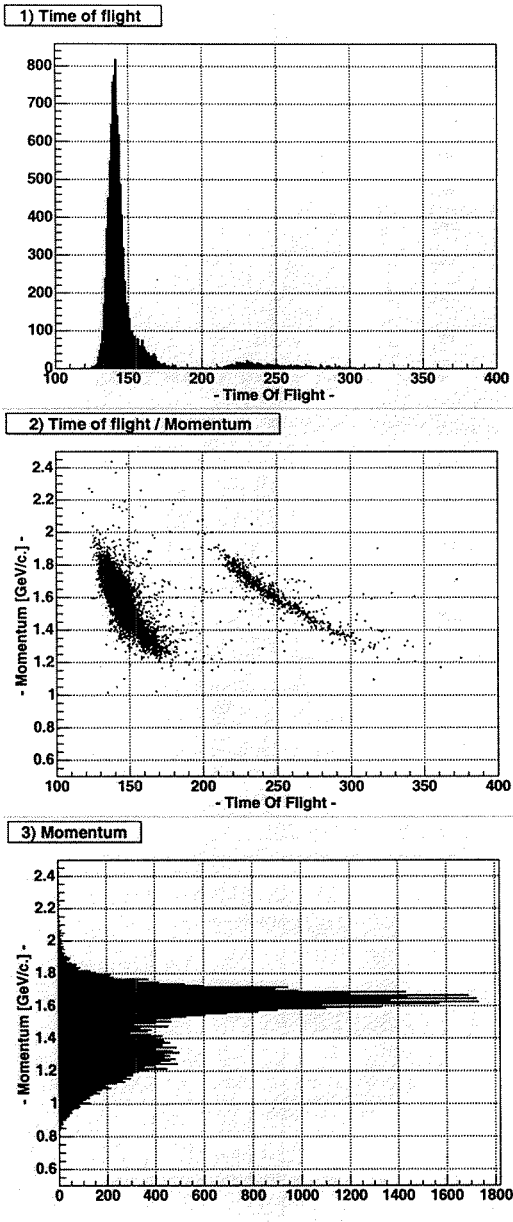


Fig. 7. The detected particle identification, using both the magnetic analysis and time-of-flight spectra

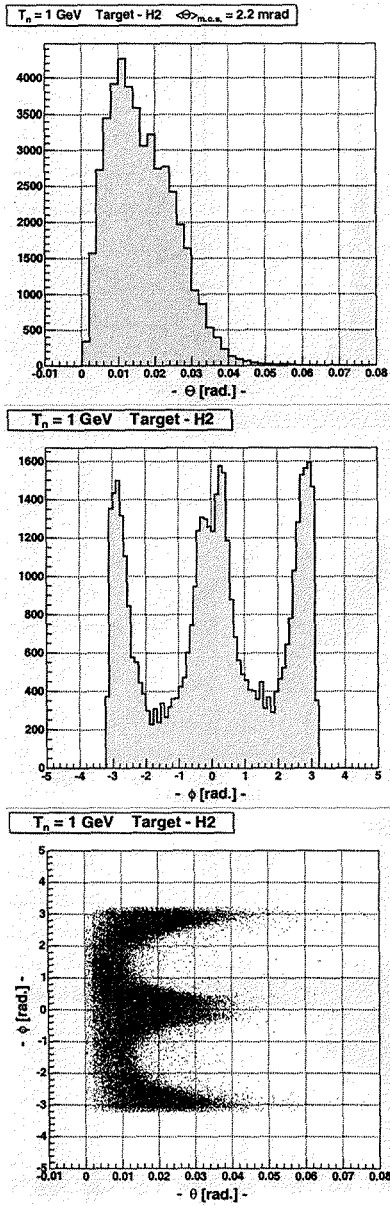


Fig. 8. Angular acceptance of spectrometer in the polar  $\theta$  and azimuthal  $\varphi$  angular planes

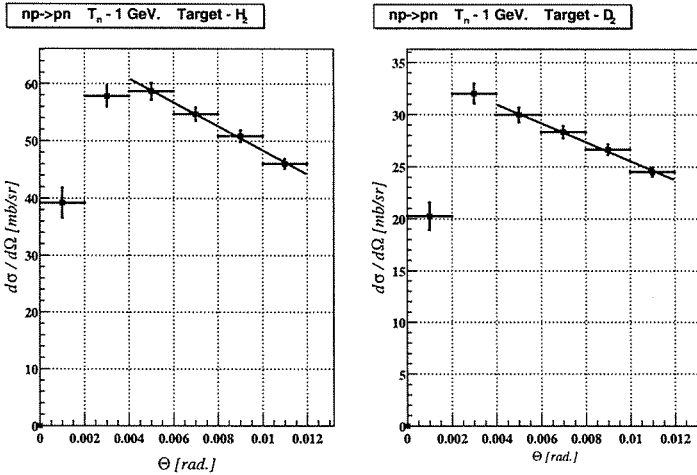


Fig. 9. Angular dependences of differential cross sections of the  $np \rightarrow pn$  process near  $0^\circ$ , obtained with  $H_2$  and  $D_2$  targets at  $T_n = 1.0$  GeV

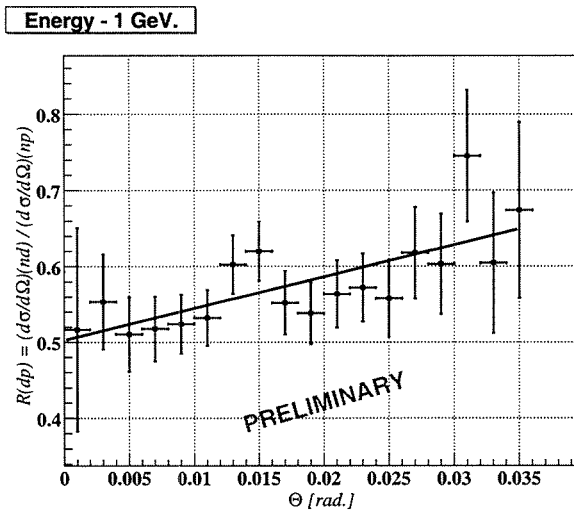


Fig. 10. An estimation of the ratio  $R_{dp}$  at neutron energy of 1.0 GeV

## References

1. V.I. Sharov, N.G. Anischenko, V.G. Antonenko, S.A. Averichev et al. *Eur.Phys.J. C* **37**, 79 (2004).
2. V.I. Sharov, N.G. Anischenko, V.G. Antonenko, S.A. Averichev et al. *Preprint JINR E1-2004-87*, Dubna, 2004. To be published in Russian Journal "Yadernaya Fizika".
3. J. Bystrický, F. Lehar and P.Winternitz. *J. Phys. (Paris)*. **39**, 1 (1978).
4. C.Lechanoine-Leluc and F.Lehar. *Rev. Mod. Phys.* **65**, 47 (1993).
5. J. Ball, N.S. Borisov, J. Bystricky, A.N. Chernikov et al. *In: Proc. Int. Workshop "Dubna Deuteron-91"*, JINR E2-92-25, p.12, Dubna, 1992.
6. E. Cherhykh, L. Golovanov, A. Kirillov, Yu. Kiselev et al. *In: Proc. Int. Workshop "Dubna Deuteron-93"*, JINR E2-94-95, p.185, Dubna, 1994; *Proc. "V Workshop on High Energy Spin Physics"*, Protvino, 20-24 September 1993, Protvino, 1994, p.478.
7. B.P. Adiasevich, V.G. Antonenko, S.A. Averichev, L.S. Azhgirey et al. *Zeitschrift für Physik C***71**, 65 (1996).
8. V.I. Sharov, S.A. Zaporozhets, B.P. Adiasevich, V.G. Antonenko et al. *JINR Rapid Communications* **3[77]-96**, 13 (1996).
9. V.I. Sharov, S.A. Zaporozhets, B.P. Adiasevich, N.G. Anischenko et al. *JINR Rapid Communications* **4[96]-99**, 5 (1999).
10. V.I. Sharov, S.A. Zaporozhets, B.P. Adiasevich, N.G. Anischenko et al. *Eur.Phys.J. C* **13**, 255 (2000).
11. F. Lehar, B. Adiasevich, V.P. Androsov, N. Angelov et al. *Nucl.Instrum.Methods* **A356**, 58 (1995).

12. N.A. Bazhanov, B. Benda, N.S. Borisov, A.P. Dzyubak et al. Nucl.Instrum.Methods **A372**, 349 (1996).
13. N.A. Bazhanov, et al., Nucl.Instrum.Methods **402**, 484 (1998).
14. I.B. Issinsky, A.D. Kirillov, A.D. Kovalenko and P.A. Rukoyatkin. Acta Physica Polonica **B25**, 673 (1994).
15. A. Kirillov, L. Komolov, A. Kovalenko, E. Matyushevsky, A.A.Nomofilov, P. Rukoyatkin, V. Sharov, A. Starikov, L. Strunov, A. Svetov. "Relativistic Polarized Neutrons at the Laboratory of High Energy Physics, JINR".  
*Preprint JINR E13-96-210*, Dubna, 1996.
16. R.A. Arndt, et al. Phys. Rev. C **56**, 3005 (1997).
17. R.A. Arndt, I.I. Strakovsky, and R.L. Workman. Phys. Rev. C **62**, 034005 (2000).
18. T.-S.H. Lee. Phys. Rev. C **29**, 195 (1984).
19. J. Ball, R.Binz, J.Bystricky et al. Eur.Phys.J. **C 5**, 57 (1998).
20. R.Binz. Ph.D. Thesis, Freiburg University, Germany (1991).
21. V.P. Dzhelepov, Yu.M. Kazarinov, B.M. Golovin, V.B. Fljagin and V.I. Satarov. Izvestia Akad. Nauk SSSR **19**, 573 (1955); Suppl. Nouvo Cimento **3**, 61 (1956).
22. G.Bizard,F.Bonthonneau,J.L.Laville, et.al. Nucl.Phys. **B 85** , 14 (1975).
23. G.Bizard,F.Bonthonneau,J.L.Laville, et.al. Nucl.Phys. **B 108**, 189 (1976).

# SENSITIVITY OF THE POLARIZATION OBSERVABLES $A_Y$ , $A_{YY}$ , $A_{XX}$ AND $A_{XZ}$ OF THE $\vec{d}d \rightarrow p\ ^3H$ AND $\vec{d}d \rightarrow p\ X$ REACTIONS TO THE DEUTERON SPIN STRUCTURE AT 270 MEV

T.A.Vasiliev<sup>1†</sup>, T.Saito<sup>2</sup>, V.P.Ladygin<sup>1</sup>, M.Hatano<sup>2</sup>, A.Yu.Isupov<sup>1</sup>, M.Janek<sup>1,5</sup>, H.Kato<sup>2</sup>, N.B.Ladygina<sup>1</sup>, Y.Maeda<sup>7</sup>, A.I.Malakhov<sup>1</sup>, S.Nedev<sup>6</sup>, J.Nishikawa<sup>4</sup>, H.Okamura<sup>8</sup>, T.Ohnishi<sup>3</sup>, S.G.Reznikov<sup>1</sup>, H.Sakai<sup>2</sup>, S.Sakoda<sup>2</sup>, N.Sakomoto<sup>3</sup>, Y.Satou<sup>2</sup>, K.Sekiguchi<sup>3</sup>, K.Suda<sup>7</sup>, A.Tamii<sup>9</sup>, T.Uesaka<sup>7</sup>, N.Uchigashima<sup>2</sup>, K.Yako<sup>2</sup>

(1) LHE JINR, Dubna, Moscow region, 141980 Russia

(2) Department of Physics, University of Tokyo, Tokyo 113-0033, Japan

(3) The Institute of Physical and Chemical Research (RIKEN), Wako 351-0198, Japan

(4) Department of Physics, Saitama University, Saitama 338-8570, Japan

(5) University of P.J.Safarik, 041-54 Kosice, Slovakia

(6) University of Chemical Technology and Metallurgy, Sofia, Bulgaria

(7) Center for Nuclear Study, University of Tokyo, Tokyo 113-0033, Japan

(8) Cyclotron and Radioisotope Center, Tohoku University, Sendai, Miyagi 980-8578, Japan

(9) Research Center for Nuclear Physics, Osaka University, Ibaraki, Osaka 567-0047, Japan

## Abstract

The experimental results on the tensor  $A_{yy}$ ,  $A_{xx}$ ,  $A_{xz}$  and vector  $A_y$  analyzing powers at  $E_d = 270\text{ MeV}$  for the  $\vec{d}d \rightarrow p\ ^3H$  reaction in angular range from  $90^\circ$  to  $180^\circ$  in c.m.s. are presented. The  $\vec{d}d \rightarrow p\ X$  data on  $A_y$ ,  $A_{yy}$  and  $A_{xx}$  near breakup threshold are also obtained. The experimental data for these reactions demonstrate the sensitivity to the spin structure of deuteron.

## 1. Introduction

Deuteron is the only bounded state of two-nucleon system. Study of its wave function is not only the most fundamental subject of nuclear physics, but also one of the most interesting subject at present. Since the spin and isospin of the deuteron are well known, it is excellent isoscalar probe with spin.

The light nuclei structure has been extensively investigated during the last few decades using both electromagnetic [1, 2] and hadronic probes [3]. A significant amount of the data devoted to the investigations of the deuteron spin structure at short distances are accumulated in the last years [4, 5, 6, 7]. The tensor analyzing  $T_{20}$  and polarization transfer coefficient  $k_0$  in backward elastic scattering,  $dp \rightarrow pd$ , have been measured at Saclay [4] and Dubna [5]. Later, the set of polarization observables was also obtained in dp-elastic scattering over wide angular range at intermediate energies at RIKEN [8, 9] and KVI [10]. Measurements of the polarization correlation coefficients  $C_{//}$  in the  $d\ ^3He \rightarrow p\ ^4He$  reaction have been performed at RIKEN [7].

All the data show the sensitivity to the deuteron spin structure at short distances. However, the remarkable deviation of the polarization observables from the One Nucleon Exchange (ONE) predictions using standard deuteron wave function occurs even at relatively small internal momenta of  $q \sim 200\text{ MeV}/c$ . Such a discrepancy can be due to the

non-adequate description of the light nuclei structure at short distances, as well as to the importance of the mechanisms in addition to ONE.

The  $\vec{d}d \rightarrow p\ ^3H$  and  $\vec{d}d \rightarrow pX$  process concern to ONE reactions. These reactions are the simplest processes with a large momentum transfer, so they could be used as a tool to study the deuteron structure at short distances. The polarization observables of these reactions are sensitive to the D/S wave ratio in the deuteron.

In this report the data on the tensor and vector analyzing powers  $A_{yy}$ ,  $A_{xx}$ ,  $A_{zz}$  and  $A_y$ , for the  $\vec{d}d \rightarrow p\ ^3H$  reaction obtained in R308n experiment at RIKEN [11] are presented. Also the data for the breakup reaction near threshold  $\vec{d}d \rightarrow pX$  are shown.

The relative momenta of nucleons in deuteron achieves  $q \sim 400\ MeV/c$  at initial deuteron kinetic energy  $E_d = 270\ MeV$ .

## 2. Experiment

The experiment was performed at RIKEN accelerator Research Facility. The Polarized Ion Source provided four modes of the beam polarization, the first one was unpolarized, others had tensor, vector and mixed polarizations, respectively. A polarized deuteron beam extracted from polarized ion source was accelerated with the AVF and the Ring cyclotrons up to the energy 270 MeV. The accelerated beam was transported to the spectrometer SMART [12] and injected onto a target placed in the scattering chamber. The momentum analysis of the scattered particles was performed with three quadrupole and two dipole magnets in QQDQD configuration. The detection system consisted of Multi Wire Drift Chambers (MWDC) and three plastic scintillation counters placed at the focal plane.

Horizontally oriented detection system was placed in the focal plane. Injection of the beam onto the target was controlled by the swinger magnet. Different angles of the swinger magnet  $\Theta_{sw}$  allowed to perform detection of the reaction products with the fixed spectrometer and in any scattering angles upto  $50^\circ$  in the lab system.

The magnitude of the beam polarization have been measured with two beam-line polarimeters based on dp-elastic scattering. Deuterated polyethylene was used as the deuteron target [13]. Measurements with a carbon target was also performed to subtract the contribution of carbon nuclei in  $CD_2$  target. For the  $\vec{d}d \rightarrow p\ ^3H$  reaction the detected protons scattered in the backward angles in the c.m.s.

Information from MWDC was transformed to the scattering angles and the momenta of the particle using the optical matrix of the spectrometer. The particle identification procedure was performed using the correlation between the ADC signals from scintillators and time of flight of the particle.

## 3. Results and discussion

The experimental results on the vector  $A_y$  and tensor  $A_{yy}$ ,  $A_{xx}$  and  $A_{zz}$  analyzing powers of the  $\vec{d}d \rightarrow p\ ^3H$  reaction at  $E_d = 270\ MeV$  are presented by the filled symbols in Fig.1. The solid, long-dashed and dotted curves are the results of ONE calculations using Paris [14], Bonn B [15], and Bonn C [15] deuteron wave functions, respectively. Urbana  $^3He$  wave function [16] was used in the calculations to describe three-nucleon (3N) system.

ONE calculations predict that the tensor analyzing power at the backward angles is sensitive to the structure of the deuteron. ONE calculation near  $90^\circ$  in the c.m.s. are sensitive to the both deuteron and  ${}^3\text{He}$  wave functions. One can see from Fig.1 that the calculations reproduce the global feature of the experimental data at the backward angles, while they remarkably deviate from the experimental results near  $90^\circ$ . These results imply that there might be some problems in the realistic  ${}^3\text{He}$  wave functions used in ONE calculations. Fig.1 shows that there are some structures in the angular distribution of  $A_y$  in spite of zero vector predicted from ONE calculations. In this respect it could be noted as requirements for extend the reaction mechanisms beyond ONE model. The signs of the tensor analyzing power  $A_{yy}$  and  $A_{xx}$  near  $180^\circ$  in the c.m.s. are positive in accordance with the sign of the deuteron wave function. The experimental and predicted data for  $A_{yy}$  and  $A_{xx}$  have the same sign and qualitatively agree each other. However, there are quantitative difference between the experimental data and the predictions. ONE predictions near  $90^\circ$  depend on both deuteron and  ${}^3\text{He}$  functions simultaneously and the experimental data for  $A_{yy}$  and  $A_{xx}$  strongly disagree with the calculations in this region. The experimental  $A_{xz}$  data and the their predictions for backward angles are in agreement. The  $A_{xz}$  experimental data near  $90^\circ$  strongly differ from the predictions.

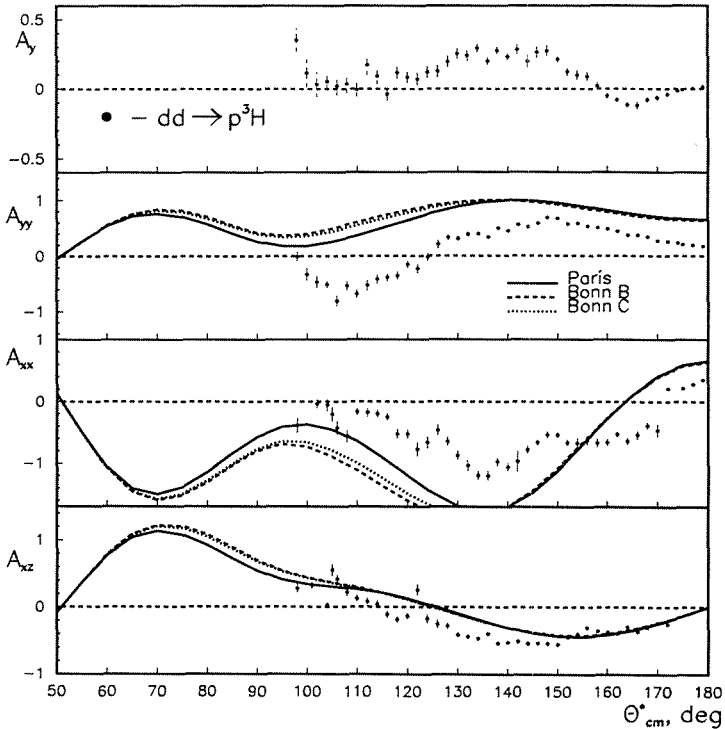
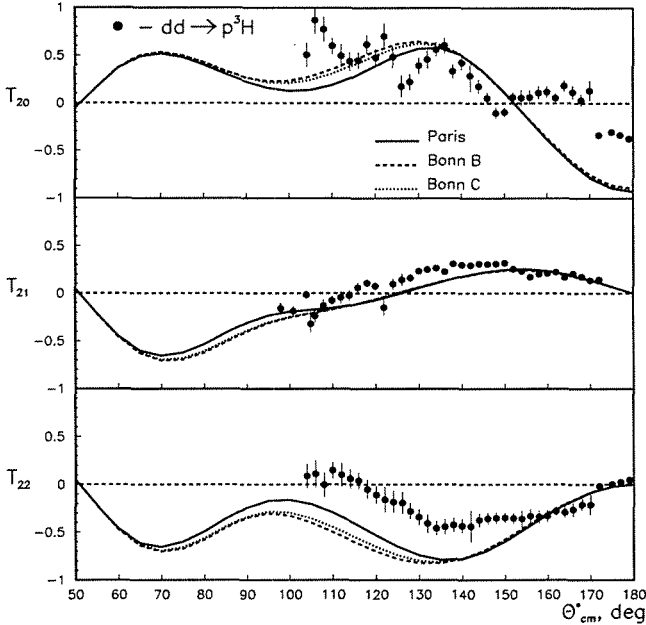


Figure 1. The experimental results on  $A_{yy}$ ,  $A_{xx}$ ,  $A_{xz}$  and  $A_y$  analyzing powers of the  $\vec{d}d \rightarrow p{}^3\text{H}$  reaction at  $E_d = 270 \text{ MeV}$

The experimental results on the tensor analyzing powers in terms of  $T_{20}$ ,  $T_{21}$ ,  $T_{22}$  of  $\vec{d}d \rightarrow p\ ^3H$  reaction at  $E_d = 270\text{ MeV}$  are presented by filled symbols in Figure.2. The curves are the same as in Figure.1. One can see, the experimental data of the tensor analyzing power  $T_{20}$  near  $0^\circ$  is negative an accordance with the sign of the deuteron wave function. The global feature of ONE predictions on  $T_{21}$  and  $T_{22}$  is reproduced by the experimental data. However for  $T_{20}$  there is strong disagreement between the experimental data and calculations.



**Figure 2.** The experimental results on  $T_{20}$ ,  $T_{21}$ ,  $T_{22}$  analyzing powers of the  $\vec{d}d \rightarrow p\ ^3H$  reaction at  $E_d = 270\text{ MeV}$

Monte Carlo (MC) simulation was performed for the  $\vec{d}d \rightarrow p\ X$  reaction at 270 MeV initial deuteron energy and small proton emission angles in accordance with 2 and 3 particle phase space [17]. It is shown that MC simulation for 2 particle phase space ( $p - dn$  in the final state) well reproduces the excitation energy spectra near threshold. The calculations in accordance with 3 particle phase space is quite small within the acceptance of the spectrometer. A peak obliged to the Final State Interaction (FSI) near breakup threshold for the 3-nucleon unbounded state is not observed in contrast with  $np$  state [5]. Thus, it gives the opportunity to conclude that FSI for the  $dn$  system is insignificant or much weaker than for the  $np$  one.

The experimental results on vector and tensor  $A_y$  and  $A_{yy}$  analyzing powers for  $\vec{d}d \rightarrow p\ X$  reaction at  $E_d = 270\text{ MeV}$  are presented by the filled symbols in Fig.3

and Fig.4, respectively. Filled stars and points are plotted for the events with 7 and 10 MeV excitation energy, respectively. The opened symbols correspond to the data for  $\vec{d}d \rightarrow p^3H$  reaction. The experimental results on  $A_{xx}$  tensor analyzing power of the  $\vec{d}d \rightarrow pX$  reaction at  $E_d = 270$  MeV and 8 MeV excitation energy are plotted in Fig.5 in comparison with the binary data.

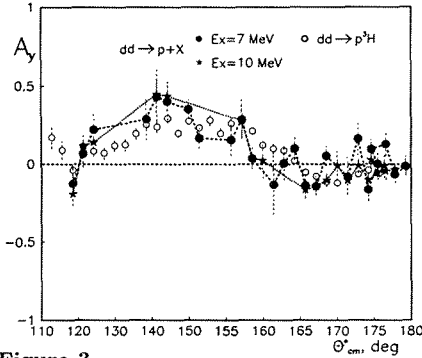


**Figure 3.**

The experimental results on  $A_y$  vector analyzing power of the  $\vec{d}d \rightarrow p^3H$  and  $\vec{d}d \rightarrow pX$  reactions at  $E_d = 270$  MeV

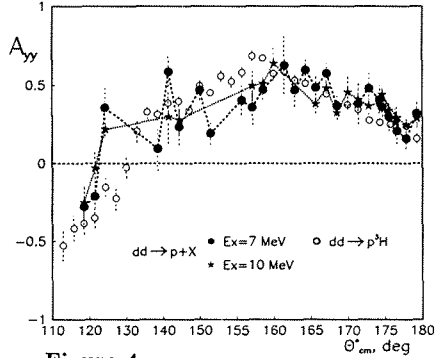


**Figure 4.**

The experimental results on  $A_{yy}$  tensor analyzing power of the  $\vec{d}d \rightarrow p^3H$  and  $\vec{d}d \rightarrow pX$  reactions at  $E_d = 270$  MeV

The comparison of the polarization observables of the breakup and the binary reactions gives an opportunity to conclude that they are in an agreement within achieved errors. The distributions of the tensor and vector analyzing powers of the breakup and the binary reactions are approximately the same within achieved experimental errors.

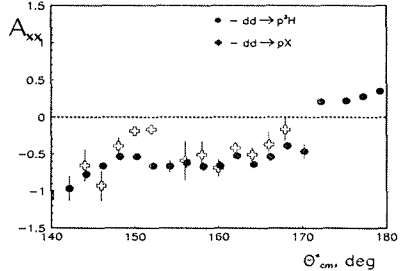


**Figure 5.** The experimental results on  $A_{xx}$  tensor analyzing power of the  $\vec{d}d \rightarrow p^3H$  and  $\vec{d}d \rightarrow pX$  reactions at  $E_d = 270$  MeV

## 4. Summary

The experimental data on the tensor and vector analyzing powers  $A_{yy}$ ,  $A_{xx}$ ,  $A_{xz}$  and  $A_y$  for the  $\vec{d}d \rightarrow p^3H$  is obtained at  $E_d = 270$  MeV in the angular range  $90^\circ - 180^\circ$  in the c.m.s. The experimental data on the tensor observables for this reaction show the sensitivity to the spin structure of the deuteron. The angular distribution of  $A_y$  indicates the necessity to take into account mechanisms beyond ONE.

The experimental data of the tensor and vector analyzing powers  $A_{yy}$ ,  $A_{xx}$  and  $A_y$  for the  $\vec{d}d \rightarrow pX$  breakup reaction are obtained. The experimental data on  $A_{yy}$  and  $A_{xx}$  for this reaction also show the sensitivity to the spin structure of deuteron.

The obtained experimental data require further development in theoretical approaches either for adequate description of the light nuclei structure at short distances and (or) taking into account mechanisms in addition to ONE.

### Acknowledgments

The work has been supported in part by the Russian Foundation for Fundamental Research (grant  $N\ 04 - 02 - 17107$ ) and by the Grant Agency for Science at the Ministry of Education of the Slovak Republic (grant  $N\ 1/1020/04$ )

## References

- [1] D.Day et al., *Phys.Rev.Lett.* **43**, 1143 (1979)  
J.S.McCarthy et al., *Phys.Rev.* **C13**, 712 (1976)
- [2] D.Abbott et al., *Phys.Rev.Lett.* **84**, 5053 (2000)
- [3] F.Lehar, *RNP: from Hundreds of MEV to TEV Vol.1, Varna, Bulgaria*, 36 (2001)
- [4] Punjabi V. et al., *Phys.Lett.* **B350**, 178 (1995)
- [5] L.S.Azhgirey et al., *Phys.Lett.* **B391**, 22 (1997)  
L.S.Azhgirey et al., *Phys. of Atom. Nucl.* Vol. **61**, 432 (1998)
- [6] L.S.Azhgirey et al., *Phys.Lett.* **B387**, 37 (1996)
- [7] T.Uesaka et al., *Phys.Lett.* **B533**, (2002)  
T.Uesaka et al., *Phys.Lett.* **B467**, 199 (1999)  
T.Uesaka, H.Sakai, H.Okamura, et al., *FewBody Systems Suppl.* **12**, 497 (2000)
- [8] N.Sakamoto et al., *Phys.Lett.* **B367**, 60 (1996)
- [9] H.Sakai et al., *Phys.Lett.* **84**, 5288 (2000)
- [10] R.Bieber et al., *Phys.Lett.* **84**, 606 (2000)
- [11] V.P.Ladygin, N.B.Ladygina, H.Sakai and T.Uesaka, *Part. and Nucl. Lett.* **3[100]**, 74 (2000)
- [12] T.Ichihara et al., *Nucl.Phys.* **A569**, 287 (1994)
- [13] Y.Maeda, H.Sakai, K.Hatanaka and A.Tamii, *Nucl.Instr. and Meth. in Phys.Res.* **A490**, 518 (2002)
- [14] M.Lacombe, B.Loiseau, R.Vinh Mau, J.Cote, P.Pires and R.de Tournell, *Phys.Lett.* **B101**, 139 (1981)

- [15] R.Machleid, K.Holinde, C.Elster, *Phys.Rep.* **149**, 1 (1987).
- [16] R.Schiavilla, V.R.Pandharipande and R.B.Wiringa, *Nucl.Phys.* **A449**, 219 (1986)
- [17] T.A.Vasiliev, et al, *In Proc. of NATO ARW DUBNA-SPIN-03 conference, Sept 16-20,2003, Dubna; E1,2-2004-80*, 440 (2004)

# SPIN AS A KINEMATICAL EFFECT OF THE RELATIVITY

O.S. Kosmachev<sup>†</sup>

(1) *Joint Institute for Nucleare Research*

† *E-mail: kos@thsun1.jinr.ru*

## Abstract

It is shown, that Pauli spin matrices are infinitesimal boost operators for irreducible representation of Lorentz group with first weight number equal  $1/2$ , which do not contain space (P) inversion and time (T) reversal. Purely relativistic effect appears under orbital motion, which is the result of so-called Wigner rotation. The similar analysis was fulfilled for (P)-, (T)- and (PT)-conjugate irreducible representation of Lorentz group with respect to standard (i.e. proper, orthochronous, homogeneous) one. In every particular case explicit form of spin matrices are changed, but components of spin operators have the same commutative relations up to phase factor  $\pm 1$  and they have the same physical sense.

**Key-words:** spin, groups, irreducible representations, discrete symmetry.

## 1. Introduction

The question on spin nature does not closed in spite of long history of spin conception [1] and it successful mathematical formalization [2] for the electron. The aim of this article is to draw attention to physical interpretation of mathematical formalism for one particular case namely spin  $1/2$ . It is singled out, exclusive case due to successes, which are symbolized the scientific progress of the past century. For example, explanation of the Mendeleev periodical low, development of the nuclear and particle physics are connected with Pauli formalism.

At first [1] electron was called "spinning". Then in Pauli article [2] it is become "magnetic". Question on a pointlike particle rotation does not yield to reasonable understanding, therefore spin was referred as inner or proper characteristic of a particle. Evidently it does not become more clear. As it was shown by Pauli situation does not improve, if we shall imagine electron as a ball with classical radius  $r_0 = e^2/m_e c^2$ . In this case contradiction arises with relativity requirement. Instantaneous velocity at the radius end exceeds light velocity 70 times.

It should be noted, that practically at that time [3] natural understanding arises that circular motion of the electron leads to magnetic manifestations. But Thomas did not refuse superposition on "inner magnetic moment". Therefore he obtained the precession of the pointlike magnet instead of the electron spin. Comparison of his calculations with proposed here shows, that so called Thomas precession has the same nature as electron spin.

Another dogma of the theory promoting initially adopted representation is a belief that interacting electron is characterized by the same properties as free one. Usual argument looks as following. It is impossible to represent why electron has four degrees of freedom in an atom and three in free state [4]. Evidently it is not a prove that the electron has

four degree of freedom in the free state . In opposition to this expression one can assume that all completeness of particle properties is become by interactions. Free Dirac equation describes both electron and positron. But it is possible to distinguish one from another by interaction with electromagnetic field.

As for our purpose main peculiarities of the 1/2 formalism are that  $\sigma$ - matrices generate finite group, it has no superfluous components as in the case of high spin fields and it satisfies relativity requirements without any stipulations.

## 2. Pauli matrices and the spin nature

Let us start from the conventional definition, that the spin is the proper angular momentum, having the quantum nature and which does not connected with particle movement as the whole [5].It is usual to describe the proper angular momentum equal 1/2 by Pauli  $\sigma$ -matrices.

$$\sigma_x = \begin{pmatrix} 0 & 1 \\ 1 & 0 \end{pmatrix}; \quad \sigma_y = \begin{pmatrix} 0 & -i \\ i & 0 \end{pmatrix}; \quad \sigma_z = \begin{pmatrix} 1 & 0 \\ 0 & -1 \end{pmatrix}.$$

It is easy to verify, that  $\sigma$ -matrices generate 16-order group. Let us denote this group as  $d_\gamma$ . The group has ten conjugate classes. Center of the group contains four elements. Group has eight one-dimensional and two inequivalent two-dimensional irreducible representations. Rank of the group is equal 3. This means that all three Pauli  $\sigma$ -matrices are necessary for generating the group.

Let us adopt the following notations [6]:

$$\sigma_z \sigma_y \equiv a_1, \quad \sigma_x \sigma_z \equiv a_2, \quad \sigma_y \sigma_x \equiv a_3$$

and

$$\sigma_x \equiv b_1, \quad \sigma_y \equiv b_2, \quad \sigma_z \equiv b_3$$

It is evidently, that

$$b_1 = a_1 c, \quad b_2 = a_2 c, \quad b_3 = a_3 c, \quad (1)$$

where  $c$  is one of four  $(I, -I, iI, -iI)$  elements of group centre and  $c = \sigma_x \sigma_y \sigma_z = iI$ . Here  $I$  is the unit  $2 \times 2$  matrix. It means, that operators  $a_1, a_2, a_3$  are connected with operators  $b_1, b_2, b_3$  by simple relations for the given irreducible representation

$$b_1 = ia_1, \quad b_2 = ia_2, \quad b_3 = ia_3. \quad (2)$$

It should be noted also, that

$$a_2 a_1 a_2^{-1} = a_1^{-1} = a_1^3, \quad a_1 a_2 \equiv a_3, \quad a_1^2 = a_2^2 = a_3^2. \quad (3)$$

It means, that elements  $a_1, a_2$  generate quaternion subgroup [7]. Let us denote it as  $Q_2[a_1, a_2]$ .

Assuming that element of the group  $d_\gamma$  are the generators of an algebra, we obtain the following commutative relations for the algebra based on the  $d_\gamma$  group (standard

representation)

$$\begin{aligned}
 [a_1, a_2] &= 2a_3, & [a_2, a_3] &= 2a_1, & [a_3, a_1] &= 2a_2, \\
 [b_1, b_2] &= -2a_3, & [b_2, b_3] &= -2a_1, & [b_3, b_1] &= -2a_2, \\
 [a_1, b_1] &= 0, & [a_2, b_2] &= 0, & [a_3, b_3] &= 0, \\
 [a_1, b_2] &= 2b_3, & [a_1, b_3] &= -2b_2, \\
 [a_2, b_3] &= 2b_1, & [a_2, b_1] &= -2b_3, \\
 [a_3, b_1] &= 2b_2, & [a_3, b_2] &= -2b_1.
 \end{aligned} \tag{4}$$

Up to the factor 2, these commutative relations coincide with commutative relations of the proper homogeneous orthochronous Lorentz group [8].

It follows from the first row of commutative relations (CR) (4), that elements  $a_1, a_2, a_3$  and all their products form the subgroup of 3-dimensional rotations. As it follows from derivation of commutative relations [8]  $b_1 = \sigma_x$ ,  $b_2 = \sigma_y$ ,  $b_3 = \sigma_z$  have the sense of infinitesimal operators of Lorentz transformations.

Taking into account anticommutation of the operators  $b_1, b_2, b_3$ , the second upper row of commutative relations (6) takes the form:

$$b_1 b_2 = -a_3, \quad b_2 b_3 = -a_1, \quad b_3 b_1 = -a_2, \tag{5}$$

All three equalities express in infinitesimal form well known fact - turn through some fixed angle one inertial system with respect to another under relativistic motion [9]. Further transition to repeating motion, for example orbital, leads to rotation. Then the total rotation and total momentum connected with total rotation will be sum of the orbital and so called spin momentum.

Thus the analysis of  $\sigma$ -matrix group on the base of CR (4), which are direct corollary of the Lorentz transformations, demonstrates, that so-called proper momentum of 1/2 spin particle is the result of a definite character of motion. It must be not free, nonlinear. This conclusion is in agreement with familiar fact. It is impossible to measure magnetic moment of the electron, connected with proper momentum, if it moves freely [4].

Explicit form of the operators  $a_1, a_2, a_3$  and  $b_1, b_2, b_3$  for irreducible representations allows to evaluate weight numbers, which specifies uniquely irreducible representations of the Lorentz group. It is necessary for this purpose to construct operators:

$$\begin{aligned}
 H_+ &= ia_1 - a_2, & F_+ &= ib_1 - b_2, \\
 H_- &= ia_1 + a_2, & F_- &= ib_1 + b_2, \\
 H_3 &= ia_3, & F_3 &= ib_3.
 \end{aligned}$$

Weight numbers is eigenvalue of the operators  $H_3 = ia_3$  and  $F_3 = ib_3$  [8]. Calculation of the eigenvalue gives  $l_0 = 1/2$  for the standard  $\sigma$ - matrices. We see, that first weight number ( $l_0$ ) coincides with spin value. One can show [11], that operators  $a_1, a_2, a_3$  as the elements of  $d_7$ -group have the same fourth order. Therefore any permutations of the elements  $a_1, a_2, a_3$  inside the operators  $H_+, H_-, H_3$  do not change value  $l_0$  and any of space axis may be selected as quantization axis.

The value of the first weight number is determined formally by operators  $a_1, a_2, a_3$ , i.e. by the subgroup of three-dimensional rotations. But generation of the spin rotation impossible without relativity, as it follows from above mentioned. It is undoubtedly truly to connect spin with quite definite quantum number, if the quantum numbers are

interpreted as indexes of groups [10]. But it is unprovable assumption to endow spin motion with physical value property, which exists in separation from motion as a whole.

Thus starting from conventional 1/2 spin formalism and taking no any additional assumption, we obtain one particular irreducible representation of the Lorentz group and as consequence physical interpretation of Pauli  $\sigma$ -matrices. Rigorously speaking it is applicable for description of the electrons or objects, which structures does not take into account.

### 3. T-conjugate representation

Exhaustive analysis of the Dirac  $\gamma$ -matrix group and consequent development [11], [12], [13] indicated necessity to supplement standard representation of Lorentz group by P-, T- and (PT)-conjugate representations. It was obtained in explicit form three groups  $f_\gamma, b_\gamma, c_\gamma$  in addition to  $d_\gamma$  group. All they realize different irreducible representations of the Lorentz group with first weight number  $l_0 = 1/2$ . These four groups are connected with four classes of transformations of the Lorentz group. It is usual to distinguish classes by determinant value ( $\pm 1$ ) and by sign change ( $\pm$ ) of the time component of the four-vector under transformations.

Four groups  $d_\gamma, f_\gamma, b_\gamma, c_\gamma$  are connected between themselves by discrete transformations or by T-, P- and (PT)-reflections. Such kind of transformations are known as an analytical continuations by group parameters.

Two groups namely  $b_\gamma$  and  $f_\gamma$  are the substructures of Dirac  $\gamma$ -matrix group besides of  $d_\gamma$  one. The group  $b_\gamma$  contains quaternion group as subgroup, but it is not isomorphic to  $d_\gamma$ . As a result commutative relations have the following form on the base of  $b_\gamma$ :

$$\begin{aligned}
 [a_1, a_2] &= 2a_3, & [a_2, a_3] &= 2a_1, & [a_3, a_1] &= 2a_2, \\
 [b'_1, b'_2] &= 2a_3, & [b'_2, b'_3] &= 2a_1, & [b'_3, b'_1] &= 2a_2, \\
 [a_1, b'_1] &= 0, & [a_2, b'_2] &= 0, & [a_3, b'_3] &= 0, \\
 [a_1, b'_2] &= 2b'_3, & [a_1, b'_3] &= -2b'_2, \\
 [a_2, b'_3] &= 2b'_1, & [a_2, b'_1] &= -2b'_3, \\
 [a_3, b'_1] &= 2b'_2, & [a_3, b'_2] &= -2b'_1.
 \end{aligned} \tag{6}$$

This set of CR is differed from (4) by sign of three commutators in the second upper row. It was named as (T)-conjugate with respect to standard one. The time as the parameter appears under Lorentz transformations just at this row. All remaining commutators are corollary of the first six commutators disposed at the first two lines.

Analog of  $\sigma$ -matrices for this representation, i.e. matrix form of  $b'_1, b'_2, b'_3$  has the view:

$$b'_1 = \begin{pmatrix} -i & 0 \\ 0 & i \end{pmatrix}; \quad b'_2 = \begin{pmatrix} 0 & -i \\ -i & 0 \end{pmatrix}; \quad b'_3 = \begin{pmatrix} 0 & -1 \\ 1 & 0 \end{pmatrix}.$$

Transition from CR (4) to CR (6) is realized by the substitution  $b_k \rightarrow b'_k = ib_k$ , ( $k = 1, 2, 3$ ). In this case we have transition between the groups  $d_\gamma \rightarrow b_\gamma$ . (T)-conjugation does not touch operators  $a_1, a_2, a_3$ , therefore it does not changes  $l_0 = 1/2$  and type of spin, i.e. all tree space axes are remained equivalent. It is the reason why particle and antiparticle have the same spin properties [13].

## 4. P-conjugate representation

Next kind of CR was obtained on the base of group  $f_\gamma$  [13]:

$$\begin{aligned}
 [a_1, a'_2] &= 2a'_3, & [a'_2, a'_3] &= -2a_1, & [a'_3, a_1] &= 2a'_2, \\
 [b'_1, b'_2] &= -2a'_3, & [b'_2, b'_3] &= 2a_1, & [b'_3, b'_1] &= -2a'_2, \\
 [a_1, b'_1] &= 0, & [a'_2, b'_2] &= 0, & [a'_3, b'_3] &= 0, \\
 [a_1, b'_2] &= 2b'_3, & [a_1, b'_3] &= -2b'_2, \\
 [a'_2, b'_3] &= -2b'_1, & [a'_2, b'_1] &= -2b'_3, \\
 [a'_3, b'_1] &= 2b'_2, & [a'_3, b'_2] &= 2b'_1.
 \end{aligned} \tag{7}$$

This representation was called (P)-conjugate, because distinctions are arisen at the level of 3-dimensional rotation subgroup with respect to standard group  $d_\gamma$ , i.e. at the first row. The transition from (4) to (7) is equivalent to following change  $a_2 \rightarrow ia'_2$ . By definition we obtain  $a_3 \rightarrow ia'_3$ . All changes of the signs in more lower rows are consequence of this primary change. In this case quaternion subgroup  $Q_2[a_1, a'_2]$  transforms in  $q_2[a_1, a_2]$  with the same determining relations between generators (see equalities (3)). One can show [13], that elements  $a_1, a_2, a_3$  of  $d_\gamma$  group have fourth order whereas elements  $a'_2, a'_3$  of  $f_\gamma$  have second order and element  $a_1$  has fourth order as previously. So that we have in the similar cases non-equivalence of space directions, or so-called asymmetry between left and right. One can show [13], that first weight number is obtained equal  $l_0 = 1/2$  for  $f_\gamma$ , if  $H_3 = ia_1$ . The number  $l_0$  is obtained pure imaginary for two other operators ( $H'_3 = a'_2, H''_3 = a'_3$ ), i.e. they have no physical sense for three-dimensional rotation subgroup.

Similar non-equivalence is observed for  $b'_1, b'_2, b'_3$  values. They explicit form is such for  $f_\gamma$  group:

$$b'_1 = \begin{pmatrix} 1 & 0 \\ 0 & -1 \end{pmatrix}; \quad b'_2 = \begin{pmatrix} 0 & 1 \\ -1 & 0 \end{pmatrix}; \quad b'_3 = \begin{pmatrix} 0 & -i \\ -i & 0 \end{pmatrix}.$$

Nevertheless the structure of commutative relations is the same on the whole as previously.

## 5. (PT)-conjugate representation

The fourth type of CR is connected with group  $c_\gamma$ :

$$\begin{aligned}
 [a_1, a'_2] &= 2a'_3, & [a'_2, a'_3] &= -2a_1, & [a'_3, a_1] &= 2a'_2, \\
 [b'_1, b'_2] &= 2a'_3, & [b'_2, b'_3] &= -2a_1, & [b'_3, b'_1] &= 2a'_2, \\
 [a_1, b'_1] &= 0, & [a_2, b'_2] &= 0, & [a_3, b'_3] &= 0, \\
 [a_1, b''_2] &= 2b''_3, & [a_1, b''_3] &= -2b''_2, \\
 [a'_2, b''_3] &= -2b''_1, & [a'_2, b''_1] &= -2b''_3, \\
 [a'_3, b''_1] &= 2b''_2, & [a'_3, b''_2] &= 2b''_1.
 \end{aligned} \tag{8}$$

This kind of CR was called (TP)-conjugate with respect to standard one (4), because it is consecutive action two conjugations. They commute between themselves therefore one can write (TP)=(PT). Comparison of CR (7) and (8) shows, that  $f_\gamma$  and  $c_\gamma$  are (T)-conjugate in the same way as  $d_\gamma$  and  $b_\gamma$ .

The first rows of CR (7) and (8) coincide, therefore all said about the first weight number  $l_0$  for  $f_\gamma$  is correctly for  $c_\gamma$ . It is confirmed a rule that T-conjugation does not

change spin properties. Matrix form of operators  $b''_1, b''_2, b''_3$ , i.e. analog of  $\sigma$ -matrices for  $c_\gamma$  has the view:

$$b''_1 = \begin{pmatrix} i & 0 \\ 0 & -i \end{pmatrix}; \quad b''_2 = \begin{pmatrix} 0 & -1 \\ -1 & 0 \end{pmatrix}; \quad b''_3 = \begin{pmatrix} 0 & i \\ -i & 0 \end{pmatrix}.$$

The study of possible types of lepton equations [12], [13],[14] exhibits, that presence in they structures of  $c_\gamma$  group leads to the particle description having longitudinal polarization only.

## 6. Conclusion

Main results of this article my be classified as a theoretical observations, because no assumptions was made. One particular irreducible representation of the Lorentz group was obtained and as a consequence we got physical interpretation of the  $\sigma$ -matrices having used well known formalism of Pauli matrices . Identical coincidence of Pauli  $\sigma$ -matrices with generators of irreducible representation Lorentz group makes words such as "spin is internal property (or proper angular momentum) of particle" not necessary or inappropriate.

Proposed interpretation of Pauli matrices does not cancel anything connected with spin electron, when it is placed in atom or in some other binding system. Difference arises from a conventional notion, when we think the free electron. The point is that particle properties are become apparent by interactions in all completeness. The spin is not exclusion, as it is shown.

## References

- [1] G.E. Uhlenbeck, S. Goudsmit, *Ersetzung der Hypothese vom unmechanischen Zwang durch eine Forderung bezüglich des inneren Verhaltens jedes einzelnen Elektrons* Naturwissenschaften. **13**, S.953 (1925). *Spinning electrons and the structure of spectra* Nature. **117**, p.264 (1926).
- [2] W.Pauli *Zur Quantenmechanik des magnetischen Electrons*, Zs f. Phys. **B.43**. S.601 (1927).
- [3] *Thomas L.H.* The Motion of the Spinning Electron (Letters to the Editor)//Nature. 1926 v 117, p.514. The kinematics of an Electron with an Axis//Philos. Mag. 1927. **3**, p.1-21.
- [4] N.F.Mott, H.S.W.Massey, *The theory of Atomic Collisions* (Clarendon Press, Oxford 1965; Mir, Moscow, 1969), p.204.
- [5] *Physical short encyclopedia* (Sov. Encyclopedia, Moscow, 1984), p.713 [in Russian].
- [6] O.S.Kosmachev, *Spin as a Kinematical Effect of the Relativity*, Preprint JINR, P2-2005-6 (Dubna, 2005) [in Russian].

- [7] O.S.Kosmachev, *A Physical Interpretation of Some Group Algebras*, Letters Part. and Nucl. v.1, N5. p.50 (2004).
- [8] M.A.Naimark, *Linear Representations of the Lorentz Group* (Fizmatgiz, Moskow, 1958), p.88 [in Russian].
- [9] C. Møller *The Theory of the Relativity*, (Clarendon Press Oxford, 1972; Atomizdat, Moscow 1975), p.39.
- [10] G.Weyl, *The Theory of Groups and Quantum Mechanics*,(Dover Publications, 1931; Nauka, Moscow, 1986 ), p.16.
- [11] O.S.Kosmachev, *On Invariants of Dirac Type Equations*, Preprint JINR, P2-2002-217 (Dubna, 2002) [in Russian].
- [12] O.S.Kosmachev, *Covariant Formulation of the Wave Equation for Doublet of Massive Neutral Leptons*, Preprint JINR, 4-2003-127 (Dubna, 2003) [in Russian].
- [13] O.S.Kosmachev, *The Wave Equation for the Neutrino Quartet* Letters Part. and Nucl. v.1, N5. p.58 (2004).
- [14] S.I.Vinitzky, A.A. Gusev, O.S.Kosmachev, *Singlet States of Lepton*, Preprint JINR, P2-2004-106 (Dubna, 2004) [in Russian].

# THE POLARISED CHARGE-EXCHANGE REACTION $\vec{d} + p \rightarrow (pp)_{1S_0} + n$

Victor Glagolev on behalf of the ANKE Collaboration<sup>1</sup>

*Joint Institute for Nuclear Research,  
Laboratory of High Energy, 141980 Dubna, Russia,  
E-mail: glagolev@sunhe.jinr.ru*

## Abstract

During our study of the  $pd \rightarrow n(pp)$  reaction in the backward direction at ANKE, we have acquired considerable expertise in measuring two protons at low relative momentum such that they are in the peak of the  $^1S_0$  final state interaction. We now wish to exploit this technique, together with the possibilities offered by the acceleration of polarised deuterons at COSY, to measure the  $\vec{d}p \rightarrow (pp)_{1S_0}n$  charge-exchange reaction near the forward direction, *i.e.* where the four-momentum transfer  $t$  between the proton and neutron is small. The cross section and analysing power data can then be interpreted in terms of the amplitudes of the  $np \rightarrow pn$  charge-exchange reaction and our results should provide information on the spin-spin terms in the amplitude in the energy range above 800 MeV (LAMPF) and up to the maximum beam energy per nucleon achievable at COSY, *viz.* 1150 MeV.

The first results of this study from the ANKE facility are presented.

## 1. Introduction

The complete description of the  $NN$  interaction requires precise data as input to phase-shift analyses (PSA), from which the scattering amplitudes can be reconstructed. The PSA generally requires experiments with both beam and target particles polarised in the initial state, as well as polarisation determination of final state particles [1]. Experiments of this type have been carried out for the  $pp$  system to about 3.0 GeV [2, 3]. Due to the absence of polarised neutron beams, there has been much less work done on spin observables in elastic  $np$  scattering above 800 MeV [4, 5]. As a consequence, the PSA for isospin  $I = 0$  are poorly tested in this region. Precise new data are needed in order to try to bridge the gap with the  $pp$  system. Information can be obtained on the spin-dependent  $np$  elastic amplitudes near the backward direction (the charge-exchange region) by measuring the charge-exchange breakup of polarised deuterons on an unpolarised hydrogen target.

### 1.1. Scientific motivation

We propose to study the spin structure of the amplitudes of the elementary  $np \rightarrow pn$  charge-exchange (CE) process *via* the deuteron-induced  $\vec{d}p \rightarrow (pp)n$  reaction, where the proton in the deuteron acts largely as a spectator. The aim is to enhance substantially the existing  $np$  data base above  $T_n = 800$  MeV at small angles  $\theta$  between incoming neutron and outgoing proton. While the ongoing proton-induced deuteron breakup experiment [6] aims at an investigation of short-range features of the deuteron structure by looking at high-momentum transfer, the new proposal focuses on the region of small four-momentum transfer  $t$  between the proton and neutron, where the cross sections are much larger.

---

<sup>1</sup>See <http://www.fz-juelich.de/ikp/anke/>

The possibility of using the CE reaction on the unpolarised deuteron in order to determine of the spin-dependent part of the elementary CE process was emphasised already in 1951 by Pomeranchuk [7]. The effect can be understood qualitatively as follows. The two nucleons in the deuteron are in  $I = 0$ ,  ${}^3S_1$  or  ${}^3D_1$ . The spatial and spin states are symmetric so that, by the generalised Pauli principle, the isospin state is antisymmetric. In the charge-exchange reaction at  $0^\circ$ , the transition to a spin antisymmetric  ${}^1S_0$  state of two protons therefore requires a spin flip. The overall intensity of the spin-dependent parts of the elementary  $np \rightarrow pn$  CE amplitude can thus be inferred from the probability of the  $dp$  CE process. Furthermore, it has been shown that by measuring the deuteron tensor analysing powers it is possible to separate the intensities of the different spin amplitudes [8, 9]. Under special kinematic conditions (scattering angle  $\theta$  close to zero and momentum transfer  $t \sim 0$ ), the  $dp$  CE differential cross section is actually fully determined by the spin-dependent parts of the elementary  $np \rightarrow pn$  amplitude.

The experimental programme is divided into two parts:

1. The first stage will utilize unpolarised and tensor polarised deuteron beams incident on an unpolarised hydrogen cluster target. The differential cross section gives only the overall intensity of the spin-dependent parts of the elementary CE process. Tensor polarised deuteron beam enables us to separate the absolute values of three spin-dependent amplitudes.
2. Using transversely polarised deuterons incident on a polarised internal hydrogen gas target and measuring the spin-correlation coefficient opens the possibility of obtaining the relative phase between amplitudes.

## 1.2. Determination of the scattering matrix

### 1.2.1. Scattering amplitudes

The amplitude of the elementary  $np \rightarrow pn$  reaction in the cm system can be written in terms of five scalar amplitudes

$$f_{np} = \alpha + i\gamma(\sigma_n + \sigma_p)\mathbf{n} + \beta(\sigma_n \cdot \mathbf{n})(\sigma_p \cdot \mathbf{n}) + \delta(\sigma_n \cdot \mathbf{m})(\sigma_p \cdot \mathbf{m}) + \varepsilon(\sigma_n \cdot \mathbf{l})(\sigma_p \cdot \mathbf{l}), \quad (1)$$

where  $\sigma_n$  and  $\sigma_p$  are the Pauli matrices for neutron and proton, respectively. The orthogonal unit vectors are defined in terms of the initial ( $\mathbf{k}$ ) and final ( $\mathbf{k}'$ ) momenta as

$$\mathbf{n} = \frac{\mathbf{k} \times \mathbf{k}'}{|\mathbf{k} \times \mathbf{k}'|}, \quad \mathbf{m} = \frac{\mathbf{k}' - \mathbf{k}}{|\mathbf{k}' - \mathbf{k}|}, \quad \mathbf{l} = \frac{\mathbf{k}' + \mathbf{k}}{|\mathbf{k}' + \mathbf{k}|}.$$

The amplitudes are normalized such that the elementary  $np \rightarrow pn$  differential cross section has the form

$$\left(\frac{d\sigma}{dt}\right)_{np \rightarrow pn} = I_{np} = |\alpha|^2 + |\beta|^2 + 2|\gamma|^2 + |\delta|^2 + |\varepsilon|^2, \quad (2)$$

where  $\alpha$  is the spin-independent amplitude,  $\gamma$  is related to the spin-orbit coupling, and  $\beta$ ,  $\delta$ , and  $\varepsilon$  are the spin-spin amplitudes. The one-pion-exchange pole is contained purely in the  $\delta$  amplitude and this gives rise to its very rapid variation with momentum transfer.

For low excitation energy  $E_{pp} < 3$  MeV of the final  $pp$  pair, and at low transferred three-momentum ( $q \approx 0$ ) from proton to neutron (or from deuteron to diproton), the

charge exchange reaction  $dp \rightarrow (pp)n$  mainly excites the  ${}^1S_0$  state of the final  $pp$  system. In impulse approximation, *i.e.* single  $np \rightarrow pn$  scattering, the resulting amplitude depends only upon the spin-dependent parts of  $f_{np}$ , *i.e.*  $\beta$ ,  $\gamma$ ,  $\delta$  and  $\varepsilon$  [9]. The form factor describing the transition from a deuteron with spin-projection  $\lambda$  to a ( ${}^1S_0$ )-state of the final  $pp$  pair contains two terms

$$S^+(k, \frac{1}{2}q) = F_S(k, \frac{1}{2}q) + \sqrt{2}F_D(k, \frac{1}{2}q), \quad (3)$$

$$S^-(k, \frac{1}{2}q) = F_S(k, \frac{1}{2}q) - \frac{1}{\sqrt{2}}F_D(k, \frac{1}{2}q). \quad (4)$$

The  $S^+$  and  $S^-$  denote the longitudinal ( $\lambda = 0$ ) and transverse ( $\lambda = \pm 1$ ) form factors. The matrix elements  $F_S$  and  $F_D$  can be expressed by the  $S$  and  $D$  components of the deuteron wave function  $u(r)$  and  $w(r)$  and the  $pp({}^1S_0)$ -scattering wave function  $\psi_k^{(-)}(r)$  as

$$F_S(k, \frac{1}{2}q) = \langle \psi_k^{(-)} | j_0(\frac{1}{2}qr) | u \rangle, \quad (5)$$

$$F_D(k, \frac{1}{2}q) = \langle \psi_k^{(-)} | j_2(\frac{1}{2}qr) | w \rangle. \quad (6)$$

Here  $k$  is the  $pp$  relative momentum, corresponding to an excitation energy  $E_{pp} = k^2/m$ , where  $m$  is the proton mass. Denoting the ratio of the transition form factors by

$$R = \frac{S^+(k, \frac{1}{2}q)}{S^-(k, \frac{1}{2}q)} \quad (7)$$

and

$$I = |\beta|^2 + |\gamma|^2 + |\varepsilon|^2 + |\delta|^2 R^2, \quad (8)$$

for the sum of squared amplitudes, differential cross section, tensor analysing powers, and spin-spin correlation parameters  $C_{y,y}$ ,  $C_{x,x}$ ,  $C_{z,z}$  of the  $dp \rightarrow (pp)_{1S_0}n$  reaction assume the forms [10, 11]

$$\frac{d^4\sigma}{dt d^3k} = \frac{1}{3} I \left\{ S^-(k, \frac{1}{2}q) \right\}^2, \quad (9)$$

$$I T_{20} = \frac{1}{\sqrt{2}} \{ |\gamma|^2 + |\beta|^2 + |\delta|^2 R^2 - 2|\varepsilon|^2 \}, \quad (10)$$

$$I T_{22} = \frac{\sqrt{3}}{2} \{ |\gamma|^2 + |\beta|^2 - |\delta|^2 R^2 \}, \quad (11)$$

$$I C_{y,y} = -2\Re(\varepsilon^* \delta) R, \quad (12)$$

$$I C_{x,x} = -2\Re(\beta^* \varepsilon), \quad (13)$$

$$I C_{z,z} = -2\Re(\delta^* \beta) R. \quad (14)$$

Thus, a measurement of the differential cross section,  $T_{20}$ , and  $T_{22}$  will allow us to extract the  $|\beta|^2 + |\gamma|^2$ ,  $|\delta|^2$ , and  $|\varepsilon|^2$  intensities over a range in  $q$  near the forward direction. Since  $\gamma$  vanishes at  $q = 0$  and is generally small in our energy and angular domain, this means that our experiment essentially leads to a determination of the absolute values of the spin-spin amplitudes in  $np$  charge exchange. It is important to note that amplitude analysis at 800 MeV shows that the spin-independent term  $\alpha$  is much smaller than  $\beta$  [12].

In order to get the relative phases of the spin-spin amplitudes requires spin-correlation and spin-transfer information and for this the situation simplifies enormously in the forward direction.

### 1.2.2. Collinear kinematics

In collinear kinematics, where all momenta lie along the beam direction,  $\mathbf{k} = \mathbf{k}'$ , the number of scalar amplitudes in Eq. (1) reduces from five to three because of the azimuthal symmetry. In this limit

$$\delta = \beta \quad \text{and} \quad \gamma = 0. \quad (15)$$

At  $q = 0$  the  $D$ -wave form factor vanishes,  $R = 1$ , and also  $T_{22} = 0$ . One then finds from Eqs. (9-13)

$$\frac{d^4\sigma}{dt d^3k} = \frac{1}{3} \{ |\varepsilon|^2 + 2|\beta|^2 \} F_S^2(k, 0), \quad (16)$$

$$I = 2|\beta|^2 + |\varepsilon|^2, \quad (17)$$

$$I T_{20} = \sqrt{2} \{ |\beta|^2 - |\varepsilon|^2 \}, \quad (18)$$

$$I C_{y,y} = I C_{x,x} = -2\Re(\varepsilon\beta^*). \quad (19)$$

Furthermore

$$I C_{xz,y} = -I C_{yz,x} = 3\Im(\beta\varepsilon^*). \quad (20)$$

Having found the moduli of the amplitudes  $\beta$  and  $\varepsilon$ , a measurement of the spin-spin correlation factor  $C_{y,y}$  yields the cosine of the relative phase,  $\cos(\varphi_\varepsilon - \varphi_\beta)$ . This will require a vector polarised deuteron beam and a hydrogen target. In order to resolve the remaining ambiguity, one has for example to measure also the sign of the spin-tensor coefficient  $C_{xz,y}$ . The deuteron charge exchange experiment is, of course, completely insensitive to the value of  $\alpha$ .

### 1.2.3. Closure approximation

Integrating Eq. (16) over the full phase space in  $d^3k$ , one can obtain closure sum rules that are insensitive to the details of the final  $pp$  interaction [13]. For example, at  $q = 0$  one finds that

$$\left( \frac{d\sigma}{dt} \right)_{dp \rightarrow (pp)n} = \frac{1}{3} (2|\beta|^2 + |\varepsilon|^2) [2 + P_D], \quad (21)$$

$$T_{20} \left( \frac{d\sigma}{dt} \right)_{dp \rightarrow (pp)n} = \frac{2\sqrt{2}}{3} (|\beta|^2 - |\varepsilon|^2) \left[ 1 - \frac{9}{10} P_D \right], \quad (22)$$

where  $P_D$  is the  $D$ -state probability in the deuteron. Although the region where  $t \approx 0$  would represent only a small part of our total data sample, it is interesting to note that the closure approximation describes to within about 10% the non-charge exchange inelastic scattering cross section  $pd \rightarrow p(pn)$  [14] at GeV energies within the Glauber-Franco theory [15].

### 1.2.4. Deuteron-induced charge-exchange (CE) reaction $dp \rightarrow (pp)n$

The deuteron-induced CE breakup reaction  $dp \rightarrow (pp)n$  was studied in the 1 m hydrogen bubble chamber (HBC) at the 3.34 GeV/c deuteron beam of the JINR Synchrophasotron. The first results, on a relatively small fraction of the processed events, were published [16, 17]. The authors returned to this problem, exploiting the final charge-exchange statistics of over  $10^5$  events [18]. Their aim was to estimate the possibilities and limitations of a counter experiment STRELA [19], which had been proposed to study the spin-dependent part of the  $np$  charge-exchange amplitudes using the JINR Nuclotron deuteron beam in the momentum range from 3.0 to 4.0 GeV/c. However, the information extracted from the bubble chamber experiment at small angles ( $\leq 3^\circ$ ) is not sufficient to observe the behavior of the differential cross section close to  $0^\circ$ .

The deuteron tensor analysing powers in the  $dp \rightarrow (pp)n$  reaction should be especially strong in regions where the  $pp$  excitation energy is small and the momentum transfer to the neutron is of the order of pion mass or less [8, 9]. This reaction provides information equivalent to that of  $(\vec{n}, \vec{p})$  [20], without the need to measure the polarisation of the outgoing particles. It has also been used as the basis of an efficient analyser of deuteron-tensor polarisations at intermediate energies [10]. The impulse approximation predictions have been tested at energies of  $T_d = 200$  MeV and 350 MeV [21] with the EMRIC apparatus and at  $T_d = 1.6$  and 2.0 GeV with the SPES4 magnetic spectrometer [22, 23]<sup>2</sup>. The kinematics of the latter experiments are quite close to those of the present proposal, though it should be noted that the acceptance of the SPES4 spectrometer for two protons was not sufficiently well understood to allow for the extraction of absolute cross sections. Nucleon-nucleon charge exchange amplitudes were therefore introduced into the analysis and, after testing on the nucleon, were used in the study of spin-isospin excitations in nuclei. The main purpose of these experiments, in fact, was the investigation of the spin structure of the  $\Delta$  excitation on a nucleon and in a nucleus.

The main effort of the other deuteron breakup experiments at large momentum transfers was focused on the study of the reaction mechanisms and deuteron structure at small distances (for a review see Ref. [24]).

Since we can measure normalized cross sections, our experiment will be the first that can provide data necessary to determine the spin-dependent part of the elementary  $np \rightarrow pn$  CE process in the energy range of about 1 GeV by investigation of the deuteron-induced CE reaction.

## 2. Charge-Exchange deuteron break-up at ANKE

The first measurement of the deuteron-induced Charge-Exchange reaction was carried out at the ANKE spectrometer [25] using a polarised deuteron beam at  $p_d = 2400$  MeV/c ( $T_d = 1170$  MeV).

In Fig. 1 those parts of the spectrometer are shown that are relevant for the present experiment. The polarised deuterons stored in the COSY ring ( $\approx 3 \times 10^9$  deuterons) impinge on a hydrogen cluster-jet target (thickness  $\approx 1 \times 10^{14}$  atoms/cm<sup>2</sup>, resulting in a luminosity of  $\approx 3 \times 10^{29}$  cm<sup>-2</sup>s<sup>-1</sup>).

---

<sup>2</sup>Double scattering effects are generally small at low angles and can be estimated in an eikonal approach [9].

Two fast protons, emitted in a narrow forward cone with momenta around half that of the deuteron beam, are detected by the Forward detector (FD) system of the ANKE set-up. The detection of proton pairs in the forward direction was already successfully achieved in our proton-induced deuteron break-up experiment [6], which was studied in the region of large momentum transfers. A silicon telescope system, consisting of three layers of silicon strip detectors [26], is mounted in the target vacuum chamber as a near-target detector.

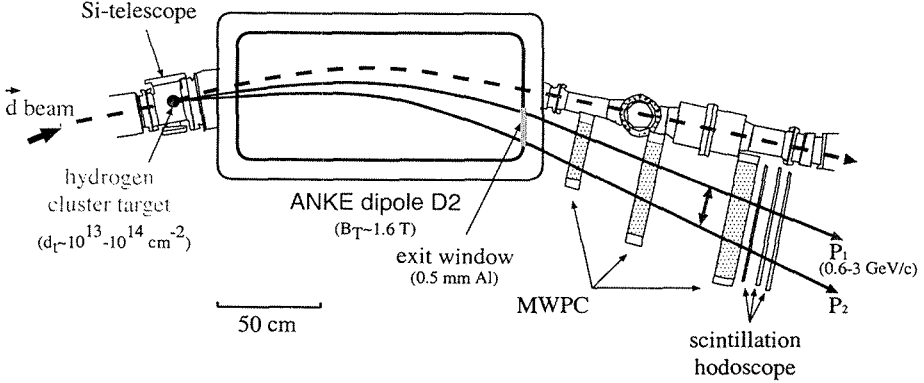


Figure 1: Schematic drawing of the part of the ANKE spectrometer used in the  $\vec{d}p \rightarrow (pp)_{1S_0} + n$  experiment

Figure 2 shows the ANKE experimental acceptance for singly charged particles for different reactions as functions of the laboratory production angle and magnetic rigidity, together with loci for the kinematics of different allowed reactions. The  $dp \rightarrow dp$  reaction has a significant acceptance for  $4^\circ < \theta_{\text{lab}}^d < 10^\circ$ . The observables  $A_y$ ,  $A_{yy}$ , and  $A_{xx}$  of this reaction were studied at Argonne[33] and SATURNE[34] for  $T_d = 1198$  MeV.

The elastic peak region in the momentum spectrum of the single track events (left panel of Fig. 3) was fitted by the sum of a Gaussian and linear function, and events selected within  $3\sigma$  of the mean. An example of such a fit is shown the right panel.

The  $dp \rightarrow {}^3\text{He}\pi^0$  reaction can be studied using just the  ${}^3\text{He}$  information. The high momentum branch of  ${}^3\text{He}$  particles was isolated well in off-line analysis, applying two-dimensional cuts in  $\Delta E$  versus momentum and  $\Delta t$  versus momentum for individual layers of the forward hodoscope.

The quasi-free  $np \rightarrow d\pi^0$  can be clearly identified in ANKE by detecting two final charged particles in the  $dp \rightarrow p_{sp}d\pi^0$  reaction, where  $p_{sp}$  is a spectator proton which has essentially half the beam momentum. The differential cross section should be half of that for  $pp \rightarrow d\pi^+$ , whereas all the analysing powers should be equal.

The charge-exchange process was identified from the missing-mass with respect to the observed proton pairs (see Fig. 4) and time difference information. The spectra for all spin modes reveal a well defined peak at  $M_{\text{miss}}$  equal to the neutron mass to within 1%; the mean value for the reconstructed neutron mass is  $M_n = 940.4 \pm 0.2$  MeV/c<sup>2</sup>. The

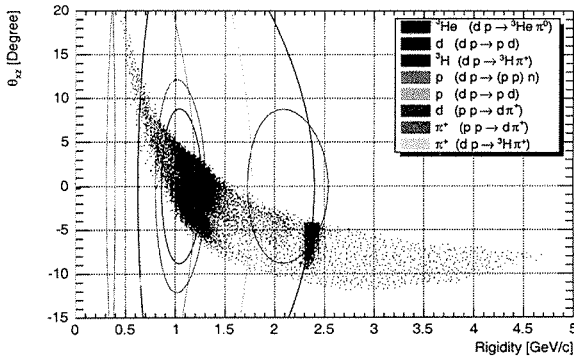


Figure 2: ANKE experimental acceptance for different reactions in  $dp$  collisions at  $T_d = 1170$  MeV

background was less than 2% and stable, so that the charge-exchange process could be reliably identified.

Using  $\vec{d}p \rightarrow dp$ ,  $\vec{d}p \rightarrow (2p)n$ ,  $\vec{n}p \rightarrow d\pi^0$ , and  $\vec{d}p \rightarrow {}^3\text{He}\pi^0$  reactions, which all have large and well determined analysing powers, a simultaneous calibration of the vector and tensor components of the polarised deuteron beam at COSY becomes possible for the first time. The results are summarized in Table 1[32].

Reaction	Facility	$\alpha_z$	$\alpha_{zz}$
$\vec{d}p \rightarrow dp$	EDDA	$0.74 \pm 0.02$	$0.59 \pm 0.05$
$\vec{d}p \rightarrow dp$	ANKE	$0.73 \pm 0.02$	$0.49 \pm 0.02$
$\vec{n}p \rightarrow d\pi^0$	ANKE	$0.70 \pm 0.03$	—
$\vec{d}p \rightarrow {}^3\text{He}\pi^0$	ANKE	—	$0.58 \pm 0.05$
$\vec{d}p \rightarrow (pp)n$	ANKE	—	$0.48 \pm 0.05$

Table 1: Values of vector and tensor beam polarisation parameters determined in different experiments. The given errors are only statistical, and other systematic effects have still to be investigated.

The average of the ANKE measurements is  $\alpha_z^{\text{ANKE}} = 0.72 \pm 0.02$  and  $\alpha_{zz}^{\text{ANKE}} = 0.52 \pm 0.03$ , which is compatible with EDDA results [35].

Figure 5 shows predictions for the values of the moduli of the two forward spin-flip amplitudes, as functions of energy[30]. In impulse approximation the forward differential cross section is proportional to  $2|\beta(0)|^2 + |\epsilon(0)|^2$  times form factors. In the region  $E_{pp} \leq 2$  MeV, the final  $pp$  system is essentially pure  $S$ -wave and acceptance corrections largely

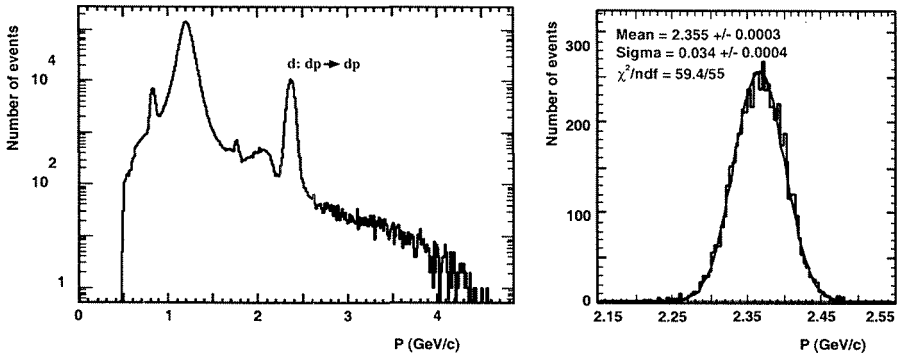


Figure 3: Left: Single-track momentum spectrum for the  $dp$  data at 2.40 GeV/c. Right: Fit result of the elastic peak region with the sum of a Gaussian and linear function

cancel out for the analysing powers. Thus, in the forward direction,

$$T_{20} = \sqrt{2} \left( \frac{|\beta(0)|^2 - |\varepsilon(0)|^2}{2|\beta(0)|^2 + |\varepsilon(0)|^2} \right),$$

so that the ratio of the two forward spin-dependent  $np \rightarrow pn$  amplitudes can already be deduced from our preliminary results.

The energy dependence of the predicted  $T_{20}$  using the SAID input is also shown in Fig. 5 along with our value of  $T_{20} = 0.39 \pm 0.04$ . Alternatively, using this value, we obtain  $|\beta(0)|/|\varepsilon(0)| = 1.86 \pm 0.15$ , to be compared to the SAID  $1.79 \pm 0.27$ . Thus our statistical error is already superior.

### 3. Conclusion

The first measurement of the CE deuteron break-up reaction  $\vec{d} + p \rightarrow (pp)_{1S_0} + n$  was carried out at the ANKE spectrometer using a polarized deuteron beam at  $P_d = 2400$  MeV/c. It has been shown, that the method of definition of the spin-dependent amplitudes of the np-scattering justified itself. The measurement of  $T_{20}$  has allowed to determine the ratio of the two spin-dependent amplitudes  $|\beta(0)|/|\varepsilon(0)| = 1.86 \pm 0.15$  with the better accuracy than in the current SAID database.

### References

- [1] J. Bystricky et al., Nucl. Phys. A444 (1985) 597.
- [2] R.A. Arndt et al., Phys. Rev. C50 (1994) 2731; C56 (1997) 3005.
- [3] M. Altmeier et al., Phys. Rev. Lett. 85 (2000) 1819.

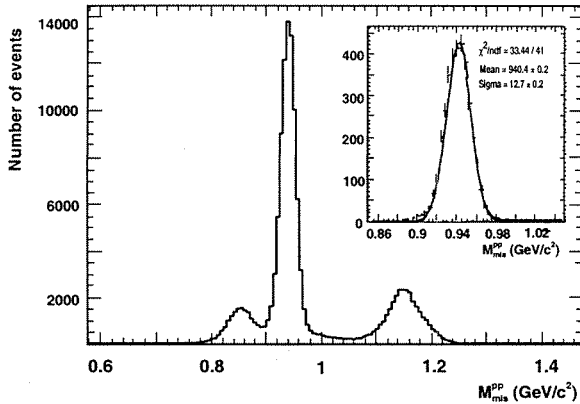


Figure 4: Missing mass distribution of all observed proton pairs. The inset shows the distribution near the neutron mass for the pairs selected by the time-of-flight difference

- [4] R.A. Arndt et al., Phys. Rev. C62 (2000) 034005; C56 (1997) 3005.
- [5] A. de Lesquen et al., Eur. Phys. J C11 (1999) 69.
- [6] V. Komarov et al., Phys. Lett. B553 (2003) 179.
- [7] I. Pomeranchuk, Doklady Akademii Nauk USSR,78 (1951) 249.
- [8] D.V. Bugg and C. Wilkin, Phys. Lett. B152 (1985) 37.
- [9] D.V. Bugg and C. Wilkin, Nucl. Phys. A467 (1987) 575.
- [10] J. Carbonell, M.B. Barbaro and C. Wilkin, Nucl. Phys. A529 (1991) 653.
- [11] M.B. Barbaro, C. Wilkin, J. Phys. J.Part. Nucl. 15 (1989) L69.
- [12] R. Dubois et al., Nucl. Phys. A377 (1982) 554.
- [13] N.W. Dean, Phys. Rev. D5 (1972) 1661; Phys. Rev. D5 (1972) 2832.
- [14] Yu.N. Uzikov. Annual Rep. IKP FZ Jülich, 2001 (2002) p.66.
- [15] V.Franco, R. Glauber. Phys. Rev. 142 (1966) 1195.
- [16] B. Aladashvili et al., Nucl. Phys. B86 (1975) 461.
- [17] B. Aladashvili et al., J. Phys. G: Nucl. Phys. 3 (1977) 1225 .
- [18] V.V. Glagolev et al., Eur. Phys. J. A15 (2002) 471.
- [19] V.V. Glagolev et al., Part. Nucl. Lett. 100 (2000) 67.

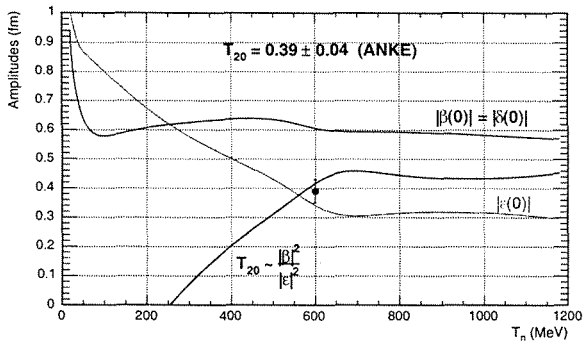


Figure 5: Predictions for the moduli of the two independent  $np \rightarrow pn$  scattering amplitudes at  $t = 0$ , taken from the SAID database[30], along with the associated prediction of  $T_{20}$  for  $\vec{d}p \rightarrow (pp)_{S_0}n$  in impulse approximation. The latter is compared to our preliminary value of  $T_{20} = 0.39 \pm 0.04$  at  $\frac{1}{2}T_d = 600$  MeV

- [20] C. Wilkin and D.V. Bugg, Phys. Lett. B154 (1985) 243.
- [21] S. Kox et al., Nucl. Phys. A556 (1993) 621.
- [22] C. Ellegard et al., Phys. Rev. Lett. 59 (1987) 974.
- [23] C. Ellegard et al., Phys. Lett. B231 (1989) 365.
- [24] S.L. Belostotski et al., Phys. Rev. C56 (1997) 50.
- [25] S. Barsov et al., Nucl. Instr. and Meth. A462 (2001) 364.
- [26] I. Lehmann et al., Nucl. Instr. and Meth. A530 (2004) 275.
- [27] C. Kerboul, Phys. Lett. 181B (1986) 28.
- [28] K. Yonehara et al., AIP Conf. Proc. 698 (2003) 763.
- [29] J.L. Friedes et al., Phys. Rev. Lett. 15 (1965) 38.
- [30] SAID database, <http://gwdac.phys.gwu.edu/analysis/>
- [31] N. Katayama et al. Nucl. Phys. A438 (1985) 685.
- [32] D. Chiladze et al., 'Deuteron Polarimetry at ANKE', Internal note, <http://www.fz-juelich.de/ikp/anke>, August (2004)
- [33] M. Haji-Said et al., Phys. Rev. C36, 2010 (1987).
- [34] J. Arvieux et al., Nucl. Instrum. Methods A273, 48 (1988).
- [35] B. Lorentz et al., submitted to the proceedings of 9<sup>th</sup> European Particle Accelerator Conference, July 5-9, 2004, Lucerne, Swiss.

# SINGLE SPIN ASYMMETRY IN HIGH $P_T$ CHARGED HADRON PRODUCTION OFF NUCLEI AT 40 GeV

V.V. Abramov<sup>1†</sup>, P.I. Goncharov<sup>1</sup>, A.Yu. Kalinin<sup>1</sup>, A.V. Khmel'nikov<sup>1</sup>, A.V. Korablev<sup>1</sup>, Yu.P. Kor'neev<sup>1</sup>, A.V. Kostitskiy<sup>1</sup>, A.N. Krinitsyn<sup>1</sup>, V.I. Kryshkin<sup>1</sup>, A.A. Markov<sup>1</sup>, V.V. Talov<sup>1</sup>, L.K. Turchanovich<sup>1</sup> and A.A. Volkov<sup>1</sup>

(1) *Institute for High Energy Physics, Protvino, Moscow region, Russia*

† *E-mail: abramov.v@mx.ihep.su*

## Abstract

The single transverse spin asymmetry data for the charged hadron production in pC and pCu interactions are presented. The measurements have been performed at FODS-2 experimental setup using 40 GeV/c IHEP polarized proton beam. The hadron transverse momentum range is from 0.5 GeV/c up to 4 GeV/c. The data obtained off the nuclear targets are compared with the proton target data measured earlier with the same experimental setup and with the data of other experiments.

**Key-words:** spin, asymmetry, hadron production, polarization, quarks, QCD.

## 1. Introduction

The experiments performed during the last 25 years show, that the single spin asymmetries in hadron hadron interactions are much larger than expected from the naive pQCD. Also the hyperon transverse polarization is unexpectedly large in collisions of unpolarized hadrons. The perturbative QCD predicts vanishing of single spin effects due to the vector nature of gluons and a small current quark mass. There were no measurements so far of single spin asymmetries of charged hadron production in the energy range between 22 and 200 GeV. We have measured the single-spin asymmetry  $A_N$  of the inclusive charged pion, kaon, proton and antiproton production cross sections at high  $x_T$  and high  $x_F$  for a 40 GeV/c polarized proton beam incident on nuclei (C, Cu), where  $A_N$  is defined as

$$A_N = \frac{1}{P_B \cdot \cos\phi} \cdot \frac{N\uparrow - N\downarrow}{N\uparrow + N\downarrow}, \quad (1)$$

where  $P_B$  is the beam polarization,  $\phi$  is the azimuthal angle of the production plane,  $N\uparrow$  and  $N\downarrow$  are event rates for the beam spin up and down respectively. The measurements were carried out at IHEP, Protvino in 2003.

## 2. Polarized beam and experimental setup

The polarized protons are produced by the parity - nonconserving  $\Lambda$  decays [1]. The schematic layout of the polarized beam line is shown in Fig. 1. The up or down beam transverse polarization is achieved by the selection of decay protons with angles near  $90^\circ$  in the  $\Lambda$  rest frame by a movable collimator. At the end of the beam line two magnets correct

the vertical beam position on the spectrometer target for the two beam polarizations. The intensity of the 40 GeV/c momentum polarized beam on the spectrometer target is  $3 \times 10^7$  ppp,  $\Delta p/p = \pm 4.5\%$ , the transverse polarization is  $39_{-3}^{+1}\%$ , and the polarization direction is changed each 18 min during 30 s. The beam intensity and the position are measured by ionization chambers and scintillation hodoscopes.

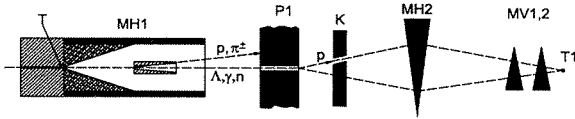


Figure 1: Schematic of polarized proton beam line

Two Cherenkov counters identify the beam particle composition to control the background contamination. At the spectrometer magnet entrance there are two scintillation hodoscopes to measure the vertical coordinates of the particles emitted from the target.

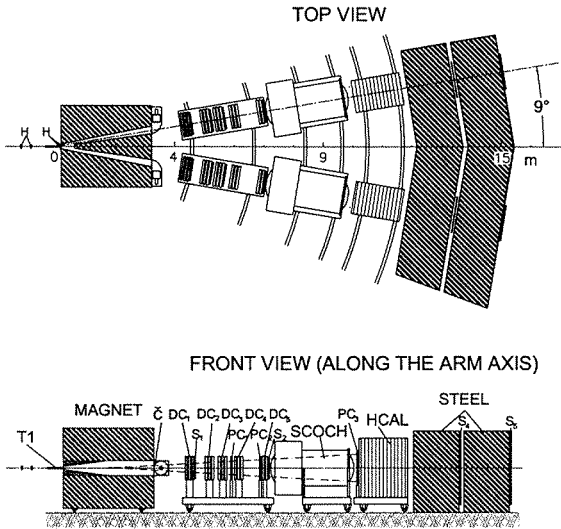


Figure 2: Schematic of experimental layout FODS-2

The measurements have been carried out with the FODS-2 [1] spectrometer (Fig. 2). It consists of an analyzing magnet, drift chambers, the Cherenkov radiation spectrometer (SCOCH) for the particle identification ( $\pi^\pm$ ,  $K^\pm$ ,  $p$  and  $\bar{p}$ ), the scintillation counters, and the hadron calorimeters to trigger on the high energy hadrons. Inside the magnet there is also a beam dump made of tungsten and copper. There are two arms which can be rotated around the target center situated in front of the magnet to change the secondary particle angle. The Cherenkov radiation spectrometer (Fig. 3) consists of a spherical mirror with the diameter 110 cm, 24 cylindrical lenses to focus the Cherenkov light on the hodoscope

photomultipliers. Measuring the particle velocity using the SCOCH and its momentum in the magnetic field one can determine the particle square mass  $M^2$  (Fig. 4). The SCOCHs are filled with Freon 13 at 8 atm.

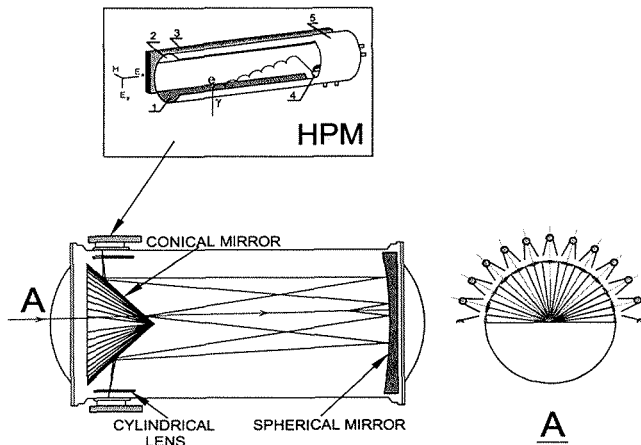


Figure 3: Schematic of the SCOCH optics

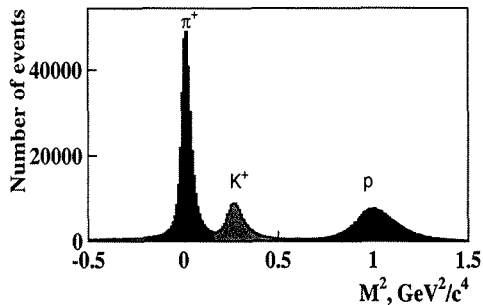


Figure 4: Reconstructed hadron mass squared  $M^2$  in the SCOCH spectrometer

There are two threshold Cherenkov counters using air at the atmospheric pressure inserted in the magnet which are used for further improvement of particle identification.

### 3. Measurements

In 1994 the study of the single spin asymmetry ( $A_N$ ) in the inclusive charge hadron production was started using FODS-2:

$$p \uparrow + p(A) \rightarrow h^\pm + X, \quad (2)$$

$$p\uparrow + p(A) \rightarrow h^\pm + h^\pm + X, \quad (3)$$

where  $h^\pm$  is a charged hadron (pion, kaon, proton or antiproton). The experimental program consists of measuring the charge hadron single spin asymmetry at high  $x_T$  and  $x_F$  in pp and pA collisions to study the asymmetry dependence on the quark flavors u, d, s and kinematical variables.

The pilot measurements of  $A_N$  for the charged hadrons carried out in 1994 with a hydrogen target for small  $x_F$  [1] are presented below for the comparison with the data obtained with nuclei. The data for large  $x_F \leq 0.7$  were also measured in 2003.

The measurements of  $A_N$  in the range  $-0.15 \leq x_F \leq 0.2$  and  $0.5 \leq p_T \leq 4$  GeV/c are carried out with symmetrical arm positions at angles of  $\pm 160$  mrad. The results for the two arms and the different values of magnetic field in the spectrometer are averaged, which partially cancels systematical uncertainties connected with the variation of the beam position in the vertical direction, the intensity monitor and the apparatus drift.

## 4. Results

The analyzing power results for six types of hadrons are shown in Fig. 5. The errors quoted are statistical ones. This report presents the first data measured with two different nuclear targets. There were no data so far for charged hadrons with  $p_T \geq 2.2$  GeV/c.

In Fig. 5a the  $\pi^+$  meson production asymmetry is shown. Within the errors there is no difference of  $A_N$  for both targets (C and Cu).  $A_N$  for the nuclear targets in the range  $1 \leq p_T \leq 2$  GeV/c is approximately 4% higher than for the hydrogen target. For the central region such a difference can be connected with the smaller portion of u quarks in the nuclear target containing neutrons. Fragmentation of u quarks ( $u \rightarrow \pi^+$ ) from the polarized beam protons as well as u quarks of the target contribute to the asymmetry. Because the target protons are not polarized their contribution in the central region reduces the measured polarization. For nuclear targets containing less u quarks in comparison with d quarks the decrease of the asymmetry is not so substantial. Quark scattering in nuclei must also lead to the decrease of the asymmetry due to the  $p_T$  shift.

The asymmetry for  $\pi^-$  meson production is presented in Fig. 5b. In the range  $0.9 \leq p_T \leq 1.6$  GeV/c it is about 4% higher for the nuclear targets than for the hydrogen target. For the central region such differences can be connected to the larger proportion of d quarks in the nuclear targets. The major contribution give d quarks ( $d \rightarrow \pi^-$  fragmentation) from the polarized beam protons and the target. For  $\pi^-$  mesons in pp collisions the asymmetry is therefore negative. Due to the large contribution of the unpolarized target in the central regions the asymmetry for nuclear targets is shifted into the positive region.

Fig. 5c shows the asymmetry for  $K^+$  production. There is no significant difference in  $A_N$  for the two nuclear targets (C and Cu) and  $A_N$  is about 3% higher than for the hydrogen target. The reason of that can be the same as for  $\pi^+$  mesons.

In Fig. 5d  $A_N$  for  $K^-$  mesons is presented. Within the errors there is no appreciable difference in  $A_N$  for all targets (p, C and Cu) and  $A_N$  is close to zero. This is expected because  $K^-$  does not contain valence quarks from the polarized beam proton.

In Fig. 5e the asymmetry for the proton production is shown which is close to zero for nuclear targets. For the hydrogen target it is slightly negative.

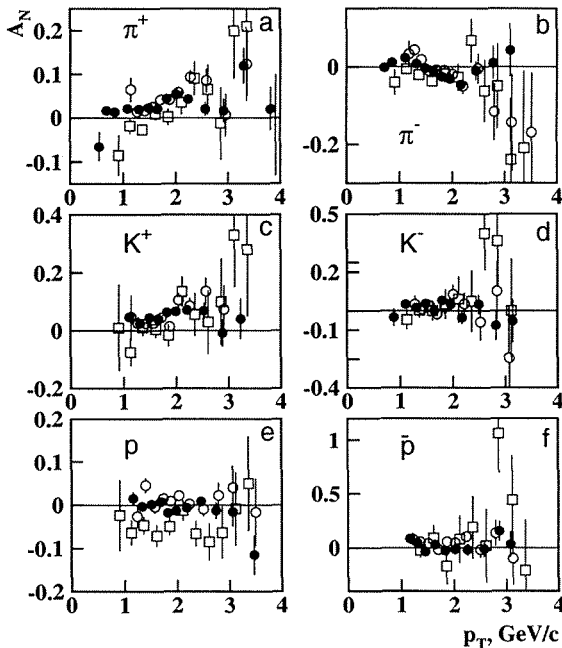


Figure 5:  $A_N$  dependence on  $p_T$  for  $p \uparrow + p(A) \rightarrow h^\pm + X$ , where  $h = \pi^+$  (a),  $\pi^-$  (b),  $K^+$  (c),  $K^-$  (d),  $p$  (e),  $\bar{p}$  (f). Closed circles correspond to C target, open circles - Cu, square - proton

The asymmetry for antiproton production presented in Fig. 5f shows no difference for all targets (p, C and Cu) and is close to zero. This result is expected because the produced antiproton does not contain valence quarks from the beam proton. Sea quarks in the most models are expected to be unpolarized. The absolute values of analyzing power for antiprotons and  $K^-$  mesons may be used as an estimate of systematic bias ( $\sim 4\%$ ) in the data in general.

## 5. Discussion

It is instructive to compare 40 GeV/c data with the other data. There are very detailed ANL measurements performed at 11.75 GeV/c [2]. There is a similarity in  $p_T$  dependence of the analyzing power for negative pions at 40 GeV/c (Fig. 5b) and 11.75 GeV/c (Fig. 6).

In particular, the  $A_N$  is rising with  $p_T$ , and then dropping back to zero or even negative values. The typical  $p_T$  values of maximum and minimum positions are increasing with the beam energy.

Another interesting similarity is between  $p_T$  dependence of the positive pion analyzing power (Fig. 5a) and the  $\Lambda$  hyperon polarization in  $\Sigma^-$  Carbon interactions [3]. In Fig. 7

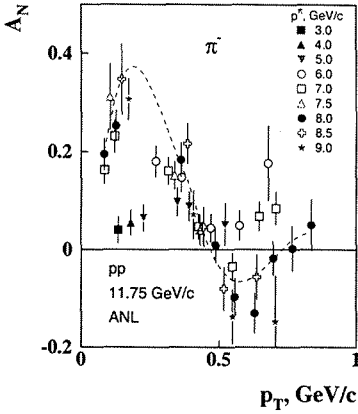


Figure 6:  $A_N$  dependence on  $p_T$  for  $p\uparrow + p \rightarrow \pi^- + X$  [2]. Different symbols correspond to different secondary pion momenta

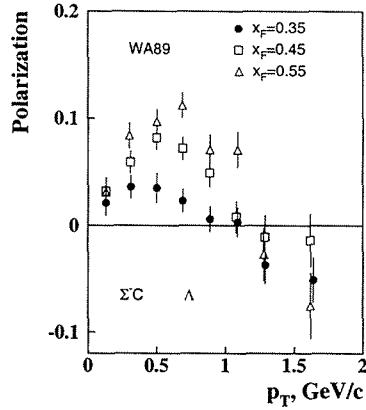


Figure 7: Polarization dependence on  $p_T$  for  $\Sigma^- + C \rightarrow \Lambda + X$  [3]. Closed circles correspond to  $x_F = 0.35$ , open circles -  $x_F = 0.45$ , square -  $x_F = 0.55$

a change-over in  $p_T$  dependence is seen. Such behaviour has never been observed before in single spin effects for high energy inclusive reactions.

## 6. Conclusion

The analyzing powers were measured for  $-0.15 \leq x_F \leq 0.2$  and  $0.5 \leq p_T \leq 4$  GeV/c in inclusive charged hadron production off carbon and copper with 40 GeV/c polarized proton beam. Three features of the results can be stressed:

- (a) there is no significant difference for the two nuclear targets (C, Cu);
- (b) for the positive charge mesons the asymmetry has a maximum at  $p_T = 2.2$  GeV/c and decreases to zero at  $p_T = 2.9$  GeV/c;
- (c) for hadrons not containing valence quarks from polarized protons ( $K^-$  and  $\bar{p}$ ) the analyzing power is close to zero.

The analysis of high  $x_F$  data measured in 2003 is still under way.

We are grateful to the IHEP staff for their assistance with setting up the experiment, and to the IHEP directorate for their support.

## References

- [1] V.V. Abramov, A.S. Dyshkant, V.N. Evdokomov *et al.*, *Nucl. Phys.* **B492**, 3 (1997).
- [2] W.H. Dragoset *et al.*, *Phys. Rev.* **D18**, 3939 (1978).
- [3] M.I. Adamovich *et al.*, *Eur. Phys. J.* **C36**, 315 (2004).

# LONGITUDINAL POLARIZATION OF $\Lambda$ AND $\bar{\Lambda}$ IN DEEP-INELASTIC SCATTERING AT COMPASS

M.G.Sapozhnikov  
on behalf of the COMPASS Collaboration

*Joint Institute for Nuclear Research, Laboratory of Particle Physics, Dubna*  
*E-mail: sapozh@sunse.jinr.ru*

## Abstract

Production of  $\Lambda$  and  $\bar{\Lambda}$  hyperons in deep-inelastic scattering of 160 GeV/ $c$  polarized muons is under study in the COMPASS (CERN NA58) experiment. Preliminary results on longitudinal polarization of  $\Lambda$  and  $\bar{\Lambda}$  hyperons from the data collected during the 2002 run are presented.

The study of longitudinal polarization of  $\Lambda(\bar{\Lambda})$  hyperons in the deep-inelastic scattering (DIS) can provide information on the fundamental properties of the nucleon, such as polarization of strange quarks in the nucleon [1], and offers a possibility to determine the mechanism of spin transfer from a polarized quark to a polarized baryon [2]-[7].

The polarized nucleon intrinsic strangeness model [1] predicts negative longitudinal polarization of  $\Lambda$  hyperons produced in the target fragmentation region [8, 9]. The main assumption of the model is negative polarization of the strange quarks and antiquarks in the nucleon. This assumption was inspired by the results of EMC [10] and subsequent experiments [11]- [13] on inclusive deep-inelastic scattering which gave an indication that the  $s\bar{s}$  pairs in the nucleon are negatively polarized with respect to the nucleon spin:

$$\Delta s \equiv \int_0^1 dx [s_{\uparrow}(x) - s_{\downarrow}(x) + \bar{s}_{\uparrow}(x) - \bar{s}_{\downarrow}(x)] = -0.10 \pm 0.02. \quad (1)$$

Recent analysis [14] of the available world data in framework of the next-to-leading order perturbative QCD including higher twist effects also concludes that  $\Delta s = -0.045 \pm 0.007$ .

The polarized strangeness model [1] was successfully applied to explain the large violation of the OZI rule in the annihilation of stopped antiprotons and its strong dependence on the spin of the initial state (for review, see [15]). The predictions of the model were confirmed in different processes of proton-proton, antiproton-proton interactions and lepton DIS. Specifically, the negative longitudinal polarization of the  $\Lambda$  hyperons at  $x_F < 0$  predicted in [8, 9] was found in the neutrino DIS experiments [16].

However, the question about polarization of the nucleon strange quarks has not been solved yet. Recently, after analysis of the semi-inclusive DIS channels in the LO approximation, the HERMES collaboration found that  $\Delta s = 0.028 \pm 0.033 \pm 0.009$  [17], i.e. consistent with zero within the errors (for the discussion of the HERMES result, see [18],[19]).

The measurement of the longitudinal  $\Lambda$  polarization in the current fragmentation region  $x_F > 0$  is traditionally related with investigations of spin transfer from quark to

hadron [2]-[6]. This spin transfer depends on the contribution of the spin of the struck quark to the  $\Lambda$  spin. There are different models of the  $\Lambda$  spin structure.

In the naive quark model the spin of  $\Lambda$  is carried by the  $s$  quark and the spin transfer from the  $u$  and  $d$  quarks to  $\Lambda$  is equal to zero. It means that the longitudinal polarization of  $\Lambda$  produced in fragmentation of the  $u$  and  $d$  quarks is  $P_\Lambda \sim 0$ .

The authors of [2], using  $SU(3)_f$  symmetry and experimental data for the spin-dependent quark distributions in the proton, predict that the contributions of  $u$  and  $d$  quarks to the  $\Lambda$  spin are negative and substantial, at the level of 20% for each light quark. One might expect that in this model the fragmentation of the dominant  $u$  quark will lead to  $P_\Lambda = -0.2$ .

In the framework of  $SU(6)$  based quark-diquark model [6] it is predicted a large and positive polarization of the  $u$  and  $d$  quarks in the  $\Lambda$  at large Bjorken scaling variable  $x_{Bj}$ . Due to this fact the spin transfer to  $\Lambda$  should be as large as +1 at  $z \sim 0.8 - 0.9$  (here  $z$  is fractional hadron energy,  $z = E_h/\nu$ ,  $\nu = E - E'$ ,  $E$  and  $E'$  are lepton energies in the initial and final state).

However the possibility to study real spin transfer from the quark to baryon at the energies of the current experiments was questioned in [9]. It turns out that even at the COMPASS energy of 160 GeV most of  $\Lambda$ , even in the  $x_F > 0$  region, are produced from the diquark fragmentation. It is predicted that in the COMPASS kinematics the longitudinal  $\Lambda$  polarization is either  $P_\Lambda = -0.004$  or  $P_\Lambda = -0.07$ , depending on the fragmentation model.

Moreover, a large part (up to 30-40%) of the  $\Lambda$ , observed in DIS, comes from decays of heavy hyperons, such as  $\Sigma^0$ ,  $\Sigma(1385)$  and  $\Xi$ , significantly changing the pattern of the spin transfer.

More clear situation is with the  $\bar{\Lambda}$  production. The contribution of  $\bar{\Lambda}$  production from diquark fragmentation is negligible. The background from decays of heavy hyperons is also absent. An interesting feature was observed in the E665 experiment at Fermilab [20]. It was found that in DIS the spin transfer to  $\Lambda$  and  $\bar{\Lambda}$  is large and has opposite signs. Though the statistical errors of the measurement were quite large, the statistics comprises only 750  $\Lambda$  and 650  $\bar{\Lambda}$  events.

The spin transfer to  $\Lambda$  and  $\bar{\Lambda}$  for the E665 experimental conditions was calculated in [7]. It is predicted, that under standard assumption that unpolarized strange quark distribution  $s(x)$  is the same as  $\bar{s}(x)$  for antistrange quarks, the spin transfer to  $\Lambda$  should be practically the same as for  $\bar{\Lambda}$ . Trying to explain the difference in  $\Lambda$  and  $\bar{\Lambda}$  spin transfer, the authors of [7] have introduced by hand some asymmetry in strange-antistrange quark distributions at small  $x_{Bj}$ . However, the calculated magnitude of the difference in  $\Lambda$  and  $\bar{\Lambda}$  spin transfer was still too small to explain the data [20].

We have studied  $\Lambda$  and  $\bar{\Lambda}$  production by polarized  $\mu^+$  of 160 GeV/c on a polarized  ${}^6\text{LiD}$  target of the COMPASS spectrometer constructed in the framework of CERN experiment NA58. A detailed description of the COMPASS experimental setup is given elsewhere [21] and only the most relevant elements for the present analysis will be given below.

The beam polarization is  $P_b = -0.76 \pm 0.04$ . The polarized  ${}^6\text{LiD}$  target consists of two oppositely polarized cells, 60 cm long. The target polarization is about 50%. For this analysis the data are averaged over the target polarization.

We have used data collected during the 2002 run. The analysis comprises about  $1.6 \cdot 10^7$  DIS events with  $Q^2 > 1$  (GeV/c) $^2$ .

The  $V^0$  events ( $V^0 \equiv \Lambda, \bar{\Lambda}$  and  $K_S^0$ ) were selected by requiring the incoming and outgoing muon tracks together with at least two hadron tracks forming the secondary vertex. The primary vertex should be inside the target. The secondary vertex must be downstream the both target cells. The angle between the vector of  $V^0$  momentum and the vector between primary and  $V^0$  vertices should be  $\theta_{col} < 0.01$  rad. Cut on transverse momentum of the decay products with respect to the direction of  $V^0$  particle,  $p_t > 23$  MeV/c was applied to reject  $e^+e^-$  pairs from the  $\gamma$  conversion seen as the band at the bottom of the Armenteros plot shown in Fig.1.

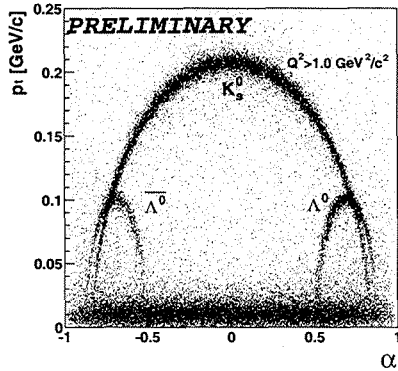


Figure 1: The Armenteros plot:  $p_t$  is the transverse momentum of the  $V^0$  decay products with respect to the direction of  $V^0$  momentum,  $\alpha = \frac{p_t^+ - p_t^-}{p_L^+ + p_L^-}$ , where  $p_L$  is the longitudinal momentum of the  $V^0$  decay particle

The typical elliptical bands from the  $K_S^0$ ,  $\Lambda$  and  $\bar{\Lambda}$  decays are seen in Fig. 1. Both  $\Lambda$  and  $\bar{\Lambda}$  signals stand out clearly. The large number of produced  $\bar{\Lambda}$  is a specific feature of the COMPASS experiment.

The DIS cuts on  $Q^2 > 1$  (GeV/c)<sup>2</sup> and  $0.2 < y < 0.8$  have been used. Here  $y = \nu/E$  is the fraction of the lepton energy carried out by the virtual photon.

To analyse  $V^0$  events, the so called bin-by-bin method was used. All angular distributions have been divided in some bins. In each angular bin the invariant mass distribution of positive and negative particles is constructed assuming  $\pi^+\pi^-$ ,  $p\pi^-$  or  $\bar{p}\pi^+$  hypothesis. The peak of the corresponding  $V^0$  particle is fitted and the number of the  $V^0$  in this peak is obtained. This number determines a point in the corresponding bin of the angular distribution. This procedure allows to construct practically background-free angular distributions. The total data sample contains about 9000  $\Lambda$  and 5000  $\bar{\Lambda}$ .

The  $x_F$  and  $Q^2$  experimental distributions (crosses) of  $\Lambda$ ,  $\bar{\Lambda}$  and  $K_S^0$  are compared with the Monte-Carlo simulated ones (hatched histograms) in Fig. 2. One can see that we are able to access mainly current fragmentation region. The averaged value of  $x_F$  is  $\langle x_F \rangle = 0.20$ , whereas for the Bjorken scaling variable it is  $\langle x_{Bj} \rangle = 0.02$ . The mean  $\Lambda$  momentum is 17 GeV/c, while decay pion momentum is 3 GeV/c. The agreement between the experimental data and the Monte-Carlo simulations is reasonable.

The angular distribution of the decay particles in the  $V^0$  rest frame is

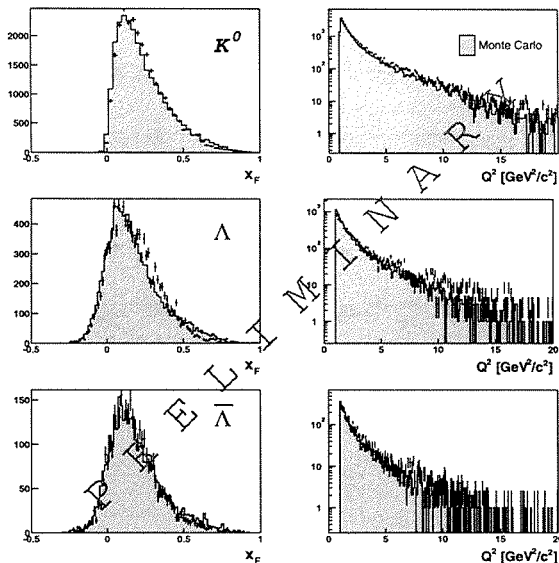


Figure 2: The  $x_F$  (left column) and  $Q^2$  (right column) distributions for  $K_S^0$  (upper row),  $\Lambda$  (middle row) and  $\bar{\Lambda}$  (lower row). The experimental data points are shown together with results of Monte-Carlo simulations (histograms)

$$w(\theta) = \frac{dN}{d \cos \theta} = \frac{N_{tot}}{2} (1 + \alpha P \cos \theta), \quad (2)$$

where  $N_{tot}$  is the total number of events,  $\alpha = +(-)0.642 \pm 0.013$  is  $\Lambda(\bar{\Lambda})$  decay parameter,  $P$  is the projection of the polarization vector on the direction of the virtual photon in the  $V^0$  rest frame,  $\theta$  is the angle between the direction of the decay proton for  $\Lambda$  (antiproton - for  $\bar{\Lambda}$ , positive  $\pi$  - for  $K^0$ ) and the direction of the virtual photon in the  $V^0$  rest frame.

Fig. 3 shows the measured angular distributions for all events of the  $K_S^0$ ,  $\Lambda$  and  $\bar{\Lambda}$  decays, corrected for the acceptance. The acceptance was determined by the Monte Carlo simulation of unpolarized  $\Lambda(\bar{\Lambda})$  decays.

One could see that the angular distribution for  $K_S^0$  decays is flat, as expected. The value of the longitudinal polarization is  $P_K = 0.007 \pm 0.017$ . The angular distribution for  $\Lambda$  decays for all events, i.e. the averaged other whole  $x_F$  interval, is also flat. The value of the longitudinal polarization is  $P_\Lambda = 0.03 \pm 0.04(stat) \pm 0.04(syst)$ . It indicates on small polarization of  $\Lambda$  in DIS processes. The same trend was observed by the HERMES collaboration [22]. The angular distribution of the  $\bar{\Lambda}$  events, averaged over  $x_F$ , exhibits some negative polarization  $P_{\bar{\Lambda}} = -0.11 \pm 0.06(stat) \pm 0.04(syst)$ .

Comparison of the spin transfer to  $\Lambda$  and  $\bar{\Lambda}$  hyperons measured in different DIS experiments is shown in Fig. 4. The spin transfer  $S$  determines which part of the beam polarization  $P_b$  is transferred to the hyperon polarization  $P$ . It is defined as  $P = S \cdot P_b \cdot D(y)$ , where  $D(y)$  is the virtual photon depolarization factor.

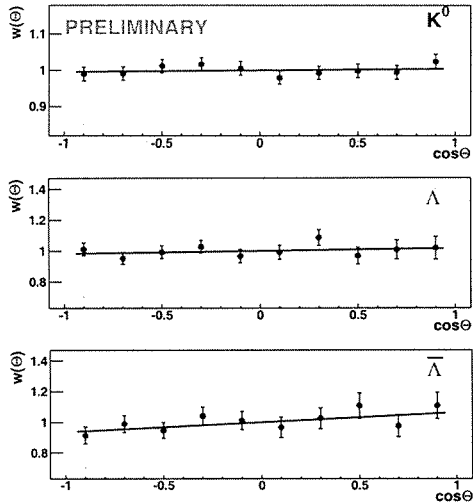


Figure 3: The angular distributions for  $K_S^0$ ,  $\Lambda$  and  $\bar{\Lambda}$  for all events

One can see that there is a reasonable agreement between the COMPASS and world data. There is an indication that the spin transfer to  $\bar{\Lambda}$  is non-zero and might be different from  $\Lambda$  case. However, for the COMPASS data only statistical errors are shown. Work to determine the systematic errors is going on.

The results from our 2002 data demonstrate a good potential of COMPASS to measure  $\Lambda$  and  $\bar{\Lambda}$  polarizations in DIS. The data samples collected in 2003 and 2004 will significantly increase the statistics.

## References

- [1] J.Ellis et al, Phys.Lett. **B353**, 319 (1995); Nucl.Phys. **A673**, 256 (2000).
- [2] M. Burkardt, R. L. Jaffe, Phys. Rev. Lett. **70**, 2537 (1993).
- [3] M.Anselmino et al, Phys. Lett. **B481**, 253 (2000); ibid. **B509**, 246 (2001).
- [4] A. M. Kotzinian, A. Bravar, D. von Harrach, Eur. Phys. J. **C2**, 329 (1998).
- [5] C. Boros, L. Zuo-Tang, Phys. Rev. **D57**, 4491 (1998).
- [6] J. J. Yang, B. Q. Ma, I. Schmidt, Phys. Lett. **B477**, 107 (2000).
- [7] B. Q. Ma, I. Schmidt, J. Soffer, J. J. Yang, Phys. Lett. **B488**, 254 (2000).
- [8] J. Ellis, D. Kharzeev, A.M. Kotzinian, Z.Physik **C69**, 467 (1996).
- [9] J. Ellis, A.M. Kotzinian, D.V. Naumov, Eur. Phys. J. **C25**, 603 (2002).

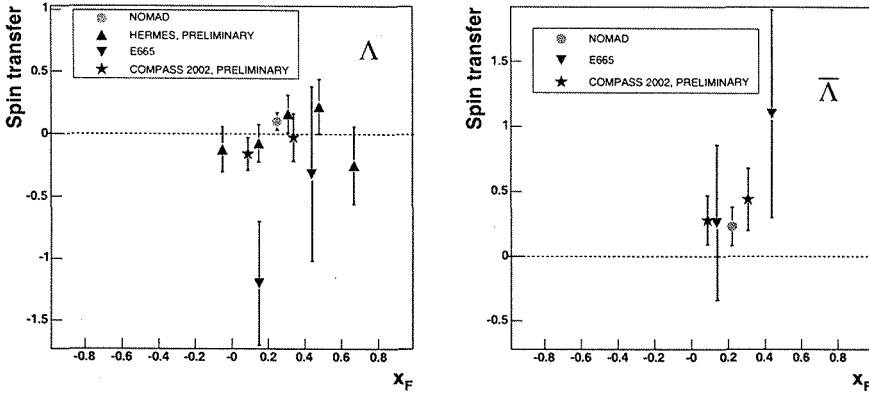


Figure 4: Comparison of the spin transfer to  $\Lambda$  (left) and  $\bar{\Lambda}$  (right) hyperons measured in different DIS experiments

- [10] The EMC Collaboration, J.Ashman et al, Phys.Lett. **B206**, 364 (1988); Nucl.Phys. **B328**, 1 (1989).
- [11] The SMC Collaboration. B.Adeva et al, Phys.Lett. **B412**, 414 (1997); D.Adams et al., Phys.Rev. **D56**, 5330 (1997).
- [12] The E143 Collaboration. K.Abe et al, Phys.Rev. **D58**, 112003 (1998).
- [13] The E155 Collaboration. P.L.Anthony et al, Phys.Lett, **B458**, 529 (1999).
- [14] E. Leader et al., Phys.Rev. **D 67**, 074017 (2003).
- [15] V.P.Nomokonov, M.G.Sapozhnikov, Phys.El.Part.At.Nucl., **34**, 184 (2003); hep-ph/0204259, 2002.
- [16] P. Astier et al., Nucl. Phys. **B588**, 3 (2000); *ibid.* **B605**, 3 (2001).
- [17] The HERMES Collaboration. A.Airapetian et al, Phys.Rev. **D 71**, 012003 (2005).
- [18] A.M.Kotzinian, Phys.Lett. **B552**, 172 (2003).
- [19] E.Leader, D.Stamenov, Phys.Rev. **D67**, 037503 (2003).
- [20] M. R. Adams et al, Eur. Phys. J. **C17**, 263 (2000).
- [21] G.Mallot, Nucl.Instr. and Methods, **A 518**, 121 (2004). L.Schmitt, Proc. Int.Conf. on Hadron Spectroscopy, Aschaffenburg, 2003, AIP Conf.Proc. n717, p.870.
- [22] A. Airapetian et al, Phys. Rev. **B64**, 112005 (2001); S. Belostotski, IXth Workshop on High-Energy Spin Physics, Dubna, Russia, Aug 2 - 7, 2001.

# DEUTERON-PROTON CHARGE EXCHANGE REACTION AT SMALL TRANSFER MOMENTUM

N.B. Ladygina<sup>1†</sup>, A.V. Shebeko<sup>2</sup>

(1) *Laboratory of High Energies, Joint Institute for Nuclear Research, 141980 Dubna, Russia,*

(2) *NSC Kharkov Institute of Physics & Technology, 61108 Kharkov, Ukraine*

† *E-mail: ladygina@sunhe.jinr.ru*

## Abstract

The charge-exchange reaction  $pd \rightarrow npp$  at 1 GeV projectile proton energy is studied. This reaction is considered in a special kinematics, when the transfer momentum from the beam proton to fast outgoing neutron is close to zero. Our approach is based on the Alt-Grassberger-Sandhas formulation of the multiple-scattering theory for the three-nucleon system. The matrix inversion method has been applied to take account of the final state interaction (FSI) contributions. The differential cross section, tensor analyzing power  $C_{0,y,y}$ , vector-vector  $C_{y,y}$  and vector-tensor  $C_{y,xz}$  spin correlation parameters of the initial particles are presented. It is shown, that the FSI effects play a very important role under such kinematical conditions. The high sensitivity of the considered observables to the elementary nucleon-nucleon amplitudes has been obtained.

## 1. Introduction

During the last decades the deuteron- proton charge exchange reaction has been studied both from the experimental and theoretical point of view. A considerable interest in this reaction is connected, first of all, to the opportunity to extract some information about the spin-dependent part of the elementary nucleon-nucleon charge exchange amplitudes. This idea was suggested by Pomeranchuk [1] already in 1951, but until now it continues to be of interest. Later, this supposition has been developed in [2, 3, 4]. It was shown, that in the plane-wave impulse approximation (PWIA) the differential cross section and tensor analyzing power  $T_{20}$  in the dp-charge exchange reaction are actually fully determined by the spin-dependent part of the elementary  $np \rightarrow pn$  amplitudes.

Nowadays the experiment on the study of the dp-charge exchange reaction at the small transfer momentum in the GeV-region is planned at ANKE setup at COSY [5]. The aim of this experiment is to provide information about spin-dependent np-elastic scattering amplitudes in the energy region where phase-shift analysis data are absent.

From our point of view, under kinematical conditions proposed in this experiment, when momentum of the emitted neutron has the same direction and magnitude as the beam proton (in the deuteron rest frame), and relative momentum of two protons is very small, the final state interaction (FSI) effects play very important role. The contribution of the D-wave in the DWF into differential cross section in this kinematics must be negligible [6]. However, for the polarization observables the influence of the D-component can be significant.

The goal of our paper is to study the importance of the D-wave and FSI effects under kinematical conditions of the planned experiment. We consider  $pd \rightarrow npp$  reaction in the approach, which has been used by us to describe the  $pd$  breakup process at 1 GeV projectile proton energy [7]. This approach is based on the Alt-Grassberger-Sandhas formulation of the multiple-scattering theory for the three-nucleon system. The matrix inversion method has been applied to take account of the FSI contributions. Since unpolarized and polarized mode of the deuteron beam are supposed to be employed in the experiment, we also calculate both the differential cross section and a set of the polarization observables. It should be noted, in this paper we have not considered the Coulomb interaction in the  $(pp)$ -pair. This problem is nontrivial and requires a special investigation.

## 2. Theoretical formalism

In accordance to the three-body collision theory, the amplitude of the deuteron proton charge exchange reaction,

$$p(\vec{p}) + d(\vec{0}) \rightarrow n(\vec{p}_1) + p(\vec{p}_2) + p(\vec{p}_3) \quad (1)$$

is defined by the matrix element of the transition operator  $U_{01}$

$$U_{pd \rightarrow npp} \equiv \sqrt{2} \langle 123 | [1 - (1, 2) - (1, 3)] U_{01} | 1(23) \rangle = \delta(\vec{p} - \vec{p}_1 - \vec{p}_2 - \vec{p}_3) \mathcal{J}. \quad (2)$$

As consequence of the particle identity in initial and final states the permutation operators for two nucleons  $(i, j)$  appear in this expression.

As was shown in ref.[7] the matrix element  $U_{pd \rightarrow npp}$  can be presented as

$$U_{pd \rightarrow npp} = \sqrt{2} \langle 123 | [1 - (2, 3)] [1 + t_{23}(E - E_1) g_{23}(E - E_1)] t_{12}^{sym} | 1(23) \rangle, \quad (3)$$

where the operator  $g_{23}(E - E_1)$  is a free propagator for the  $(23)$ -subsystem and the scattering operator  $t_{23}(E - E_1)$  satisfies the Lippmann-Schwinger (LS) equation with two-body force operator  $V_{23}$  as driving term

$$t_{23}(E - E_1) = V_{23} + V_{23} g_{23}(E - E_1) t_{23}(E - E_1). \quad (4)$$

Here  $E$  is the total energy of the three-nucleon system  $E = E_1 + E_2 + E_3$ .

Let us rewrite the matrix element (3) indicating explicitly the particle quantum numbers,

$$U_{pd \rightarrow npp} = \sqrt{2} \langle \vec{p}_1 m_1 \tau_1, \vec{p}_2 m_2 \tau_2, \vec{p}_3 m_3 \tau_3 | [1 - (2, 3)] \omega_{23} t_{12}^{sym} | \vec{p} m \tau, \psi_{1M_d 00}(23) \rangle,$$

where  $\omega_{23} = [1 + t_{23}(E - E_1) g_{23}(E - E_1)]$  and the the spin and isospin projections denoted as  $m$  and  $\tau$ , respectively. The operator  $t_{12}^{sym}$  is symmetrized NN-operator,  $t_{12}^{sym} = [1 - (1, 2)] t_{12}$ .

In this paper we consider the special kinematics, when transfer momentum  $\vec{q} = \vec{p} - \vec{p}_1$  is close to zero. In other words, the neutron momentum has the same value and direction as the beam proton. In fact, since the difference between proton and neutron masses and deuteron binding energy take place, the transfer momentum is not exactly zero,  $q \approx 1.8$

MeV/c. But because of this value is very small and has no significant influence on the results, we shall suppose  $q = 0$  in the subsequent calculations.

Under such kinematical conditions one can anticipate that the FSI in the  $^1S_0$  state is prevalent at comparatively small  $p_0$ -values. In such a way we get the following expression for amplitude of the dp charge exchange process [8]

$$\mathcal{J} = \mathcal{J}_{PWIA} + \mathcal{J}_{1S_0}$$

$$\begin{aligned} \mathcal{J}_{PWIA} &= \langle LM_L 1 \mathcal{M}_S | 1 M_D \rangle u_L(p_0) Y_L^{M_L}(\widehat{p}_0) \\ &\quad \left\{ \langle \frac{1}{2} m'_2 \frac{1}{2} m_3 | 1 \mathcal{M}_S \rangle \langle m_1 m_2 | t^0(\vec{p}, \vec{p}_0) - t^1(\vec{p}, \vec{p}_0) | m m'_2 \rangle - \right. \\ &\quad \left. \langle \frac{1}{2} m'_2 \frac{1}{2} m_2 | 1 \mathcal{M}_S \rangle \langle m_1 m_3 | t^0(\vec{p}, \vec{p}_0) - t^1(\vec{p}, \vec{p}_0) | m m'_2 \rangle \right\} \end{aligned} \quad (5)$$

$$\begin{aligned} \mathcal{J}_{1S_0} &= \frac{(-1)^{1-m_2-m'_2}}{\sqrt{4\pi}} \delta_{m_2 -m_3} \langle \frac{1}{2} m'' \frac{1}{2} -m'_2 | 1 M_D \rangle \\ &\quad \langle m_1 m'_1 | t^0(\vec{p}\vec{p}_0) - t^1(\vec{p}, \vec{p}_0) | m m'' \rangle \int dp'_0 p_0'^2 \psi_{00}^{001}(p'_0) u_0(p'_0). \end{aligned} \quad (6)$$

The wave function of the final  $pp$ -pair  $\psi_{00}^{001}(p'_0)$  can be expressed by a series of  $\delta$ -functions, what enables us to perform the integration over  $p'_0$  in this expression. We use the phenomenological model suggested by Love and Franey [9] for description the high energy nucleon-nucleon matrix  $t(\vec{p}, \vec{p}_0)$ .

### 3. Results and discussions

We define general spin observable related with polarization of initial particles in terms of the Pauli  $2 \times 2$  spin matrices  $\sigma$  for the proton and a set of spin operators  $S$  for deuteron as following

$$C_{\alpha\beta} = \frac{Tr(\mathcal{J} \sigma_\alpha S_\beta \mathcal{J})}{Tr(\mathcal{J} \mathcal{J}^+)}, \quad (7)$$

where indices  $\alpha$  and  $\beta$  refer to the proton and deuteron polarization, respectively;  $\sigma_0$  and  $S_0$  corresponding to the unpolarized particles are the unit matrices of two and three dimensions. In such a way, Eqs.(5) for dp- charge exchange amplitude enables us to get the relation for any variable of this process taking into account two slow protons final state interaction in  $^1S_0$ -state. So, we have following expression for the spin- averaged squared amplitude in kinematics, when one of the slow protons is emitted along the beam direction as well as neutron ( $\theta_2 = 0^0$ )

$$\begin{aligned} C_0 &= \frac{1}{2\pi} \left( \frac{m_N + E_p}{2E_p} \right)^2 \{ (2B^2 + F^2) (\mathcal{U}^2(p_2) + w^2(p_2)) + \\ &\quad (F^2 - B^2) w(p_2) (w(p_2) - 2\sqrt{2} Re \mathcal{U}(p_2)) \}, \end{aligned} \quad (8)$$

where  $\mathcal{U}(p_2) = u(p_2) + \int dp'_0 p_0'^2 \psi_{00}^{001}(p'_0) u(p'_0)$  is the S-component of the DWF  $u(p_2)$  corrected on the FSI of the (pp)-pair and  $w(p_2)$  is the D-component of the DWF;  $B$  and  $F$  are the spin dependent nucleon-nucleon amplitudes [9].

We use a right-hand coordinate system defined in accordance to the Madison convention [10]. The quantization  $z$ -axis is along the beam proton momentum  $\vec{p}$ . Since the direction of  $\vec{p} \times \vec{p}_1$  is undefined in the collinear geometry, we choose the  $y$ -axis normal to the beam momentum. Then third axis is  $\vec{x} = \vec{y} \times \vec{z}$ .

The tensor analyzing power can be presented in the following form

$$C_{0,yy} \cdot C_0 = \frac{1}{4\pi} \left( \frac{m_N + E_p}{2E_p} \right)^2 \{2(F^2 - B^2)(\mathcal{U}^2(p_2) + w^2(p_2)) + (2F^2 + B^2)w(p_2)(w(p_2) - 2\sqrt{2}\text{Re}\mathcal{U}(p_2))\} \quad (9)$$

Note, that only squared nucleon-nucleon spin-flip amplitudes  $B^2$  and  $F^2$  are in expression for the tensor analyzing power  $C_{0,yy}$  and differential cross section. However, the spin-correlation due to vector polarization of deuteron and beam proton contains the interference terms of this amplitudes

$$C_{y,y} \cdot C_0 = -\frac{2}{4\pi} \left( \frac{m_N + E_p}{2E_p} \right)^2 \{ \text{Re}(FB^*)[2\mathcal{U}^2(p_2) - 2w^2(p_2) - \sqrt{2}\text{Re}\mathcal{U}(p_2)w(p_2)] - 3\sqrt{2}\text{Im}(FB^*)\text{Im}\mathcal{U}(p_2)w(p_2) \} \quad (10)$$

It is interesting, that there is the term proportional to the imaginary part of  $\mathcal{U}(p_2)$ . It has a non-zero value only in case when FSI is taken into account. The analogous result we have obtained for the vector-tensor spin correlation

$$C_{y,xz} \cdot C_0 = -\frac{3}{4\pi} \left( \frac{m_N + E_p}{2E_p} \right)^2 \{ \text{Im}(FB^*)[2\mathcal{U}^2(p_2) - 2w^2(p_2) - \sqrt{2}\text{Re}\mathcal{U}(p_2)w(p_2)] + 3\sqrt{2}\text{Re}(FB^*)\text{Im}\mathcal{U}(p_2)w(p_2) \} \quad (11)$$

The differential cross section and three polarization observables are presented in figs.(1-4). The Love and Franey parametrization with a set of parameters obtained by fitting of the modern phase shift data SP00 [11, 12] has been employed for NN-amplitude. All calculations were carried out with Paris NN-potential [13] and Paris DWF [14].

One can see, the FSI contribution to the differential cross section (fig.1) is significant even at the very small proton momentum, while for the polarization observables the difference between PWIA and PWIA+FSI is visible only for  $p_2 \geq 10 - 15$  MeV/c. However, with increase of the proton momentum up to 50 MeV/c the importance of the FSI corrections to the PWIA also increases.

Note, the absolute value of the tensor analyzing power  $C_{0,yy}$  (fig.2) in the momentum interval of interest is near zero. In order to understand the source of that, we disregard the D-wave in the DWF. Then the polarization observables are defined by the ratio of the nucleon-nucleon charge exchange amplitudes only

$$\begin{aligned} C_{0,yy} &= \frac{1}{2} \cdot \frac{F^2 - B^2}{2B^2 + F^2} \\ C_{y,y} &= -2 \cdot \frac{\text{Re}(FB^*)}{2B^2 + F^2} \\ C_{y,xz} &= -3 \cdot \frac{\text{Im}(FB^*)}{2B^2 + F^2} \end{aligned} \quad (12)$$

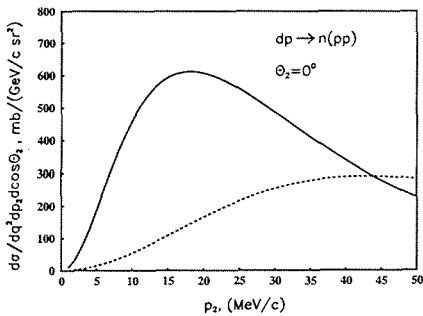


Figure 1: The differential cross section at  $\vec{q} = 0$  as a function of one of the slow proton momentum. The dashed and full line correspond to the PWIA and PWIA+FSI, respectively

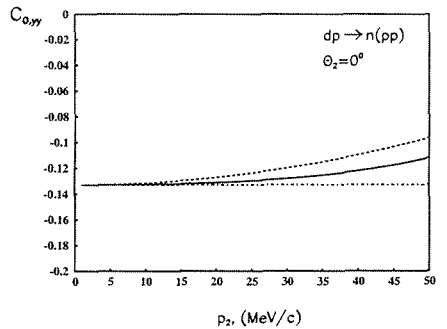


Figure 2: The tensor analyzing power  $C_{yy}$  vs.  $p_2$ . The dashed line corresponds to PWIA; dash-dotted and full lines are PWIA+FSI without D-component in the DWF and with it, respectively

Thus, the nearness of the tensor analyzing power to zero indicates that the absolute values of the spin-flip NN-amplitudes approximately equal each other,  $|B| \approx |F|$ .

The vector-tensor spin correlation  $C_{y,xz}$  (fig.4) has also very small value,  $|C_{y,xz}| \approx 0.06$ . The magnitude of this observable decreases up to zero for  $p_2 \approx 50$  MeV/c, if the FSI corrections and D-wave in the deuteron are taken into account, while it is almost constant in the PWIA and PWIA+FSI without D-wave. One can see from Eqs.(11, 12) for  $C_{y,xz}$ , the reason of this behaviour is connected with the small value of the imaginary part of the nucleon-nucleon amplitudes product,  $Im(FB^*)$ . In such a way, the great contribution into  $C_{y,xz}$  gives the term proportional to  $Re(FB^*)$ , which defined by D-wave and imaginary part of the generalized function  $\mathcal{U}(p_2)$ . Note, that  $Im\mathcal{U}(p_2) \neq 0$ , if FSI taken into account.

The other situation is for the vector-vector spin correlation  $C_{y,y}$  (fig.3). The term proportional to  $Re(FB^*)$  gives also a considerable contribution in this observable, but it is multiplied on the  $\mathcal{U}^2(p_2)$ . The magnitude of  $C_{y,y}$  is close to the theoretical limit  $-2/3$ , that confirms to the conclusion about approximate equality of the nucleon-nucleon amplitudes,  $|B|$  and  $|F|$ . Besides, this allows to conclude, that the relative phase between these amplitudes is close to zero. It is seen from Eq.(12), where D-wave was neglected.

## 4. Conclusion

We have studied the deuteron -proton charge exchange reaction at 1 GeV energy in special kinematics,  $\vec{q} \approx 0$ . The influence of the D-wave in the deuteron and FSI between two slow protons has been considered. It was shown, that D-wave and FSI effects are negligible for the polarization observables at proton momentum up to 10-15 MeV/c. As a result, in this region the polarization observables are defined by the ratio of the nucleon- nucleon charge exchange amplitudes only. However, it should not be ignored that the importance of the D-wave and, especially, FSI into polarization observables increases at  $p_2 \geq 15$  MeV/c. In

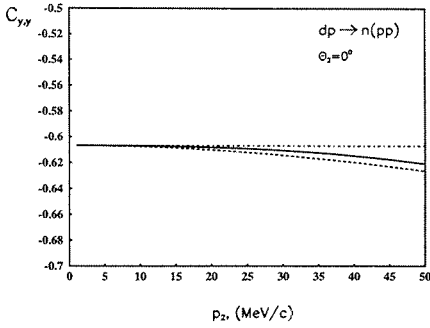


Figure 3: The spin-correlation  $C_{yy}$  due to the vector polarization of the deuteron. The curves are the same as in fig.2

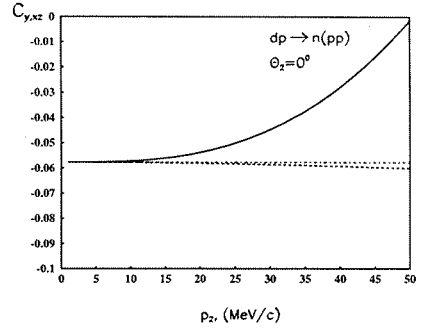


Figure 4: The spin-correlation  $C_{y,xz}$  due to the tensor polarization of the deuteron. The curves are the same as in fig.2

such a way, we conclude, that the ratio of the nucleon- nucleon charge exchange amplitudes and phase shift between them can be extracted from experimental data rather simple, if the experimental conditions and technical setup possibilities allow to work in this small momentum interval. In the opposite case, this procedure is more complicated and model dependent. It should be remembered that the FSI contribution to the differential cross section is very significant in comparison with PWIA predictions even at very small proton momentum. This fact does not enable us to get the absolute value of the nucleon-nucleon spin flip amplitudes without considering the FSI corrections.

We are grateful to V.V.Glagolev, M.S.Nioradze and A.Kacharava for inspiration of interest to this problem. The authors are thankful to V.P. Ladygin for fruitful discussions.

## References

- [1] I.Pomeranchuk, Doklady Akademii Nauk USSR **78**, 249 (1951)
- [2] N.W.Dean, Phys.Rev. D**5**, 1661 (1972); Phys.Rev. D**5**, 2832 (1972)
- [3] D.V.Bugg, C.Wilkin, Nucl.Phys. A**467**, 575 (1987)
- [4] J.Carbonell, M.B.Barbaro, C.Wilkin, Nucl.Phys. A**529**, 653 (1991)
- [5] A.Kacharava, F.Rathmann (spokespersons) *et al.*, COSY proposal # 125, 2003
- [6] V.V.Glagolev *et al.* Eur.Phys.J. A**15**, 471 (2002)
- [7] N.B.Ladygina, A.V.Shebeko, Few Body Syst.**33**, 49 (2003)

- [8] N.B.Ladygina, A.V.Shebeko, Eur.Phys.J. **A22**, 29 (2004)
- [9] W.G.Love, M.A.Franey, Phys.Rev. **C24**, 1073 (1981); W.G.Love, M.A.Franey, Phys.Rev. **C31**, 488 (1985)
- [10] *Proceedings of the 3-d Int.Symp., Madison,1970* edited by H.H. Barshall, W.Haeberli (Madison, WI: University of Wisconsin Press)
- [11] R.A.Arndt, I.I.Strakovsky, R.L.Workman, Phys.Rev. **C62**, 034005 (2000)
- [12] <http://gwdac.phys.gwu.edu>
- [13] M.Lacombe *et al.*, Phys.Rev. **C21**, 861 (1980)
- [14] M. Lacombe *et al.*, Phys.Lett.B **101**, 139 (1981)

# NUCLEAR SPIN IN DIRECT DARK MATTER SEARCH

V.A. Bednyakov<sup>1†</sup>, F. Šimkovic<sup>2</sup> and I.V. Titkova<sup>1</sup>

(1) *Joint Institute for Nuclear Research, Dzhelapov Laboratory of Nuclear Problems, 141980 Dubna, Moscow Region, Russia, † E-mail: bedny@jinr.ru*

(2) *Department of Nuclear Physics, Comenius University, Mlynská dolina F1, SK-842 15 Bratislava, Slovakia*

## Abstract

The Weakly Interacting Massive Particles (WIMPs) are among the main candidates for the relic dark matter (DM). The idea of the direct DM detection relies on elastic spin-dependent (SD) and spin-independent (SI) interaction of WIMPs with target nuclei. The importance of the SD WIMP-nucleus interaction for reliable DM detection is argued. The absolute lower bound for the detection rate can naturally be due to SD interaction. An experiment aimed at *detecting* DM with sensitivity higher than  $10^{-5}$  event/day/kg should have a non-zero-spin target.

## 1. Introduction

The lightest supersymmetric (SUSY) particle (LSP) neutralino is assumed to be the Weakly Interacting Massive Particle (WIMP) and the best dark matter (DM) candidate. It is believed that for heavy enough nuclei this spin-independent (SI) interaction of DM particles with nuclei usually makes the dominant contribution to the expected event rate of its detection. The reason is the strong (proportional to the squared mass of the target nucleus) enhancement of SI WIMP-nucleus interaction. Nevertheless there are at least three reasons to think that SD (or axial-vector) interaction of the DM WIMPs with nuclei could be very important. First, contrary to the only one constraint for SUSY models available from the scalar WIMP-nucleus interaction, the spin WIMP-nucleus interaction supplies us with two such constraints (see for example [1] and formulas below). Second, one can notice [2, 3] that even with a very sensitive DM detector (say, with a sensitivity of  $10^{-5}$  events/day/kg) which is sensitive only to the WIMP-nucleus scalar interaction (with spin-less target nuclei) one can, in principle, miss a DM signal. To safely avoid such a situation one should have a spin-sensitive DM detector, i.e. a detector with non-zero-spin target nuclei. Finally, there is a complicated nuclear spin structure, which, for example, characterized by the so-called long  $q$ -tail form-factor behavior. Therefore for heavy target nuclei and heavy WIMP the SD efficiency to detect a DM signal is much higher than the SI efficiency [4]. However, simultaneous study of both spin-dependent and spin-independent interactions of the DM particles with nuclei significantly increases the chance to observe the DM signal.

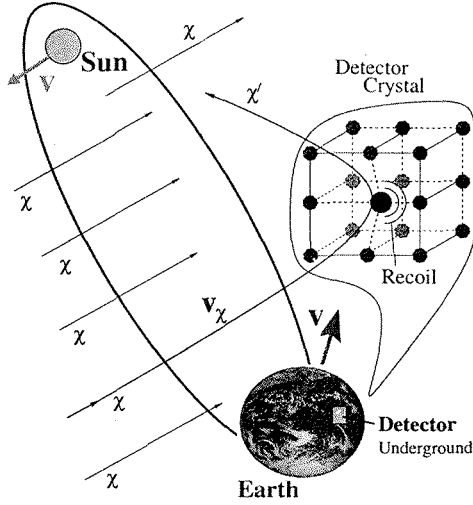


Figure 1: Due to the expected annual modulation signature of the event rate (1) only the Sun-Earth system is a proper setup for the successful direct DM detection

## 2. Two constraints for SUSY due to the spin

One believes to detect directly a DM particle  $\chi$  via its elastic scattering on a target nucleus  $(A, Z)$ . The nuclear recoil energy  $E_R$  ( $E_R \sim 10^{-6}m_\chi \approx \text{few keV}$ ) is measured by a proper detector (Fig. 1). The differential event rate depends on the distribution of the relic DM particles in the solar vicinity  $f(v)$  and the cross section of LSP-nucleus elastic scattering [5]–[12]:

$$\frac{dR}{dE_R} = N \frac{\rho_\chi}{m_\chi} \int_{v_{\min}}^{v_{\max}} dv f(v) v \frac{d\sigma}{dq^2}(v, q^2), \quad E_R = q^2/(2M_A). \quad (1)$$

Here,  $N = \mathcal{N}/A$  is the number density of target nuclei.  $\mathcal{N}$  and  $A$  stand for the Avogadro number and the atomic mass in AMU, respectively.  $M_A$  denotes the nuclear mass.  $v_{\max} = v_{\text{esc}} \approx 600 \text{ km/s}$ ,  $v_{\min} = (M_A E_R / 2\mu_A^2)^{1/2}$ , the DM density  $\rho_\chi = 0.3 \text{ GeV}\cdot\text{cm}^{-3}$ . The neutralino-nucleus elastic scattering cross section for spin-non-zero ( $J \neq 0$ ) nuclei is a sum of the coherent (spin-independent) and axial (spin-dependent) terms [4, 13, 14, 15]:

$$\begin{aligned} \frac{d\sigma^A}{dq^2}(v, q^2) &= \frac{\sum |\mathcal{M}|^2}{\pi v^2 (2J+1)} = \frac{S_{\text{SD}}^A(q^2)}{v^2 (2J+1)} + \frac{S_{\text{SI}}^A(q^2)}{v^2 (2J+1)} \\ &= \frac{\sigma_{\text{SD}}^A(0)}{4\mu_A^2 v^2} F_{\text{SD}}^2(q^2) + \frac{\sigma_{\text{SI}}^A(0)}{4\mu_A^2 v^2} F_{\text{SI}}^2(q^2). \end{aligned} \quad (2)$$

It is useful to separate the zero-momentum transfer cross sections and introduce the normalized-to-unity ( $F_{\text{SD,SI}}^2(0) = 1$ ) nonzero-momentum-transfer nuclear form-factors:

$$F_{\text{SD,SI}}^2(q^2) = \frac{S_{\text{SD,SI}}^A(q^2)}{S_{\text{SD,SI}}^A(0)}. \quad (3)$$

The SD structure function  $S_{\text{SD}}^A(q)$  contains the isoscalar  $S_{00}$ , isovector  $S_{11}$  and the interference  $S_{01}$  terms:

$$S_{\text{SD}}^A(q) = a_0^2 S_{00}(q) + a_1^2 S_{11}(q) + a_0 a_1 S_{01}(q). \quad (4)$$

Here the isoscalar  $a_0 = a_n + a_p$  and isovector  $a_1 = a_p - a_n$  effective coupling constants are used (see (9)). For  $q = 0$  the nuclear SD and SI cross sections take the forms

$$\sigma_{\text{SI}}^A(0) = \frac{4\mu_A^2 S_{\text{SI}}(0)}{(2J+1)} = \frac{\mu_A^2}{\mu_p^2} A^2 \sigma_{\text{SI}}^p(0), \quad (5)$$

$$\sigma_{\text{SD}}^A(0) = \frac{4\mu_A^2 S_{\text{SD}}(0)}{(2J+1)} = \frac{4\mu_A^2}{\pi} \frac{(J+1)}{J} \{a_p \langle \mathbf{S}_p^A \rangle + a_n \langle \mathbf{S}_n^A \rangle\}^2. \quad (6)$$

Here,  $\mu_A = \frac{m_\chi M_A}{m_\chi + M_A}$  is the reduced  $\chi$ -nucleus mass and  $\mu_n^2 = \mu_p^2$  is assumed. The dependence on effective neutralino-quark couplings  $C_q$  and  $\mathcal{A}_q$  in the underlying (SUSY) theory

$$\mathcal{L}_{eff} = \sum_q (\mathcal{A}_q \cdot \bar{\chi} \gamma_\mu \gamma_5 \chi \cdot \bar{q} \gamma^\mu \gamma_5 q + C_q \cdot \bar{\chi} \chi \cdot \bar{q} q) + \dots \quad (7)$$

and on the spin ( $\Delta_q^{(p,n)}$ ) and the mass ( $f_q^{(p,n)}$ ) structure of *nucleons* enter into these formulas via the zero-momentum-transfer proton and neutron SI and SD cross sections:

$$\sigma_{\text{SI}}^p(0) = 4 \frac{\mu_p^2}{\pi} C_0^2, \quad \sigma_{\text{SD}}^{p,n}(0) = 12 \frac{\mu_{p,n}^2}{\pi} a_{p,n}^2; \quad (8)$$

$$\sigma_0^{p,n} = \sum_q C_q f_q^{(p,n)}, \quad a_p = \sum_q \mathcal{A}_q \Delta_q^{(p)}, \quad a_n = \sum_q \mathcal{A}_q \Delta_q^{(n)}. \quad (9)$$

The factors  $\Delta_q^{(p,n)}$ , which parametrize the quark spin content of the nucleon, are defined as  $2\Delta_q^{(n,p)} s^\mu \equiv \langle p, s | \bar{\psi}_q \gamma^\mu \gamma_5 \psi_q | p, s \rangle_{(p,n)}$ . The  $\langle \mathbf{S}_{p(n)}^A \rangle$  is the total spin of protons (neutrons) averaged over all  $A$  nucleons of the nucleus ( $A, Z$ ):

$$\langle \mathbf{S}_{p(n)}^A \rangle \equiv \langle A | \mathbf{S}_{p(n)}^A | A \rangle = \langle A | \sum_i \mathbf{s}_{p(n)}^i | A \rangle \quad (10)$$

The mean velocity  $\langle v \rangle$  of the relic DM particles of our Galaxy is about 300 km/s =  $10^{-3}c$ . For not very heavy  $m_\chi$  and  $M_A$  one can use the SD matrix element in *zero momentum transfer limit* [15, 16]

$$\mathcal{M} \propto \langle A | a_p \mathbf{S}_p + a_n \mathbf{S}_n | A \rangle \cdot \mathbf{s}_\chi. \quad (11)$$

Note a coupling of the spin of  $\chi$ ,  $\mathbf{s}_\chi$ , to the spin carried by the protons and the neutrons. The uncertainties arising from electroweak and QCD scale physics are incorporated in the

Table 1: Zero momentum spin structure of nuclei in different models. The measured magnetic moments used as input are enclosed in parentheses. From [17]

$^{19}\text{F}$ ( $L_J = S_{1/2}$ )	$\langle S_p \rangle$	$\langle S_n \rangle$	$\mu$ (in $\mu_N$ )
ISPSM, Ellis–Flores [18, 19]	1/2	0	2.793
OGM, Engel–Vogel [20]	0.46	0	(2.629) <sub>exp</sub>
EOGM ( $g_A/g_V = 1$ ), Engel–Vogel [20]	0.415	-0.047	(2.629) <sub>exp</sub>
EOGM ( $g_A/g_V = 1.25$ ), Engel–Vogel [20]	0.368	-0.001	(2.629) <sub>exp</sub>
SM, Pacheco-Strottman [21]	0.441	-0.109	
SM, Divari et al. [22]	0.4751	-0.0087	2.91
$^{23}\text{Na}$ ( $L_J = P_{3/2}$ )	$\langle S_p \rangle$	$\langle S_n \rangle$	$\mu$ (in $\mu_N$ )
ISPSM	1/2	0	3.793
SM, Ressel-Dean [15]	0.2477	0.0198	2.2196
OGM, Ressel-Dean [15]	0.1566	0.0	(2.218) <sub>exp</sub>
SM, Divari et al. [22]	0.2477	0.0199	2.22
$^{27}\text{Al}$ ( $L_J = D_{5/2}$ )	$\langle S_p \rangle$	$\langle S_n \rangle$	$\mu$ (in $\mu_N$ )
ISPSM, Ellis–Flores [18, 19]	1/2	0	4.793
OGM, Engel–Vogel [20]	0.25	0	(3.642) <sub>exp</sub>
EOGM ( $g_A/g_V = 1$ ), Engel–Vogel [20]	0.333	0.043	(3.642) <sub>exp</sub>
EOGM ( $g_A/g_V = 1.25$ ), Engel–Vogel [20]	0.304	0.072	(3.642) <sub>exp</sub>
SM, Engel et al. [16]	0.3430	0.0296	3.584
$^{73}\text{Ge}$ ( $L_J = G_{9/2}$ )	$\langle S_p \rangle$	$\langle S_n \rangle$	$\mu$ (in $\mu_N$ )
ISPSM, Ellis–Flores [18, 19]	0	0.5	-1.913
OGM, Engel–Vogel [20]	0	0.23	(-0.879) <sub>exp</sub>
IBFM, Iachello et al. [23] and [14]	-0.009	0.469	-1.785
IBFM (quenched), Iachello et al. [23] and [14]	-0.005	0.245	(-0.879) <sub>exp</sub>
TFFS, Nikolaev–Klapdor-Kleingrothaus, [24]	0	0.34	—
SM (small), Ressel et al. [14]	0.005	0.496	-1.468
SM (large), Ressel et al. [14]	0.011	0.468	-1.239
SM (large, quenched), Ressel et al. [14]	0.009	0.372	(-0.879) <sub>exp</sub>
“Hybrid” SM, Dimitrov et al. [25]	0.030	0.378	-0.920
$^{127}\text{I}$ ( $L_J = D_{5/2}$ )	$\langle S_p \rangle$	$\langle S_n \rangle$	$\mu$ (in $\mu_N$ )
ISPSM, Ellis–Flores [19, 26]	1/2	0	4.793
OGM, Engel–Vogel [20]	0.07	0	(2.813) <sub>exp</sub>
IBFM, Iachello et al. [23]	0.464	0.010	(2.813) <sub>exp</sub>
IBFM (quenched), Iachello et al. [23]	0.154	0.003	(2.813) <sub>exp</sub>
TFFS, Nikolaev–Klapdor-Kleingrothaus, [24]	0.15	0	—
SM (Bonn A), Ressel–Dean [15]	0.309	0.075	2.775 {2.470} <sub>eff</sub>
SM (Nijmegen II), Ressel–Dean [15]	0.354	0.064	3.150 {2.7930} <sub>eff</sub>
$^{131}\text{Xe}$ ( $L_J = D_{3/2}$ )	$\langle S_p \rangle$	$\langle S_n \rangle$	$\mu$ (in $\mu_N$ )
ISPSM, Ellis–Flores [18, 19]	0	-0.3	1.148
OGM, Engel–Vogel [20]	0.0	-0.18	(0.692) <sub>exp</sub>
IBFM, Iachello et al. [23]	0.000	-0.280	(0.692) <sub>exp</sub>
IBFM (quenched), Iachello et al. [23]	0.000	-0.168	(0.692) <sub>exp</sub>
TFFS, Nikolaev–Klapdor-Kleingrothaus, [24]		-0.186	—
SM (Bonn A), Ressel–Dean [15]	-0.009	-0.227	0.980 {0.637} <sub>eff</sub>
SM (Nijmegen II), Ressel–Dean [15]	-0.012	-0.217	0.979 {0.347} <sub>eff</sub>
QTDA, Engel [4]	-0.041	-0.236	0.70

factors  $a_p$  and  $a_n$ . The nuclear matrix element  $\mathcal{M}$  in Eq. (11) is often related to the matrix element of the nuclear magnetic moment, which also consists of the matrix elements of the total proton and neutron spin operators:

$$\mu = \langle A | g_n^s \mathbf{S}_n + g_n^l \mathbf{L}_n + g_p^s \mathbf{S}_p + g_p^l \mathbf{L}_p | A \rangle. \quad (12)$$

The *free particle*  $g$ -factors (gyromagnetic ratios) are (in nuclear magnetons):  $g_n^s = -3.826$ ,  $g_n^l = 0$ ,  $g_p^s = 5.586$ ,  $g_p^l = 1$ . The nuclear magnetic moment  $\mu$  is often used as a benchmark for the accuracy of the calculation of  $\mathbf{S}_p$  and  $\mathbf{S}_n$  [14, 15]. For the most interesting isotopes either  $\langle \mathbf{S}_p^A \rangle$  or  $\langle \mathbf{S}_n^A \rangle$  dominates ( $\langle \mathbf{S}_{n(p)}^A \rangle \ll \langle \mathbf{S}_{p(n)}^A \rangle$ ). See, for example, Table 1.

Figure 2: Exclusion curves for the spin-dependent WIMP-proton cross section ( $\sigma_{SD}^p$  as a function of the WIMP mass). DAMA/NaI-7a(f) contours for the WIMP-proton SD interaction in  $^{127}\text{I}$  are obtained on the basis of the positive signature of *annual signal modulation* [27, 28]. The scattered points are calculations of [29].

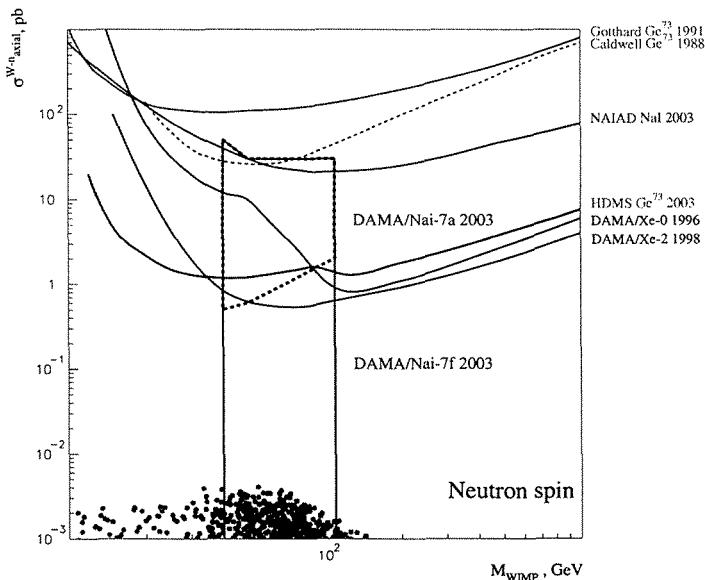


Figure 3: Exclusion curves for the SD WIMP-neutron cross section ( $\sigma_{SD}^n$  versus WIMP mass).

From Eqs. (6) one can conclude the spin observables in DM search give us TWO independent constraints on a SUSY model via  $\sigma_{SD}^p(0)$  and  $\sigma_{SD}^n(0)$ , or, equivalently, via  $a_p$  and  $a_n$ . These constraints are usually presented in the form of exclusion curves obtained with different target nuclei (Figs. 2 and 3). There is only one similar constraint from

spin-independent DM search experiments (Eq. (5)). This presentation is a bit obsolete [27, 28, 29], but it allows one to compare sensitivities of different experiments.

### 3. Long-tail $q$ -behaviour due to the spin

As  $m_\chi$  becomes larger, the finite momentum transfer limit must be considered for heavier mass  $M_A$  nuclei. The differential SD event rate with structure function  $S_{\text{SD}}^A(q)$  (4) has now the form

$$\frac{dR_{\text{SD}}^A}{dq^2} = \frac{\rho}{m_\chi m_A} \int v dv f(v) \frac{8G_F^2}{(2J+1)v^2} S_{\text{SD}}^A(q). \quad (13)$$

Comparing this formula with the observed recoil spectra for different targets (Ge, Xe, F, NaI, etc) one can directly and simultaneously restrict both isoscalar and isovector neutralino-nucleon effective couplings  $a_{0,1}$ . These constraints will impose most model-independent restrictions on the MSSM parameter space. Another attractive feature of the SD WIMP-nucleus interaction is the  $q$ -dependence of SD structure function (4). The ratio of SD to SI rate in the  $^{73}\text{Ge}$  detector grows with the WIMP mass [2, 3]. The growth is much greater for heavy target isotopes like xenon. The reason is the different behavior of the spin and scalar structure functions with increasing momentum transfer. For example, the xenon SI structure function vanishes for  $q^2 \approx 0.02 \text{ GeV}^2$ , but the SD structure function is a non-zero constant in the region (Fig. 4). As noted by Engel in [4], the relatively long tail of the SD structure function is caused by nucleons near the Fermi surface, which do the bulk of the scattering. The core nucleons, which dominate the SI nuclear coupling, contribute much less at large  $q$ . Therefore the SD efficiency for detection of a DM signal is higher than the SI efficiency, especially for very heavy neutralinos.

### 4. One does not miss a DM signal due to the spin

To estimate the DM detection rate we traditionally use the so-called effective scheme of MSSM (effMSSM) whose parameters are defined directly at the electroweak scale, relaxing completely constraints following from any unification assumption (see, for example [30]–[36]). Our MSSM parameter space is determined by the entries of the mass matrices of neutralinos, charginos, Higgs bosons, sleptons and squarks. The relevant definitions can be found in [31]. We have included the current experimental upper limits on sparticle and Higgs masses from the Particle Data Group. Also, the limits on the rare  $b \rightarrow s\gamma$  decay have been imposed. For each point in the MSSM parameter space (MSSM model) we have evaluated the relic density of the light neutralinos  $\Omega_\chi h_0^2$  with our code [37, 38, 39] based on [40], taking into account all coannihilation channels with two-body final states that can occur between neutralinos, charginos, sleptons, stops and sbottoms. We assume  $0.1 < \Omega_\chi h^2 < 0.3$  for the cosmologically interesting region and we also consider the WMAP reduction of the region to  $0.094 < \Omega_\chi h^2 < 0.129$  [41, 42].

From Fig. 5 one sees that the SD contribution obviously dominates in the domain of large expected rates in the non-zero-spin germanium detector ( $R > 0.1 \text{ event/day/kg}$ ). But as soon as the total rate drops down to  $R < 0.01 \text{ event/day/kg}$  or, equivalently, the SI (scalar) neutralino-proton cross section becomes smaller than  $10^{-9}$ – $10^{-10} \text{ pb}$ , the

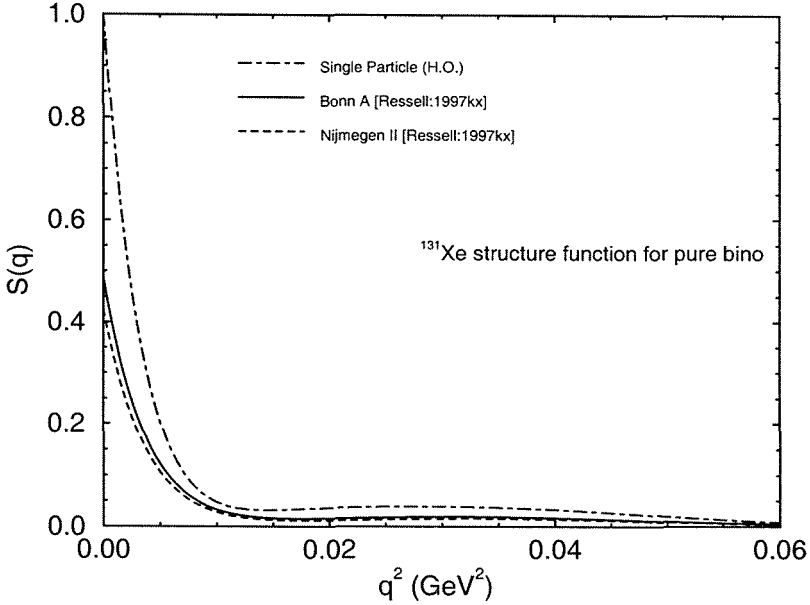


Figure 4: The  $^{131}\text{Xe}$  structure function for a pure bino neutralino. The single-particle structure function is normalized to  $S(0) = 1$ . From [15]

SD interaction may produce a rather non-negligible contribution to the total event rate. Moreover, if the scalar cross section further decreases ( $\sigma < 10^{-12}$  pb), it becomes obvious that the spin contribution alone saturates the total rate and protects it from decreasing below  $R \approx 10^{-6}$ – $10^{-7}$  event/day/kg [44]. With only a spinless detector one can miss a signal caused by SD interaction. An experiment aimed at *detecting* dark matter with sensitivity higher than  $10^{-5}$  event/day/kg should have a non-zero-spin target. Indeed, while the scalar cross sections governed mostly by Higgs exchange can be rather small, the spin cross section cannot be arbitrarily small because the mass of the  $Z$  boson [29], which makes the dominant contribution, is well defined, provided one ignores any possible fine-tuning cancellations. Therefore, if an experiment with sensitivity  $10^{-5}$ – $10^{-6}$  event/day/kg fails to detect a dark matter signal, an experiment with higher sensitivity should have a non-zero-spin target and will be able to detect dark matter particles only due to the spin neutralino-quark interaction.

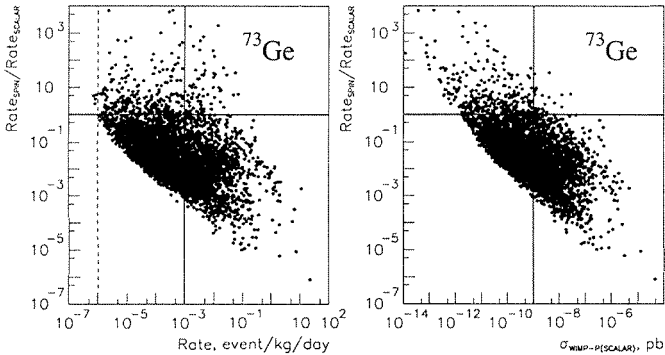


Figure 5: Ratio of the SD (spin) event rate to the SI (scalar) event rate in the  $^{73}\text{Ge}$  isotope (spin = 9/2) as a function of the total (SD+SI) event rate (left) and the scalar cross section of the neutralino-proton interaction (right). The solid vertical lines give the expected sensitivity of one of the best future projects GENIUS [43]. In the region above the horizontal line the spin contribution dominates

## 5. Conclusion

There are at least three reasons to think that spin-dependent interaction of the DM WIMPs with nuclei could be very important. First, contrary to the only one constraint for SUSY models available from the spin-independent WIMP-nucleus interaction, the SD WIMP-nucleus interaction supplies us with two such constraints. Second, for heavy target nuclei and heavy WIMP masses the SD efficiency to detect a DM signal is much higher than the SI efficiency. Finally, the absolute lower bound for the DM detection rate can naturally be due to SD interaction. An experiment aimed at *detecting* DM with sensitivity higher than  $10^{-5}$  event/day/kg should have a non-zero-spin target.

The authors have a pleasure to thank Prof. H.V.Klapdor-Kleingrothaus for fruitful and permanent cooperation as well as the organizers of the Baldin Seminar for their invitation to give this pedagogical review talk whose subject is beyond the traditional scope of the Seminar.

## References

- [1] V. A. Bednyakov, H. V. Klapdor-Kleingrothaus, and S. G. Kovalenko, Phys. Lett. **B329** (1994) 5.
- [2] V. A. Bednyakov and H. V. Klapdor-Kleingrothaus, Phys. Rev. **D63** (2001) 095005.
- [3] V. A. Bednyakov, Phys. Atom. Nucl. **66** (2003) 490.
- [4] J. Engel, Phys. Lett. **B264** (1991) 114.
- [5] G. Jungman, M. Kamionkowski, and K. Griest, Phys. Rept. **267** (1996) 195.

- [6] J. D. Lewin and P. F. Smith, *Astropart. Phys.* **6** (1996) 87.
- [7] P. F. Smith and J. D. Lewin, *Phys. Rept.* **187** (1990) 203.
- [8] V. A. Bednyakov and H. V. Klapdor-Kleingrothaus, *Phys. Atom. Nucl.* **62** (1999) 966.
- [9] V. A. Bednyakov, S. G. Kovalenko, and H. V. Klapdor-Kleingrothaus, *Phys. Atom. Nucl.* **59** (1996) 1718.
- [10] V. A. Bednyakov, H. V. Klapdor-Kleingrothaus, and S. G. Kovalenko, *Phys. Rev.* **D55** (1997) 503.
- [11] V. A. Bednyakov, S. G. Kovalenko, H. V. Klapdor-Kleingrothaus, and Y. Ramachers, *Z. Phys.* **A357** (1997) 339.
- [12] V. A. Bednyakov, H. V. Klapdor-Kleingrothaus, and S. Kovalenko, *Phys. Rev.* **D50** (1994) 7128.
- [13] J. Engel, S. Pittel, and P. Vogel, *Int. J. Mod. Phys.* **E1** (1992) 1.
- [14] M. T. Ressell *et al.*, *Phys. Rev.* **D48** (1993) 5519.
- [15] M. T. Ressell and D. J. Dean, *Phys. Rev.* **C56** (1997) 535.
- [16] J. Engel, M. T. Ressell, I. S. Towner, and W. E. Ormand, *Phys. Rev.* **C52** (1995) 2216.
- [17] V. A. Bednyakov and F. Simkovic, hep-ph/0406218.
- [18] J. R. Ellis and R. A. Flores, *Nucl. Phys.* **B307** (1988) 883.
- [19] J. R. Ellis and R. A. Flores, *Phys. Lett.* **B263** (1991) 259.
- [20] J. Engel and P. Vogel, *Phys. Rev.* **D40** (1989) 3132.
- [21] A. F. Pacheco and D. Strottman, *Phys. Rev.* **D40** (1989) 2131.
- [22] P. C. Divari, T. S. Kosmas, J. D. Vergados, and L. D. Skouras, *Phys. Rev.* **C61** (2000) 054612.
- [23] F. Iachello, L. M. Krauss, and G. Maino, *Phys. Lett.* **B254** (1991) 220.
- [24] M. A. Nikolaev and H. V. Klapdor-Kleingrothaus, *Z. Phys.* **A345** (1993) 373.
- [25] V. Dimitrov, J. Engel, and S. Pittel, *Phys. Rev.* **D51** (1995) 291.
- [26] J. R. Ellis and R. A. Flores, *Nucl. Phys.* **B400** (1993) 25.
- [27] R. Bernabei *et al.*, *Riv. Nuovo Cim.* **26** (2003) 1.
- [28] R. Bernabei *et al.*, *Phys. Lett.* **B509** (2001) 197.
- [29] V. A. Bednyakov and H. V. Klapdor-Kleingrothaus, hep-ph/0404102.

- [30] V. A. Bednyakov and H. V. Klapdor-Kleingrothaus, Phys. Rev. **D59** (1999) 023514.
- [31] V. A. Bednyakov and H. V. Klapdor-Kleingrothaus, Phys. Rev. **D62** (2000) 043524.
- [32] L. Bergstrom and P. Gondolo, Astropart. Phys. **5** (1996) 263.
- [33] P. Gondolo, hep-ph/0005171.
- [34] L. Bergstrom, Rept. Prog. Phys. **63** (2000) 793.
- [35] A. Bottino, F. Donato, N. Fornengo, and S. Scopel, Phys. Rev. **D63** (2001) 125003.
- [36] J. R. Ellis, A. Ferstl, K. A. Olive, and Y. Santoso, Phys. Rev. **D67** (2003) 123502,
- [37] V. A. Bednyakov, H. V. Klapdor-Kleingrothaus, and V. Gronewold, Phys. Rev. **D66** (2002) 115005.
- [38] V. A. Bednyakov, H. V. Klapdor-Kleingrothaus, and E. Zaiti, Phys. Rev. **D66** (2002) 015010.
- [39] V. A. Bednyakov, hep-ph/0208172.
- [40] P. Gondolo, J. Edsjo, L. Bergstrom, P. Ullio, and E. A. Baltz, astro-ph/0012234.
- [41] D. N. Spergel *et al.*, Astrophys. J. Suppl. **148** (2003) 175.
- [42] C. L. Bennett *et al.*, Astrophys. J. Suppl. **148** (2003) 1.
- [43] H. V. Klapdor-Kleingrothaus, Phys. Atom. Nucl., **61**, 967 (1998), and Int. Journal of Modern Physics A **13**, 3953 (1998). H. V. Klapdor-Kleingrothaus and Y. Ramachers. Eur. Phys. J. A **3**, 85 (1998); H. V. Klapdor-Kleingrothaus *et al.*, GENIUS: A Super-sensitive Germanium Detector System for Rare Events, Proposal, MPI-H-V26-1999, August 1999, hep-ph/9910205.
- [44] V. A. Bednyakov and H. V. Klapdor-Kleingrothaus, Phys. Rev. D **62** (2000) 043524.

# CHARM PRODUCTION IN NN AND $\gamma N$ COLLISIONS

Egle Tomasi-Gustafsson<sup>†</sup>

*DAPNIA/SPhN, CEA/Saclay, 91191 Gif-sur-Yvette Cedex, France*

<sup>†</sup> *E-mail: etomasi@cea.fr*

## Abstract

The processes of open and hidden charm production in  $NN$  collisions and of open charm production in  $\gamma N$  collisions are studied. The near-threshold cross section is predicted and polarization phenomena are calculated in frame of an effective Lagrangian approach.

## 1. Introduction

New experimental facilities, planned in the near future [1], will be able to make detailed measurements of open charm production in  $pN$ ,  $NA$  or  $AA$  collisions, in a wide energy region, starting from threshold. The upgraded machine at Jefferson Laboratory will open the possibility to produce charmed particles at threshold in photoproduction experiments [2].

One can expect that the physics of close-to-threshold  $\Lambda_c D$ -production is similar to  $\Lambda K$ -production and use  $SU(4)$  symmetry to make predictions in the charm sector.

Few or no experimental data exist at threshold for open charm hadro and photoproduction on the nucleon. More data exist for  $J/\Psi$  production, sometimes indirectly derived from nuclear reactions.

The theoretical activity, for inclusive charm production, is mainly focused on QCD-inspired approaches, and it cannot be easily extrapolated to the threshold region. Moreover exclusive processes cannot be described in QCD approaches without additional assumptions. For a reliable description of the overall charm dynamics in  $AA$  collisions, it is necessary to have a good parametrization of the elementary processes of open charm production in  $\pi N$  and  $NN$  collisions. The parametrization of the energy behavior of the total cross section for different processes of  $D$  and  $\bar{D}$ -production for  $\sqrt{s} \geq 10$  GeV, generally used in simulation codes, cannot be applied near threshold as it violates the general threshold behavior for two or three particle production.

In this contribution we present some of the results recently obtained for the processes  $N + N \rightarrow \Lambda_c(\Sigma_c) + \bar{D} + N$  [3],  $N + N \rightarrow N + N + J/\Psi$  [7] in the threshold region and for  $\gamma + N \rightarrow \Lambda_c(\Sigma_c) + \bar{D} + N$  [4, 6]. We derive, in model independent way, the spin structure of the matrix element for these processes. For quantitative predictions, we calculate the cross section and the polarization phenomena in the framework of a model based on meson exchanges in an effective Lagrangian (ELA) approach. ELA gives a very convenient frame for this study, as all the observables can be calculated with the help of few parameters, such as masses, coupling constants, and magnetic moments, which have a definite physical meaning.

## 2. Open charm production in NN collisions

An important characteristic of the threshold  $NN$ -dynamics is the strong correlation between the spin and isospin structures of the threshold matrix element for the  $N + N \rightarrow \Lambda_c(\Sigma_c) + \bar{D} + N$  reactions. Using the isotopic invariance of the strong interaction and taking into account that  $I(\Sigma_c) = 1$ ,  $I(\bar{D}) = 1/2$ , one can express the matrix element for the seven different processes  $N + N \rightarrow \Lambda_c(\Sigma_c) + \bar{D} + N$ , in terms of three (complex) isotopic amplitudes,  $A_{I_1 I_2}$ , corresponding to the total isospin  $I_1$  for the initial nucleons and the total isospin  $I_2$  for the produced  $\bar{D}N$ -system:

$$\begin{aligned}
 \mathcal{M}(pp \rightarrow \Sigma_c^{++} D^- p) &= A_{11} + \sqrt{2}A_{10}, \\
 \mathcal{M}(pp \rightarrow \Sigma_c^{++} \bar{D}^0 n) &= A_{11} - \sqrt{2}A_{10}, \\
 \mathcal{M}(pp \rightarrow \Sigma_c^+ \bar{D}^0 p) &= -\sqrt{2}A_{11}, \\
 \mathcal{M}(np \rightarrow \Sigma_c^{++} D^- n) &= A_{11} + \sqrt{2}A_{01}, \\
 \mathcal{M}(np \rightarrow \Sigma_c^+ \bar{D}^0 p) &= -A_{11} + \sqrt{2}A_{01}, \\
 \mathcal{M}(np \rightarrow \Sigma_c^+ D^- p) &= A_{10} - A_{01}, \\
 \mathcal{M}(np \rightarrow \Sigma_c^+ \bar{D}^0 n) &= -A_{10} - A_{01},
 \end{aligned} \tag{1}$$

Generally, each isospin structure contains the contribution of all possible spins. However, the interferences  $A_{11} \otimes A_{01}^*$  and  $A_{10} \otimes A_{01}^*$ , vanish in the threshold region (after summing over the polarizations of the colliding nucleons) and we can derive the following relations, between the differential cross sections, which hold for any model, at threshold:

$$\frac{d\sigma}{d\omega}(np \rightarrow \Sigma_c^{++} D^- n) = \frac{d\sigma}{d\omega}(np \rightarrow \Sigma_c^+ \bar{D}^0 p), \quad \frac{d\sigma}{d\omega}(np \rightarrow \Sigma_c^+ D^- p) = \frac{d\sigma}{d\omega}(np \rightarrow \Sigma_c^+ \bar{D}^0 n).$$

Following the ideology of meson production in  $NN$ -collisions, we calculate the cross section for  $NN$  collisions, in terms of  $D$ -meson exchange in  $t$ -channel, neglecting, as it was done for strange particle production, the light mesons exchange. The cross section can be expressed in terms of the isotopic amplitudes of elastic  $\bar{D}N$  scattering,  $a_0$  (singlet) and  $a_1$  (triplet). Using isotopic invariance, one finds for the ratio  $\mathcal{R}_D$  of the cross sections of  $\Lambda_c \bar{D}$ -production for  $np$  over  $pp$  collisions:

$$\mathcal{R}_D = \frac{\sigma(np \rightarrow \Lambda_c^+ \bar{D}^0 n)}{\sigma(pp \rightarrow \Lambda_c^+ \bar{D}^0 p)} = \frac{\sigma(np \rightarrow \Lambda_c^+ D^- p)}{\sigma(pp \rightarrow \Lambda_c^+ \bar{D}^0 p)} = \frac{1}{4} \left( 1 + \frac{a_0^2}{3a_1^2} \right) > \frac{1}{4}, \tag{2}$$

where the index  $D$  underlines that this prediction is valid only in framework of  $D$ -exchange. These large isotopic effects can, in principle, be modified by initial (ISI) and final (FSI) state interaction. However, as the reaction threshold is quite large, one can assume that ISI are similar for  $np$  and  $pp$ . Moreover, assuming  $|a_0/a_1| \simeq 0.1$  as for elastic  $KN$  scattering, FSI would also be negligible.

Based on phase space arguments, one can estimate the relative cross section of the processes  $p + p \rightarrow \Lambda_c^+ + \bar{D}^0 + p$  ( $D$ -exchange) and  $p + p \rightarrow \Lambda + K^+ + p$  ( $K$ -exchange). Charm production turns out to be lower by three order of magnitude than strange particle production. This is mainly due to the difference in the reaction threshold and in the propagators, as well as to the necessary phenomenological form factors. Taking the experimental data on the total cross section for  $p + p \rightarrow \Lambda + K^+ + p$  [5], one can predict the following energy dependence for the cross section of open charm production, valid near threshold:

$$\sigma(pp \rightarrow \Lambda_c^+ \bar{D}^0 p) \simeq 0.2(Q/0.1 \text{ GeV})^2 \text{ nb}. \tag{3}$$

In Fig. 2 a comparison between the calculations [4] (thick lines) and [8] (thin lines) is shown for  $\overline{D}^0$  production (solid lines) and for  $D^-$ -production (dashed lines).

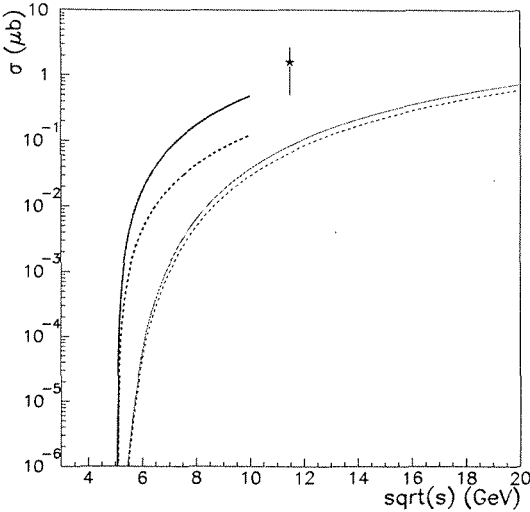


Fig. 1 Comparison between the calculations [4] (thick lines) and [8] (thin lines) for  $\overline{D}^0$  production (solid lines) and for  $D^-$ -production (dashed lines)

### 3. $J/\Psi$ production in $NN$ collisions

$J/\Psi$  production has a specific interest: the production and the propagation of charm in ion-ion collisions has been considered as one of the most promising probe of quark-gluon plasma (QGP) formation. The suppression of charmonium production in heavy ion collisions has been indicated as a signature of QGP [10], but in order to state the evidence of a clear signal, it is necessary to analyze in detail all possible mechanisms for  $J/\Psi$  production in ion-ion collisions, and also all other processes which are responsible for the dissociation of the produced  $J/\Psi$  meson, such as  $J/\Psi + N \rightarrow \Lambda_c + D$ , for example. The knowledge of the elementary process  $p + N \rightarrow p + N + J/\Psi$  is very important for a realistic calculation of  $J/\Psi$  production in nucleus-nucleus collisions.

In principle, the 'elastic'  $J/\Psi$  production in  $NN$ -collisions can be treated in full analogy with processes of light vector meson production. All symmetry properties of the strong interaction, such as the Pauli principle, the isotopic invariance, the P-invariance, which have been successfully applied to light vector meson production in  $NN$ -collisions [11], hold for  $J/\Psi$  production, too. A formalism can be built, which is particularly simplified in the threshold region, where all final particles are produced in  $S$ -state. Simple considerations indicate that this region may be quite wide: the effective proton size, which is responsible for charm creation, has to be quite small,  $r_c \simeq 1/m_c$ , where  $m_c$  is the  $c$ -quark mass [12]. Therefore the  $S$ -wave picture can be applied for  $q \leq m_c$ , where  $q$  is the  $J/\Psi$  three-momentum in the reaction center of mass (CMS). In the general case the spin structure of the matrix element for the process  $N + N \rightarrow N + N + V$  is described by a set of 48 independent complex amplitudes, which are functions of five kinematical variables.

One can see that the values can differ by an order of magnitude. This comes from the fact that the correct  $Q$ -behavior at threshold, from phase space considerations, should be quadratic, whereas the best fit parameters of Ref. [8] give an exponent  $\simeq 5$ . The difference is also due to the fact that the isotopic relations among  $\overline{D}^0$  and  $D^-$ -cross sections are not respected in the parametrization [8]. This induces very large effect in particular in the threshold region. Note that the calculation [9], which is based on the Quark-Gluon String model and the Regge phenomenology, is in agreement with [4], for a specific choice of form factors.

The same reaction, in coplanar kinematics, is described by 24 amplitudes, functions of four variables. In collinear kinematics the number of independent amplitudes is reduced to 7 and the description of this reaction is further simplified in case of threshold  $V$ -meson production, where all final particles are in  $S$ -state.

Applying the selection rules following from the Pauli principle, the  $P$ -invariance and the conservation of the total angular momentum, it is possible to prove that the threshold process  $p + p \rightarrow p + p + V^0$  is characterized by a single partial transition:

$$S_i = 1, \ell_i = 1 \rightarrow \mathcal{J}^P = 1^- \rightarrow S_f = 0, \quad (4)$$

where  $S_i$  ( $S_f$ ) is the total spin of the two protons in the initial (final) states and  $\ell_i$  is the orbital momentum of the colliding protons. In the CMS of the considered reaction, the matrix element corresponding to transition (4) can be written as:

$$\mathcal{M}(pp) = 2f_{10}(\tilde{\chi}_2 \sigma_y \vec{\sigma} \cdot \vec{U}^* \times \hat{k} \chi_1) (\chi_4^\dagger \sigma_y \tilde{\chi}_3^\dagger), \quad (5)$$

where  $\chi_1$  and  $\chi_2$  ( $\chi_3$  and  $\chi_4$ ) are the two-component spinors of the initial (final) protons;  $\vec{U}$  is the three-vector of the  $V$ -meson polarization,  $\hat{k}$  is the unit vector along the 3-momentum of the initial proton;  $f_{10}$  is the S-wave partial amplitude, describing the triplet-singlet transition of the two-proton system in  $V$ -meson production.

In case of  $np$ -collisions, applying the conservation of isotopic invariance for the strong interaction, two threshold partial transitions are allowed:

$$S_i = 1, \ell_i = 1 \rightarrow \mathcal{J}^P = 1^- \rightarrow S_f = 0, \quad S_i = 0, \ell_i = 1 \rightarrow \mathcal{J}^P = 1^- \rightarrow S_f = 1, \quad (6)$$

with the following spin structure of the matrix element:

$$\mathcal{M}(np) = f_{10}(\tilde{\chi}_2 \sigma_y \vec{\sigma} \cdot \vec{U}^* \times \hat{k} \chi_1) (\chi_4^\dagger \sigma_y \tilde{\chi}_3^\dagger) + f_{01}(\tilde{\chi}_2 \sigma_y \chi_1) (\chi_4^\dagger \vec{\sigma} \cdot \vec{U}^* \times \hat{k} \sigma_y \tilde{\chi}_3^\dagger). \quad (7)$$

Here  $f_{01}$  is the S-wave partial amplitude describing the singlet-triplet transition of the two-nucleon system in  $V$ -meson production. In the general case the amplitudes  $f_{10}$  and  $f_{01}$  are complex functions, depending on the energies  $E$ ,  $E'$  and  $E_V$ , where  $E$ , ( $E'$ ) and  $E_V$  are the energies of the initial (final) proton and of the produced  $V$ -meson, respectively.

Note that  $f_{10}$  is the common amplitude for  $pp$ - and  $np$ -collisions, due to the isotopic invariance of the strong interaction. This explains the presence of the coefficient two in Eq. (5). All dynamical information is contained in the partial amplitudes  $f_{01}$  and  $f_{10}$ , which are different for the different vector particles. Some polarization phenomena show common characteristics, essentially independent from the type of vector meson. For example, vector mesons produced in  $pp$ - and  $np$ -threshold collisions are transversally polarized, and the elements of the density matrix  $\rho$  are independent from the relative values of the amplitudes  $f_{01}$  and  $f_{10}$ :  $\rho_{xx} = \rho_{yy} = \frac{1}{2}$ ,  $\rho_{zz} = 0$ .

All other single spin polarization observables, related to the polarizations of the initial or final nucleons, identically vanish, for any process of  $V$ -meson production. The dependence of the differential cross section for threshold collisions of polarized nucleons (where the polarization of the final particles is not detected) can be parameterized as follows:

$$\frac{d\sigma}{d\omega}(\vec{P}_1, \vec{P}_2) = \left( \frac{d\sigma}{d\omega} \right)_0 \left( 1 + \mathcal{A}_1 \vec{P}_1 \cdot \vec{P}_2 + \mathcal{A}_2 \hat{k} \cdot \vec{P}_1 \hat{k} \cdot \vec{P}_2 \right), \quad (8)$$

where  $\vec{P}_1$  and  $\vec{P}_2$  are the axial vectors of the beam and target nucleon polarizations, and  $d\omega$  is the element of phase-space for the three-particle final state. The spin correlation coefficients  $\mathcal{A}_1$  and  $\mathcal{A}_2$  are real and they are different for  $pp$ - and  $np$ - collisions:

- $\vec{p} + \vec{p} \rightarrow p + p + V^0$ :  $\mathcal{A}_1(pp) = 0$ ,  $\mathcal{A}_2(pp) = 1$ .
- $\vec{n} + \vec{p} \rightarrow n + p + V^0$ :  $\mathcal{A}_1(np) = -\frac{|f_{01}|^2}{|f_{01}|^2 + |f_{10}|^2}$ ,  $\mathcal{A}_2(np) = \frac{|f_{10}|^2}{|f_{01}|^2 + |f_{10}|^2}$ ,

with the following relations  $-\mathcal{A}_1(np) + \mathcal{A}_2(np) = 1$  and  $0 \leq \mathcal{A}_2(np) \leq 1$ .

Defining  $\mathcal{R}$  as the ratio of the total (unpolarized) cross section for  $np$ - and  $pp$ - collisions, taking into account the identity of final particles in  $p + p \rightarrow p + p + V^0$ , we find:

$$\mathcal{R} = \frac{\sigma(np \rightarrow npV^0)}{\sigma(pp \rightarrow ppV^0)} = \frac{1}{2} + \frac{1}{2} \frac{|f_{01}|^2}{|f_{10}|^2}, \quad \text{and} \quad \mathcal{A}_1 = -1 + \frac{1}{2\mathcal{R}}. \quad (9)$$

Similar expressions for the polarization transfer from the initial neutron to the final proton can be given in terms of the partial amplitudes  $f_{01}$  and  $f_{10}$ .

One can show that the most probable mechanism to describe the threshold dynamics of  $J/\Psi$ -production in NN-collisions is meson exchange in  $t$ -channel, with  $\mathcal{J}^P = 0^+$  (scalar mesons) and  $\mathcal{J}^P = 0^-$  (pseudoscalar meson).

For the exchange of one meson,  $\pi$ ,  $\rho$  or  $\eta$ , one finds that only one amplitude enters in the cross section, and the observables take definite values (Table I).

	$\pi(f_{01} = -3f_{10})$	$\eta(f_{01} = f_{10})$	$\sigma(f_{01} = -f_{10})$
$\mathcal{R}$	5	1	1
$\mathcal{A}_1$	-9/10	1/2	-1/2
$\mathcal{P}_1$	-3/5	-1	1

Table 1: Numerical values of the isotopic ratio and single spin polarization observables for  $\pi$ ,  $\eta$  or  $\sigma$  exchange

If one considers the exchange of two mesons,  $\pi + \eta$ , for example, one can still express the observables in terms of a parameter,  $r$ , which characterizes the relative role of  $\pi$  and  $\eta$  exchange and contains coupling constants, propagators and kinematical factors:

$$r = \frac{g_{\eta NN} h_{1\eta}}{g_{\pi NN} h_{1\pi}} \left( \frac{t - m_\pi^2}{t - m_\eta^2} \right).$$

The single spin polarization observables in  $n + p \rightarrow n + p + V^0$  and the ratio  $\mathcal{R}$  of the total cross section for  $n + p$ - and  $p + p$ -collisions can be written as a function of  $r$  as:

$$\mathcal{A}_1 = -\frac{9 + 6\mathcal{R}e r + |r|^2}{2(5 + 2\mathcal{R}e r + |r|^2)}, \quad \mathcal{P}_1 = -\frac{3 - 2\mathcal{R}e r - |r|^2}{5 + 2\mathcal{R}e r + |r|^2}, \quad \mathcal{R} = \frac{5 + 2\mathcal{R}e r + |r|^2}{|1 - r|^2}, \quad (10)$$

where  $h_{1\eta}$  ( $h_{1\pi}$ ) is the partial amplitude which describes the threshold spin structure for the subprocess  $\pi^{0*}(\eta^*) + N \rightarrow V^0 + N$  at threshold.

In order to make an estimation of the cross section, one can compare  $\phi$  and  $J/\Psi$  production, in framework of a model based on  $\rho$  exchange. One finds that

$$\sigma(pp \rightarrow pp\phi) \simeq 206 \left( \frac{Q}{0.1 \text{ GeV}} \right)^2 \text{ nb}$$

and

$$\sigma(pp \rightarrow ppJ/\Psi) \simeq 9.7 \cdot 10^{-5} \left( \frac{Q}{0.1 \text{ GeV}} \right)^2 \left[ F(t_{J/\Psi})/F(t_\phi) \right]^2 \text{ nb} . \quad (11)$$

This value is too small, when compared with the existing experimental value for the lowest  $\sqrt{s} = 6.7 \text{ GeV}$ , namely  $\sigma_{exp}(pp \rightarrow ppJ/\Psi) = 0.3 \pm 0.09 \text{ nb}$ . To explain this discrepancy, one can note that the  $\rho$ -exchange model for  $\sigma(\pi N \rightarrow J/\Psi)$  gives a cross section one order of magnitude smaller in comparison with other possible theoretical approaches [13, 14, 15]. Another possibility is to take  $\left[ F(t_{J/\Psi})/F(t_\phi) \right]^2 \simeq 10$ , which can be plausible, because the  $J/\Psi = c\bar{c}$ -system must have a smaller size in comparison with  $\phi = s\bar{s}$ . This can be realized by the following form factor:

$$F_V(t) = \frac{1}{1 - t/\Lambda_V^2}, \quad \Lambda_V \simeq m_V.$$

The cross section, based on Eq. (11) normalized the the experimental point at  $\sqrt{s} = 6.7 \text{ GeV}$ , i.e., taking the ratio  $\left[ F(t_{J/\Psi})/F(t_\phi) \right]^2 = 10$ , is plotted in Fig. 2, together with the experimental data from the compilation [16], where different symbols differentiate  $J/\Psi$  production in  $pp$  or extrapolated from  $pA$  collisions. Note, that, for  $r$  real and  $\simeq 0$ ,

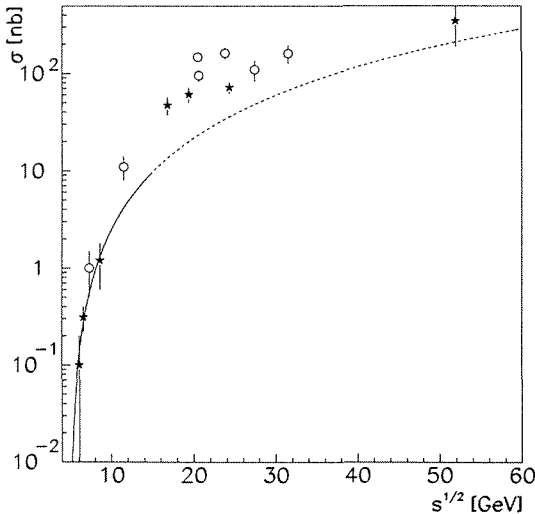


Fig. 2 Cross section for  $J/\psi$  production in  $pp$  collisions. Data are from [16]

The experimental determination of the ratio of the total cross sections for  $np$  and  $pp$  collisions is very important for the identification of the reaction mechanism.

#### 4. $\gamma$ -nucleon collisions

We give here model independent considerations for the reaction  $\gamma + p \rightarrow \Lambda_c^+ + \bar{D}^0$ , where the spins involved are  $1 + 1/2 \rightarrow 1/2 + 0$ . In collinear kinematics, due to the conservation

of the spin projection, the collision of  $\gamma$  and  $p$  with parallel spins cannot take place for collinear regime. Therefore, the asymmetry in the collision of circularly polarized photons with a polarized target, takes its maximum value. This result holds for any process of pseudoscalar and scalar meson photoproduction on a nucleon target (if the final baryon has spin 1/2) and it is independent on the  $\mathcal{P}$ -parity of produced meson. It is a model independent result, based uniquely on the assumption of the spins of the particle, the conservation of helicity in collinear kinematics, and applies also to the threshold region, for any angle.

One can suggest a model independent method to determine the parity of the charmed mesons, more exactly, the relative  $P(N\Lambda_c D)$  parity. We will use the standard parametrization [17] of the spin structure for the amplitude of pseudoscalar meson photoproduction on the nucleon:

$$\mathcal{M}(\gamma N \rightarrow Y_c \bar{D}_c) = \chi_2^\dagger \left[ i\vec{\sigma} \cdot \vec{e} f_1 + \vec{\sigma} \cdot \hat{q} \vec{\sigma} \cdot \hat{k} \times \vec{e} f_2 + i\vec{e} \cdot \hat{q} \vec{\sigma} \cdot \hat{k} f_3 + i\vec{\sigma} \cdot \hat{q} \vec{e} \cdot \hat{q} f_4 \right] \chi_1, \quad (12)$$

where  $\hat{k}$  and  $\hat{q}$  are the unit vectors along the three-momentum of  $\gamma$  and  $\bar{D}_c$ ;  $f_i$ ,  $i=1,4$  are the scalar amplitudes, which are functions of two independent kinematical variables, the square of the total energy  $s$  and  $\cos\vartheta$ , where  $\vartheta$  is the  $\bar{D}_c$ -meson production angle in the reaction center of mass (CMS) with respect to the direction of the incident photon,  $\chi_1$  and  $\chi_2$  are the two-component spinors of the initial nucleon and the produced  $Y_c$ -baryon. Note that the pseudoscalar nature of the  $\bar{D}_c$ -meson is not experimentally confirmed up to now, therefore Eq. (12) corresponds to the prescription of the quark model for the  $\mathcal{P}$ -parities of  $\bar{D}_c$  and  $Y_c$ -charm particles.

It is possible to derive in a model independent way, that for the reaction  $\gamma + p \rightarrow \Lambda_c^+ + \bar{D}^0$ , the triple polarization correlation coefficient is sensitive to  $P(N\Lambda_c D)$ . In collinear kinematics, the spin structure (12) reduces to one amplitude, which depends on  $P(N\Lambda_c D)$ :

$$\begin{aligned} \mathcal{F}_{col}^{(-)} &= \vec{\sigma} \cdot \vec{e} f_{col}^{(-)}, \\ \mathcal{F}_{col}^{(+)} &= \vec{\sigma} \cdot \vec{e} \times \hat{k} f_{col}^{(+)}, \end{aligned} \quad (13)$$

where  $f_{col}^{(\pm)}$  is the collinear amplitude for  $P(N\Lambda_c D) = \pm 1$ . Due to the presence of a single allowed amplitude in collinear kinematics, all polarization observables have definite numerical values, which are independent on the model chosen for  $f_{col}^{(\pm)}$ .

The dependence of the  $\Lambda_c$  polarization on the polarization of the colliding particles can be written as:

$$-(\vec{e} \cdot \vec{e})(\vec{P}_1 \cdot \vec{P}_2) + 2(\vec{e} \cdot \vec{P}_1)(\vec{e} \cdot \vec{P}_2), \quad \text{if } P(N\Lambda_c D) = -1,$$

$$(\vec{e} \cdot \vec{e})[(\vec{P}_1 \cdot \vec{P}_2) - 2(\hat{k} \cdot \vec{P}_1)(\hat{k} \cdot \vec{P}_2)] - 2(\vec{e} \cdot \vec{P}_1)(\vec{e} \cdot \vec{P}_2), \quad \text{if } P(N\Lambda_c D) = +1, \quad (14)$$

where  $\vec{P}_1$  and  $\vec{P}_2$  are the polarization vectors for the initial and final baryons.

One can see from (14), that only the linear photon polarization affects the triple polarization correlations in  $\vec{\gamma} + \vec{p} \rightarrow \Lambda_c^+ + \bar{D}^0$ , due to the  $\mathcal{P}$ -invariance of the electromagnetic interaction of charmed particles. Let us define the coordinate system for the considered collinear kinematics with the  $z$ -axis along  $\hat{k}$  and the  $x$ -axis along the vector  $\vec{e}$  of the photon linear polarization. The correlations (14) can be written in such system as:

$$-(\vec{P}_1 \cdot \vec{P}_2) + 2P_{1x}P_{2x} = P_{1x}P_{2x} - P_{1y}P_{2y} - P_{1z}P_{2z}, \quad \text{if } P(N\Lambda_c D) = -1,$$

$$(\vec{P}_1 \cdot \vec{P}_2) - 2P_{1z}P_{2z} - 2P_{1x}P_{2x} = -P_{1x}P_{2x} + P_{1y}P_{2y} - P_{1z}P_{2z}, \text{ if } P(N\Lambda_c D) = +1. \quad (15)$$

From (15) one can find a connection between the components of the vectors  $\vec{P}_1$  and  $\vec{P}_2$  for the different  $P(N\Lambda_c D)$ , assuming, for simplicity, that initially one has 100% linearly polarized photons:

$$\begin{aligned} P_{2x} &= +P_{1x}, P_{2y} = -P_{1y}, P_{2z} = -P_{1z}, \text{ if } P(N\Lambda_c D) = -1, \\ P_{2x} &= -P_{1x}, P_{2y} = +P_{1y}, P_{2z} = -P_{1z}, \text{ if } P(N\Lambda_c D) = +1, \end{aligned} \quad (16)$$

One can see that both transversal components of the  $\Lambda_c$ -polarization are sensitive to  $P(N\Lambda_c D)$ , through the relative sign between  $P_{2i}$  and  $P_{1i}$ :

$$P_{2x} = -P(N\Lambda_c D)P_{1x}, P_{2y} = P(N\Lambda_c D)P_{1y}, \quad (17)$$

whereas  $P_{2z} = -P_{1z}$  for any value of  $P(N\Lambda_c D)$ .

Therefore, the relations (17) allow one to determine, in a model-independent way, the  $D$ -meson P-parity. This model independent result holds for any nucleon photoproduction of a spin 1/2 baryon and a spin zero meson. It requires the assumption on P-parity conservation in  $\gamma + p \rightarrow \Lambda_c^+ + \bar{D}^0$  and helicity conservation in the collinear regime. Similar arguments apply to the reaction  $\bar{\gamma} + \bar{p} \rightarrow \Theta^+ + K$  and allow to suggest a method for the determination of the parity of pentaquark [18].

The suggested experiment, measuring the triple polarization correlations in  $\bar{\gamma} + \bar{p} \rightarrow \bar{\Lambda}_c^+ + \bar{D}^0$ , can be in principle realized by the Compass collaboration [19], which has a polarized target and where linearly polarized photons can be obtained in muon-proton collisions, at small photon virtuality, by tagging the photon through the detection of the scattered muon. The  $\Lambda_c$ -polarization can be measured through the numerous weak decays of the  $\Lambda_c^+$ -hyperon, for example  $\Lambda_c^+ \rightarrow \Lambda + e^+ + \nu_e$  [20], which is characterized by a large decay asymmetry. In other words, the  $\Lambda_c$  is a self-analyzing particle.

Eqs. (17) show that only the relative sign of the transversal components of the polarization of the target proton and the produced  $\Lambda_c^+$ -hyperon is important for the determination of the  $P(N\Lambda_c D)$ -parity. Therefore such experiment does not need very large statistics, only well identified events. The energy of the photon beam has not to be necessarily monochromatic.

The charm particle photo and electroproduction at high energy is usually interpreted in terms of photon-gluon fusion,  $\gamma + G \rightarrow c + \bar{c}$ . Near threshold, other possible mechanisms, based on the subprocess  $q + \bar{q} \rightarrow G \rightarrow c + \bar{c}$  should also be taken into account. In case of exclusive reactions, such mechanism is equivalent to the exchange of a  $\bar{c}q$ -system, in  $t$ -channel [21]. The mesonic equivalent of such exchange is the exchange by pseudoscalar  $\bar{D}_c$  and (or) vector  $\bar{D}_c^*$  mesons, in the  $t$ -channel of the considered reaction.

In order to insure the gauge invariance, baryonic exchanges in  $s$ - and  $u$ -channels have also to be taken into account. Due to the virtuality of the exchanged hadrons, in this approach, form factors (FFs) are introduced in the pole diagrams.

The largest cross section on the neutron target belongs to the process  $\gamma + n \rightarrow \Sigma_c^0 + \bar{D}^0$ , the  $D^-$  production being essentially suppressed. The  $D^-$  production is also small in the  $\gamma p$  interaction,  $\gamma + p \rightarrow \Sigma_c^{++} + D^-$ , in agreement with the experiment [22]. Large isotopic effects are an expected property of ELA approach, because the relative values of  $s$ ,  $u$ , and  $t$ -channel contributions are different for the different channels (Fig. 4).

Polarization effects are generally large (in absolute value), characterized by a strong  $\cos\vartheta$ -dependence, which results from a coherent effect of all the considered pole contributions.

Large isotopic effects (i.e. the dependence on the electric charges of the participating hadrons) are especially visible in the  $\cos\vartheta$ -distributions for all these observables.

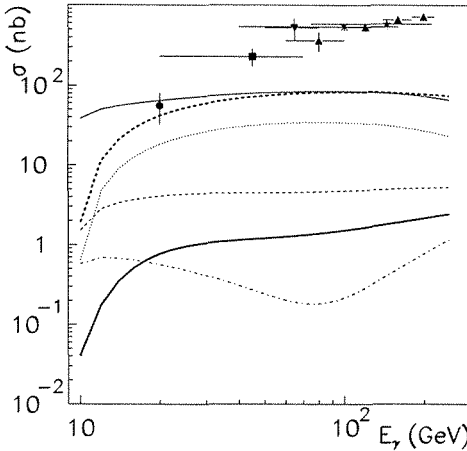


**Fig. 3**  $E_\gamma$ -dependence of the total cross section for photoproduction of charmed particles for model I. The curves correspond to different reactions:  $\gamma + p \rightarrow \Lambda_c^+ + \bar{D}^0$  (solid line),  $\gamma + p \rightarrow \Sigma_c^{++} + D^-$  (dashed line),  $\gamma + p \rightarrow \Sigma_c^+ + \bar{D}^0$  (dotted line),  $\gamma + n \rightarrow \Lambda_c^+ + D^-$  (dot-dashed line),  $\gamma + n \rightarrow \Sigma_c^+ + D^-$  (thick solid line),  $\gamma + n \rightarrow \Sigma_c^0 + \bar{D}^0$  (thick dashed line). The data correspond to the total charm photoproduction cross section ([4] and refs. herein)

In frame of the considered model, the asymmetry  $\Sigma_B$  is positive in the whole angular region, in contradiction with the predictions of PGF [23] and in agreement with the SLAC data [24].

## 5. Instead of Conclusions

*This talk is dedicated to Prof. Michail P. Rekalov. The results presented here would not have been realized without his deep and wide knowledge in different fields of physics. I met him in for the first time in this Hall of the Bogoliubov Laboratory of Theoretical Physics, ten years ago. Since then, I could profit of many enthusiastic discussions and of his clear explanations.*

*Extremely creative, full of ideas, he was always ready to interact with people. Very generous in scientific discussions, he had a prompt humour, sometimes very sharp.*

*He was able to think deeply and to concentrate on physics. He could focus very quickly on the essential aspects of a problem: complicated and difficult questions were suddenly made very simple and solvable.*

*His absence is an unvaluable loss for our community.*

## References

- [1] H. Feldmeier, J. Knoll, W. Norenberg and J. Wambach, Structure of Hadrons: 29th International Workshop on Gross Properties of Nuclei and Nuclear Excitations, Hirschegg, Austria, 14-20 Jan 2001.

- [2] See the website <http://www.jlab.org/gen/charm/>.
- [3] M. P. Rekaló and E. Tomasi-Gustafsson, *Eur. Phys. J. A* **16**, 575 (2003).
- [4] E. Tomasi-Gustafsson and M. P. Rekaló, *Phys. Rev. D* **69**, 094015 (2004).
- [5] P. Moskal, M. Wolke, A. Khoukaz and W. Oelert, *Prog. Part. Nucl. Phys.* **49**, 1 (2002).
- [6] M. P. Rekaló and E. Tomasi-Gustafsson, *Phys. Lett. B* **541**, 101 (2002).
- [7] M. P. Rekaló and E. Tomasi-Gustafsson, *New J. Phys.* **4**, 68 (2002).
- [8] W. Cassing, E. L. Bratkovskaya and A. Sibirtsev, *Nucl. Phys. A* **691**, 753 (2001).
- [9] A. M. Gasparyan, V. Y. Grishina, L. A. Kondratyuk, W. Cassing and J. Speth, *arXiv:nucl-th/0210018*.
- [10] T. Matsui and H. Satz, *Phys. Lett. B* **178**, 416 (1986).
- [11] M. P. Rekaló *et al.* *Z. Phys. A* **357**, 133 (1997).
- [12] S. J. Brodsky, E. Chudakov, P. Hoyer and J. M. Laget, *Phys. Lett. B* **498**, 23 (2001).
- [13] J. F. Bolzan, K. A. Geer, W. F. Palmer and S. S. Pinsky, *Phys. Rev. Lett.* **35**, 419 (1975).
- [14] J. Kodaira and K. Sasaki, *Lett. Nuovo Cim.* **26**, 417 (1979).
- [15] E. L. Berger and C. Sorensen, *Phys. Lett. B* **62**, 303 (1976).
- [16] R. Vogt, *Phys. Rept.* **310**, 197 (1999).
- [17] G. F. Chew, M. L. Goldberger, F. E. Low and Y. Nambu, *Phys. Rev.* **106**, 1345 (1957).
- [18] M. P. Rekaló and E. Tomasi-Gustafsson, *J. Phys. G* **30**, 1459 (2004).
- [19] G. Baum *et al.* [COMPASS Collaboration], CERN-SPSLC-96-14
- [20] S. Eidelman *et al.*, *Phys. Lett. B* **592**, 1 (2004).
- [21] V. O'Dell *et al.* [SLAC Hybrid Facility Photon Collaboration], *Phys. Rev. D* **36**, 1 (1987).
- [22] M. I. Adamovich *et al.* [Photon Emulsion Collaboration], *Phys. Lett. B* **187**, 437 (1987).
- [23] D. W. Duke and J. F. Owens, *Phys. Rev. Lett.* **D44**, 1173 (1980).
- [24] K. Abe *et al.* [SLAC Hybrid Facility Photon Collaboration], *Phys. Rev. D* **33**, 1 (1986).

# TENSOR $A_{yy}$ AND VECTOR $A_y$ ANALYZING POWERS OF THE $(d, p)$ AND $(d, d)$ REACTIONS AT 5 GeV/c AND 178 MR

V.P.Ladygin<sup>1,†</sup>, L.S.Azhgirey<sup>1</sup>, S.V.Afanasiev<sup>1</sup>, V.N.Zhmyrov<sup>1</sup>, L.S.Zolin<sup>1</sup>, V.I.Ivanov<sup>1</sup>, A.Yu.Isupov<sup>1</sup>, N.B.Ladygina<sup>1</sup>, A.G.Litvinenko<sup>1</sup>, V.F.Peresedov<sup>1</sup>, A.N.Khrenov<sup>1</sup> and N.P.Yudin<sup>2</sup>

(1) *JINR, 141980, Dubna, Moscow region, Russia*

(2) *Moscow State University, Moscow, Russia*

† *E-mail: ladygin@sunhe.jinr.ru*

## Abstract

New data on the tensor analyzing power  $A_{yy}$  of the  ${}^9\text{Be}(d, p)X$  reaction at an initial deuteron momentum of 5 GeV/c and secondary particles (protons and deuterons) detection angle of 178 mr have been obtained at the JINR Synchrophasotron.

The proton data obtained are analyzed within the framework of an approach based on the light-front dynamics using Karmanov's relativistic deuteron wave function. Contrary to the calculations with standard non-relativistic deuteron wave functions, we have managed to explain the new data within the framework of our approach without invoking degrees of freedom additional to nucleon ones.

The  ${}^9\text{Be}(d, d)X$  data are obtained in the vicinity of the excitation of baryonic resonances with masses up to  $\sim 1.8$  GeV/ $c^2$ . The  $A_{yy}$  data are in a good agreement with the previous data obtained at 4.5 and 5.5 GeV/c when they are plotted versus  $t$ . The results of the experiment are compared with the predictions of the plane wave impulse approximation and  $\omega$ -meson exchange models.

## 1. Introduction

The interest to the  $(d, p)$  reaction at relativistic energies is mostly due to the possibility to observe the manifestation of the non-nucleonic degrees of freedom and relativistic effects in the simplest bounded system.

Large amount of the polarization data in deuteron breakup obtained at a zero degree last years can be interpreted from the point of view  $NN^*$  configurations in the deuteron, where relativistic effects are taken into account by the minimal relativization scheme with the dependence of the deuteron structure on single variable  $k$ . In addition the considering of multiple scattering is required to obtain the agreement with the data[1].

On the other hand, it was shown that  $T_{20}$  data for the pion-free deuteron breakup process  $dp \rightarrow ppn$  in the kinematical region close to that of backward elastic  $dp$  scattering depended on the incident deuteron momentum in addition to  $k$ [2]. The recent measurements of the tensor analyzing power  $A_{yy}$  of deuteron inclusive breakup on nuclear targets [3, 4] have demonstrated a significant dependence on the transverse secondary proton momentum  $p_T$  being plotted at a fixed value of the longitudinal proton momentum. This forces one to suggest that description of this quantity requires an additional independent variable, aside from  $k$ .

At the same time, the interest to deuteron inelastic scattering off hydrogen and nuclei at high energies is due to the possibilities to study nucleon-baryon ( $NN^*$ ) interaction; to investigate the deuteron structure at short distances (as complementary method to the elastic  $pd$ - and  $ed$ -scatterings, deuteron breakup reaction, electro- and photodisintegration of the deuteron); to learn amplitudes of  $NN^* \rightarrow NN^*$  processes in the kinematical range, where the contribution of double scattering diagrams is significant; to get information on the formation of  $6q$  configuration in the deuteron, at large momentum transfers.

Since the deuteron is an isoscalar probe,  $A(d, d')X$  reaction is selective to the isospin of the unobserved system  $X$ , which is bound to be equal to the isospin of the target  $A$ . Inelastic scattering of deuterons on hydrogen,  $H(d, d')X$ , is selective to the isospin  $1/2$  and can be used to obtain information on the formation of baryonic resonances  $N^*(1440)$ ,  $N^*(1520)$ ,  $N^*(1680)$ , and others.

The polarized deuterons of high energies have been used to study the tensor analyzing power  $T_{20}$  in the vicinity of the Roper resonance ( $P_{11}(1440)$ ) excitation on hydrogen and carbon targets at Dubna [5] and on hydrogen target at Saclay [6]. The measurements of  $T_{20}$  in the deuteron scattering at 9 GeV/c on hydrogen and carbon have been performed for missing masses up to  $M_X \sim 2.2$  GeV/c<sup>2</sup> [7]. The experiments have shown a large negative value of  $T_{20}$  at momentum transfer of  $t \sim -0.3$  (GeV/c)<sup>2</sup>. Such a behaviour of the tensor analyzing power has been interpreted in the framework of the  $\omega$ -meson exchange model [8] as due to the longitudinal isoscalar form factor of the Roper resonance excitation [9]. The measurements of the tensor and vector analyzing powers  $A_{yy}$  and  $A_y$  at 9 GeV/c and 85 mr of the secondary deuterons emission angle in the vicinity of the undetected system mass of  $M_X \sim 2.2$  GeV/c<sup>2</sup> have shown large values [10]. The obtained results are in satisfactorily agreement with the plane wave impulse approximation (PWIA) calculations [11]. It was stated that the spin-dependent part of the  $NN \rightarrow NN^*$  ( $\sim 2.2$  GeV/c<sup>2</sup>) process amplitude is significant. The measurements of  $A_{yy}$  at 4.5 GeV/c and 80 mr [12] also shown large value of the tensor analyzing power. The exclusive measurements of the polarization observables in the  $H(d, d')X$  reaction in the vicinity of the Roper resonance excitation performed recently at Saclay [13] also demonstrated large spin effects.

In this report the  $A_{yy}$  data in deuteron inclusive breakup on beryllium at 5.0 GeV/c and 178 mr are presented [14]. The results are compared with the relativistic calculations using Paris, CD-Bonn and Karmanov's deuteron wave functions (DWFs). Also new results on the tensor and vector analyzing powers  $A_{yy}$  and  $A_y$  in deuteron inelastic scattering on beryllium target at the incident deuteron momentum of 5.0 GeV/c and  $\sim 178$  mr of the secondary emission angle in the vicinity of light baryonic resonances excitation are reported [15].

## 2. Experiment

The experiment has been performed using a polarized deuteron beam at Dubna Synchrotron at the Laboratory of High Energies of JINR and the SPHERE setup shown in Fig.1 and described elsewhere [10, 12]. The polarized deuterons were produced by the ion source POLARIS [16]. The sign of the beam polarization was changed cyclically and spill-by-spill, as "0", "−", "+", where "0" means the absence of the polarization, "+" and "−" correspond to the sign of  $p_{zz}$  with the quantization axis perpendicular to the plane containing the mean beam orbit in the accelerator.

The tensor polarization of the beam has been determined during the experiment by the asymmetry of protons from the deuteron breakup on berillium target,  $d + Be \rightarrow p + X$ , at zero emission angle and proton momentum of  $p_p \sim \frac{2}{3}p_d$  [17]. It was shown that deuteron breakup reaction in such kinematic conditions has very large tensor analyzing power  $T_{20} = -0.82 \pm 0.04$ , which is independent on the atomic number of the target ( $A > 4$ ) and on the momentum of incident deuterons between 2.5 and 9.0 GeV/c [18]. The tensor polarization averaged over the whole duration of the experiment was  $p_{zz}^+ = 0.716 \pm 0.043(stat) \pm 0.035(sys)$  and  $p_{zz}^- = -0.756 \pm 0.027(stat) \pm 0.037(sys)$  in " + " and " - " beam spin states, respectively.

The stability of the vector polarization of the beam has been monitored by measuring of the asymmetry of quasi-elastic  $pp$ -scattering on thin  $CH_2$  target placed at the  $F_3$  focus of VP1 beam line. The values of the vector polarization were obtained using the results of the asymmetry measurements at the momenta 2.5 GeV/c per nucleon and  $14^\circ$  of the proton scattering angle with corresponding value of the effective analyzing power of the polarimeter  $A(CH_2)$  taken as 0.234 [19]. The vector polarization of the beam in different spin states was  $p_z^+ = 0.173 \pm 0.008(stat) \pm 0.009(sys)$  and  $p_z^- = 0.177 \pm 0.008(stat) \pm 0.009(sys)$ .

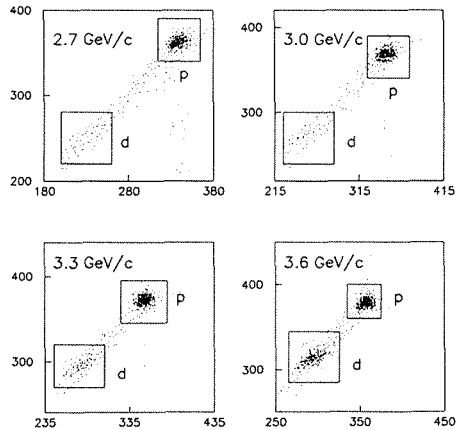


Figure 1: The TOF spectra obtained for different magnetic elements tuning

The coincidences of signals from three scintillation counters were used as a trigger. For particle identification the time-of-flight (TOF) information with a base line of  $\sim 28$  ns between the start counter and the stop counters were used in the off-line analysis. The TOF resolution was better than  $0.2$  ns ( $1\sigma$ ). The TOF spectra obtained for all four cases of magnetic elements tuning are shown in Fig.1. At the higher momentum of the detected particles only deuterons appear in TOF spectra, however, when the momentum decreases the relative contribution of protons becomes more pronounced. In data processing useful events were selected as the ones with at least two measured time of flight values correlated. This allowed to rule out the residual background completely.

The tensor  $A_{yy}$  and vector  $A_y$  analyzing powers were calculated from the yields of

deuterons  $n^+$ ,  $n^-$  and  $n^0$  for different states of the beam polarization after correction for dead time of the setup, by means of the expressions

$$A_{yy} = 2 \cdot \frac{p_z^- \cdot (n^+ / n^0 - 1) - p_z^+ \cdot (n^- / n^0 - 1)}{p_z^- p_{zz}^+ - p_z^+ p_{zz}^-},$$

$$A_y = -\frac{2}{3} \cdot \frac{p_{zz}^- \cdot (n^+ / n^0 - 1) - p_{zz}^+ \cdot (n^- / n^0 - 1)}{p_z^- p_{zz}^+ - p_z^+ p_{zz}^-}. \quad (1)$$

### 3. Results

The results on the tensor analyzing power  $A_{yy}$  of the reaction  ${}^9\text{Be}(d,p)X$  at the initial deuteron momentum of 5 GeV/c and a proton emission angle of 178 mr are compared with the calculation performed in the framework of relativistic hard scattering model in Fig. 2. The details of the calculations and the final expressions for the tensor analyzing power of  $(d,p)$  reaction can be found in ref. [20].

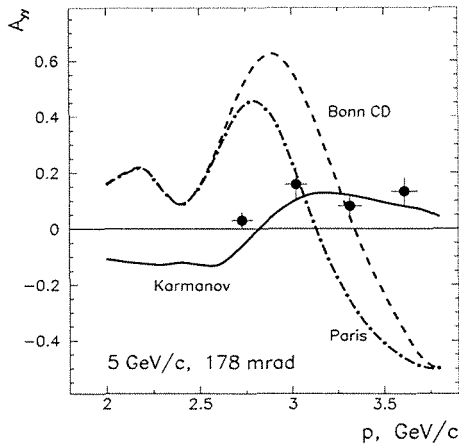


Figure 2:  $A_{yy}$  in the reaction  ${}^9\text{Be}(d,p)X$  at an initial deuteron momentum of 5 GeV/c and a proton emission angle of 178 mr as a function of the detected proton momentum. The solid curve was calculated with the Karmanov's relativistic deuteron wave function [21]. The calculations were made with the deuteron wave functions for the Bonn CD [23] (dashed curve) and the Paris [22] (dash-dotted curve) potentials.

It is seen that the experimental data are rather good reproduced using the Karmanov's relativistic deuteron wave function (DWF) [21] depending on 2 internal variables as opposed to the calculations with the standard DWFs [22, 23]; the last curves change sign at the proton momentum  $\sim 3.2$  GeV/c.

In Fig.3 the data on the tensor analyzing power  $A_{yy}$  in the inelastic scattering of 5.0 GeV/c deuterons on beryllium at an angle of 178 mr are shown as a function of the transferred 4-momentum  $t$  by the solid triangles. The  $A_{yy}$  has a positive value at  $|t| \sim 0.9$  (GeV/c) $^2$  and crosses a zero at larger  $|t|$ . The data on tensor analyzing power

obtained at zero emission angle at 4.5 GeV/c and 5.5 GeV/c [5] on hydrogen are given by the open triangles and squares, respectively (recall that for these data  $A_{yy} = -T_{20}/\sqrt{2}$ ). The data obtained at 4.5 GeV/c and at an angle of 80 mr [12] are shown by the open circles. As it was established earlier [5, 12], there is no significant dependence of  $A_{yy}$  on the  $A$ -value of the target. The observed independence of the tensor analyzing power on the atomic number of the target indicates that the rescattering in the target and medium effects are small. Hence, nuclear targets are also appropriate to obtain information on the baryonic excitations in the deuteron inelastic scattering [5, 7, 10, 12].

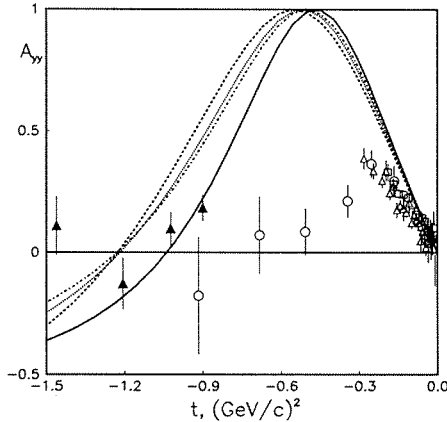


Figure 3:  $A_{yy}$  in deuteron inelastic scattering on beryllium at 5.0 GeV/c at an angle of 178 mr and at 4.5 GeV/c at an angle of 80 mr [12] given by the full triangles and open circles, respectively; on hydrogen at 4.5 and 5.5 GeV/c at zero angle [5] shown by the open triangles and squares, respectively, as a function of the 4-momentum  $t$ . The solid, dashed, dotted and dash-dotted lines are predictions in the framework of PWIA [11] using DWFs for Paris [22] and Bonn A, B and C [23] potentials, respectively.

The sensitivity of the tensor analyzing power in the deuteron inelastic scattering off protons to the excitation of baryonic resonances has been pointed out in [8] in the framework of the  $t$ -channel  $\omega$ -meson exchange model. In this model the  $t$ -dependence of the tensor analyzing power in deuteron inelastic scattering is defined by the  $t$ -dependence of the deuteron form factors and the contribution of the Roper resonance due to its nonzero isoscalar longitudinal form factor [9]. Since, the isoscalar longitudinal amplitudes of  $S_{11}(1535)$  and  $D_{13}(1520)$  vanish due to spin-flavor symmetry, while both isoscalar and isovector longitudinal couplings of  $S_{11}(1650)$  vanish identically, the tensor analyzing power  $A_{yy}$  in inelastic deuteron scattering with the excitation one of these resonances has the value of +0.25 independent of  $t$  [12].

The  $t$  dependence of  $A_{yy}$  at  $M_X \sim 1550$  MeV/c<sup>2</sup> is shown in Fig.4. The full triangles are the results of the present experiment, open squares, circles and triangles are obtained earlier at 4.5 and 5.5 GeV/c [5, 12]. The solid curves are the results of the PWIA calculations [11] using Paris DWF [22]. The dashed lines are the expectations of the

$\omega$ -meson exchange model [8, 9]. One can see that the behaviour of  $A_{yy}$  at  $M_X \sim 1550$  MeV/ $c^2$  is not in contradiction with the  $\omega$ -meson exchange model prediction [9].

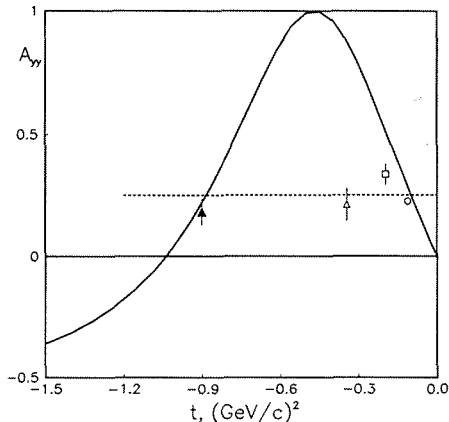


Figure 4: The  $A_{yy}$  data from the present experiment (full triangles) along with the data obtained with 4.5 and 5.5 GeV/c deuterons at zero angle [5] (open circles and squares, respectively) and the data at 4.5 GeV/c at an angle of 80 mr [12] plotted versus 4-momentum  $t$  for the missing mass  $M_X \sim 1550$  MeV/ $c^2$ . The solid curve is the calculations in PWIA using DWFs for Paris [22]. The dashed line is the predictions within the  $\omega$ -meson exchange model [9]

The behaviour of the vector analyzing power  $A_y$  obtained in the present experiment is plotted in Fig.5 versus  $t$ . The calculations are performed using the expression for  $A_y$  from ref.[11] with the ratio  $r$  of the spin-dependent to spin-independent parts of the  $NN \rightarrow NN^*$  process taken in the form  $r = a \cdot \sqrt{|t|}$  with the value of  $a = 1.0$ . The solid curve in Fig.5 is obtained with the DWF for Paris potential [22], while the dashed, dotted and dash-dotted lines correspond to the DWFs for Bonn A, B and C potentials [23], respectively. The PWIA calculations give approximately the same results at the value of  $a \sim 0.8 \div 1.2$ . It should be noted that  $a$  value might have different values for the different  $M_X$ , however, we took the fixed value for the simplicity due to lack of the data.

## 4. Conclusions

New experimental data on the tensor and vector analyzing powers  $A_{yy}$  and  $A_y$  in the  ${}^9\text{Be}(d,p)X$  and  ${}^9\text{Be}(d,d')X$  reactions at 5.0 GeV/c and at an angle of  $\sim 178$  mr are presented.

The calculation of the tensor analyzing power of  $(d,p)$  reaction in the frame of light-front dynamics using Karmanov's relativistic DWF is in good agreement with the new experimental data whereas the calculations with the standard non-relativistic DWFs are in sharp contradiction with the data. New data favour the view of ref. [20] that the

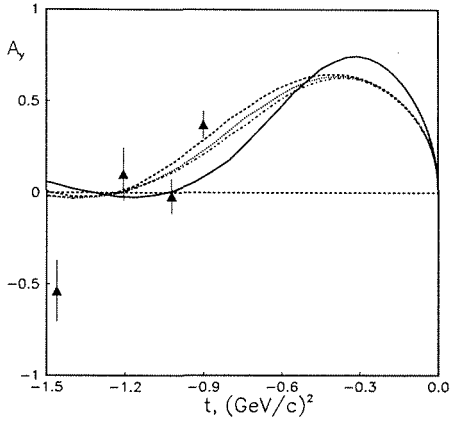


Figure 5: Vector analyzing power  $A_y$  in deuteron inelastic scattering on beryllium at 5.0 GeV/c at an angle of 178 mr as a function of the 4-momentum  $t$ . The solid, dashed, dotted and dash-dotted lines are predictions in the framework of PWIA [11] using DWFs for Paris [22] and Bonn A, B and C [23] potentials, respectively

relation between the  $k_L$  and  $k_T$  in a moving deuteron differs essentially from that in the non-relativistic case. The method of relativization proposed by Karmanov et al. [21] appear to reflect correctly this relation, at least up to  $p_T \sim 0.7$  GeV/c.

The data on  $A_{yy}$  in the  $(d, d')X$  reaction are in good agreement with the data obtained in previous experiments at the momenta between 4.5 GeV/c and 5.5 GeV/c [5, 12] when they are compared versus variable  $t$ .

It is observed also that  $A_{yy}$  data in the  $(d, d')X$  reaction are in good agreement with PWIA calculations [11] using conventional DWFs [22, 23]. On the other hand, the behaviour of the  $A_{yy}$  data obtained in the vicinity of the  $S_{11}(1535)$  and  $D_{13}(1520)$  resonances is not in contradiction with the predictions of the  $\omega$ -meson exchange model [9], while at higher excited masses this model may require taking into account the additional baryonic resonances with nonzero longitudinal form factors.

The vector analyzing power  $A_y$  has a large value at  $M_X \sim 1500$  MeV/c<sup>2</sup>, that could be interpreted as a significant role of the spin-dependent part of the elementary amplitude of the  $NN \rightarrow NN^*$  reaction.

Authors are grateful to the LHE accelerator staff and POLARIS team for providing good conditions for the experiment. This work was supported in part by the Russian Foundation for Fundamental Research (grant No. 03-02-16224).

## References

- [1] A.P.Kobushkin et al., Phys.Lett.**B421**, 53 (1998).
- [2] L.S. Azhgirey et al., Phys. Lett. **B391**, 22 (1997); Yad. Fiz.**61**, 494 (1998).

- [3] S.V. Afanasiev et al., Phys. Lett. **B434**, 21 (1998).
- [4] V.P. Ladygin et al., Few-Body Systems **32**, 127 (2002); L.S. Azhgirey et al., Yad. Fiz. **66**, 719 (2003).
- [5] L.S. Azhgirey et al., Phys.Lett.**B361**, 21 (1995).
- [6] Experiment LNS-E250 (unpublished).
- [7] L.S. Azhgirey et al., JINR Rapid Comm. **2[88]-98**, 17 (1998).
- [8] M.P. Rekaló and E. Tomasi-Gustafsson, Phys.Rev. **C54**, 3125 (1996).
- [9] E. Tomasi-Gustafsson, M.P. Rekaló, R. Bijker, A. Leviatan and F. Iachello, Phys.Rev. **C59**, 1526 (1999)
- [10] L.S. Azhgirey et al., Yad.Fiz.**62**, 1796 (1999). [Phys.Atom.Nucl.**62**, 1673 (1999)].
- [11] V.P. Ladygin and N.B. Ladygina, Yad.Fiz. **65**, 188 (2002) [Phys.Atom.Nucl.**65**, 182 (2002)].
- [12] V.P.Ladygin et al., Eur.Phys.J. **A8**, 409 (2000); L.S.Azhgirey et al., Yad.Fiz.**64**, 2046 (2001). [Phys.Atom.Nucl.**64**, 1961 (2001)]
- [13] L.V.Malinina et al., Phys.Rev. **C64**, 064001 (2001).
- [14] L.S. Azhgirey et al., Phys.Lett. **B595**, 151 (2004).
- [15] L.S. Azhgirey et al., *nucl-ex/0404021*, to be published in Yad.Fiz. (2005).
- [16] N.G. Anishchenko et al., in Proceedings of the 5-th Int. Symp. on High Energy Spin Physics, Brookhaven, 1982 (AIP Conf. Proc. **N95**, N.Y., 1983) p.445
- [17] L.S. Zolin et al., JINR Rapid Comm. **2[88]-98**, 27 (1998).
- [18] C.F. Perdrisat et al., Phys. Rev.Lett. **59**, 2840 (1987);  
V. Punjabi et al., Phys. Rev. **C39**, 608 (1989);  
V.G. Ableev et al., Pis'ma Zh.Eksp.Teor.Fiz. **47**, 558 (1988);  
JINR Rapid Comm. **4[43]-90**, 5 (1990);  
T. Aono et al., Phys.Rev.Lett. **74**, 4997 (1995).
- [19] L.S. Azhgirey et al., PTE **1**, 51 (1997)[Instr. and Exp.Tech.**40**, 43 (1997)];  
L.S. Azhgirey et al., Nucl.Instr.Meth. in Phys.Res. **A497**, 340 (2003).
- [20] L.S. Azhgirey and N.P. Yudin, to be published in Yad. Fiz.
- [21] J. Carbonell and V.A. Karmanov, Nucl. Phys. **A581**, 625 (1994).
- [22] M. Lacombe et al., Phys. Lett. **B101**, 139 (1981).
- [23] R. Machleidt, Phys. Rev. **C63**, 024001 (2001).

# MEASUREMENTS OF THE TENSOR $A_{xx}$ , $A_{yy}$ , $A_{xz}$ AND VECTOR $A_y$ ANALYZING POWERS FOR THE $d + d \rightarrow {}^3\text{H} + p$ AND $d + d \rightarrow {}^3\text{He} + n$ REACTIONS AT 270 MeV

M. Janek<sup>1,2†</sup>, T. Saito<sup>3</sup>, V.P. Ladygin<sup>1</sup>, M. Hatano<sup>3</sup>, A.Yu. Isupov<sup>1</sup>, H. Kato<sup>3</sup>, N.B. Ladygina<sup>1</sup>, A.I. Malakhov<sup>1</sup>, Y. Maeda<sup>3</sup>, S. Nedev<sup>4</sup>, J. Nishikawa<sup>5</sup>, H. Okamura<sup>5</sup>, T. Onishi<sup>6</sup>, S.G. Reznikov<sup>1</sup>, H. Sakai<sup>3</sup>, N. Sakamoto<sup>6</sup>, S. Sakoda<sup>3</sup>, Y. Satou<sup>3</sup>, K. Sekiguchi<sup>6</sup>, K. Suda<sup>5</sup>, N. Uchigashima<sup>3</sup>, T. Uesaka<sup>3</sup>, A. Tamii<sup>3</sup>, T.A. Vasiliev<sup>1</sup>, K. Yako<sup>3</sup>

(1) *LHE-JINR, 141-980 Dubna, Moscow region, Russia*

(2) *University of P.J. Šafárik, 041-54 Košice, Slovakia*

(3) *Department of Physics, University of Tokyo, Tokyo 113-0033, Japan*

(4) *University of Chemical Technology and Metallurgy, Sofia, Bulgaria*

(5) *Department of Physics, Saitama University, Saitama 338-8570, Japan*

(6) *RIKEN, 351-0198 Wako, Japan*

† *E-mail: janek@sunhe.jinr.ru*

## Abstract

The experimental results on the tensor  $A_{xx}$ ,  $A_{yy}$ ,  $A_{xz}$  and vector  $A_y$  analyzing powers at  $E_d = 270$  MeV for the  $d + d \rightarrow {}^3\text{H} + p$  and  $d + d \rightarrow {}^3\text{He} + n$  reaction are presented. The energy dependence of the tensor analyzing power  $T_{20}$  at a zero degree as well as the angular dependences of the tensor analyzing powers  $T_{20}$  and  $T_{22}$  are shown. The  ${}^3\text{He} - {}^3\text{H}$  analyzing powers difference are presented, but the results require further investigation at small angles.

## 1. Introduction

The structure of light nuclei can be investigated by electromagnetic and hadronic probes.

Simple reactions with large transfer momentum (short distances) and one-nucleon-exchange (ONE) mechanism are  $d + p \rightarrow p + d$  [1]-[2],  $d + {}^3\text{He} \rightarrow p + {}^4\text{He}$  [3]-[4] or  $d + {}^3\text{He} \rightarrow {}^3\text{He} + d$  [5]. In the framework of ONE approximation the polarization observables of these reactions are expressed in terms of the D/S-waves ratios in these nuclei.

However, the remarkable deviation of the polarization observables on the ONE predictions using standart deuteron and  ${}^3\text{He}$  wave functions occurs even at relatively small internal momenta of  $\approx 200$  MeV/c. Such a discrepancy can be due to the non-adequate description of the light nuclei structure at short distances, as well as to the importance of the mechanisms in addition to ONE.

## 2. Experiment

The experiment was performed at RIKEN Accelerator Research Facility (RARF) (see Fig. 1). The direction of symmetric axis of the beam polarization was controlled with a Wien filter located at the exit of polarized ion source (PIS).

# RIKEN Accelerator Research Facility (RARF)

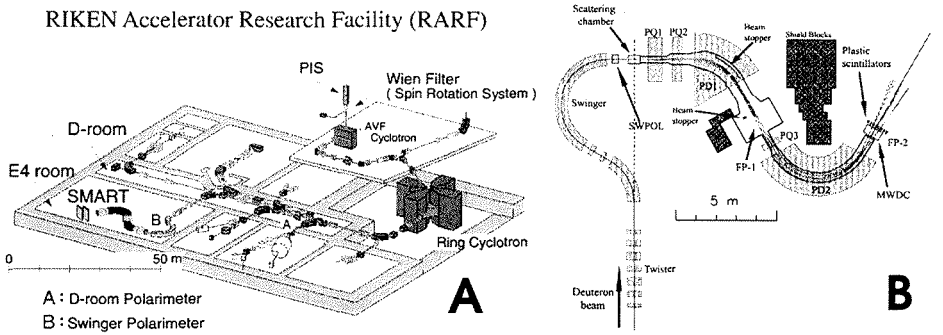


Figure 1: A) RIKEN Accelerator Research Facility (RARF), B) SMART spectrograph

The deuteron vector ( $p_Z$ ) and tensor ( $p_{ZZ}$ ) beam polarization with respect to their cylindrically symmetric axis  $Z$  are defined by

$$p_Z = N_+ - N_-, \quad (1)$$

$$p_{ZZ} = N_+ + N_- - 2N_0, \quad (2)$$

where  $N_+$ ,  $N_-$  and  $N_0$  denotes the fractions of deuteron beam in magnetic substates +1, -1 and 0, respectively. In this experiment, four spin modes were used, whose ideal magnitudes of polarizations are

$$\text{mode 0: } (p_Z, p_{ZZ}) = (0, 0), \quad (3)$$

$$\text{mode 1: } (p_Z, p_{ZZ}) = (0, -2), \quad (4)$$

$$\text{mode 2: } (p_Z, p_{ZZ}) = (-2/3, 0), \quad (5)$$

$$\text{mode 3: } (p_Z, p_{ZZ}) = (1/3, 1). \quad (6)$$

The mode 0 - unpolarized mode, mode 1 - pure tensor mode, mode 2 - pure vector mode and mode 3 is the mixed mode. The obtained polarization values were  $\sim 75\%$  of the ideal values. The polarized deuteron beam was accelerated up to 270 MeV by the combination of the AVF cyclotron and Ring cyclotron. The beam polarizations were measured with D-room polarimeter (DroomPOL) located at D-room and Swinger polarimeter (SWPOL) just before the target. Both polarimeters utilize  $d + p$  elastic scattering for polarimetry and value of polarization were derived using known analyzing powers  $A_y$ ,  $A_{yy}$ ,  $A_{xx}$  and  $A_{xz}$  [6] [7].

Deuterated polyethylene ( $CD_2$ ) sheets with 0.72 and 0.32  $\text{mg/mm}^2$  were used as a target and carbon foil with 0.34  $\text{mg/mm}^2$  was used for measurement of background spectra.

The scattering angle of the polarized deuteron beam was controlled by rotating of the Swinger. Scattered particles ( $^3\text{H}$ ,  $^3\text{He}$  or  $p$ ) were momentum analyzed with quadrupole and dipole magnets (Q-Q-D-Q-D) and detected with MWDC followed by the three plastic scintillators at the second focal plane.

Criteria used for the identification of the scattered particles  ${}^3\text{H}$ ,  ${}^3\text{He}$  or proton from the reaction  $d + d \rightarrow {}^3\text{H} + p$  ( $d + d \rightarrow {}^3\text{He} + n$ ) are the following. Particle must be registered in the all three scintillation detectors and it was selected by the correlation of the energy losses in the 1st and the 2nd and the 1st and the 3rd scintillation detectors. Radio frequency signal of the cyclotron was used as a reference of time-of-flight measurement.

The main source of the background was  ${}^3\text{He}$ ,  ${}^3\text{H}$  and protons from the  $d + {}^{12}\text{C}$  interaction. The number of useful events were obtained by the subtraction of the momenta spectra on the  $\text{CD}_2$  and C foils.

To obtain the analyzing powers  $A_y$ ,  $A_{yy}$ ,  $A_{xx}$  and  $A_{zz}$  for the  $d + d \rightarrow {}^3\text{H} + p$  ( ${}^3\text{He} + n$ ) reactions we used the asymmetries and beam polarization values for the three different spin modes.

### 3. Results and discussion

The tensor analyzing power  $T_{20}$  at  $\Theta_{cm} = 0^\circ$  or  $180^\circ$  (see Fig. 2) is given by [8], [9]

$$T_{20} = \frac{1}{\sqrt{2}} \frac{2\sqrt{2}u(k)w(k) - w(k)^2}{u(k)^2 + w(k)^2}, \quad (7)$$

where  $u(k)$  and  $w(k)$  are the S- and D-wave functions for  ${}^3\text{He}$  ( ${}^3\text{H}$ ) or deuteron for  $\Theta_{cm} = 0^\circ$  or  $180^\circ$ , respectively.

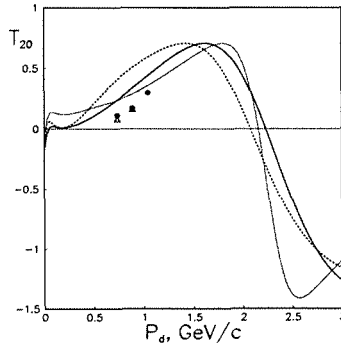


Figure 2: Tensor analyzing power  $T_{20}$  at  $\Theta_{cm} = 0^\circ$  at  $E_d = 270, 200$  and  $140$  MeV [10]. The  ${}^3\text{He} + n$  ( ${}^3\text{H} + p$ ) channel are presented by solid and open symbols, respectively. The solid and dashed curves are calculated using Urbana  ${}^3\text{He}$  wave function

One can see that the ONE predictions reproduce incident energy dependence and the sign of the experimental data. Since the  $T_{20}$  at  $0^\circ$  is directly connected with D/S ratio of  ${}^3\text{He}$  ( ${}^3\text{H}$ ) (1), the sign of  $T_{20}$  at  $0^\circ$  reflects the relative sign of wave functions  $u(k)$  and  $w(k)$  for  ${}^3\text{He}$  ( ${}^3\text{H}$ ).

The angular dependences for the tensor  $A_{xx}$ ,  $A_{yy}$ ,  $A_{zz}$  and vector  $A_y$  analyzing powers at energy  $E_d = 270$  MeV are presented in Fig. 3.

ONE calculations predict that the vector analyzing power  $A_y$  equals to zero, but some structures are observed in the experimental results. The angular distribution of  $A_y$  indicates the necessity of description of its reaction mechanism beyond the ONE.

In the ONE calculations the tensor analyzing powers at forward angles are sensitive to the structure  ${}^3\text{H}$  ( ${}^3\text{He}$ ) but they remarkably deviate from the experimental results. These results may imply that there is a problem in the realistic  ${}^3\text{H}$  ( ${}^3\text{He}$ ) wave functions used in the ONE calculations.

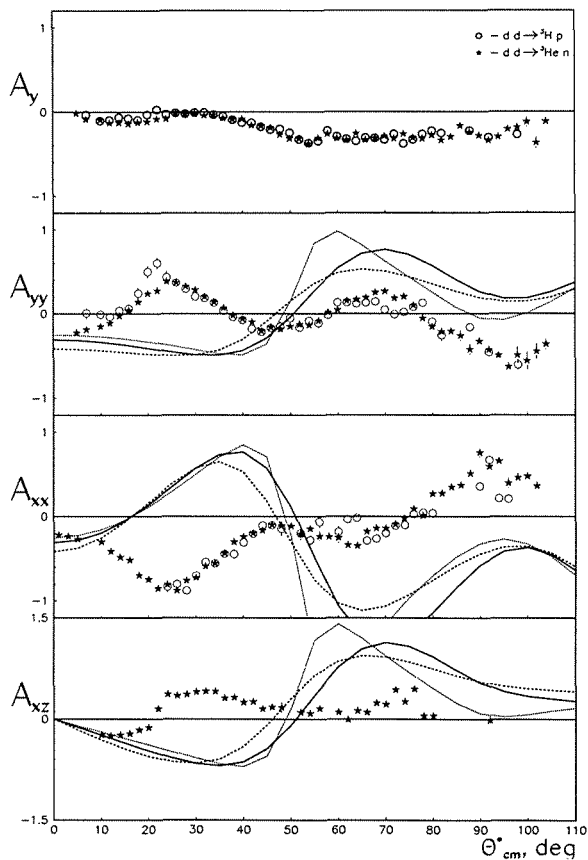


Figure 3: The results for the vector  $A_y$  and tensor  $A_{yy}$ ,  $A_{xx}$  and  $A_{xz}$  analyzing powers in the centre-of-mass frame at energy  $E_d=270$  MeV. The open and solid circles are for case of the  ${}^3\text{H} + \text{p}$  and  ${}^3\text{He} + \text{n}$  channels, respectively. The solid, dot-dashed and long-dashed curves are the results of ONE calculations [8] using Urbana [11], Paris [12] and Reid soft core [13]  ${}^3\text{He}$  wave functions, respectively

The tensor analyzing powers  $T_{20}$  and  $T_{22}$  can be expressed via  $A_{xx}$  and  $A_{yy}$  as

$$T_{20} = \frac{1}{\sqrt{2}}(A_{xx} + A_{yy}), \quad (8)$$

$$T_{22} = \frac{(A_{xx} - A_{yy})}{2\sqrt{3}}. \quad (9)$$

The angular dependences for the tensor  $T_{20}$  and  $T_{22}$  analyzing powers at energy  $E_d=270$  MeV are presented in Fig. 4.

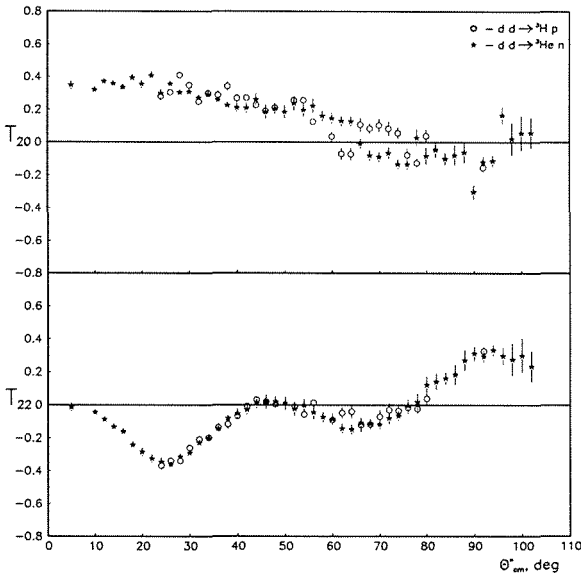


Figure 4: Angular dependences of tensor analyzing powers  $T_{20}$  and  $T_{22}$  at  $E_d=270$  MeV. The  ${}^3\text{He}n$  ( ${}^3\text{H}p$ ) channel are presented by filled (opened) symbols

Tensor analyzing power  $T_{20}$  at small angles have the same sign and approximately the same values as the  $T_{20}$  at zero degree [10]. In this region the  $T_{20}$  values are approximately constant. The  $T_{20}$  intersects the axis at  $\sim 60$  degrees (internal impulse  $\sim 600$  MeV/c).

The experimental results for the  ${}^3\text{H}$  and  ${}^3\text{He}$  at angles larger than  $30^\circ$  are in the agreement within statistical errors. At smaller angles the difference in the analyzing powers is observed, however these results require further investigation of the systematics. Therefore at the moment, we cannot conclude that the effect of charge symmetry breaking was observed (Fig. 5).

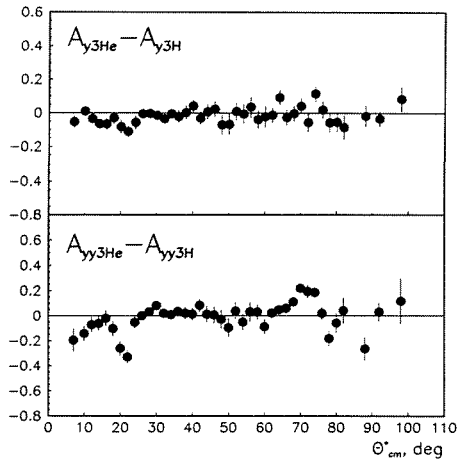


Figure 5:  $A_{y3He} - A_{y3H}$  and  $A_{yy3He} - A_{yy3H}$  difference

## Acknowledgements

The investigation has been supported in part by the Russian Foundation for Fundamental Research (grant N° 04-02-17107) and by the Grant Agency for Science at the Ministry of Education of the Slovak Republic (grant No.1/1020/04).

## References

- [1] N. Sakamoto, H. Okamura, T. Uesaka *et al.* Phys. Lett. **B367** 60 (1996).
- [2] H. Sakai, K. Sekiguchi, H. Witala *et al.* Phys. Lett. **84** 5288 (2000).
- [3] T. Uesaka, H. Sakai, H. Okamura *et al.* Phys. Lett. **B467** 199 (1999).
- [4] T. Uesaka, H. Sakai, H. Okamura *et al.* Few-body Syst. Suppl. **12** 497 (2000).
- [5] M. Tanifuji *et al.* Phys. Rev. **C61** 024602 (2000).
- [6] N. Sakamoto: Doctor Thesis, University of Tokyo (1996), unpublished.
- [7] T. Uesaka *et al.* Riken Accel. Prog. Rep. **33** 153 (2000).
- [8] V. P. Ladygin *et al.* Part. Nucl. Lett. **3[100]** 74 (2000).
- [9] V. P. Ladygin and N. B. Ladygina Phys. Atom. Nucl. **59** 789 (1996).
- [10] V. P. Ladygin *et al.* Phys. Lett. **B589** 47 (2004).
- [11] R. Schiavilla *et al.* Nucl. Phys. **A449** 219 (1996).
- [12] J. M. Laget *et al.* Nucl. Phys. **A370** 479 (1981).
- [13] F. D. Santos *et al.* Phys. Rev. **C19** 238 (1979).

# INCLUSIVE AND SEMI-INCLUSIVE ASYMMETRIES AT COMPASS

A.Yu. Korzenev, on behalf of the COMPASS collaboration

*Institute for Nuclear Physics, Mainz University  
on leave from JINR, LPP, Dubna  
E-mail: korzenev@mail.cern.ch*

## Abstract

We present preliminary results for the measurement of the inclusive asymmetry,  $A_{1d}$ , and semi-inclusive asymmetries for positive and negative hadrons,  $A_{1d}^{h+}$  and  $A_{1d}^{h-}$ . These asymmetries will be used to determine contributions of quarks and anti-quarks to the nucleon spin. Data obtained by scattering polarized muons of 160 GeV off a polarized  ${}^6\text{LiD}$  target are presented. The analysis is based on data collected in years 2002 and 2003. The covered kinematic range is  $Q^2 > 1 \text{ GeV}^2$  and  $0.004 < x_{Bj} < 0.7$ .

## 1. Introduction

In view of the spin crisis in the QPM the understanding of the spin structure of the nucleon is the one of the most interesting issues in particle physics. The investigation of this subject is the primary goal of the COMPASS experiment [1] at CERN SPS. The analysis of deep inelastic scattering (DIS) of polarized muons off a polarized deuteron target gives access to the spin dependent structure of the nucleon. The large acceptance of a two stage forward spectrometer with excellent particle identification allows a precise measurement of  $\mu$ -nucleon double-spin asymmetries. The large statistics of the experiment will reduce significantly the error for the inclusive and hadron asymmetries in the region of low  $x$ -Bjorken.

The scattering processes are classified as inclusive or semi-inclusive depending on what is detected in the final state of the reaction (fig. 1). In the inclusive process we detect only the scattered muon,  $\mu'$ , in the final state. For semi-inclusive scattering, in addition the reconstruction of at least one hadron is required. In both cases we determine the photon-nucleon asymmetry  $A^{\gamma^*N}$  which is defined as

$$A^{\gamma^*N} = \frac{\sigma_{1/2} - \sigma_{3/2}}{\sigma_{1/2} + \sigma_{3/2}},$$

where  $\sigma_{3/2}$  and  $\sigma_{1/2}$  are cross sections for reactions when the spin of the exchanging photon and target nucleon are parallel (3/2) and anti-parallel (1/2). In the experiment we measure the muon-nucleon asymmetry which is related to the gamma-nucleon asymmetry via depolarization factor  $A^{\mu N} = D A^{\gamma^*N}$ . The  $A^{\gamma^*N}$  can be decomposed into longitudinal ( $A_1$ ) and transverse ( $A_2$ ) parts:  $A^{\gamma^*N} = A_1 + \eta A_2$ . In the kinematic region of COMPASS the second term is suppressed due to the smallness of the kinematic factor  $\eta$ , therefore  $A^{\mu N} \simeq D A_1$ .

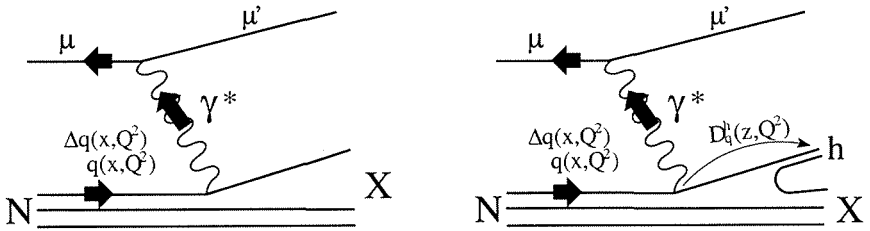


Figure 1: Diagrams of DIS process: inclusive (*left*), semi-inclusive (*right*). Big arrows show the spin direction of the particle. Quark distribution and fragmentation functions are indicated as well

In case of an inclusive process one can express  $A_1$  as a function of unpolarized quark distributions ( $q$ ) and helicity distributions ( $\Delta q$ ) in the LO of QCD as

$$A_1(x) = \frac{\sum_q e_q^2 (\Delta q(x) + \Delta \bar{q}(x))}{\sum_q e_q^2 (q(x) + \bar{q}(x))}. \quad (1)$$

This asymmetry is sensitive only to the sum of quark and anti-quark distributions. Individual polarized parton distributions can be extracted via study of semi-inclusive DIS asymmetries when in addition to the scattered muon  $\mu'$  a hadron  $h$  is detected. In the LO of QCD this asymmetry is written as

$$A_1^h(x) = \frac{\sum_q e_q^2 (\Delta q(x) \int D_q^h(z) dz + \Delta \bar{q}(x) \int D_{\bar{q}}^h(z) dz)}{\sum_q e_q^2 (q(x) \int D_q^h(z) dz + \bar{q}(x) \int D_{\bar{q}}^h(z) dz)}, \quad (2)$$

where  $D_q^h$  is the hadron fragmentation function, which is the density number of hadrons  $h$  originating from fragmentation of quark  $q$ . Since in general  $D_q^h \neq D_{\bar{q}}^h$  the individual quark and anti-quark flavor contributions can be separated in contrast to the inclusive measurement where quark flavors enter in the combination  $\Delta q + \Delta \bar{q}$ .

Tagging events with an identified hadron allows us to determine the flavor of the struck quark. For instance, the observation of a strange particle (kaon) indicates that a  $s$ -quark took part in the process. However, having a deuteron target only limited flavor separation is possible. The isospin symmetry of proton and neutron inside the deuteron allows us to select only three independent combined parton densities  $\vec{\Delta q} = \{\Delta u + \Delta d, \Delta \bar{u} + \Delta \bar{d}, \Delta s\}$ , assuming that  $\Delta s = \Delta \bar{s}$ . If combined with results on proton target a full flavor separation is in principle possible:  $\vec{\Delta q} = \{\Delta u, \Delta \bar{u}, \Delta d, \Delta \bar{d}, \Delta s, \Delta \bar{s}\}$ .

## 2. COMPASS spectrometer

The experiment is located at the M2 muon beam line of the SPS at CERN. The muon beam of 160 GeV has an intensity of  $2 \cdot 10^8 \mu/\text{spill}$  during 4.8 s and a cycle time of 16.8 s. The polarization is acquired by muons in weak decays of  $\pi$  and K. The selection of muons produced in the narrow cone around the momentum of parent hadron allows to obtain the average  $\mu$ -beam polarization of -76%. The muons are scattered off a polarized solid state target located inside a superconducting solenoid which provides a field of 2.5

T. The target consists of two 60 cm long cells filled with  ${}^6\text{LiD}$ . The two cells, separated by 10 cm, are immersed in a bath of a  ${}^3\text{He}/{}^4\text{He}$  mixture. They are polarized in opposite directions with a typical polarization value of 50%.

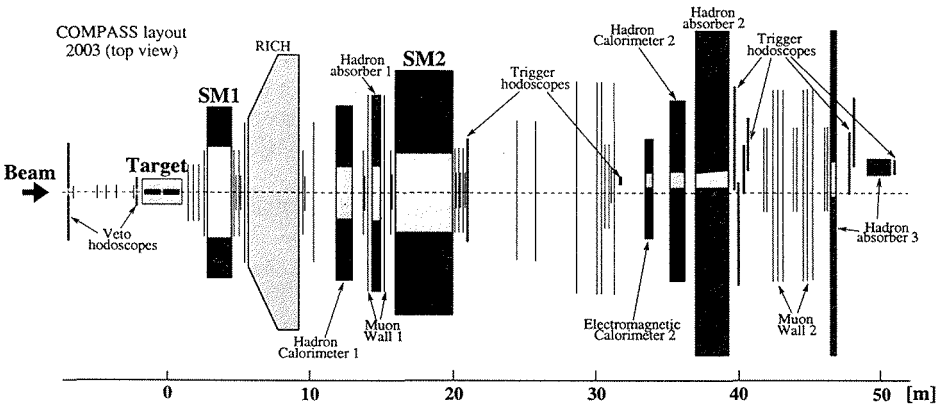


Figure 2: Schematic drawing of the COMPASS experiment

The scattered muons and the forward produced hadrons are detected in a large acceptance two stage spectrometer (fig. 2) associated with two dipole magnets SM1 and SM2. A large gap 1 Tm dipole magnet (SM1) is used in the first stage to measure low momentum tracks, mainly of hadrons produced in the target, whereas in the second stage a 4.4 Tm dipole magnet (SM2), bending the particles in the same direction as the first one, is used for the scattered muons and other high momentum particles. A large number of tracking detectors determine the trajectories with a high precision. Both stages are equipped with hadronic calorimetry and hadron absorber walls for hadron and muon identification. The first stage contains a RICH which provides hadron identification in the momentum range 2.5–50 GeV. The threshold momenta for emission of Cherenkov photons are 2.5, 8.9 and 17.0 GeV for  $\pi$ ,  $K$  and  $p$ , respectively. A description of the apparatus can be found in [2].

In the downstream part of the second spectrometer trigger hodoscopes are located. Every trigger requires a coincidence between two hodoscope planes. The recording system is activated by a signal indicating the presence of a scattered muon at a given angle or in a given energy range. To suppress hadrons at least one of hodoscopes is placed behind of a hadron absorber. For triggers which cover small scattering angles (quasi-real photon events) additionally the presence of a hadron signal in the calorimeters is demanded. In a part of the 2003 data taking, the acceptance has been further extended towards high  $Q^2$  values by the addition of a standalone calorimetric trigger in which only an energy deposit in the hadron calorimeter exceeding 9 times the typical muon response is required.

### 3. Data selection and asymmetry extraction approach

In the analysis we require for all events to have a reconstructed primary interaction vertex defined by the incoming and the scattered muons. For hadron asymmetries an extra track

outgoing from the vertex is required. The energy of the beam muon is constrained to be in the interval  $140 < P_\mu < 180$  GeV. To equalize fluxes through the two target cells it is required for the trajectory of incoming muon to cross both cells. This is essential for the asymmetry extraction since it allows to get rid of the muon flux normalization. Cuts are made on  $Q^2$ , the photon virtuality, and on  $y$ , the fractional energy transferred from the beam muon to the virtual photon. The requirement  $Q^2 > 1$  GeV<sup>2</sup> defines the region of DIS. Events with small energy transfer, which have a large kinematic smearing, are rejected by requiring  $y > 0.1$ . Also  $y < 0.9$  is demanded to eliminate the region most affected by radiative corrections. These cuts lead to  $x$ -Bjorken interval accessible by COMPASS:  $0.004 < x < 0.7$ .

To reject the kinematic region of target remnants in semi-inclusive analysis additionally the cut on the hadron variable  $z = E_h/E_\gamma$  was required to be  $z > 0.2$ .

The primary vertex distribution for inclusive events is shown on fig.3. One can see clearly the effect of acceptance. Hadrons have less chance to leave the target if they are produced in the upstream cell what results in a depletion of events in this region. In order to cancel this effect the data with opposite target spin configurations are combined together. Denoting the number of events in upstream and downstream cells as  $N_U$  and  $N_D$ , and priming events after the spin reversal we get

$$A^{\mu N} = \frac{1}{2} \left( \frac{N_U - N_D}{N_U + N_D} - \frac{N'_U - N'_D}{N'_U + N'_D} \right) \cdot \frac{1}{P_t P_b f}, \quad (3)$$

where  $P_b$  is the incoming muon polarization,  $P_t$  is the target polarization and  $f$  is dilution factor which is the ratio of the absorption cross-section on the deuteron and on all nuclei in the target material ( $f \approx 0.37$ ). In general the spin directions in the two target cells are reversed every 8 hours by rotating the magnetic field direction. In order to minimize the effect of detectors instability only groups of runs with opposite spin configurations which are close in time are combined for the asymmetry extraction.

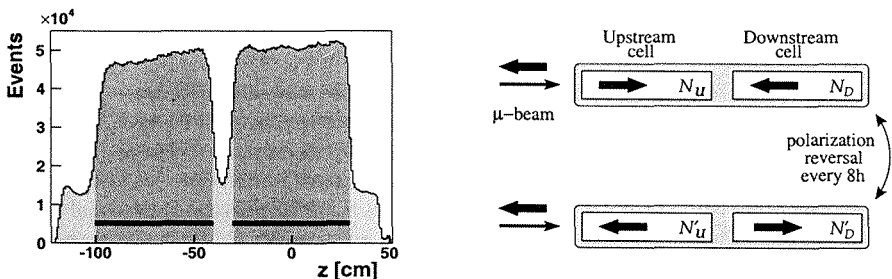


Figure 3: The distribution of the reconstructed interaction point along the beam direction (*left*). Two horizontal lines indicate the position of two target cell. The cells polarization is reversed every 8 hours by rotating the magnetic field direction (*right*)

In order to minimize the statistical error events are weighted with the weight factor  $w = fDP_b$ . This gives about 10% gain in precision.

## 4. Results

The preliminary results on  $A_{1d}$ ,  $A_{1d}^{h+}$  and  $A_{1d}^{h-}$  are shown on fig.4 and 5. For comparison the points of COMPASS are shown together with data from previous experiments: SMC [5],[3]; HERMES [6],[4]; and SLAC experiments E143 [7] and E155 [8]. One can observe the good agreement over the full range of  $x$ . COMPASS contributes significantly to the low  $x$  region previously covered only by SMC. For the 4 points at  $x < 0.03$  the statistical error of COMPASS is factor of 2-3 smaller for both inclusive and hadron asymmetries. It should be mentioned as well that for the case of  $A_{1d}$  the negative trend at low  $x$  which was observed by SMC is not confirmed by present COMPASS data.

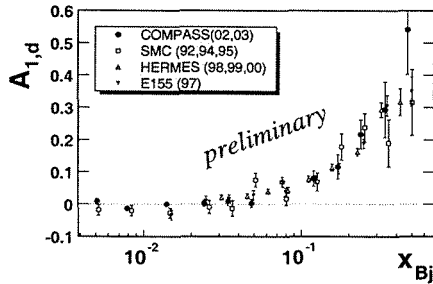


Figure 4: Inclusive  $A_{1d}$  asymmetry measured in COMPASS with superimposed points from other experiments

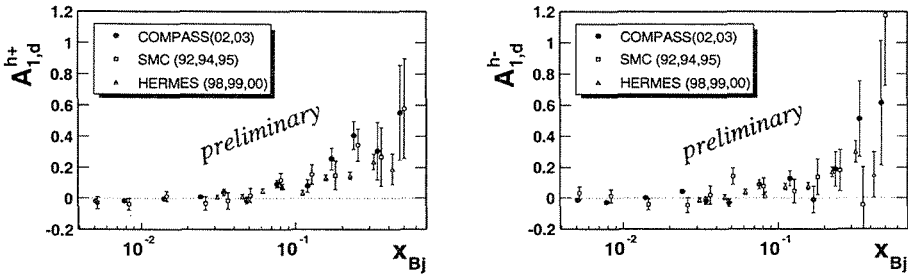


Figure 5: Hadron asymmetries measured by COMPASS, SMC and HERMES experiments. *Left:* positive hadron asymmetry  $A_{1d}^{h+}$ . *Right:* negative hadron asymmetry  $A_{1d}^{h-}$

There are several sources of systematic uncertainties in the asymmetry determination. The measurement of the target polarization and parametrization of the beam polarization together give the multiplicative error 6.4%. The uncertainty related to the dilution factor  $f$  is 6% over the full range of  $x$ . The depolarization factor  $D$  gives another multiplicative error order of 4%. A neglecting of the term  $A_2$  mainly affects the highest  $x$  region and its contribution is estimated to be  $\leq 0.005$ . The systematic error due to radiative corrections does not exceed 2% of statistical accuracy.

The multiplicative errors dominate at large  $x$  values where asymmetries show essentially nonzero effect. The study of false asymmetry generated by a variation of detector efficiencies in time is ongoing.

The publication of results on inclusive asymmetry  $A_{1d}$  is expected at the beginning of the year 2005.

## 5. The prospect for semi-inclusive analysis

The extraction of polarized quark distribution functions  $\Delta q$  is the final goal of semi-inclusive analysis. According to equations 1 and 2 the measured asymmetries are linear combinations of quark and anti-quark helicity distributions. One can rewrite these equations as  $\vec{A}_1 = B(q, D_q^h) \cdot \vec{\Delta}q$ . The matrix  $B$  is a function of known quantities: unpolarized quark distributions  $q$  which were determined by many experiments and fragmentation functions  $D_q^h$  which either were measured or can be taken from Monte Carlo simulations.

It is planned to use in analysis 6 asymmetries:  $\vec{A}_1 = \{A_1, A_1^{h+}, A_1^{h-}, A_1^{K+}, A_1^{K-}, A_1^{K_S^0}\}$ . The results on the first three were already discussed. The analysis on kaon asymmetries is in progress. Kaon asymmetries have the main role in the  $\Delta s$  determination since the strange quark is the valence quark for kaon. Due to the trigger settings the large part of DIS statistics of the experiment occupies the region of low  $x$  which is dominated by sea quarks. The strange quarks contribute only to the sea therefore COMPASS has a potential to determine  $\Delta s$  with a good accuracy. The theoretical constraint for  $\Delta s$  coming from unpolarized quark distributions is very weak at low  $x$  and the precise measurement of  $\Delta s$  is very important for the further theoretical elaboration. In particular the knowledge of the this quantity is necessary to have an interpretation for the Ellis-Jaffe sum rule [9] violation.

The analysis of the kaon asymmetries is more difficult. Charged kaons will be identified by the RICH and  $K_S^0$  from their decay geometry and reconstructed mass. This work is in progress.

## References

- [1] COMPASS proposal CERN/SPSLC 96-14 (Geneva 1996)
- [2] G.K.Mallot, NIM A518: 121-124, 2004.
- [3] B. Adeva et al., Phys. Lett. B420 (1998) 180-190
- [4] A. Airapetian et al., hep-ex/0407032, submitted to Phys. Rev D
- [5] B. Adeva et al., Phys. Rev. D58 (2001) 112001
- [6] A. Airapetian et al., Phys. Lett. B442 (1998) 484
- [7] K. Abe et al., Phys.Rev.D58:112003,1998
- [8] P.L.Anthony et al., Phys.Lett.B493:19-28,2000
- [9] J.Ellis and R.Jaffe, Phys.Rev D9, 1444 (1974)

**IX.**  
**PROGRESS**  
**IN EXPERIMENTAL**  
**STUDIES**  
**AT THE HIGH**  
**ENERGY**  
**ACCELERATORS**



# FULL SIMULATION OF HIGGS BOSON DECAYS INTO FOUR LEPTONS FOR ATLAS AT THE LHC

Alexander Khodinov<sup>1</sup>, Michael Rijssenbeek<sup>1</sup> and Sanjay Padhi<sup>2</sup>

<sup>1</sup>State University of New York at Stony Brook, New York, 11794-3800, USA

<sup>2</sup>Brookhaven National Laboratory, New York, 11973-5000, USA

## Abstract

Standard Model Higgs boson decays into leptons were studied using the complete ATLAS detector simulation. The reconstructed Higgs boson mass was obtained using a Z-mass constraint on leading leptons. The ATLAS detector resolution was convoluted on an event-by-event basis with the Breit-Wigner shape for the Z bosons. The muon reconstruction efficiency was found to be around 95% as a function of its transverse momentum. These results are consistent with the ATLAS technical design report.

In the framework of the Standard Model (SM), spontaneous symmetry breaking is generated according to the Higgs mechanism, and therefore the search for a massive spin zero particle  $H_0$ , called the Higgs boson, the self-interaction of the Higgs field, is considered as the main tasks of the ATLAS experiment [1] presently under construction at CERN. The SM does not predict the Higgs mass, but the constraints due to experimental data from LEP at CERN and the Tevatron at Fermilab [2] suggest that the SM Higgs mass is expected to be within the window of  $114 < M_H \text{ (GeV)} < 212$  at 95% confidence level. Among Higgs decay modes with the highest discovery potential, the channel  $H_0 \rightarrow ZZ^*$  with subsequent  $Z(Z^*)$  decay into lepton pairs provides a clear signal for the Higgs boson with a peak in the invariant mass spectrum of the final state leptons.

In this study we explore single lepton reconstruction efficiencies and Higgs boson mass resolutions, obtained from the full ATLAS detector simulation in proton-proton collisions at the center-of-mass energy 14 TeV. The physics processes have been simulated using PYTHIA 6.2 [3] Monte Carlo particle generator. The Higgs bosons were allowed to decay only into Z or  $Z^*$ , and Z bosons only into  $e^+e^-$  or  $\mu^+\mu^-$  pairs. Thus, the simulated data sample consists of the three processes  $H_0 \rightarrow 4e$  (25%),  $H_0 \rightarrow 4\mu$  (25%) and  $H_0 \rightarrow 2e2\mu$  (50%). These channels are important in terms of software and physics validation and are used as benchmark processes for electron and muon detectors at the LHC. Also, the high statistics, background-free process of single Z-production with subsequent  $Z \rightarrow e^+e^-$ , is considered the main tool for calibration of the electromagnetic (EM) calorimeter in ATLAS. The largest backgrounds to  $H_0 \rightarrow ZZ^* \rightarrow 4l$  are from top pair production and from  $Zbb^-$ . They are significantly reduced by requiring the final-state leptons to be isolated using the isolation criteria [4], which consists of cuts on the minimum angular distance,  $\Delta R = \sqrt{(\Delta\eta)^2 + (\Delta\phi)^2}$ , between the lepton and other clusters in either the Muon Spectrometer or the EM Calorimeter, and on maximum transverse energy deposited in the cone around the single lepton candidate.

The complete detector simulation was performed using the GEANT3 simulation program in the DC1 geometry layout (2003). The reconstruction used the ATLAS software ATHENA release 7.0.2 [5].

Single muon reconstruction efficiency as a function of transverse momentum,  $p_T$ , integrated over the pseudorapidity  $|\eta| < 2.5$  is shown in Figure 1(a), and as a function of pseudorapidity integrated over  $40 < p_T(\text{GeV}) < 60$  in Figure 1(b) for three different muon reconstruction algorithms: MUONBOX [6], MUID [7]-standalone, and MUID-combined. The first two algorithms track a muon candidate from the Muon Spectrometer back to the interaction point and take into account energy-loss information from the calorimeters. The third algorithm combines the ATLAS tracker (Inner Detector) and the Muon Spectrometer measurements, which is found to improve the overall muon momentum resolution and rejects muons from secondary pion decays. MUID-combined matches a muon track reconstructed independently in the Inner Detector by the iPatRec [8] pattern recognition procedure with a track found in the Muon Spectrometer by MUID-standalone. The iPatRec algorithm searches for track candidates in the Pixel and Semi Conductor Tracker [1], which are closest to the collision point, and extrapolates them to Transition Radiation Tracker. iPatRec is relatively insensitive to the multiple interactions and energy loss due to the amount of material in front of the EM Calorimeter, which may reach several radiation lengths. The muon reconstruction efficiency was found to be around 95% and is a function of its transverse momentum.

Electrons have been identified using EM clusters matched to charged iPatRec tracks with very loose energy over momentum ( $E/p$ ) matching ratio. The average efficiency for electrons is found to be 78%, worse than for muons.

The event sample is required to have isolated leptons with  $\Delta R < 0.1$  and  $E_T^{\text{ISO}} > 10$  GeV for electrons and  $E_T^{\text{ISO}} > 5$  GeV for muons. According to the ATLAS Physics Technical Design Report [1] an event is accepted in the sample if:

1. there are two leptons  $e^+e^-$  or  $\mu^+\mu^-$  with  $p_T > 20$  GeV and  $|\eta| < 2.5$ ;
2. there are two more leptons with  $p_T > 7$  GeV and  $|\eta| < 2.5$ ;
3. the leading  $e^+e^-$  or  $\mu^+\mu^-$  pair has invariant mass  $m_{12}$  within a 6 GeV window around the Z boson mass  $M_Z$ ;
4. the sub-leading  $e^+e^-$  or  $\mu^+\mu^-$  pair's invariant mass  $m_{34}$  is larger than 20 GeV.

All possible 4-lepton combinations for leading and sub-leading pairs of appropriate charge and flavor are tested. Only the combination in which the leading pair is reconstructed with an invariant mass closest to  $M_Z$  is selected. Under the assumption that the leading pair comes from an on-shell Z boson of mass  $M_Z$ , the leading lepton 4-momenta are rescaled on an event-by-event basis so that:

$$p \rightarrow p \times m_0/m_{ll}, \quad (1)$$

where  $m_{ll}$  is the reconstructed (measured) invariant mass of the two leading leptons;  $m_0$  is the maximum of the convolution of the Z mass detector resolution function (chosen to be Gaussian) with the Breit-Wigner shape (BW):

$$m_0 = \max(\text{Gaussian}(m_{ll}, \sigma_0) \times \text{BW}(M_Z, \Gamma_Z)), \quad (2)$$

where  $\sigma_0$  is the width of the  $m_{ll}$  distribution found to be 2.80 GeV for MUID combined muons and 2.85 GeV for iPatRec electrons.

Figure 2 shows the Higgs boson mass distribution for  $H_0 \rightarrow 4l$ . At the moment of writing, the  $H_0 \rightarrow 4\mu$  resolution of 1.56 GeV (Figure 2c) is the best value obtained with the new software, and is in a good agreement with the TDR.

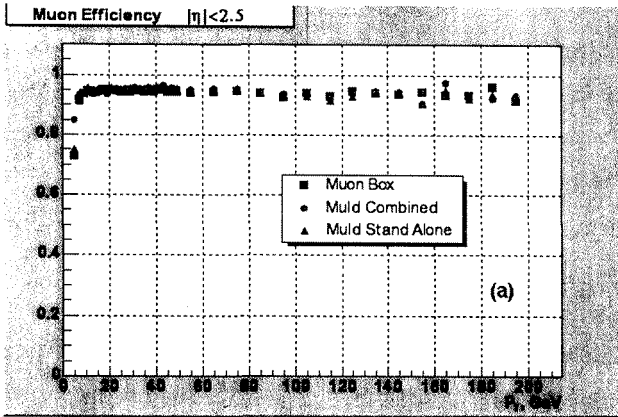


Figure 1(a): Single muon reconstruction efficiency as a function of its transverse momentum

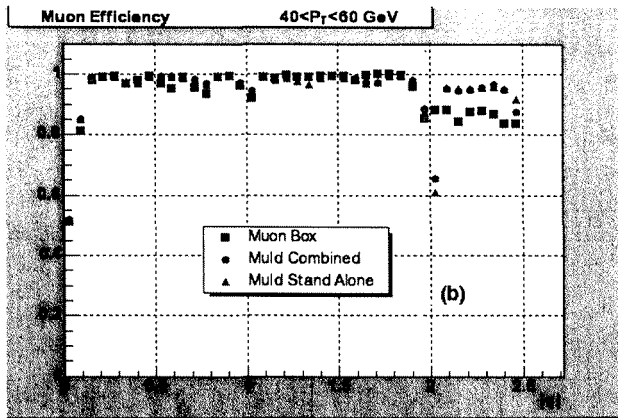


Figure 1(b): Single muon reconstruction efficiency integrated over  $40 < p_T(\text{GeV}) < 60$  as a function of  $|\eta|$

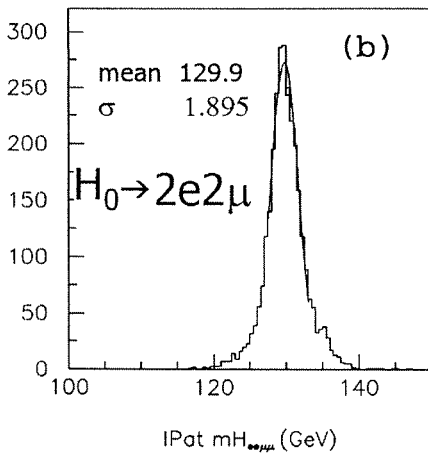
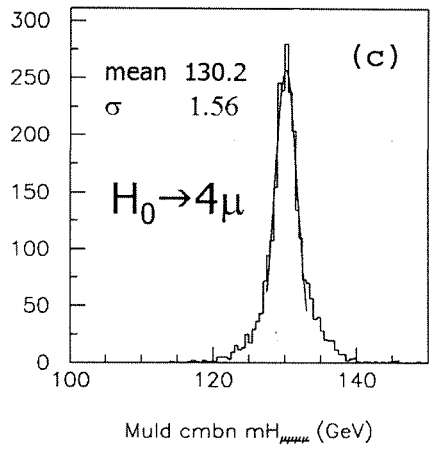
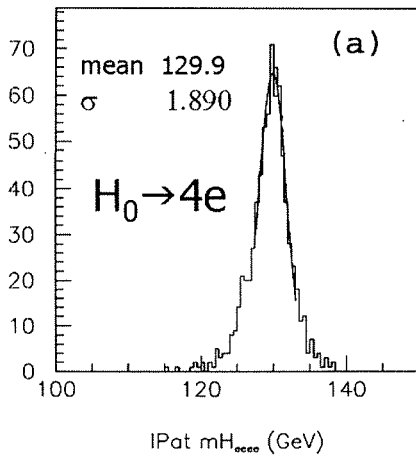


Figure 2: The four lepton invariant mass distribution (histogram) with the Gaussian fit (solid curve) around the peak over  $(-1.5\sigma, 2\sigma)$  are shown for  $H_0 \rightarrow 4e$  (a),  $H_0 \rightarrow 2e2\mu$  (b) and  $H_0 \rightarrow 4\mu$  (c)

References:

- [1] ATLAS Detector and Physics Performance Technical design Report, Volume I, II, ATLAS TDR 14, 15 CERN/LHCC 99-14, 15, May 25, (1999).
- [2] Search for the Standard Model Higgs Boson at LEP CERN-EP/2001-055 (2001); and the results of the Electroweak Working Group: <http://lepewwg.web.cern.ch/LEPEWWG/>
- [3] T. Sjöstrand, P. Edén, C. Friberg, L. Lönnblad, G. Miu, S. Mrenna and E. Norrbin, Computer Phys. Commun. 135 (2001) 238.
- [4] O. Linossier and L. Poggioli, ATLAS Internal Note ATL-PHYS-97-010, (101).
- [5] <http://atlas.web.cern.ch/Atlas/GROUPS/SOFTWARE/OO/architecture>
- [6] M. Virchaux et. al, "MUONBOX: a full 3D tracking program for Muon reconstruction in the ATLAS Detector," ATLAS Internal Note ATL-SOFT-94-009 (1994) .
- [7] "A Muon Identification and Combined Reconstruction Procedure for the ATLAS Detector at the LHC at CERN", CERN-ATL-CONF-2003-011, (2003).
- [8] R. Clift and A. Poppelton, "iPatRec: Inner Detector pattern-recognition and track-fitting," ATLAS Internal Note, ATL-SOFT-94-009 (1994).

# STUDY OF A POSSIBILITY TO DETECT $\Upsilon$ IN p-Pb AND Pb-p COLLISIONS AT THE LHC IN THE MUON SPECTROMETER OF ALICE

A. Morsch<sup>1</sup>, C. Mitu<sup>2</sup>, A. Sevchenko<sup>2</sup>, G. Shabratova<sup>2</sup>, A. Vodopianov<sup>2</sup> and A. Zinchenko<sup>2†</sup>

(1) *CERN, Geneva, Switzerland*

(2) *JINR, Dubna, Russia*

† *E-mail: zinchenk@laxpub00.jinr.ru*

## Abstract

Results of a Monte Carlo study of upsilon family production in p-Pb and Pb-p collisions at the LHC and its detection in the muon spectrometer of the ALICE detector are presented. The study was done on the basis of the fast simulation method developed within the ALICE simulation and reconstruction framework AliRoot. In this method, the expected efficiency, momentum and mass resolution of the spectrometer have been taken into account for smearing the generated particle parameters in the muon spectrometer acceptance. The upsilon production has been simulated using the  $p_t$  and rapidity parameterization for the resonances. Secondary interactions and decays of bottom quarks are the main sources of background. The simulation of the background, i.e. the bottom quark pair production has been carried out by the Pythia generator. The merging of the background and signal was done with weights proportional to corresponding production cross sections. The signal to background ratio and significance have been estimated for each member of upsilon family for the collider running scenario. The Bjorken variable  $x$  distributions for the target and projectile are presented. A good separation between the signal and background is demonstrated.

## 1. Introduction

Hard processes such as heavy-flavor production will play a central role in the physics of ALICE. Heavy quarks (charm and bottom) provide sensitive probes of the collision dynamics at both short and long timescales. On one hand, heavy-quark production is a perturbative phenomenon, which takes place on a timescale of the order of  $1/m_Q$ , where  $m_Q$  is the heavy-quark mass. On the other hand, the long lifetime of charm and bottom quarks allows them to live through the thermalization phase of the plasma and to possibly be affected by its presence. In addition, the high temperature of the plasma may generate heavy-quark pairs of thermal origin. Finally, heavy-quark-antiquark pairs can form quarkonium states, which are bound by energies of the order of a few hundred MeV. These binding energies are comparable in size with the mean energies ( $3 T_c$ ) of the plasma, implying a large probability for quarkonium breakup. Less than 1% of all heavy-quark pairs form quarkonium bound states. Therefore, phenomena such as quarkonium suppression do not have any impact on the open heavy-quark production [1].

The uncertainties in the initial conditions for heavy-ion collisions at the LHC translate into significant ambiguities for separating initial- from final-state medium effects. With

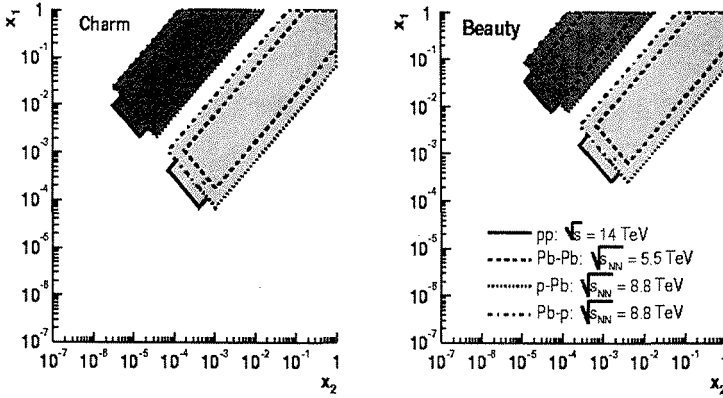


Figure 1: ALICE acceptance in the  $(x_1, x_2)$  plane for charm(left) and beauty(right) in pp, Pb-Pb, p-Pb and Pb-p collisions

p-A or d-A collisions we can separate those two effects better and together with p-p results we can have a more reasonable interpretation of A-A data. The observables measured in p-A collisions are more sensitive to final state rescattering and energy loss of a fast parton in a hot and cold nuclear matter and in the interpretation of open-charm(beauty) and onium data one must add up the production and the suppression mechanism in p-A.

The LHC will allow to probe the parton distribution function (PDF) of nucleons and in the case of proton nucleus and nucleus-nucleus collisions also their modification in the nucleus down to unprecedented low values of  $x$ , where  $x$  is the Bjorken variable defined as a fraction of the proton momentum carried by the parton that enters the hard scattering process. The charm and beauty production cross section at the LHC are significantly affected by parton dynamics in the small  $x$ -region. The measurement of heavy flavour production could provide information of the nuclear parton densities. Measurements of p-A collisions allow us to reduce the uncertainties in the nuclear parton distribution functions and in particular in the gluon structure function. In principle, measuring the yields in p-Pb relative to pp collisions at 8.8 TeV allows us to explore values of  $x$  down to  $10^{-4}$ .

The square of the invariant mass of the  $Q\bar{Q}$  pair for the case of the gluon-gluon fusion  $gg \rightarrow Q\bar{Q}$  in the collision of two ions with  $(A_1, Z_1)$  and  $(A_2, Z_2)$  in the leading order will be equal to [2]:

$$M_{Q\bar{Q}}^2 = x_1 x_2 s_{NN} = x_1 \frac{Z_1}{A_1} x_2 \frac{Z_2}{A_2} \quad (1)$$

and its longitudinal rapidity in the laboratory system is

$$y_{Q\bar{Q}} = \frac{1}{2} \ln \left[ \frac{E + p_z}{E - p_z} \right] = \frac{1}{2} \ln \left[ \frac{x_1 Z_1 A_2}{x_2 Z_2 A_1} \right] \quad (2)$$

Thus, Bjorken variables  $x_1$  and  $x_2$  can be expressed as

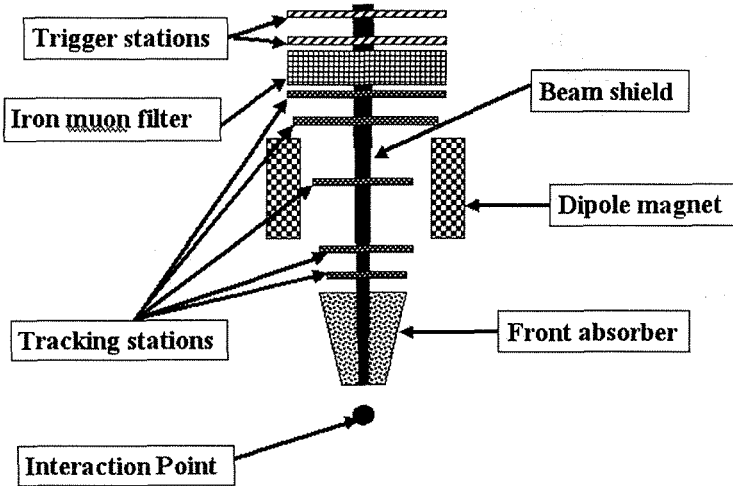


Figure 2: Layout of the muon arm of ALICE detector at the LHC

$$x_{1,2} = \frac{A_{1,2} M_{Q\bar{Q}}}{Z_{1,2} \sqrt{s_{pN}}} \exp(\pm y_{Q\bar{Q}}) \quad (3)$$

In the case of asymmetric collisions, e.g. p-Pb and Pb-p, the center of mass moves with a longitudinal rapidity, resulting in the rapidity shift:  $\Delta y = y_{cm}$ , corresponding  $+0.47$  ( $-0.47$ ) for p-Pb (Pb-p) collisions. Therefore, running with both p-Pb and Pb-p will allow to cover the largest interval in  $x$ . Fig. 1 presents [2] a first idea of the regimes for  $x_1$  and  $x_2$  accessible with the detector ALICE, specialized for studies of nucleus-nucleus collisions at LHC energies. The ALICE rapidity acceptance cuts, presented in this plot, were applied to the rapidity of the  $Q\bar{Q}$  pair, and not to that of the particles which are actually detected. Investigation of  $\Upsilon$  family production in p-Pb (Pb-p) collisions via detection of  $\mu\mu$  pairs from their decay is an aim of this work. The layout of the muon spectrometer used for this study is presented in Fig. 2 [3].

## 2. Simulation

The study of the  $\Upsilon$  family production was done with simulated data. The simulation used the FASTSIM (fast simulation) package [4] developed within the ALICE simulation and reconstruction framework AliRoot. The simulation of  $c\bar{c}$ ,  $b\bar{b}$  pairs and  $\Upsilon$  family was done in the rapidity range 1.-6.

The signal was generated using AliGenMUONlib with the new functions (Vogt pA and Vogt Ap) included, describing parameterizations for  $p_t$  and rapidity distributions for the simulation of  $\Upsilon$  family production. (Fig. 3-top). In the simulation of the signal the shadowing effect and rapidity shift were also taken into account (Fig. 3-bottom).

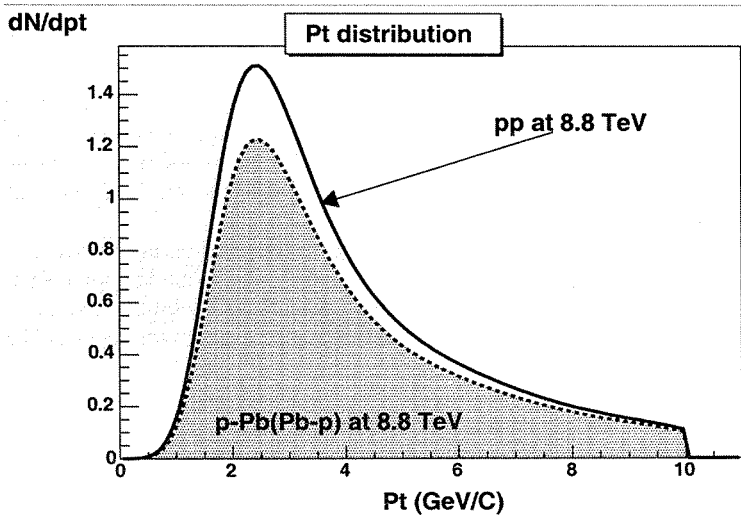
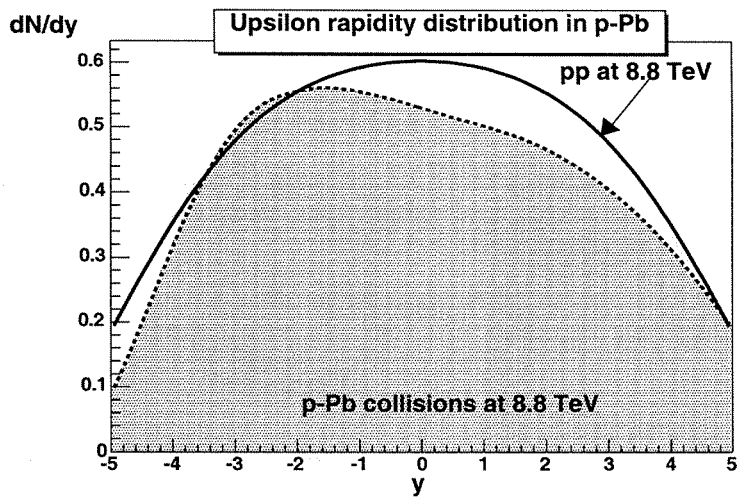


Figure 3: Rapidity and  $p_t$  distributions for  $\Upsilon$ 's created in p-Pb collisions

For the background simulation the Pythia package was used (AliGenPythia library) to generate  $c\bar{c}$  and  $b\bar{b}$  pairs at 8.8 TeV p-Pb and Pb-p collisions. The decay muons from the same or different events were used to represent the correlated or uncorrelated background, respectively. The produced particles in the muon spectrometer acceptance were smeared in accordance with the expected efficiency, momentum and mass resolution of the spectrometer [3].

The background and signal were merged together (a “detected” event) with weights proportional to corresponding cross sections. Cross sections for different states in p-Pb (Pb-p) collisions are presented in table 1 [2],[5].

State	$\sigma_{prod.}$ (b)	$\sigma \times BR$ , (b)
$c\bar{c}$	1.49	0.22
$b\bar{b}$	0.056	0.0056
$\Upsilon$		$3.53 \times 10^{-6}$

Table 1: Cross sections used for simulation of signal and background

### 3. Data analysis

The prepared “detected” events were then analysed as follows. The parameterized background was subtracted from the total  $M_{eff}$  distribution (a la experiment) (Fig. 4-top). The remaining signal was fitted to a sum of three Gaussian functions, corresponding to the  $\Upsilon$ ,  $\Upsilon'$  and  $\Upsilon''$  resonances (Fig. 4-bottom). From the two resulted distributions, the signal to background ratio was calculated.

In order to estimate the number of signal and background events for the current LHC running scenario the following numbers were taken: the required luminosity for p-Pb collisions is  $1.1 \times 10^{29} \text{ cm}^{-2} \text{ s}^{-1}$  [6]; the running time for p-Pb interaction  $10^6 \text{ s}$ , i.e. the same as for Pb-Pb collisions [3]. The number of background events was calculated using the following formula:

$$N_{BGR} = tL\sigma BRh_{simul}h_{detect},$$

where  $t$  - running time,  $L$  - luminosity,

$\sigma BR$  - production cross section multiplied by branching ratio,

$h_{simul}$  - ratio of  $b\bar{b}$  produced in the rapidity range 1.-6. to all  $b\bar{b}$  pairs,

$h_{detect}$  - ratio of  $\mu\mu$  pairs detected in the muon spectrometer acceptance(2.5-4.) to simulated  $b\bar{b}$  pairs in the rapidity range 1.-6.

The numbers of  $\Upsilon$  events for each member of the family were calculated using the signal to background ratio taken from the parameterized  $M_{eff}$  multiplied by the number of events from background:

$$N_{signal} = N_{BGR}S/B$$

The numbers of events obtained after the analysis are of the order of  $10^3$  particles for the background and signal. The numbers correspond to the interval of  $\pm 1\sigma$  around the resonance mass. In addition to the signal to background ratios, the significance ( $S/\sqrt{S+B}$ )

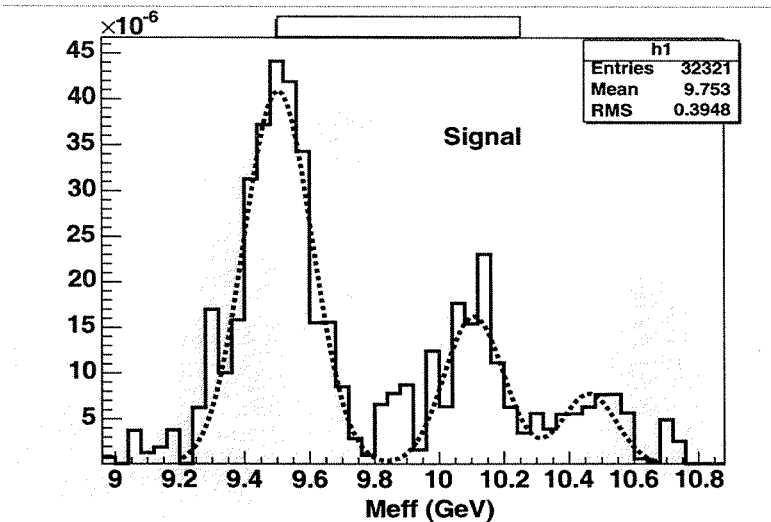
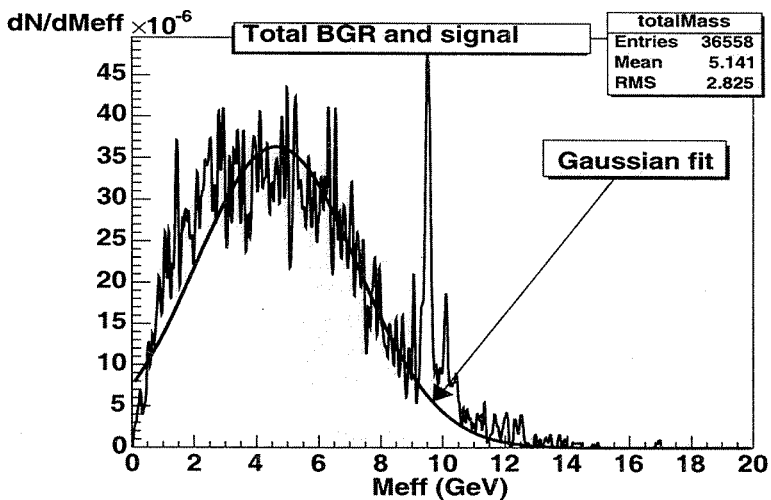


Figure 4: Distributions of the effective mass for the Pb-p collisions with  $p_t > 3$  GeV/c of decay muons. Upper plot - signal + background case, lower - signal after subtraction of the background

was calculated, showing good results. The calculation of signal and background events, signal to background ratio and significance was done without  $p_t$  cuts and with  $p_t > 3$  GeV cuts for decay muons.

$p_t > 3$ GeV					
Collisions	State	Backgr.(B)x $10^3$	Signal (S)x $10^3$	S/B	$S/\sqrt{S+B}$
p-Pb	$\Upsilon$	3.14	5.77	2.70	64.9
	$\Upsilon'$	1.16	1.56	1.26	29.5
	$\Upsilon''$	1.13	1.08	0.94	22.9
Pb-p	$\Upsilon$	2.91	13.01	4.47	103.1
	$\Upsilon'$	2.62	6.17	2.35	65.8
	$\Upsilon''$	1.07	2.22	2.07	38.7

Table 2: Background and signal rates, signal to background ratio and significance

The Bjorken variables  $x_1$  and  $x_2$  were extracted according to (3) using the effective mass of  $\mu\mu$  pair and their longitudinal rapidity. A good separation between background and signal (in the upsilon family mass range) was obtained (Fig. 5)

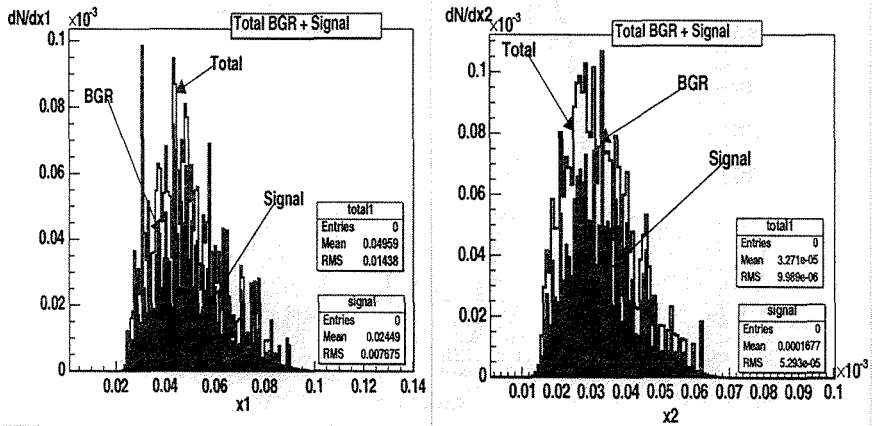


Figure 5:  $x_1$  and  $x_2$  of  $\Upsilon$ 's created in p-Pb collisions with  $p_t > 3$  GeV of decay muons in the effective mass region of 9.2-10.6 GeV

## 4. Conclusion

Production of the upsilon family can be studied with a good efficiency in the muon spectrometer of ALICE for p-Pb and Pb-p collisions at LHC.

## References

- [1] G. Marchesini, hep-ph/9307376.
- [2] N. Carrer and A. Dainese, ALICE-INT-2003-019.
- [3] CERN/LHCC 96-32 LHCC/P3-Addendum 1.
- [4] A. De Falco et al, <http://gosset.home.cern.ch/gosset/ALICE/dimuonoffline/DOCUMENTS>.
- [5] K.J. Eskola et al, hep-ph/0308248.
- [6] A. Morsch ALICE-INT-2001-10.

# PERFORMANCE OF THE SILICON DRIFT DETECTOR IN THE CASE OF PERPENDICULAR TRACKS AND INCLINED TRACKS

S.Kouchpil <sup>1,2†</sup> for the ITS ALICE collaboration

(1) *JINR, Dubna, Russia.*

(2) *NPI, Řež near Prague, Czech Republic.*

† *E-mail:skushpil@ujf.cas.cz*

## Abstract

The Silicon Drift Detector is well suited for secondary vertex reconstruction, particle identification and tracking of low-momentum particles in the ALICE experiment where will be in central Pb-Pb collisions reached very high particle multiplicity. The ALICE SDD performance was studied during beam tests carried out at the CERN SPS facility. The data analysis results, presented here, were focused on the evaluation of spatial resolution for various incident angles of particles traversing the detector.

## 1. Introduction

The Silicon Drift Detectors (SDD) [1] will equip the third and the fourth layers of the ALICE Inner Tracking System (ITS) [2]. They offer the high granularity required by the high particle density predicted in heavy-ion reactions and provide the energy-loss measurement needed for particle identification. Several prototypes have been tested using beam particles to evaluate the detector performance in real experimental conditions. An overview of the results of these studies can be found in [3]-[10]. This article presents the study of the influence of the incident particle angle with respect to the detector on the performance of the ALICE SDD.

## 2. Experimental details

### 2.1. The detector

All the studies were carried out with the ALICE SDD D2 prototype [3] (very close to the final design for ALICE) produced by Canberra Semiconductors N.V., Belgium. Each SDD is produced from a  $300\ \mu\text{m}$  thick, 5 inch diameter n-type silicon wafer of resistivity  $3\ \text{k}\Omega\ \text{cm}$ . The detector has a bi-directional structure with two opposite drift directions. For each drift region  $292\ p^+$  cathodes are implanted on both sides of the wafer with  $120\ \mu\text{m}$  pitch. A voltage divider, implanted in the wafer, connects all adjacent cathode strips with  $170\ \text{k}\Omega$  resistors. For each half of the detector the drift length is  $35.0\ \text{mm}$ , and the drifting charge is collected by 256 anodes with a pitch of  $294\ \mu\text{m}$ , so that the sensitive area is  $70 \times 75\ \text{mm}$ . The active area of the SDD is 85% of its total area. Since the drift velocity is very sensitive to the detector temperature variation the monitoring of this quantity is performed by means of three rows of 33 implanted point-like MOS charge injectors [4].

## 2.2. Experimental setup

The experimental results presented in Section 3 were obtained from the analysis of the data taken at the CERN SPS with a pion beam at  $p = 140 \text{ GeV}/c$  in August 2000. The SDD was placed on the beam trajectory between two microstrip telescopes which measured the particle impact point on the SDD with a precision of  $\sim 5 \mu\text{m}$  r.m.s. Each of the microstrip detectors had an area of about  $20 \times 20 \text{ mm}^2$  and  $50 \mu\text{m}$  pitch between strips. Two pairs of scintillating counters placed at the both ends of the setup provided the beam trigger signal. The microstrip telescopes were aligned with these trigger counters. The signals induced on the SDD anodes were amplified using OLA chips [11], specially developed for this type of detector, and sampled at 40 MHz by non-linear 8 bit Flash ADCs. A relevant linearization procedure was applied to the data during the off-line analysis.

## 2.3. Data

The data taking was organized in *runs*, in which a certain number of events in the same experimental conditions, i.e. the SDD position, connected anodes etc., were recorded. All runs were taken at the nominal drift field ( $667\text{V}/\text{cm}$ ), with single tracks. The detector support structure rotated at 22.5 degrees and 36 degrees with respect to the beam direction respectively. The ranges of connected anodes for these two sets of data were different in order to avoid the presence of material from the mechanical support on the beam line.

From geometrical considerations, a significant improvement of the resolution along the anode axis is expected, due to the reduction of the fraction of single-anode clusters, whereas the drift axis cluster size should not change significantly. A small improvement of the spatial resolution along the drift direction is expected from the higher value of the signal-to-noise ratio ( $S/N$ ) due to the inclination of the detector with respect to the beam axis. However, AliRoot simulations [12] have shown that a negligible influence is expected by increasing the  $S/N$  ratio of 20%.

# 3. Results

## 3.1. Cluster reconstruction

A cluster can be defined as a set of adjacent samples with a signal amplitude higher than a certain threshold. In order to take into account the signal fluctuations coming from the noise, it is required that for each anode at least two adjacent samples pass the threshold. Since the OLA amplifier has a linear response, for each channel the integral of the output signal is expected to be proportional to the charge collected by the anode. Under the condition that the threshold is sufficiently low compared to the maximum amplitude of the signal, that the signal has no undershoot, and that the sampling period is small enough compared to the signal shaping time, the sum of the sample linearized amplitudes of the cluster is, in a good approximation, proportional to the total collected charge. All these conditions were verified in our experiment. In the following, this sum will be called *charge*. The drift axis coordinate is calculated in first approximation as the time signal centroid multiplied by a uniform drift velocity and the anode coordinate is calculated by

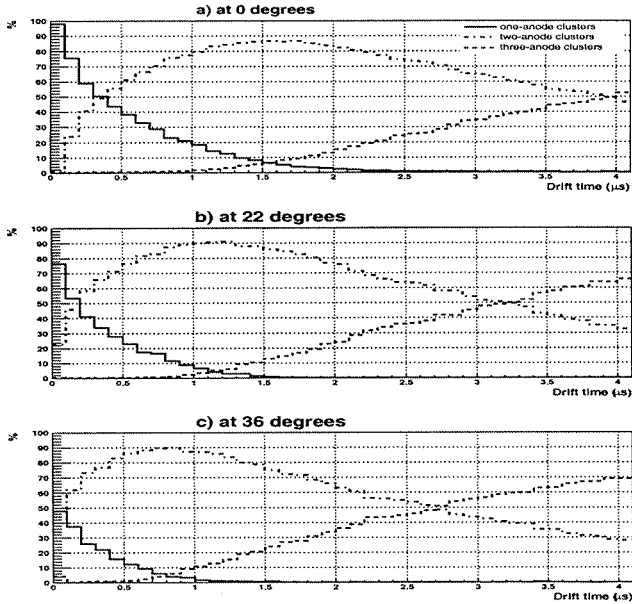


Figure 1: Percentages of the events in which a cluster is collected by one, two or tree anodes as a function of the drift time

the centroid of charge distribution measured on the anodes. After that, the systematic errors caused by the dopant inhomogeneities are successively corrected [8].

### 3.2. Cluster size

A measurement of the cluster size was performed in the anode and the drift directions. The time evolution of the amplifier output signal results from the convolution of the anodic current and the time response of the amplifier. The anodic current shape is, in good approximation, similar to the electron collection time distribution. The nominal value of the OLA shaping time is  $55\text{ ns}$  for a zero input capacitance [11] but was larger and not known precisely in our experimental conditions. This uncertainty didn't allow us to determine precisely the size of the electron cloud along the drift axis. However, since the shaping time of the OLA was constant during all the data taking and of the same order of magnitude of the anodic signal duration, a qualitative comparison of this duration is possible by calculating the drift direction cluster *r.m.s.* We studied the distribution of the *r.m.s.* of the signal as a function of the drift time for the various values of the incident angle. No significant difference is observed, confirming the independence of the cluster size along the drift axis versus the angle  $\theta_{rz}$ .

Figure 1 shows the relative amounts of clusters collected by one, two or three anodes as a function of the drift time for  $\theta_{rz} = 0^\circ, 22.5^\circ, 36^\circ$ . The number of clusters collected by more than three anodes is less than 1%. As expected, the number of multi-anode

clusters increases with the inclination angle of the tracks. The number of single anode clusters in the anode region decreases with  $\theta_{rz}$  changing from 11% of the total number of clusters for  $0^\circ$  to 4% for  $36^\circ$ . The number of three anode clusters increases with drift time and  $\theta_{rz}$  from 20% (for  $0^\circ$ ) to 41% (for  $36^\circ$ ) of the total amount of clusters.

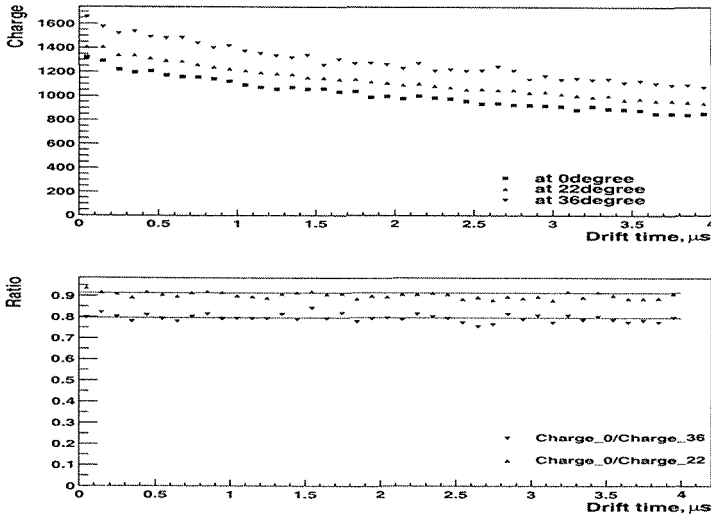


Figure 2: Top: dependence of the most probable values of the charge collected for inclined tracks and for perpendicular tracks versus the drift time. Bottom: ratio of MPV of the charges versus drift time. The lines indicate the values of  $\cos 22.5^\circ$  and  $\cos 36^\circ$

### 3.3. Charge

In Fig. 2 (top) the *MPVs* (Most Probable Values) of the cluster charge versus the drift distance are shown for the perpendicular tracks and inclined tracks for each group of the analyzed runs. Due to a defect of the used detector caused by the fabrication process, the collected charge decreases as a function of the drift distance. Nevertheless, the ratio between the *MPV* for perpendicular tracks and the *MPV* for the inclined tracks has, apart from the experimental fluctuations, a constant value versus the drift time. The ratio between the *MPVs* for  $0^\circ$  and  $22.5^\circ$  (Fig. 2 bottom) is  $0.917 \pm 0.009$ , which is in agreement with the expected value  $\cos 22.5^\circ = 0.923$ ; the ratio between the *MPV* for  $0^\circ$  and  $36^\circ$  gives  $0.805 \pm 0.011$ , that is consistent with  $\cos 36^\circ = 0.809$ . This increase in the cluster size along the anode axis allows us to expect an improvement of the anodic resolution when  $\theta_{rz}$  increases.

### 3.4. Resolution

The spatial resolution is defined as the *r.m.s.* of the residual distribution between the coordinate of the electron cloud measured by the SDD and the reference coordinate given

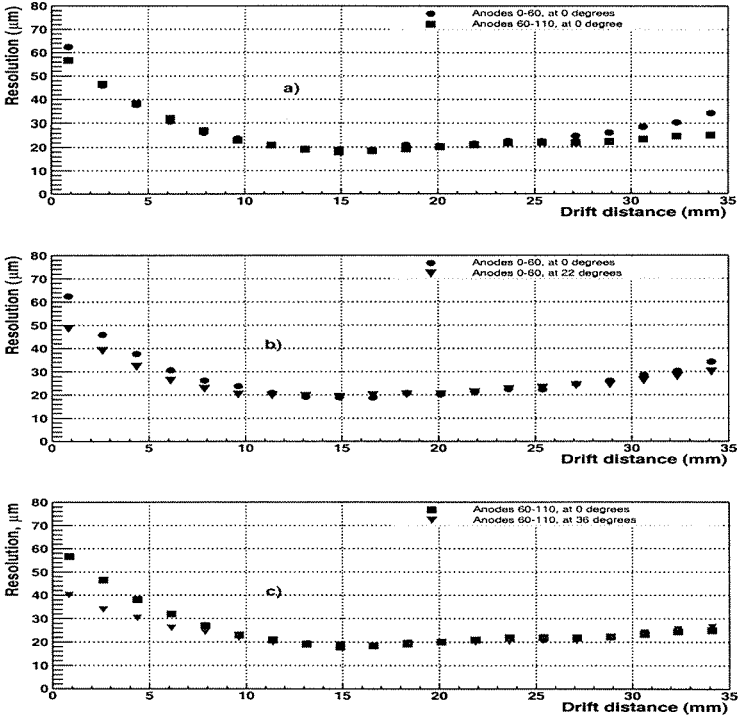


Figure 3: Spatial resolution along the anode axis as a function of the drift distance: (a) comparison of the resolution for the case of perpendicular tracks for two different regions of the SDD, corresponding to groups of the indicated anodes; (b) comparison of the resolution for the case of tracks inclined at 22.5 degrees and the perpendicular tracks obtained for the region between anodes 0 and 60; (c) comparison of the resolution for the case of tracks inclined at 36 degrees and perpendicular tracks for the group of anodes 60-110.

by the microstrip telescopes. The spatial resolution with inclined tracks was studied only along the anode axis, where an improvement, with respect to the one with perpendicular tracks, is expected. Figure 10 shows the spatial resolution along the anode direction as a function of the drift distance. The resolution for perpendicular tracks obtained for the two groups of anodes is presented in Fig. 3a. At short drift distances, the anodic charge centroid is affected by uncertainty due to the charge cloud being much smaller than the anode pitch. As a consequence, the corresponding value of the resolution is higher than for longer drift distances. The deterioration of the resolution at the long drift distances is due to the decrease of the signal to noise ratio caused by the diffusion. The values of resolution for different groups of anodes are compatible for all drift distances, although there is an evident difference from distances large than 25 mm. This discrepancy may come from the difficulty to correct for the large values of the systematic deviations (up to several hundreds of  $\mu\text{m}$ ) in this region.

In Fig. 3.b the comparison between the measured resolution for perpendicular tracks and for an inclination of  $22.5^\circ$  in the SDD region between anodes 0 and 60 is shown. Fig. 3.c shows the comparison of the resolution for incident angles of  $0^\circ$  and  $36^\circ$ , obtained in the region corresponding to anodes 60-110. We observe, that in the vicinity of the SDD anodes the values of the anodic resolution for inclined tracks become better with respect to those for perpendicular tracks. This behaviour is caused by the decrease of the fraction of narrow clusters in the inclined track events. For longer drift distances the values of the resolution are very similar to those for perpendicular tracks. Except at short drift distances, the average value of the resolution is below  $30 \mu m$ . The resolution reached the best value of  $19 \mu m$  at a drift distance of  $15 mm$ .

## 4. Conclusion

The results of the SDD data analysis for the inclined tracks, concerning total charge, are in excellent quantitative agreement with the expected behaviour. The study of the cluster size and the spatial resolution is in agreement with expected results. In particular, the anode resolution at a small drift paths is, on average, better for the inclined tracks than for the perpendicular tracks. The value of the resolution would be adequate for the performance of the SDDs in the ALICE experiment.

## References

- [1] E. Gatti, P. Rehak, Nucl. Instr. and Meth. **A 225** (1984) 608.
- [2] ALICE Collaboration, Technical Design Report of the ITS, CERN/LHCC 99-12.
- [3] A. Rashevsky *et al.*, Nucl. Instr. and Meth. **A461** (2001) 133-138
- [4] W. Bonvicini *et al.*, Nucl. Instr. and Meth. **A439** (2000) 476
- [5] D. Nouais *et al.*, Nucl. Instr. and Meth. **A477** (2002) 99-103
- [6] D. Nouais *et al.*, Nucl. Phys. B (Proc.Suppl.) 78 (1999) 252-258
- [7] D. Nouais *et al.*, Nucl. Instr. and Meth. **A450** (2000) 338
- [8] D. Nouais *et al.*, Nucl. Instr. and Meth. **A461** (2001) 222-225
- [9] E. Crescio *et al.*, CERN/ALICE/PUB 00-29, ALICE-INT-2001-09
- [10] S. Kouchpil, Part. Nucl. Lett. 2004. V.1, No. 4(121),P. 70-79
- [11] W. Dabrowski *et al.*, Nucl. Phys. **B44** (1995) 637
- [12] P. Cerello *et al.*, ALICE-INT-2001-34

# PRODUCTION AND IDENTIFICATION OF THE SUPERHEAVY HYDROGEN HYPERNUCLEUS ${}^6_{\Lambda}\text{H}$

L. Majling<sup>1,2†</sup>, Yu. Batusov<sup>1</sup>, J. Lukstins<sup>1</sup>, A. Parfenov<sup>1</sup>, M. Solar<sup>3</sup> and B. Sopko<sup>3</sup>

(1) *Joint Institute for Nuclear Research, Dubna, Russia*

(2) *Nuclear Physics Institute, CAS, Řež, Czech Republic*

(3) *Czech Technical University, Prague, Czech Republic*

† *E-mail: majling@ujf.cas.cz*

## Abstract

The hypernucleus  ${}^6_{\Lambda}\text{H}$ , existence of which has been suggested recently, could be identified unambiguously in experiments with light relativistic hypernuclei prepared for Nuclotron.

**Key-words:** relativistic hypernuclei, exotic nuclei

## 1. Introduction. Nuclei with a Neutron Halo

In the last twenty years a new branch of nuclear physics, namely physics of nuclei in the vicinity of the neutron drip line has been constituted [1]. The dripline is the limit of the nuclear landscape, where additional neutrons can no longer be kept in the nucleus. This dripline has been really reached for light nuclei ( $Z \leq 6$ ), see Fig. 1. One can see irregularities at the border of neutron stability. There is considerable interest in unbound nuclear systems close to the driplines, both in themselves and as subsystem of Borromean halo nuclei. The term Borromean was coined in ref. [2] to denote a bound three-body system (core + n + n) for which no binary subsystem is bound. In Fig. 1, the  $\beta$ -stable isotopes are marked by ( $\oplus$ ) and the type of neutron halo is also given.

The short range of the nuclear force and the low separation energy of the valence nucleons results, in some cases, in considerable tunneling into the classical forbidden region and more or less pronounced halo may be formed. As a result the valence and the core subsystems are to a large extent separable. Therefore, halo nuclei may be viewed as an inert core surrounded by a low density halo of valence nucleons and described in few-body or cluster models.

There have been used different experiments which have contributed to the present picture of nuclei with neutron halo. The development of techniques for the production of exotic radioactive nuclei and making beams of them, has been of key importance for the progress of the field. The ground-state properties such as mass, spin and moments are mainly measured with stopped low-energy beams at ISOL facilities. The energetic radioactive beams obtained with the in-flight technique are the main tool for studies of nuclei at the driplines. In this contribution, we discuss the potential of hypernuclear physics.

## 2. Stabilizing role of the $\Lambda$ hyperon

It is well known that  $\Lambda$  hyperon makes the nuclear system more stable. In the lower part of Fig. 1, the solid line determines hyperfragments observed in emulsion [3]. The stabilizing influence of the  $\Lambda$  hyperon is obvious: the 'lake of instability' ( ${}^8\text{Be}$ ,  ${}^9\text{B}$ ) is filled as well as irregularities at the border ( ${}^5\text{He}$ ,  ${}^7\text{He}$ ). Large scale systematic studies of hypernuclei began with the advent of separated  $K^-$  beams, which permitted the use of counter technique and confirmed the brilliant suggestion of Podgoretsky [4]: instead of hunting down decays of random fragments, to study hypernuclear production in strangeness exchange reaction  ${}^A_Z(K^-, \pi^-) {}^A_{\Lambda}Z$ . In one-step direct reactions such as  $(K^-, \pi^-)$  or  $(\pi^+, K^+)$  [5, 6] and  $(K^-, \pi^0)$  or  $(e, e' K^+)$  [7, 8] the level structure of hypernuclei can be experimentally studied and information on structure can be obtained.

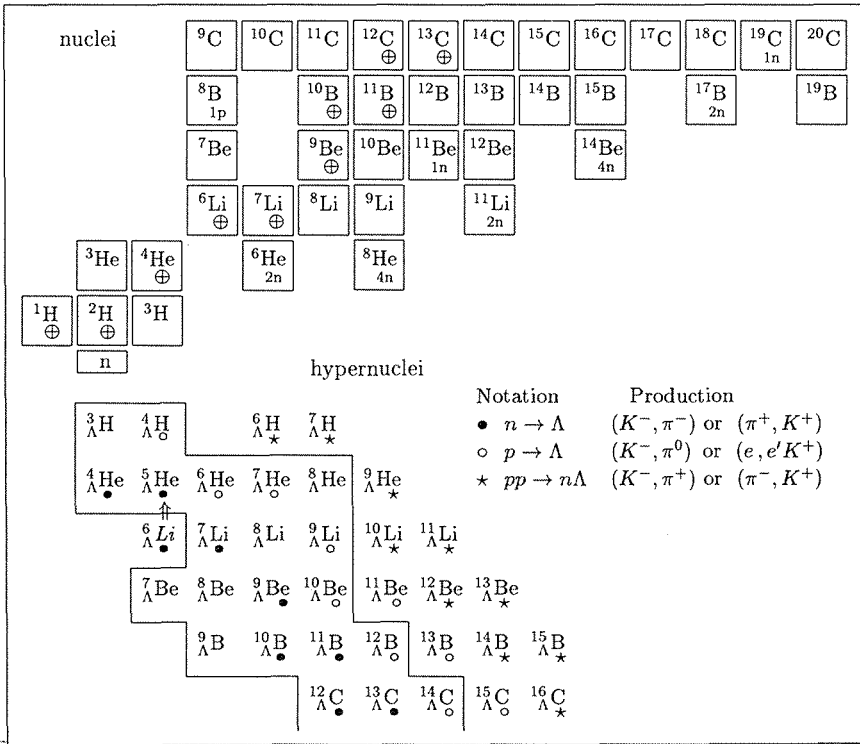


Figure 1: N/Z diagram of light nuclei and hypernuclei. Hypernuclei are shown together with their production reaction. See text for detail

Recently, Tamura solved the huge technical problems and constructed "Hyperball", a large acceptance Ge detector array dedicated to hypernuclear  $\gamma$ -ray spectroscopy [9]. An impressive result has been obtained: the observed  $\gamma$ -rays from  ${}^7_{\Lambda}\text{Li}$  hypernucleus indicate a significant ( $\approx 20\%$ ) contraction of the  ${}^6\text{Li}$  ( $= \alpha + d$ ) core in  ${}^7_{\Lambda}\text{Li}$ . So, HYPERNU-

CLEAR PHYSICS COULD BE USED IN THE STUDIES OF THE LOOSELY BOUND NUCLEAR SYSTEMS such are nuclei with neutron halo. However, there is only one hypernucleus with neutron halo,  ${}^7_{\Lambda}\text{He}$ , which can be produced in one-step direct reaction,  $p \rightarrow \Lambda$ .

The announcement of the plan for the new hypernuclear facility FINUDA at the  $\phi$ -factory DAΦNE (Frascati) [11], initiated great expectations. It opens unprecedented possibilities: very low energy of kaons from the  $\phi$  decay allow the use of very thin solid stopping targets. The detector is designed to register both the  $\pi^-$  from the formation reaction and charge products from the hypernuclear decay. We suggested [12] to study there STRANGENESS AND DOUBLE CHARGE EXCHANGE (S&DCX) reaction ( $K^-, \pi^+$ ), which opens way to the production of neutron-rich hypernuclei. There are two paths how to arrive at the  $\Lambda n p^{-2}$  states:

$$\begin{array}{ll} \text{either by the pion charge exchange:} & K^- p \rightarrow \Lambda \pi^0, \quad \pi^0 p \rightarrow n \pi^+ \\ \text{or through the } \Sigma N \rightarrow \Lambda N \text{ conversion:} & K^- p \rightarrow \pi^+ \Sigma^-, \quad \Sigma^- p \rightarrow \Lambda n. \end{array}$$

Hypernuclei produced in such a reaction are marked by  $\star$  in Fig. 1. As we can see no  $\Lambda$  hypernucleus produced in S&DCX reaction has been observed until now.

Unfortunately, both protons have to be in the same target nucleus, so cross sections are inevitably low. Nevertheless, the search for neutron-rich  $\Lambda$  hypernuclei is one of the items on the FINUDA's list [13].

The current status of experimental efforts to produce neutron-rich  $\Lambda$  hypernuclei is given in Table 1. We have not only upper limits for reactions with stopped kaons, [14], [15], but even first positive results [16] for another type of S&DCX reaction, namely ( $\pi^-, K^+$ ). In the experiment KEK-PS-E521, about 40 events were registered in the bound region of  ${}^9_{\Lambda}\text{Li}$ . The results confirmed qualitatively the calculations given by Tretyakova and Lansky [17, 18, 19]: The cross sections of the ( $\pi^-, K^+$ ) reaction are smaller by three orders of magnitude than those of ( $\pi^+, K^+$ ) reaction; the two-step mechanism dominates over the single-step mechanism [17] (via virtual  $\Sigma^-$  admixture in the hypernuclear state appearing due to  $\Sigma^- p \leftrightarrow \Lambda n$  coupling [20]); the cross section is larger for targets with neutron orbit vacancy.

Table 1: Status of the hypernuclei production in S&DCX reactions

Reaction	Ref.	${}^6_{\Lambda}\text{H}$	${}^7_{\Lambda}\text{H}$	${}^9_{\Lambda}\text{He}$	${}^{10}_{\Lambda}\text{Li}$	${}^{12}_{\Lambda}\text{Be}$	${}^{16}_{\Lambda}\text{C}$
$(K^-_{st}, \pi^+)$	[14] (KEK)					< 6.1	< 6.2
	[15] (FINUDA)	< 3.5	< 4.9	< 23		< 2.6	
$(\pi^-, K^+)$	[16] (KEK)				12±2	7	
	[19] (calculation)				22	2.5	

The results of a recent experiment [21], revived our interest in lightest neutron-rich hypernuclei. There, the primary beam of the radioactive ion  ${}^6\text{He}$  was used for the production of the resonance state in proton knock-out reaction  ${}^6\text{He} ({}^1\text{H}, {}^2\text{He}) {}^5\text{H}$ . The two protons from the decay of  ${}^2\text{He}$  from the reaction were detected as a peak at an energy 1.7 MeV above the  ${}^3\text{H}+n+n$  threshold. In the next section we will show that  ${}^6_{\Lambda}\text{H}$  [22], can be identified unambiguously through its pionic decay  ${}^6_{\Lambda}\text{H} \rightarrow \pi^- + {}^6\text{He}$ .

### 3. Experiment

At the LHE JINR, an original approach of hypernuclear experiments was elaborated on the basis of beam nuclei excitation to produce high energy hypernuclei (up to 3.5 A·GeV the experiments, carried out at the Synchrophasotron and 6 A·GeV planned at the Nuclotron). Data on the hypernuclear lifetimes and the production cross sections were obtained [23] using the streamer chamber in the Synchrophasotron beams. The Nuclotron beams offer new possibilities of carrying out hypernuclear experiments under condition of the significantly increased data collection rate. It was suggested [24, 25, 26] to investigate the properties of the lightest hypernuclei by using the SPHERE spectrometer. We hope that in a short period the spectrometer based on the proportional chamber trackers will be commissioned. In addition, the extracted Nuclotron beam energy is expected to be increased soon up to 4-6 A·GeV – the value necessary for hypernuclear experiments. In this context we see that the hypernuclear research program for the first year could be extended.

The measurement of the binding energy of the lightest  ${}^3_{\Lambda}\text{H}$ ,  ${}^6_{\Lambda}\text{He}$  hypernuclei and the lifetimes of light hypernuclei are planned among the first, with the ultimate task [27] of the scheduled experiments to investigate the  $\Lambda\text{N}$  weak interaction matrix in nonmesonic decays of  ${}^A_{\Lambda}\text{B}$ . Recently, it was proposed to search for the neutron halo hypernucleus  ${}^6_{\Lambda}\text{H}$  in the very beginning of the research program. The suggestion is based on physical interest and the advantages of the experimental approach.

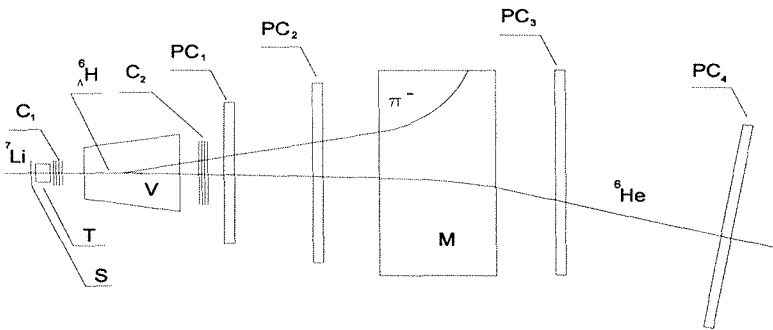


Figure 2: SPHERE spectrometer adapted for the first hypernuclear experiments, for example, for  ${}_{\Lambda}\text{H}$  production (particularly,  ${}^6_{\Lambda}\text{H}$ ) in the  ${}^7\text{Li}$  beam. The stripping proton from  ${}^7\text{Li} \rightarrow {}^6_{\Lambda}\text{H} + p$  is not shown. T – target; S,  $C_{1,2}$  – trigger counters; V – vacuum decay volume; M – magnet;  $PC_{1-4}$  – proportional chambers

Let us note some advantages of the research method and analyze how they can be achieved at the Nuclotron experiments. Since hypernuclei (hyperfragments) in the experiments are produced by the excitation of high energy nuclei (up to 6 A·GeV) the energy of the produced hypernuclei is just a little bit lower than that of an incident beam. In

such a case, hypernuclei decay at tens cm beyond the target. For example, the mean hypernuclei decay range should be about 40-45 cm. For experiments at the SPHERE spectrometer, it was suggested to observe hypernuclear decays in a vacuumed volume of 60 cm (approximately 70% of hypernuclei will decay inside of this volume). If the decay vertex was fixed inside of 60 cm path there is no doubt that the event was the decay of a hypernucleus since no background process can produce the vertex in vacuum. In other words one can obtain a pure sample of hypernuclei decays. **HYPERNUCLEI CAN BE IDENTIFIED UNAMBIGUOUSLY.** To be sure that the decay vertex was inside vacuum one must use an adequate tracker to measure the direction of secondary particles (to calculate the vertex coordinates). On the other hand, if an incident nuclear beam is not  $^3\text{He}$ , different hypernuclei and isotopes can be produced. While the charge of hypernuclei is measured with the trigger counters, isotopes can be identified by the daughter nuclei momentum measurement. Since the momenta of positive decay products should also be measured, a tracker should be installed beyond the analyzing magnet. Estimates show that the expected accuracy of the measurement of the vertex position and the daughter nuclei momenta is good enough to obtain sample of the safely identified hypernuclei in our case of the proposed spectrometer and hypernuclear experiments.

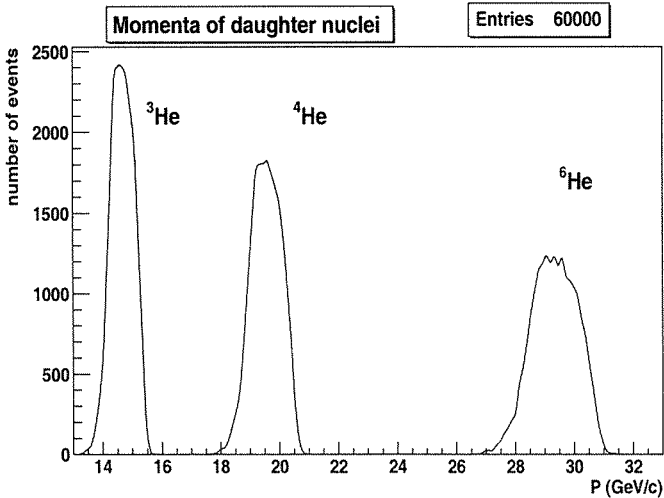


Figure 3: Momenta distributions of recoil nuclei  $^3\text{He}$ ,  $^4\text{He}$  and  $^6\text{He}$

It is suggested to start the hypernuclear research program with the investigation of  $^4_{\Lambda}\text{H}$  and  $^3_{\Lambda}\text{H}$  production in the helium beam. Such an experiment is similar to the previous one and allows one to check all systems of the set up (including data processing). *At the NEXT STEP helium beam should be changed to the  $^7\text{Li}$  beam to search for  $^6_{\Lambda}\text{H}$  together with  $^4_{\Lambda}\text{H}$  and  $^3_{\Lambda}\text{H}$ .* The number of hypernuclear decays (N) expected to be observed in 24 hours is given in Table 2. The trigger in both experiments is tuned to detect charge equal to one of hydrogen hypernuclei (regardless to the mass value) in the counters  $C_1$  (see Fig. 2) and the charge equal to two (counters  $C_2$ ). To be more precise, in case of the  $^7\text{Li}$  beam an additional trigger fine-tuning should be applied to take into account stripping

Table 2: Production and decay

beam	target	production	decay	N
${}^3\text{He}$	+ ${}^{12}\text{C}$	$\rightarrow {}^3_{\Lambda}\text{H} + \dots$	$\rightarrow {}^3\text{He} + \pi^-$	100
${}^4\text{He}$	+ ${}^{12}\text{C}$	$\rightarrow {}^4_{\Lambda}\text{H} + \dots$	$\rightarrow {}^4\text{He} + \pi^-$	600
		$\rightarrow {}^3_{\Lambda}\text{H} + \dots$	$\rightarrow {}^3\text{He} + \pi^-$	
${}^7\text{Li}$	+ ${}^{12}\text{C}$	$\rightarrow {}^6_{\Lambda}\text{H} + \dots$	$\rightarrow {}^6\text{He} + \pi^-$	400
		$\rightarrow {}^4_{\Lambda}\text{H} + \dots$	$\rightarrow {}^4\text{He} + \pi^-$	
		$\rightarrow {}^3_{\Lambda}\text{H} + \dots$	$\rightarrow {}^3\text{He} + \pi^-$	

proton (fragment) of charge one but this does not change the approach significantly. To discriminate the masses of the isotopes of the hypernuclear daughter nuclei one should measure the corresponding momenta. The momentum values of  ${}^3\text{He}$ ,  ${}^4\text{He}$  and  ${}^6\text{He}$  are concentrated in the  $\approx 14$  GeV/c,  $\approx 19$  GeV/c and  $\approx 29$  GeV/c bands correspondingly. Such difference can be measured easily to separate three possible reactions of the hydrogen hypernuclei production and decay in the  ${}^7\text{Li}$  beam, see Fig. 3.

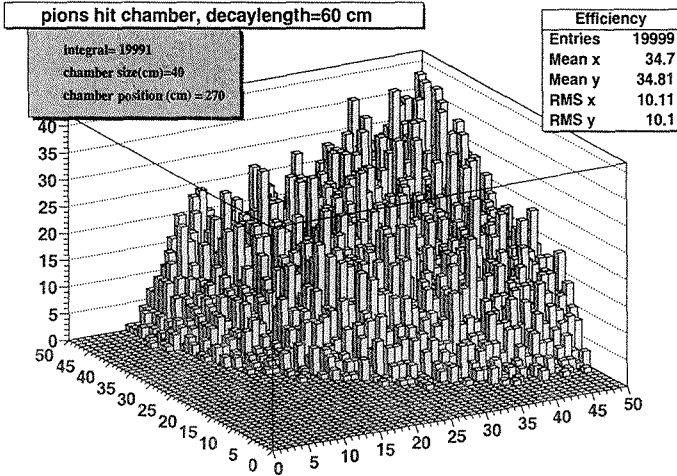


Figure 4: The  $80 \times 120$  cm proportional chambers are large enough to register pions from the hypernuclear decays. The calculation for the chambers situated at the 270 cm distance beyond the target. All the pions hit the chamber approximately inside a ring of 60 cm diameter. A quadrant of the chamber is presented in the histogram

In the first experiments dedicated to the observation of pionic decays of the lightest hypernuclei, proportional chambers of a 2 mm wire separation will be used.  $38 \times 38$  cm chambers ( $\text{PC}_1$ ) will be installed just behind (at a distance of 20 cm) the vacuumed decay vol-

ume V (see Fig. 2) while at the distance of 220 cm the second set of larger (80×120 cm) chambers will operate to fix the second point of the decay products trajectory. The size of these chambers were chosen large enough to register all the decay pions emitted at more wide angles than the daughter nuclei (see Fig. 4). Beyond the analyzing magnet (M) 2 meter chambers previously used in the EXCHARM experiments are mounted. In spite of that the chambers are collected from different experiments, they are adjusted to the electronics of the same type. So, one can use the same readout software, gas refilling system etc. for all the chambers. Of course, the properties of all the chambers are also very similar. For example, the resolution of 38 cm chambers is estimated to be of the same order as it was measured (0.7-0.8 mm) for the 2 m chambers [30]. Naturally, it was much easier to tune the 38 cm chambers and to obtain 99% efficiency in comparison with  $\approx 95\%$  for the 2 m chambers.

#### 4. What can we learn from this experiment ?

A serious obstacle in exploiting the beam of protons [31, 32] or relativistic light nuclei [33] for hypernuclear studies is a huge background in production vertex, consequently, one have to identify hyperfragments by they weak decay modes. Here, we confine ourselves to the study of the production of hyperhydrogen isotopes  ${}^A_{\Lambda}H$  ( $A = 3, 4$  and  $6$ ) only, which decay through pionic channel. As one can see in Fig. 3, different isotopes could be separated unambiguously. This way, we could determine the 'source' of neutron-rich hypernucleus  ${}^6_{\Lambda}H$ . The nuclei of our beam ( ${}^7Li$ ) interacting with a target are also fragmented ( ${}^6Li + n$ ,  ${}^6He + p$ ,  ${}^4He + {}^3H$ ), so the outgoing beam is rather complicated mixture of primary and secondary hypernuclei given in Table 3.

Table 3: Hypernuclei: primary (pr) and secondary (sc)

nuclei: hypernuclei	${}^7Li$		${}^6Li$		${}^6He$		${}^4He$		${}^3H$
	${}^7_{\Lambda}Li$	${}^7_{\Lambda}He$	${}^6_{\Lambda}Li$	${}^6_{\Lambda}He$	${}^6_{\Lambda}H$	${}^4_{\Lambda}He$	${}^4_{\Lambda}H$	${}^3_{\Lambda}H$	
${}^7_{\Lambda}Li$	pr								
${}^7_{\Lambda}He$		pr							
${}^6_{\Lambda}He$	sc	sc		pr					
${}^6_{\Lambda}H$		sc			pr				
${}^5_{\Lambda}He$	sc	sc	sc	sc					
${}^4_{\Lambda}He$			sc			pr			
${}^4_{\Lambda}H$	sc	sc	sc	sc	sc		pr		
${}^3_{\Lambda}H$	sc		sc	sc				pr	

The Fig. 5 shows clearly why the highly excited states of  ${}^7_{\Lambda}He$ , in which the "INNER PROTON" is substituted by  $\Lambda$  (transition  $p_s \rightarrow \Lambda_s$ ) are the source of hyperfragments  ${}^4_{\Lambda}H$  and  ${}^6_{\Lambda}H$ . The thresholds for these decay channels are rather high, but large changes in the structure of these states prevents the neutrons or  $\Lambda$  from emission.

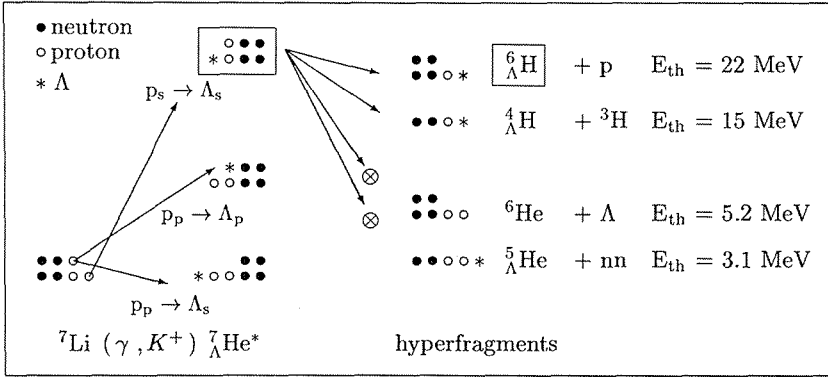


Figure 5: Different decay channels of  ${}^7_{\Lambda}\text{He}$  hypernucleus

We recall that states of such type ( $s_{\Lambda} s^{-1}$ ) have been recognized in the 'in-flight' ( $K^{-}, \pi^{-}$ ) reactions [34]. The structure of the  ${}^6_{\Lambda}\text{Li}$  spectrum was described successfully [35] under assumption that resonances of type  $|s_{\Lambda} s^3 p^k\rangle$  preserve their individuality (see also [36]). The thresholds and global structure characteristics, Young schemes  $[f_i]$ , are displayed in Table 4.

Table 4: Decay modes

${}^A_Z\text{X} \rightarrow {}^A'_{Z'}\text{Y}$	$E_{\text{thres}}$	$[f_1] \cdot [f_2]$	${}^A_Z\text{X} \rightarrow {}^A'_{Z'}\text{Y}$	$E_{\text{thres}}$	$[f_1] \cdot [f_2]$
${}^7_{\Lambda}\text{He} \rightarrow {}^6_{\Lambda}\text{He} + n$	2.82	[41] · [1]	${}^6_{\Lambda}\text{He} \rightarrow {}^5_{\Lambda}\text{He} + n$	0.17	[4] · [1]
${}^7_{\Lambda}\text{He} \rightarrow {}^5_{\Lambda}\text{He} + nn$	3.08	[4] · [2]	${}^6_{\Lambda}\text{He} \rightarrow {}^4_{\Lambda}\text{H} + {}^2\text{H}$	18.93	[3] · [2]
${}^7_{\Lambda}\text{He} \rightarrow {}^4_{\Lambda}\text{H} + {}^3\text{H}$	15.49	[3] · [3]	${}^6_{\Lambda}\text{He} \rightarrow {}^3_{\Lambda}\text{H} + {}^3\text{H}$	20.84	[2] · [3]
${}^7_{\Lambda}\text{He} \rightarrow \boxed{{}^6_{\Lambda}\text{H}} + {}^1\text{H}$	22.0	[32] · [1]			
${}^7_{\Lambda}\text{Li} \rightarrow {}^5_{\Lambda}\text{He} + {}^2\text{H}$	3.12	[4] · [2]	${}^6_{\Lambda}\text{Li} \rightarrow {}^5_{\Lambda}\text{He} + {}^1\text{H}$	-0.59	[4] · [1]
${}^7_{\Lambda}\text{Li} \rightarrow {}^6_{\Lambda}\text{He} + {}^1\text{H}$	5.99	[41] · [1]	${}^6_{\Lambda}\text{Li} \rightarrow {}^4_{\Lambda}\text{He} + {}^2\text{H}$	18.50	[3] · [2]
${}^7_{\Lambda}\text{Li} \rightarrow {}^3_{\Lambda}\text{H} + {}^4\text{He}$	6.92	[2] · [4]	${}^6_{\Lambda}\text{Li} \rightarrow {}^4_{\Lambda}\text{H} + {}^2\text{He}$	20.31	[3] · [2]
${}^7_{\Lambda}\text{Li} \rightarrow {}^4_{\Lambda}\text{H} + {}^3\text{He}$	19.33	[3] · [3]	${}^6_{\Lambda}\text{Li} \rightarrow {}^3_{\Lambda}\text{H} + {}^3\text{He}$	20.76	[2] · [3]

The appearance of the exotic **hyperfragment**  ${}^6_{\Lambda}\text{H}$  together with determining the yields ratios  $Y({}^6_{\Lambda}\text{H}) : Y({}^4_{\Lambda}\text{H}) : Y({}^3_{\Lambda}\text{H})$  could shed some light to the hypernuclear production in relativistic nuclei collisions.

The work of L.M. was supported by grant 202/02/0930 of the Grant Agency of Czech Republic.

## References

- [1] B. Jonson, Phys. Reports **389**, 1 (2004).
- [2] M.V. Zhukov *et al.*, Phys. Reports **231**, 154 (1993).
- [3] D.H. Davis, J. Pniewski, Contemp. Phys. **27**, 91 (1986).
- [4] M.I. Podgoretsky, Zh. Eksp. Teor. Fiz. **44**, 695 (1963).
- [5] R.E. Chrien, C.B. Dover, Ann. Rev. Nucl. Part. Sci. **39**, 113 (1989).
- [6] T. Hagesawa *et al.*, Phys. Rev. **C53**, 1210 (1996).
- [7] T. Miyoshi *et al.*, Phys. Rev. Lett. **90**, 232502 (2003).
- [8] M.W. Ahmed *et al.*, Phys. Rev. **C68**, 064004 (2003).
- [9] H. Tamura *et al.*, Phys. Rev. Lett. **84**, 5963 (2000).
- [10] K. Tanida *et al.*, Phys. Rev. Lett. **86**, 1982 (2001).
- [11] T. Bressani, in Proc. Workshop on physics and Detectors for DAΦNE, Frascati, 1991.
- [12] L. Majling, Nucl. Phys. **A585**, 211c (1995).
- [13] T. Bressani, Proc. Int. School "E. Fermi", Course **153**, p. 323 (2003).
- [14] K. Kubota *et al.*, Nucl. Phys. **A602**, 327 (1996).
- [15] A. Filippi (FINUDA), Proc. 19th Few-Body Conference, Gronningen, August 2004.
- [16] P. K. Saha (KEK-PS-E521), Proc. HYP2003, Nucl. Phys., to be publ.
- [17] T. Tretyakova, D. Lanskoj, Nucl. Phys. **A691**, 51c (2001).
- [18] T. Tretyakova, D. Lanskoj, Phys. of At. Nuclei **66**, 1651 (2003).
- [19] D.E. Lanskoj, arXiv: nucl-th/0411004.
- [20] Y. Akaishi *et al.*, Phys. Rev. Lett. **84**, 3539 (2000).
- [21] A. Korshennikov *et al.*, Phys. Rev. Lett. **87**, 092502 (2001).
- [22] K. S. Myint, Y. Akaishi, Prog. Theor. Phys. Suppl. **146**, 599 (2002).
- [23] A. Abdurakhimov *et al.*, N. Cim. **102A**, 645 (1989);  
S. Avramenko *et al.*, Nucl. Phys. **A547**, 95c (1992).
- [24] S.A. Avramenko *et al.*, JINR Rapid Comm., **5[68]**, 14 (1994).
- [25] S.A. Avramenko *et al.*, Nucl. Phys. **A 585**, 91c (1995).
- [26] J. Lukstins, Nucl. Phys. **A691**, 491c (2001).
- [27] L. Majling *et al.*, Czech. J. Phys. **53**, 667 (2003).
- [28] M.V. Evlanov *et al.*, Nucl. Phys. **A632**, 624 (1998).
- [29] L. Majling *et al.*, Mesons and Light Nuclei, 8th Conf., Prague, 2001,  
AIP Conf. Proc. **603**, p. 453, New York, 2001.
- [30] A.N. Aleev *et al.*, Instr. and Exp. Techniques, **38**, 425 (1995).
- [31] E. Hungerford, Proc. Int. School "E. Fermi", Course **158**, (2004).
- [32] W. Cassing *et al.*, Eur. Phys. J. **A16**, 549 (2003).
- [33] H. Bandō, T. Motoba, J. Žofka, Int. J. Mod. Phys. **A5**, 4198 (1990).
- [34] R. Bertini *et al.*, Nucl. Phys. **A368**, 365 (1981).
- [35] L. Majling *et al.*, Phys. Lett. **92B**, 256 (1980).
- [36] L. Majling, Nucl. Phys. **A639**, 134c (1998).

# THE DIPOLE MAGNET IRON YOKE DESIGN FOR THE ALICE DIMUON ARM SPECTROMETER

V.Arefiev<sup>1</sup>, I.Boguslavsky<sup>1</sup>, V.Borisov<sup>1</sup>, Zh.Bunzarov<sup>2</sup>, D.Cacaut<sup>3</sup>, A.Efremov<sup>1</sup>,  
O.Fedorov<sup>1</sup>, E.Kochournikov<sup>1†</sup>, A. Makarov<sup>1</sup>, I.Olex<sup>1</sup>, E.Ustenko<sup>1</sup>, A.Shurygin<sup>1</sup>,  
M.Shurygina<sup>1</sup>, A.Sissakian<sup>1</sup>, D.Swoboda<sup>3</sup>, A.Vodopianov<sup>1</sup>

(1) *JINR Joint Institute for Nuclear Research, Dubna, Russia*

(2) *St.K.Ohridski University, Sofia, Bulgaria*

(3) *CERN European Organization for Nuclear Research, Geneva 23, Switzerland*

† *E-mail address: root@magnet.spb.su*

## Abstract

Iron Yoke of about 820 tons for the Dipole Magnet with aluminium water cooled winding has been produced for the DiMuon Arm Spectrometer of ALICE experiment at the LHC. This magnet provides the bending power to measure the momenta of muons. The initial design of the magnet was prepared by JINR. The main feature of this magnet is the huge uncompensated force applied from the neighbouring solenoid magnet L3. The yoke of the magnet was manufactured and preliminary assembled in Russia in Tver region at SMZ manufacturing company and transported to CERN. The results of electromagnetic forces calculations and deflected mode analysis are presented. Design, following up of the yoke production and the main features of the technology process are discussed.

**Key-words:** Electromagnetic Forces, Magnetic Core, Iron Yoke, Spectrometry, Magnetic Field Calculations.

## 1. Introduction

A large conventional Dipole Magnet (DM) is required for the DiMuon Arm Spectrometer of ALICE experiment at the LHC. It provides the bending power to measure muons momenta. Design work has been performed at JINR (Dubna) and at CERN. A general description of the design of the magnet and current status of the work are presented in [1] - [4]. An important component part of the DM is 820 tons iron yoke. The general view of the iron yoke preliminary assembled in horizontal position is shown at fig.1.

## 2. Iron yoke design description

The general concept of the DM is based on a window frame return yoke, fabricated from low carbon steel sheets. The flat vertical poles follow the defined acceptance angle of 9 degrees. The excitation coils are of saddle type. The coils are wound from hollow aluminium conductor and cooled by circulating de-mineralized water. The main flux direction in the gap is horizontal and perpendicular to the LHC beam axis. The DM will work in a cyclic regime over a period of ten years - the full number of operation cycles will be about 4000. The general view of the iron yoke is shown at fig.2.

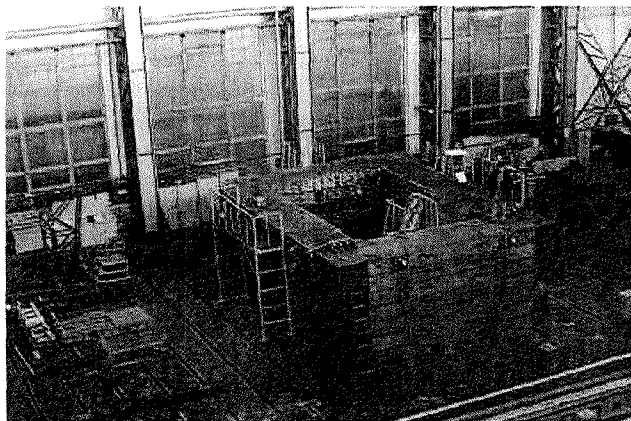


Figure 1: Yoke of the ALICE DM assembled in horizontal position

The DM iron yoke is of mountable-and-dismountable type. It's mass is about 820 tons, the height - 9022 mm, the width - 6896 mm, the length - 3120 mm. The iron yoke consists of four blocks: bottom and top blocks and two uprights, which produce a trapeze form aperture  $\pm 9^\circ$  (2972 mm minimum width), 6090 mm in height. A block consists of seven modules each, which have been rigidly connected by means of bolt flanges and a tie rods system. The modules has mass within 26-30 tons. These steel modules initially have been prepared for other purposes, but have never been used. Each module consists of about 15 metal plates 30 mm in thickness connected with each other by welding trough drilled holes  $\varnothing 40$  mm with pitch 800 mm as on a chess-board. The material of the iron plates is a low carbon steel - Steel 10 (GOST 1577-93). Content of carbon according to the Russian standard is 0.07 - 0.14%. The flanges are welded by arc welding at the extremities of all bottom and vertical beams to provide mutual fixation of the beams. At the beam extremities for fixation of the vertical and top beams there are additional special slots for inserts, supplied with threaded holes. The surfaces of the beams have been machined to provide the precise dimensions and to minimize the gaps between the the beams. To provide the bending resistance of the beams under action of attractive forces in L3 direction the metal palates  $30 \times 400$  mm have been welded to the vertical beams to create a "box" profile. The vertical beams have the rests ( $50 \times 400$  mm in cross section) on the bottom and top beams to resists attractive forces between pole beams. There are vertical, 40 mm plates on the bottom beams extremities which are used to fixate the yoke to the foundation.

For securing of the base requirements special design decisions have been accepted as follows:

- The first assembly of the yoke is to be in horizontal position;
- The geometrical reproducibility of the aperture within 3mm is to be provided by shim polishing in the vertical/horizontal beams connections;
- Mutual fixation of the beams by dowel pins ( $\varnothing 40 \times 150$  mm Steel 45) is to be done

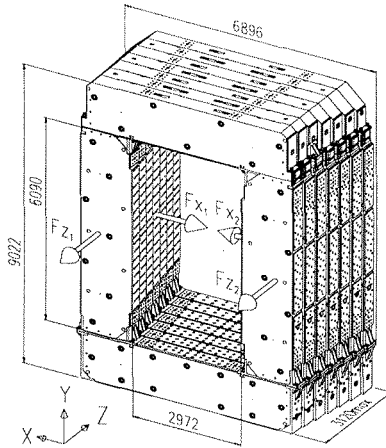


Figure 2: General view of the iron yoke

at the first horizontal assembly. All subsequent assemblies have to be done without additional mutual adjustment of the beams and correction of the shims;

- Space position of the DM aperture is adjusted by means of shims between the foundation surface and the seat surface of the magnet.

The horizontal and vertical beams have been tightened by means of tie rods and bolts M36 (steel 40X). The layers of the magnet have been tightened by tie rods M72 (high-strength steel 40HN2MA) through  $\varnothing 87$  mm holes. The nuts M72 at the ends of the tie rods have been embedded into the side beams 1 and 7. Standard nuts (steel 40X) have been mounted in couples at the downstream side of the yoke and SUPERBOLT High Strength Tensioners CY-M72 $\times$ 6/W (steel 4340HT) have been used at the upstream side. These special nuts have been used to lighten the tightening process of the nuts up to 190 tons. Additionally, after final assembly of the yoke at the operation position, the vertical beams in couples and horizontal beams in couples, are to be welded by arc welding at the outer surface of the yoke.

The DM will be installed on a concrete foundation with a metal plate embedded in the foundation surface, which can be aligned before assembly of the yoke and serves as a geometrical reference. The finally assembled yoke will be fixed there by means of arc welding of brackets to the bottom beams and to the above-mentioned steel plates.

Several assemblies of the DM yoke have been planned. The construction concept takes this into account. The first "horizontal" assembly of the yoke has been necessary in order to verify and correct the geometry and to establish all reference surfaces and locate the reference and alignment dowels. The assemblies of the DM in the underground area at the experimental hall UX25 will be carried out at temporary position to validate the assembly procedure, followed by the final assembly of the magnet at the operation position.

### 3. Calculations of magnetic forces

Vector Fields TOSCA Version 8.7 code has been applied for the ALICE dipole magnet field/forces calculations. The calculations of magnetic forces have been undertaken to estimate mechanical stability of the yoke for different options of the magnetic circuit configuration:

- Preliminary assembly of the magnet - Detached Dipole Magnet,
- The entire magnet system geometry including L3 Magnet, Dipole Magnet and Muon Filter (Entire model),
- An option of the entire geometry when L3 Magnet switched off ("L3 off"),
- An option of the entire geometry when Dipole Magnet switched off ("DM off").

The whole region has no symmetry planes because:

- the field induced by the solenoid of the L3 Magnet is symmetrical with respect to the z-y plane, while the field induced by the Dipole Magnet winding is anti-symmetrical with respect to the same plane;
- the geometrical centre of the Dipole Magnet is shifted by 0.3 m in y-direction relative the central axe of the L3 Magnet.

Electromagnetic forces applied to the yoke elements have been analyzed in conformity with requirements of OPERA-3D Reference Manual. The results of magnetic forces calculations can be seen in table1.

Table 1: Components of the forces applied to the Dipole Magnet parts at operational conditions

	$F_x$ , kN	$F_y$ , kN	$F_z$ , kN
Yoke	140	47	-1368
Coils	-53	9	628
Sum	87	57	-740

### 4. Strength analysis

ANSYS 5.3 code has been used to perform structural finite element analysis of the yoke [5]. Additionally, all ANSYS calculations have been controlled by theory of elasticity simplified calculation procedures. The results of these simplified calculations have been used for estimation of safety margin of the constructive elements strength. Comparison of the results shows that the stresses obtained by ANSYS calculations are lower than results of simplified procedures of theory of elasticity. This means there is an addition to the safety margin of the yoke.

Volumetrical electromagnetic forces, gravity, thermal and seismic loads have been considered in the calculations. The immediate proximity of the DM and L3 solenoid

exerts a very sufficient influence on the force interaction of the magnets - the attractive force of 1370 kN is applied to the DM. The forces, which are applied to the yoke vertical beams are unsymmetrical ones, because of unsymmetrical character of the magnetic field. For example unequal forces 767 kN and 632 kN are applied to the vertical beams. These beams which serve as magnet poles are attracting to each other by force of 4700 kN. In vertical direction the beams are pressed by force of 11500 kN, which is applied to the flange connections of the horizontal and vertical beams. The electromagnetic loads, applied to the coil parts and thermal loads, caused by temperature drop across the coil width are transmitted from the coils to the yoke beams in some fixation points with the help of the coil supports. Seismic load calculations have been fulfilled in accordance with Code project [6], which is based on [7].

The mechanical loads applied to the yoke will be different in operation regimes, as follows:

1. **Normal operational regime.** The yoke is loaded by the electromagnetic forces of nominal value (the currents in L3 and Dipole Magnets are 100% of the operational values). Temperature drop across the coil width is 30K.
2. **Violation of normal operation regime.** This regime corresponds to overloading of the yoke by the electromagnetic forces of 110% of nominal value and by temperature drop 40 K.
3. **Emergency regime.** In the emergency regime the dipole magnet is loaded by the forces of the normal operational regime and by seismic load simultaneously.
4. **Test regime.** The loads are in conformity with the detached dipole magnet is tested without L3 magnet.

Design criteria and the yoke loading regimes have been established according to Russian National standards [8, 9]. Initial coefficient value of friction between neighbouring beam surfaces without special machining, is to be  $f_0 = 0.25$ . Reliability index required the calculated value of friction coefficient to be equal to  $f = 0.12$ . Frictional forces between the beams, which correspond to this friction coefficient, are not sufficient to transmit shear loads between the beams. Cylindrical pins and welded connections have been used to transfer the shear loads between the beams. Vertical beams have been reinforced with side steel plates to increase the rigidity and strength for the shear loads (fig.3)

Design model of a beam includes a rectangle box, which is created by side steel plates, joined by weld seams and flexible filler (steel plates), which is not rigid for shear. This filler has been represented as a solid anisotropic material to decrease the number of finite elements in the calculations. Equivalent shear modulus of the metal plates, joined by the local weld seams, is 240 MPa according to ANSYS calculations. It has appeared that the compressive forces are not distributed for the whole volume of the material, and are concentrated in the areas bordering to the tie rods. In the uncompressed areas the modulus of elasticity for tension has been accepted to be  $E = 0$  MPa. In the same areas the modulus of elasticity for compression has been accepted to be  $E = 200$  GPa. The shear moduli between metal plates in these areas are  $G = 240$  GPa. In other areas the material characteristics are equivalent the characteristics of the steel  $E = 200$  GPa,  $E = 77$  GPa.

In case of the normal operational regime violation, the effecting loads are increased 1.1 times. According to the standards, the permissible stresses are to be increased by

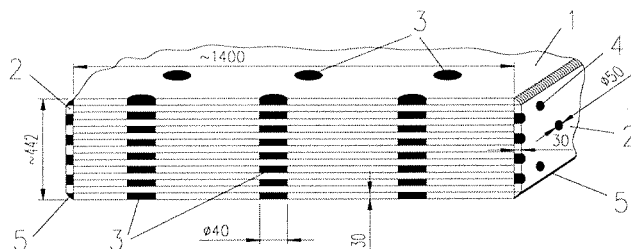


Figure 3: Cross section of a beam: 1 - Beam plates, 2 - Outside plates, 3 - Inner weld points, 4 - Weld points on the side plates, 5 - Weld seams

20%. This means that in the case of the normal operational regime violation the safety margins will not be less than those under the normal conditions. In the emergency regime the permissible stresses are to be increased by 40%. In spite the additional seismic load, the yoke will keep the stability in emergency regime.

#### Strength Analysis of the iron yoke

Upon analysis of calculated eigenfrequencies of the yoke, we concluded that in Z direction the yoke has a sufficient part of shear deformation, which is created by insignificant shear rigidity of the anisotropic beam filler. Maximal sag of the yoke is about 1.7 mm in L3 direction in the normal operation regime. At that the gaps up to 0.8 mm may appear between the vertical beams in different parts of the yoke. The main cause of the displacement is the weak pin contact joints between the beams. The sags of the vertical beams inside of the aperture (x-direction) are within 0.04 - 0.16 mm. According to calculations maximal stresses in the yoke units do not exceed acceptable levels. Strength of yoke is sufficient in the normal operational conditions and in the case of the normal regime violation. To estimate the actual reserve of the constructive elements strength the relative coefficient of strength reserve  $\eta$  was considered in the calculations. It is equal the ratio of permissible stress  $[\sigma]$  and actual stress  $\sigma$ :

$$\eta = \frac{[\sigma]}{\sigma}$$

It is appeared that for all yoke units  $\eta > 1.0$ , namely:

for pin joints between the beams  $\eta = 2 - 2.5$ ;

for bolts M42 connections between horizontal and vertical beams  $\eta = 1.9$ ;

for weld connections including the local weld points between steel plates of the beams, brackets weld seams and the outside weld seams between the vertical beams and between horizontal beams  $\eta = 1.3 - 4.0$ ;

for frictional force in the joints between the vertical walls and the bottom beams and between the bottom beams  $\eta = 1.2 - 1.5$ ;

for tie rod nuts barrels :

- bearing strain of bottom washer  $\eta = 1.39$ ,

- the barrel bottom bearing strain  $\eta = 1.02$ ,
- the barrel bottom shear  $\eta = 1.5$ ,
- bearing strain of the beam sheets under the barrel  $\eta = 1.5$ ,
- barrel wall  $\eta = 2$ ;

Tie rods prestressed by 90% of the full load. If the normal operational regime is violated, the relative safety margins are

- thread  $\eta = 1.1$ ,
- groove  $\eta = 1.02$ .

Brackets in the joints of the vertical and bottom beams

- washer bearing strain  $\eta = 1.7$
- plate bending strength  $\eta = 1.06$
- weld joints strength  $\eta = 1.8$

The analysis of yoke fixation units to the foundation treats a case of emergency loading, i.e. loading generated by electromagnetic forces under the normal operation regime and by seismic forces simultaneously. Strength of the yoke attachment to the foundation is sufficient to withstand the case of combined loading of the normal regime and an earthquake. Safety margin for the welded units including fixation units of the face sides of the yoke, units of the beams B1 - B7 is  $\eta = 1.3 - 2.9$ .

## 5. QA

Integrated approach to quality maintenance in the process of the yoke production has been based on State and Branch standards, currently in force in RF, as well as on SMZ quality regulations. Besides the producer elaborated and coordinated with JINR the program "Program of quality maintenance in the process of the yoke construction" which included:

- Control of technology compliance of the units and assembly units production; certification of the machinery and the personal;
- Input control of the material documentation. Input control of the physical and chemical properties of the materials by testing laboratory of SMZ (chemical contents, strength properties);
- Functional inspection and final control of geometrical characteristics of the units, assembly units and test assembly of the yoke by the Quality Division personal;
- Acceptance of the critical units of the yoke by the JINR representative according to elaborated by JINR test manual.

Control of geometrical characteristics of the fastening elements has been exercised not only in the machine shops, but in the SMZ testing laboratory. Control protocols have been provided. Strength properties of the critical units have been controlled for the witness samples after heat treatment process, or for samples prepared from ready made units. In the process of the yoke production JINR designers executed follow up of the project.

## 6. Results of tests and measurements

Strength of the load-carrying weld seams of the yoke beams, as well as strength of the screwed holes, used for lifting has been verified by strengthening tests, according to test manual prepared by JINR. An acceptance board has fulfilled the tests with SMZ and JINR representatives. The test results have been fixed in the test protocol.

Control assembly of the yoke bottom part and the yoke in horizontal position has been fulfilled by the producer to verify the assembly procedure and to control the geometrical sizes. Assembly in horizontal position has been stipulated by the lack of assembly area at the factory with bearing capacity above  $80t/m^2$ . The specific load for the horizontal assembly is about  $25t/m^2$ , which is acceptable for the bearing capacity of the assembly floor  $25t/m^2$ .

The assembly area has been aligned relative horizon by metal strips to within 2 mm. The sag of the foundation has been controlled along the perimeter of the yoke after placing of every four beams yoke layer with precision of 0.1 mm.

Assembly of the bottom part in vertical position has been provided by means of technology tie rods, which are identical to the tie rods, used for the vertical assembly in CERN and to Super Nuts of P&S Tensioning Systems Ltd. Tightening of the Super Nuts has been done according to the manual [9]. The tie rods tightening has been increased stepwise (10, 30, 50, 75 and 100 % of rated force). The elongation of the tie rods, the gaps between the beams and the thickness of the 7 beam package (in several cross-sections) as well as space position and geometrical characteristics of the mating surfaces of the beams have been controlled in the tightening process. The elongations of both controlled tie rods amount to 5 and 7.1 mm. It corresponds to calculated value of 7.2 mm as a whole. After tightening of the tie rods all bottom part dimensions have corresponded to the targeted dimensions.

Assembly of the iron yoke in horizontal position has been fulfilled layerwise - bottom and upper beams and two vertical beams create one layer. The tightening of the beams has been done with the set of technology tie rods, spacer tubes and Super Nuts. The mutual positions of the beams of a layer and the mutual positions of the beams in the neighbouring layers have been controlled with space templates to within 0.5 mm. The positions of the beams of a layer have been corrected by means of compensate gaskets between mating surfaces of the vertical and the horizontal beams. Mutual positions of the beams in the neighbouring layers after tightening have been fixed by means of dowel pins.

According to the measurements, the foundation sags have been near the calculated ones, after assembly of every layer (fig.4)

Simultaneously, the mutual space positions of the beams have been measured and fixed in the certificate for future assembly in vertical position. The gaps at the interfaces between the vertical and horizontal beams, as well as gaps between neighbouring layer beams, have been monitored. Changes of the gaps as the new layers have been added and tie rods and bolts have been tightened, have not exceeded 0.2 mm. Actual gaps have not exceeded 0.5 mm instead of planned gaps up to 2 mm.

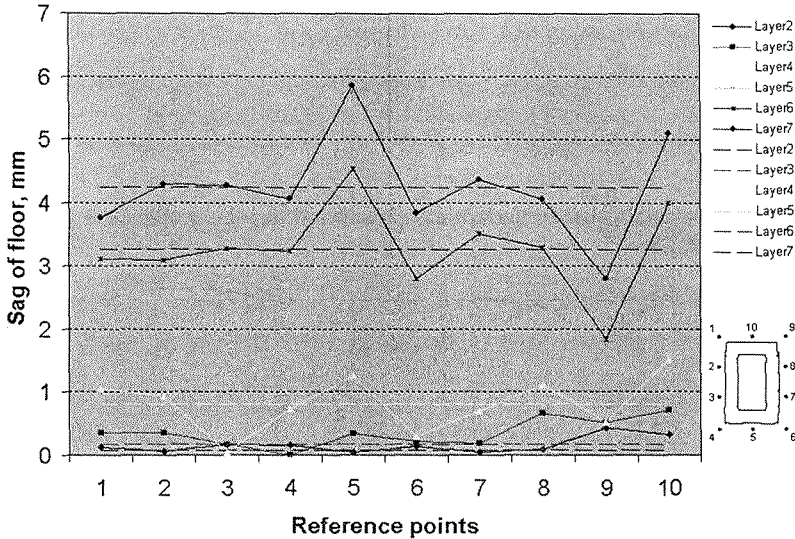


Figure 4: Evaluation of the foundation sag

## 7. Conclusion

- Design of the iron yoke of the dipole magnet of ALICE spectrometer is intended to withstand the huge uncompensated attractive force of about 1370 kN applied in direction of the neighbouring solenoid magnet L3.
- The iron yoke of the magnet has been manufactured, preliminary assembled in horizontal position by SMZ (Savelovo, Moscow region) and transported in disassembled condition to CERN, Geneva in accordance with collaboration agreement between JINR and CERN.
- Special design measures and high quality of machining of the yoke critical parts guarantee a very high level of geometrical shape reproducibility at the subsequent vertical assemblies.

## References

- [1] Dimuon forward spectrometer ALICE. Technical design report. CERN/LHCC 99-22 ALICE TDR 5. 13 August 1999.
- [2] D. Swoboda et al, Design and Status of the Dipole Spectrometer Magnet for the ALICE Experiment. IEEE Transaction on applied superconductivity., vol. 10, 1999, p.411-414.
- [3] D. Swoboda et al, Status of the ALICE Magnet System., IEEE Transaction on applied superconductivity. vol. 12, 2002, p. 432-437.

- [4] P.Akishin et al., Dipole Magnet Design for the ALICE DiMuon Arm Spectrometer. IEEE Transaction on applied superconductivity. vol. 12, 2002, p.399-402.
- [5] A. Vodopianov et al. Analysis of the deflected mode of the muon spectrometer ALICE dipole magnet iron yoke. Proceedings of 4th Conference of CAD-FEM GmbH software users. Moscow, April 21-22 2004. Edited by A. Shadsky, M., Poligon-press, 2004, pp. 96-101.
- [6] Norms to calculate the strength of equipment and pipe-lines of nuclear power plants. PNAE-G-002-86.
- [7] Regles de construction parasismique PS 92 (NF P 06-013).
- [8] Construction Directives, Steel Constructions, SNiP II-23-81, M., 1983, 92.
- [9] Installation and Removal Procedure. Super Nuts of P&S Tensioning Systems Ltd.

# INCLUSIVE $\pi^0$ PRODUCTION BY PROTONS AND LIGHT NUCLEI ON C AND Cu TARGETS AT A MOMENTUM OF 4.5 GeV/c PER NUCLEON

**Kh.U.Abraamyan, M.N.Khachaturian, M.A.Kozhin, G.L.Melkumov**  
*Joint Institute for Nuclear Research, 141980 Dubna, Moscow Region, Russia*

**A.H.Khudaverdyan**  
*Yerevan State University, 375049, Yerevan, Armenia*

## Abstract

The cross sections for the inclusive production of  $\pi^0$ -mesons in the reactions  $(p, d, \alpha, C^{12}) + (C, Cu) \rightarrow \pi^0 + x$  at an incident momentum of 4.5 GeV/c per nucleon are measured for the kinematical region specified by the inequalities  $\theta_\pi \leq 16^\circ$  and  $E_\pi \geq 2$  GeV (lab. sys.). The cumulative number  $X$ , Feynman variable  $x_F$  and transverse momentum dependences of the exponent  $n$  in the cross section parametrization  $Ed^3\sigma/d^3p \sim A_T^n$  are investigated by comparing of the observed cross sections for  $\pi^0$  production on carbon and copper targets in the intervals  $0.6 \leq X \leq 1.8$  and  $0.04 \leq P_T^2 \leq 0.40$  (GeV/c)<sup>2</sup>. The dependence of the cross sections on the mass of the target is approximately  $A_T^{0.37-0.40}$  and is in agreement with the predictions of the parton recombination model. Under the assumption that the invariant cross section as a function of the projectile atomic number  $A_p$  can be parametrized in the form  $Ed^3\sigma/d^3p \sim A_p^m$ , the  $X$  and  $P_T^2$  dependences of the exponent  $m$  are investigated by comparing the cross sections for the reactions  $C + A_T \rightarrow \pi^0 + x$  ( $A_T = C, Cu$ ) with those for the analogous reactions induced by incident  $\alpha$  particles. At  $X = 1.9$ , the parameter  $m$  is found to reach a value of  $2.1 \pm 0.1$ . The  $A_p$  dependence of the cross section under study shows a significant variation with  $X$  and only a weak variation with the pion transverse momentum. The probabilities of the formation of six-quark configurations in  ${}^2d$ ,  ${}^4He$  and  ${}^{12}C$  nuclei are estimated. For the parametrization  $Ed^3\sigma/d^3p \sim \exp(-X/X_0)$ , the values of the slope parameter  $X_0$  corresponding to various energies of deuteron, helium and carbon projectiles are compared. The double differential cross section of the reaction  $d + C \rightarrow \pi^0 + x$  is first measured using statistics of more than 40000  $\pi^0$  mesons. The obtained regularity of the energy spectra of pions in different intervals of emission angle indicates the absence of intermediate objects (hadronic clusters or fireballs) responsible for pion production in above-mentioned kinematical region.

## 1. Introduction

We report here on a measurement of inclusive  $\pi^0$  production by relativistic protons and  ${}^2d$ ,  ${}^4He$  and  ${}^{12}C$  nuclei on carbon and copper targets. The fragmentation of nuclei in high energy collisions into elementary particles with momenta far exceeding the average momentum per nucleon in the nucleus is one of the most interesting phenomena in high energy physics. This phenomenon, so called cumulative production of particles was first observed by Baldin [1]. As in the previous investigations of our group [2-5], which were also performed with the multichannel Cherenkov  $\gamma$ -spectrometer [6] installed at the Laboratory of High Energies (JINR, Dubna), we aim at clarifying the mechanism of neutral pion emission near and beyond the kinematic limit for free nucleon-nucleon and nucleon-nucleus collisions. We have also investigated how  $\pi^0$  production depends on the numbers of nucleons in the projectile and in the target and compare our results with a quark-parton models of the nucleus [7,8].

Moreover, our experiments allow to study the double differential cross sections of the reactions and thus to study the properties of objects (hadronic clusters or fireballs; quarks; six-

quark configurations) responsible for pion production in above-mentioned kinematical region and to estimate the transverse component of valence quarks momenta in protons and nuclei.

## 2. Experimental procedure

The experiment was performed at the synchrofasotron of the High Energy Laboratory using a single arm lead glass Cherenkov spectrometer with scintillator counter hodoscopes. A schematic drawing of the experimental apparatus is given in fig.1 The primary beam was focused producing at the target an elliptical beam spot with a horizontal axis of 3 cm and a vertical axis of 4 cm. To monitor the number of beam particles hitting the target, a monitor telescope composed of three scintillation counters was used. A carbon or a copper target was exposed to beams of deuterons,  $\alpha$  and  $^{12}\text{C}$  with a momentum of 4.5 GeV/c per nucleon, a momentum spread of  $\Delta p/p = \pm 2\%$  and an intensity up to  $10^5$  particles per pulse. Our experimental apparatus made it possible to measure both the energies and emission angles of photons from  $\pi^0$  decays. The FOTON setup has previously been described in detail in ref. [2,6].

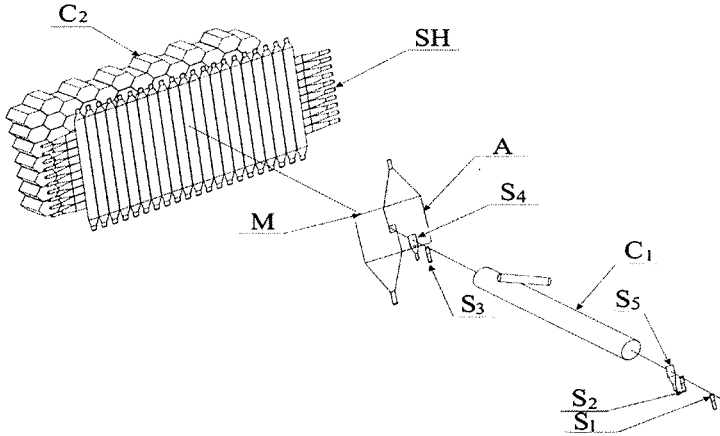


Fig. 1

The distance along the beam between the target center and the upstream face of the spectrometer was 340 cm for the carbon target and 520 cm for the copper target. The corresponding acceptances in the laboratory emission angle for  $\pi^0$  mesons were  $\theta_\pi \leq 16^\circ$  and  $10^\circ$ , respectively.

For charge particle identification forty scintillation counter hodoscopes composed  $2 \cdot 10 \cdot 100 \text{ cm}^3$  scintillators were used in front of the lead glass resulting in a 99 % detection probability for charged particles.

The lead glass modules are divided into 14 groups. The output signals in each group summed up linearly and after discrimination by amplitude used in fast triggering. In this experiment the thresholds of the discriminators were at the level of 1.0 – 1.5 GeV.

Triggering takes place when there is a coincidence of signals from beam counters, halo counters (in anticoincidence) and two or more groups of lead glass counters with total energy

exceeding 2 GeV. The mean velocity of triggering was about 15 events per spill. A total of about  $1.5 \cdot 10^6$  triggers was recorded during this experiment.

### 3. Event selection

The  $\pi^0$  mesons are detected through their two-photon decay mode as a narrow peak in the invariant mass distribution.

Photons are recognized as isolated and confined clusters (an area of adjacent modules with a signal above threshold) in the electromagnetic calorimeter. The photon energy is calculated from the energy of the cluster by applying a position-dependent leakage correction. Assuming that the photon originates at the target, its direction is determined from the geometrical positions of the constituent crystals, weighted by the corresponding energy deposits.

Inclusive spectra of  $\pi^0$  have been extracted from the raw data under the following selection criteria:

- (1)  $N_\gamma \geq 2$ ,
- (2)  $E_\gamma \geq 500$  MeV,
- (3)  $E_{\gamma T} \geq 120$  MeV,

where  $N_\gamma$  is the number of  $\gamma$ -quanta (clusters) in the event,  $E_\gamma$  is the energy of  $\gamma$ -quanta,  $E_{\gamma T}$  is the transverse momentum of  $\gamma$ -quanta.

### 4. Inclusive spectra of $\pi^0$ mesons

In order to identify  $\pi^0$  mesons all photon pair combinations are used to calculate the invariant mass in the each event. The combinatorial invariant mass spectra of the  $\gamma\gamma$  combinations selected according to the criteria (1) – (3) for different reactions are shown in fig. 2. The dotted histogram in fig.2 represents the invariant mass distribution for  $\gamma\gamma$  pairs combinations selected accidentally from different events. These combinatorial distributions were used for background calculations. The dashed histogram in the inset in fig.2c is the predicted  $\pi^0 \rightarrow \gamma\gamma$  signal obtained through a Monte Carlo simulation (for details, see [3]).

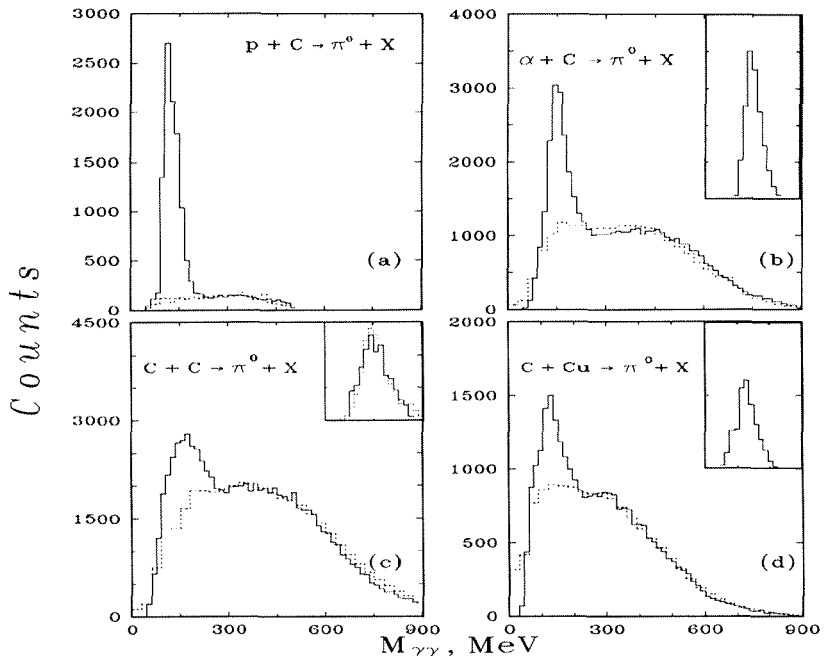


Fig. 2

There is an excess of  $\gamma\gamma$  pairs at small decay angles for background events. The influence of these events of the invariant mass distribution are essential for  $M < 100$  MeV only. These masses were excluded in the data analysis.

In fig. 3 we compare invariant neutral pion inclusive cross sections obtained in our experiments for the deuteron, helium and carbon nuclei at 4.5 GeV/c per nucleon on carbon target averaged in the range  $\theta_\pi \leq 16^\circ$  and  $E_\pi \geq 2$  GeV versus the cumulative number X.

An overall normalization uncertainty of  $\sim 20\%$  [5] is not included in the experimental data.

The slope parameter B of the exponential form  $Ed^3\sigma / d^3p \sim \exp(-BX)$  is:  $6.0 \pm 0.2$ ;  $7.4 \pm 0.1$  and  $8.0 \pm 0.1$  for fragmenting d,  $\alpha$ , and  $^{12}\text{C}$  projectiles, respectively.

The experimental values of  $X_0 = 1 / B_0$  (where  $B_0$  is the value of the slope parameter B for pion emission at zero angle) - a parameter that characterizes the quark-parton structure function of the fragmenting nucleus [9], are plotted in fig. 4 for various momenta of the fragmenting nuclei d,  $\alpha$ , and  $^{12}\text{C}$  - our data and the data from [10-13] (when the transition to the antilaboratory frame is required, the data are presented for  $\theta_\pi = 180^\circ$ ). It is suggested by the data in fig. 4 that the values of  $X_0$  are different for different light nuclei, what may be explained by difference of six-quark configurations formation probabilities (see below).

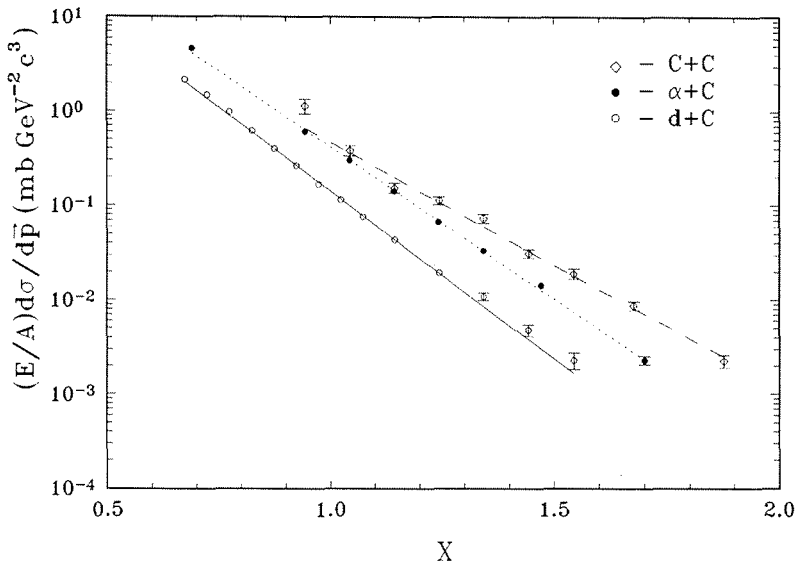


Fig.3

The  $A_p$  dependence of the invariant cross section can be parametrized in the form  $E d^3\sigma / d^3p \sim A_p^m$ . We derive the values of  $m$  by comparing the data for  $\alpha + C \rightarrow \pi^0 + x$  and  $C + C \rightarrow \pi^0 + x$  reactions. The resulting dependence of  $m$  on the cumulative number  $X$  is illustrated in fig. 5(a). For the region  $0.6 < X < 2.0$ , the dependence of  $m$  on the square of the  $\pi^0$  transverse momentum is shown in fig.5(b). It can be seen from fig. 5(a) that, over the region  $X > 0.9$ , the cross section for  $\pi^0$  production reveals an anomalously strong  $A_p$  dependence ( $m > 1$ ), which becomes even more pronounced with increasing  $X$ . That the exponent  $m$  increases with  $X$  suggests the redistribution of momenta among quarks from different nucleons, which is due to the formation of multi-quark configurations [14].

We denote by  $p_i$  ( $i=6,9,\dots$ ) the probability of the formation of an  $i$ -quark configuration within the nucleus. In the region around  $X \sim 1$ , where the formation of nine-quark and still higher configurations is unlikely [14], assuming that the probability of the absence of any correlations,  $p_3$ , is equal to  $p_3 \approx 1 - p_6$  and invoking the data in fig. 5(a) we estimated the probabilities of the formation of six-quark configurations in the deuteron, helium and carbon nuclei at (for details, see [5]):

$$p_6(^2d) \approx 2\%; \quad p_6(^4He) \approx 5 \div 10\%; \quad p_6(^{12}C) \approx 20 \div 40\%.$$

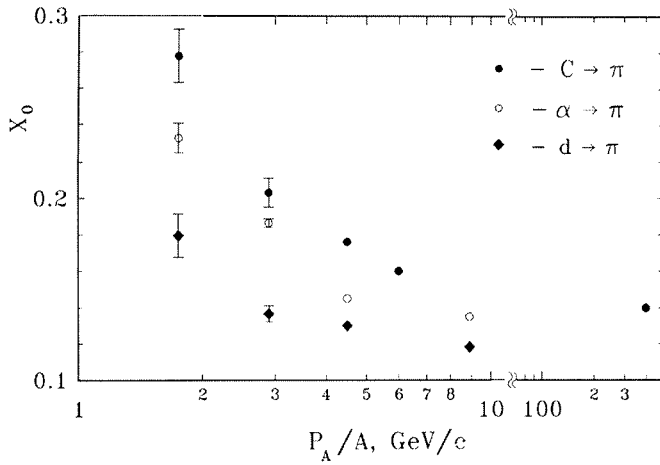


Fig. 4

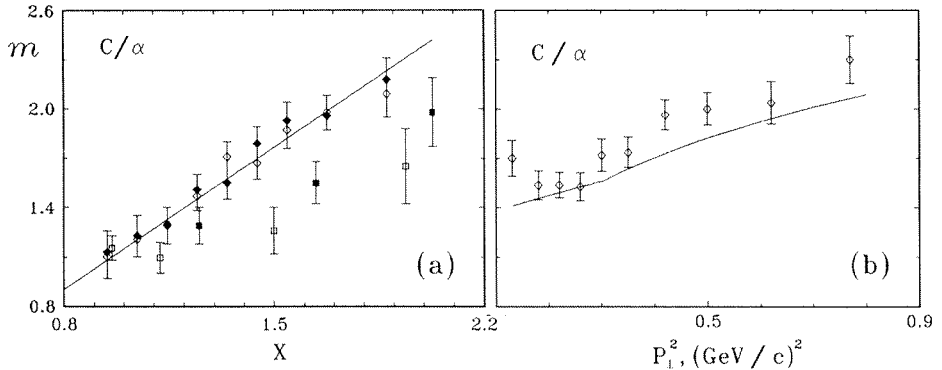


Fig. 5

The dependence of  $m$  on  $p_{\perp}^2$  (see fig. 5(b)) indicates that the parameter  $m$  is determined by  $X$ : the curve in fig. 5(b) was computed by considering that the mean value of  $X$  increases with  $p_{\perp}^2$  in the kinematical region specified by the inequalities  $\theta_{\pi} \leq 16^{\circ}$  and  $E_{\pi} \geq 2$  GeV (lab. sys.) and assuming the same  $p_{\perp}^2$  dependence of the invariant cross section for the fragmenting  $\alpha$  particle and  $^{12}\text{C}$  nucleus.

We present the target dependence in the form  $\text{Ed}^3\sigma / d^3p \sim A_T^n$ , where  $A_T = 12$  and  $63.5$  is the nucleon number of the target. The results are shown in fig. 6 where we have plotted  $n$  against cumulative number  $X$ .

The parton models [7,8] predict that  $n$  is independent of  $X$  and  $p_T$  at large  $X$  and small  $p_T$ . According to these models, an incident hadron fragments when one of its constituent quarks collides in the target. The spectator quarks that escape collision and thus retain their original fraction  $X$  of the projectile CM momentum can fragment or recombine with a slow quark ( $X \approx 0$ ) and form the large  $X$ -low  $p_T$  fragments.  $n$  has been estimated quantitatively assuming that

the recombination does not depend on  $X$  [7]. From calculations [2] in frame of this model we obtain  $\approx 0.38$  for  $n$ . The mean experimental value of  $n$  is:  $0.37 \div 0.40$ .

Thus the parton recombination model reproduces well both the mean value of  $n$  and the behaviour of the dependence  $n(X)$  in the region  $X > 0.6$ .

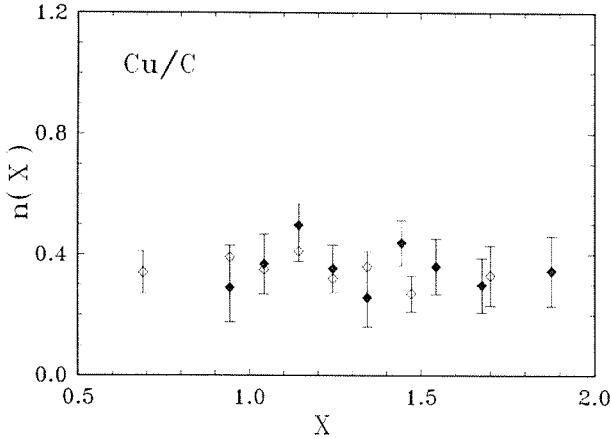


Fig. 6

### 5. Double differential cross section

The double differential cross section of the reaction  $d + C \rightarrow \pi^0 + x$  is first measured at 4.5 GeV/c per nucleon using statistics of 45000  $\rightarrow \pi^0$  mesons (fig. 7).

The invariant cross section of this reaction versus the energy  $E_\pi$  and emission angle  $\theta_\pi$  of the neutral pion in the lab.system is analysed at  $4^\circ \leq \theta_\pi \leq 16^\circ$  and  $2 \leq E_\pi \leq 4.7$  GeV.

We have obtained the slope parameters in the energy spectra  $Ed^3\sigma / d^3p$  ( $E, \theta$ -fixed)  $\sim \exp(E/T_0)$ , for each interval of  $\theta_\pi$  and expressed  $T_0$  as  $T_0 = T_0 (1 - \beta^2)^{1/2} / (1 - \beta \cdot \cos\theta_\pi)$ .

Interpreting the parameter  $T_0 \sim m_\pi$  as the universal hadron temperature [16]:  $Ed^3\sigma / d^3p \sim \exp(-E^*/T_0)$ , we have obtained the values of  $\beta$  - the velocity of an intermediate object (cluster) which decays into a final pion. The parameter  $\beta$  obtained at  $T_0=160$  MeV versus emission angle  $\theta$  is shown in fig. 8 (the same values of  $\beta$  for the interval  $\theta_\pi \leq 8^\circ$  at  $T_0=140$  MeV are shown by dashed line).

The obtained regularity of the  $\beta(\theta)$  in the interval  $\theta_\pi \leq 8^\circ$  qualitatively agree with the predictions of the cluster models (the existence of an intermediate object with velocity  $\beta$  which decays into a final pion). However, for explanation of such small values of  $\beta$  one have to suppose second or more collisions in the target which contradicts with observed target mass dependence (see fig. 6 or [5]).

Thus the obtained regularity of the  $\beta(\theta)$  indicates the absence of intermediate objects (hadronic clusters or fireballs) responsible for pion production in above-mentioned kinematical region.

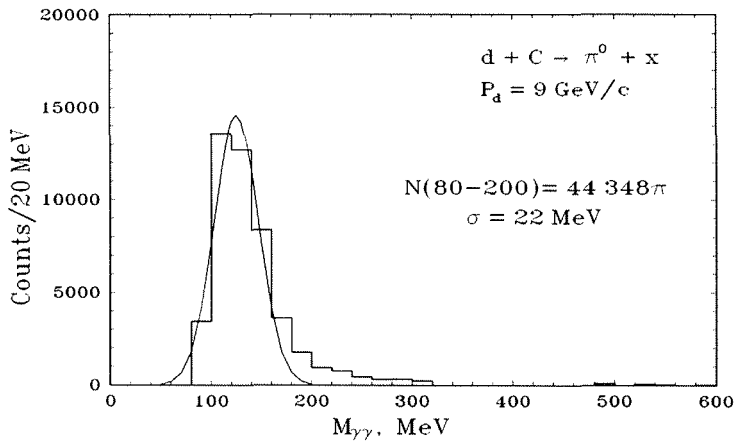
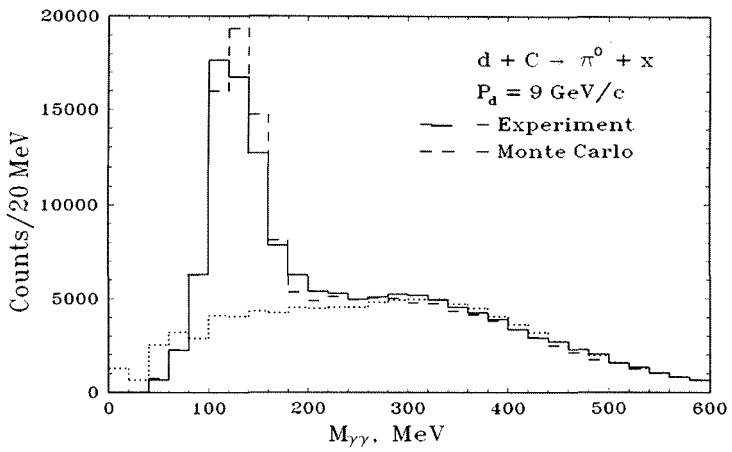


Fig. 7

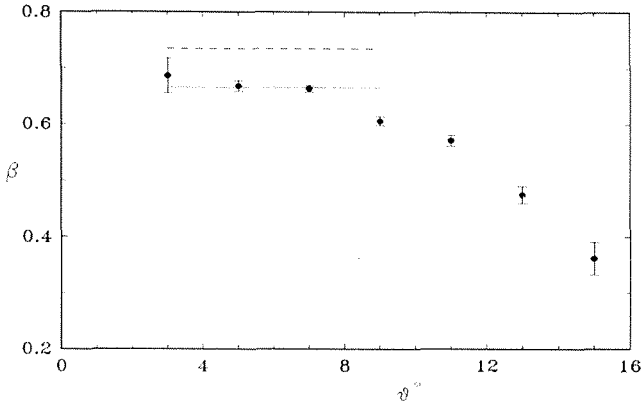


Fig. 8

## 5. Conclusion

1. The dependence of the cross sections on the mass of the target is approximately  $A_T^{=0.37-0.40}$  and is in agreement with the predictions of the parton recombination model.

2. Under the assumption that the invariant cross section as a function of the projectile atomic number  $A_p$  can be parametrized in the form  $Ed^3\sigma/d^3p \sim A_p^m$ , the  $X$  and  $P_{\perp}^2$  dependences of the exponent  $m$  are investigated by comparing the cross sections for the reactions  $C + A_T \rightarrow \pi^0 + x$  ( $A_T = C, Cu$ ) with those for the analogous reactions induced by incident  $\alpha$  particles. At  $X = 1.9$ , the parameter  $m$  is found to reach a value of  $2.1 \pm 0.1$ . The  $A_p$  dependence of the cross section under study shows a significant variation with  $X$  and only a weak variation with the pion transverse momentum.

3. The probabilities of the formation of six-quark configurations in  $^2d$ ,  $^4He$  and  $^{12}C$  nuclei are estimated at  $\sim 2\%$ ; 5-10% and 20-40% respectively.

4. For the parametrization  $Ed^3\sigma/d^3p \sim \exp(-X/X_0)$ , the values of the slope parameter  $X_0$  corresponding to various energies of deuteron, helium and carbon projectiles are compared: the values of  $X_0$  are different for different light nuclei, what may be explained by difference of six-quark configurations formation probabilities.

5. The double differential cross section of the reaction  $d + C \rightarrow \pi^0 + x$  is first measured using statistics of more than 40000  $\pi^0$  mesons. The obtained regularity of the energy spectra of pions in different intervals of emission angle indicates the absence of intermediate objects (hadronic clusters or fireballs) responsible for pion production in above-mentioned kinematical region.

## Acknowledgement

We are grateful to Professor A.I.Malakhov for his support and to S.G.Reznikov, V.V.Arhipov, S.N.Plyashkevich and the VBLHE accelerator staff for contributions to the success of this experiment.

## REFERENCES

1. Baldin A.M. et al. Part. Nucl. 8 (1977) 429; Preprint of JINR, Dubna, 1971, no.R7-5808.
2. Abraamyan Kh.U. et al. Phys. Lett. B 323 (1994) 1.
3. Abraamyan Kh.U. et al. Yad. Fiz. 59 (1996) 271 [Phys. At. Nucl. (Engl. Transl.) 59 (1996) 252].

4. Abraamyan Kh.U. et al. *Yad. Fiz.* 60 (1997) 2014 [*Phys. At. Nucl. (Engl. Transl.)* 60 (1997) 1843].
5. Abraamyan Kh.U. et al. *JINR*, P1-2004-37, Dubna, 2004; *Proc. of the XVI Intern. Baldin Seminar on High Energy Physics Problems. JINR, E1,2-2004-76, Dubna, 2004, V. 2, p. 13.*
6. Astvatsaturov R.G. et al. *Nucl.Instr.and Meth.* 163 (1979) 343.
7. Berlad G. and Dar A. *Phys. Lett.* B102 (1981) 385.
8. Baldin A.M. *Proc. Intern. Conf. on Extreme States in Nuclear Systems. Dresden, 1980, v.2, p.1.*
9. Baldin A.M. *Proc. of the VI Intern. Seminar on High Energy Physics Problems. JINR, D1,2-81-728, Dubna, 1981.*
10. E.Moeller et al. *Phys.Rev.*C28 (1983) 1246.
11. Baldin A.M. et al. *JINR*, 1-82-28, Dubna, 1982.
12. Baldin A.M. et al. *Yad. Fiz.*, 20 (1974) 1201.
13. Leksin G.A. et al. *ITEP*, 37, Moscow, 1980.
14. Lukyanov V.Љ. and Titov A.I. *Phys. of Elem. Part. and At. Nucl.*, 10 (1979) 815.
15. Hans J. Pirner and James P. Vary. *Phys. Rev. Lett.*, 46 (1981) 1376.
16. Gorenshteyn M.I., Zinovyev G.M., Shelest V.P. // *Yad. Phys.*, 1977. V.26. P.788.

## CLUSTER-FLUCTONS REVELATION IN NUCLEAR INTERACTIONS AT 4.2 (GEV/C)/N

V.N. Penev, A.I. Shklovskaya  
*INRNE, Sofia and JINR, Dubna*

E.N. Kladnitskaya  
*JINR, Dubna*

The question about the correlations between nucleons in the nuclei and the conservation of their own individualities has always been, for many researchers, an interesting puzzle. As early as 1949 K.Brueckner et.al. [1] brought a report about space nucleon correlations in nuclei. In 1950 J.Hadley et.al. [2] studied forward emission of high momentum deuterons in p+nucleus interactions. M.G. Mescheriakov et.al. [3], Ajgirei et.al. [3] discovered the effect of deuterons knocking out from Li, Be, C... In 1956 Bete mentioned the short-range interactions between the pairs of nucleons in nuclei. Further, in 1957 D.I. Blokhintsev proposed [5] a very productive idea, that high momentum components of particles produced are connected, with some clusters, consisting of nucleons, also called fluctons. In the seventies many papers were published [6] on nuclear fragmentation, pions production in nuclear interactions, etc. Particularly, it was shown, that pions spectra couldn't be reproduced by any model, in which the pions generation is attributed to collisions between individual nucleons inside the nucleus only.

Cumulative particles, i.e. particles with momentum greater, than that allowed by nucleon-nucleon kinematics, began to be an object of intensive studies after the publications of G.A. Leksin et.al.[7], and A.M. Baldin [8]. Strictly speaking, all products of the nuclear-nuclei interactions are cumulative ones, just because of the existence of Fermi momentum. But in this case the particles are meant that had obtained an unusually great moment, and the total situation has become quite different. In this field a lot of experimental data were obtained by Stavinskiy V.S. et. al. [9]. Cumulative processes with high momentum transfer enjoy nowadays a special interest. A review of the first experimental cumulative data and the analysis of these data from the point of view of the new hypotheses were made by V.K. Lukyanov and A.I. Titov [10]. It was shown, that the hypothesis about the nuclear density fluctuations and quark-parton interaction mechanism existence can be the base of the large momentum transfer and etc.

That study was undertaken in order to pick out and to analyze the groups of events, in which two, three or more nucleons had taken part at the interactions. By comparing such events with collisions of elementary particles, it is possible to study the interactions of groups of nucleons as a whole object: flucton. The

quazy-nucleons and fluctons that may compose the nucleus, we shall sign as 'F'. One nucleon flucton is  $N_F$ , two nucleon – is  $d_F$ . The type of the nucleus is signed by upper index.

In this situation the experimental data of protons, deuterons and carbons interactions with protons and carbons from propane ( $C_3H_8$ ), obtained in propane bubble chamber at 4.2 (GeV/c)/N [11] were used. The interactions  $p + C_3H_8$ ,  $d + C_3H_8$ ,  $C + C_3H_8$  were divided on  $p+p$  and  $p+C$ , on  $d + C$  and  $d + p$ ; on  $C+C$  and  $C+p$ -collisions correspondently by the way, proposed in [12].

The calculation and analyses of some total values for every event, based on charged particles, registered inside the chamber, represent an important part of this study. These values are as follows:

$\Sigma P_y^i$  –total longitudinal momenta of all charged particles. As long as all particles run along the y-axis, the registered value should be  $\Sigma P_y^i = nP_0$ , where  $P_0$  is the momentum of the beam and  $n=1, 2, 3, \dots$  depending on the number of the initial interaction nucleons. There is obviously, that for  $p+C$ ,  $p+p$ -collisions:  $n=1$ , but for  $d+C$ ,  $d+p$ , when both nucleons take part in the interaction:  $n=2$ . In case, that one initial nucleon takes part at the interaction ( $n=1$ ), one maximum may be seen in the  $\Sigma P_y^i$ -spectrum. Observation of several maxima corresponds to the superimposition of a number of spectra, having the next maximum values of summary momentum:  $\approx 4.2, \approx 8.4, \approx 12.8$  GeV/c, ... It accords to the fact, that 1, 2, 3, ... nucleons from the flying nuclei interact with the target.

The next value is the interaction energy  $M_{tot,0}^2 = (\Sigma E_0^{1,2})^2 - (\Sigma P_0^{1,2})^2$ , where  $E_0^{1,2}$  and  $P_0^{1,2}$  – are the energy and momenta of initial particles. On the other hand the value of interaction energy may be calculated, using the reaction products:  $M_{tot}^2 = (\Sigma E_i)^2 - (\Sigma P_i)^2$ , where  $E_i, P_i$ -are the energies and momenta of all particles produced. If all products are registered,  $M_{tot,0}^2 = M_{tot}^2$ .

Let us consider  $C+C$ ,  $C+p$ ,  $d+C$  – interactions, (or more exactly  $d_F^C + N_F^C$ ,  $d_F^C + p$  and  $d + N_F^C$ ), for which  $\Sigma P_y^i \approx 8.4$  GeV/c. There are two nucleons from the flying carbon which have taken part at the interaction:  $n=2$ . If both nucleons interact with two target nucleons independently, or – with one "quazy-deuteron" (that is  $n_{part}=4$ , where  $n_{part}$  is the number of interacted particles), than such events will come to the region of  $39 \div 40$  (GeV)<sup>2</sup> in  $M_{tot}^2$  spectra. However, it does not seem to be the case: most of the events, coming from the  $\Sigma P_y^i \approx 8.4$  GeV/c- interval, settled down near  $M_{tot}^2 \approx 20$  (GeV)<sup>2</sup>, i.e.  $n_{part}=3$ .

The  $M_{tot}^2$ -distributions for  $C+C$ ,  $C+p$ -, and  $d+C$ ,  $d+p$  –collisions for two  $\Sigma P_y^i$ -stripes:  $\Sigma P_y^i \approx 4.2$  GeV/c,  $n=1$ , and  $\approx 8.4$  GeV/c,  $n=2$  are shown on fig. 1 and fig. 2, correspondently. As seen on figs. 1 and 2 again the events are grouped near the two  $M_{tot}^2$  values:  $M_{tot}^2 \approx 9.8$  and  $20$  (GeV/c)<sup>2</sup>. So, the events with  $n=1$  and  $n_{part}=2$  are in accordance with nucleon-nucleon kinematics, obviously are included in the first group. The second group of events corresponds to the

interactions of two flying protons with one target's nucleon successively via secondary collisions or simultaneously.

It was shown[14], that the events with three nucleons interaction differ from two nucleons interactions strongly, both in one particle longitudinal momentum spectra and in multiplicities of generated particles.

For example, let us consider the  $P_y^i$ -spectra of all charged particles for the reactions of quazy-nucleon or free nucleon with two nucleons from the carbon - target:  $N_F^C + d_F^C$ ,  $N_F^d + d_F^C$ ,  $p + d_F^C$ . Further, let us suppose, that the coming fly nucleon interacts with the two target nucleons "successively": one flying nucleon interacts with one target nucleon, followed by another target nucleon interacting with the product from the first interaction. In that case on the basis of mean momentum particles analysis [14], it is necessary to suppose that more than 85% of particles, produced in the first collision, interact with the other nucleon. But it is not possible, because it leads to strong increasing of charged particles multiplicity (see table. 1). For example, as it is seen from the table 1, the ratio of particle multiplicity observed of two nucleon ("flucton") – nucleon interactions to multiplicity of nucleon-nucleon collisions turn out:

$$\begin{aligned} n_{ch}(p+d_F^C)/n_{ch}(p+p) &= 1.26 \pm 0.10, \text{ and } - \\ n_{ch}(d_F^C + p)/n_{ch}(d(\text{one nucleon}) + p) &= 1.25 \pm 0.06. \end{aligned}$$

So, from the charged particle multiplicity analysis the next conclusion is follows: (20÷30)% of all produced particles interact in the nuclei again.

So, the secondary interactions contributions, calculated on the basics of mean momenta of one particle spectra and from mean values of charged particles multiplicities are not agreed one with another. It is quite possible that secondary interactions mechanism do not work here at all.

The cumulative particles, well known from some experiments, were observed in these reactions too.

Let us mark, that the appearance of protons with moment  $P_y^p > 4.2 \text{ GeV}/c$  in  $d_F^C + N_F^C$  – reaction, show up the maximum violation of nucleon- nucleon collision kinematics. The number of such protons compiles (12.5±1.5)% from all produced protons. Cumulative particles generations moving backward in the same reaction are due to secondary interactions and to Fermi movement only. Therefore, the number of such particles is very small: less than 1.0% of all protons fly backward. It was proved in [9] that abundant production of cumulative particles, moving in beam direction or backward, especially – production of protons flying backward in reaction  $N_F^C + d_F^C$ , for example, can be explained neither by Fermi-momentum nor by secondary interactions in the nuclei. As seen from distribution of longitudinal proton momenta for reaction  $N_F^C + d_F^C$ , ( $n=1$ ,  $n_{part}=3$ ) more than (14±2)% of all protons move in direction opposed to the nucleons beam.

So, longitudinal momenta spectra and multiplicities of charge particle analysis and distinction of cumulative particles production in  $d_F^C+p$  and  $d_F^C+p$ -reactions suggest reasonable assumption that two nucleons are combined as one flucton even before interaction. Then high momentum  $P_t^+$  and  $P_y^+$  appearance become more probable when a flucton with momentum 8.4 GeV/c instead of a nucleon with momentum 4.2 GeV/c, interacts with the target. So, for example abundant production of cumulative protons, coming fly backward may be explained easily if it is supposed that one nucleon interacts with two nucleons, i.e. with a flucton.

Let us note, that the values of mean transverse momenta of positively charged particles  $\langle P_t^+ \rangle$  increase for nuclear-nuclei interactions compared with nucleon-nucleon ones. And they become even greater for the reactions with fluctons participations (see table 2).

We are realizing, that the conclusion obtained must be tested in future on a high statistics basis. Also all particles registrations are needed for the better channels separation.

We are thankful to people of 2m. propane chamber Collaboration for providing us with experimental data, which was used here. We thank Malakhov A.I. for discussions, for support and hospitality. We are very grateful to prof. Troyan Yu.A., Tokarev M.A., Rogachevskiy O.V. and to Lukyanov V.K. especially for useful discussion and support. Authors are grateful to Zhelyu Bunzarov for reading and edition of manuscript.

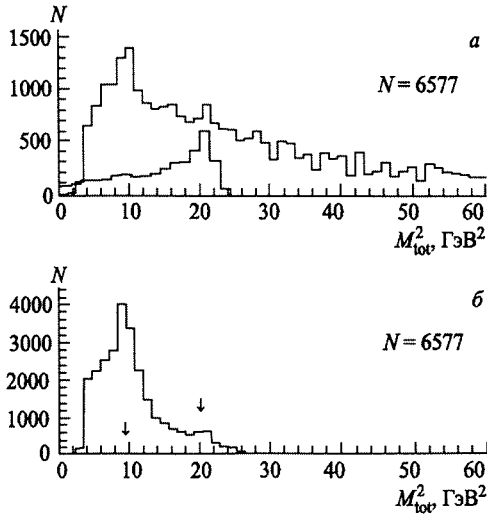


Fig. 1A, B. Distributions of total energy  $M_{tot}^2$  (GeV)<sup>2</sup> for (A) C+C and (B) C+p-collisions for the two groups of events with summary longitudinal particle momentum  $\Sigma P_y^* \approx 4.2$  GeV/c and  $\approx 8.4$  GeV/c. The inside histogram [14] is the particles spectrum for  $n=2$  nucleon interaction with the nucleon target. It is not normalized

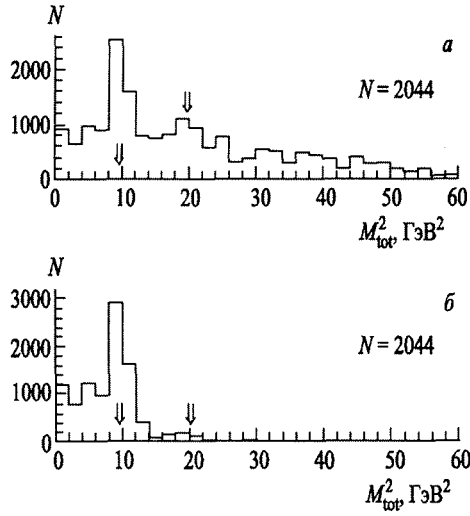


Fig.2A, B. Distributions of total particle energy  $M_{tot}^2$  ( $GeV$ )<sup>2</sup> for (A)  $d+C$ - and (B)  $d+p$ -collisions for the two groups of events with summary longitudinal particle momentum  $\Sigma P_y^i \approx 4.2$   $GeV/c$  and  $\approx 8.4$   $GeV/c$ .

Table 1. Mean values of charged particles multiplicity

Target	$d_F^C$	$N_F^C$	p
Initial coming fly particle	$n_{ch}$	$n_{ch}$	$n_{ch}$
p [15]	$4.05 \pm 0.27$	$2.97 \pm 0.12$	$2.86 \pm 0.22$ $2.37 \div 2.60$
$N_F^C$	$3.73 \pm 0.79$	$2.94 \pm 0.46$	$2.73 \pm 0.25$
$d_F^C$	$3.30 \pm 0.20$	$3.82 \pm 0.76$	$3.37 \pm 0.58$
d(both nucleons)	-	$3.05 \pm 0.14$	$2.95 \pm 0.18$
d(one nucleon)	-	$2.78 \pm 0.20$	$2.70 \pm 0.21$

Table 2

Reactions	$\langle P^{i+}_x \rangle$ GeV/c	$\langle P^{i+}_y \rangle$ , GeV/c
p+p	0.464±0.009	1.508±0.030
$N_F^C$ +p	0.496±0.014	1.819±0.058
p+ $d_F^C$	0.474±0.025	1.189±0.075
$N_F^C$ + $d_F^C$	0.519±0.029	1.176±0.072
$d_F^C$ +p	0.550±0.024	2.479±0.118
d(both nucleons)+ $N_F^C$	0.563±0.070	2.265±0.283
d(both nucleons)+ p	0.532±0.093	2.350±0.616
d+p	{0.458±0.009}	{1.525±0.033}

- [1] K. Brueckner, R. Eden, N. Francis. Phys. Rev.,98,1445,1955
- [2] J. Hadley, H. York. Phys.Rev.80, 345, 1950
- [3] M.G. Meshcheriakov et.al. DAN USSR, 109, 499, 1956; L.S. Ajgirei et.al. JETF, 33, 5(11), 1957
- [4] H. Bethe. Phys.Rev. 103, 1354, 1956
- [5] D.I. Blokhintsev, JETF, ò. 33, 5(11),1957;
- [6] See in Harry H. Heckman Proc. of Int. Conf. On High Energy Physics and Nuclear Structure, Uppsala, Sweden, June, 18-22,1973; Herbert Steiner Lecture on Adriatic Meeting on particle Physics, Rovinj, Yugoslavia, September 23 oct. 5,1973
- [7] G.A. Leksin et.al. JETF, 32, 445, 1957; Nuclear Scaling, M. MIFI, 1975.
- [8] A.M. Baldin, Physics of Elementary Particles and Atomic Nuclei 1977, v. 8, p. 429
- [9] V.S. Stavinskiy, Physics of Elementary Particles and Atomic Nuclei, vol. 10, part 5, (1979).
- [10] V.K.Lukyanov, A.I. Titov, Physics of Elementary Particles and Atomic Nuclei 10,815, (1979)
- [11] G.N. Agakishiev et. al. Yadernaia Fizika 1984,40,1209; D. Armutliiski et.al. Zett Phys. A, v.328, 455, 1987; L.J.Simic et. al. Phys Rev D, v.34, 692,1986
- [12] Ö.N. Agakishiev et. al. JINR communication,1-83-662, 1983; A.I. Bondarenko et.al. JINR Rapid Communication P1-98-292.
- [13] A.G. Litvinenko, A.I. Malakhov, P.I. Zarubin, Proc. Of the Xith Int. Seminar on High Energy Physics Problems, Dubna, JINR, p. 228, 1994.
- [14] V.N. Penev, A.I. Shklovskaya and E.N. Kladnitskaya, JINR COMMUNICATION P1-2004-98

# INVESTIGATIONS IN VEKSLER AND BALDIN LABORATORY OF HIGH ENERGIES

A.I. Malakhov

Joint Institute for Nuclear Research, Dubna, Russia  
e-mail: malakhov@lhe.jinr.ru

## 1. Introduction

Today the Veksler and Baldin Laboratory of High Energies (VBLHE) of the Joint Institute for Nuclear Research (JINR) is an accelerator center where research in the transition energy region is carried out. VBLHE co-operates with CERN, many physics centers in Russia, JINR member states, research institutes in the US, Germany, France, Japan, and other countries.

In 2004 the scientific programme of VBLHE, as in the previous years, was focused on Relativistic Nuclear Physics [1, 2].

This report presents the new results obtained at VBLHE in 2004 and the research programme for the next three years.

## 2. Main results of the Nuclotron development in 2004 and plan for next three years

The annual running time of the VBLHE accelerator complex is presented in fig.1 The Synchrophasotron was stopped in 2003. The Nuclotron annual running time has reached 2500 hours in 2004. It is planned to increase it up to 4000 hours in the coming three years.

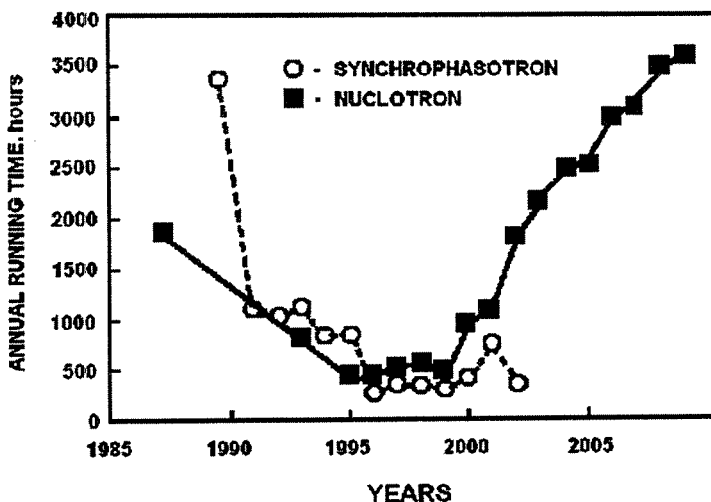


Fig.1. The annual running time of the VBLHE accelerator complex

The Nuclotron main parameters achieved in 2004 are presented in Table 1.

Table.1. The Nuclotron main parameters

Parameter	Planned	Achieved
Particles	$1 < Z < 92$	$1 < Z < 36$
Maximum energy, A·GeV	$6(A/Z=2)$	4.2
Maximum magnetic field, Tl	2.0	1.5
Injection energy, A·MeV	5	5
Slow extraction, s	10	10
Vacuum, Torr	$1 \cdot 10^{-10}$	$1 \cdot 10^{-10}$
Pulse repetition rate, Hz	0.5	0.2
Magnetic field ramp, T/s	2	1

The parameters of the Nuclotron beams are shown in Table 2.

Table 2. Extracted beams of Nuclotron

Beam	Intensity (Particles per cycle)		
	Year 2002	Year 2004	Year 2005
p	$3 \cdot 10^{10}$	$1 \cdot 10^{11}$	$2 \cdot 10^{11}$
d	$5 \cdot 10^{10}$	$5 \cdot 10^{10}$	$1 \cdot 10^{11}$
$^4\text{He}$	$8 \cdot 10^8$	$3 \cdot 10^9$	$2 \cdot 10^{10}$
$^7\text{Li}$	$8 \cdot 10^8$	$1 \cdot 10^9$	$2 \cdot 10^9$
$^{10}\text{B}$	$2.3 \cdot 10^7$	$2 \cdot 10^8$	$2 \cdot 10^9$
$^{12}\text{C}$	$1 \cdot 10^9$	$2 \cdot 10^9$	$1 \cdot 10^{10}$
$^{14}\text{N}$	-	$1 \cdot 10^7$	$5 \cdot 10^7$
$^{16}\text{O}$	$5 \cdot 10^8$	$7 \cdot 10^8$	$1 \cdot 10^9$
$^{24}\text{Mg}$	$2 \cdot 10^7$	$1 \cdot 10^8$	$3 \cdot 10^8$
$^{40}\text{Ar}$	$1 \cdot 10^6$	$3 \cdot 10^7$	$2 \cdot 10^9$
$^{56}\text{Fe}$	-	$1.2 \cdot 10^6$	$5 \cdot 10^7$
$^{84}\text{Kr}$	$1 \cdot 10^3$	-	$5 \cdot 10^6$
$^{131}\text{Xe}$	-	-	$1 \cdot 10^6$

The main task of the Nuclotron development in 2004 was to accelerate deuterons to the maximum energy 6 A·GeV. Works dedicated to this goal were provided during the December run of Nuclotron.

The next important task for 2005-2007 is to increase the beam intensity  $3 \div 5$  times. To fulfill this, beam losses during the first 100 mksec of acceleration time should be reduced. Adiabatic capture of particles in the acceleration process will be used for this purpose.

During 2004 construction of the new internal target station at Nuclotron was completed [3,4]. The Prague Vacuum plant and the Physical Institute of SAS, Bratislava took active part in this work. The layout of the internal target station is presented in fig.2.

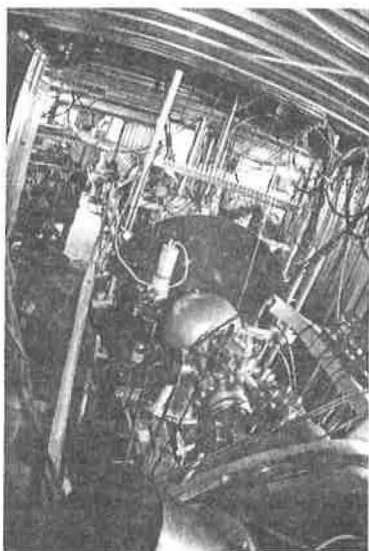


Fig.2. The view of the internal target station in the Nuclotron ring

A very important event in 2004 was signing an agreement between the Indiana University and JINR on handing over the CIPIOS polarized ion source to be mounted at Nuclotron. The source parameters are:

- Pulsed 1 Hz to 4 Hz
- 25 keV beam energy
- Polarized H or d
- Normal polarization > 80%
- 1.5 mA (peak) from source
- > 25 mA (peak) unpolarized

Using this source at Nuclotron it will be possible to provide intensity of the external beam of polarized deuterons up to  $10^{10}$  per cycle. Reaching such intensity of polarized deuterons is the main task in 2005-2007. INR RAS (Troitsk) will take active part in this work.

At present this source is ready for transportation to Dubna (fig. 3).

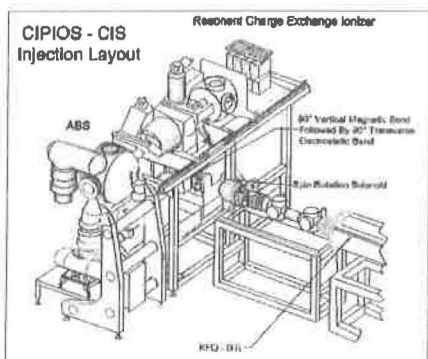


Fig.3. The CIPIOS polarized source (left); the packing process (right)

During 2005-2007 a project of the Nuclotron booster and prototype superconductive magnets and magnetic lenses for the beam lines of the VBLHE accelerator complex will be developed.

The prototypes of the superconductive magnets for the new international accelerator center FAIR at GSI, Germany will also be tested.

Nuclotron operation opens new possibilities for different research programs with ion beams and polarized ion beams. The experience of its maintenance and exploitation is very helpful for design and construction of new accelerators.

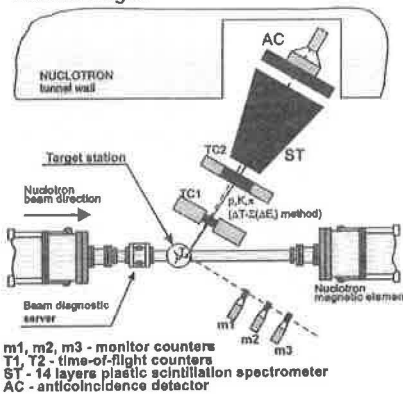
### 3. Physics results in 2004 and plans for 2005-2007

#### 3.1. Results obtained at the VBLHE accelerator center and plans for 2005-2007

##### Search for resonant structure in pion production reaction using the Nuclotron internal beam

We have searched for an enhancement in the excitation function of the pion yield in the  $p+d$  reaction at projectile energies near 350 MeV/nucleon. The measurements were carried out on DELTA-2 setup at the Nuclotron internal beam with Ag, Cu, Al and C targets during two runs in March and June, 2004. The layout of the DELTA-2 setup and preliminary experimental results are presented in fig. 4. It is seen that for heavier targets (beginning with Cu) a narrow peak appears in the region of the beam energy 350 MeV/nucleon. It means that this effect has a nuclear nature.

The installation layout at the NUCLOTRON internal target.



March and June 2004 Nuclotron Runs. Pion yield for C, Al, Cu and Ag targets for proton and deuteron beam near 350 MeV bombarding energy.

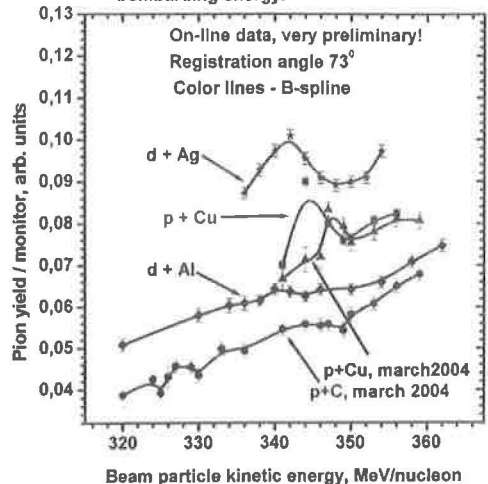


Fig.4. Layout of the DELTA-2 setup (left); preliminary normalized pion yields in  $d + A$  and  $p + A$  reactions as functions of beam energy (right)

The possible physical explanations of the observed effect are the following:

- Excitation of a narrow dibaryon state
- Increased transparency of nuclei for low energy pions
- Large binding energy of nuclear matter leading to a narrow  $2\Delta$  state
- Localized  $\Delta$  isobar in nuclear matter: "Snow ball", " $\Delta$  ball" (a meta-stable localized  $\Delta$  isobar, effect of the medium)
- Two-pion Cooper pair in nuclei (two pion states when two pions scatter within nuclear matter)

For final interpretation more experimental data are required. It is planned to study the effect in more detail for various targets, projectiles and pion emission angles in 2005-2006.

**Observation of the narrow exotic baryons (pentaquarks)**

Three VBLHE groups participated in search for the narrow exotic baryons (pentaquarks). Two groups used the existing data from the VBLHE bubble chambers for analysis. The group headed by Yu.A. Troyan used the data obtained at the VBLHE 1m hydrogen bubble chamber and the group of R. Togoo (Mongolia) used the data from the VBLHE 2m propane bubble chamber.

The group of G.L. Melkumov actively participated in obtaining the data on pentaquarks at NA49 setup (SPS CERN).

A special project NIS (in collaboration with LPP) exists aimed at the search for such objects at Nuclotron. The leaders of the project NIS are: A.G. Litvinenko (VBLHE) and E.A. Stokovsky (LPP).

The group of Yu.A. Troyan analyzed the reaction  $np \rightarrow npK^+K^-$  at neutron momentum  $P_n = (5.20 \pm 0.12)$  GeV/c. Narrow exotic baryons were studied in the  $K^+n$  system. The results were published in [5]. Some plots are shown in Fig.5. Three peaks with significance exceeding  $5\sigma$  can be seen. These peaks are produced by the resonances with the masses  $M = 1.541, 1.606$  and  $1.687$  GeV/c<sup>2</sup>.

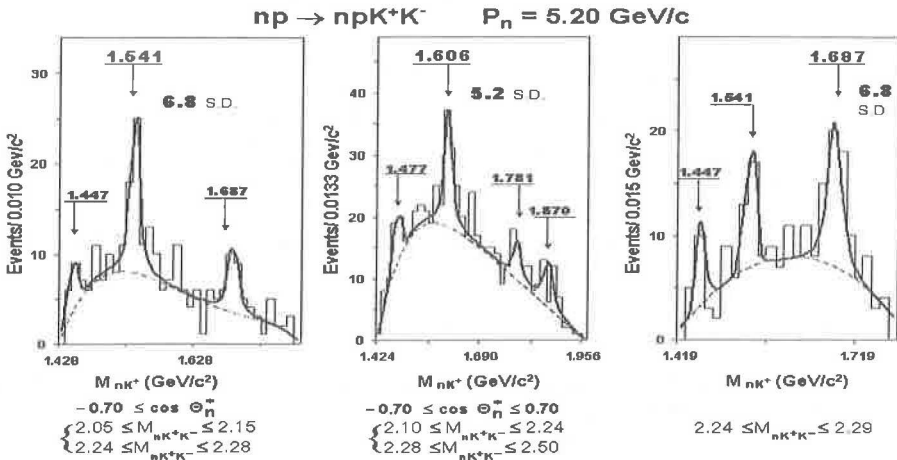


Fig.5. Three peaks with significance exceeding  $5\sigma$  are observed in the  $K^+n$  system. The data were obtained using the VBLHE hydrogen bubble chamber

One of the possible mechanisms of  $\Theta^+$  production is presented in fig.6.

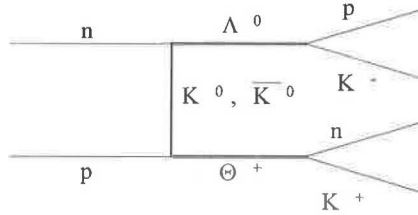


Fig.6. One of the possible mechanisms of  $\Theta^+$  ( $uudd\bar{s}$ ) production

The results on observation of pentaquarks were obtained by the group of P. Togo (Mongolia) using the data from the VBLHE 2m propane bubble chamber. This group studied the reaction  $C + C_3H_8 \rightarrow K_s^0 p + x$  at carbon beam momenta  $P_C = 4.2 \text{ A}\cdot\text{GeV}/c$ . A narrow peak with  $M = (1532 \pm 6) \text{ MeV}/c^2$  and width  $\Gamma \approx (26 \pm 4) \text{ MeV}/c^2$  was observed in the  $K_s^0 p$  effective mass spectrum (fig.7) [6].

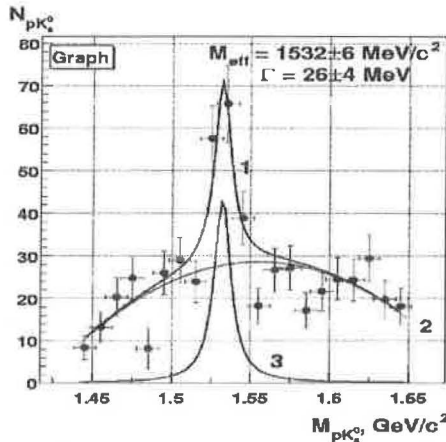


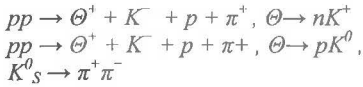
Fig.7. The spectrum of  $K_s^0 p$  effective masses in  $C + C_3H_8 \rightarrow K_s^0 p + x$  reaction at carbon beam momenta  $P_C = 4.2 \text{ A}\cdot\text{GeV}/c$

The results of NA49 experiment on observation of pentaquarks in the  $\Xi\pi$  system are published in [7].

The physical programme of the NIS experiment at Nuclotron includes:

(A) Search for effects of nucleon polarized strangeness in production of  $\phi$  and  $\omega$  mesons in  $pp$  and  $np$  scattering close to thresholds (at  $\varepsilon \approx 30 \div 100 \text{ MeV}$  above the thresholds).

(B) Search for production of the  $\Theta^+$  baryons in  $pp$  interactions close to threshold in reactions:



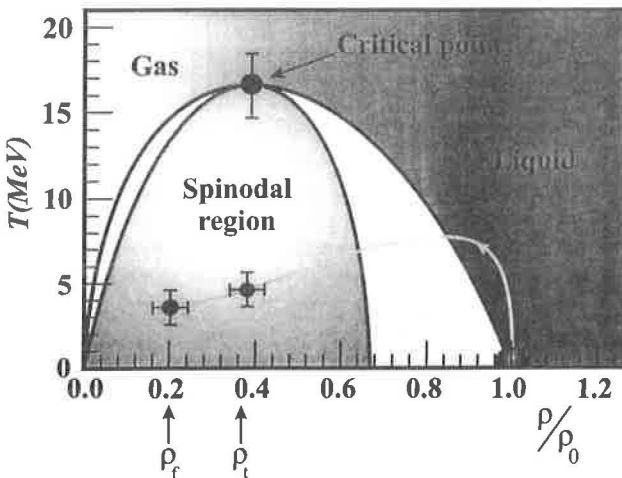
**Study of thermal multifragmentation induced by light relativistic ions and nuclear phase transitions**

It has been shown in the previous studies at the FAZA setup (leader V.A. Karnaukhov, DLNP) that nuclear disintegration takes place after an expansion of the exited nucleus. The break up density is  $\rho_t = (0.3 \div 0.4) \rho_0$  and the temperature is  $T_b = 5 \div 7$  MeV. Thermal multifragmentation can be interpreted as the first order nuclear *liquid-fog* phase transition at this temperature.

An important model parameter of the scenario of spinodal decomposition is the critical temperature for the nuclear *liquid-gas* phase transition  $T_c = 17 \pm 2$  MeV which was measured by FAZA collaboration. That is a very important result as it gives direct evidence, that multifragmentation takes place deep inside the spinodal region.

A very significant observation was made recently [8, 9]. It was proved experimentally that the multifragmentation process has two characteristic densities. The first one,  $\rho_t$ , determined from the intermediate mass fragments (IMF,  $2 < Z < 20$ ) charge distribution, corresponds to the moment of fragment formation, when the properly extended hot target spectator transforms into a configuration consisting specified prefragments. They are not yet fully developed, there are still links (nuclear interaction) between them. The final channel of disintegration is completed during the evolution of the system up to the moment when receding and interacting prefragments become completely separated at the mean density  $\rho_f$  (freeze-out density). This is just as in ordinary fission. The saddle point (which has a rather compact shape) resembles the final channel of fission by way of having a fairly well-defined mass asymmetry. Nuclear interaction between fission prefragments ceases after descent of the system from the top of the barrier to the scission point.

Figure 8 presents the proposed spinodal region in the T- $\rho$  plane with the experimental data obtained by FASA. The points for the partition and freeze-out configurations are located at  $\rho_t$



and  $\rho_f$ . These points are deep inside the spinodal region, the top of which is specified by the critical temperature,  $T_c$ , for the liquid-gas phase transition.

Fig.8. The proposed spinodal region for a nuclear system. The experimental points were obtained by the FASA collaboration. The arrow line shows the way of

These studies will be continued. The first priority tasks (for the next 3 years) are the following:

1. Further investigation of the evolution of the thermal multifragmentation mechanism with increasing the projectile mass from the relativistic protons to neon. As a result, the nature of the collective flow observed for the beams heavier than helium will be found out.

2. Obtaining and analysis of the experimental data on IMF multiplicity, their charge and energy distributions, as well as the angular and velocities correlations, to get new information on the nuclear liquid-fog phase transition.

3. Study of the dependence of the IMF-IMF correlation function (with respect to the relative angle and velocity) on the entrance channel conditions to obtain new information about spatial configuration of the system at the break-up.

4. Investigation of the expansion dynamics of hot nuclei driven by thermal pressure, measuring the mean time of expansion. Experimental method for that is now under development.

### Anomalous behavior of the $dp$ elastic cross-section (Sagara discrepancy)

Anomalous behavior of the  $dp$  elastic cross-section is called Sagara discrepancy. This effect reflects the experimental fact that modern nucleon-nucleon potentials can not reproduce the behavior of the cross section in deuteron-proton elastic scattering in the vicinity of  $120^\circ$  in the c.m.s. (fig.9). Only taking into account strong contribution of the 3 nucleon forces allows to reach an agreement with the data. The influence of the 3 nucleon forces on this effect is studied at the LNS setup (leader V.P. Ladygin). The LNS detectors are now at stage of construction and calibration and the first measurements are beginning (fig.10).

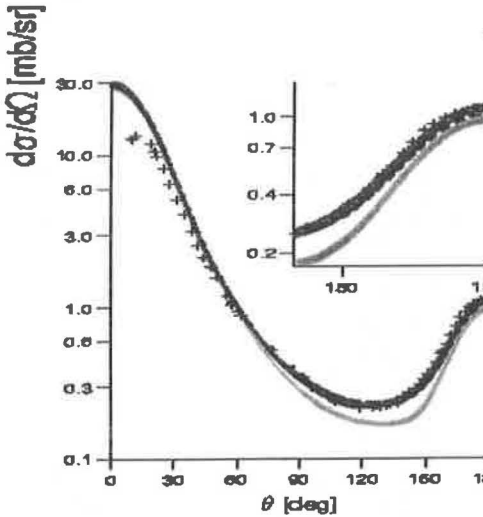
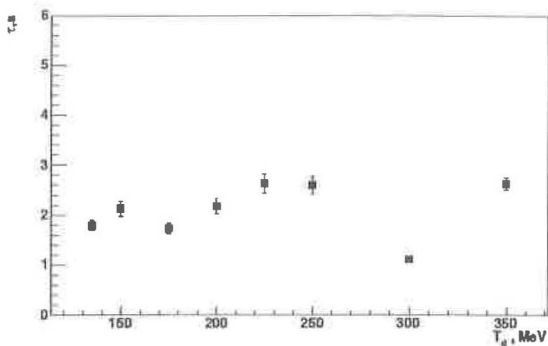


Fig.9. Sagara discrepancy effect: modern nucleon-nucleon potentials can not reproduce the behavior of the cross section in  $dp$  elastic scattering in the vicinity of  $120^\circ$  in c.m.s.

Fig.10. Deuteron beam lifetime at the internal Nuclotron target station vs deuteron kinetic energy  $T_d$



### The study of spin structure of three nucleon systems

The main objective of the joint VBLHE-RIKEN experiment (pHe3 project, leaders V.P. Ladygin and T. Uesaka, Japan) is to study the  ${}^3\text{He}$  ( ${}^3\text{H}$ ) structure at distances, beyond the reach of electromagnetic probes at present, by measuring the angular dependences of the tensor analyzing powers  $A_{yy}$ ,  $A_{xx}$  and  $A_{zz}$  in the  $d+d \rightarrow {}^3\text{He}+n$  and  $d+d \rightarrow {}^3\text{H}+p$  reactions [10]. These polarization observables are sensitive to the neutron (proton) spin distributions in  ${}^3\text{He}$  ( ${}^3\text{H}$ ) at small distances in the framework of one-nucleon data exchange. On the other hand, both  ${}^3\text{He}$  and  ${}^3\text{H}$  are mirror nuclei with respect to the number of protons and neutrons, and the difference in their observed values can be interpreted in terms of charge symmetry violation.

An interesting fact is that interactions of polarized deuterons with polarized  ${}^3\text{He}$  nucleus are allowed only in D state (D wave). This fact is demonstrated in fig.11. So, since interaction of polarized deuterons with polarized  ${}^3\text{He}$  nucleus is possible only in D state, a pure D wave in a deuteron can be studied in this process.

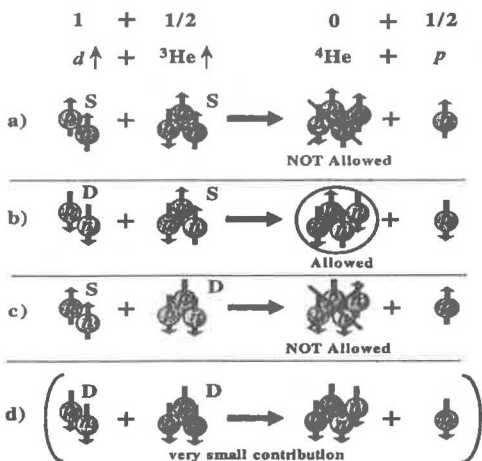


Fig.11. Possible interaction mechanisms between polarized deuterons and polarized  ${}^3\text{He}$  nuclei

The view of the He3 polarized target manufactured at CNS, Japan, is presented in fig.12.

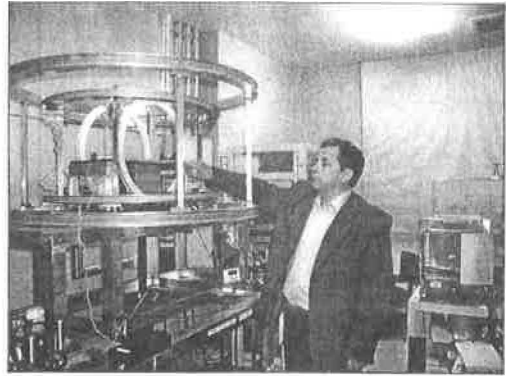


Fig.12. The view of the He3 polarized target manufactured at CNS, Japan for pHe3 project

### New results on measurement of np total cross section difference $\Delta\sigma_L(np)$

New accurate results of the neutron-proton spin-dependent total cross section difference  $\Delta\sigma_L(np)$  at the neutron beam kinetic energies 1.39, 1.69, 1.89 and 1.99 GeV were obtained [11]. The results are shown in fig.13.

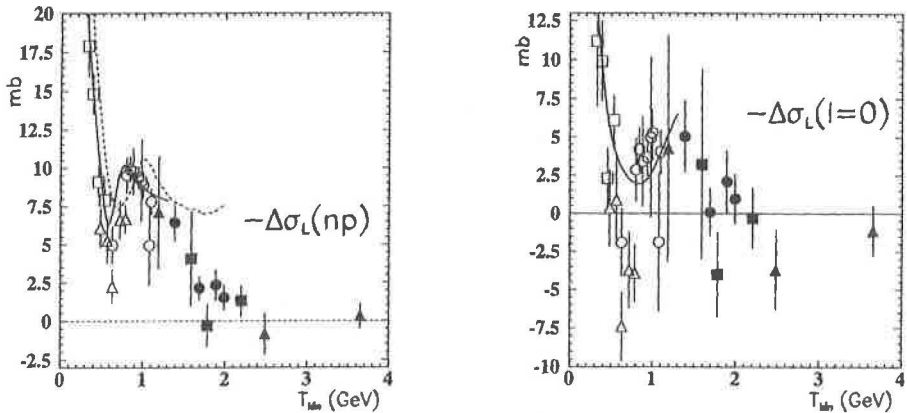


Fig.13. Energy dependence of  $-\Delta\sigma_L(np)$  (left) and  $-\Delta\sigma_L(l=0)$  (right). The symbols denote: black dots – our experimental data, black triangles and black squares - our earlier data, open squares - PSI data, open triangles – LAMPF data, open circles – Saturn II data

The measured  $\Delta\sigma_L(np)$  values are compatible with the existing np results, using free neutrons. The rapid decrease of  $\Delta\sigma_L(np)$  values above 1.1 GeV is confirmed and a minimum or a “shoulder” around 1.8 GeV is observed.

The  $\Delta\sigma_L(I=0)$  values obtained from the measured  $\Delta\sigma_L(np)$  values and the existing  $\Delta\sigma_L(np)$  data are also presented. They show a plateau or a weak maximum around 1.4 GeV, followed by a rapid drop with energy growth and by a minimum around 1.8 GeV.

The obtained results were compared with the dynamic model predictions and with the recent ED GW/VPI PSA fit. The necessity of further accurate  $\Delta\sigma_L(np)$  measurements around 1.8 GeV and new  $\Delta\sigma_L(np)$  data in the kinetic energy region above 1.1 GeV is emphasized. The spin-dependent results were supplemented by the measurement of unpolarized total cross sections  $\sigma_{\text{tot}}(np)$  and  $\sigma_{\text{tot}}(nC)$ .

### Clustering pattern of light nuclei in peripheral dissociation above 1 A·GeV

In 2004, emulsion stacks were exposed to 2.0 A·GeV/c  ${}^9\text{Be}$ ,  ${}^8\text{B}$ , and  ${}^9\text{C}$  nuclei (The BECQUEREL project, leader P.I. Zarubin).

The clear production of “white” stars with  $\alpha$  particle pairs is initiated in the  ${}^9\text{Be}$  fragmentation with removal of a loosely bound neutron (fig.14). An analysis of the data will allow one to conclude about clustering in the  ${}^9\text{Be}$  nucleus and extent experience of  ${}^8\text{Be}$  identification in  $n$ - ${}^8\text{Be}$ ,  $n$ - ${}^8\text{Be}^*$ , and  $\alpha n\alpha$  excitations [12-15].

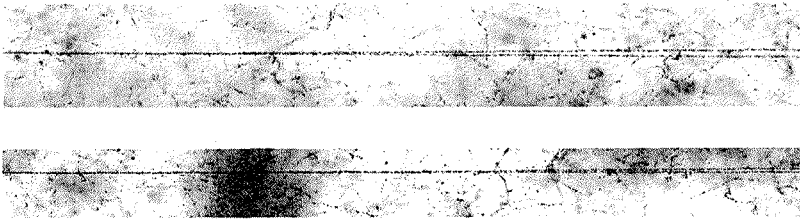


Fig. 14. Examples of the events of the peripheral  ${}^9\text{Be}$  in emulsion at 1.3 A·GeV: a splitting to two  $\text{He}$  fragments (upper photo) without target nucleus excitation or visible recoil and to two  $\text{He}$  fragments with a recoil proton (lower photo).

It is planned to determine the relative probabilities of  ${}^8\text{B}^* \rightarrow p{}^7\text{Be}$ ,  $p{}^3\text{He}\alpha$ ,  $pp{}^6\text{Li}$ , and  $ppd\alpha$ . There arises a possibility of studying the decays  ${}^7\text{B} \rightarrow ppp\alpha$  and  $p{}^3\text{He}{}^3\text{He}$  since a nuclear stability border gets crossed in the  ${}^8\text{B} \rightarrow {}^7\text{B}$  fragmentation. In the relativistic case such decays would be appearing as narrow jets convenient for analysis.

### Using carbon-12 beam for cancer therapy

The JINR Program advisory committee approved in 2004 a new MED-NUCLOTRON project. During the first stage of this project it is planned to prepare the Nuclotron carbon beam with the parameters required for irradiation of patients. The first measurements of the Bragg peak at the  ${}^{12}\text{C}$  Nuclotron beam are presented in fig.15. The energy of the carbon beam was 500 A·MeV.

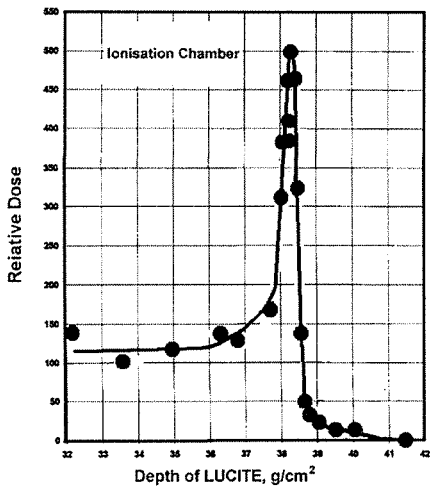


Fig.15. The Bragg peak of 500 A·MeV <sup>12</sup>C ions from Nuclotron

During the next three years the required carbon beam and a special place for irradiation of biological samples will be prepared.

### 3.2. Results obtained at other accelerator centers and plans for 2005-2007

#### Suppression of high $p_t$ hadrons

The VBLHE group (leader A.G.Litvinenko) participated in design and manufacturing of the aerogel detector for the PHENIX setup. The detector system consisting of 80 aerogel counters was assembled, tested and installed at the PHENIX setup and used for obtaining new physical information at RHIC in 2004.

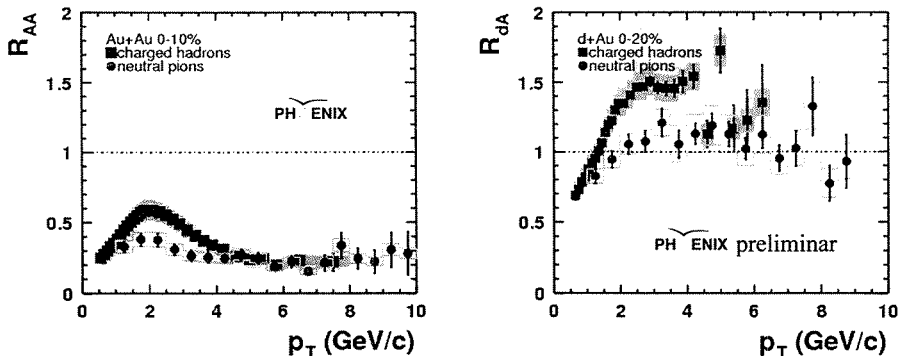


Fig.16. High  $p_t$  hadron suppression in  $Au + Au$  collisions (left) and in  $d + Au$  collisions (right) obtained in PHENIX experiment at RHIC

At the PHENIX setup the new data on suppression of high  $p_t$  hadrons in  $d + Au$  collisions were obtained in addition to the earlier obtained data on such suppression in  $Au + Au$  collisions (fig.16). As seen from this picture, significant suppression of high  $p_t$  hadrons is observed in  $Au + Au$  interactions, while in  $d + Au$  interactions such suppression is not observed [16]. High  $p_t$  hadron suppression in the  $Au + Au$  collisions is interpreted as a result of strong energy losses in quark-gluon plasma in central collisions at RHIC energies (Jet Quenching Effect).

The similar result was obtained in the STAR experiment at RHIC. The VBLHE group headed by Yu.A. Panebratsev took active part in this work (fig.17).

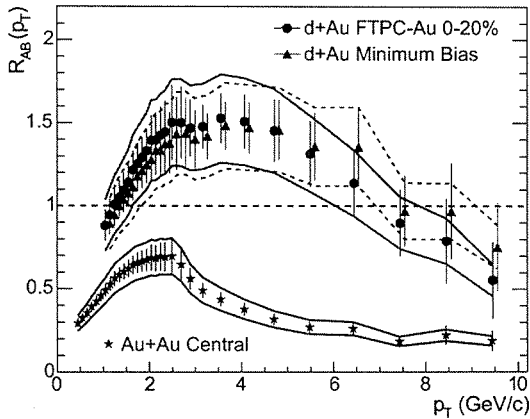


Fig.17. High  $p_t$  hadron suppression in  $Au + Au$  collisions and in  $d + Au$  collisions obtained in STAR experiment at RHIC

High  $p_t$  hadron suppression in central  $Au + Au$ , but not in  $d + Au$ , clearly proves Jet Quenching Effect to be a final-state phenomenon, indicating very strong interactions of hard-scattered partons or their fragments with dense, dissipative medium.

Participation in PHENIX and STAR experiments at RHIC will be continued in 2005-2007.

### Heavy ions interaction at CERN SPS

The  $e^+e^-$  invariant-mass spectrum obtained at the NA45 setup (SPS, CERN) is presented in fig.18. The enhancement of the experimental data compared to the hadron cocktail in the mass range  $m_{c+c^-} > 200 \text{ MeV}/c^2$  is  $3.1 \pm 0.3$  (stat.) The VBLHE group (leader Yu.A. Panebratsev) conducted comparison of the experimental data with various models in 2004. The NA45 spectrometer offers a unique possibility to study  $\phi$ -meson production in the  $K^+K^-$  decay channel also. The group obtained the new data on  $\phi$ -meson production in nuclear matter in  $Pb + Au$  collisions (invariant mass and transverse momentum spectra).

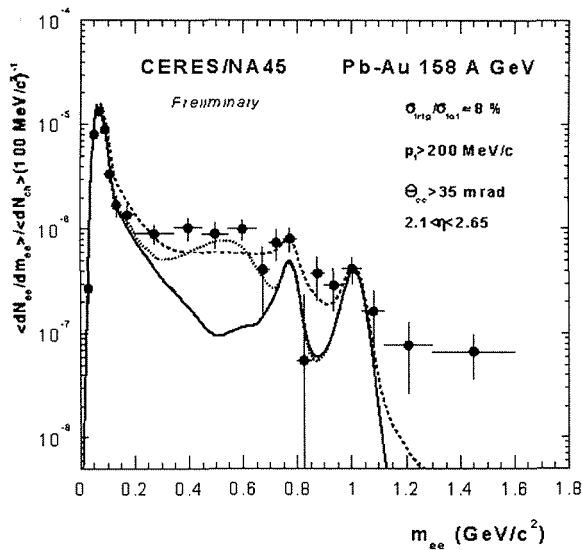


Fig.18. The  $e^+e^-$  invariant-mass spectrum obtained in the NA45 experiment at SPS, CERN

The group of Yu.A. Panebratsev also participated in the preparation for study of  $e^+e^-$  production in heavy ion collisions at LHC CERN.

The group of G.L. Melkumov actively participate in the NA49 experiment. During 2004 the following results were obtained [17-19]:

1. The results on the pentaquark baryon with  $S = -2$  and strangeness production from 20 to 158 A-GeV, and energy and centrality dependence of deuteron and proton production in  $Pb+Pb$  collisions at the CERN-SPS were published.
2. Presentations at the conference Quark Matter 2004 and Strange Matter 2004 were made.
3. A new proposal from NA49 was prepared and presented at the SPSC workshop in Villars in September 2004.

It is planned participate in the NA49 experiment in future. The nearest plans of participation in the NA49 experiment are the following:

1. Calibration of the TOF data. Processing and analysis of the antiproton and antideuteron data and submission of the results for publication.
2. Upgrade of the NA49 detector for the experiments after 2005. Inspection and repairment of the Dubna TOF detector.
3. Further analysis of the data obtained at the NA49 on the energy, centrality and size dependence of particles produced in  $pp$ ,  $pA$ ,  $CC$ ,  $SiSi$  and  $PbPb$  collision.

## Participation in preparation of the experiments for LHC in CERN

The group of A.S. Vodopianov continued to participate in ALICE project for LHC in CERN.

The main results obtained in 2004 are the following:

1. The yoke of the dipole magnet was successfully assembled in the ALICE underground area by the JINR team.
2. 230 lead tungstate crystals were delivered for the photon spectrometer (PHOS) from Kharkov (Ukraine) to JINR.
3. The data analysis program for the PHOS beam test data was performed.
4. During the summer of 2004 JINR physicists took part in the beam test of PHOS calorimeter prototype of 256 crystals at the CERN beams.
5. The construction of drift chambers for TRD detector started at JINR (leader Yu.V. Zanevsky). Further development of the Kalman filter method for the dimuon spectrometer tracking is going on in collaboration with SUBATECH (Nantes, France).
6. Simulation of  $p$ - $Pb$  and  $Pb$ - $p$  interactions for the production of Upsilon family was performed.

Some expected results in 2005-2007:

1. Production of the crystals for the photon spectrometer.
2. Construction of the spectrophotometer to test crystals.
3. Participation in the assembly of the 1<sup>st</sup> PHOS module at CERN.
4. Preparation of the test setup to test PHOS module at RHIC (BNL).
7. Continuation of the construction of the drift chambers for TRD detector.
8. Continuation of the study of the quarkonia production at  $pA$  and  $Ap$  interaction for the dimuon spectrometer for the various level of collision centrality.
9. Organization of the ALICE-Russia and ALICE-JINR participation in the Data Challenge in the framework of GRID.

Another VBLHE group (leader A.I. Malakhov) participated in CMS project. This group participated in development of Heavy Ion Program for CMS and in the test beam run of the hadronic calorimeter and electronics at CERN in 2004. V.P.Ladygin and T.A.Vasiliev took part in the test beam run on calibration of the Hadron Endcap Calorimeter at CERN. The express online analysis of some data was performed. In particular, the VBLHE group obtained the ratios of the calibration coefficients for different types of particles. With these coefficients the resolution of Hadron Endcap Calorimeter  $\sigma_E/E \approx 12.5\%$  for 150 GeV pion beam was obtained (see Fig.19).

The VBLHE group also continued the analysis of the wire-source calibration data for Hadron Endcap Calorimeter. The semi-automatic procedure to obtain the calibration constants was developed. The effect of geometry due to the various sizes of the scintillators obtained as a ratio of the signal from the wire source to the collimated source was studied. This effect was found to be several per cents, which is essential for correct calibration of the Hadron Endcap Calorimeter.

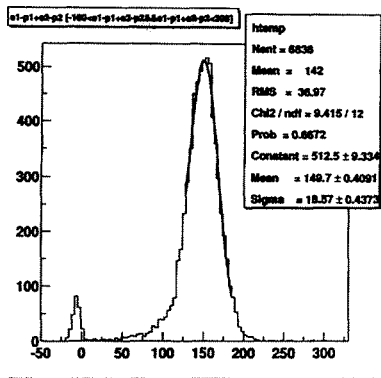


Fig.19. Signal from 150 GeV pions in Hadron Endcap Calorimeter

### Collaboration with GSI

The group of Yu.V. Zanevsky continued participation in HADES experiment. The following was carried out for HADES:

- six low mass multilayer inner drift chambers were constructed, tested and integrated into the HADES spectrometer.
- Front End Electronics for Drift Chambers system was developed and tested.
- track reconstruction software was developed and successfully applied for data analysis.

The preliminary effective mass spectrum of  $e^+e^-$  pairs obtained at HADES for  $Ca + Ca$  interactions at 2.2 A-GeV is presented in fig.20. It is in a good agreement with the simulation.

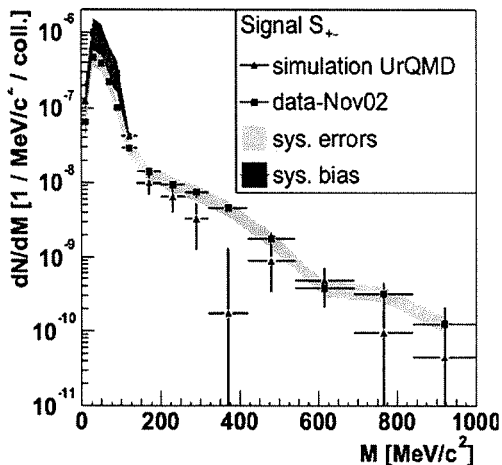


Fig.20. The preliminary effective mass spectrum of  $e^+e^-$  pairs obtained at HADES

The following studies are planned in 2005-2007:

- dielectrons from  $pp/pd$  interactions
- threshold  $\eta$  production in  $d + p$  collisions
- $\omega$  production in  $pp$  collisions
- dielectrons from  $Ca + Ca$  interactions.

The VBLHE participates in R&D for the New Facility at GSI (FAIR – Facility for Antiproton and Ion Research) (accelerators, detectors, and physics):

- fast-ramped magnets (Nuclotron-type)
- SIS100/SIS300 lattice optimization
- cryogenic magnetic system, superconductive beam lines
- TRD detector for the CBM project
- superconductive magnets for the CBM and PANDA projects
- simulation (track fitter and track finder)
- physical program (production of vector mesons and lambda particles in nuclear collisions)

The main topics of the VBLHE research programme in 2005-2007 are presented in table.3.

Table 3. Main topics of the VBLHE research programme in 2005-2007

<b>Polarization Phenomena at Relativistic Energies</b>
<ul style="list-style-type: none"> <li>▪ Spin effects in the interactions of polarized nucleons and the lightest nuclei at energies above 1 GeV: <i>ALPOM, KAPPA, SMS MSU, DISK, SPIN, BES, SINGLET</i></li> <li>▪ Spin structure of the <math>np</math> forward scattering amplitude: <i>DELTA-SIGMA</i></li> <li>▪ Spin-dependent part of the nucleon scattering amplitude: <i>STRELA</i></li> <li>▪ Search for the role of three nucleon forces: <i>pHe3, LNS</i></li> <li>▪ Investigation of the spin structure of the lightest nuclei at short distances: <i>PIKASO</i></li> <li>▪ Investigation of meson production and resonances in collisions of polarized nucleons and the lightest nuclei: <i>DELTA-2, NIS and WASA (CELSIUS, Uppsala)</i></li> </ul>
<b>Nuclear Beams at Relativistic Energies</b>
<b>Study of multiple production processes in collisions of relativistic nuclei from the lightest to the heaviest ones at energies from hundreds of MeV to TeV</b>
<ul style="list-style-type: none"> <li>▪ Investigation of multiple particle production at the Nuclotron energies in inclusive and semi-inclusive measurements and measurements in <math>4\pi</math>- geometry: <ul style="list-style-type: none"> <li>○ External Beams: <i>BECQUEREL, MARUSYA, SMS MSU, DISK</i></li> <li>○ Internal Beams: <i>MARUSYA, DELTA-2, LNS</i></li> </ul> </li> <li>▪ Study of asymptotic multiple particle production at ultrarelativistic energies: <i>STAR, PHENIX (BNL), ALICE, NA49 and Heavy_Ions@CMS (CERN)</i></li> <li>• Participation in the new International Project at GSI.</li> </ul>
<b>Manifestation of the structure and excited states of nuclei at relativistic energies</b>
<ul style="list-style-type: none"> <li>▪ Research of clusterization in light stable and radioactive nuclei: <i>BECQUEREL</i></li> <li>▪ Investigation of multifragmentation of the medium and heavy target nuclei: <i>FAZA</i></li> <li>▪ Investigation of light hypernuclei: <i>GIBS</i></li> <li>▪ Observation of eta-mesonic nuclei: <i>ETA-NUCLEI</i></li> <li>▪ Search for pentaquarks: <i>NIS (Together with LPP), GIBS, NA49</i></li> <li>▪ Investigation of lepton pairs: <i>NA45 (CERN), HADES (GSI)</i></li> </ul>
<b>Applied Research using the Nuclotron Relativistic Nuclear Beams</b>
<ul style="list-style-type: none"> <li>▪ Provision of space apparatus elements with ground tests</li> <li>▪ Radiobiology and space biomedicine (in cooperation with DRRR). Transmutation of radioactive wastes, problems of the electronuclear energy generation method: <i>GAMMA-2, Energy+Transmutation</i></li> <li>▪ Use of the carbon beam for medical purposes (in cooperation with DLNP): <i>MED-NUCLOTRON</i></li> </ul>

## References

1. A.I.Malakhov. Research program for the Nuclotron. Nuclear Physics, A734C, (2004) pp. 82-90.
2. A.I.Malakhov. Relativistic Nuclear Physics at the Veksler and Baldin Laboratory of High Energies. Physics of Particles and Nuclei. Vol.1, No.6 (2004) pp.314-324.
3. Yu.S.Anisimov et al., Polarimeter for Nuclotron Internal Beam. Particles and Nuclei, Letters. 2004, №1[118], p.68-79.
4. A.Yu.Isupov. DAQ Systems for the High Energy and Nuclotron Internal Target Polarimeters with Network Access to Polarization Calculation Results and Raw Data. JINR Preprint, E10-2004-13, Dubna (2004).
5. Yu. A.Troyan et al., D1-2004-39, Dubna, 2004; hep-ex/0404003.
6. P. Togoo et al., Proc.of the Mongolian Academy of Sciences, vol.170, No.4, p.3, 2003.
7. C.Alt, T.Anticic, B.Baatar, D.Barna, ..., V.I.Kolesnikov, ..., A.I.Malakhov, G.L.Melkumov et al. (NA49 Collaboration). Evidence for an Exotic  $S = -2$  and  $Q = -2$  Barion Resonance in Proton-Proton Collisions at the CERN SPS. Phys.Rev.Lett., V.92, No.4, (2004) pp. 042003-1 – 042003-5.
8. V.A.Karnaukhov, et al., Nucl.Phys.A 734 (2004) 520.
9. V.A.Karnaukhov, et al., Phys. Rev.C 70 (2004) 1 (R)
10. V.P.Ladygin, T.Uesaka, T.Saito, M.Hatana, A.Yu.Isupov, H.Kato, N.B.Ladygina, Y.Maeda, A.I.Malakhov, J.Nishikawa, T.Ohnishi, H.Okamura, S.G.Reznikov, H.Sakai, N.Sakamoto, S.Sakoda, Y.Satou, K.Sekiguchi, K.Suda, A.Tamii, N.Uchigashima, K.Yako. Measurements of tensor analyzing power  $T_{20}$  in  $dd \rightarrow {}^3\text{He} n$  and  $dd \rightarrow {}^3\text{He} p$  at intermediate energies and at zero degree. Phys.Lett. B598, (2004) pp. 47-54.
11. V.I.Sharov, N.G.Anischenko, V.G.Antonenko, S.A.Averichev, L.S.Azhgirey et al. Measurement of the np total cross section difference  $\Delta\sigma_1(np)$  at 1.39, 1.69, 1.89 and 1.99 GeV. Eur.Phys.J. C37, (2004) 79-90.
12. V.Bradnova, M.M.Chernyavsky, A.Sh.Gaitinov, L.A.Goncharova, L.Just, S.I.Kharlamov, A.D.Kovalenko, M.Haiduc, V.G.Larionova, F.G.Lepekhin, A.I.Malakhov, G.I.Orlova, N.G.Peresadko, N.G.Polukhina, P.A.Rukoyatkin, V.V.Rusakova, N.A.Salmanova, B.B.Simonov, S.Vokal, P.I.Zarubin, I.G.Zarubina. Studies of Light Nucleus Clustering in Relativistic Multifragmentation Processes. Acta Physica Slovaca, Vol.54, No.4, (2004) pp.1-15.
13. M.I.Adamovich, V.Bradnova, S.Vokal, S.G.Gerasimov, V.A.Dronov, P.I.Zarubin, A.D.Kovalenko, K.A.Kotelnikov, V.A.Krasnov, V.G.Larionova, F.G.Lepekhin, A.I.Malakhov, G.I.Orlova, N.G.Peresadko, N.G.Polukhina, P.A.Rukoyatkin, V.V.Rusakova, N.A.Salmanova, B.B.Simonov, M.M.Chernyavsky, M.Haiduc, S.P.Kharlamov, and L.Just. Phys. of Atomic Nuclei, Vol.67, No.3 (2004), pp.514-517.
14. V.Bradnova, M.M.Chernavsky, L.Just, M.Haiduc, S.P.Kharlamov, A.D.Kovalenko, V.A.Krasnov, V.G.Larionova, A.I.Malakhov, G.I.Orlova, N.G.Peresadko, N.G.Polukhina, P.A.Rukoyatkin, V.V.Rusakova, N.A.Salmanova, S.Vokal, P.I.Zarubin. Nuclear Clustering Quest in Relativistic Multifragmentation. Proceedings of the XVI International Baldin Seminar on High Energy Physics Problems. Relativistic Nuclear Physics and Quantum Chromodynamics. Edditors: A.N.Sissakian et al, Vol.II, (2004) pp.131-134.

15. N.P.Andreeva et al. (BECQUEREL Collaboration), Toplogy of “White Stars” in Relativistic Fragmentation of Light Nuclei. Preprint of JINR, P1-2004-91, Dubna (2004).
16. S.S.Adler, S.Afanasiev,...,A.Isupov, V.Ladygin, A.Litvinenko, A.Malakhov, V.Peresedov, L.Zolin et al. High- $p_T$  charged hadron suppression in Au+Au collisions at  $\sqrt{s_{NN}} = 200$  GeV. Physical Review C **69**, 034910 (2004).
17. T.Anticic, B.Baatar, D.Barna, ..., V.I.Kolesnikov, ..., A.I.Malakhov, G.L.Melkumov et al.  $\Lambda$  and anti- $\Lambda$  in Central Pb-Pb Collisions at 40, 80 and 158 A GeV. Phys.Rev.Lett, V. 93, No.2, (2004) pp. 022302-1 – 022302-5.
18. T.Anticic, B.Baatar, D.Barna, ..., V.I.Kolesnikov, ..., A.I.Malakhov, G.L.Melkumov et al. Transverse momentum fluctuations in nuclear collisions at 158 A GeV. Physical Review C **70** (2004) pp.034902-1 – 034902-14.
19. T.Anticic, B.Baatar, J.Bartke,..., V.I.Kolesnikov, ..., A.I.Malakhov, ..., G.L.Melkumov et al. Energy and centrality dependence of deuteron and proton production in  $Pb+Pb$  collisions at relativistic energies. Physical Review C **69**, 024902 (2004).

# INVARIANT ANALYSIS OF THE FRAGMENTATION OF RELATIVISTIC NUCLEI IN EMULSION

D. A. Artemenkov<sup>1)</sup>, V. Bradnova<sup>1)</sup>, M. M. Chernyavsky<sup>2)</sup>, L. A. Goncharova<sup>2)</sup>,  
M. Haiduc<sup>3)</sup>, A. D. Kovalenko<sup>1)</sup>, A. I. Malakhov<sup>1)</sup>, G. I. Orlova<sup>2)</sup>, N. G. Polukhina<sup>2)</sup>,  
P. A. Rukoyatkin<sup>1)</sup>, V. V. Rusakova<sup>1)</sup>, E. Stan<sup>1,3)</sup>, R. Stanoeva<sup>1,5)</sup>, E. Stefan<sup>3)</sup>,  
T. V. Schedrina<sup>1)</sup>, I. Tsakov<sup>5)</sup>, S. Vokal<sup>1,4)</sup>,  
A. Vokalova<sup>1)</sup>, J. Vrlakova<sup>4)</sup>, P. I. Zarubin<sup>1)</sup>, I. G. Zarubina<sup>1)</sup>

<sup>1)</sup>Joint Institute for Nuclear Research, Dubna, Russia.

<sup>2)</sup>Lebedev Institute of Physics, Moscow, Russia.

<sup>3)</sup>Institute of Space Sciences, Bucharest-Maguerele, Romania.

<sup>4)</sup>P. J. Safarik University, Kosice, Slovak Republic.

<sup>5)</sup>Institute for Nuclear Research and Nuclear Energy, Sofia, Bulgaria.

The pattern of the fragmentation of relativistic nuclei of energy above 1 A GeV in emulsion is represented in invariant variables. New data extracted from emulsions exposed to 2.1 A GeV <sup>14</sup>N and 1.2 A GeV <sup>9</sup>Be nuclei suggest the advantages of the emulsion technique in obtaining unique information on the decay of light nuclei to a few fragments with charges 1 and 2.

## INTRODUCTION

A detailed study of relativistic fragment systems formed in the dissociation of nuclei of energy above 1 A GeV provides a qualitatively better understanding of the structure of nuclear excitations above the decay thresholds. In accordance with the classification developed in papers [1-6], fragmentation results in the production of fragment jets which are determined by the invariant variable region concentrated within  $10^{-4} < b_{ik} < 10^{-2}$ , where  $b_{ik} = -(P_i/m_i - P_k/m_k)^2$ ,  $P$  and  $m$  are the four-momenta and the masses of the  $i$  and  $k$  fragments.

The lower limit corresponds to the decay <sup>8</sup>Be → 2α (decay energy 92 KeV), while the upper one - to the upper limit of non-relativistic nuclear processes as suggested by A. M. Baldin. The latter go at the level of nucleon-nucleon interactions without inclusion of the meson degrees of freedom. For the sake of illustration of the events of this class, fig. 1 gives as an example an event of relativistic <sup>14</sup>N dissociation without visual target-nucleus excitation or meson production.

The expression of the data via the relativistic invariant variable  $b_{ik}$  makes it possible to associate in a common form data on multiple target-nucleus and relativistic projectile fragmentation. There is a close connection between the  $b_{ik}$  variables and the invariant mass of the system of fragments  $M^{*2} = (\Sigma P_j)^2 = \Sigma(P_i \cdot P_k)$  and the excitation energy  $Q = M^* - M$ , where  $M$  is the mass of the ground state of the nucleus corresponding to the charge and the weight of the system being analyzed.

Within the invariant approach, an optimal strategy which would take into account the formulation of the problem, the properties of the nucleus studied and limitations on real measurements is chosen by experiment. In the present talk, the advantages of this approach are discussed using the available data on nuclear fragmentation in emulsion (see [7-8] and references herein). New data for 2.1 A GeV <sup>14</sup>N and 1.2 A GeV <sup>9</sup>Be nuclei are extracted from a minor portion of the processed material. They enable one only to outline promising approaches to future analysis. A significant difference in the energy of the nuclei studied was due to practical circumstances in emulsion exposure. The presentation of the data in the invariant form makes it possible to overcome this obstacle when comparing them.

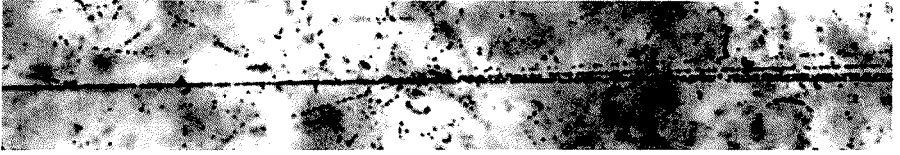


Fig. 1. Fragmentation of  $^{14}\text{N}$  nucleus at 1.2 A GeV in emulsion. The interaction vertex and a fragment jet in a narrow angle cone are seen on the photograph. Following the direction of the fragment jet it is possible to make out 3 fragments with  $Z = 2$  and 1 fragment with  $Z = 1$

The nuclear emulsion technique seems to be most suitable for the study of fragmentation of relativistic nuclei up to a total breakup to single-charged fragments. More images reflecting capabilities of emulsion technique can be found via the Web [10]. It should be noted that this method imposes some restrictions on the determination of the four-momentum components of fragments. Firstly, the possibility of obtaining the value of the spatial momentum per nucleon of a fragment is limited. As a rule, it is suggested to be equal within a few percent to the primary nucleus value which is a quite reasonable approximation. Secondly, the mass identification is possible only for relativistic hydrogen isotopes and hardly for helium isotopes. Therefore the alpha particle mass is taken for the mass of two-charged fragments which also is a good approximation when selecting stable nuclear fragments in a narrow fragmentation cone. The scalar product of unit vectors which determine the direction of fragment emission plays the decisive role in  $b_{ik}$ ,  $M$  and  $Q$  estimates. Thus, owing to a record spatial resolution the nuclear emulsion method can yield unique evidence about the characteristics of narrow jets of  $Z = 1, 2$  fragments with a total nuclear dissociation.

### $^{22}\text{Ne}$ NUCLEUS FRAGMENTATION

The formation of a nuclear state analogous to a dilute Bose gas at the atomic level can be revealed in narrow jets of doubly charged relativistic fragments near the threshold of production of an ensemble consisting of few alpha particles [11]. Such ensembles are inwardly non-relativistic systems and can possess quantum coherence. It can be predicted that these systems would have similar characteristics when they are produced under various conditions. Another property of these systems is a very narrow distribution in velocities in the c.m.s. [11]. The determination of the system c.m.s. for each event is rather complicated and not efficient. It is just in this case that the analysis of jets in the  $b_{ik}$  four-velocity space enables one to formulate the properties of few body systems in the most universal manner.

We have at our disposal data on 4100 events from 3.3 A GeV  $^{22}\text{Ne}$  interactions which contain classification of secondly tracks by ionization and angles. Tracks classified as relativistic alpha particles were in a  $6^\circ$  cone with respect to the primary nucleus track. The helium isotopes can play a more significant role as compared to the symmetric nuclei due to the presence of a pair of external neutrons. This fact can be used for more effective generation and detection of five alpha particle systems in stimulating dissociation by a neutron knockout process.

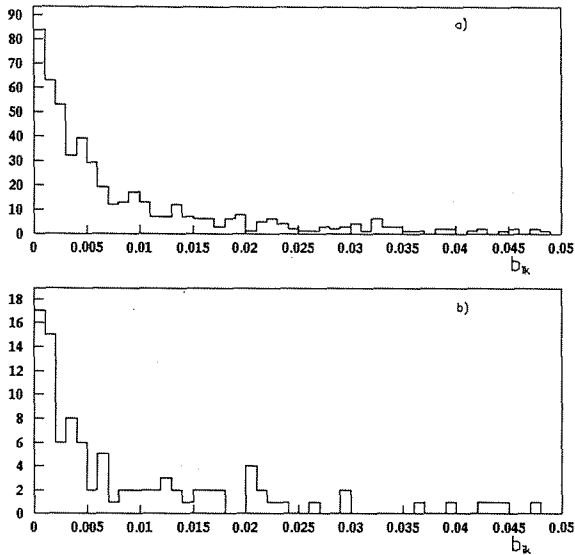


Fig. 2. The  $b_{ik}$  distribution for the fragmentation channels  $^{22}\text{Ne} \rightarrow 2\alpha$  (a) and  $^{22}\text{Ne} \rightarrow 5\alpha$  (b)

Fig.2 shows the  $b_{ik}$  distribution for the fragmentation channel  $^{22}\text{Ne} \rightarrow 2\alpha$  (a) and  $^{22}\text{Ne} \rightarrow 5\alpha$  (b) channel (10 events). The dominant fraction of the relative velocities defining the dispersion of relativistic jets satisfies a non-relativistic criterion  $b_{ik} < 10^{-2}$ . It appears that the distribution "tails" are due to the  $^3\text{He}$  nucleus formation proceeding at a higher momentum transfer. In spite of a significant difference in the composition of the systems, both distributions look rather similar. Fig. 3 give the ratios of the distributions in the channels  $^{22}\text{Ne} \rightarrow 3\alpha$  (a) and  $^{22}\text{Ne} \rightarrow 4\alpha$  (b) to the one in the  $^{22}\text{Ne} \rightarrow 2\alpha$  channel. The narrow "helium" jet production process is seen to be universal with high statistical provision.

3 events of a decay  $^{22}\text{Ne} \rightarrow 5\alpha$  are found with the secondary tracks are within a  $3^\circ$  cone and are accompanied by neither target fragments nor produced mesons ("white" stars). Of them, in 2 events all tracks are within no more than  $1^\circ$ . For these two events the invariant excitation energy normalized to the nucleon number  $(M_{5\alpha}^* - 5m_\alpha)/4n_\alpha$  is estimated to be 400 and 600 KeV. These values are essentially lower than the Coulomb barrier. The detection of such events in emulsion and their preliminary metrology are serious arguments in favor of systematic studies of the phase transition of nuclei to a dilute Bose gas of alpha particles on the basis of much larger statistics and for a great variety of nuclei.

### $^{14}\text{N}$ NUCLEUS FRAGMENTATION

We are presently engaged in accumulating statistics on the interactions of  $^{14}\text{N}$  nuclei of an energy of 2.1 A GeV in emulsion for the study of "white" stars  $^{14}\text{N}^* \rightarrow d(p)\alpha\alpha\alpha$  in a forward cone to  $8^\circ$  degrees. The major task is a rapid search for "white" stars the cross section for which constitutes a few percent of the inelastic cross section. By viewing over primary tracks 540 events of interactions of  $^{14}\text{N}$  nuclei with emulsion nuclei, including 25 "white" stars, were already found. There is an indication of an important role of the charge configuration  $2+2+2+1 - 12$  such events were found. An example of such star is given in fig. 1.

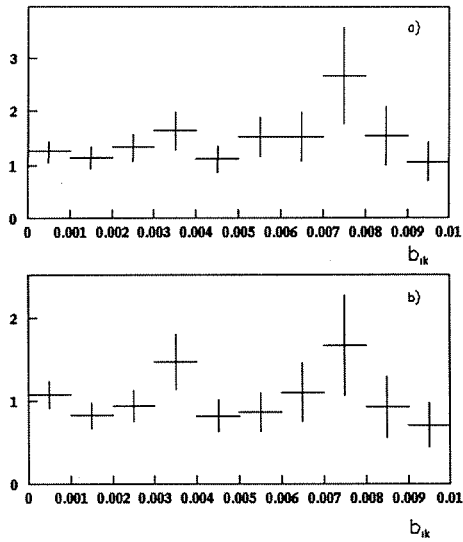


Fig. 3. The ratio of the  $b_{ik}$  distributions for the fragmentation channels  $^{22}\text{Ne} \rightarrow 3\alpha$  (a) and  $^{22}\text{Ne} \rightarrow 4\alpha$  (b)

A 6+1 configuration which is similar to the events with separation of  $Z=1$  fragments in the dissociation of heavier symmetric nuclei (6 events) is found to be important. A multiple scattering of  $Z=1$  tracks in emulsion is analyzed for the purpose of identifying it in mass. Preliminary data indicate that the ratio of protons to deuterons is approximately as 2:1. This implies that the fraction of fragments-deuterons noticeably decreases as compared with the cases of relativistic fragmentation of  $^6\text{Li}$  and  $^{10}\text{B}$  nuclei (2+2+1 channel), where the proton and deuteron yields are equal. It is seen that the role of clustering in the form of deuterons becomes evidently less important which is in agreement with a large threshold of their separation as compared to protons.

A leading role of the channel 2+2+2+1 in the  $^{14}\text{N}$  fragmentation implies that the exploration of three alpha particle systems at  $b_{ik} < 10^{-2}$  is prospective. For the sake of illustration, we consider several events for which angular measurements are already performed. The  $b_{ik}$  distribution (fig. 4) is of the same nature as for the above-considered  $^{22}\text{Ne} \rightarrow n\alpha$  events. Further accumulation of statistics can enable one to study in more detail the question to what extent this distribution is universal.

To estimate the excitation scale fig. 5 (a) presents the distribution in an invariant excitation energy normalized to the nucleon number  $(M_{3\alpha}^* - 3m_\alpha)/4n_\alpha$ . In just the same way as in the case of "white"  $^{22}\text{Ne}$  stars, it is indicated that there is a concentration of events in the region of very low energies. A distribution in which the energy is counted out from the  $^{12}\text{C}$  nucleus mass, that is  $M_{3\alpha}^* - m_{\text{C}}$ , is given in fig. 5 (b). It is interesting that events are concentrated around  $^{12}\text{C}$  nucleus levels of 10-14 MeV. It is possible that the detected events would give a better understanding of the nature of these excited states. These preliminary observations serve as a serious motivation for further accumulation of statistics and for detailed measurements.

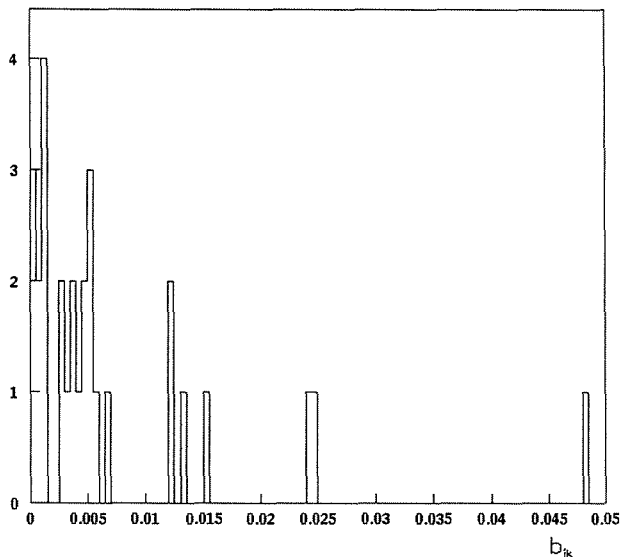


Fig. 4. The  $b_{ik}$  distribution for the fragmentation  $^{14}\text{N} \rightarrow 3\text{He}$  channel

An important fact is that there is no indication of a decay from lower 7.65 MeV level proceeding in the  $^{12}\text{C}^* \rightarrow \alpha\text{ }^8\text{Be}$  channel. The latter should reveal itself in the formation of events with three alpha particles two of which have an extremely small  $5 \cdot 10^{-3}$  rad dispersion angle at the available energy. Owing to this fact the search for a reliable method of identifying relativistic  $^8\text{Be}$  decays under the simpler conditions is topical.

### $^9\text{Be}$ NUCLEUS FRAGMENTATION

The relativistic  $^9\text{Be}$  nucleus fragmentation is an attractive source for  $^8\text{Be}$  nucleus generation since the energy threshold of neutron separation of the  $^8\text{Be}$  nucleus is only 1.7 MeV. The estimation of the  $^8\text{Be}$  production probability will make it possible to clear up the role of this nuclear structure as a core in the  $^9\text{Be}$  nucleus. In addition, the relation between  $n\text{ }^8\text{Be}$  and three-body excitation modes is expected to be established which is very important for the determination of the fragmentation scenario for heavier nuclei.

A secondary  $^9\text{Be}$  nucleus was formed via fragmentation of the primary  $^{10}\text{B}$  beam of energy of 1.2 A GeV. The beam was enriched about 80% by  $^9\text{Be}$  nuclei. The background is lighter nuclei with a close charge-to-weight ratio. In viewing emulsions exposed to  $^9\text{Be}$  nuclei we found by the present time 200 interactions in which the total charge of secondary tracks in the relativistic fragmentation cone is equal to the primary charge of a primary track. Fig. 6 shows a distribution for the 50 measured events over the opening angle between fragment pairs. One can resolve the peak at  $4 \cdot 10^{-3}$  rad corresponding to the  $^8\text{Be}$  decay from the ground state  $0^+$ . The angle value  $26 \cdot 10^{-3}$  rad corresponds to decay from the first excited state  $2^+$ .

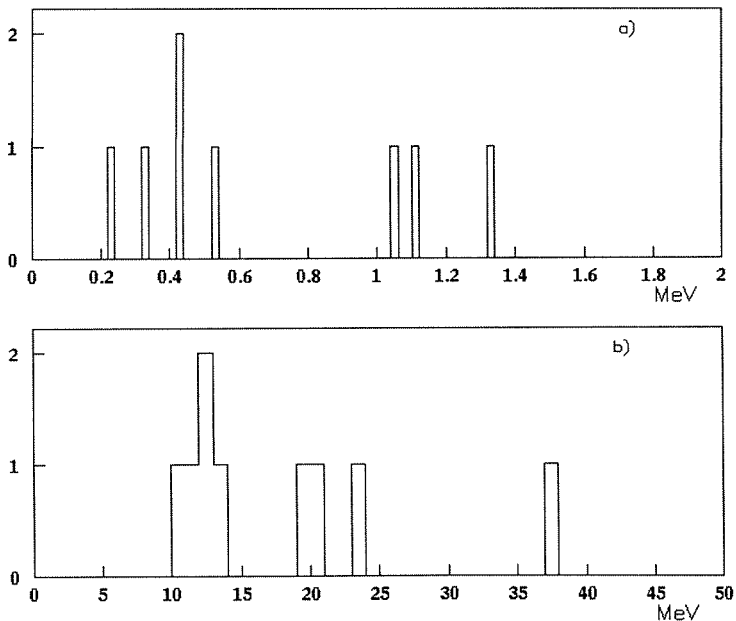


Fig. 5. Distribution in invariant excitation energy for the  $^{14}\text{N} \rightarrow 3\text{He}$  channel at an energy of 2.1 A GeV normalized to the nucleon number (a) and with respect to the ground state of the nucleus  $^{12}\text{C}$  (b)

Fig. 7 (a) shows the  $b_{ik}$  distribution for two-charged fragment pairs from 50 measured events. The distribution is seen to be limited by a region  $b_{ik} < 10^{-2}$  in this case as well. A part of this distribution zoomed near zero is presented in fig. 7 (b). One can see a concentration of 14 events for  $b_{ik} < 2 \cdot 10^{-4}$  corresponding to a  $^8\text{Be}$  decay from the ground state. The decay energy defined using them is  $88 \pm 10$  KeV. In spite of the fact that the statistics is rather restricted these distributions show that further accumulation of statistics is prospective.

### CONCLUSIONS

In the present talk use is made of the invariant approach to analyzing the fragmentation of a number of nuclei of energy above 1 A GeV in emulsion. New results are obtained from the exposure of emulsion to  $^{14}\text{N}$  nuclei at 2.1 A GeV and to  $^9\text{Be}$  at 1.2 A GeV. In spite of limited statistics it can be asserted that the use of the relativistic invariant approach to the analysis of multiple fragmentation of light nuclei in emulsion, suggested by A.M.Baldin in a rather general form, is an effective mean of obtaining sufficiently clear conclusions about the behavior of systems involving a few lightest nuclei at energies typical of quantum coherence.

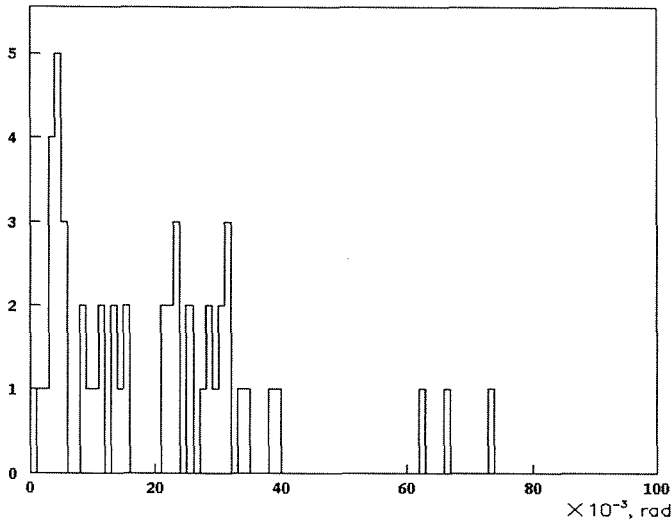


Fig. 6. Distribution in the opening angle between fragment pairs for the  ${}^9\text{Be} \rightarrow 2\text{He}$  fragmentation channel

Relativistic fragments are concentrated in a cone defined by  $b_{ik} < 10^{-2}$  and their differential distributions in this domain are alike. This approach makes it possible to explore the particular features of decay of individual nuclei. The excitation energy of a system involving a few fragments over the ground state with the same baryon number can be estimated in an invariant form up to the  ${}^8\text{Be}$  nucleus decays.

The work was supported by the Russian Foundation for Basic Research (Grants nos. 96-1596423, 02-02-164-12a, 03-02-16134, 03-02-17079, 04-02-16593 and 04-02-17151), VEGA 1/9036/02 Grant from the Agency for Science of the Ministry for Education of the Slovak Republic and the Slovak Academy of Sciences and Grants from the JINR Plenipotentiaries of Bulgaria, Czech Republic, Slovak Republic, and Romania in 2002-2004.

## REFERENCES

1. A. M. Baldin, B. V. Batyunya, I. M. Gramenitsky, V. G. Grishin, L. A. Didenko, A. A. Kuznetsov, Z. V. Metreveli. *Yad. Fiz.* **44**:1209 (1986) [*Sov. J. Nucl. Phys.* **44**: 785 (1986)].
2. A. M. Baldin, B. V. Batyunya, V. G. Grishin, L. A. Didenko, A. A. Kuznetsov, Z. V. Metreveli. *Z. Phys.* **C33** 363 (1987).
3. A. M. Baldin, V. G. Grishin, L. A. Didenko, A. A. Kuznetsov, Z. V. Metreveli. *Yad. Fiz.* **48**: 995 (1988) [*Sov. J. Nucl. Phys.* **48**: 633 (1986)].
4. A. M. Baldin, V. G. Grishin, L. A. Didenko, A. A. Kuznetsov. *Yad. Fiz.* **49**:1034 (1989) [*Sov. J. Nucl. Phys.* **49**: 640 (1989)].

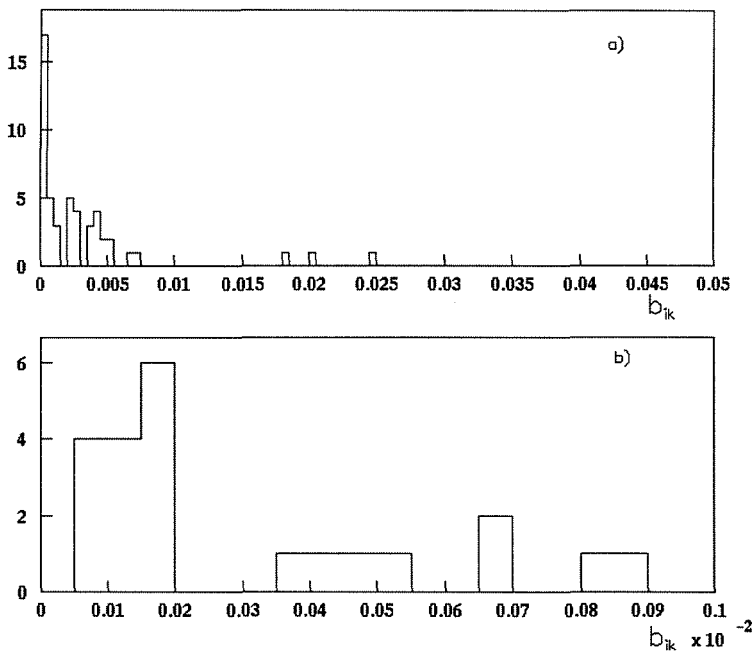


Fig. 7. Full scale distribution over  $b_{ik}$  for the  ${}^9\text{Be} \rightarrow 2\text{He}$  fragmentation channel (a) and zoomed one (b)

5. A. M. Baldin, V. G. Grishin, L. A. Didenko, A. A. Kuznetsov. *Yad. Fiz.* **52**:1427 (1990) [*Sov. J. Nucl. Phys.* **52**: 903 (1990)].
6. A. M. Baldin and L. A. Didenko. *Fortsch. Phys.* **38**, 261 (1990).
7. V. Bradnova et al. *Acta Phys. Slov.* **54** 351 (2004).
8. M. I. Adamovich et al. *Yad. Fiz.* **67**, 514 (2004) [*Phys. At. Nucl.* **68**, 533 (2004)].
9. N. P. Andreeva et al. *Yad. Fiz.* **68**, 484 (2005) [*Phys. At. Nucl.* **68**, 455 (2005)].
10. Web site of the BECQUEREL Project, <http://becquerel.lhe.jinr.ru>.
11. P. Schuck, H. Horiuchi, G. Ropke, and A. Tohsaki. *C. R. Physique* **4**, 537(2003).

# PHYSICS AT COSY

H. Machner

*Inst. für Kernphysik, FZ Jülich, 52425 Jülich, Germany*

## Abstract

The COSY accelerator in Jülich is presented together with its internal and external detectors. The physics programme performed recently is discussed with emphasis on strangeness physics.

Key-words: strangeness physics; isospin symmetry; threshold production

## 1. The accelerator complex

COSY is a synchrotron with electron cooling at injection energy and stochastic cooling at higher energies. It provides beams of unpolarised as well as polarised protons and deuterons up to 3700 MeV/c momentum. COSY can be used as a storage ring to supply internal experiments with beam. The beam can also be stochastically extracted within time bins ranging from 10 s to several minutes to external experiments. The emittance of the extracted cooled beam is only  $\epsilon = 0.4\pi$  mm mrad. This allows excellent close to target tracking. Hence a large fraction of the experimental programme is devoted to meson production close to threshold.

Here we will concentrate on hadron physics thus leaving out detectors built for different purposes. These are COSY-11, ANKE and EDDA internally and TOF and BIG KARL externally. The physics at EDDA will be presented in the contribution by Hinterberger [1] and is therefore neglected here. COSY-11 and ANKE are magnetic detectors. The former [3] employs an accelerator dipole magnet while the latter [2] is a chicane consisting of three dipoles with the middle one as analysing magnet. TOF [4] is a huge vacuum vessel with several layers of scintillators. Time of flight is measured between start detectors in the target area and the scintillators. The target area detectors are especially suited for the identification of delayed decays and TOF is thus a geometry detector. BIG KARL [5, 6] is a focussing magnetic spectrograph of the 3Q2D-type. Particle tracks are measured in the focal plane area with packs of MWDC's followed by scintillator hodoscopes allowing for a time of flight path of 3.5 m. Additional detectors exist. MOMO [7] measures the emission vertex of charged particles. The Germanium Wall [8] is a stack of four annular germanium diodes being position sensitive. It acts as a recoil spectrometer.

## 2. Strangeness physics

One strong item in COSY physics is the study of strangeness production in various processes in  $pp$ ,  $pd$  and  $pA$  interactions. Here we have to concentrate on a few of these reactions.

The  $pp \rightarrow pK\Lambda(\Sigma)$  reactions, associated strangeness production were measured by COSY-11 [9, 10, 11] and TOF [12]. In Fig. 1 the ratio  $\sigma(pK^+\Lambda)/\sigma(pK^+\Sigma^0)$  is shown as function of the excess energy. The ratio rises strongly to threshold. This unexpected

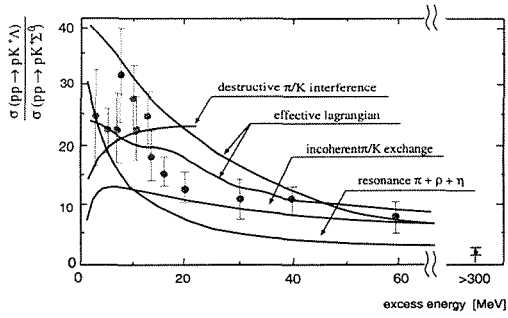


Figure 1: Ratio of the cross sections for the indicated associated strangeness production. The curves are model calculations discussed in the text

behaviour is studied within several models, including pion and kaon exchange added coherently with destructive interference [13] or incoherently [16], the excitation of nucleon resonances [14, 15] (labeled effective lagrangian), resonances with heavy meson exchange ( $\pi, \rho, \eta$ ) [17] and heavy meson exchange ( $\rho, \omega$  and  $K^*$ ) [14, 15]. The corresponding curves are also shown in the figure. All models show a decrease of the ratio with increasing excitation energy but none of them accounts for all data.

The associated strangeness production is also a useful tool to study the nucleon-hyperon interaction via FSI. At present a high resolution study of this interaction runs at BIG KARL. The measurement of Dalitz diagrams enables even the investigation of the importance of intermediate  $N^*$  excitation.

Connected with the associated strangeness production is the question whether pentaquarks exist. Most of the experimental searches were performed with electromagnetic probes on the neutron, which, of course, is embedded in a nucleus. A cleaner environment is the  $pp$  interaction. The reaction studied with TOF is the

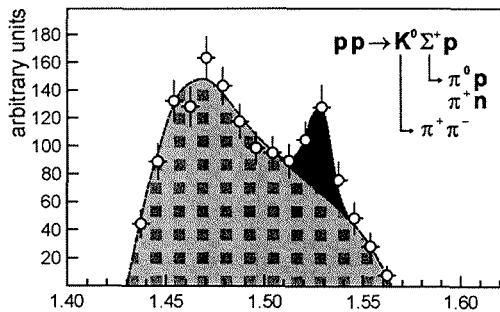


Figure 2: Evidence for a pentaquark produced in  $pp$  collision

$$pp \rightarrow K^0 \Sigma^+ p \quad (1)$$

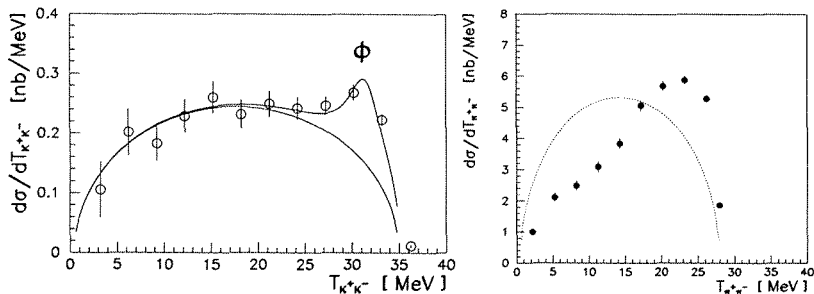


Figure 3: Left: Energy spectrum of the two kaons at a maximal excess energy of 35 MeV. Right: Same as left but for two pions for a maximal excess energy of 28 MeV

reaction. The  $K^0$  is identified via its decay into two pions and the  $\Sigma$  via its delayed decay. The data are shown in Fig. 2 [18]. There is evidence on a  $4\sigma$  level for the production of a pentaquark

$$pp \rightarrow \Theta^+ \Sigma^+ \quad (2)$$

with a subsequent decay of the  $\Theta^+$  into  $K^0$  and  $p$ . For the enormous body of papers related to pentaquark we refer to the talk by Stancu [19].

Another interesting reaction is

$$pp \rightarrow dK^+ \bar{K}^0. \quad (3)$$

On order to reach the threshold of this reaction the maximal energy of COSY had to be lifted above its design value of 2.5 GeV. The data were taken at an energy of 2.65 GeV. The analysis of the data [21] resulted in a dominance of the channel

$$pp \rightarrow da_0^+ \quad (4)$$

with a subsequent decay  $a_0^+ \rightarrow K^+ \bar{K}^0$ .

At the BIG KARL spectrograph the reaction

$$pd \rightarrow {}^3HeK^+K^- \quad (5)$$

was studied with the MOMO vertex wall. The interest in this reaction stems from the surprising behaviour of two pions in the

$$pd \rightarrow {}^3He\pi^+\pi^- \quad (6)$$

reaction [22]. The latter reaction showed a p-wave between the two pions even close to threshold. In Fig. 3 the energy spectrum of two kaons for a maximal energy of 35 MeV are shown. Besides a smooth continuum the production of  $\phi$ -mesons is visible. The energy distribution follows phase space, hence it is s-wave. The same conclusion holds for the  $KK-{}^3He$  system. Also the excitation function for the  $\phi$  production is in accord with the assumption of s-wave. To summarise: the  $KK-{}^3He$  behaves as expected while the  $\pi\pi-{}^3He$  system shows an unexpected behaviour. In order to proof the findings for this

system the experiment was repeated but with inverse kinematics. The advantage of doing so is a smaller number of settings of the spectrograph. A result of this measurement is also shown in Fig. 3. It supports the previous findings.

One aspect of strangeness physics is the  $s\bar{s}$  content in the nucleon. This is connected to a violation of the OZI-rule in the ratio

$$R = \frac{\sigma(pp \rightarrow pp\phi)}{\sigma(pp \rightarrow pp\omega)}. \quad (7)$$

These two mesons have almost ideal quark mixing and hence the  $\omega$  has negligible  $s\bar{s}$  content while the  $\phi$  is an almost pure  $s\bar{s}$  state (see previous reaction). TOF measured  $\omega$  production at exactly the same excess energy as previous  $\phi$  production, thus allowing the deduction of  $R$  as function of excess energy. This yields  $R = (3 \pm 1) \times 10^{-2}$  while the OZI-rule predicts  $R = 4 \times 10^{-3}$ . This may point to a serious content of  $s\bar{s}$  pairs in the nucleon.

### 3. Threshold production, symmetries

There is a wealth of data of light meson production measured at COSY in the threshold region. The data were taken mainly by the COSY-11 and GEM collaborations for the nucleon-nucleon channel [24, 25, 26]. The  $\eta$  and  $\eta'$  production were discussed by Moskal [27] at this meeting. Here we will concentrate on  $pd \rightarrow {}^3AX$  reactions with  $A = H$  or  $He$  and  $X = \pi, \eta$ . The latter reaction is of interest since the  $\eta$ -nucleus interaction might be attractive. From the differential cross sections one can deduce a matrix element  $f$  as

$$|f(\theta)|^2 = \frac{k^2 d\sigma}{q^2 d\Omega}(\theta) = |f_p|^2 |T(q)|^2. \quad (8)$$

This quantity is shown in the left part of Fig. 4 as function of the of the  $\eta$  momentum  $q$ . Close to threshold the final state interaction is an s-wave and one can apply the Watson-Migdal theorem (right side of Eq. 8) to extract the FSI amplitude  $|T(q)|$  and from this the  $\eta$ - ${}^3He$  scattering length. Sibirtsev et al. [28] performed such an analysis with the result  $a = |4.3 \pm 0.3| + i(0.5 \pm 0.5)$  fm. This result is also shown in the figure. The second curve is from A. Khoukaz which includes the preliminary COSY-11 data.

The GEM collaboration studied isospin symmetry breaking by comparing neutral and charged pion production in  $pp \rightarrow d\pi^+$  and  $np \rightarrow d\pi^0$  [5] reactions, and  $pd \rightarrow {}^3H\pi^+$  and  $pd \rightarrow {}^3He\pi^0$  reactions [29]. For the latter reactions it was found that the angular distribution of the matrix elements consists of two parts. an exponential part showing scaling which is attributed to a one step reaction. This part shows isospin symmetry breaking. The second component is isotropic and is related to two step processes. It does not show isospin symmetry breaking. The origin of isospin symmetry breaking is in addition to the Coulomb force a difference in the masses of the up and down quark. It was suggested [30] to study the  $pd \rightarrow {}^3He\pi^0$  reaction at maximal momentum transfer around the  $\eta$ -production threshold. This channel should be sensitive to  $\pi^0$ - $\eta$  mixing with the mixing angle being dependent on the different quark masses. On the contrary the  $pd \rightarrow {}^3H\pi^+$  reaction should not show such an interference effect. This was indeed found in an experiment [31] and the ratio of both reactions is shown in Fig. 4. Baru et al. [32]

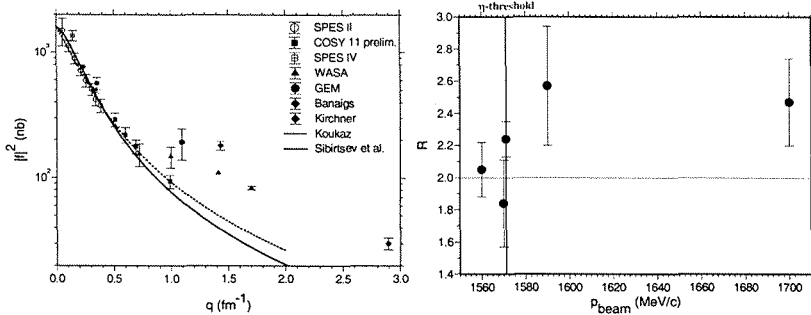


Figure 4: Left: Excitation function of the matrix element squared for the  $pd \rightarrow {}^3\text{He}\eta$  reaction. The references can be found in [28]. Right: Excitation functions for the ratio of the two pion production reactions at maximal momentum transfer (zero degree in the lab. system). The  $\eta$ -production threshold is indicated as line

claimed this effect to be most probably to be most probably to FSI. However, if the data are analysed on terms of the model from Ref. [30] the mixing angle results into  $\theta = 0.006 \pm 0.005$ . Green and Wycech used a K-matrix formalism and derived  $\theta = 0.010 \pm 0.005$ . From this formalism a rather large  $\eta$ -nucleon scattering length is extracted making a bound  $\eta$ -nucleus very likely. The search for such a system is in progress. Also the question of  $\pi^0$ - $\eta$  mixing will be further studied via isospin forbidden decays of  $\eta$  and  $\eta'$  mesons with WASA at COSY.

## Acknowledgements

I am grateful to the members of GEM for their collaboration. The contributions and discussions with Dres. M. Büscher, A. Gillitzer, R. Jahn, A. Khoukaz and F. Rathmann are gratefully acknowledged.

## References

- [1] F. Hinterberger, contribution to this conference.
- [2] S. Barsov et al., *Nucl. Instr. Methods in Physics Research A* **462**, 364 (2001).
- [3] S. Brauksiepe et al., *Nucl. Instr. Methods in Physics Research A* **376**, 397 (1996).
- [4] M. Dahmen et al., *Nucl. Instr. Methods in Physics Research A* **348**, 97 (1994).
- [5] M. Drochner et al. (GEM Collaboration), *Nucl. Phys. A* **643**, 55 (1998).
- [6] J. Bojowald et al., *Nucl. Instr. Methods in Physics Research A* **487**, 314 (2002).
- [7] F. Bellemann et al. (COSY-MOMO Collaboration), *Phys. Rev. C* **60**, 0601002 (1999).

- [8] M. Bettigeri et al. (GEM Collaboration), *Nucl. Instr. Methods in Physics Research A* **421**, 447 (1999).
- [9] J.T. Balewski et al., *Phys.Lett. B* **420**, 211 (1998).
- [10] S. Sewerin et al., *Phys. Rev. Lett.* **83**, 682 (1999).
- [11] P. Kowina et al., e-Print Archive nucl-ex/0402008, *Eur. Phys. J. A*, in print.
- [12] S. Marcello et al., *Nucl. Phys. A* **691**, 344c (2001).
- [13] A. Gasparian et al., *Phys. Lett. B* **480**, 273 (2000).
- [14] R. Shyam et al., *Phys. Rev. C* **63**, 022202 (2001).
- [15] R. Shyam hep-ph/0406297.
- [16] A. Sibirtsev et al., *Nucl.Phys. A* **646**, 427-443 (1999).
- [17] A. Sibirtsev et al., nucl-th/0004022 v2 (2000).
- [18] M. Abdel Bary et al., (COSY-TOF Collaboration), *Phys. Lett. B* **595**, 127 (2004).
- [19] F. Stancu, contribution to this conference.
- [20] V.Kleber et al., *Phys.Rev.Lett.* *91*, 172304 (2003).
- [21] V. Yu. Grishina, L. A. Kondratyuk, M. Büscher, W. Cassing, *Eur. Phys. J. A* **21**, 507 (2004).
- [22] R. Bellemann et al. (COSY-MOMO Collaboration), *Phys. Rev. C* **60**, 061002 (1999).
- [23] S. Abd El-Samad et al. (COSY-TOF Collaboration), *Phys. Lett. B* **522**, 16 (2001).
- [24] H. Machner and J. Haidenbauer, *J. Phys. G* **25**, R231 (1998).
- [25] P. Moskalet al., *Progress in Part. Nucl. Phys.* **49**, 1 (2002).
- [26] M. Bettigeri et al., *Phys. Rev. C* **65**, 064001 (2002)
- [27] P. Moskal, contribution to this conference.
- [28] A. Sibirtsev, J. Haidenbauer, C. Hanhart and J.A. Niskanen, e-Print Archive **nucl-th/0310079**.
- [29] S. Abdel-Samad et al., *Phys. Lett. B* **553**,31 (2003).
- [30] A. Magiera and H. Machner, *Nucl. Phys. A* **674**, 515 (2000).
- [31] M. Abdel-Bary et al., *Phys. Rev. C* **68**, 021603(R) (2003).
- [32] V. Baru, J. Haidenbauer, C. Hanhart, J.A. Niskanen, . *Phys. Rev. C* **68**, 035203 (2003).
- [33] A. M. Green and S. Wycech, *Phys. Rev. C* **68**, 062601 (2003)

# POLARIZED DEUTERONS AT THE NUCLOTRON <sup>1</sup>

Yu.K.Pilipenko, S.V.Afanasiev, L.S.Azhgirey, A.Yu.Isupov,  
V.P.Ershov, V.V.Fimushkin, L.V.Kutuzova, V.F.Peresedov,  
V.P.Vadeev, V.N.Zhmyrov, L.S.Zolin

*Joint Institute for Nuclear Research, Dubna*

† *E-mail: pilipen@sunhe.jinr.ru*

## Abstract

The first acceleration of polarized deuterons was done at the accelerator nucleotron since the old machine synchrophasotron has been shutdown. Simulation shows that depolarization resonances are absent under polarized deuteron acceleration almost at all energy range of the machine. The  $\uparrow D^+$  source POLARIS was used. The polarization of the beam was measured by some polarimeters: at the exit of the 10 MeV linac, inside the accelerator ring and after the beam extraction. The high vector polarization value of the deuteron beam during acceleration conformed by all polarimeters. Its measured  $P_z$  as: - 0.56 and + 0.62. The intensity of the polarized deuteron beam in a short one turn injection mode (8  $\mu s$ ) is observed as  $1.3 \cdot 10^8 \uparrow d/pulse$ . To increase the intensity of the accelerated polarized beam up to  $0.7 \cdot 10^{10} \uparrow d/pulse$  a multyturn charge exchange injection of negative ions (20-30 turns) should be applied. The polarized  $\uparrow D^-$  ion source is required. The existing  $\uparrow D^+$  source POLARIS is reconstructed into the  $\uparrow D^-$  source. New plasma  $\uparrow D^-$  charge exchange ionizer developed and tested. The source design and first results of the beam polarization measurements are presented.

## 1. $\uparrow D^+$ source POLARIS

An intensive study of polarization phenomena in high energy spin physics was carried out at the Dubna 10 GeV synchrophasotron during last 20 years. In fall of 2002 last polarized beam run has passed before that historical machine was shutdown. All that time cryogenic source POLARIS was used to produce polarized deuteron beam [1,2,3]. It was design at the end of 1970-ies, when turbopump oilfree technology hasn't been developed yet. The source atomic beam forming process is required to pump a large mass of injected gas. It was decided insted of conventional pumping to apply cryocondensation of deuterium molecules on cooled surfaces. POLARIS is compact atomic beam source with internal 4.2 K surfaces for effective gas cryopumping, cold nozzle, superconducting magnets. It consists of two LHe cryostats:

- a pulsed atomic beam stage with two superconducting sextupole magnets,
- the Penning plasma ionizer with high field SC solenoid.

The energy of the deuteron beam at the output of the source is about 3 keV, the current: 0.3-0.4 mA. The vector and tensor polarizations are:  $P_z = \pm 0.54$ ;  $P_{zz} = \pm 0.76$ .

---

<sup>1</sup>This work is supported by the Russian Fund of Fundamental Research, the Grant 04-02-17410.

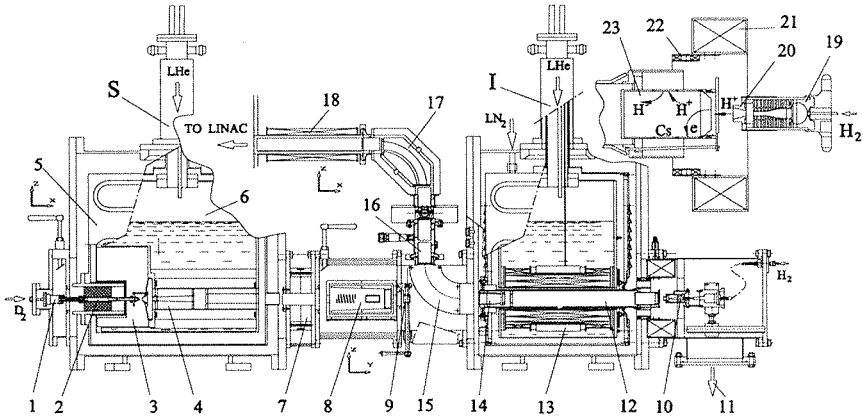


Figure 1: Schematic view of the polarized deuteron source POLARIS. S - polarized atomic source, I - charge exchange ionizer. 1- pulsed  $D_2$  valve, 2- dissociator, 3- nozzle chamber, 4- SC sextupole magnets, 5- nitrogen shield, 6- helium cryostat, 7- permanent sextupole, 8- RF cell, 9- vacuum gate, 10-  $H^-$  plasma generator, 11- two 500 l/s turbopumps, 12- HV charge exchange space, 13- SC solenoid, 14- extraction electrodes, 15-  $90^\circ$  bending magnet, 16- ion optics, 17- electrostatic mirror, 18- solenoid of spin-precessor, 19- Cu cathode, 20- anode, 21- magnetic coil, 22- transverse magnetic filter, 23- molybdenum converter

The commissioning of the new superconducting accelerator nuclotron supposes to continue the spin physics program. A first test polarized run at the new machine took place since the synchrophasotron has been shutdown. Simulation shows that depolarizing resonances are absent under polarized deuteron acceleration almost at all energy range of the nuclotron [4]. There is a project to produce a polarized deuteron beam. It is supposed to modify  $\uparrow D^+$  source POLARIS into the  $\uparrow D^-$  one and to realize multyturn charge exchange injection in the nuclotron ring.

## 2. Charge Exchange Ionizer

The new machine nuclotron has a short one turn injection ( $8 \mu s$ ) of positive ions (factor 50 less compared to the synchrophasotron). To get a large beam current a new plasma charge exchange ionizer has been developed [5,6,7] (Fig.1). It has similar the Penning ionizer LHe cryostat with the 60 mm cold bore SC solenoid. A short pulse ( $300 \mu s$ )  $H^+$  arc plasma generator is installed at the solenoid entrance.  $0.05-0.1 \text{ cm}^3 H_2$  gas at pressure 0.5-1.2 bar is injected into a hollow cathode space of the plasma generator by a fast

thyristor triggered valve. High current arc discharge and  $H^+$  plasma beam are started due to ignition pulse in 0.9 ms. An acceleration potentials of the plasma generator and the HV charge exchange pipe are +(13-17) kV. A nuclear polarized deuterium atomic beam is injected into the solenoid space towards the plasma beam. The charge exchange reaction between polarized deuterium atoms and hydrogen plasma ions  $\uparrow D^0 + H^+ = \uparrow D^+ + H^0$  takes place inside the HV space.  $\uparrow D^+, H^+, H_2^+$  three component plasma is extracted by extraction grids to separation magnet.

Using POLARIS atomic beam stage, about 1 mA polarized  $D^+$  (mass 2) current accompanied by 9 mA  $H_2^+$  (mass 2) background from the plasma generator, has been measured output of the charge exchange ionizer behind the  $90^\circ$  bending magnet. To get proper vertical orientation of spin the polarized beam should be passed through electrostatic mirror and spin rotator. A beam space charge limit of the mirror is around 10-12 mA. An efficiency of the new ionizer is 3-5% instead of 1-2% for the our old Penning ionizer. It is clear the  $\uparrow D^+$  charge exchange ionizer can't sufficiently rise intensity accelerated beam in one turn injection mode.

To reach the accelerated polarized beam intensities up to  $0.7-1 \cdot 10^{10}$   $\uparrow d$ /pulse a multyturn charge exchange injection (20-30 turns) could be be applied. It is realized by injection into the nuclotron ring of  $\uparrow D^-$  ions and stripping them inside the ring. A polarized  $\uparrow D^-$  beam from the source is required.

The existing  $D^+$  plasma charge exchange ionizer has been modified into  $\uparrow D^-$  one using an external converter-emitter [7,8,9]. At output of the  $H^+$  plasma generator, a molybdenum surface converter is placed to produce  $H^-$  ions (Fig.2). Titanium-cesium chromate pellets are loaded into an O-ring groove of the converter and heated up to 300-500°C. Cesium molybdenum surfaces of the converter are exposed to an intense flux of superheated hydrogen atoms, positive ions and effectively generate  $H^-$  ions.

Fast plasma electrons, accompanying  $H^+$  plasma beam, are removed by a transverse magnetic field of a permanent magnet, to avoid of  $H^-$  ion destruction.  $H^-$  ions, generated inside the converter, space charge compensated by residual  $H^+$  ions, are entered axial region and fill up a charge exchange volume of the HV pipe -(17-20) kV. The reaction  $\uparrow D^0 + H^- = \uparrow D^- + H^0$  takes place. Polarized negative deuterium ions, confined in the radial direction by magnetic field of the solenoid, drift to the extracting grids. The  $90^\circ$  bending magnet separates accelerated  $H^-$  plasma and polarized  $\uparrow D^-$  ions.

Vacuum in the ionizer is provided by cryopumping and by some turbopumps. Hydrogen vapor pressure at 4.2 K cryostat is  $1-2 \cdot 10^{-6}$  mbar. Reconstruction of the ionizer cryostat is finished, cryogenic tests have done. A study of the surface conversion technology  $H^+$  to  $H^-$  ions took place simultaneously. Some configurations of the  $H^+$  generator and molybdenum converter have been modified and tested:

- converter diameter, cone shape, length,
- plasma source magnetic coil length,
- arc discharge configuration space,
- filter magnetic field,
- extraction electrode configuration,
- arc discharge feeding scheme.

A scheme of the extraction electrodes is shown on Fig.2. Extraction of positive and negative ions from the charge exchange space are different for the same acceleration volt-

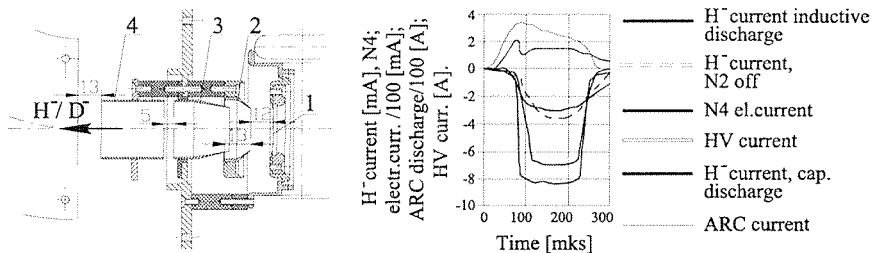


Figure 2: Scheme of test bench extraction electrodes and  $H^-$  current pulses behind bending magnet. 1- HV plasma wire mesh, 2,3,4- electrodes

age range ( $U_{acc}=12-17$  kV). An extraction grid length of positive ions consist of two fine wire mesh, with gap 10-15 mm. Extraction electrodes N2, N3 for negative ions have a cone shape. A changing of the N2 electrode potential from 0 to -9 kV is heighten  $H^-$  current double from 4 to 8 mA.  $H^-$  current pulse is raised if two middle sections of the solenoid magnetic coils are tuned. A direct discharge scheme of the arc feeding is preferable. Duration of the plasma current pulse is about 200  $\mu s$  in that case. It is correspond to 25 turns of the injected beam.  $H^-$  currents at the output of 90° bending magnet, electron current of the N2 electrode and total current of the HV power supply are shown on Fig.2.

A conditioning of the converter surfaces and theirs covering by Cs are very important. There is small  $H^-$  current (0.2-0.5 mA) accompanying large quantity of plasma electrons first time after installation. The current is slowly raised with time. It is depend on arc voltage, pulse frequency, clean vacuum, converter temperature, Cs covering. Quantity of the injected gas strongly influences on the negative current value. Surface activation process takes place in a pulse time while an adsorption of residual gas molecules occur between pulses.

The 10 mA  $H^-$  current was observed at the frequency 0.3 pulse/s. It is expected to get the larger current in real ionizer configuration, using cryostat with SC solenoid and cryopumping. Estimation shows, 0.3-0.5 mA  $\uparrow D^-$  polarized beam should be got, using POLARIS atomic stage.

The plasma charge exchange ionizer of the polarized source has another important feature. It can be used as the intensive source of unpolarized proton or deuteron beams (10-15 mA). In that case the bending separation magnet is adjusted not for polarized but for the plasma beam. Development of the ionizer will be continued.

### 3. Test run at the nuclotron

A test run has been done at the nuclotron using the existing  $\uparrow D^+$  source POLARIS with Penning ionizer.

The polarizations of low and high energy beams during acceleration were measured:

- low energy polarimeters with  $He^3$ ,  $He^4$  targets behind the 10 MeV linac,
- internal target polarimeter during an acceleration,
- two-arm relative polarimeter with polyethylene target.

The results of measurements are:

	Pz (1-4)	Pz (3-6)
1. Beam polarization measured behind the linac	- 0.56+/-0.07	0.62+/-0.07
2. Internal target measurements at 3.5 GeV/c	-0.58+/-0.04	0.59+/-0.04
at 5.0 GeV/c	-0.56+/-0.03	0.60+/-0.03
3. Polarization of the extracted beam		
at 3.5 GeV/c	-0.55+/-0.03	0.53+/-0.03
at 5.0 GeV/c	-0.58+/-0.02	0.63+/-0.02

The vector polarization of the deuteron beam is retained during an acceleration and conformed by all polarimeters. As expected, the intensity of the polarized deuteron beam in one turn injection mode is observed as  $1.3 \cdot 10^8$   $\uparrow$ d/pulse. The charge exchange multyturn injection is required.

## Acknowledgments

This work is supported by the Russian Fund of Fundamental. Research, the Grant 04-02-17410.

## References

- [1] N.G. Anischenko *et al.* -In: The 5th Int. Symp. on High Energy Spin Physics, Brookhaven 1982, AIP Conf. Proc. N.Y. **N95**, 445 (1983).
- [2] N.G. Anischenko *et al.* 6th Int. Symp. on High Energy Spin Physics, Marseille 1984, Journ.De Phys. Colloquia C2, Supplement an n° 2, **46**, C2-703 (1985).
- [3] V.P. Ershov *et al.* - In: Int. Workshop on Polarized Beams and Polarized Gas Targets, Cologne 1995, (World Scientific, Singapore) 193 (1996).
- [4] A.M. Kondratenko *et al.* - In: The 6th Workshop on High Energy Spin Physics. Protvino 1995, **v.2**, 212 (1996).
- [5] A.S. Belov *et al.* Nucl. Instr. and Meth., vol.**A255**, 3, 442 (1987).
- [6] V.P. Ershov *et al.* -In: The 13th Int. Symp. on High Energy Spin Physics Protvino 1998, (World Scientific, Singapore) 615 (1999).
- [7] V.P. Ershov *et al.* -In: Int. Workshop on Polarized Sources and Targets, Erlangen 1999, (Druckerei Lengfelder, Erlangen) 456 (1999).
- [8] A.S. Belov *et al.* Rev. Sci. Instr. vol.**67**, 3, 1293 (1996).
- [9] V.P. Ershov *et al.* -In: Int. Workshop on Polarized Sources and Targets, Nashville 2001, (World Scientific, Singapore) 225 (2002).

The results of measurements are:

	Pz (1-4)	Pz (3-6)
1. Beam polarization measured behind the linac	- 0.56+/-0.07	0.62+/-0.07
2. Internal target measurements at 3.5 GeV/c	-0.58+/-0.04	0.59+/-0.04
at 5.0 GeV/c	-0.56+/-0.03	0.60+/-0.03
3. Polarization of the extracted beam		
at 3.5 GeV/c	-0.55+/-0.03	0.53+/-0.03
at 5.0 GeV/c	-0.58+/-0.02	0.63+/-0.02

The vector polarization of the deuteron beam is retained during an acceleration and conformed by all polarimeters. As expected, the intensity of the polarized deuteron beam in one turn injection mode is observed as  $1.3 \cdot 10^8$   $\uparrow$ d/pulse. The charge exchange multyturn injection is required.

## Acknowledgments

This work is supported by the Russian Fund of Fundamental. Research, the Grant 04-02-17410.

## References

- [1] N.G. Anischenko *et al.* -In: The 5th Int. Symp. on High Energy Spin Physics, Brookhaven 1982, AIP Conf. Proc. N.Y. **N95**, 445 (1983).
- [2] N.G. Anischenko *et al.* 6th Int. Symp. on High Energy Spin Physics, Marseille 1984, Journ.De Phys. Colloquia C2, Supplement an n° 2, **46**, C2-703 (1985).
- [3] V.P. Ershov *et al.* - In: Int. Workshop on Polarized Beams and Polarized Gas Targets, Cologne 1995, (World Scientific, Singapore) 193 (1996).
- [4] A.M. Kondratenko *et al.* - In: The 6th Workshop on High Energy Spin Physics. Protvino 1995, **v.2**, 212 (1996).
- [5] A.S. Belov *et al.* Nucl. Instr. and Meth., vol.**A255**, 3, 442 (1987).
- [6] V.P. Ershov *et al.* -In: The 13th Int. Symp. on High Energy Spin Physics Protvino 1998, (World Scientific, Singapore) 615 (1999).
- [7] V.P. Ershov *et al.* -In: Int. Workshop on Polarized Sources and Targets, Erlangen 1999, (Druckerei Lengfelder, Erlangen) 456 (1999).
- [8] A.S. Belov *et al.* Rev. Sci. Instr. vol.**67**, 3, 1293 (1996).
- [9] V.P. Ershov *et al.* -In: Int. Workshop on Polarized Sources and Targets, Nashville 2001, (World Scientific, Singapore) 225 (2002).

# Scientific Programme

September 27, Monday

PLENARY SESSION  
BOGOLIUBOV CONFERENCE HALL OF BLTP

10.30 *A. Sissakian (JINR)*

Opening

10.40 *V. Kadyshvsky (JINR)*

Welcome from the JINR Directorate

*Quantum chromodynamics at the large distances*

Chairman A. Sissakian

10.40 *C. Perdrisat (USA)*

Proton form factor measurements at Jefferson Lab

Coffee break 11.30 - 12.00

*Quantum chromodynamics at the large distances*

Chairman A. Malakhov

12.00 *G. Efimov (JINR)*

Masses of light mesons and analytical confinement

12.20 *V. Burov (JINR)*

Bethe-Salpeter approach with separable interaction for the deuteron

13.00 *Yu. Pokrovsky (Russia)*

Could leptons be composed from quarks or antiquarks?

Break 13.40 - 15.00

*Quantum chromodynamics at the large distances*

Chairman V. Burov

15.00 *D. Blaschke (Germany)*

Color superconductivity and cooling of compact stars

15.40 *M. Musakhanov (Uzbekistan)*

Instanton vacuum effective action beyond chiral limit

16.10 *N. Konopleva (Russia)*

On the motion of matter in the geometrical gauge field theory

Coffee break 16.30-17.00

- 17.00 *O. Pavlovsky* (Russia)  
Random lattice QCD and chiral Born-Infeld theory
- 17.20 *N. Yudin* (Russia)  
The microscopic approach to quasielastic knock-out of mesons out of nucleons by electrons
- 17.40 *N. Khokhlov* (Russia)  
The nucleon-nucleon scattering description at  $E_{tab}=0-6$  GeV, the deuteron properties and deuteron photodisintegration in the relativistic quasipotential optical model, based on the Moscow potential
- 18.00 *B. Krippa* (Russia)  
Exact renormalization group and its application in many-fermions systems
- 18.20 *S. Eliseev* (JINR)  
Production of cumulative protons in DIS of nuclei, the role of fluctons, LPM effect and all that
- 18.40 *I. Pestov* (JINR)  
On electrodynamics of constituent quarks and QCD potential
- 19.00 *H.-J. Lee and N. Kochelev* (JINR)  
Instantons and structure of pentaquark

**20.00 Welcome Party**

September 28, Tuesday

PARALLEL SESSION A  
BOGOLIUBOV CONFERENCE HALL OF BLTP  
*Quantum chromodynamics at the large distances*

Chairman C. Perdrisat

9.00 *S. Gerasimov* (JINR)

On relations between leptonic and two-photon decay widths of lowest mass S-wave

9.40 *A. Shebeko* (Ukraine)

The clothed particle representation in quantum field theory: mass renormalization

10.00 *A. Vinnikov* (JINR)

Gluonic contribution to  $\rho^0$  electroproduction at intermediate energy

10.20 *S. Goloskokov* (JINR)

Electroproduction of vector mesons at small  $x$

10.40 *M. Zomorrodian* (Iran)

The influence of fragmentation models in production of hadron jets in electron-positron annihilations

11.00 *N. Faddev* (JINR)

Physical nature of Lobachevsky parallel lines and a new inertial frame transformation

Coffee break 11.20 - 11.50

*Relativistic heavy ion collisions*

Chairman S. Gerasimov

11.50 *B. Batyunya* (JINR)

Simulation of  $\Phi \rightarrow K^+K^-$  detection in ALICE experiment

12.10 *V. Vechernin* (Russia)

Multiplicity and  $pt$  correlations in relativistic nuclear collisions

12.50 *G. Feofilov* (Russia)

Long-range correlations in PbPb collisions at 158 A\*GeV

13.30 *A. Shakel* (India)

On spatial and event-by-event fluctuations in relativistic heavy-ion collisions

Break 13.30 - 15.00

*Relativistic heavy ion collisions*

Chairman A. Kovalenko

15.00 *G. Lykasov* (JINR)

Charm production in hadronic and heavy ion collisions

15.20 *M. Suleymanov* (JINR)

Search for signal on percolation cluster formation in nucleus- nucleus collisions at relativistic energies

- 15.40 *N. Topilskaya* (Russia)  
Investigation of charmonium states production  
in p-A and A-A collisions at SPS CERN
- 16.20 *N. Zotov* (Russia)  
Structure function  $F_L$  in the  $k_T$  factorization approach
- 16.40 *K. Hanna* (Egypt)  
Model for restoration of heavy-ion potentials at intermediate energies

Coffee break 17.00 - 17.30

*Relativistic heavy ion collisions*

Chairman N. Yudin

- 17.30 *S. Vokal* (JINR)  
Azimuthal structures of produced particles in heavy ion interactions
- 17.50 *G. Orlova* (Russia)  
The extraordinary interaction of  $^{14}\text{N}$  - nucleus in photoemulsion
- 18.10 *Yu. Sinyukov* (Ukraine)  
Pion phase-space densities in relativistic heavy ion collisions
- 18.50 *S. Timoshenko* (Russia)  
 $\rho$ -meson production in ultraperipheral heavy ion collisions at STAR
- 19.10 *E. Shahaliev* (JINR)  
Random matrix theory and analysis of nucleus-nucleus collision at high energies
- 19.30 *A. Tarasov* (JINR)  
Lepton pair production in nucleus-nucleus collisions

**September 28, Tuesday**

PARALLEL SESSION B  
BLOKHINTSEV AUDITORIUM OF BLTP  
*Structure functions of hadrons and nuclei*

Chairman A. Baldin

- 9.00 *G. Skoro* (Serbia and Montenegro)  
Jet energy density in hadron-hadron collisions at high energies
- 9.20 *A. Stadnik* (JINR)  
Wavelet applications for jet analysis
- 9.40 *M. Tokarev* (JINR)  
Z-scaling at RHIC
- 10.00 *I. Zborovskiy* (Czech Republic)  
Anisotropy in relativistic nuclear collisions and Michelson's experiments with light.
- 10.20 *T. Dedovich* (JINR)  
Z-scaling of jet production at Tevatron

10.40 *M. Gaidarov* (Bulgaria)

Scaling in inclusive electron scattering from nuclei

Coffee break 11.00 - 11.50

*Structure functions of hadrons and nuclei*

Chairman *M. Tokarev*

11.50 *A. Krutov* (Russia)

Electromagnetic properties of deuteron in the new relativistic constituent model

12.10 *N. Tsirova* (Russia)

New aspects in the asymptotics of the deuteron electromagnetic form factor

12.30 *S. Kulagin* (Russia)

Isospin effects in nuclear parton distributions

13.00 *N. Ivanov* (JINR)

Theoretical method of the polarized semi-inclusive deep inelastic scattering data analysis in the next-to-leading QCD order

Break 13.20 - 15.00

*Structure functions of hadrons and nuclei*

Chairman *I. Zborovsky*

15.00 *V. Kozhukalov* (JINR)

Relativistic description of the elastic pD scattering

15.20 *E. Rogochaya* (JINR)

Electro-disintegration of the deuteron in the Bethe-Salpeter approach

15.40 *D. Shulga* (Russia)

Final-state interaction contribution to the deuteron photodisintegration in the Bethe-Salpeter formalism

16.00 *V. Pozdnyakov* (JINR)

Study of the multihadron production in gamma-gamma collisions

Coffee break 17.00 - 17.30

*Progress in experimental studies at the high energy accelerators*

Chairman *A. Vodopianov*

17.00 *A. Khodinov* (USA)

Higgs Boson decays into four leptons in full simulation with ATLAS at LHC

17.50 *A. Zinchenko* (JINR)

Study of a possibility to detect Upsilon in p-Pb and Pb-p collisions at the LHC energy in the muon spectrometer of ALICE

18.10 *S. Kushpil* (JINR)

Performance of the silicon drift detector for particle identification in the case perpendicular and inclined tracks

- 18.30** *S. Gmuca* (Slovak Republic)  
Relativistic mean field approach to asymmetric nuclear matter in beta-equilibrium
- 18.50** *L. Majling* (Czech Republic)  
Production and identification of the superheavy hydrogen hypernucleus  ${}^6_{\Lambda}\text{H}$
- 19.30** *E. Koshurnikov* (JINR)  
The dipole magnet iron yoke for the ALICE DiMuon arm spectrometer

## September 29, Wednesday

PARALLEL SESSION A  
BOGOLIUBOV CONFERENCE HALL OF BLTP  
*Hadron spectroscopy*

Chairman V. Kukulín

- 9.00** *E. Strokovsky* (JINR)  
Search and study of exotic narrow baryons at JINR Nuclotron
- 9.40** *Yu. Troyan* (JINR)  
The search and study of the baryonic resonances with the strangeness  $S=+1$  in the system of  $nK^+$  from the reaction  $np \rightarrow npK^+K^-$  at the momentum of incident neutrons  $P_n=(5.20\pm 0.12)\text{GeV}/c$
- 10.00** *P. Aslanyan* (JINR)  
Observation of  $S=+1$  narrow resonances in the system  $K_s^0 p$  from  $p+C_3H_8$  collision at 10 GeV/c
- 10.20** *V. Henner* (Russia)  
Analysis of light vector and scalar mesons in  $e^+e^-$  annihilation and  $\pi\pi$  scattering

**Coffee break 11.00 - 11.30**

*Relativistic heavy ion collisions*

Chairman E. Strokovsky

- 11.30** *V. Kukulín* (Russia) and *M. Shikhalev* (JINR)  
Dibaryons in hadronic physics and nuclear structure
- 12.10** *B. Tatischeff* and *E. Tomasi-Gustafsson* (France)  
New Evidence for narrow baryonic and dibaryonic structures
- 12.40** *I. Cherednikov* (JINR)  
Instantons in high energy QCD processes
- 13.00** *G. Ganbold* (JINR)  
Two-quark bound states: meson spectra and Regge trajectories

**Break 13.30 - 15.00**

PLENARY SESSION  
BOGOLIUBOV CONFERENCE HALL OF BLTP  
*Polarization phenomena and spin physics*

Chairman N. Piskunov

- 15.00 *L. Azhgirey* (JINR)  
Investigation of the angular dependence of the tensor  
analyzing power of 9 GeV/c deuteron breakup
- 15.40 *L. Strunov* (JINR)  
Measurements of neutron-proton spin observables at 0 degrees  
using highest energy polarized d,n probes
- 16.10 *V. Sharov* (JINR)  
Measurements of energy behaviors of spin dependent  
neutron-proton observables over a GeV region

Coffee break 16.40 - 17.10

*Polarization phenomena and spin physics*

Chairman L. Azhgirey

- 17.10 *L. Zolin* (JINR)  
Study of polarized deuteron fragmentation into high momentum mesons  
at Dubna 9 GeV polarized deuteron facility (PIKASO Project)
- 17.30 *T. Vasiliev* (JINR)  
Sensitivity of the polarization observables  $A_{yy}$ ,  $A_{xx}$  and  $A_{zz}$   
of the  $\bar{d} + d \rightarrow p + {}^3\text{H}$  and  $\bar{d} + d \rightarrow p + X$  reactions to the deuteron spin structure
- 17.50 *O. Kosmachev* (JINR)  
Spin as a kinematical effect of the relativity

September 29, Wednesday

PARALLEL SESSION B  
BLOKHINTSEV AUDITORIUM OF BLTP  
*Applied use of relativistic beams*

Chairman N. Agapov

- 9.00 *A. Sosnin* (JINR)  
Thorough comparison of the neutron fluxes generated in the uranium/lead  
assembly (installation "energy plus transmutation") under irradiation  
with protons at energy in the range from 0.7 to 2.0 GeV
- 9.20 *A. Khilmanovich* (Belarus)  
On solution of the nuclear problems reduced to a system of first order  
integral fredholm equations

**9.40 M. Krivopustov (JINR)**

Transmutation studies of I-129, Np-237 and other nuclides in the electronuclear installation "Energy plus Transmutation" irradiated with 1.5 GeV protons from the Nuclotron at the JINR in Dubna

**10.00 M. Majerle (Czech Republic)**

Experimental studies of transmutation of iodide isotopes by spallation neutrons using JINR Dubna Phasotron

**10.30 M. Bielewicz (Poland)**

On the experiment of neutron spectrum investigation on U/Pb-assembly using 0.7 GeV proton beam from the JINR Nuclotron (Dubna)

**Coffee break 11.00 - 11.30**

*Applied use of relativistic beams*

Chairman N. Agapov

**11.30 I. Zhuk (Belarus)**

Theoretical and experimental determination of  $^{235}\text{U}$  and  $^{238}\text{U}$  fission rate distributions in the U/Pb assembly bombarded with 1.5 GeV protons

**12.00 M. Kievets (Belarus)**

Investigation of neutron fields on the surface of the massive lead target under its bombardment by protons with kinetic energies of 1.5 and 5.0 GeV

**12.30 V. Wagner (Czech Republic)**

Experimental studies of spatial distributions of neutrons inside and around the set-up consisted from thick target and large uranium blanket irradiated by relativistic protons

**Break 13.00 - 15.00**

**September 30, Thursday**

PLENARY SESSION

BOGOLIUBOV CONFERENCE HALL OF BLTP

*Polarization phenomena and spin physics*

Chairman A. Shebeko

**9.00 V. Glagolev (JINR)**

Charge-exchange np-pn reaction on the polarized deuteron beam (ANKE, COSY)

**9.30 A. Abramov (Russia)**

Single spin asymmetry in high Pt charged hadron production off nuclei at 40 GeV

**10.00 M. Sapozhnikov (JINR)**

Longitudinal polarization of Lambda and antiLambda hyperons in deep-inelastic scattering at COMPASS (on behalf of the COMPASS collaboration)

**10.20 N. Ladygina (JINR)**

Deuteron-proton charge exchange reaction at small transfer momentum

10.40 *V. Bednyakov* (JINR)  
Nuclear spin in dark matter search

Coffee break 11.00 - 11.30

*Polarization phenomena and spin physics*

Chairman G. Feofilov

- 11.30 *E. Tomasi-Gustafsson* (France)  
Charm production in gamma-N and NN collisions
- 12.10 *V. Ladygin* (JINR)  
Tensor  $A_{yy}$  and vector  $A_y$  analyzing powers of the (d,p)  
and (d,d) reactions at 5 GeV/c and 178 mr
- 12.30 *M. Janek* (JINR)  
Measurements of the tensor  $A_{xx}$ ,  $A_{yy}$ ,  $A_{xz}$  and vector  $A_y$  analyzing powers  
for the  $d+d \rightarrow {}^3\text{H}+p$  and  $d+d \rightarrow {}^3\text{He}+n$  reactions at 270 MeV
- 12.50 *A. Korzenev* (JINR)  
Inclusive and semi-inclusive asymmetries at COMPASS

14.30 Boat Trip

October 1, Friday

PARALLEL SESSION A  
BOGOLIUBOV CONFERENCE HALL OF BLTP  
*Multiparticle dynamics*

Chairman I. Manjavidze

- 9.00 *P. Aslanyan* (JINR)  
Lambda and neutral Kaon production in p+C collisions at 10 GeV/c
- 9.20 *B. Slowinski* (Poland)  
Search for scaling properties in many-particle stochastic processes
- 9.40 *E. Kokoulina* (JINR)  
Analysis multiparticle production in two stage gluon model at high multiplicity
- 10.00 *G. Kozlov* (JINR)  
Multiparticle dynamics via BEC in finite temperature QFT
- 10.20 *A.A. Baldin* (JINR)  
Development of the ideas of Academician A.M. Baldin on the theory  
of relativistic nuclear interactions in relative 4-velocity space

Coffee break 11.00 - 11.30

Multiparticle dynamics

Chairman B. Slowinski

- 11.30 *A. Sissakian and I. Manjavidze* (JINR)  
The thermalization phenomena and VHM physics
- 11.50 *E. Baldina* (JINR)  
Interaction of ultra-short laser and ion beams with nuclear matter - a new direction of research at high-energy particle accelerators
- 12.10 *E. Bubelev* (JINR)  
Realization and development of Lobachevsky and Poincar'e ideas and methods in high energy particle physics
- 12.30 *V. Lyuboshitz* (JINR)  
Strangeness conservation and structure of pair correlations of neutral kaons with low relative momenta in inclusive processes

Break 13.00 - 15.00

PLENARY SESSION  
BOGOLIUBOV CONFERENCE HALL OF BLTP  
*Accelerator Facilities: status and perspectives*

Chairman S. Vokal

- 15.00 *A. Vodopianov* (JINR)  
Status of the ALICE experiment
- 15.40 *D. Dinev* (Bulgaria)  
Beam - based measurement of dynamical characteristics in Nuclotron
- 16.00 *Yu. Panebratchev* (JINR)  
Participation in STAR experiment
- 16.40 *S. Shimanskiy* (JINR)  
Spin as an additional tool for QGP investigations

Coffee break 17.00 - 17.30

*Accelerator Facilities: status and perspectives*

Chairman E. Krasavin

- 17.30 *A. Litvinenko* (JINR)  
The features of hadrons transverse momentum spectra in Au+Au and d+Au obtained by PHENIX detector at RHIC
- 18.10 *W. Westmeier* (Germany)  
Transmutation experiments using the Nuclotron accelerator
- 18.30 *G. Timoshenko* (JINR)  
Heavy nuclei dosimetry in radiobiological experiments at the Nuclotron
- 18.50 *S. Smolyansky* (Russia)  
Electron-positron pair creation in fields of high-power optical lasers

October 1, Friday

PARALLEL SESSION B  
BLOKHINTSEV AUDITORIUM OF BLTP  
*Hadron spectroscopy*

Chairman D. Blaschke

- 9.00 *S. Semikh* (JINR)  
Solving the non-homogeneous Bethe-Salpeter equation
- 9.20 *M. Dineykh* (JINR)  
Determination of the glueball mass spectrum with the spin-orbit interaction in nonperturbative QCD
- 9.40 *A. Machavariani* (JINR)  
Three dimensional field-theoretic equations for the three-body systems with the electromagnetic interactions and with the  $\Delta$ -resonance degrees of freedom
- 10.20 *I. Anikin* (JINR)  
Exotic hybrid mesons in the hard reactions

Coffee break 11.00 - 11.30

*Progress in experimental studies at the high energy accelerators*

Chairman I. Boguslavsky

- 11.30 *S. Afanasiev* (JINR)  
Measurement of the cross-section for the  $p(d,pp)n$  reaction in the GeV/c region at the Nuclotron
- 11.50 *Kh. Abraamyan* (JINR)  
Inclusive  $\pi^0$  production by protons and light nuclei on C and Cu targets at a momentum of 4.5 GeV/c per nucleon
- 12.30 *V. Krasnov* (JINR)  
Search for resonant structure in the pion production reaction on the Nuclotron internal beam
- 12.50 *V. Penev* (JINR)  
Cluster-fluctons revelation in nuclear interactions at 4.2 (GeV/c) per nucleon

Break 13.30 - 15.00

October 2, Saturday

PLENARY SESSION

BOGOLIUBOV CONFERENCE HALL OF BLTP

*Progress in experimental studies at the high energy accelerators*

Chairman E. Tomasi-Gustafsson

9.00 A. Malakhov (JINR)

Investigations in V.I. Veksler and A.M. Baldin Laboratory of High Energies

9.40 A. Kovalenko (JINR)

Status of the Nuclotron

10.20 P. Zarubin (JINR)

Experimental studies of clustering in multifragmentation of relativistic nuclei

Coffee break 11.00 - 11.30

*Progress in experimental studies at the high energy accelerators*

Chairman A. Malakhov

11.30 H. Machner (Germany)

Physics at COSY

12.10 Yu. Pilipenko (JINR)

Polarized deuterons at the Nuclotron

12.40 E. Krasavin (JINR)

Nuclotron as a unique tool for modeling biological effects  
of Galactic space radiation

13.10 V. Burov and A. Malakhov (JINR)

Closing

Coffee 13.30

# List of Participants

**Abraamyan, Kh.U.**  
<*abraam@sunhe.jinr.ru*>  
JINR

**Abramov, V.V.**  
<*abramov.v@mz.ihep.su*>  
Russia

**Afanasiev, S.V.**  
<*afanasev@lhe.jinr.ru*>  
JINR

**Agapov, N.N.**  
<*agapov@lhe.jinr.ru*>  
JINR

**Anisimov, Yu.S.**  
<*anisimov@lhe.jinr.ru*>  
JINR

**Arakelyan, S.G.**  
JINR

**Aslanian, P.Z.**  
<*petros@spp.jinr.ru*>  
JINR

**Azhgirey, L.S.**  
<*azhgirey@jinr.ru*>  
JINR

**Babchik, V.I.**  
JINR

**Bakaev, V.V.**  
<*bakaev@lhe.jinr.ru*>  
JINR

**Baldin, A.A.**  
<*Anton.Baldin@sunhe.jinr.ru*>  
JINR

**Baldina, E.G.**  
<*Elina.Baldina@sunhe.jinr.ru*>  
JINR

**Baldina, I.S.**  
JINR

**Batyunya, B.V.**  
<*batyunya@sunhe.jinr.ru*>  
JINR

**Bednyakov, V.A.**  
<*bedny@ru.jinr.ru*>  
JINR

**Belova, L.B.**  
JINR

**Belyaev, A.V.**  
JINR

**Bielewicz, M.**  
<*m.bielewicz@cyf.gov.pl*>  
Poland

**Blaschke, D.**  
<*blaschke@physik.uni-bielefeld.de*>  
Germany

**Boguslavsky, I.V.**  
<*biv@sunse.jinr.ru*>  
JINR

**Bondarenko, S.G.**  
<*bondarenko@jinr.ru*>  
JINR

**Brovko, O.I.**  
<*brovko@sunhe.jinr.ru*>  
JINR

# List of Participants

**Abraamyan, Kh.U.**  
<abraam@sunhe.jinr.ru>  
JINR

**Abramov, V.V.**  
<abramov.v@mz.ihep.su>  
Russia

**Afanasiev, S.V.**  
<afanasev@lhe.jinr.ru>  
JINR

**Agapov, N.N.**  
<agapov@lhe.jinr.ru>  
JINR

**Anisimov, Yu.S.**  
<anisimov@lhe.jinr.ru>  
JINR

**Arakelyan, S.G.**  
JINR

**Aslanian, P.Z.**  
<petros@spp.jinr.ru>  
JINR

**Azhgirey, L.S.**  
<azhgirey@jinr.ru>  
JINR

**Babchik, V.I.**  
JINR

**Bakaev, V.V.**  
<bakaev@lhe.jinr.ru>  
JINR

**Baldin, A.A.**  
<Anton.Baldin@sunhe.jinr.ru>  
JINR

**Baldina, E.G.**  
<Elina.Baldina@sunhe.jinr.ru>  
JINR

**Baldina, I.S.**  
JINR

**Batyunya, B.V.**  
<batyunya@sunhe.jinr.ru>  
JINR

**Bednyakov, V.A.**  
<bedny@ru.jinr.ru>  
JINR

**Belova, L.B.**  
JINR

**Belyaev, A.V.**  
JINR

**Bielewicz, M.**  
<m.bielewicz@cyf.gov.pl>  
Poland

**Blaschke, D.**  
<blaschke@physik.uni-bielefeld.de>  
Germany

**Boguslavsky, I.V.**  
<biv@sunse.jinr.ru>  
JINR

**Bondarenko, S.G.**  
<bondarenko@jinr.ru>  
JINR

**Brovko, O.I.**  
<brovko@sunhe.jinr.ru>  
JINR

**Bubelev, E.G.**  
<bubelev@sunhe.jinr.ru>  
JINR

**Burov, V.V.**  
<burov@thsun1.jinr.ru>  
JINR

**Cherednikov, I.**  
<igorcb@thsun1.jinr.ru>  
JINR

**Dedovich, T.G.**  
<dedovich@sunhe.jinr.ru>  
JINR

**Dinev, D.**  
<dinnet@inrne.bas.bg>  
Bulgaria

**Dineykh, M.**  
<dineykh@thsun1.jinr.ru>  
JINR

**D'yachenko, V.M.**  
<dyachenko@lhe.jinr.ru>  
JINR

**Efimov, G.V.**  
<efimovg@thsun1.jinr.ru>  
JINR

**Eliseev, S.M.**  
<selis@thsun1.jinr.ru>  
JINR

**Elishev, A.F.**  
JINR

**Fadeev, N.G.**  
<fadeev@sunse.jinr.ru>  
JINR

**Feofilov, G.A.**  
Russia

**Gaidarov, M.K.**  
<gaidarov@inrne.bas.bg>  
Bulgaria

**Ganbold, G.**  
<ganbold@thsun1.jinr.ru>  
JINR

**Gerasimov, S.B.**  
<gerasb@thsun1.jinr.ru>  
JINR

**Glagolev, V.V.**  
<glagolev@sunhe.jinr.ru>  
JINR

**Gmuca, S.**  
<gmuca@savba.sk>  
Slovakia

**Gogoleva, S.V.**  
<gogoleva@lhe.jinr.ru>  
JINR

**Goloskokov, S.V.**  
<goloskkv@thsun1.jinr.ru>  
JINR

**Gorelikova, N.A.**  
<gorelikova@lhe.jinr.ru>  
JINR

**Hanna, K.M.**  
<rukhanna@hotmail.com>  
Egypt

**Henner, V.K.**  
<Victor.Henner@psu.ru>  
Russia

**Ierusalimov, A.P.**  
<ierusalimov@vxjinr.jinr.ru>  
JINR

**Il'ina, L.G.**  
JINR

**Issinsky, I.B.**  
JINR

**Isupov, A.Yu.**  
JINR

**Ivanova, S.P.**  
JINR

**Janek, M.**  
Slovakia, JINR

**Kadyshevsky, V.G.**  
<kadyshev@jinr.ru>  
JINR

**Karachuk, J.-T.**  
<karachuk@jinr.ru>  
JINR

**Kartashov, V.V.**  
JINR

**Khilmanovich, A.M.**  
<ifanbel@ifanbel.bas-net.by>  
Belarus

**Khodinov, A.I.**  
<khodinov@bnl.gov>  
USA

**Khokhlov, N.A.**  
<khokhlov@email.kht.ru>  
Russia

**Khorozov, S.A.**  
JINR

**Kievets, M.**  
<kievets@sosny.bas-net.by>  
Belarus

**Knyr, V.A.**  
<knyr@fizika.khstu.ru>  
Russia

**Kochelev, N.I.**  
<kochelev@thsun1.jinr.ru>  
JINR

**Kokoulina, E.S.**  
<Elena.Kokoulina@sunse.jinr.ru>  
JINR

**Konopleva, N.P.**  
<nelly@thsun1.jinr.ru>  
Russia

**Korneichuk, L.P.**  
JINR

**Korol, A.P.**  
JINR

**Korzenev, A.Yu.**  
<korzenev@mail.cern.ch>  
Germany

**Koshurnikov, E.K.**  
JINR

**Kosmachev, O.S.**  
<kos@thsun1.jinr.ru>  
JINR

**Kotsev, N.**  
JINR

**Kovalenko, A.D.**  
<kovalen@sunhe.jinr.ru>  
JINR

**Kozhukalov, V.A.**  
<kozhlv@thsun1.jinr.ru>  
JINR

**Kozlov, G.A.**  
<kozlov@thsun1.jinr.ru>  
JINR

**Krasavin, E.A.**

<krasavin@jinr.ru>

JINR

**Krasnov, V.A.**

<krasnov@sunhe.jinr.ru>

JINR

**Krippa, B.V.**

<boris@al20.inr.troitsk.ru>

Russia

**Krivopustov, M.I.**

<krivopustov@lhe.jinr.ru>

JINR

**Krutov, A.F.**

<krutov@ssu.samara.ru>

Russia

**Kukulin, V.I.**

<kukulin@nucl-th.sinp.msu.ru>

Russia

**Kulagin, S.**

<kulagin@ms2.inr.ac.ru>

Russia

**Kushpil, S.A.**

<skushpil@ujf.cas.cz>

JINR

**Kuznetsov, S.N.**

JINR

**Kuznetsov, A.A.**

JINR

**Ladygin, V.P.**

<ladygin@sunhe.jinr.ru>

JINR

**Ladygina, N.B.**

<ladygina@sunhe.jinr.ru>

JINR

**Litvinenko, A.G.**

<litvin@moonhe.jinr.ru>

JINR

**Livanov, A.N.**

<livanov@lhe.jinr.ru>

JINR

**Loschilov, M.G.**

JINR

**Lukstins, Ju.**

<juris@sunhe.jinr.ru>

JINR

**Lukyanov, V.K.**

<lukyanov@thsun1.jinr.ru>

JINR

**Lyadnovich, L.A.**

<liadn@lhe.jinr.ru>

JINR

**Lykasov, G.I.**

<lykasov@nu.jinr.ru>

JINR

**Lyuboshitz, V.V.**

<Valery.Lyuboshitz@jinr.ru>

JINR

**Lyuboshitz, V.L.**

<lyubosh@sunhe.jinr.ru>

JINR

**Machavariani, A.**

<machavar@thsun1.jinr.ru>

JINR

**Machner, K.**

<h.machner@fz-juelich.de>

Germany

**Majerle, M.**

<mitja.majerle@guest.arnes.si>

Czech Republic

**Majling, L.**  
<majling@ujf.cas.cz>  
Czech Republic

**Malakhov, A.I.**  
<malakhov@lhe.jinr.ru>  
JINR

**Manjavidze, Io.D.**  
JINR

**Martinska, G.**  
<martinov@kosice.upjs.sk>  
JINR

**Matyushevsky, E.A.**  
<matyush@sunhe.jinr.ru>  
JINR

**Matyushin, V.T.**  
JINR

**Melkumov, G.L.**  
JINR

**Migulina, I.I.**  
JINR

**Molchanov, E.M.**  
<dnsp@dubna.ru>  
JINR

**Musakhanov, M.Yu.**  
<musakhanov@pusan.ac.kr>  
Uzbekistan

**Okorokov, V.A.**  
<okorokov@bnl.gov>  
Russia

**Orlova G.I.**  
<orlova@sci.lebedev.ru>  
Russia

**Panebratsev, Yu.A.**  
<panebrat@sunhe.jinr.ru>  
JINR

**Parfenov, A.N.**  
<parfenov@cv.jinr.ru>  
JINR

**Pavlovsky, O.V.**  
<ovp@goa.bog.msu.ru>  
Moscow, Russia

**Penev, V.N.**  
<penev@lhe.jinr.ru>  
JINR

**Perdrisat, Ch.**  
<perdrisa@jlab.org>  
USA

**Peresedov, V.F.**  
JINR

**Pestov, I.**  
<pestov@thsun1.jinr.ru>  
JINR

**Pilipenko, Yu.K.**  
<pilipen@sunhe.jinr.ru>  
JINR

**Piskaleva, G.V.**  
JINR

**Piskunov, N.M.**  
<piskunov@sunhe.jinr.ru >  
JINR

**Plekhanov, E.B.**  
<plekhanov@lhe.jinr.ru>  
JINR

**Plis, Yu.A.**  
<plis@nusun.jinr.ru>  
JINR

**Pokrovsky, Yu.E.**

Russia

**Pozdnyakov, V.**

<Valeri.Pozdniakov@cern.ch>

JINR

**Punjabi, V.**

<punjabi@jlab.org>

USA

**Rogochaya, E.P.**

<rogoch@thsun1.jinr.ru>

JINR

**Rukoyatkin, P.A.**

JINR

**Rusakovich, E.N.**

JINR

**Rusakovich, N.A.**

JINR

**Saitov, I.S.**

<saitov@lhe.jinr.ru>

JINR

**Sapozhnikov, M.G.**

JINR

**Semikh, S.S.**

<semikh@thsun1.jinr.ru>

JINR

**Shahaliev, E.**

<shah@sunhe.jinr.ru>

JINR

**Shakeel, A.**

<sa\_hep@yahoo.com>

India

**Sharov, V.I.**

<sharov@sunhe.jinr.ru>

JINR

**Shebeko, A.V.**

<shebeko@fbsyst.comcom.kharkov.ua>

Ukraine

**Shelaev, I.A.**

<shelaev@lhe.jinr.ru>

JINR

**Shevchenko, O.**

JINR

**Shikhalev, M.A.**

<shehalev@thsun1.jinr.ru>

JINR

**Shimanskiy, S.S.**

<shimansk@sunhe.jinr.ru>

JINR

**Shirkov, D.V.**

JINR

**Shirkov, G.V.**

<shirkov@sunse.jinr.ru>

JINR

**Shklovskaya, A.Io.**

<alla@lhe.jinr.ru>

JINR

**Shulga, D.V.**

<denis@ift.phys.dvgu.ru>

Russia

**Sinyukov, Yu.M.**

<sinyukov@bitp.kiev.ua>

Ukraine

**Sissakian, A.N.**

<sisakian@jinr.ru>

JINR

**Sitnik, I.M.**

<sitnik@sunhe.jinr.ru>

JINR

**Skokov, V.V.**  
<*vskokov@thsun1.jinr.ru*>  
JINR

**Slowinski, B.**  
<*slowb@if.pw.edu.pl*>  
Poland

**Smolyansky, S.**  
<*smol@sgu.ru*>  
Russia

**Sokol, G.A.**  
<*gsokol@x4u.lpi.ruhep.ru*>  
Russia

**Sosnin, A.N.**  
<*sosnin@cv.jinr.ru*>  
JINR

**Stadnik, A.V.**  
<*stadnik@sunhe.jinr.ru*>  
JINR

**Starchenko, B.M.**  
JINR

**Stetsenko, S.G.**  
JINR

**Strokovsky, E.A.**  
<*strok@sunhe.jinr.ru*>  
JINR

**Strunov, L.N.**  
<*strunov@sunhe.jinr.ru*>  
JINR

**Suleimanov, M.K.**  
<*mais@sunhe.jinr.ru*>  
JINR

**Szuta, M.**  
<*mszuta@cyf.gov.pl*>  
Poland

**Tetereva, T.V.**  
Russia

**Timoshenko, G.N.**  
<*drrr@jinr.ru*>  
JINR

**Timoshenko, S.L.**  
<*tim@intphys3.mephi.ru*>  
Russia

**Tchoubakova, S.V.**  
<*svetlana@sunse.jinr.ru*>  
JINR

**Tokarev, M.V.**  
<*tokarev@sunhe.jinr.ru*>  
JINR

**Tomasi-Gustafsson, E.**  
<*etomasi@cea.fr*>  
France

**Topil'skaya, N.S.**  
<*topilska@inr.ru*>  
Russia

**Troyan, A.Yu.**  
JINR

**Troyan, Yu.A.**  
JINR

**Tsakov, I.**  
<*itsak@inrne.bas.bg*>  
Bulgaria

**Tsirova, N.A.**  
<*ntsirova@ssu.samara.ru*>  
Russia

**Tumanov, Yu.A.**  
JINR

**Vasiliev, T.A.**  
JINR

**Vechernin, V.V.**  
<vecherni@pink.phys.spbu.ru>  
St. Petersburg, Russia

**Vinnikov, A.V.**  
<vinnikov@thsun1.jinr.ru>  
JINR

**Vodopianov, A.S.**  
<vodopian@sunhe.jinr.ru>  
JINR

**Vokal, S.**  
<vokal@lhe.jinr.ru>  
JINR

**Voronov, V.V.**  
<voronov@thsun1.jinr.ru>  
JINR

**Wagner, V.**  
<wagner@ujf.cas.cz>  
Czech Republic

**Westmeier, W.**  
<westmeier@t-online.de>  
Germany

**Yanev, Jo.**  
JINR

**Yudin, N.P.**  
<yudin@helene.sinp.msu.ru>  
Russia

**Zarubin, P.I.**  
<zarubin@lhe.jinr.ru>  
JINR

**Zarubina, I.**  
JINR

**Zborovsky, I.**  
<zborovsky@ujf.cas.cz>  
Rez, Czech Republic

**Zhabitsky, V.M.**  
JINR

**Zhuk, I.V.**  
<zhuk@sosny.bas-net.by>  
Belarus

**Zhuravlev, V.I.**  
JINR

**Zinchenko, A.I.**  
<zinchenk@lxpub00.jinr.ru>  
JINR

**Zolin, L.S.**  
<zolin@sunhe.jinr.ru>  
JINR

**Zomorrodian, M.E.**  
<zomorrod101@yahoo.com>  
Mashhad, Iran

**Zotov, N.P.**  
<zotov@theory.sinp.msu.ru>  
Russia